AN X-RAY APPROACH TO LOW LUMINOSITY ACTIVE GALACTIC NUCLEI

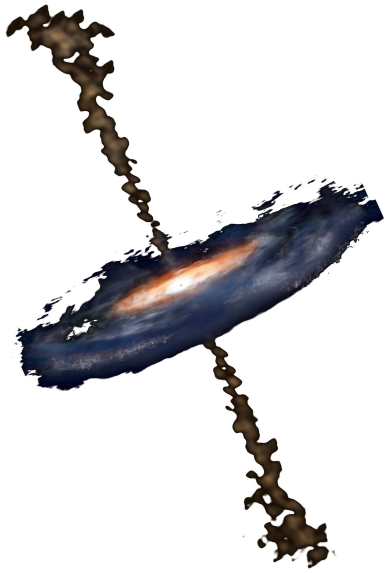

Omaira González Martín

Instituto de Astrofísica de Andalucía

Memoria de Tesis
presentada en la Universidad de Granada
para optar al grado de Doctor en Astrofísica.

Directoras de Tesis
Dra. Josefa Masegosa Gallego
Dra. Isabel Márquez Pérez

Junio 2008

Editor: Editorial de la Universidad de Granada
Autor: Omaira González Martín
D.L.: GR.1607-2008
ISBN: 978-84-691-4840-2

Universidad de Granada

Instituto de Astrofísica de Andalucía

Consejo Superior de Investigaciones Científicas

Abstract

Active Galactic Nuclei (AGNs) are one of the most energetic phenomena ever observed in the Universe. They produce luminosities as high as 10^{44} erg s^{-1} in very compact volumes. The classification of AGNs is essentially observational and is based on their luminosities and optical spectral characteristics. As a consequence of that, the taxonomy of AGNs tend to be rather confusing and its complexity leads to an heterogeneous family of sources.

Despite the lack of direct evidence it is today accepted that accretion of matter by supermassive black holes (SMBH) is the primary energy source in AGNs. The material is accreted onto the SMBH by an accretion disk and a region with high velocity clouds (Broad Line Region, BLR) is surrounding this accretion disk. Finally a region composed by low velocity clouds (Narrow Line Region, NLR), extend up to several kpc scales, shows evidence of interaction with a radio jet.

Antonucci et al. (1993) proposed a unified model to explain all the families of AGNs. The key elements in this simple scheme is the obscuring torus between the BLR and the NLR. If the torus is seen face-on, our view of the central regions is unobscured and we detect the broad lines; if our view is closer to edge-on, the central regions are not seen directly and no broad lines are detected. However, although this general scenario is widely accepted, there are still several discrepancies that need to be explained.

This thesis is focused in one of these subclasses of active nuclei known as Low Ionisation Narrow Emission-line Regions (LINERs). They were discovered by Heckman (1980), which classified them as a subgroup of AGNs by an optical spectra dominated by emission lines of moderate intensities arising from gas in lower ionisation states than classical AGN and line widths approaching those of the NLR in Seyfert galaxies.

The X-ray domain is plenty of AGN signatures (X-ray luminosity, FeK emission line or hydrogen column density) resulting in one of the most important tools to determine the nature of doubtful AGN, as it is the case of LINERs.

The analysis of a large sample of LINERs carried out in this thesis demonstrates that a high percentage of them (60% for the full sample, 68% for the sub sample with spectral fit) shows compact unresolved nuclear sources at high energies ($4.5 - 8$ keV) band, being excellent candidates to host a nuclear AGN. The modelling of their X-ray spectra shows that most of them agree with the Baseline model of AGNs. 70% of the sample need two power-laws while a thermal model at energies below 2 keV is needed in the vast majority of the cases (95%).

The obscuring material scenario is consistent with a two absorber media claimed for AGNs, an extended medium associated with the host galaxy and a compact nuclear absorber likely associated with the BLR. Multiwavelength diagnostics also suggests that 50% of the LINER nuclei are good candidates to host a hidden AGN, even at X-ray frequencies (Compton-thick), higher than that reported for Seyfert nuclei (closest AGNs in terms of luminosities).

Taken all the known multiwavelength tracers of AGN activity together, our main conclusion is that the vast majority of LINERs (around 90% of our sample) show evidence of AGN activity in their nuclei. However, the results of UV, radio and X-ray studies are controversial for some objects, i.e. showing AGN characteristics at UV that are not seen at X-ray frequencies. We argue that such variations might be compatible with the existence of a clumpy torus, which will be the responsible for such discrepancies due to the probability of finding a high-velocity thick cloud in the line-of-sight when non simultaneous observations are analysed.

The NLR and ENLR of a low luminosity Seyfert 1 galaxy NGC 4151 is studied at optical, radio and X-ray frequencies. It suggests that most of the emission seen at soft X-ray energies, both in the NLR and in the ENLR, is due to photoionized material from the central source, and not to in-situ stellar photoionization. The other important conclusion on this work is the explanation of the orientation mismatch of the optical NLR/ENLR and the radio jet. It is suggested that a different (or precessing) jet is the origin of the the X-ray and optical cone-like morphology.

Finally, Ultra-Luminous X-ray sources (ULX, defined as X-ray sources with L(2-10 keV) $> 10^{39}\ \mathrm{erg\ s^{-1}}$*) seen in front of the High Velocity System of NGC 1275, are mostly associated with a region of very active star formation, although the brightest does not seem to be connected. This relation of ULX with star formation regions are also reported by several archetypal galaxies as the Antennae or the Cartwheel system.*

Resumen

Los Núcleos Activos de Galaxias (AGN, del inglés Active Galactic Nuclei) son uno de los fenómenos mas energéticos en el Universo. Emiten luminosidades de hasta 10^{44} erg s^{-1} en volumenes muy compactos. La clasificación de estos objectos es esencialmente observacional, basándose en sus características espectroscópicas y luminosidades. Debido a esto, su clasificación tiende a ser confusa, resultando una familia heterogénea de objetos.

Aunque no hay evidencias directas, hoy en día está aceptado que este fenómeno se basa en la acreción de materia sobre un agujero negro supermasivo (SMBH, del inglés supermassive black hole). Dicha acreción proviene de un disco de acreción que está, a su vez, rodeado por nubes de alta velocidad o región de lineas anchas (BLR, del inglés Broad Line Region). Finalmente, una región compuesta de nubes de baja velocidad o región de lineas estrechas (NLR, del inglés Narrow Line Region) se extiende hasta algunos kilo-parsecs de distancia. Esta última región muestra evidencias de interacción con un chorro relativista proveniente del núcleo, cuyo pico de emisión se encuentra en radio frecuencias.

Antonucci y colaboradores (1993) propusieron un escenario unificado para explicar las diferentes familias the AGNs, que recibió el nombre the Modelo Unificado. La clave de dicho modelo es un toroide que oscurece, localizado entre la NLR y la BLR. Si el toroide es visto de cara, nuestra línea de visión permite observar la región central por lo que detectamos la BLR; si es visto de canto las regiones central no queda accesible y la BLR no se detecta. Sin embargo, aunque este escenario está ampliamente aceptado, existen algunas discrepancias entre el modelo y las observaciones que necesitan ser revisadas.

Esta tesis está centrada en una de estas sub-categorias de AGNs, conocida como Regiones de líneas estrechas de baja ionización (LINERs, Low Ionisation Narrow Emission-line Regions). Esta categoría fué descubierta por Heckman (1980), que los clasificó como un subgrupo de AGNs diferenciado del resto por presentar un espectro óptico dominado por líneas de emisión de intensidad moderada que proceden de gas ionizado con un estado de ionización más bajo que el observado en galaxias Seyfert.

El rango de frecuencias en rayos X posee muchas características que permiten el estudio de la actividad AGN (la luminosidad en rayos X, la emisión de la línea de hierro a 6.4 keV o la columna de densidad de hidrógeno), resultando una de las herramientas mas poderosa para investigar la naturaleza AGN de los LINERs.

El análisis de una muestra extensa de LINERs realizado en el desarrollo de esta tesis demuestra que un alto porcentaje de ellos (60% para la muestra completa, 68% para la submuestra con ajuste espectral) presentan una fuente compacta en la banda de rayos X duros ($4.5 - 8$ keV), indicando que albergan un AGN en sus núcleos. La modelización de sus espectros indica que para la mayoría el mejor ajuste se obtiene con el modelo propuesto para AGNs. De hecho el 70% de la muestra necesita dos leyes de potencias y el 95% necesita de un modelo térmico adicional para explicar el espectro a bajas energías.

Del estudio del material que oscurece estas fuentes, concluímos que es necesaria la presencia de dos absorventes, como ha sido propuesto para otro tipo de AGNs, uno extendido asociado a la galaxia albergadora y otro de origen nuclear más compacto asociado con la

BLR. Como resultado de los estudios multifrecuencia presentados en esta tesis obtenemos que el 50% de las LINERs son buenos candidatos a albergar un AGN oscurecido, incluso a las frecuencias observadas en el rango X (conocidos como Compton-thick). Este porcentaje es mayor que el encontrado en otros estudios para galaxias tipo Seyfert (AGNs inmediatamente próximos en luminosidad a los LINERs).

Nuestra conclusión principal, tomando en cuenta toda la información multi-frequencia, es que la gran mayoría de los LINERs (en torno a un 90%) muestran evidencias de actividad AGN en sus núcleos. Sin embargo, en algunos casos los resultados multifrequencia son controvertidos, mostrando por ejemplo características de AGN a frecuencias UV pero no a frecuencias de rayos X. Del análisis realizado sugerimos que dichas variaciones podrían ser debidas a la existencia de un toroide conformado por nubes gruesas de alta velocidad que, cuando se localizan en la línea de visión oscurecen el núcleo.

La NLR y NLR extendida (ENLR, del ingés Extended NLR) de la galaxia tipo Seyfert 1 NGC 4151 ha sido estudiada en frecuencias ópticas, radio y rayos X. Sugerimos que la emisón observada en rayos X suaves (menor que 2 keV) de ambas regiones, NLR y ENLR, es debida a material fotoinizado por el núcleo. Además este objeto presenta un desalineamiento entre le extensión the la NLR y ENLR y la direción del chorro relativista visto en radio. La segunda conclusión importante del trabajo presentado tiene que ver con la falta de alineamiento entre la NLR/ENLR observada en el óptico y el chorro relativista en radio frecuencias. Encontramos que dicho desalineamiento podría atribuirse a la existencia de o de otro chorro secundario o de un movimiento de precesión del chorro primario.

Finalmente, se presenta un estudio de las fuentes Ultra-Luminosas en rayos X (ULXs, del inglés Ultra-Luminous X-ray sources), definidas como fuentes no coincidentes con el núcleo con L(2-10 keV) $> 10^{39}$ erg s^{-1}) vistas en la dirección del Sistema de Alta velocidad (HVS, del inglés High Velocity System) de la galaxia NGC 1275. Dichas fuentes están mayoritariamente asociadas a regiones de formación estelar muy activa, exceptuando la más brillante que no parece estar conectada con ninguna de estas regiones. Esta relación ha sido también sugerida en diversas galaxias bien conocidas como La Antena o Cartwheel.

Contents

Chapter 1

Introduction

1.1 Background

Active Galactic Nuclei (hereinafter AGN) are one of the most energetic phenomena ever observed in the Universe. They produce luminosities as high as 10^{44} erg s^{-1} in very compact volumes (probably less than 1 pc^3). These large energies have been hypothesised to be gravitational in origin: the accretion of matter onto a massive black hole (Rees, 1984). It is remarkable what M. Rees pointed out at that time that massive black holes should exist in the nuclei of all galaxies and 24 years later it has been found that massive black holes do exist in almost all the galaxies with a well developed bulge (Gebhardt et al., 2000; Ferrarese and Merritt, 2000). The main question is to properly understand the accretion-disk physic in relation to the observations for the different types of AGNs, how they relate to each other. To do so it is needed to explore the entire parameter space defined by mass and accretion rate. Thus, by using all the data available at the different frequencies a full analysis is required from the very low luminosity AGNs (low accretion but high mass) till the highest luminosity AGNs (high accretion and high mass). Much information is expected to be obtained from multiwavelength analysis to understand how the energy is extracted from the central black hole, which is a fundamental issue in the study of AGNs.

On the other hand, due to their extreme brightness, AGNs can be detected up to very high redshifts, making them optimal tracers of the large scale structure of the Universe (Cappelluti et al., 2007). Thus, they also offer the possibility to get crucial information on how galaxies form and evolve at very early epochs in the evolution of the Universe.

1.1.1 A Few Historical Remarks

The observational study of AGNs began in 1908 when Fath took the first optical spectrum of a well known AGN, NGC 1068. He noted the presence of strong emission lines in its central nebula. In 1926, Hubble in a study of extragalactic nebula,

found "Planetary Nebula" in three galaxy centers. The discovery of such objects as a special class has to wait till 1943, when Karl Seyfert realised that there were a group of galaxies with similar nuclear properties. K. Seyfert made optical spectroscopy of a galaxy sample, finding that several nuclei (NGC 1068, NGC 1275, NGC 3516, NGC 4051, NGC 4151 and NGC 7469) were dominated by high-excitation emission lines. That was the starting point for the AGN research, although the emission mechanisms was still unknown. The work made by Seyfert allowed to characterise for the first time a few fraction of galaxies, specially luminous and showing broad emission lines in their nuclei, that were called "Seyfert galaxies" in his honour. But this work did not produce strong impact till it was realised that these exotic galaxies and their radio properties are related to quasars (hereinafter, QSOs).

QSOs were originally discovered by radio surveys which identified, together with the counterparts of a large amount of optical known galaxies, a population of star-like objects. The first known QSOs that opened this field of research was 3C 48, identified by Matthews and Sandage (1963) as 16 magnitude star, but which appeared in the spectral photographic plate as a very enigmatic object since the identification of a single line was not possible. Another identified enigmatic source was 3C 273 (Hazard et al., 1963). The first breakthrough in understanding them came when Schmidt (1963) noted that the unidentifiable lines of 3C 48 were just the Balmer- series and Mg II lines at a redshift of 0.158. Soon after, the relationship between QSOs and Seyfert galaxies (same spectral characteristics broad emission permitted lines and narrow high excitation emission lines in their optical spectra) was noted and their importance started to be realised. In 1968, another type of active nuclei appeared, the BL Lac objects, with a continuum radiation very similar to that found in QSOs but without intense emission lines. All of them, Seyfert galaxies, QSOs and BL Lac objects were located into the same family: the Active Galactic Nuclei.

The possible role of AGNs in galaxy formation and evolution appeared very early (Burbidge et al., 1963) as Cosmological probes to understand the Universe at very early epochs. Moreover, the suggestion that a massive black hole might be involved in the observed energetic phenomena came from the work by Zel'Dovich and Novikov (1964). All these considerations lead to the large amount of research in this field since then. As a curiosity, looking into the ADS for papers within this denomination, more than 10000 papers have been published since 1968 on this very *active* field.

1.2 AGN populations

The classification of AGNs is essentially observational and it is mainly based on their luminosities and optical spectroscopic characteristics, like intensity and broadening of the emission lines, and intensity ratios. As a consequence of that, the taxonomy of AGNs tends to be rather confusing and its complexity leads to a heterogeneous family of sources. Along the last decades a complete family of objects were defined. The main groups are:

- **Quasars**. Their nuclear sources emit more than a hundred times the host galaxy emission, and their spectra show broad permitted emission lines and narrow forbidden emission lines. They present variability in many cases and radio sources are observed in a small percentage of them.

- **Seyferts**. Seyfert nuclei emit a total energy of the order of that from the host galaxy and the optical spectrum is characterised by high ionisation lines, as [OIII] $\lambda 5007$, [OI] $\lambda 4861$, [NII] $\lambda 6583$ and [SII] $\lambda\lambda 6716, 6731$. They were subclassified as type 1 and type 2 objects attending to the presence or absence of broad permitted emission lines, respectively. Osterbrock et al. (1989) defined the intermediate classes Seyfert 1.5 (strong broad and narrow emission lines), Seyfert 1.8 (weak broad emission lines and strong narrow emission lines), and Seyfert 1.9 (a weak broad emission line only seen in Hα but not in Hβ). Morphologically, the host galaxy of Seyferts tends to be spiral galaxies. Seyfert 2s appear to be strong radio sources whereas Seyfert 1s do not, in close resemblance to what is found in QSOs.

- **Radio galaxies**. These galaxies have radio luminosities of the order of, or even higher, than the optical luminosity. They are also divided into broad-line radio galaxies (BLRG), similarly to Seyfert 1s, and narrow Line Radio Galaxies (NLRG), similarly to Seyfert 2 nuclei.

- **Blazars**. They are characterised by strong continua, highly polarised, and rapid variability, with weak or even lacking emission lines. They are divided in BL Lac and OVVs (Optically Violent Variable quasars), the latter showing emission lines when the continuum is weak.

- **LINERs**. They come from the acronym "Low Ionisation Narrow Emission-Line Regions", and are the main subject in the current investigation. LINERs were first discovered by Heckman (1980), being typically less luminous than powerful Seyferts and quasars. According to their optical spectra, they resemble Seyfert 2 galaxies, but the low-ionisation lines are remarkable strong

whereas the high ionisation lines are much fainter that what is observed in Seyfert 2s. While the unusual line ratios typical of LINERs cannot be the result of normal stellar processes, the true nature of ionising mechanisms in these sources is still ambiguous. More information about the efforts trying to disentangle emission mechanism of LINERs will be given in Sect. 1.5.

Within the family of Starburst a large variety of star-forming galaxies are included. The common characteristic for all of them is that a recent burst of star formation is manifest through the presence of ionised Hα and UV excess. They can be distinguished from other AGNs because they show weak low ionisation emission lines, as e.g. [SII], [OI] or [NII] at variance with what is observed in LINERs, but with intense high ionisation lines [OIII], [SIII] and [NeIII]. Since they are known to be produced by stellar processes they are not normally included into the AGN family.

In all the AGN previously described, excepting Blazars, the object must show an optical spectrum plenty of prominent emission lines to be considered within the AGN family. A fundamental characteristic is that an AGN produces as much light as up to several trillion stars in a volume that is significantly smaller than a cubic parsec. Then, AGN refer to the existence of energetic phenomena in the nuclei of galaxies in which the fast variability (on timescales from hours to years, i.e. Leighly, 1999) and high luminosity of these sources requires radiation mechanisms that are more efficient than ordinary stellar processes (Fabian, 1979). This phenomenon implies the existence of a central supermassive black hole of billions solar masses.

The following is an attempt to specify the most conspicuous observational properties of AGNs:

1. *Continuum emission*. The continuum of the spectral energy distribution (SED) of most AGNs look extraordinarily different from the spectra of normal galaxies. The continuum of AGN spectra, at least in first-order approximation, can be described as a power law of the form $F_\nu \simeq \nu^{-\alpha}$, where α is generally between zero and unity. One of the most prominent features in the optical/UV range is the so-called *big blue bump*, which is generally attributed to thermal emission from an accretion disk. Most AGNs show a local minimum in their SED in the vicinity of 1 μm. This is thought to represent the minimum between a hot thermal spectrum (the big blue bump) and a cold thermal spectrum due to emission by warm dust grains, known as the 'IR bump'.

2. *Broad-Line Region (BLR)*. Broad emission lines are one of the dominant features of many AGN spectra observed in the optical/UV range, with typical widths about 3000 km s^{-1}. The BLR is composed by large column density

high density gas clouds, at a distance of 0.01-0.1 pc. The physical conditions of this region are such that the ionisation parameter is U $\sim 10^{-2}$. This means that only the illuminated surface of the cloud is highly ionised. The energy source that drives the broad emission lines in AGN spectra is almost certainly photoionization by the continuum radiation from the central source, since the emission-line fluxes vary strongly in response to changes in the continuum flux.

3. *Narrow-line Region (NLR)*. It comprises low column density, low density clouds. The emission comes from a spatially extended region, so the extended physical and kinematical distributions can be mapped out directly with the current instrumentation. A wide variety of ionisation states are present in narrow-line spectra. Both low ionisation lines and high ionisation lines are strong, and in same cases very highly ionised species have been detected, as iron coronal lines. The [OIII] λ5007/Hβ flux ratio is usually larger than 3, indicating that the NLR gas is indeed photoionized by the AGN spectrum, and not by stars in the central regions. The FWHM for narrow emission lines falls in the range 200-900 km s^{-1}. Both density and velocity dispersion increase as we get closer to the nucleus, merging naturally with the BLR. In general, the NLR morphology is found to be axisymmetric, and the NLR axis uses to be coincident with the radio axis in sources where extended radio emission is detected. This indicates that there is some connection between the thermal narrow-line gas and the non-thermal plasma. The picture that emerges is that the outflowing plasma, responsible for the radio emission, creates shock fronts as it collides with the ambient NLR gas. The most dramatic morphological features seen in AGNs are 'ionisation cones', which are visible clearly in high-excitation maps as traced by [OIII] λ5007. The sizes of the ionisation cones are smaller than a few kpcs, and constitute what it is sometimes referred to as the Extended NLR (ENLR). The gas velocities in the ENLR seem to be consistent with galactic rotation, without acceleration by interaction with the radio emitting plasma as in classical NLR. Then, although the morphology suggests outflows from the nucleus, the gas velocities argue in contradictory ways. The study of the ENLR is part of the contribution of this thesis work.

1.3 AGN unification

Although there are several types of AGNs, a unified model (Antonucci, 1993) to explain them all is widely accepted. Direct proofs are lacking but the evidences point towards gravitational accretion of matter by a supermassive black holes (SMBH)

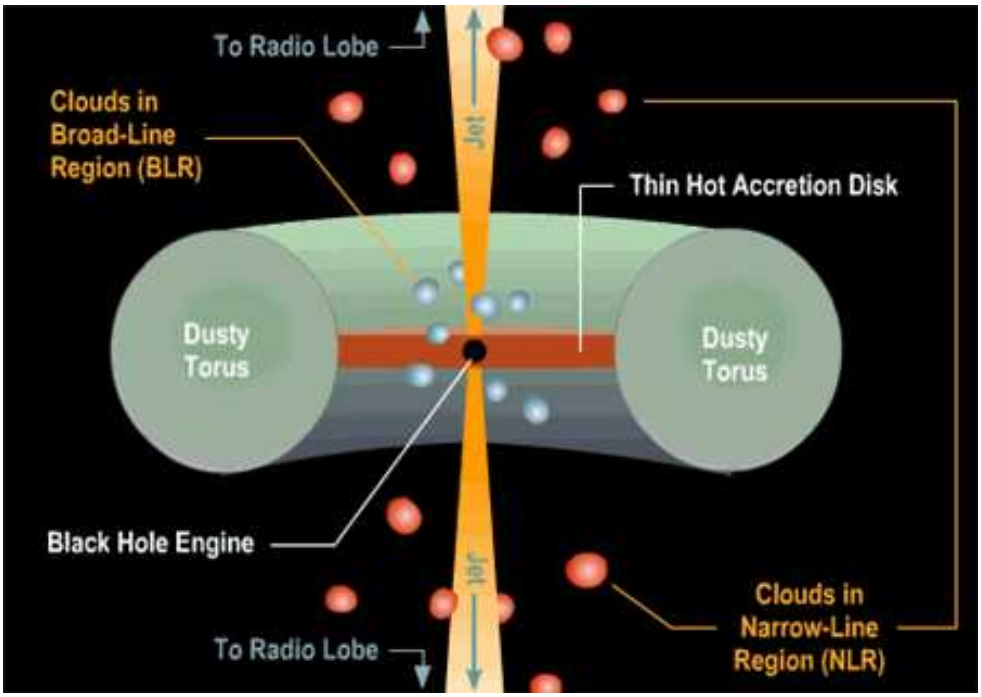

Figure 1.1: *Unified Model of Active Galactic Nuclei.*

as being the primary energy source in AGNs. Gravitational potential energy is converted into radiation via dissipation in an accretion disk surrounding the black hole. Kinematical observations of a number of galaxies have yielded evidences for central black holes with masses between 10^6-10^9 $M_\odot$ (Kormendy and Richstone, 1995). The measure of the UV/optical continuum-emitting region implies sizes of the accretion disk smaller than $\sim 10^{15}$ cm. The corresponding X-ray-emitting region appears to be smaller, few times 10^{13} cm. The BLR, which has a typical size of 10^{16} cm, surrounds it, but its specific geometry and kinematics are poorly understood. NLR gas motions are dominated by gravity but we see evidence of interaction with the radio jet, in terms of shock-heating and outflowing gas. The NLR is the smallest scale of the AGN in which the details can be spatially resolved for nearby galaxies. Its appearance is axisymetric rather than spherical, and it is argued that an optically thick obscuring torus that permits the AGN radiation to escape only along the torus axis, is the responsible for the axisymetry. The radio axis tends to align with this NLR.

The unification ideas try to find the minimum number of parameters needed to cover all the AGN families and to determine the relationships among various

parameters in the hope that this will lead to physical insights. The assumption is that there is less intrinsic diversity among AGNs that we observe, and that this wide variety of AGN phenomena come from the coupling of (1) a combination of real differences in a small number of physical parameters and (2) apparent differences which are due to the point of view of the observer.

A representation of the Unified Model is shown in Fig. 1.1. The key elements in this simple scheme are the obscuring torus and, in the case of the radio sources, a synchrotron-emitting jet. Then, Seyfert 1s and BLRGs are distinguished from their counterparts, Seyfert 2s and NLRGs, by the orientation of the obscuring torus. If the torus is seen face-on, our view of the central region is unobscured and we detect the broad lines; if our view is closer to edge-on, the central region is not seen directly and broad lines are not detected. BL Lacs and OVVs are both face-on versions of radio sources, in which the differences reside in the intensity of the radio luminosity.

Arguments in favour of Seyfert unification do indeed exist. For instance, the properties of the narrow-line components on Seyfert 1s and 2s are statistically indistinguishable (Cohen, 1983) and, in fact, at least some Seyfert 2s are undoubtedly Seyfert 1s in which we observe the Seyfert 1 spectrum only in polarised light (Antonucci and Miller, 1985; Tran, 2001).

Another strong support has been obtained from X-ray observations of many Seyfert 2 type nuclei, that show heavy photoelectric absorption due to cold gas which is likely associated with the dusty torus (Matt, 2002). However, there are definitely other possible absorbers: the BLR ((Risaliti et al., 2005; Elvis et al., 2004)), the host galaxy disc (Maiolino and Rieke, 1995), dust lanes (Malkan et al., 1998; Matt, 2002) and starburst regions (Weaver, 2001). In fact, not all the Seyfert 2s are intrinsically Seyfert 1s in their polarised spectrum. Panessa and Bassani (2002) found a sample of unabsorbed Seyfert 2s with indications of Compton-thin nature (10%-30% the population of type 2 Seyfert galaxies). Then, the molecular torus is not likely to be the responsible for the type 2 class of these sources and the obscuration could be due to dust lanes at large scales or a weak or even absent BLR ('true Seyfert 2', Tran, 2001). Then, it is worth to note that the unified model illustrated above is very simplified and a more complex scenario must be invoked in order to include all the subclasses of objects within the AGN family. We do not have any direct observational evidence that gas indeed accretes onto SMBH. Instead we quite commonly observe the opposite, i.e. gas outflows in AGN. Broad absorption lines (BALs) in UV spectral of QSOs are the most spectacular manifestation for such outflows (Proga, 2007, for a review). They indicates the presence of winds with velocities as large as 0.2c (Turnshek, 1998). Other evidence for AGN winds include narrow absorption lines (BAL) that are blushifted as much as 50000 $\mathrm{km\ s^{-1}}$ (Hamann et al., 1997). Both BAL and NAL are found also in the X-ray domain (Chartas et al., 2003; Kaastra et al.,

2000).

A refinement of the unified model is the modification proposed by Elvis (2000) to be able to include all the classes of AGNs into the same scheme. The model proposes that a funnel-shaped thin shell outflow creates all of these features.

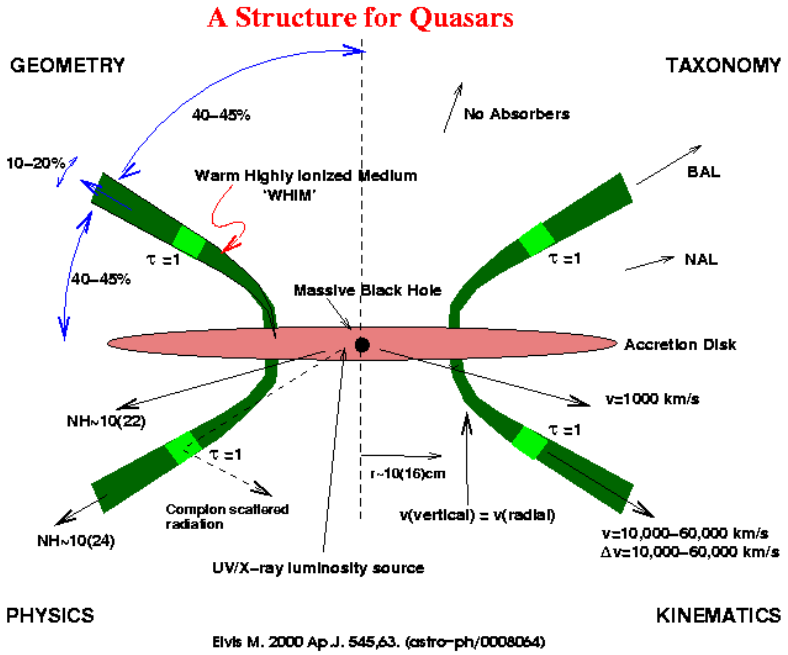

Figure 1.2: *Unified Model modification proposed by Elvis (2000).*

A flow of warm gas first rises vertically from a small range of radii on an accretion disk rotating, tornado-like, with an initial Keplerian disk velocity, comparable to broad emission line (BEL) velocities. The flow then angles outward and accelerates to broad absorption line (BAL) velocities, until it makes an angle of $\sim 60^o$ to the quasar axis, with a divergence angle of $\sim 6^o$ - 12^o (see Fig. 1.2). Viewed along the flow a BAL is seen. Dust in low luminosity objects prevents the BALs from being seen in Seyfert 1 galaxies (they appear as Seyfert 2 galaxies). Viewed across the flow, narrow absorption lines (NALs) and X-ray warm absorbers are observed. Viewed from above, no absorbers are apparent. The angles are set in order to produce the

correct ratios of NAL, BAL, and non-absorbed quasars. The medium is warm ($\sim 10^6$ K), has a high density ($n_e \sim 10^9$ cm^3), and is highly ionised, as required by X-ray observations. We call this the warm highly ionised medium (WHIM). In spite of its at least phenomenon logically simplicity, this model shows many complications when applied to the different types of objects: no calculations can currently reproduce all the observed properties of the broad emission lines, there are no calculations that support the arguments suggesting that the outflow can reach the NLR and form larger condensations, and the model predicts the existence of BAL Seyferts, which have not been observed jet (Alloin, 2006).

Another field of investigation concerns to the dusty torus. The classification of AGNs into type 1 and 2 is only based, under the unified model, in the viewing angle of a dusty torus. However, it does not explain the misclassification between different observations of the same objects (Alonso-Herrero et al., 2003) and transitions between type 1 and 2 objects (Aretxaga et al., 1999). Within the clumpy torus modification, the differences between types are not a matter of orientation but of probability for intercepting a cloud that obscures the AGN direct view. Then, if a cloud happens to obscure the AGN from an observer that objects would be classified as type 2 irrespective of viewing angle. In cases of such single cloud obscuring the nucleus may move out of the line-of-sight, showing a transition between type 2 to type 1 spectrum. However, X-ray observations gives evidence for the orientation dependent absorption, according with Unified ideas (Maiolino and Risaliti, 2007). Elitzur (2007) discusses the possibility that the "dusty torus" does not correspond to what we observe at X-rays, or "X-ray torus". In this sense the bulk of the X-ray absorption likely comes in most cases from the clouds in the dust-free inner portion of the torus. It can explains the discovery of type 1 QSOs that show *Compton-thick* X-ray absorption but no UV absorption (Gallagher et al., 2006).

1.4 X-ray emission

The study of astronomical objects at the highest energies of X-rays and gamma-rays really began only in the early 1960's. Then it is a relatively short history. In the 1970's, dedicated X-ray Astronomy satellites, such as *Uhuru*, *Ariel 5*, *SAS-3*, *OSO-8*, and *HEAO-1*, were essential for the development of this field of research at an astounding pace. In the last decades, several missions have been developed as *HEAO* series, *EXOSAT*, *Ginga*, *CGRO*, *RXTE*, *ROSAT* and *ASCA*. Nowadays, three satellites are in operation: *Chandra*, *XMM-Newton* and, in the last 2 years, *Suzaku*.

X-ray telescopes generally use a Wolter telescope consisting of cylindrical paraboloid and hyperboloid surfaces coated with iridium or gold. X-ray photons would be

absorbed by normal mirror surfaces, so mirrors with a low grazing angle are necessary to reflect them. *Chandra* uses four pairs of nested iridium mirrors, together with their support structure while *XMM-Newton* holds three X-ray telescopes (PN, MOS, RGS), each of which contains 58 Wolter-type concentric mirrors.

XMM-Newton instruments is better suited for spectral analysis because the high number of concentric mirrors increase the sensitivity of the instrument. On the other hand, the angular resolution of *Chandra* (0.5 arcseconds) is over one thousand times better than that of the first orbiting X-ray telescope. Then, the combination of *Chandra* and *XMM-Newton* will allow to achieve high resolution and high sensitivity data.

1.4.1 Active Galactic Nuclei at X-rays

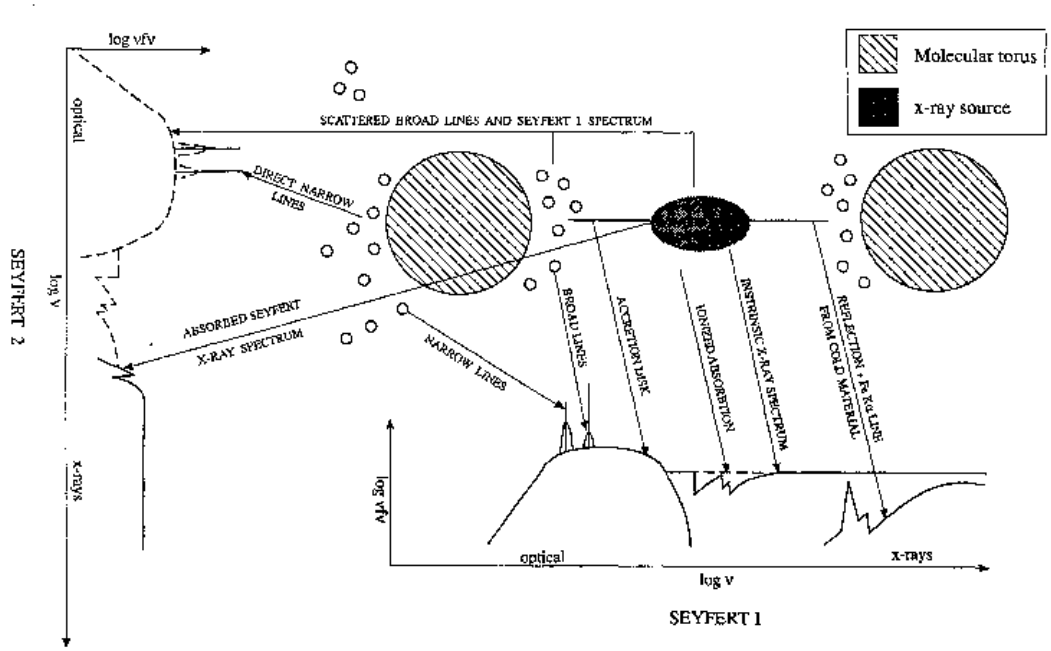

Figure 1.3: *Figure from Mushotzky et al. (1993)*

AGNs are one of the most powerful sources at X-ray frequencies being, in fact, one of the most robust indication of AGN activity. Since the primary source of opacity in the hard X-ray spectrum is electron scattering, very large column densities ($N_H > 10^{24} cm^{-2}$), are required to attenuate the X-ray emission, what allows to study

the internal parts of AGNs only through X-ray frequencies. The UV thermal photons emitted by the accretion disk are Comptonized by hot electrons in an optically thin corona. Such a hot corona has been explained by using three different scenarios: magnetic flares (Haardt et al., 1994), clumpy discs (Guilbert and Rees, 1988) and aborted jet (Henri and Petrucci, 1997). However, none of the above scenarios can be ruled out with the present observations. The resulting X-ray spectrum of AGNs is, as a first approximation, a power law with a high energy cut-off of the form $F(E)=AE^{-\Gamma}$ with a spectral index of $\Gamma \simeq 1.8$.

The X-ray source itself is close to the black hole, and illuminates an optically thick, geometrically thin accretion disk giving rise to a Compton reflection spectrum and an iron Kα line (6.4 keV), which is the most prominent feature in AGNs at energies in the range 2-10 keV (Ogle et al., 2000). The majority of the X-ray flux incident on the accretion disk is thermalized and reprocessed into UV/soft X-ray emission, enhancing the UV/soft X-ray emission processes in the disk itself. Along the line of sight that intercept the torus, much of the nuclear flux is absorbed. Thus, the broad lines, the UV spectrum, and the soft X-rays cannot be seen directly, leading to a classification of a less active type 2 Seyfert. However, some nuclear flux scattered over the top of the torus by the ionised material can be detected, through the observation of polarised broad lines, weak UV and soft X-ray emission. The torus is generally transparent to X-rays at energies greater than 4 keV, so that the hard X-ray nuclear flux can be seen directly (see Fig. 1.3, by Mushotzky et al., 1993).

At least 50% of the low-resolution X-ray spectra of type 1 AGNs show the presence of a broad absorption feature at 0.7-0.8 keV, ascribed to absorption edges of O VIII and O VII due to a warm ionised gas along our line-of-sight (Crenshaw et al., 1999). Nowadays, higher-resolution X-ray spectra have revealed that they are actually the blend of various absorption lines and absorption edges (see Maiolino and Risaliti, 2007, and reference therein). It is explained as outflowing material with column densities of a few times 10^{22} cm^{-2} with velocities ranging from a few to several 100 km s^{-1}, which is located at a 0.2-3 pc scale from the nucleus.

Also, many AGNs show X-ray spectra which rise smoothly below 1 keV above the extrapolated 2-10 keV emission. This soft X-ray excess lacks of features and cannot be resolved into a series of emission lines with gratings. Thus, it seems that it is a continuum component. Two explanations are under consideration: an optically thick material seen via reflection out of the line of sight, or optically thin material seen in absorption in the line of sight (Done et al., 2007).

The most striking broad spectral feature observed in X-ray spectra of AGNs is the soft absorption by material associated with the interstellar medium in our Galaxy and by *in-situ* material of the galaxy and/or AGN; this is called as 'Cold absorber'. This material suppresses the primary power law continuum *via* photoelectric ab-

sorption.

When column densities are higher than $1.5\times10^{24}\mathrm{cm}^{-2}$, the primary source is completely suppressed below 10 keV giving rise to what is called a *Compton-thick* object. If the column density is smaller than this but still in excess of the Galactic one, the source is called *Compton-thin*. If the absorbing medium has column a density $10^{24} - 10^{25}$ cm^{-2}, the transmitted component can still be observed above 10 keV while for column densities well above 10^{25} cm^{-2}, the entire X-ray high energy spectrum is suppressed over the whole X-ray energy range (Matt, 1997; Maiolino and Risaliti, 2007). In this case, the obscured luminosity below 10 keV does not provide a measure of the intrinsic luminosity of the objects.

Under the Unified Model, type 1 objects must be free of obscured matter (i.e. column densities compatible with the Galactic one) whereas type 2 objects are the result of matter obscuration through a dusty torus. Then, the column density measurements is an important tool in order to study the dusty torus, within the Unified scheme. Actually early investigations with hard X-ray satellites clearly revealed an excess of absorption in type 2 Seyfert, in agreement with the expectations from the Unified Model. However, such early studies could identify only a few *Compton-thick* sources, suggesting that they are a very rare class. However, Risaliti et al. (1999), by extracting a subsample selected with [OIII] fluxes could determine, for the first time, the distribution of column densities of an unbiased sample of Seyfert nuclei. They found that *Compton-thick* sources among the Seyfert 2 class are as numerous as *Compton-thin* sources. Moreover, generally the optical classification is consistent with the X-ray properties under the assumption of the Unified model, where type 1 Seyfert tend to be less affected by absorption than type 2 Seyfert. However, the size, location and morphology of the absorbing medium is still under debate.

Strong biases are imposed in optically selected studies, since *Compton-thick* sources are naturally completely buried at such energy ranges. Hard X-ray observations (Vignali et al., 1999; Guainazzi et al., 2000; Ceca et al., 2002) have revealed the presence of heavily obscured, relatively luminous Seyfert nuclei in galaxies optically classified as Starburst. Maiolino et al. (2003) investigated the statistical properties of these elusive AGNs, finding that most of them are *Compton-thick*.

About the extension of the cold absorber two main components have been proposed: an extended medium (on scales 10-100 pc) probably associated to the host galaxy disk (Maiolino and Rieke, 1995; Malkan et al., 1998) and a compact, nuclear absorber ($< 1 - 10$pc) probably co-spatial with the BLR (Risaliti et al., 2005; Elvis et al., 2004).

With respect to the origin of the cold absorber, various studies have shown that X-ray and optical nuclear absorption do not match in AGNs. The measured optical dust extinction is systematically lower than that estimated from X-rays, assuming

reasonable dust-to-gas ratio (Maiolino, 2001).

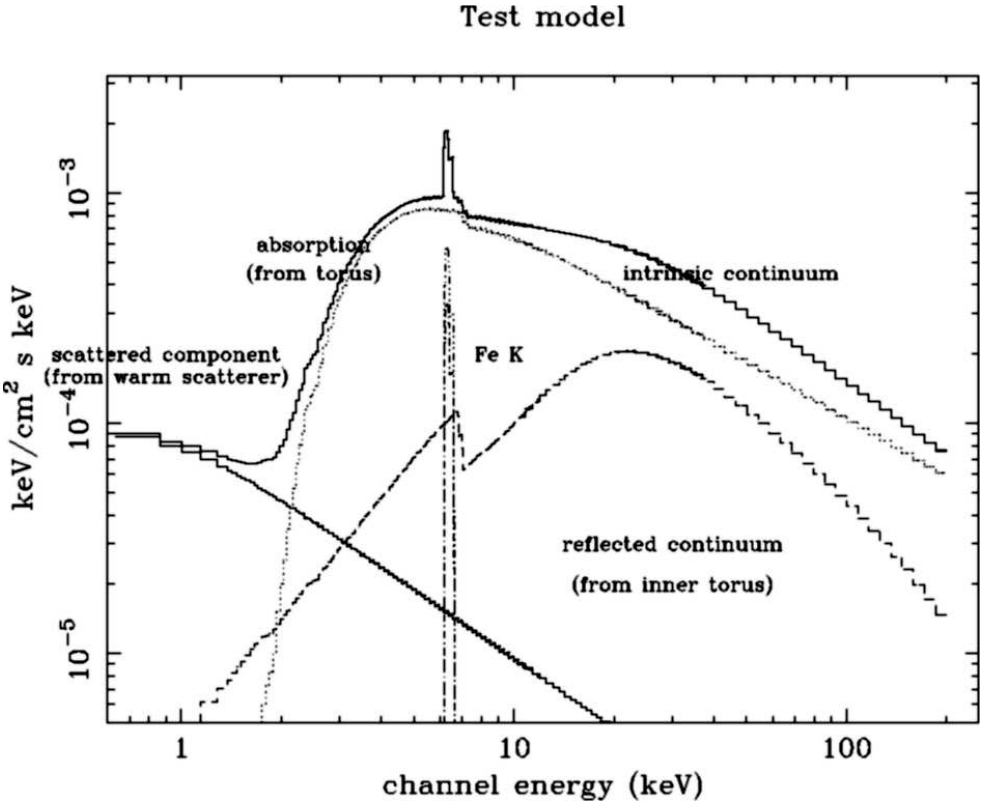

Figure 1.4: *Baseline model. Figure retrieved form Cappi et al. (1999)*

Cappi et al. (1999) proposed that the general picture for an AGN in X-rays can be modelled by the so-called *Baseline* model for AGNs (see Fig. 1.4). This *Baseline* model includes the following components: (a) The primary continuum described by a power law; (b) a Compton reflection component from cold matter (fitted with PEXRAV model); (c) a narrow Kα iron line modelled with a Gaussian profile; and (d) for the soft X-ray spectrum (< 2 keV), a combination of a thermal component model (MEKAL) and a scattering component by ionised material (described with a power-law).

Then, the X-ray domain is plenty of AGN signatures resulting in one of the most important tools to determine the nature of doubtful AGNs, as is the case of LINERs.

1.4.2 Additional sources contributing at X-ray frequencies

However, AGNs are not the only sources that contribute to the X-ray range (see Fabbiano, 2004, for a review). Point-like off-nuclear X-ray sources with luminosities well in excess of the Eddington limit for a stellar mass black hole, have been discovered in a large number of nearby galaxies (Fabbiano, 2006). The X-ray 2-10 keV luminosities of these sources fall in the range 10^{39-41}erg s^{-1}, one order of magnitude larger than the X-ray binaries in our Galaxy. If ULXs are black holes that accretes at the Eddington limit, their masses might range from 10 to 10000$M_{\odot}$, i.e., they are intermediate mass black holes (IMBH). However, optical studies (Fabbiano and White, 2006; Fabbiano, 2006) have found that ULXs are preferentially associated with massive star forming regions such as OB associations and, at the high-mass limit, superstar clusters, connecting these sources with star-forming processes.

1.5 LINERs

Almost three decades ago, Heckman (1980) found a large amount of Active Galactic Nuclei which spectroscopic properties departed from those of either "normal" HII regions or classical AGNs. Their principal signature was the enhancement of the low ionisation lines, what made him to propose for them the name of "Low Ionisation Nuclear Emission Line Region" (LINERs). They were characterised by optical spectra dominated by emission lines of moderate intensities arising from gas in lower ionisation states than classical AGN and line widths approaching those of the NLR in Seyfert galaxies. In some of them, a compact nuclear radio source was detected. In that early work, Heckman noticed that a sequence between LINERs and AGNs could be drawn in which LINERs occupy the low luminosity end. However, whereas AGNs were broadly recognised as regions photoionized by power-law continuum (Halpern and Steiner, 1983), LINERs were best explained in the context of shock ionization (Fosbury et al., 1978; Dopita et al., 1996) and photoionization by post-AGB stars in the case of weak LINERs in ellipticals (Binette et al., 1994). After more than a decade, the debate is still open (see Ho et al., 2008, for a full discussion on this topic) and no consensus exists on whether LINERs do represent the low luminosity end of the sequence of the AGN phenomenon. Thus, their study is essential for a full understanding on the AGN demography and evolution.

The low luminosity of these nuclear sources makes them difficult targets for observational studies, even in nearby galaxies. One would expect that 0.5 arcsecond, the information coming from different spectral ranges could help to disentangle and eventually classify the LINER family. However, unless much progress has been done on the last decade, the study of data at different wavelengths open new ques-

tions. Here we will summarise the discussion as it stands now at different frequencies:

- **Radio emission.** Since the nuclei of LINERs may be very heavily obscured, observations at UV, optical, near-infrared, and even far-infrared may not penetrate the dust to reach the nucleus. The most important recent data constraining the nature of LINER nuclei have come from radio and X-rays surveys because in these spectral regions it is possible to detect central engines that are completely obscured in the optical and UV. In a *VLA* survey, Nagar et al. (2000) found that 64% LINER 1s and 36% LINER 2s have compact radio cores (Nagar et al., 2005). The objects bright enough for VLBI observations at 5GHz were studied by Falcke et al. (2000) (see also Filho et al., 2004); all showed compact, high-brightness-temperature cores, suggesting that an AGN, rather than a starburst, is responsible for the radio emission. Moreover, the core radio fluxes have been found to be variable by a factor of up to a few in about half of the $\sim$10 LINERs observed several times during 3 years (Nagar et al., 2002). A radio survey looking for 1.3 cm water mega-maser emission, an indicator of dense circumnuclear molecular gas, detected LINER nuclei at the same rate as type 2 Seyfert nuclei (Braatz et al., 1997). Such mega-maser emission is only seen in AGNs. Finally, it is worthwhile to mention that a type of NLR behaviour is found in a few LINERs, with indications of a Seyfert-like ionisation cone oriented along their radio axis (Pogge et al., 2000).

- **IR emission.** Lawrence et al. (1985) found that LINERs show strong excess in the range between 10-20 μm, while they are stellar dominated in the range 1-5 μm. However, Seyferts, where the reemission of the hot dust is very important, show a flat spectrum until 5 μm and a rapidly enhancement in the range of 10-20 μm. This excess in 10 μm in LINERs is interpreted as relatively few hot dust, reinforcing the existence of a non thermal component. But still a large amount of work remains to be done specially at mid-IR frequencies, where hints for the AGN nature of LINERs can be found. The unique study done so far by Sturm et al. (2006) has shown that two different LINER populations seems to exist: infrared-faint LINERs, with LINER emission arising mostly in compact nuclear regions, and infrared-luminous LINERs, which often show spatially extended (non-AGN) LINER emission. IR-luminous LINERs show mid-IR SEDs typical of starburst galaxies, while the mid-IR SEDs of IR-faint LINERs are much bluer. Fine-structure emission lines from highly excited gas, such as [O IV], were detected in both populations, suggesting the presence of an additional AGN in a large fraction of IR-bright LINERs as well, although it contributes little to the combined mid-IR light.

- **UV emission.** Several attempts have been made to detect UV emission in LINERs, since the stellar contamination in the old population-dominated bulges disappears in the UV. The UV imaging surveys by Barth et al. (1996) and Maoz et al. (2005) (also Pogge et al., 2000) found nuclear UV emission in $\sim$25% of the LINERs that were observed. About half of them appeared as point-like at the resolution of *HST* and thus were good candidates for being genuine LLAGNs with non-stellar continua. Barth et al. (1996) show that the low UV detection rate is primarily due to dust obscuration of the nuclei. Thus, the majority of LINERs probably have UV sources in their nuclei (which could be either AGN or young-star clusters), but in most cases the UV sources lie behind too large amounts of dust to render it visible. Therefore, the foreground dust plays an important role in blocking our view of the central engines. A UV-variability campaign that monitored 17 known UV-bright LINERs by Maoz et al. (2005) found that almost all objects varied on either short or long timescales, indicating the presence of an AGN component.

- **X-ray emission.** Only a reduced number of X-ray observations of LINER 2s has been performed so far. X-ray observations with *Einstein* and *ROSAT* were limited to soft energies, where heavily obscured AGN are difficult to detect. The *ROSAT HRI* images showed compact soft X-ray ($\leq$ 2 keV) emission in 70% of the LINERs and Seyfert galaxies (Roberts & Warwick 2000). Satyapal et al. (2005) (see also Ho et al., 2001; Satyapal et al., 2004; Dudik et al., 2005) estimated the 2-10 keV luminosities of a sample of LINERs with *Chandra* data. They found that AGNs were very frequent among the LINER population and based on the derived Eddington ratios, they concluded that LINERs were the faintest end of the fundamental correlation between mass accretion and star formation rates, being very inefficient systems in the accretion process onto the putative nuclear black hole. Flohic et al. (2006) studied a sample of 19 LINERs through archival *Chandra* data to investigate the presence of an AGN. They found that AGNs contributed in median 60% to the 0.5-10 keV luminosity although they suggested that the AGN power is not enough to produce the observed optical emission lines, invoking shocks or stellar processes. The study at X-ray frequencies of LINERs is one of the main goals of the research work presented in this thesis.

1.6 Open questions and outline of this work

The main topic of this thesis has been to understand which is the nature of the energy source observed in LINERs. As reported in this introduction, although the

astronomical community shows a common consensus about the general picture of the Unified Model, many aspects related to the different manifestation of activity as it is observed in a number of different objects, QSOs, Seyferts, LINERs, are still matter of debate. This thesis will tackle with: (1) LLAGN re-unification, (2) torus obscuration in LINERs and (3) origin of the ENLR/NLR.

About the main task, LINERs have been discussed in Chapter 2 and 3. Chapter 2 is focused in the discussion of its origin trying to disentangle the AGN/Starburst contribution in 51 LINERs. This topic is also tackled in Chapter 3. However, the large number of objects (81) and, specially the large number of X-ray spectra used for the analysis (60) added to the multiwavelength data, allow studying the location and amount of obscure matter around these objects. Within this analysis it must be remarked the study of *Compton-thick* candidates and its implications in the distribution of accretion-rates in LINERs. Note that the difference between Chapter 2 and 3 is also a matter of process in which the Chapter 2 raises some questions that open other questions that are tackled in Chapter 3.

Another approach to study the Unification ideas of AGN is the multiwavelength analysis, performed in Chapter 4, of the NLR/ENLR of a special case, NGC 4151. This gives the opportunity to test the possibilities of multiwavelength analysis of AGNs, nowadays accessible thanks to the high performance of the new instrumentation.

Finally, Chapter 5 is devoted to the study of ULXs, important in our analysis mainly for two reasons: 1) the contribution of ULXs in LLAGN might be an ingredient to be considered; and 2) some theoretical frameworks advocate that they are IMBHs, plaussible connection with SMBHs in the center of galaxies.

The following subsections attempts to retrieve the main work presented in each chapter:

1. **X-RAY NATURE OF 51 LINER NUCLEAR SOURCES WITH *Chandra***

   We report the results from a homogeneous analysis of the X-ray (*Chandra* ACIS) data available for a sample of 51 LINER galaxies selected from the catalogue by Carrillo et al. (1999) and representative of the population of bright LINER sources. The nuclear X-ray morphology has been classified by their nuclear compactness in the hard band (4.5–8.0 keV) into 2 categories: active galactic nuclei (AGN) candidates (with a clearly identified unresolved nuclear source) and starburst (SB) candidates (without a clear nuclear source). Sixty percent of the total sample are classified as AGN, with a median luminosity of L_X(2-10 keV)= 2.5×10^{40} erg s^{-1}, which is an order of magnitude higher than for SB-like nuclei. The spectral fitting allows us to conclude that most of the objects need a non-negligible power-law contribution. When no spectral fitting can be

performed (data with a low signal-to-noise ratio), the color-color diagrams allow us to roughly estimate physical parameters, such as column density, temperature of the thermal model, or spectral index for a power-law, and therefore to better constrain the origin of the X-ray emission. The X-ray morphology, the spectra, and the color-color diagrams together allow us to conclude that a high percentage of LINER galaxies, at least $\approx 60\%$, could host AGN nuclei, although contributions from high-mass X-ray binaries or ultra-luminous X-ray sources cannot be ruled out for some galaxies.

2. **AN X-RAY VIEW OF 82 LINERs WITH *Chandra* AND *XMM-Newton***

We present the results of a homogeneous X-ray analysis of 82 LINERs selected from the catalogue by Carrillo et al. (1999) with available *Chandra* (68 sources) and *XMM-Newton* (55 sources) observations. Both together they comprise the largest sample of LINERs with X-ray spectral fit ever analysed (60 out of the 82 objects). Information from the literature on the black hole masses, optical morphology with *HST* data, optical emission lines, radio compactness and stellar populations have been added for the analysis. The nuclear X-ray morphology has been classified according to the compactness of the detected nuclear source in the hard band (4.5-8.0 keV). 60% of the sample shows such a compact nuclear source. The analysis of their spectra has shown that they can be best fitted by composite models (a combination of a thermal and a power law component with two absorbers, MEPL and ME2PL). The resulting median spectral parameters are: $<\Gamma>$=2.11$\pm$ 0.52 , $<kT>$=0.54$\pm$ 0.30 keV, $<\log(NH1)>$=21.32$\pm$ 0.71 and $<\log(NH2)>$=21.93$\pm$ 1.36 . The Compton-thickness nature of the LINER nuclei in our sample has been investigated by means of the Fez iron emission line (detected in 13 galaxies) and the $F_X(2-10keV)/F([OIII])$ ratios. 58% of the analysed LINER nuclei are found to be Compton-thick candidates. After Compton-thickness correction, they have quite large median soft and hard luminosities, <log(L(0.5-2 keV))>= 40.51$\pm$ 1.41 and <log(L(2-10 keV))>= 40.87$\pm$ 1.38 , respectively, pretty similar to the ranges found for nearby low luminosity Seyferts. The investigation of the origin of the obscuring material allows us to conclude that, whereas the column density NH1 reflects what is found with the optical extinction, the column density NH2 seems to be most probably associated to the inner parts of the dusty torus. The calculated Eddington ratios cover the range from 10^{-2} to 10^{-6}, unexpectedly overlapping with those reported for Seyfert 2 galaxies. Finally, adding all the multiwavelength existing data for these LINERs, we conclude that evidences do exist supporting the AGN nature of their nuclear engine for 90% of the sample (74 out of 82 objects). Therefore, the main con-

tributions in this paper have been, first to illustrate that AGN are much more frequent among LINERs than previously reported and, second, that the reason for the differences between LINERs and Seyferts 2 are not due to different accretion rates as claimed before. Clumpy dusty models need to be further investigated for an eventual explanation of the nature of different AGN populations.

3. **THE EXTENDED NARROW EMISSION LINE REGION OF NGC 4151: AN OPTICAL, RADIO AND X-RAY STUDY**

   We present a new interpretation of archival *Chandra*, Hubble Space Telescope (*HST*), and *VLA* imaging observations of the circumnuclear extended emission in the nearby Type 1.5 Seyfert galaxy NGC 4151. A conical structure is seen in [SII]/Hα and [OIII]/Hβ ratios, extending up to 14″. The morphological comparison between both ratios suggests photoionization from the nucleus in the Narrow Line Region (NLR) and Extended NLR (ENLR). This is confirmed by diagnostic diagrams in a number of regions along the NLR and ENLR. The resolved soft X-ray emission is spatially coincident with the [OIII]/Hβ ratio distribution. The X-ray spectra of the ENLR, as in the NLR, are dominated by emission lines from the photoionized medium up to 14″. We detect not only the radio jet with an overall P.A.$\sim 77°$, but also a secondary jet traced by a weaker radio knots along P.A.$\sim 53°$. The appearance of the radio spectral index map may be interpreted as the superposition of two linear structures along P.A.$\sim 53°$ and $\sim 77°$. The computed lifetime of the radio sources are larger values for the south knot located at P.A.$\sim 53°$, suggesting that these secondary jet is older than the first jet. This second structure is aligned with the conical distribution as seen in X-ray and optical wavelengths. We point out to the possibility that the jet has precessed between 45° and 77° or alternatively, two jets have been ejected from the galaxy nucleus at different times.

4. **THE ULTRA LUMINOUS X-RAY SOURCES IN THE HVS OF NGC 1275**

   We report the results of a study of X-ray point sources coincident with the *High Velocity System* (HVS) projected in front of NGC 1275. A very deep X-ray image of the core of the Perseus cluster made with the *Chandra Observatory* has been used. We find a population of Ultra-Luminous X-ray sources (ULX; 7 sources with $L_X(0.5-7.0\,\mathrm{keV}) > 7\times10^{39}\ \mathrm{erg\ s^{-1}}$). As with the ULX populations in the Antennae and Cartwheel galaxies, those in the HVS are associated with a region of very active star formation. Several sources have possible optical counterparts found on *HST* images, although the X-ray brightest one does not. Absorbed power-law models fit the X-ray spectra, with most having a photon index between 2 and 3.

This thesis is mainly based on the following papers:

- I. X-ray nature of the LINER nuclear sources
  O. González-Martín, J. Masegosa, I. Márquez, M. A. Guerrero, & D. Dultzin-Hacyan, 2006, A&A, 460, 45
- II. The ultraluminous X-ray sources in the high-velocity system of NGC1275
  González-Martín, O., Fabian, A. C., & Sanders, J. S. 2006, MNRAS, 367, 1132
- III. An X-ray aproach to LINERs nuclei I: Sample properties
  O. González-Martín, J. Masegosa, I. Márquez, M. Guainazzi and E. Jiménez-Bailón, to be submitted.
- IV. An X-ray aproach to LINERs nuclei II: Obscuring matter
  O. González-Martín, J. Masegosa, I. Márquez, M. Guainazzi and E. Jiménez-Bailón, to be submitted.
- V. The Extended Narrow Emission Line Region OF NGC 4151: An optical, radio and X-ray study
  O. González-Martín, M. Karovska, C. Carrasco-González, M. Elvis, I. Márquez and J. Masegosa, to be submitted.

1.7 Conclusions and Outline of the Future Prospects

LINERs:

- **X-ray image and spectral analysis**. The analysis of a large sample of LINERs has demonstrate that a high percentage of them (60% for the full sample, 68% for the sub sample with spectral fit) shows compact unresolved nuclear sources at high energies ($4.5 - 8$ keV) band, being excellent candidates to host a nuclear AGN.

  The modelling of their X-ray spectra has shown that most of them agree with the *Baseline* model of AGNs. Moreover 70% of the sample need two power-laws and a thermal model (MEKAL model) at energies below 2 keV is needed in the vast majority of the cases (95%).

  OUTLINE: The full characterisation of the soft emission need to be analysed, which has been out of the scope of this thesis. Such soft excess, fitted as thermal model in a first approximation, will be analysed in the future by using high resolution RGS *XMM-Newton* spectra. It will allow to disentangle the nature of the observed emission, i.e. whether this contribution comes from

ionisation due to the central engine or it is better associated to the phenomena occurring in the host galaxy.

- **Obscuration**. The comparison between optical extinction and column densities suggests that NH1 (the column density associated with energies below 2 keV) is related to this optical extinction while NH2 (the column density associated with energies above 2 keV) is much higher than it. It is suggested that the first absorber is associated with the host galaxy and the process that obscure at optical wavelength while NH2 arise in a medium much closer to the center which cannot be seen at optical wavelength. This scenario is consistent with a two absorber media claimed for AGNs, an extended medium associated with the host galaxy and a compact nuclear absorber probably associated with the BLR (Maiolino and Risaliti, 2007).

  Compton-thickness diagnostics have been used to search for hidden AGNs amongst the LINER population. We have concluded that 50% of the LINER nuclei are good candidates to host a hidden AGN. Such a percentage is higher than that reported for Seyfert nuclei. It has been also shown that the large equivalent width of the FeKα emission line, claimed as a powerful indicator of the *Compton-thick* nature of AGN , does not appear to be so large for confirmed *Compton-thick* LINERs. Then, studies on the local Universe are important to estimate the contribution of heavily obscured AGNs to the X-ray background.

  OUTLINE: Higher S/N ratio data with *XMM-Newton* need to be taken to study in a bigger sample, the FeKα emission line in *Compton-thick* objects. The hidden AGN population amongst the family of normal Starburst galaxies needs also to be analysed in future works using the same methodology presented in this thesis work. Moreover for the *Compton-thick* candidates suspected so far, a confirmation of their nature need to be tackled both with present, *SUZAKU* and *INTEGRAL*, and future planned X-ray missions, *XEUS*, *Simbol-X* and/or *Constellation-X*.

- **Multiwavelength**. Taken all the known multiwavelength tracers of AGN activity together, our main conclusion is that the vast majority of LINERs (around 90% of our sample) show evidence of AGN activity in their nuclei. The main argument is coming from the X-ray image and the spectroscopic analysis but information from optical, radio and UV wavelength reinforce this AGN rate, even increasing it. However, information coming from UV, radio and X-rays sometimes present discrepant results for some objects, i.e. showing characteristic of AGNs at UV that are not seen at X-ray frequencies. We argue that such variations might be compatible with the existence of a clumpy torus, which will be the responsible of such discrepancies due to the probability of finding

a high-velocity thick cloud in the line-of-sight when non simultaneous observations are analysed.

OUTLINE: One of the best ways to test the clumpy medium theories are variability studies of LINERs to search for transitions between *Compton-thick* to *Compton-thin* states. Risaliti et al. (2007) show that this is the case for the Seyfert 2 galaxy NGC 1365. On the other hand, near IR spectroscopy (SOFI /NTT) of obscured AGNs are still lacking, since these AGNs might emit the bulk of their luminosity at IR frequencies.

- **LINER/Seyfert connection.** The spectral parameters of LINERs, like spectral indices and luminosities (i.e. accretion rate) after *Compton-thick* correction, are consistent with what it is found for Seyfert galaxies. However, we find a correlation between NH1 (associated with soft spectrum) and the optical extinction that have never been reported before for Seyfert galaxies. However, previous work on Seyfert galaxies only deals with a single absorber.

  OUTLINE: We stress that a uniform homogeneous analysis of complete samples of Seyfert 1 and 2 at X-ray frequencies with both *Chandra* and *XMM-Newton* is needed. These will be of particular importance to find whether the hydrogen column density of these objects is related with the optical extinction, in the same way that LINERs.

NGC 4151:

The NLR and ENLR of NGC 4151 have been studied with optical, radio and X-ray observations. It is suggested that most of the emission seen at soft X-ray energies, both in the NLR and in the ENLR, is due to photoionized material from the central source, and it is not to *in-situ* stellar photoionization. The other important conclusion on this work has been the explanation of the orientation mismatch of the optical NLR/ENLR and the radio jet. It is suggested that a different (or precessing) jet is the origin of the the X-ray and optical cone-like morphology.

OUTLINE: This kind of multiwavelength analysis are still lacking, excepting for exceptional cases as NGC 1068. A study of a complete sample of the diffuse emission of Seyferts will help to make statistical analysis of the properties on NLR/ENLR. They are difficult targets because powerful AGNs hide the extended emission at X-ray frequencies. In this sense, the low luminosity of the central source at X-ray frequencies, makes LINERs also better targets to study the NLR/ENLR since it is not hidden by the nuclear illumination. Then multiwavelngth analysis, as for NGC 4151 is a future project, not only in Seyfert galaxies but also in our sample of LINERs, for which NLR has been detected.

ULXs:

Finally, ULX seen in front of the High velocity system of NGC 1275, are mostly associated with a region of very active star formation, although the brightest does not seem to be connected. This relation of ULX with star formation regions are also reported by several archetypal galaxies as the Antennae or the Cartwheel.

OUTLINE: ULX are also an interesting field of study since many of the LINERs show an extremely high population of sources close to the nuclear sources. As a future prospect, the study of the discrete sources in LINERs is another interesting field to be searched since the coincidence of a ULX in the nuclear source, although it is highly unlikely, cannot be rule out. We guess that multiwavelength analysis, specially at IR and radio data will help to understand the nature of these objects.

Bibliography

Alloin, D.: 2006, Vol. 693

Alonso-Herrero, A., Quillen, A. C., Rieke, G. H., Ivanov, V. D., and Efstathiou, A.: 2003, *Astronomical Journal* **126**, 81

Antonucci, R.: 1993, *Annual Review of Astronomy and Astrophysics* **31**, 473

Antonucci, R. R. J. and Miller, J. S.: 1985, *Astrophysical Journal* **297**, 621

Aretxaga, I., Joguet, B., Kunth, D., Melnick, J., and Terlevich, R. J.: 1999, *Astrophysical Journal* **519**, L123

Barth, A. J., Reichert, G. A., Filippenko, A. V., Ho, L. C., Shields, J. C., Mushotzky, R. F., and Puchnarewicz, E. M.: 1996, *Astronomical Journal* **112**, 1829

Binette, L., Magris, C. G., Stasinska, G., and Bruzual, A. G.: 1994, *Astronomy and Astrophysics* **292**, 13

Braatz, J. A., Wilson, A. S., and Henkel, C.: 1997, *Astrophysical Journal Supplement Series* **110**, 321

Burbidge, G. R., Burbidge, E. M., and Sandage, A. R.: 1963, *Reviews of Modern Physics* **35**, 947

Cappelluti, N., Bohringer, H., Schuecker, P., Pierpaoli, E., Mullis, C. R., Gioia, I. M., and Henry, J. P.: 2007, *Astronomy and Astrophysics* **465**, 35

Cappi, M., Bassani, L., Comastri, A., Guainazzi, M., Maccacaro, T., Malaguti, G., Matt, G., Palumbo, G. G. C., Blanco, P., Dadina, M., dal Fiume, D., di Cocco, G., Fabian, A. C., Frontera, F., Maiolino, R., Piro, L., Trifoglio, M., and Zhang, N.: 1999, *Astronomy and Astrophysics* **344**, 857

Carrillo, R., Masegosa, J., Dultzin-Hacyan, D., and Ordonez, R.: 1999, *Revista Mexicana de Astronomia y Astrofisica* **35**, 187

Ceca, R. D., Ballo, L., Tavecchio, F., Maraschi, L., Petrucci, P. O., Bassani, L., Cappi, M., Dadina, M., Franceschini, A., Malaguti, G., Palumbo, G. G. C., and Persic, M.: 2002, *Astrophysical Journal* **581**, L9

Chartas, G., Brandt, W. N., and Gallagher, S. C.: 2003, *Astrophysical Journal* **595**, 85

Cohen, R. D.: 1983, *Astrophysical Journal* **273**, 489

Crenshaw, D. M., Ruiz, J. R., and Kraemer, S. B.: 1999, Vol. 195, p. 1543

Done, C., Gierlinski, M., Sobolewska, M., and Schurch, N.: 2007, Vol. 373, p. 121

Dopita, M. A., Koratkar, A. P., Evans, I. N., Allen, M., Bicknell, G. V., Sutherland, R. S., Hawley, J. F., and Sadler, E.: 1996, Vol. 103, p. 44

Dudik, R. P., Satyapal, S., Gliozzi, M., and Sambruna, R. M.: 2005, *Astrophysical Journal* **620**, 113

Elitzur, M.: 2007, Vol. 373, p. 415

Elvis, M.: 2000, *New Astronomy Review* **44**, 559

Elvis, M., Risaliti, G., Nicastro, F., Miller, J. M., Fiore, F., and Puccetti, S.: 2004, *Astrophysical Journal* **615**, L25

Fabbiano, G.: 2004, Vol. 20, pp 46–49

Fabbiano, G.: 2006, Vol. 230, pp 180–184

Fabbiano, G. and White, N. E.: 2006, *Compact stellar X-ray sources in normal galaxies*, pp 475–506

Fabian, A. C.: 1979, *Royal Society of London Proceedings Series A* **366**, 449

Falcke, H., Nagar, N. M., Wilson, A. S., and Ulvestad, J. S.: 2000, *Astrophysical Journal* **542**, 197

Fath, E. A.: 1908, *Lick Observatory Bulletin* **5**, 71

Ferrarese, L. and Merritt, D.: 2000, *Astrophysical Journal* **539**, L9

Filho, M. E., Fraternali, F., Markoff, S., Nagar, N. M., Barthel, P. D., Ho, L. C., and Yuan, F.: 2004, *Astronomy and Astrophysics* **418**, 429

Flohic, H. M. L. G., Eracleous, M., Chartas, G., Shields, J. C., and Moran, E. C.: 2006, *Astrophysical Journal* **647**, 140

Fosbury, R. A. E., Mebold, U., Goss, W. M., and Dopita, M. A.: 1978, *Monthly Notices of the Royal Astronomical Society* **183**, 549

Gallagher, S. C., Brandt, W. N., Chartas, G., Priddey, R., Garmire, G. P., and Sambruna, R. M.: 2006, *Astrophysical Journal* **644**, 709

Gebhardt, K., Pryor, C., O'Connell, R. D., Williams, T. B., and Hesser, J. E.: 2000, *Astronomical Journal* **119**, 1268

Guainazzi, M., Oosterbroek, T., Antonelli, L. A., and Matt, G.: 2000, *Astronomy and Astrophysics* **364**, L80

Guilbert, P. W. and Rees, M. J.: 1988, *Monthly Notices of the Royal Astronomical Society* **233**, 475

Haardt, F., Maraschi, L., and Ghisellini, G.: 1994, *Astrophysical Journal* **432**, L95

Halpern, J. P. and Steiner, J. E.: 1983, *Astrophysical Journal* **269**, L37

Hamann, F., Barlow, T., Cohen, R. D., Junkkarinen, V., and Burbidge, E. M.: 1997, in *Mass Ejection from Active Galactic Nuclei*, Vol. 128, p. 19

Hazard, C., Mackey, M. B., and Shimmins, A. J.: 1963, *Nature* **197**, 1037

Heckman, T. M.: 1980, *Astronomy and Astrophysics* **87**, 152

Henri, G. and Petrucci, P. O.: 1997, *Astronomy and Astrophysics* **326**, 87

Ho, L. C., Darling, J., and Greene, J. E.: 2008, *A New H I Survey of Active Galaxies*

Ho, L. C., Feigelson, E. D., Townsley, L. K., Sambruna, R. M., Garmire, G. P., Brandt, W. N., Filippenko, A. V., Griffiths, R. E., Ptak, A. F., and Sargent, W. L. W.: 2001, *Astrophysical Journal* **549**, L51

Kaastra, J. S., Mewe, R., Liedahl, D. A., Komossa, S., and Brinkman, A. C.: 2000, *Astronomy and Astrophysics* **354**, L83

Kormendy, J. and Richstone, D.: 1995, *Annual Review of Astronomy and Astrophysics* **33**, 581

Lawrence, A., Ward, M., Elvis, M., Fabbiano, G., Willner, S. P., Carleton, N. P., and Longmore, A.: 1985, *Astrophysical Journal* **291**, 117

Leighly, K. M.: 1999, *Astrophysical Journal Supplement Series* **125**, 297

Maiolino, R.: 2001, *X-ray Astronomy: Stellar Endpoints, AGN, and the Diffuse X-ray Background* **599**, 199

Maiolino, R., Comastri, A., Gilli, R., Nagar, N. M., Bianchi, S., Beker, T., Colbert, E., Krabbe, A., Marconi, A., Matt, G., and Salvati, M.: 2003, *Monthly Notices of the Royal Astronomical Society* **344**, L59

Maiolino, R. and Rieke, G. H.: 1995, *Astrophysical Journal* **454**, 95

Maiolino, R. and Risaliti, G.: 2007, Vol. 373, p. 447

Malkan, M. A., Gorjian, V., and Tam, R.: 1998, *Astrophysical Journal Supplement Series* **117**, 25

Maoz, D., Nagar, N. M., Falcke, H., and Wilson, A. S.: 2005, *Astrophysical Journal* **625**, 699

Matt, G.: 1997, *Memorie della Societa Astronomica Italiana* **68**, 127

Matt, G.: 2002, Vol. 258, p. 3

Matthews, T. A. and Sandage, A. R.: 1963, *Astrophysical Journal* **138**, 30

Mushotzky, R. F., Done, C., and Pounds, K. A.: 1993, *Annual Review of Astronomy and Astrophysics* **31**, 717

Nagar, N. M., Falcke, H., and Wilson, A. S.: 2005, *Astronomy and Astrophysics* **435**, 521

Nagar, N. M., Falcke, H., Wilson, A. S., and Ho, L. C.: 2000, *Astrophysical Journal* **542**, 186

Nagar, N. M., Falcke, H., Wilson, A. S., and Ulvestad, J. S.: 2002, *Astronomy and Astrophysics* **392**, 53

Ogle, P. M., Marshall, H. L., Lee, J. C., and Canizares, C. R.: 2000, *Astrophysical Journal* **545**, L81

Osterbrock, D. E., Shaw, R. A., and Veilleux, S.: 1989, Vol. 134, p. 298

Panessa, F. and Bassani, L.: 2002, *Astronomy and Astrophysics* **394**, 435

Pogge, R. W., Maoz, D., Ho, L. C., and Eracleous, M.: 2000, *Astrophysical Journal* **532**, 323

Proga, D.: 2007, in *The Central Engine of Active Galactic Nuclei*, Vol. 373, p. 267

Rees, M. J.: 1984, *Annual Review of Astronomy and Astrophysics* **22**, 471

Risaliti, G., Elvis, M., Fabbiano, G., Baldi, A., and Zezas, A.: 2005, *Astrophysical Journal* **623**, L93

Risaliti, G., Elvis, M., Fabbiano, G., Baldi, A., Zezas, A., and Salvati, M.: 2007, *Astrophysical Journal* **659**, L111

Risaliti, G., Maiolino, R., and Salvati, M.: 1999, *Astrophysical Journal* **522**, 157

Satyapal, S., Dudik, R. P., O'Halloran, B., and Gliozzi, M.: 2005, *Astrophysical Journal* **633**, 86

Satyapal, S., Sambruna, R. M., and Dudik, R. P.: 2004, *Astronomy and Astrophysics* **414**, 825

Schmidt, M.: 1963, *Nature* **197**, 1040

Seyfert, C. K.: 1943, *Astrophysical Journal* **97**, 28

Sturm, E., Rupke, D., Contursi, A., Kim, D.-C., Lutz, D., Netzer, H., Veilleux, S., Genzel, R., Lehnert, M., Tacconi, L. J., Maoz, D., Mazzarella, J., Lord, S., Sanders, D., and Sternberg, A.: 2006, *Astrophysical Journal* **653**, L13

Tran, H. D.: 2001, *Astrophysical Journal* **554**, L19

Turnshek, D. A.: 1998, in *Structure et Evolution du Milieu Inter-Galactique Revele par Raies D'Absorption dans le Spectre des Quasars, 13th Colloque d'Astrophysique de l'Institut d'Astrophysique de Paris*, p. 263

Vignali, C., Comastri, A., Cappi, M., Palumbo, G. G. C., Matsuoka, M., and Kubo, H.: 1999, *Astrophysical Journal* **516**, 582

Weaver, K. A.: 2001, Vol. 249, p. 389

Zel'Dovich, Y. B. and Novikov, I. D.: 1964, *Soviet Physics Doklady* **9**, 246

Chapter 2

X-RAY NATURE OF 51 LINER NUCLEAR SOURCES WITH *Chandra*

We report the results from a homogeneous analysis of the X-ray (Chandra ACIS) data available for a sample of 51 LINER galaxies selected from the catalogue by Carrillo et al. (1999) and representative of the population of bright LINER sources. The nuclear X-ray morphology has been classified by their nuclear compactness in the hard band (4.5–8.0 keV) into 2 categories: active galactic nuclei (AGN) candidates (with a clearly identified unresolved nuclear source) and starburst (SB) candidates (without a clear nuclear source). Sixty percent of the total sample are classified as AGNs, with a median luminosity of $L_X(2-10\ keV) = 2.5 \times 10^{40}\ erg\ s^{-1}$*, which is an order of magnitude higher than for SB-like nuclei. The spectral fitting allows us to conclude that most of the objects need a non-negligible power-law contribution. When no spectral fitting can be performed (data with a low signal-to-noise ratio), the color-color diagrams allow us to roughly estimate physical parameters, such as column density, temperature of the thermal model, or spectral index for a power-law, and therefore to better constrain the origin of the X-ray emission. The X-ray morphology, the spectra, and the color-color diagrams together allow us to conclude that a high percentage of LINER galaxies, at least* $\approx 60\%$*, could host AGN nuclei, although contributions from high-mass X-ray binaries or ultra-luminous X-ray sources cannot be ruled out for some galaxies.*

2.1 Introduction

Active galactic nuclei (AGN) produce enormous luminosities in extremly compact volumes. Large luminosity variations on time scales from years to hours are common (e.g. Leighly, 1999). The combination of high luminosity and short variability time scales implies that the power of AGN is produced by phenomena that are more efficient in terms of energy release per unit mass than ordinary stellar processes (Fabian, 1979).

A quantitative definition of what constitutes an active galaxy is perhaps not very useful, since galaxies showing low-level activity (e.g. Heckman, 1980; Stauffer, 1982; Hawley and Phillips, 1980) may be in either a pre- or post- eruptive stage, so may yield important clues into the origin and evolution of nuclear activity. The question of whether similar unification ideas can also apply to low-luminosity AGNs (LLAGNs), which make up the vast majority of the AGN population, has been explored (see Barth, 2002). In this sense, LLAGNs might constitute a perfect laboratory for investigating the connection between galaxies in which the central black holes are active and those in which they are quiescent. However, such AGNs may be difficult to identify because of extinction (e.g. Keel, 1980; Lawrence and Elvis, 1982) or contamination by star-forming processes in circumnuclear regions (e.g. Veron et al., 1981). The number of weak AGNs increases every time deep searches are made. Heckman (1980) (see also Heckman et al., 1980; Ho et al., 1997) has shown that one third of a complete sample of 'normal' galaxies exhibit signs of nuclear activity.

LINERs (low-ionization nuclear emission-line regions) were originally defined as a subclass of these LLAGNs by Heckman (1980) and are characterized by optical spectra dominated by emission lines of moderate intensities arising from gas in lower ionization states than classical AGNs. LINERs where defined as galaxies whose spectra satisfy $[\mathrm{OII}]\lambda3727/[\mathrm{OIII}]\lambda5007 \geq 1$ and $[\mathrm{OI}]\lambda6300/[\mathrm{OIII}]\lambda5007 \geq 1/3$ (Heckman, 1980). These LINERs typically are less luminous than powerful Seyferts and QSOs. It is still unclear whether all LINERs are essential AGNs at all, but if LINERs represent the low-luminosity end of the AGN phenomenon, they are the nearest and most common examples, and their study is essential for understanding AGN demographics and evolution. One fundamental question that needs to be addressed is whether the nuclear emission of these galaxies results from starbursts or accretion onto super-massive black holes (SMBHs).

The low luminosity of these nuclear sources makes them difficult targets for observational studies, even in very nearby galaxies. The origin of the optical narrow emission lines of LINERs has long been a source of controversy because the optical line ratios can be reproduced reasonably well by models based on a variety of different physical mechanisms, including shock heating (Fosbury et al., 1978; Dopita et al., 1996), photo-ionization by a non stellar continuum (Ferland and Netzer, 1983; Halpern and Steiner, 1983), photo-ionization by a young starburst containing Wolf-Rayet stars (Filippenko and Halpern, 1984; Terlevich and Melnick, 1985; Barth and Shields, 2000), or photo-ionization by hot stars (Filippenko and Terlevich, 1992; Shields, 1992).

One would expect that information coming from different spectral ranges could help disentangle and eventually classify the LINER family. However, the study of

data at different wavelengths has provoked even more discussion. The UV imaging surveys by Barth et al. (1998) and Maoz et al. (2005) (see also Pogge et al., 2000) found nuclear UV emission in ∼25% of the LINERs that were observed. About half of them appear point-like at the resolution of *HST* and thus are good candidates for being genuine LLAGNs with non-stellar continua. Barth et al. (1998) show that the low UV detection rate is primarily due to dust obscuration of the nuclei. Thus, the majority of LINERs probably have UV sources in their nuclei (which could be either AGNs or young-star clusters), but in most cases the UV sources lie behind large amount of dust to render it visible. Therefore, the foreground dust plays an important role in blocking our view of the central engines. A UV-variability campaign that monitored 17 known UV-bright LINERs by Maoz et al. (2005) found that almost all objects varied on either short or long timescales, indicative of an AGN component.

Since the nuclei of LINERs may be very heavily obscured, observations in UV, optical, near-infrared, and even the far-infrared may not penetrate the dust to reach the nucleus. The most important recent data constraining the nature of LINER nuclei have come from radio and X-rays surveys because it is possible in these spectral regions to detect central engines that are completely obscured in the optical and UV. In a VLA survey, Nagar et al. (2000) found that 64% of LINER 1 and 36% of LINER 2 have compact radio cores (Nagar et al., 2005). The objects bright enough for VLBI observations at 5GHz were studied by Falcke et al. (2000) (see also Filho et al., 2004); all showed compact, high-brightness-temperature cores, suggesting that an AGN, rather than a starburst, is responsible for the radio emission. Moreover, the core radio fluxes have been found to be variable by a factor of up to a few in about half of the ∼10 LINERs observed several different times over 3 years (Nagar et al., 2002). A radio survey looking for 1.3 cm water mega-maser emission, an indicator of dense circunnuclear molecular gas, detected LINER nuclei at the same rate as type 2 Seyfert nuclei (Braatz et al., 1997). Such mega-maser emission is seen only in AGNs. Some LINERs have indications of a Seyfert-like ionization cone oriented along their radio axis (Pogge et al., 2000).

X-ray observations provide another direct probe of the central engines. Pure starburst galaxies, at low redshift, do not exhibit unresolved hard X-ray (2.0-8.0 keV) nuclei. In contrast, starbursts such as M82 have extended hard X-ray emission from both diffuse gas and unresolved X-ray binaries (Griffiths et al., 2000). The detection of a hard X-ray continuum, as well as Fe K emission (Iyomoto et al., 1996; Ishisaki et al., 1996; Terashima et al., 1998; Terashima, 1999; Terashima et al., 2000; Roberts et al., 1999; Jimenez-Bailon et al., 2005; Streblyanska et al., 2005), indicate AGN activity. Only a reduced number of X-ray observations of LINER 2s have been performed so far. X-ray observations with *Einstein* and *ROSAT* were limited to soft energies, where heavily obscured AGNs are difficult to detect. The *ROSAT HRI* images show

compact soft X-ray ($\leq$ 2 keV) emission in 70% of the LINERs and Seyfert galaxies (Roberts and Warwick, 2000). Nevertheless, the lack of spectral information, low spatial resolution, and inadequate bandpass of these observations cannot distinguish the thermal emission of the host galaxy from the emission from the AGN. These problems are overcome by *Chandra*, whose spatial resolution is 10 times superior to that of the *ROSAT HRI*, thus allowing us to resolve the emission at lower physical sizes.

In this paper we present a homogeneous analysis of a sample of LINERs observed by *Chandra* and examine the probable ionization mechanism in LINERs. The paper is organized as follows. In Sect. 2.2 we summarize the *Chandra* and *HST* observations and describe the galaxy sample. Image and spectral reduction and analysis of X-ray data and *HST* imaging are reported in Sect. 2.3. We discuss the origin of the X-ray emission in our sample in Sect. 2.4. Finally, a summary of our findings is presented in Sect. 2.5.

2.2 The Sample and the data

The starting list for the sample selection has been the multi-wavelength catalogue of LINERs (MCL) compiled by Carrillo et al. (1999). The MCL includes most of the LINER galaxies known until 1999, providing information on broad-band and monochromatic emission from radio frequencies to X-rays for 476 objects classified as LINERs. The initial galaxy sample was constructed by using the *Chandra* archive to select all the galaxies in MCL with Advanced CCD Imaging Spectrometer (ACIS[1]) observations already public in November 2004, which yielded a set of 137 out of the 476 galaxies.

The optical classification was reanalyzed (by using the line-ratio diagrams by Veilleux, 1987), and 15 objects were eliminated from the sample due to misclassification in MCL; 5 of them appear to be Starburst systems (NGC 1808, NGC 3077, ESO 148-IG002N, ESO 148-IG002S, and NGC 253), 6 are Seyfert-like galaxies (NGC 4258, MRK 0266SW, 3C452, NGC 4565, NGC 4501, and NGC 3079), and 4 are transition objects (NGC 0224, NGC 0404, AN 0248+43B, and NGC 4303). For the selected sample, we noticed that data with exposure times shorter than 10 ksec had less than 25 counts in the 0.5-10.0 keV energy range. Therefore, only data with longer exposure times were taken into account. The final sample, with high-quality data and optical re-identification as LINER nuclei, amounts to 51 objects. Almost all objects (except NGC 3607, NGC 3608, NGC 3690B, NGC 4636, NGC 5746, and NGC 6251)

[1]Comprising two back-illuminated CCD chips and eight front-illuminated CCD chips of 1024 pixels square, with a plate scale of 0.″492 pixel^{-1}.

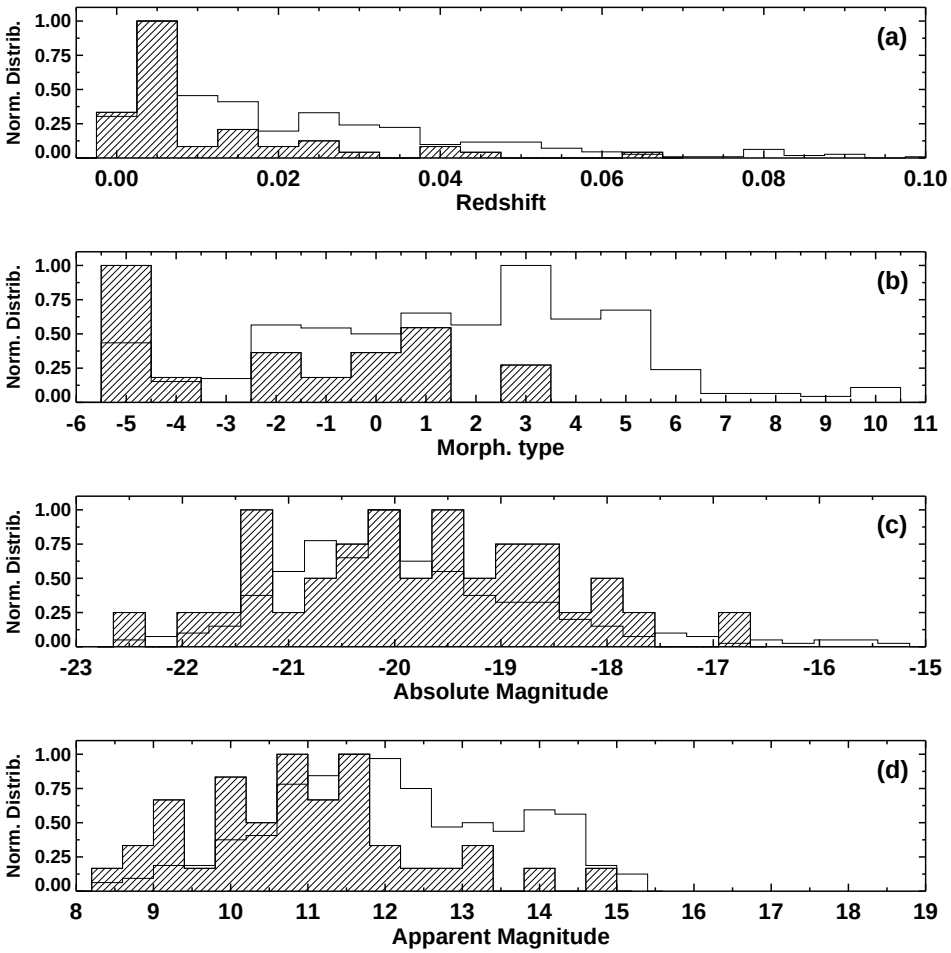

Figure 2.1: *(a) Redshift, (b) morphological types (from the RC3 catalog: t<0 are for ellipticals, t=0 for S0, t=1 for Sa, t=3 for Sb, t=5 for Sc, t=7 for Sd, and t>8 for Irregulars), (c) absolute magnitudes, and (d) apparent magnitudes distribution for the total sample of LINERs in MCL (empty histogram) and for our X-Ray sample (full histogram), normalized to the peak in each sample.*

were observed with ACIS-S mode. The 51 galaxies were observed between August 2000 and April 2004. A list of the objects, including the details of their observations, is provided in Table 2.1 in which name (Col. 1), X-ray position in right ascension and declination (Cols. 2 and 3), X-ray radii selected for the nuclear sources (Col. 4) and offset with respect to the 2MASS coordinates (Col. 5), *Chandra* Observational

Identifier (Col. 6), and exposure time after removal of background flares (Col. 7) are given.

The data provided in Table 2.2 were extracted from Carrillo et al. (1999) and include properties of the host galaxies such as: source name (Col. 1), redshift z (Col. 2), distances (Col. 3), spatial scale at the distance of the galaxy (Col. 4), source radii of the selected X-ray nuclear source regions (Col. 5), B magnitude (Col. 6), E(B-V) (Col. 7), and morphological type (Col. 8). The codes for the assumed distances correspond to those extracted from (a) Ferrarese and Merritt (2000), (b) from assuming a cosmology with $H_o = 75\ km\ s^{-1}\ Mpc^{-1}$ and $q_o = 0$, (c) Tonry et al. (2001), (d) Tully (1998), and (e) Karachentsev and Drozdovsky (1998).

In Fig. 2.1, from top to bottom, the normalized redshifts, morphological types and absolute and apparent magnitudes distributions are shown for the MCL catalogue (empty histogram) and the X-ray sample (filled histogram). In the MCL catalogue, the z distribution shows that most of the LINERs are hosted in nearby galaxies (Fig. 2.1a); the Hubble-type histogram shows that host galaxies of LINERs are mainly normal spirals (Fig. 2.1b) with a median B magnitude of $M_B = -20.0 \pm 1.5$ (Fig. 2.1c). It has to be noticed that, whereas the redshift and absolute magnitude distributions are very similar to those of the total sample, the X-ray selected sample resides mostly in the earliest Hubble-type galaxies. This bias might be produced by the way in which these galaxies have been selected for observations: they are part of guaranteed and open-time programs with differing scientific goals. In Fig. 2.1d the bias produced by the apparent magnitude selection can be seen. Most of the galaxies in the X-ray sample come from the bright LINER sample catalogued by Ho et al. (1997), but for some particular and peculiar cases that were observed because of their interest: NGC 6240, UGC 08696, and UGC 05101 belong to the class of ultraluminous infrared galaxies (ULIRGs); CGCG 162-010 is the central cluster galaxy in Abell 1795; and NGC 0833 (Arp 318B) lies in a Hickson compact group, HCG 16. Therefore we believe that this sample can be considered representative only of the bright galaxy population but not for all the LINER population. It should be noticed, for instance, that the sample does not include the strong IR emitters, which seem to be a large percentage of all known LINERs (Veilleux et al., 1999; Masegosa and Marquez, 2003); in fact, the LINER galaxies in our X-ray sample with far IR data from the IRAS Point Source Catalogue appear to be rather faint IR emitters with an average IR luminosity of $10^{10} erg\ s^{-1}$.

Together with *Chandra* X-ray data, we make use of the high-resolution, optical information provided by *HST* imaging for our sample galaxies. Out of the total 51, 45 galaxies have been observed with WFPC2 in several different programs, so with different filters and exposure times. The observations in the red broad filter F814W were selected (31 galaxies), but observations in other broad filters (mainly F606W

and F702W) were used otherwise. The summary of the selected data is given in Cols. 8, 9, and 10 in Table 2.1, including filter, proposal identifier and exposure time of the archival data. In Sect. 2.3.2 the analysis of *HST* data is described.

2.3 Data reduction and analysis

2.3.1 X-ray Data

Level 2 event data from ACIS instrument were extracted from *Chandra* archive. The data products were analyzed in a uniform, self-consistent manner using the *CXC Chandra Interactive Analysis of Observations* (CIAO[2]) software version 3.1. The spectral analysis was performed with *XSPEC*[3] (version 11.3.2). Background "flares" (periods of enhanced count rate) can seriously affect the scientific value of an observation, increasing the count rate by a factor of up to 100. These "flares" are due to low-energy protons interacting with the detector. Such flares were observed everywhere in the orbit, including near the apogee, so there cannot be due to the Van Allen belt effect. Images could be dominated by the background if time intervals affected by flares are not excluded. The exposure time was therefore processed to exclude background flares, using the task LC_CLEAN.SL[4] in source-free sky regions of the same observation. For all observations (except NGC 4486, excluded in the spectral analysis), the nuclear counts were insufficient for photon pile-up to be significant.

Spectral analysis

To distinguish which emission mechanisms are involved in these objects and to estimate the X-ray luminosity, a careful analysis of the spectra based on model fittings was performed. X-ray luminosities in the hard band (2.0–10.0 keV) can otherwise be estimated following Ho et al. (2001), who assume a power law with a spectral index of 1.8 for the SED. Since most of our objects show a clear compact nuclear source, suggestive of an AGN nature, large departures from a power-law index 1.8 are not expected (see Terashima, 1999). Nevertheless, this approach has been shown to be too simplistic in some cases (i.e. NGC 3077, by Ott et al., 2003), hence our attempt to calculate luminosities *via* the spectral fitting.

To extract the nuclear spectra, we first determined the position of the nuclear sources as catalogued by near-IR observations from the *Two Micron All Sky Survey*

[2]See http://asc.harvard.edu/ciao
[3]See http://cxc.heasarc.gsfc.nasa.gov/docs/xanadu/xspec/
[4]see http://cxc.harvard.edu/ciao/download/scripts/

(2MASS) (see Fig. 2.2). NGC 4636 and NGC 4676B were not found in the near-IR catalog, so their positions from NED were taken as reference.

Nuclear spectra were extracted from a circular region centered in the object using regions defined to include as many of the source photons as possible, but at the same time minimizing contamination from nearby sources and background. In order to determine appropriate source extraction, the radius of each source aperture on the detector was estimated as follows: (1) 4–6 pixels for a single source, (2) 3–4 pixels for objects with few knots close to the nucleus to exclude nearby sources, and (3) ≥ 6 pixels for sources dominated by diffuse emission, since a good signal-to-noise (S/N) is required for extracting the spectra. Positions from near-IR in 48 out of the 49 objects with 2MASS coordinates have been found to agree with the X-ray nuclear position within the X-ray radii of the sources, consistent with the astrometry accuracy provided by these data. The offset for NGC 4696 is 7.5″, about double the size of the nuclear extraction, but NGC 4696 presents a complex morphology with a number of knots embedded in strong diffuse emission in the hard and soft X-ray energies, making identification of the nuclear source ambiguous. X-ray radii and offsets are included in Col. 4 and 5 in Table 2.1. The spatial regions sampled by the nuclear extractions generally cover the innermost 500 pc, but in a few cases (7) they are larger than 1 kpc (see Col. 5 in Table 2.2). Nevertheless, the number of these more distant objects is evenly distributed between AGN and SB candidates (see below,) and therefore no bias in the results is expected due to this effect.

The background region is defined either by a source-free circular annulus close to the nuclei (cases (1) and (3)) or by several circles around the sources (case (2)), in order both to take the spatial variations of the diffuse emission into account and to minimize effects related to the spatial variation of the CCD response. For each source, we extracted spectra from each of the datasets. Response and ancillary response files were created using the CIAO MKACISRMF and MKWARF tools.

The spectra were fitted using XSPEC v.11.3.2. To be able to use the χ^2 as the fit statistics, the spectra were binned to give a minimum of 20 counts per spectral bin before background subtraction. The task GRPPHA included in FTOOLS software has been used for this purpose. Of the 51 objects in our sample, 23 fulfill this criterion (hereafter the spectral fitting (SF) subsample). In the SF we excluded any events with energies above 10 keV or below 0.5 keV.

Since our aim is to try to disentangle whether the emission mechanism might be due to an AGN or to star formation, two models were used: a single power-law and a single-temperature optically-thin plasma emission (MEKAL or Raymond Smith (Raymond and Smith, 1977) model. For each object, five models were attempted: (1) power-law (PL), (2) Raymond-Smith (RS), (3) MEKAL (ME), (4) PL+RS, and (5) PL+ME. The power-law plus thermal combinations (models 4 and 5) have been

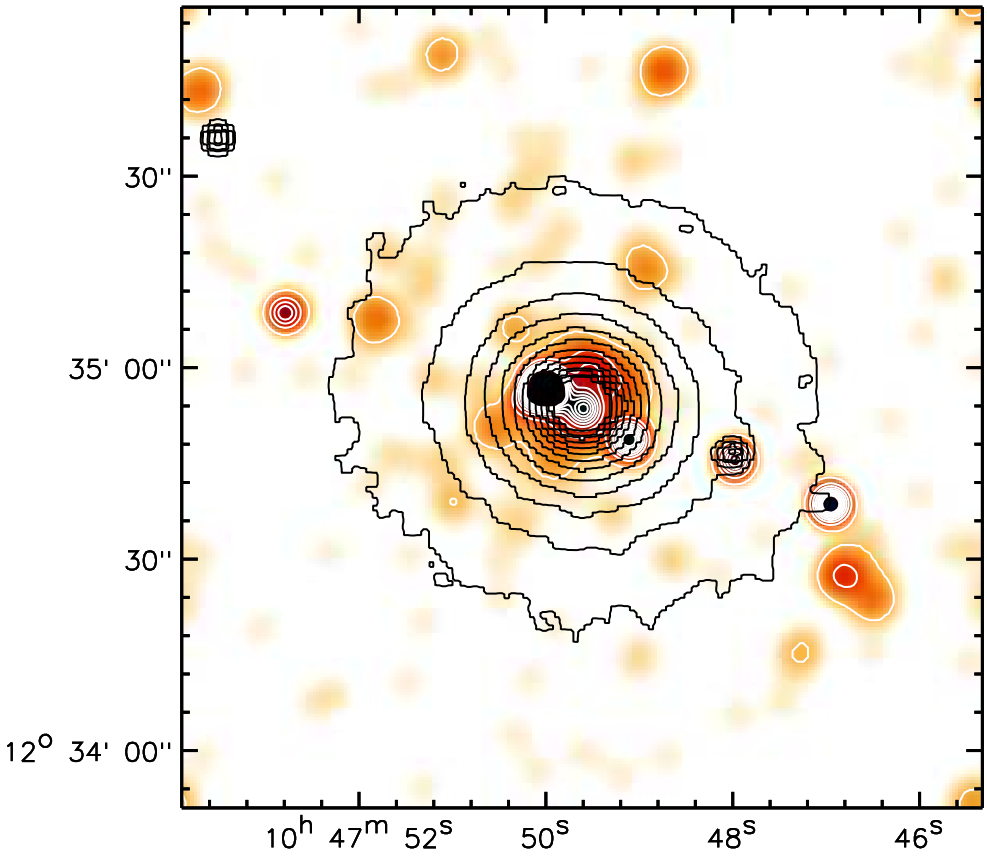

Figure 2.2: *NGC 3379 smoothed X-Ray image from 0.9 to 1.2 keV with K-band contours from 2MASS over-plotted.*

taken into account to include the possibility that the two emission mechanisms are relevant. We did not expect large differences between MEKAL and Raymond-Smith models. Furthermore, we included a photoelectric absorption law (called 'phabs' in XSPEC software) to fit the absorbers in the line of sight with a cross section called 'bcmc' by Balucinska-Church and McCammon (1992). To decide which is the best-fit model for each nuclear source, we selected the model that gives χ^2 reduced closer to 1. The results from the spectral fittings for the five models are given in Table 2.3. The best model was chosen as that with the best χ^2-reduced statistic. When a combination of power-law plus thermal model is the best model, we used the FTEST task to determine whether the inclusion of an additional component is needed or a single thermal or power-law model could be a good fit for the spectrum. The selected

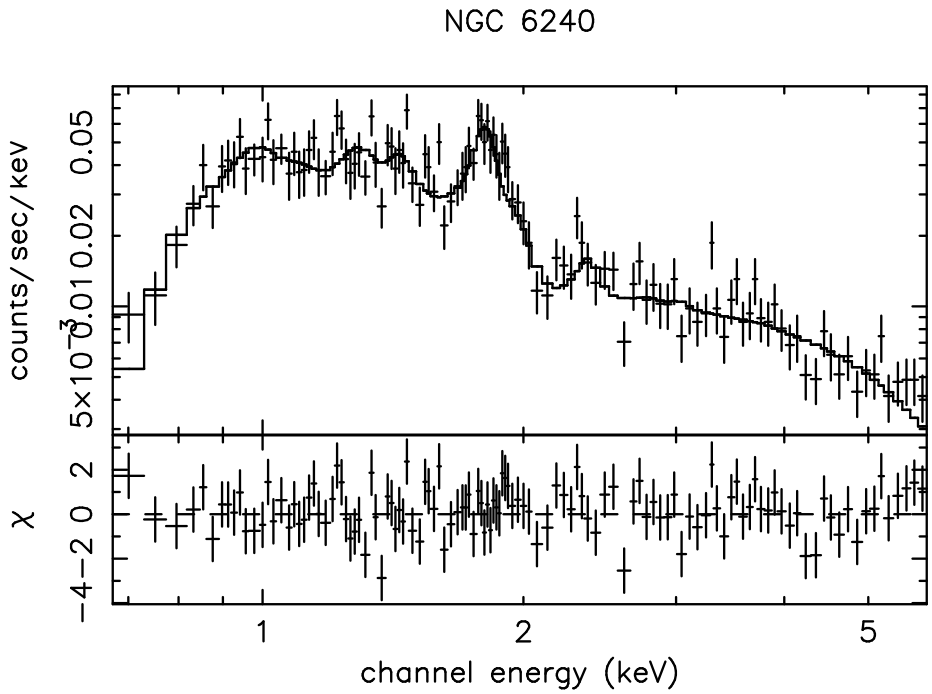

Figure 2.3: *The ACIS-S spectrum of NGC 6240 is shown in the top panel. The solid line corresponds to a power-law plus Raymond-Smith model. Residuals from the fitting are presented in the bottom panel.The spectral fitting for all the galaxies in the SF subsample are shown in the electronic edition.*

model for each case is indicated by an asterisk.

NGC 6240 was selected as a model example of the process since the number counts for this source guarantee that the errors in the fitting due to S/N are minimal. The resulting parameters for the different fittings of NGC 6240 are shown in Table 2.3. The best-fit model is a combination PL+RS (Fig. 2.3, *Top*) with the best χ^2-reduced statistic (Fig. 2.3, *Bottom*). The soft X-ray spectrum (below 2 keV) shows clear signatures of thermal emission well-described by a optically thin plasma, which probably originates in a powerful starburst. Strong, hard X-ray emission is also detected, and its spectrum above 3 keV is extremely flat.

NGC 4261 was not included in the SF subsample due to the spectral complexity that results in unphysical parameters for any of our five models. The fits are statistically acceptable for all the remaining objects ($\chi^2_\nu \sim 1$), except in NGC 2681 ($\chi^2_\nu = 0.54$) and NGC 7130 ($\chi^2_\nu = 1.43$). The resulting fittings are plotted in Fig. 2.3 in the electronic edition for the whole SF subsample.

Only for NGC 6482 did the single thermal model provide a statistically acceptable fit ($\chi^2_\nu \sim 1$). Therefore, in 22 of 23 objects the power-law component is needed to describe the hard-energy spectrum observed, indicating a non-negligible non-thermal contribution in our sample. Seven objects are described with a single power-law (NGC 3690B, NGC 4374, NGC 4395, NGC 4410A, NGC 5494, NGC 4696, NGC 5746). Although a combination of thermal plus power law model gives smaller χ^2 for NGC 3690B, NGC 4410B and NGC 5746, the thermal component is not needed to describe their spectrum according to the FTEST tool. Furthermore, the same spectral indices are found, including error bars, assuming a single power-law or a combination with a thermal model (see Table 2.3). Nevertheless, in 15 out of 22 objects strong residuals remained at low energies indicating that a single power-law model was not completely satisfactory. In these cases, a significant improvement was achieved when a power-law plus optically thin emission was considered, according to the FTEST tool. It has to be noted that ME+PL and RS+PL with solar metallicity give the same fitted parameters within the error.

Table 2.4 gives the mean (Col. 1), median (Col. 2), and mean standard deviation (Col. 3) for the logarithm of the 2-10 keV band luminosity, column density, temperature, and spectral index (the first row for each entry). Galactic absorptions can be derived from the HI map (Dickey and Lockman, 1990) using the NH tool provided by the HEASARC. The SF sample of LINERs with enough counts to constrain absorption, showed column densities exceeding the expected N_H from HI map, ranging between (0.01-2.87)$\times 10^{22}$ cm^{-2}, with a mean value of 3.5×10^{20} cm^{-2}. Therefore it is very likely that LINERs generally are much more absorbed than the Galactic value indicated. The mean temperature from the SF subsample is kT=0.64$\pm$0.17 keV, while the mean spectral index is Γ=1.89$\pm$0.45. The spectral fits provide 2.0-10.0 keV unabsorbed luminosities for the SF subsample, thereby expanding a wide range between 1.4×10^{38} erg s^{-1} and 1.5×10^{42} erg s^{-1} with a mean value of 1.4×10^{40} erg s^{-1}.

In order to get a luminosity estimation of the whole sample, we obtained a count rate to flux conversion factor between 2.0–10.0 keV, assuming a power-law model with a spectral index of 1.8 and the Galactic interstellar absorption (3×10^{20} cm^{-2}). In Fig. 2.4, the estimated 2.0–10.0 keV luminosity of the SF subsample is plotted ($L_{estimated}$) against the value obtained from the direct integration of the spectrum (L_{fitted}). The luminosities are correlated well, always less than a factor of 3 within the real luminosity. Monte Carlo simulations have granted confidence of the proposed calibration at 95% level. We therefore inferred a self-consistent estimate of the 2.0–10.0 keV luminosities for the whole sample, using the SED fitting for the SF subsample and from this calibration otherwise. In Table 2.5 we list the 2–10 keV fluxes (Col. 2) and unabsorbed luminosities (Col. 3) of the nuclear sources for the whole sample, using the empirical calibration (denoted by 'e' in Col. 4) or the spec-

tral fitting (denoted by 'f' in Col. 4). In those cases where the flux and luminosity were obtained from the spectral fitting the estimated errors are also included.

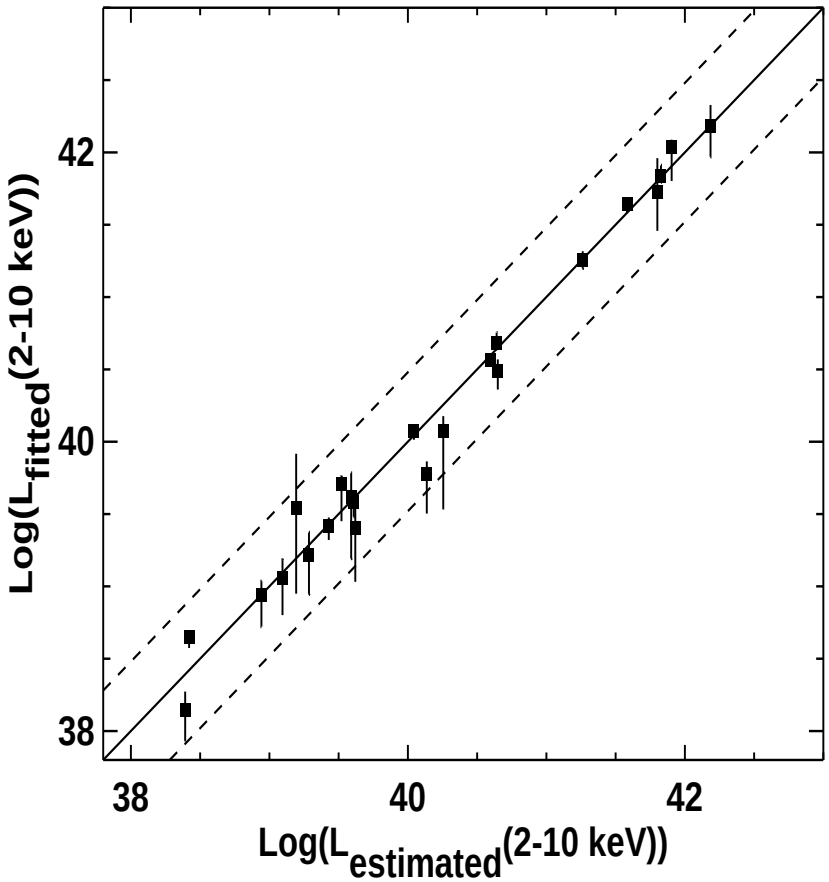

Figure 2.4: *Luminosities estimated assuming a power law with an spectral index of 1.8 (Log(Lx_estimated)) versus luminosities computed through the spectral fittings (Log(Lx_fitted)). Objects with the same results with both methods are shown with the continuous line; dashed lines are luminosities from our estimate, which are 3 times higher and lower than the luminosities from spectral fitting, respectively (Log(Lx_estimated)=Log(Lx_fitted)±0.48). SF subsample.*

Image analysis

In order to gain insight into the emission mechanisms in the whole sample, we studied the X-ray morphology of the sources in six energy bands: 0.6–0.9, 0.9–1.2, 1.2–1.6, 1.6–2.0, 2.0–4.5, and 4.5–8.0 keV. The bands were chosen to maximize the detection, as well as to obtain a good characterization of the spectra, as is illustrated in the next section. In the last energy band (4.5–8.0 keV), the range from 6.0 to 7.0 keV was excluded to avoid possible contamination due to the FeK emission line (the corresponding band will be called (4.5–8.0)* hereafter). The most common emission features in the 2-10 keV band of AGN spectra are those of iron between 6.4–6.97 keV (depending on the ionization state of Fe), related to the reflexion in the accretion disk. Only 5 objects (NGC 5194, UGC 08696, NGC 6240, NGC 7130, and UGC 05101) have a point-like source after continuum extraction. Although UGC 08696 shows a compact nuclear source in this energy band, it cannot be directly associated with an FeK line because it has a broad high-energy component (See Appendix B of UGC 08696 for details).

The images were adaptively smoothed (the smoothing depends on the count rate of the pixel vicinity) with the CIAO task CSMOOTH, using a *fast Fourier transform* algorithm and a minimum and maximum significance S/N level of 3 and 5, respectively. Smoothing algorithms are useful when the count-rate of the diffuse emission is close to the background level. Adaptively smoothed images were not used for any quantitative analysis, but only for a morphological classification. The images in the four bands 0.6–0.9, 1.6–2.0, 4.5–8.0*, and 6–7 keV are given in Figs. 2.5 and 2.6 (for all the galaxies, see published paper).

Since we focus our attention on the nuclear sources, no attempt has been made to fully characterize the flux and the spectral properties (when possible) of the extranuclear sources, whose study is beyond the scope of the paper. As a first insight into the nature of LINERs, we have taken the existence of an unresolved compact nuclear source in the hard band (4.5–8.0 keV) as evidence of an AGN. Of course, detection of broad emission lines at multi-wavelength observations will be needed to assess their nature. The sample has been grouped into 2 categories:

- **AGN candidates:** We include all the galaxies with a clearly identified, unresolved nuclear source in the hard band (4.5–8.0)* keV. In Fig. 2.5 we show NGC 4594, as an example of AGN candidate, where a clear point-like source exists in the hardest band (*Center-Left*). Fifty nine percent (30/51) of our sample galaxies have been classified as AGN-like nuclei; the median luminosity is $L_X(2-10\,\mathrm{keV}) = 1.2 \times 10^{40}\,\mathrm{erg\,s^{-1}}$, whereas it is $L_X(2-10\,\mathrm{keV}) = 3.8 \times 10^{39}\,\mathrm{erg\,s^{-1}}$ for the whole sample (Fig. 2.7).
- **Starburst candidates:** Here we include all the objects without a clearly iden-

tifiable nuclear source in the hard band. In Fig. 2.6 we show the images of CGCG 162-010 as an example of these systems. Note that there does not appear to be a nuclear source in the hardest energy band (*Center-Left*). Fourty one percent (21/51) of the sample of LINERs falls into this category. The median luminosity is $L_X(2-10\ \mathrm{keV}) = 1.7 \times 10^{39}\ \mathrm{erg\ s^{-1}}$ (Fig. 2.7).

The classification of each object is included in Col. 6 in Table 2.5. The histogram of the derived X-ray luminosities for the two groups is presented in Fig. 2.7. The median luminosity is higher for AGN like nuclei ($\sim$ 10 times), but a clear overlap exists in the range ($[10^{37} - 10^{42}]\mathrm{erg\ s^{-1}}$). We do not find clearcut differences in luminosities between AGN and SB candidates.

With respect to the SF subsample (see Table 2.4), the spectral index and its standard deviation in AGN-like (18/23) is $\Gamma = 1.7 \pm 0.3$, and the temperature is $kT = 0.6 \pm 0.2$ keV. In the SF subsample, 5 objects have been classified as SB-like nuclei (namely, NGC 4438, NGC 4696, CGCG 162-010, NGC 5846, and NGC 6482). Excepting NGC 6482, fitted with a single thermal model, all the objects were fitted by including a power-law component. The origin of this power-law contribution from the presence of an AGN remains therefore an open possibility for our sample objects. A full discussion is made in Sect. 2.4 and in the Appendix B for individual sources.

Color-color diagrams

We explored the possibility of using X-ray colors to obtain information about the emission mechanism in these objects. Previous works have explored this possibility in an AGN sample (Ceballos and Barcons, 1996), X-ray surveys of galaxies (Hasinger et al., 2001), X-ray source populations in galaxies (Grimm et al., 2005; Heinke et al., 2005), or diffuse emission in star-forming galaxies (Strickland et al., 2004). We built color-color diagrams, using different hardness ratios of the form $Q_i = (H_i\text{-}S_i)/(H_i+S_i)$ (i = A, B, C), with the same bands used for imaging classification: S_A=0.6-0.9 keV, H_A=0.9-1.2 keV (Q_A), S_B=1.2-1.6 keV, H_B=1.6-2.0 keV (Q_B), and S_C=2.0-4.5 keV, H_C=(4.5-8.0)* keV (Q_C). These six bands defining three hardness ratios were selected after verifying that they are specially well-suited to maximize the differences between a thermal plasma model and emission in the form of a power law; while at the low energy range (below 2 keV), the thermal contribution becomes more significant, at higher energy ranges a larger flux is expected whenever the power law contribution is needed. The use of the same bands as for the imaging analysis allows direct quantification of the properties of the nuclear sources used for morphological classification.

Counts were extracted directly from the source, and background event files described for the spectral extraction. Error bars were computed as one standard deviation in the count rates. Hardness ratios were calculated for all the bands in which the measured error in the count rates were less than 80%.

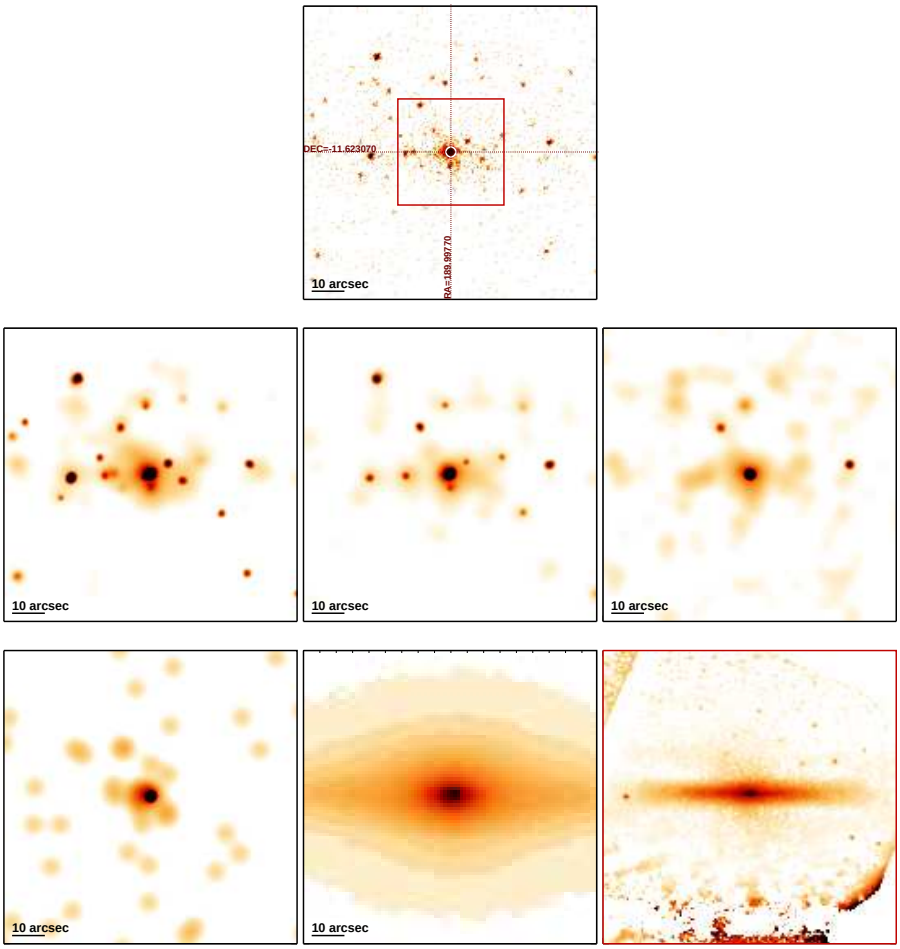

Figure 2.5: *Images for the AGN candidate NGC 4594. The top image corresponds to the 0.6-8.0 keV band without smoothing. The following 4 images correspond to the X-ray bands 0.6–0.9 (*Center-Left*), 1.6–2.0 (*Center-Center*), 4.5–8.0** *(*Centre-Right*) and 6.0–7.0 keV (*Bottom-Left*). The 2MASS image in Ks band is plotted in the top box. The enlarged view of the region marked as a rectangle in the* Center-Right *image is the sharp-divided* HST *optical image in the filter F814W (*Bottom-Right*). All the galaxies are presented in the electronic edition.*

In Fig. 2.8 we plot Q_A versus Q_B (*Top-Right*), Q_B versus Q_C (*Top-Left*), and Q_A versus Q_C (*Bottom*). To compare the observed X-ray colors of the sources with different spectral shapes, we computed the colors of pure power law, Raymond Smith model, and a combination of both models. In both models, photoelectric absorption by cold

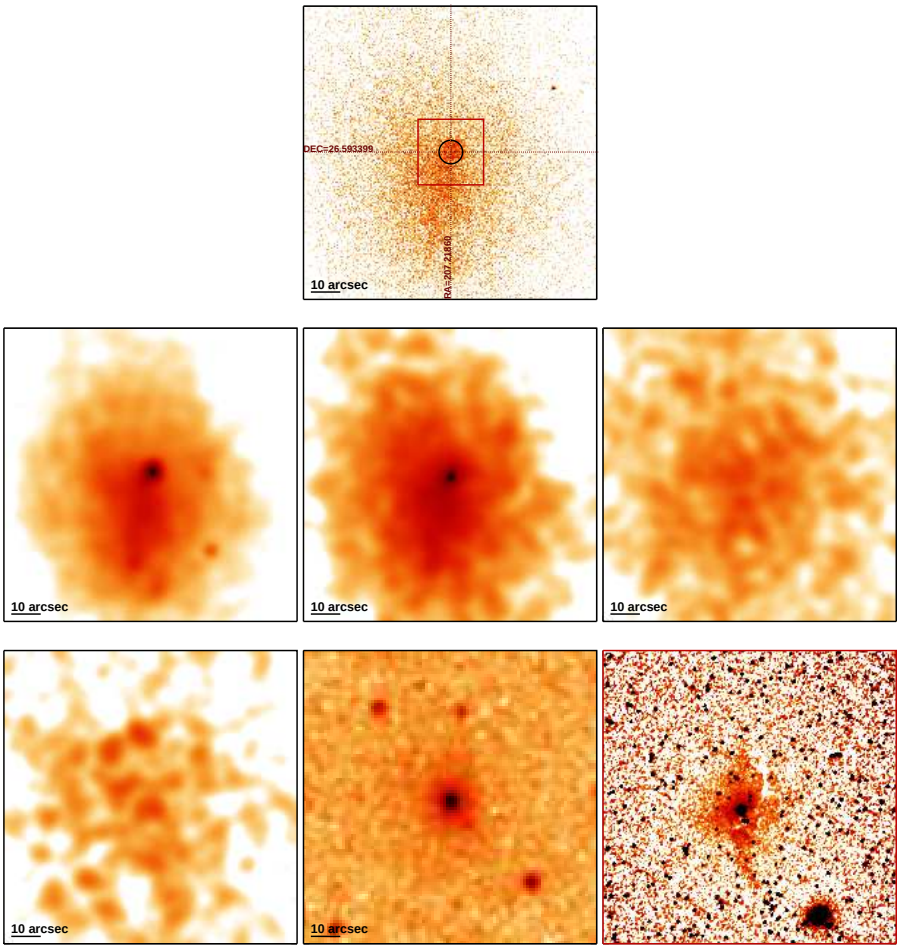

Figure 2.6: *Images for the SB candidate CGCG 162-010. The top image corresponds to the 0.6-8.0 keV band without smoothing. The following 4 images correspond to the X-ray bands 0.6–0.9 (*Center-Left*), 1.6–2.0 (*Center-Center*), 4.5–8.0** *(*Centre-Right*) and 6.0–7.0 keV (*Bottom-Left*). The 2MASS image in Ks band is plotted in the top box. The enlarged view of the region marked as a rectangle in the* Center-Right *image is the sharp-divided* HST *optical image in the filter F814W (*Bottom-Right*). All the galaxies are presented in the electronic edition.*

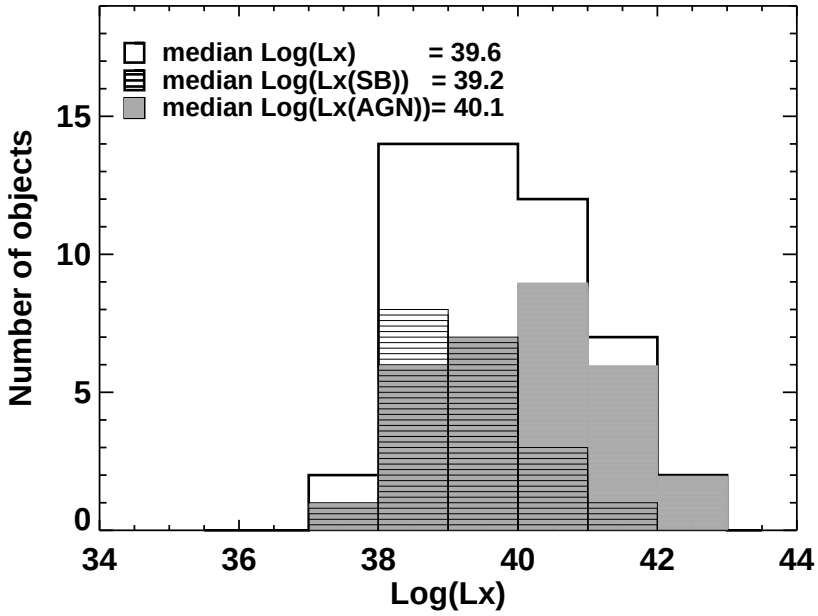

Figure 2.7: *Luminosity (2-10 keV) histogram for our whole sample (empty histogram), objects classified as AGN candidates (grey histogram), and for SB candidates (dashed histogram). Median values are included.*

gas was included. For each column density (N_H) and model parameter (Γ or kT) pair, XSPEC generated a model spectrum that was then multiplied by the effective area at each energy (obtained from the response matrices for the actual data) and sampled appropriately. The output was thus a model of the number of photons detected per second as a function of energy, which could be compared with the observations. These simulated data were then used to calculate the hardness ratio of ACIS-S observations as a function of N_H, Γ, and/or kT. Grids of points were determined for parameters $\Gamma = 0.4 - 2.6$ and kT = 0.1–4.0 keV for the power law (Fig. 2.8 dark grey grid) and Raymond-Smith (Fig. 2.8 light grey grid) models, respectively, and for $N_H = [1 - 30] \times 10^{20}$ cm^{-2} in the single models. Several grids were computed in the combination model with $N_H = [10^{20}, 10^{21}, 10^{22}, 10^{23}]$ cm^{-2}, with 50% of contribution from both models at 1 keV. Note that variation in the column density in the combination model result in a shifting of the grid up and right, with higher values at low energies (Fig. 2.8). This effect is smaller for low N_H, but it is quite noticeable for higher column densities ($N_H > 10^{22}$ cm^{-2}). In Fig. 2.8, two combination models are given for $N_H = 10^{20}$ cm^{-2} (*Left*) and 10^{22} cm^{-2} respectively. Therefore, these

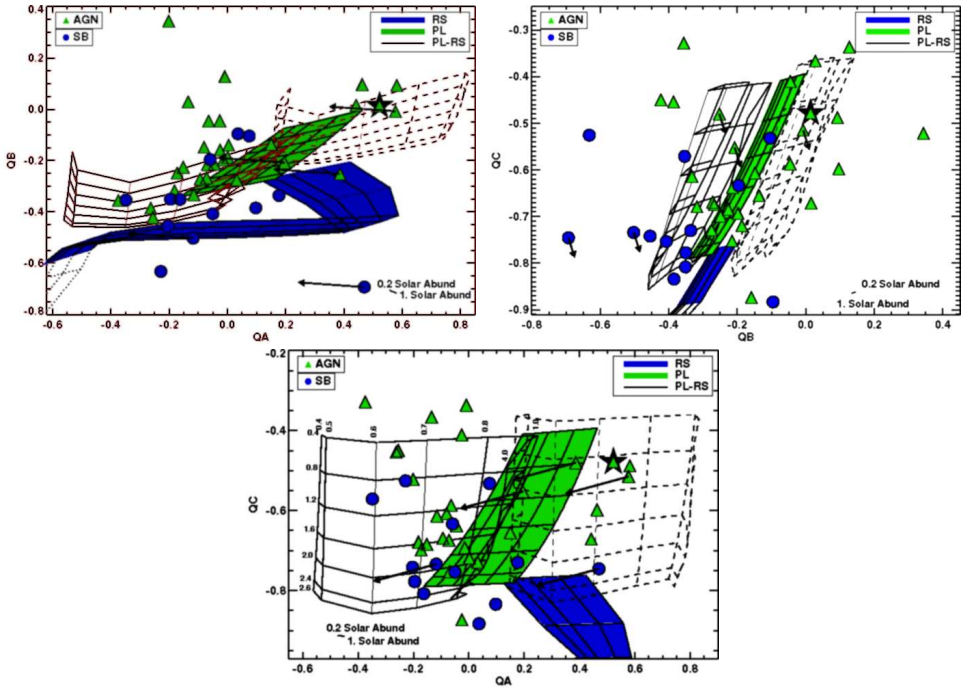

Figure 2.8: *Color-color diagrams for an RS model (light-grey filled grid), PL model (dark-grey filled grid), and combination model (empty grid) for* $N_H = 10^{20}$ cm^{-2} *(continuum line) and* $N_H = 10^{22}$ cm^{-2} *(dashed line). Light-grey triangles are AGN-like objects and dark-grey circles are SB-like objects. NGC 6240 is plotted as a black star. The grids were calculated for* $\Gamma = 0.4$ to 2.6 *(from up to down) for PL model, for* $kT = 0.4$ to 4.0 keV *(from down to up in the thermal model and from left to right in the combination model) for the RS model and* $N_H = (0.5 - 30.) \times 10^{20}$ cm^{-2} *(from left to right) in the single-model case.*

grids could help to distinguish whether these objects are strongly obscured. For less energetic colors, both absorption effects and thermal contribution become more important, thus both column density and temperature could be better estimated. The highest energetic color (Q_C) is better suited to estimate the power law contribution. Note that the grid of models were computed for ACIS-S observations, but for the objects observed with ACIS-I (namely, NGC 3608, NGC 3690B, NGC 4636, NGC 5746, and NGC 6251) an arrow was included to represent the correction to be done to take the different sensitivities into account. This correction is important at low energies (i.e. Q_A) where the different sensitivity of both instruments become more important. The parameters were estimated with this correction. Although our grid of models

has been computed for solar abundances, the variation between solar abundance and 0.2 below solar abundance is always smaller than other effects (see Fig. 2.8).

In Fig. 2.8 we plot Q_A versus Q_B (*Top*), Q_B versus Q_C (*Center*) and Q_A versus Q_C (*Bottom*) for the subset of 42 sources for which the three Q_i values are available. The resulting Q_A, Q_B, and Q_C values are given in Table 2.7.

The reliability of hardness ratio diagrams can be tested by comparing their results with those given by the more conventional method of fitting models to the observed spectrum. For this comparison, we used first the bright source NGC 6240 (Fig. 2.8), since we determined the spectral parameters from the spectral fitting with high reliability. Considering the error bars, the spectral index estimated from color diagrams is Γ = [0.8-1.0], the temperature is kT = 0.7-0.8 keV, and the column density may be high ($N_H \sim 10^{22} cm^{-2}$). From the spectral fitting parameters we have obtained $\Gamma = 1.03^{+0.14}_{-0.15}$, $kT = 0.76^{+0.06}_{-0.06}$ keV, and $N_H = 1.1^{+0.1}_{-0.1} \times 10^{22} cm^{-2}$, well within the range of values provided by the estimation from the color-color diagrams.

The method has then been tested with the SF subsample. The parameters estimated from color-color diagrams are included in Table 2.6, where the name is shown in Col. 1; SB/AGN classification is shown in Col. 2; the chosen model is included in Col. 3 for the objects in the SF subsample, the absorbed column density from the fitted spectra (Col. 4) or color-color diagram estimation (Col. 5); as well as power law index (Cols. 6 and 7); and temperature (Cols. 8 and 9). Note that the column density estimation from color-color diagrams has been included as "$\sim 10^{22}$" only those cases where color-color diagrams provide a clear indication of high obscuration.

Seventeen objects (12 SB-like and 5 AGN candidates) do not have any estimation from the color-color diagrams. 9 of them have large errors in the highest energy band, and consequently Q_C is not reliable enough. The remaining 8 objects (ARP 318B, NGC 1052, NGC 4395, NGC 4494, MRK 266NE, UGC 08696, NGC 5866 and NGC 6482) fall out from at least two of the three color-color diagrams: NGC 1052, MRK 0266NE and UGC 08696 have a too high value for Q_C (> 0.3), most probably due to the contamination of jet-related X-ray emission (see Appendix B on the individual sources). ARP 318B, NGC 4494 and NGC 6482 are out of the grid because of low values of Q_C; NGC 6482 is the only galaxy resulting to be best fitted by a single thermal component, and its position in the color-color diagrams is indeed closer to the thermal model. The situation for the other two galaxies, NGC 4395 and NGC 5866, is however less clear.

Fig. 2.9 (*Top*) shows the comparison of the temperature obtained from the spectral fitting with that estimated from color-color diagrams. Excepting NGC 0315, NGC 6251 and IC 1459 that show temperatures estimated from color-color diagrams much higher than the fitted ones, it can be concluded that color-color diagrams provide a good temperature estimation. NGC 0315 has been fitted by Donato et al.

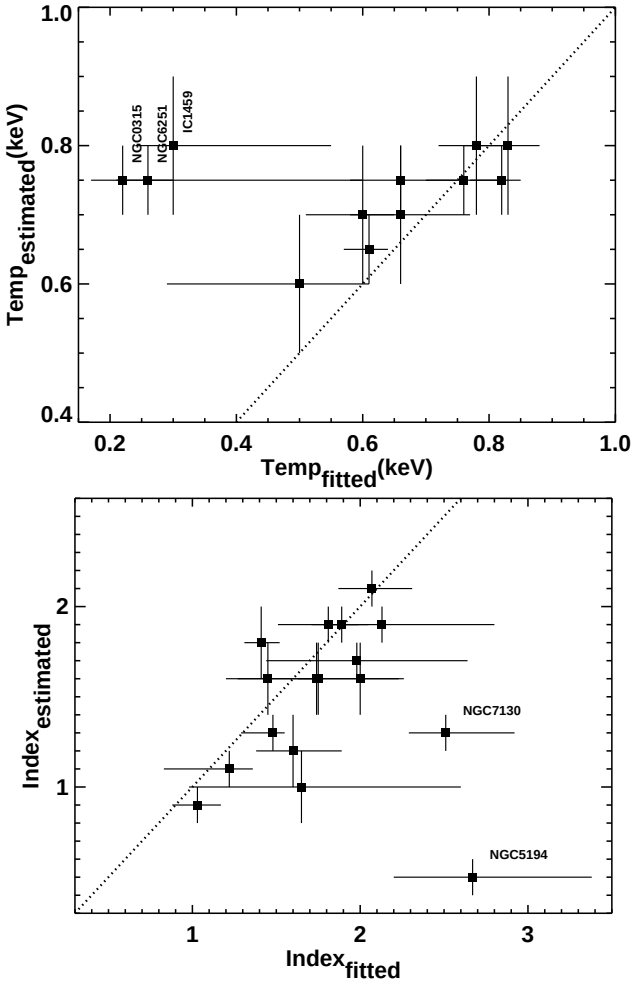

Figure 2.9: *Temperature (*Top*) and spectral index (*Bottom*) comparison between estimated from color-color diagram values and fitted values. Objects with large departures from the fitted value have been included with the names. Details are given in the text.*

(2004) with kT=0.51 keV, much closer to our estimated temperature. Considering the extended structure and the jet-like emission in this galaxy, differences in the back-

ground subtraction methods may explain such a discrepancy. Note that NGC 6251 and IC 1459 are the only galaxies for which PL+RS and PL+MEKAL fitting provide very different values of kT; even if PL+MEKAL model is selected in these cases, the statistical estimator is not so sharp and, if a PL+RS is considered, the resulting temperatures are in good agreement with the estimated ones.

Fig. 2.9 (*Bottom*) shows the spectral index correlation between the values from the spectral fitting versus those estimated from color-color diagrams. The spectral indices estimated from the color-color diagrams result to be somewhat underestimated, but within less than 40% of the fitted values, excepting for NGC 5194 and NGC 7130, for which the fitted values are rather unrealistic. All the estimated column densities corresponds with the fitted ones.

Therefore, it seems reasonable to conclude that the information provided by color-color diagrams can be used as a rough estimate of the physical parameters describing the X-ray SED of our targets, this method being specially valuable for the objects where no spectral fitting can be made.

For the whole sample, the main general conclusion from the diagrams in Fig. 2.8 is that the spectra of LINERs cannot be described in general by a single power law. At least two components are needed: a hard power law and a soft component represented by a thermal model. We find that the best fit MEKAL model for a soft component in most of LINER galaxies has kT between 0.6-0.8 keV and it appears quite clearly that an AGN power law component may be needed for most of them, since Q_C values are in general too high for a thermal emission. In particular, AGN-like nuclei show systematically high Q_C values; SB-like nuclei mostly fall in the power law region as well. This result further emphasizes that the AGN contribution in our sample of LINER galaxies might be rather important.

2.3.2 HST-imaging analysis

To gain some insight into the nature of the X-ray emission, especially for the LINERs without a detected compact component, we have searched for the optical counterpart of the X-ray compact sources. The high spatial resolution provided by *HST* observations is needed for our purposes. In order not to make our analysis dependent on the model used for describing the underlying host galaxy, we have decided to remove such a contribution by applying the sharp-dividing method to the original *HST* images. This technique has been proved to be very well suited to remove large-scale galactic components and therefore is a very convenient way to look for subtle, small-scale variations and discuss the possible presence of both dust extinguished and more luminous regions (Sofue et al., 1994; Marquez and Moles, 1996; Marquez et al., 2003; Laine et al., 1999). It consists on applying a filtering to the orig-

inal image, with a box size several times that of the PSF FWHM, and then dividing the original image by the filtered one. The resulting so-called sharp-divided images are plotted in Figs.2.5 and 2.6 (*Bottom-Right*). We note that absolute astrometry has been performed by using the position of the coordinates of those objects in the images cataloged by USNO, excepting NGC 4410, NGC 4596 and NGC 4696 for with the position of the central galaxy had to be taken from the RC3 catalogue due to the lack of reference stars.

According to the appearance of the central regions, two main groups can be distinguished: (a) galaxies with compact nuclear sources, when a knot coincident with the central X-ray source is detected in the sharp-divided image (see for instance catalogue of images for NGC4552) (C in Col. 7, Table 2.5); 35 objects fall into this category; and (b) galaxies with dusty nuclear regions, when dust-lanes like features are seen but no central knot is detected (see for instance catalogue of images for NGC4438) (D in Col. 7, in Table 2.5) with 8 objects belonging to this class. Two galaxies, namely NGC 3608 and NGC 4636, cannot be classified because of saturation or rather low S/N.

2.4 Discussion

According to their X-ray morphologies in the hard band (4.5-8* keV), the LINER galaxies in our sample were classified into two broad main categories. We defined AGN-like nuclei as those objects displaying a hard nuclear point source, coincident with a 2MASS position of the nucleus. Of the 51 galaxies in the LINER sample, 30 meet this criterion (59%). We called SB candidates those lacking a hard nuclear source because they either 1) lack an energetically significant AGN or 2) contain highly obscured AGN with column densities higher than $\sim 10^{23}\mathrm{cm}^{-2}$. Ho et al. (2001) classify the X ray morphology into four categories: class (I) objects exhibit a dominant hard nuclear point source (2-10 keV), class (II) objects exhibit multiple hard off-nuclear point sources of comparable brightness to the nuclear source, class (III) objects reveal a hard nuclear point source embedded in soft diffuse emission, and class (IV) objects display no nuclear source. Dudik et al. (2005) analyzed a sample of IR-Bright LINERs and classified the objects following the same scheme. Because we can assimilate classes (I) and (III) into our group of AGN-candidates and that their class (II) is equivalent to our SB candidates, they obtained similar percentages of AGN-like objects since 51% (28/55) of their LINERs fall into classes (I) and (III), and 13% (7/55) were classified as belonging to class (IV). A detailed comparison of the 18 galaxies in common shows that 15 objects share the same classification. The odd classification for the remaining three nuclei (NGC 3628, NGC 4696, and

CGCG 162-010) can be attributed to our use of a harder X-ray band for the detection of unresolved nuclear sources.

As seen in Fig. 2.7, the 2-10 keV luminosities of the AGN-like in our LINER sample range from 10^{37}erg s^{-1} to 10^{43}erg s^{-1}, while SB-like luminosities range from 10^{37}erg s^{-1} to 10^{42}erg s^{-1} and both classifications overlap in the range 10^{37}erg s^{-1} to 10^{42}erg s^{-1}. The 2-10 keV X-ray luminosities were calculated by fitting the SED between 0.5-10 keV in the SF subsample and assuming a generic power-law model with photon index $\Gamma = 1.8$ and the Galactic absorption otherwise. A similar method is proposed by Ho et al. (2001) who used an empirical estimate from the count rates. Satyapal et al. (2005), by using Ho estimate of the luminosity, have found a range in luminosities from $\sim 2 \times 10^{38}$ to $\sim 1 \times 10^{44}$erg s^{-1} for the AGN LINERs. For the 31 objects in common, the resulting luminosities agree within the errors but only for 3 objects. The differences can be attributed to the presence of bright FeK lines in the spectra of NGC 5194 and NGC 6240; this is clearly the case for NGC 6240, with the highest luminosity they derive (Vignati et al., 1999, obtain $\sim 1 \times 10^{44}$erg s^{-1} once the FeK line contribution is included in the fit as a Gaussian component). For NGC 3245 the luminosity we estimate is much fainter than the one given by them; we stress however that our estimation agrees very well with that of Filho et al. (2004) (see Appendix C on images).

We found that LINER X-ray SED can be interpreted as a combination of a soft thermal component with temperatures of about 0.6-0.8 keV, maybe due to circumnuclear star formation and a hard power law produced by an obscured AGN. Regarding the soft component, Ptak et al. (1999) based on *ASCA* data found that similar models apply to starbursts that usually show a temperature higher than 0.6 keV. This result is confirmed with *Chandra* observations for starburst galaxies by Ott et al. (2005) and Grimes et al. (2005), while Teng et al. (2005) find that the best-fit MEKAL model for the soft component in Seyfert 1 galaxies has kT$\sim$0.25 keV and that the low temperatures of the Seyfert 1 galaxies suggest that starburst activity may not be the dominant energy source of the soft component. The same conclusion was made by Boller et al. (2002) for F01572+0009. LINER nuclei have similar values to what we expect in starbursts, indicating that star formation activity may be the dominant energy source of the soft component. Except in 2 objects (NGC 0315 and IC 1459), the temperature obtained from the spectral fit is about 0.6 keV, therefore hinting that a starburst component can be inferred in most cases. The spectral index in the sample galaxies for which the power-law component is needed to fit spectra (22 objects) range from $\sim$1.0 till 4.3 with a mean value of 1.9 (see Table 2.4 for a detailed analysis). In 3 out of 22 objects (NGC 4494, NGC 5746, and NGC 6240), the slope tends to be significantly flatter ($\Gamma < 1.4$) than what is typically observed in AGNs. Ptak et al. (2003) explain this flattening in a *Compton-thick* scenario as due

to a combination of reflection from optically thick central material, scattering from optically-thin (unlikely to be highly ionized) material and leakage of X-ray through patches in the obscuring material. Nevertheless, we recall that simple models have been used to test the need of power-law and/or thermal components to fit these spectra, and some artifacts may be consequently produced for more complex situations where the presence of several components is absolutely needed to explain the spectral features.

Our sample can be compared to X-ray observations of nearby Seyfert 2 galaxies. In their recent survey of nearby Seyfert galaxies taken from the compilation by Ho et al. (1997), Cappi et al. (2006) analyze *Chandra* data for 27 Seyfert 1 and 2 galaxies (mainly Seyfert 2), obtaining values for the power-law index of 1.56 for type 1 Seyfert and 1.61 for type 2, which are not too far from our quoted median value for LINERs (1.75 ± 0.45). Their most remarkable result is that the range of column densities they find for Seyferts is quite similar to what we find for LINERs, with N_H between 10^{20} and 10^{22} cm^{-2}. Finally, when a thermal component is needed (in 15 out of the 27 galaxies), kT is found in the range between 0.2-0.8 keV, as is the case for our LINERs, although their spectral fitting technique is quite different from ours: they fit the spectra between 2-10 keV by a single power law, and then a thermal component is added to the cases where the extrapolation from the power law to lower energies (below 2 keV) results in a soft excess. The mean value for their (2-10 keV) luminosities ($10^{39.8}$ ergs s^{-1} for Seyfert 2 and 10^{41} ergs s^{-1} for Seyfert 1) is also in good agreement with our estimated mean value ($10^{40.16}$ erg s^{-1}). These results are at variance with those by Guainazzi et al. (2005), with luminosities higher than 10^{41} ergs s^{-1} for a sample of 49 Seyfert 2. Note, however, that their galaxies are more heavily obscured than those in the analysis by Cappi et al. (2006). On the other hand, the comparison of our data with those reported by Mateos et al. (2005) and Gallo et al. (2006) for galaxies at higher redshifts, results in power-law spectral indices fully consistent with ours: note that, even if their galaxies are more luminous, more obscured objects, they obtain Γ values varying between 1.7 for AGN type 1 and 1.9 for type 2 AGNs. Hence this comparison leads to the conclusion that it is not clear whether LINERs in the X-ray represent a lower scaled version of AGN activity. For a more definitive conclusion, a full, homogeneous analysis using the same methodology and similar selection criteria is therefore needed. In this respect, we have collected archival X-ray data for a sample of Seyfert galaxies that will be studied with the same methods we used for LINERs, and their analysis will be the subject of a forthcoming paper.

To gain some insight into the nature of the X-ray emission, especially for the LINERs without a detected compact component, we searched for the optical counterpart of the X-ray compact sources. We note that all the galaxies classified as AGN

by their X-ray imaging show compact nuclei (28 galaxies). Among those showing SB X-ray morphology (17 objects), 8 galaxies (NGC 3507, NGC 3607, NGC 4438, NGC 4676A, NGC 4676B, NGC 4698, CGCG 162-010, and NGC 5846) show dusty nuclear sources; 5 out of 8 showing low column densities and 3 (NGC 3507, NGC 3607, NGC 4676B) without any estimated column density. The remaining 7 galaxies classified as SB candidates nevertheless host compact nuclear sources in the optical (namely NGC 3245, NGC 3379, NGC 4314, NGC 4459, NGC 4596, NGC 4696, and NGC 7331). Both NGC 3608 and NGC 4636 remain unclassified. We stress that NGC 4696 is obscured at X-rays (like some of the objects in Chiaberge et al., 2005), so in this case the AGN would only be visible in the optical; i.e., a low optical extinction has to be coupled with a relatively high X-ray column density. This kind of situation might be explained by, e.g., unusual dust-to-gas ratios (Granato et al., 1997) or by the properties of the dust grains (Maiolino, 2001). Moreover, in NGC 4696 a broad balmer Hα line was detected by Ho et al. (1997). NGC 3245 also shows evidence of its AGN nature from the optical, with double-peaked Hα and [NII] profiles indicative of the presence of spatially unresolved rapid rotation near the nucleus (Barth et al., 2001) and the radio frequencies, where an unresolved nuclear radio source is detected (Wrobel and Heeschen, 1991). Unresolved nuclear radio cores have also been found for NGC 7331 (Cowan et al., 1994) and NGC 4314 (Chiaberge et al., 2005). For NGC 4596, Sarzi et al. (2001) have determined a black hole mass of 7.8 x 10^7 M$\odot$ from an STIS kinematic analysis of the source. Thus it appears that even in the cases we called SB candidates, the existence of a mini or an obscured AGN cannot be completely ruled out, since the region mapped by these observations may correspond to distances from the center that are not as close to the AGN, which may be much more obscured; they would map regions much farther out instead, which would explain that thermal mechanisms most probably due to star-forming processes seem to be the dominant energy source in these systems (Rinn et al., 2005).

The unambiguous determination of the presence of an AGN, however needs a detailed study of the individual sources to discard the eventual mechanisms producing unresolved hard X-ray nuclear morphologies originating in star-forming processes. Eracleous et al. (2002) argue in favor of the SB nature of NGC 4736 (see Appendix B). In particular, the contribution of high mass X-ray binaries (HMXBs) and ultra-luminous X-ray sources (ULXs)[5] needs to be estimated, since they are expected to dominate the emission of star-forming galaxies (see for instance the data for the Antennae by Zezas et al., 2002). The high X-ray luminosity found for a ULX in the star-forming galaxy NGC 7714 (Soria and Motch, 2004), amounting to 6×10^{40} erg s^{-1}, proves how important the contamination produced by such objects can be if they are found at nuclear positions, making this analysis extremely difficult and

[5]See Fabbiano (2006) for a review of the different X-ray source populations in galaxies.

implying that only indirect proofs can be invoked. Hence, we should keep in mind that contribution from ULXs cannot be discarded.

Stellar population synthesis will help investigating the relevance of the contribution from HMXBs since they are short-lived (10^{6-7} years). Data on population synthesis exist for 14 out of the 51 galaxies of Fernandes et al. (2004) and Delgado et al. (2004). Only in one galaxy, NGC 3507, a large contribution of a young population with age $< 10^8$ years ($\sim$ 27%) does exist. For the remaining galaxies, the contribution is always less than 3%. Then it is not clear that HMXBs may be an important ingredient in the nuclear X-ray emission. It has to be noticed that the mapped region of the optical data (1.5″) is the same as used in our X-ray analysis.

Data at radio frequencies are also crucial for understanding the AGN character of LINERs. An unresolved nuclear radio core and flat continuum spectra have been taken as the best evidence for their AGN nature (see Nagar et al., 2005; Filho et al., 2004, for a full discussion). Thirty-three out of the 51 objects have been observed at radio-frequencies (Filho et al., 2000, 2002, 2004; Nagar et al., 2000, 2002, 2005; Falcke et al., 2000). From these 33 objects, 16 galaxies seem to be detected with good confidence, but only upper limits can be given for 17 objects. Three out of the 16 radio detected (NGC 3628, NGC 4636, and NGC 5846) show a radio-steep spectrum that can be taken as evidence of their Starburst nature. The remaining 13 galaxies show AGN nature according to radio diagnosis; 9 of them show X-ray AGN morphology and 4 have an SB classification (NGC 3245, NGC 4459, NGC 5866, and NGC 7331). In principle, compact radio cores should appear as compact sources at X-ray frequencies, unless the X-ray nucleus is obscured due to large amounts of dust; nevertheless, this does not seem to be the case for these 4 SB galaxies with compact radio cores since they do not appear to have high column densities. Thus the reason for the discrepancy needs to be found. For NGC 3245 and NGC 4459, the AGN radio classification was made by (Filho et al., 2004) on compactness arguments based on 5-arcsecond-resolution radio imaging, so much better resolution data are needed. NGC 7331 also needs better data due to the marginal nuclear source identification. The only clear radio-AGN is NGC 5866. A closer inspection of this source (see our Fig. 5) shows that a weak nuclear source can be identified in the hard band. Then we should use the available data to conclude that AGN radio cores appear as AGN-like systems at X-ray frequencies.

Additional evidence of an AGN nature comes from variability studies. Maoz et al. (2005) use *HST* UV data for a sample of 17 galaxies showing LINER emission in their nuclei and compact nuclear UV sources, and find significant variability in all but four objects with peak-to-peak amplitudes up to 50%. For the 7 objects in common with their sample (NGC 1052, NGC 4486, NGC 4552, NGC 4579, NGC 4594, NGC 4736, and NGC 5055), five (excepting NGC 1052 and NGC 5055) show time

variability that hints at their AGN nature. We note that all of them belong to our class of AGN candidates.

It is clear from the preceding analysis that a multi-frequency approach is needed to gain insight into the AGN nature of these galaxies, but since most of the hard emission between 4.5-8 keV is coming from an unresolved nuclear source, the natural explanation seems to be that the X-ray unresolved nuclear source is due to a low-luminosity AGN. Low-luminosity AGNs in the nucleus of early type galaxies being quiescent at optical or UV frequencies have been invoked by Soria et al. (2006b) and Soria et al. (2006a) due to the existence of SMBHs in the nucleus of these galaxies and in their X-ray properties. Therefore, since a SMBH has been detected for most of the LINERs (Satyapal et al., 2005), the AGN nature of the X-ray emission seems to be appropriate.

2.5 Conclusions

The primary goal of our study was to determine the X-ray nuclear characteristics of a statistically significant sample of LINERs that were selected based on their optical emission properties (Veilleux, 1987). Archival *Chandra* ACIS data were used to study the nature of our sample, with the aim of analyzing whether the observed X-ray emission is consistent with AGN-powered emission and whether star-forming emission can be ruled out in our sample or not. We first classified the nuclear morphology, according to the compactness in the hard band, as AGN candidates whenever a clearly identified unresolved nuclear source is found in the 4.5 to 8.0 keV band and as SB candidates otherwise. Color-color diagrams for the whole sample and the spectral analysis for the SF subsample lead to the following conclusions:

1. Morphologically, 30 out of 51 of LINERs can be classified as AGN-like candidates.

2. A thermal plus power-law model with a median temperature of $\sim$0.6 keV (0.6-0.9 keV from color-color diagrams) and median spectral index of $\sim$1.9 (1.4-1.7 from color-color diagrams) reproduces the X-ray energy distribution better. This indicates a non-negligible contribution of a non-thermal component in our sample.

3. Luminosities in the energy band 2-10 keV span a wide range between 1.4×10^{38} erg s^{-1} and 1.5×10^{42}erg s^{-1} with a mean value of 1.4×10^{40}erg s^{-1}. For the two groups separately, AGN candidates range between 7.8×10^{37} erg s^{-1} and 1.5×10^{42} erg s^{-1}, while SB candidates range between 8.7×10^{37} erg s^{-1} and 5.3×10^{41} erg s^{-1}. The broad overlap in X-ray luminosities indicates that this

parameter cannot be used to distinguish between AGN and SB candidates in LINERs.

4. We stress that color-color diagrams are a valid tool for roughly estimating the values of the physical parameters used in the models for the spectral fitting by providing important clues to the amount of nuclear absorption. Their use is especially interesting when spectral fitting is not possible.

5. The estimated column densities from either the spectral analysis or color-color diagrams show that it is very likely that LINERs are generally significantly obscured, especially in SB candidates. This result is consistent with the hypothesis that they may host an obscured AGN.

6. All the galaxies classified as AGN by the X-ray imaging show compact nuclei at the resolution of *HST* images. Eight out of 14 galaxies showing SB X-ray morphology have dusty nuclear sources, indicating that the objects can be dust-obscured, in agreement with the X-ray analysis.

These new data offer some insight into the long-standing dispute about the nature of the ionizing source in LINER. Although contributions from HMXBs and ULXs cannot be ruled out for some galaxies, we can conclude that for a high percentage of LINERs, 59% at most, an AGN does exist in their nuclei. For the remaining 41%, their existence cannot be discarded based on the available data. Diagnostics at other wavelengths have to be explored to determine the possible contribution of an embedded AGN. Future papers will be devoted to studying whether a link exists in objects with higher activity levels by comparing the properties of our AGN-like LINER nuclei with those of a sample of Seyfert nuclei.

Note added in proof.- After submition of the current paper, Flohic et al. (2006) published an X-ray analysis of a sample of 19 LINERs observed with *Chandra*, 18 of which are also in our sample. They fitted the spectra for 8 objects and the spectral parameters, and luminosities derived from the spectral fitting are in good agreement with ours for the objects in common. They also conclude that in about 60% of the nuclear sources an AGN is present.

Acknowledgements

This work was financed by DGICyT grants AYA2003-00128 and the Junta de Andalucía TIC114. OGM acknowledges financial support by the Ministerio de Educación y Ciencia through the Spanish grant FPI BES-2004-5044. MAG is supported by the Spanish National program Ramón y Cajal. We thank X. Barcons and E.

Jimenez-Bailon for helpful comments, D.W. Kim for useful advice in data reduction, and J. Cabrera for providing us with the Monte Carlo simulations. This work benefited from fruitful previous work with A.C. Fabian and J.S. Sanders. We acknowledge D. Maoz for his valuable comments. This research made use of the NASA/IPAC extragalactic database (NED), which is operated by the Jet Propulsion Laboratory under contract with the National Aeronautics and Space Administration. We acknowledge an anonymous referee for her/his comments and advice on our work, which resulted in great improvement of the manuscript.

Table 2.1: *Observational details.*

	X-ray Position		X-ray	Offset	X-ray Obs.			HST Obs.	
Name	α (2000)	δ (2000)	Radii (arcsec)	2MASS (arcsec)	Obs.ID	Expt. (ks)	Filt.	Prop.ID	Expt. (s)
(1)	(2)	(3)	(4)	(5)	(6)	(7)	(8)	(9)	(10)
NGC 0315	00 57 48.9	+30 21 08.7	1.968	0.81	4156	52.3	F814W	6673	460
ARP 318A	02 09 38.5	−10 08 45.4	4.920	1.26	923	12.5	...	...	...
ARP 318B	02 09 42.7	−10 11 02.2	2.952	0.54	923	12.5	...	...	...
NGC 1052	02 41 04.8	−08 15 20.6	1.476	0.57	385	10.9	F555W	3639	1000
NGC 2681	08 53 32.8	+51 18 48.8	2.460	0.83	2060	78.3	F555W	4854	1000
UGC 05101	09 35 51.7	+61 21 11.1	2.952	0.61	2033	48.2	F814W	6346	800
NGC 3226	10 23 27.0	+19 53 54.6	1.476	0.26	860	46.3	F702W	6357	1000
NGC 3245	10 27 18.3	+28 30 27.2	1.968	0.59	2926	9.6	F702W	7403	140
NGC 3379	10 47 49.6	+12 34 53.7	1.968	0.20	1587	31.3	F814W	5512	1340
NGC 3507	11 03 25.3	+18 08 07.3	2.460	1.27	3149	38.0	F606W	5446	160
NGC 3607	11 16 54.6	+18 03 04.4	2.952	2.22	2073	38.4	F814W	5999	320
NGC 3608	11 16 58.9	+18 08 53.7	1.968	1.53	2073	38.4	F814W	5454	460
NGC 3628	11 20 16.9	+13 35 22.8	2.952	1.60	2039	54.8	...	...	...
NGC 3690B.....	11 28 30.9	+58 33 40.5	3.198	2.64	1641	24.3	F814W	8602	700
NGC 4111	12 07 03.1	+43 03 57.3	2.952	1.95	1578	14.8	F702W	6785	600
NGC 4125	12 08 06.0	+65 10 27.6	2.460	0.81	2071	61.9	F814W	6587	2100
NGC 4261	12 19 23.2	+05 49 30.4	3.444	1.49	834	31.3	F702W	5476	280
NGC 4314	12 22 32.1	+29 53 44.8	5.904	2.71	2062	14.5	F814W	6265	600
NGC 4374	12 25 03.7	+12 53 13.2	1.476	0.90	803	28.2	F814W	6094	520
NGC 4395	12 25 48.9	+33 32 48.4	1.476	0.78	5301	26.3	F814W	6464	2160
NGC 4410A	12 26 28.2	+09 01 10.8	1.968	1.00	2982	34.8	F606W	5479	500
NGC 4438	12 27 45.6	+13 00 33.0	2.952	2.26	2883	24.6	F814W	6791	1050
NGC 4457	12 28 59.0	+03 34 14.3	2.952	0.45	3150	35.6	...	...	...
NGC 4459	12 29 00.0	+13 58 41.7	1.968	1.17	2927	9.8	F814W	5999	320
NGC 4486	12 30 49.4	+12 23 28.3	2.460	0.35	2707	98.7	F814W	6775	1480
NGC 4494	12 31 24.1	+25 46 29.8	1.968	0.94	2079	15.8	F814W	6554	1800
NGC 4552	12 35 39.8	+12 33 23.3	2.460	1.91	2072	54.3	F814W	6099	1500
NGC 4579	12 37 43.5	+11 49 05.5	1.968	1.53	807	30.6	F791W	6436	600
NGC 4594	12 39 59.4	−11 37 23.0	1.476	0.71	1586	18.5	F814W	5512	1470
NGC 4596	12 39 56.0	+10 10 35.3	3.690	1.61	2928	9.2	F606W	5446	160
NGC 4636	12 42 49.8	+02 41 15.9	2.214	...	4415	74.1	F814W	8686	400
NGC 4676A	13 30 03.3	+47 12 41.4	3.936	1.31	2043	27.9	F814W	8669	320
NGC 4676B.....	13 30 04.6	+47 12 08.9	3.936	...	2043	27.9	F814W	8669	320
NGC 4696	12 48 48.8	−41 18 43.3	3.936	7.51	1560	47.7	F814W	8683	1000
NGC 4698	12 48 22.9	+08 29 14.6	2.214	0.71	3008	29.4	F814W	9042	460
NGC 4736	12 50 53.1	+41 07 13.2	1.476	0.82	808	46.4	F814W	9042	460
NGC 5055	13 15 49.2	+42 01 45.9	1.476	1.33	2197	27.7	F814W	9042	460
NGC 5194	13 29 52.8	+47 11 40.4	3.444	2.87	3932	45.2	...	...	...
MRK 0266NE...	13 38 17.9	+48 16 41.1	1.968	0.84	2044	17.4	F606W	5479	500
UGC 08696	13 44 42.1	+55 53 13.1	1.968	0.66	809	40.4	F814W	8645	800
CGCG 162-010 .	13 48 52.5	+26 35 36.3	3.936	1.59	493	19.6	F702W	5212	300
NGC 5746	14 44 56.0	+01 57 18.1	1.476	1.06	3929	36.8	F814W	9046	800
NGC 5846	15 06 29.2	+01 36 19.6	4.920	1.13	4009	24.0	F814W	5920	2300
NGC 5866	15 06 29.5	+55 45 46.1	4.428	2.22	2879	31.9	...	...	...
NGC 6251	16 32 31.9	+82 32 15.7	1.968	1.68	847	25.4	F814W	6653	1000
NGC 6240	16 52 58.9	+02 24 02.6	1.680	0.99	1590	36.7	F814W	6430	1200
IRAS 17208-0014	17 23 22.0	+00 17 00.6	2.460	1.04	2035	48.4	F814W	6346	800
NGC 6482	17 51 48.8	+23 04 18.9	2.460	0.46	3218	19.1	...	...	...
NGC 7130	21 48 19.5	−34 57 05.0	1.968	0.73	2188	36.9	F606W	5479	1900
NGC 7331	22 37 04.0	+34 24 56.0	1.968	1.75	2198	29.5	F814W	7450	170
IC 1459	22 57 10.6	−36 27 43.6	2.952	1.81	2196	51.8	F814W	5454	460

Table 2.2: *Host-galaxy properties.*

Name [1]	z [2]	Dist. [3]	Spatial Scale [4] (pc/arcsec)	Radii [5] (pc)	B [6]	E(B-V) [7]	Morph. Type [8]
NGC 0315	0.016465	65.8[b]	319.0	627.8	12.2	0.065	E
ARP 318A	0.013586	54.3[b]	263.3	1295.4	12.91	0.025	SAB(r)ab;pec
ARP 318B	0.012889	54.3[b]	263.3	777.3	13.69	0.025	(R')Sa;pec
NGC 1052	0.004903	19.4[c]	94.1	138.9	11.41	0.027	E4
NGC 2681	0.002308	17.2[c]	83.4	205.2	11.09	0.023	(R')SAB(rs)0/a
UGC 05101	0.039390	157.3[b]	762.6	2251.2	15.2	0.033	S?
NGC 3226	0.003839	23.6[c]	114.4	168.9	12.3	0.023	E2;pec
NGC 3245	0.004530	20.9[c]	101.3	199.4	11.7	0.025	SA(r)0
NGC 3379	0.003069	10.6[c]	51.4	101.2	10.24	0.024	E1
NGC 3507	0.003266	19.8[d]	96.0	236.2	11.73	0.024	SB(s)b
NGC 3607	0.003119	22.8[c]	110.5	326.2	10.82	0.021	SA(s)0
NGC 3608	0.003696	22.9[c]	111.0	218.4	11.7	0.021	E2
NGC 3628	0.002812	7.7[d]	37.3	110.1	14.8	0.027	Sb;pec;sp
NGC 3690B	0.010411	41.6[b]	201.7	645.0	...	0.017	GPair
NGC 4111	0.002692	15.0[c]	72.7	214.6	11.63	0.015	SA(r)0+:;sp
NGC 4125	0.004523	23.9[c]	115.9	285.1	10.65	0.019	E6;pec
NGC 4261	0.007372	29.4[c]	142.5	490.8	11.41	0.018	E2-3
NGC 4314	0.003212	9.7[d]	47.0	277.5	11.43	0.025	SB(rs)a
NGC 4374	0.003336	18.4[c]	89.2	131.7	12.1	0.040	I
NGC 4395	0.001064	4.2[e]	20.4	30.1	10.64	0.017	SA(s)m
NGC 4410A	0.025174	100.5[b]	487.2	958.8	14.92	0.024	S0;pec
NGC 4438	0.000237	16.8[d]	81.4	240.3	11.02	0.028	SA(s)0/a;p:
NGC 4457	0.002942	17.4[d]	84.4	249.1	11.76	0.022	(R)SAB(s)0/a
NGC 4459	0.004036	16.1[c]	78.1	153.7	11.32	0.046	SA(r)0+
NGC 4486	0.004276	16.1[c]	78.1	192.1	9.59	0.022	E+0-1;pec
NGC 4494	0.004416	17.1[c]	82.9	163.1	10.71	0.021	E1-2
NGC 4552	0.001071	15.4[c]	74.7	183.8	10.73	0.041	E
NGC 4579	0.005067	16.8[d]	81.4	160.2	10.48	0.041	SAB(rs)b
NGC 4594	0.003639	9.8[c]	47.5	70.1	8.98	0.051	SA(s)a
NGC 4596	0.006251	16.8[d]	81.4	300.4	11.35	0.022	SB(r)0+
NGC 4636	0.003653	14.7[c]	71.3	157.9	10.43	0.028	E/S0_1
NGC 4676A	0.022059	88.0[b]	426.6	1679.1	14.7	0.017	Irr
NGC 4676B	0.022039	88.0[b]	426.6	1679.1	14.4	0.017	SB(s)0/a;pec
NGC 4696	0.009867	35.5[c]	172.1	677.4	11.39	0.113	E+1;pec
NGC 4698	0.003342	16.8[d]	81.4	180.2	1.46	0.026	SA(s)ab
NGC 4736	0.001027	5.2[c]	25.2	37.2	8.99	0.018	(R)SA(r)ab
NGC 5055	0.001681	7.2[d]	34.9	51.5	9.31	0.018	SA(rs)bc
NGC 5194	0.001544	7.7[c]	37.3	128.5	8.96	0.035	SA(s)bc;pec
MRK 0266NE	0.028053	112.0[b]	543.0	1068.6	14.1	0.013	Compact;pec:
UGC 08696	0.037780	150.9[b]	731.6	1439.8	15.07	0.008	Ring galaxy
CGCG 162-010	0.063260	252.6[b]	1224.6	4820.0	15.2	0.013	cD;S0?
NGC 5746	0.005751	29.4[d]	142.5	210.3	11.29	0.040	SAB(rs)b?;sp
NGC 5846	0.006078	24.9[c]	120.7	593.8	11.05	0.055	E0-1
NGC 5866	0.002242	15.4[c]	74.7	330.8	10.74	0.013	S0_3
NGC 6251	0.023016	91.9[b]	445.5	876.7	13.64	0.087	E
NGC 6240	0.024480	97.8[b]	474.1	796.5	13.8	0.076	I0:;pec
IRAS 17208-0014	0.042810	171.0[b]	829.0	2039.3	15.1	0.344	...
NGC 6482	0.013176	52.6[b]	255.0	627.3	12.35	0.099	E
NGC 7130	0.016151	64.5[b]	312.7	615.4	12.98	0.029	Sa;pec
NGC 7331	0.002739	15.1[a]	73.2	144.1	10.35	0.091	SA(s)b
IC 1459	0.005641	22.0[d]	106.7	315.0	10.97	0.016	E3

Table 2.3: *Results from spectral fitting of the five models tested.*

Name	ME			RS			PL		
	N_H (10^{22})	kT (keV)	χ^2/d.o.f	N_H (10^{22})	kT (keV)	χ^2/d.o.f	N_H (10^{22})	Γ	χ^2/d.o.f
NGC 0315	0.23	63.99	285.15/163	0.22	79.89	284.03/163	0.20	1.18	282.77/163
NGC 2681	0.51	0.64	78.02/28	0.45	0.58	77.75/28	0.28	3.68	82.58/28
NGC 3690B...	0.79	1.40	118.70/25	1.09	1.10	112.04/25	0.02	1.45	21.81/25 (*)
NGC 4374	0.97	0.64	168.94/33	0.93	0.62	179.05/33	0.14	2.07	32.20/33 (*)
NGC 4395	2.73	28.01	120.52/106	2.77	24.01	119.41/106	2.87	1.44	123.68/106 (*)
NGC 4410A ..	0.92	0.60	337.45/45	0.89	0.58	353.98/45	0.01	1.75	33.11/45 (*)
NGC 4438	0.43	0.66	68.13/36	0.41	0.57	53.97/36	0.89	7.69	148.92/36
NGC 4457	0.51	0.63	74.99/20	0.43	0.52	78.02/20	0.32	4.08	68.80/20
NGC 4494	0.78	0.61	27.90/7	0.73	0.56	29.40/7	0.12	2.38	16.47/7
NGC 4552	0.75	0.66	354.09/63	0.71	0.61	368.32/63	0.12	2.39	117.28/63
NGC 4594 . ..	0.19	18.77	115.89/87	0.19	18.49	116.02/87	0.20	1.41	118.72/87 (*)
NGC 4696	0.37	0.70	26.71/17	0.35	0.62	24.47/17	0.13	4.26	21.98/17 (*)
NGC 4736	0.82	0.59	635.49/81	0.71	0.56	673.96/81	0.12	2.38	130.19/81
NGC 5194	0.09	0.68	185.59/50	0.09	0.60	114.83/50	0.82	8.00	340.52/50
UGC 08696 ...	0.09	8.72	88.79/42	0.09	9.51	78.50/42	0.27	2.34	72.20/42
CGCG 162-010	0.51	0.86	117.41/63	0.90	0.35	118.54/63	0.39	3.99	83.83/63
NGC 5746	0.64	63.97	15.91/17	0.62	79.90	15.90/17	0.60	1.22	15.66/17 (*)
NGC 5846	0.16	0.65	80.52/27	0.25	0.48	45.59/27	0.79	7.20	160.99/27
NGC 6251	0.03	32.62	74.98/64	0.03	31.18	75.08/64	0.05	1.36	73.08/64
NGC 6240	0.29	48.10	181.56/114	0.30	37.87	181.24/114	0.31	1.31	181.95/114
NGC 6482	0.30	0.78	15.90/18	0.31	0.68	16.41/18 (*)	1.02	9.24	41.40/18
NGC 7130	0.57	0.63	284.55/59	0.54	0.51	266.72/59	0.32	4.23	192.78/59
IC 1459	0.06	7.04	341.31/168	0.06	7.16	335.79/168	0.16	1.89	290.02/168

Table 2.3 *(Continuation)*

Name	RS+PL				ME+PL			
	N_H (10^{22})	Γ	kT (keV)	χ^2/d.o.f	N_H (10^{22})	Γ	kT (keV)	χ^2/d.o.f
NGC 0315	0.71	1.48	0.22	188.77/161(*)	0.48	1.30	0.27	213.89/161
NGC 2681	0.04	1.68	0.76	9.40/26	0.08	1.74	0.66	13.94/26 (*)
NGC 3690B...	0.10	1.45	0.98	20.28/23	0.07	1.43	1.08	20.13/23
NGC 4374	0.12	1.80	0.77	18.76/31	0.14	1.83	0.64	18.34/31
NGC 4395	2.93	1.48	0.03	123.62/104	2.97	1.51	0.08	123.69/104
NGC 4410A ..	0.01	1.69	0.58	31.21/43	0.01	1.68	0.50	30.32/43
NGC 4438	0.11	2.13	0.78	32.27/34 (*)	0.23	2.42	0.60	29.04/34
NGC 4457	0.07	1.98	0.66	18.68/18 (*)	0.13	1.96	0.53	19.23/18
NGC 4494	0.01	1.13	0.82	5.03/5	0.11	1.37	0.63	5.59/5 (*)
NGC 4552	0.04	1.81	0.83	57.19/61 (*)	0.05	1.82	0.79	70.58/61
NGC 4594 . ..	0.22	1.41	0.45	117.65/85	0.25	1.43	0.39	117.03/85
NGC 4696	0.41	4.67	0.27	19.94/15	0.62	2.33	0.18	5.80/15
NGC 4736	0.08	2.02	0.66	71.96/79	0.08	2.00	0.60	72.90/79 (*)
NGC 5194	0.02	2.98	0.69	68.32/48	0.03	2.67	0.61	49.74/48 (*)
UGC 08696 ...	0.39	1.74	0.75	55.63/40 (*)	0.38	1.70	0.68	56.81/40
CGCG 162-010	0.09	2.44	1.12	59.95/61 (*)	0.12	2.71	1.33	58.43/61
NGC 5746	1.13	1.51	0.11	14.81/15	0.95	1.43	0.08	15.79/15
NGC 5846	0.10	2.56	0.63	38.16/25	0.12	1.65	0.50	21.91/25 (*)
NGC 6251	0.15	1.42	0.49	67.85/62	0.44	1.60	0.26	65.27/62 (*)
NGC 6240	1.11	1.03	0.76	126.79/112 (*)	1.17	1.08	0.75	133.10/112
NGC 6482	0.02	2.42	0.87	13.21/16	0.02	2.64	0.83	14.51/16
NGC 7130	0.06	2.51	0.82	81.43/57 (*)	0.12	2.74	0.67	90.75/57
IC 1459	0.18	1.80	0.61	193.27/166	0.28	1.89	0.30	189.47/166 (*)

Table 2.4: *Result of the model fitting to the spectra of the SF subsample. The top line in each parameter corresponds to the whole sample of 24 objects, bottom-left shows the result in the AGN-like nuclei (19 objects), and bottom-right shows the result in the SB-like objects (5 objects).*

	Mean (1) AGN/SB	Median (2) AGN/SB	Mean Std Dev. (3) AGN/SB
$\mathrm{Log(L_X)}$	40.16 40.22/39.93	39.78 40.07/39.54	0.96 1.03/0.64
$\mathrm{N_H}$ $(10^{22}\mathrm{cm}^{-2})$	0.35 0.40/0.15	0.12 0.14/0.12	0.35 0.41/0.06
kT (keV)	0.64 0.59/0.77	0.66 0.66/0.78	0.17 0.17/0.18
Γ	1.89 1.73/2.62	1.75 1.74/2.44	0.45 0.32/0.82

Table 2.5: *X-ray and HST results.*

Name	Flux $\mathrm{erg\,cm^{-2}\,s^{-1}}$	Log(L_X(2–10 keV)) $\mathrm{erg\,s^{-1}}$	Ref.	Obscuration	Classif.	HST-Classif.
(1)	(2)	(3)	(4)	(5)	(6)	(7)
NGC 0315.....	-12.08 $^{+0.04}_{-0.06}$	41.64 $^{+0.03}_{-0.06}$	(f)	SF+CD	AGN	C
ARP 318A	-13.24	39.48	(e)		SB	
ARP 318B.....	-13.32	40.20	(e)	CD	SB	
NGC 1052.....	-11.95	40.78	(e)	CD	AGN	C
NGC 2681.....	-13.61 $^{+0.09}_{-0.20}$	38.94 $^{+0.10}_{-0.22}$	(f)		AGN	C
UGC 05101.....	-13.32	41.24	(e)		AGN	C
NGC 3226.....	-12.83	39.62	(e)	CD	AGN	C
NGC 3245.....	-13.48	39.08	(e)		SB	C
NGC 3379.....	-14.36	37.89	(e)		SB	C
NGC 3507.....	-14.37	38.31	(e)		SB	D
NGC 3607.....	-14.05	38.45	(e)	CD	SB	D
NGC 3608.....	-13.97	38.64	(e)	CD	SB	U
NGC 3628.....	-13.61	38.24	(e)	CD	AGN	C
NGC 3690B	-12.64 $^{+0.07}_{-0.06}$	40.63 $^{+0.07}_{-0.05}$	(f)	CD	AGN	C
NGC 4111.....	-13.21	39.33	(e)		AGN	C
NGC 4125.....	-13.91	38.93	(e)		AGN	C
NGC 4261.....	-12.58	40.65	(e)		AGN	C
NGC 4314.....	-13.92	37.94	(e)		SB	C
NGC 4374.....	-13.03 $^{+0.06}_{-0.12}$	39.58 $^{+0.07}_{-0.10}$	(f)	SF	AGN	C
NGC 4395.....	-11.61 $^{+0.06}_{-0.25}$	39.71 $^{+0.05}_{-0.26}$	(f)	SF	AGN	C
NGC 4410A.....	-12.85 $^{+0.06}_{-0.06}$	41.26 $^{+0.06}_{-0.06}$	(f)		AGN	C
NGC 4438.....	-13.32 $^{+0.11}_{-0.37}$	39.22 $^{+0.16}_{-0.28}$	(f)	SF	SB	D
NGC 4457.....	-13.51 $^{+0.14}_{-0.24}$	39.05 $^{+0.13}_{-0.25}$	(f)		AGN	
NGC 4459.....	-13.66	38.83	(e)	CD	SB	C
NGC 4486.....	-11.75	40.75	(e)		AGN	C
NGC 4494.....	-12.93 $^{+0.19}_{-0.45}$	39.62 $^{+0.17}_{-0.43}$	(f)	SF	AGN	C
NGC 4552.....	-13.04 $^{+0.06}_{-0.09}$	39.41 $^{+0.06}_{-0.09}$	(f)		AGN	C
NGC 4579.....	-11.38	41.15	(e)		AGN	C
NGC 4594.....	-11.99 $^{+0.04}_{-0.05}$	40.07 $^{+0.04}_{-0.06}$	(f)	SF	AGN	C
NGC 4596.....	-13.88	38.65	(e)		SB	C
NGC 4636.....	-13.16	39.25	(e)		SB	U
NGC 4676A.....	-13.93	40.06	(e)	CD	SB	D
NGC 4676B	-13.78	40.21	(e)	CD	SB	D
NGC 4696.....	-13.42 $^{+0.13}_{-0.23}$	39.78 $^{+0.09}_{-0.27}$	(f)	SF	SB	C
NGC 4698.....	-13.84	38.72	(e)	CD	SB	D
NGC 4736.....	-12.86 $^{+0.04}_{-0.07}$	38.65 $^{+0.05}_{-0.08}$	(f)		AGN	C
NGC 5055.....	-13.42	38.37	(e)		AGN	C
NGC 5194.....	-13.71 $^{+0.15}_{-0.19}$	38.14 $^{+0.13}_{-0.21}$	(f)		AGN	
MRK 0266NE	-13.22	40.98	(e)		AGN	C
UGC 08696.....	-12.28 $^{+0.15}_{-0.21}$	42.18 $^{+0.14}_{-0.22}$	(f)	SF	AGN	C
CGCG 162-010	-13.23 $^{+0.19}_{-0.29}$	41.73 $^{+0.23}_{-0.27}$	(f)	CD	SB	D
NGC 5746.....	-12.73 $^{+0.11}_{-0.56}$	40.07 $^{+0.10}_{-0.54}$	(f)	CD	AGN	C
NGC 5846.....	-13.34 $^{+0.35}_{-0.59}$	39.54 $^{+0.38}_{-0.59}$	(f)	SF	SB	D
NGC 5866.....	-13.85	38.80	(e)		SB	
NGC 6251.....	-12.18 $^{+0.07}_{-0.04}$	41.84 $^{+0.07}_{-0.05}$	(f)	SF	AGN	C
NGC 6240.....	-12.04 $^{+0.06}_{-0.23}$	42.04 $^{+0.05}_{-0.24}$	(f)	CD	AGN	C
IRAS 17208-0014 ..	-13.45	41.14	(e)	CD	AGN	C
NGC 6482.....	-14.16 $^{+0.14}_{-0.30}$	39.40 $^{+0.15}_{-0.37}$	(f)	SF+CD	SB	
NGC 7130.....	-13.23 $^{+0.07}_{-0.11}$	40.49 $^{+0.08}_{-0.13}$	(f)		AGN	C
NGC 7331.....	-13.73	38.72	(e)		SB	C
IC 1459	-12.20 $^{+0.02}_{-0.02}$	40.56 $^{+0.02}_{-0.03}$	(f)	SF	AGN	C

NOTES.- (f) Indicates flux and unabsorbed luminosity from spectral fitting and while (e) indicates flux and luminosity estimated from empirical calibration. (SF) obscuration indicators from spectral fitting and (CD) thought color-color diagrams. (C) compact, (D) dusty and (U) unclassified opticla (HST) morphology.

Table 2.6: *Results from spectral fitting and estimate from color-color diagrams (CC).*

Name	Classif.	Model	N_H ($10^{22}cm^{-2}$)	N_H(CC)	Γ	Γ(CC)	kT (keV)	kT(CC) (keV)	χ^2/d.o.f
NGC 0315	AGN	RS+PL	$0.71^{+0.07}_{-0.16}$	$\sim 10^{22}$	$1.48^{+0.07}_{-0.19}$	[1.2-1.4]	$0.22^{+0.08}_{-0.01}$	[0.7-0.8]	188.77/161
ARP 318A	SB	...	...	...	...	[1.8-2.0]	...	[0.6-0.8]	...
ARP 318B	SB	...	...	...	...	...	...	...	...
NGC 1052	AGN	...	...	...	...	...	...	...	...
NGC 2681	AGN	ME+PL	$0.08^{+0.07}_{-0.08}$	...	$1.74^{+0.52}_{-0.47}$	[1.4-1.8]	$0.66^{+0.09}_{-0.08}$	[0.7-0.8]	13.94/26
UGC 05101	AGN	...	...	...	...	[0.4-0.6]	...	...	...
NGC 3226	AGN	...	...	$\sim 10^{22}$	...	[0.8-1.2]	...	[0.7-0.8]	...
NGC 3245	SB	...	...	...	...	[2.0-2.4]	...	[0.6-0.8]	...
NGC 3379	SB	...	...	...	...	...	...	...	...
NGC 3507	SB	...	...	...	...	...	...	...	...
NGC 3607	SB	...	...	...	...	...	...	...	...
NGC 3608	SB	...	...	...	...	...	...	[1.0-4.0]	...
NGC 3628	AGN	...	...	$\sim 10^{22}$	...	[1.2-1.6]	...	[0.6-0.8]	...
NGC 3690B	AGN	PL	$0.02^{+0.15}_{-0.02}$	...	$1.45^{+0.33}_{-0.25}$	[1.4-1.8]	...	[0.6-0.7]	21.81/25
NGC 4111	AGN	...	...	...	...	[0.4-0.6]	...	[0.6-0.7]	...
NGC 4125	AGN	...	...	...	...	[1.4-1.8]	...	[0.6-0.8]	...
NGC 4261	AGN	...	...	...	...	[1.5-1.6]	...	...	...
NGC 4314	SB	...	...	...	...	...	...	...	...
NGC 4374	AGN	PL	$0.14^{+0.06}_{-0.05}$	...	$2.07^{+0.24}_{-0.20}$	[2.0-2.2]	...	[0.7-0.8]	32.20/33
NGC 4395	AGN	PL	$2.87^{+0.53}_{-0.38}$	...	$1.44^{+0.26}_{-0.19}$	...	...	...	123.68/106
NGC 4410A	AGN	PL	$0.01^{+0.04}_{-0.01}$	...	$1.75^{+0.19}_{-0.12}$	[1.4-1.8]	...	[0.7-0.8]	33.11/45
NGC 4438	SB	RS+PL	$0.11^{+0.07}_{-0.04}$	...	$2.13^{+0.67}_{-0.62}$	[1.8-2.0]	$0.78^{+0.04}_{-0.06}$	[0.7-0.9]	32.27/34
NGC 4457	AGN	RS+PL	$0.07^{+0.08}_{-0.07}$	...	$1.98^{+0.66}_{-0.54}$	[1.6-1.8]	$0.66^{+0.11}_{-0.08}$	[0.6-0.8]	18.68/18
NGC 4459	SB	...	...	...	...	...	...	...	...
NGC 4486	AGN	...	...	...	...	[1.2-1.6]	...	[0.7-0.8]	...
NGC 4494	AGN	ME+PL	$0.11^{+0.15}_{-0.01}$	...	$1.37^{+0.91}_{-0.88}$	...	$0.63^{+0.20}_{-0.13}$	...	5.59/5
NGC 4552	AGN	RS+PL	$0.04^{+0.02}_{-0.04}$	...	$1.81^{+0.24}_{-0.10}$	[1.8-2.0]	$0.83^{+0.05}_{-0.07}$	[0.7-0.9]	57.19/61
NGC 4579	AGN	...	...	...	...	[1.2-1.6]	...	...	...
NGC 4594	AGN	PL	$0.20^{+0.02}_{-0.04}$	$\sim 10^{22}$	$1.41^{+0.11}_{-0.10}$	[1.6-2.0]	...	[0.4-0.6]	118.72/87
NGC 4596	SB	...	...	...	...	...	...	...	...
NGC 4636	SB	...	...	...	...	[2.0-2.2]	...	[0.7-0.8]	...
NGC 4676A	SB	...	...	...	...	[0.8-1.2]	...	...	...
NGC 4676B	SB	...	...	...	...	...	...	...	...
NGC 4696	SB	PL	$0.13^{+0.18}_{-0.13}$	...	$4.26^{+0.96}_{-0.62}$	...	...	...	21.98/17
NGC 4698	SB	...	...	...	...	[1.2-1.6]	...	[0.7-0.8]	...
NGC 4736	AGN	ME+PL	$0.08^{+0.04}_{-0.04}$	...	$2.00^{+0.23}_{-0.06}$	[1.4-1.8]	$0.60^{+0.05}_{-0.09}$	[0.6-0.8]	72.90/79
NGC 5055	AGN	...	...	...	...	[1.6-2.0]	...	[0.7-0.9]	...
NGC 5194	AGN	ME+PL	$0.03^{+0.06}_{-0.03}$	...	$2.67^{+0.71}_{-0.47}$	[0.4-0.6]	$0.61^{+0.03}_{-0.04}$	[0.6-0.7]	49.74/48
MRK 266NE	AGN	...	...	...	...	...	...	...	...
UGC 08696	AGN	RS+PL	$0.39^{+0.06}_{-0.06}$	...	$1.74^{+0.81}_{-0.61}$	...	$0.75^{+0.12}_{-0.12}$	...	55.63/40
CGCG 162-010	SB	RS+PL	$0.09^{+0.21}_{-0.09}$	...	$2.44^{+1.51}_{-0.43}$	...	$1.12^{+0.18}_{-0.21}$	...	59.95/61
NGC 5746	AGN	PL	$0.60^{+0.36}_{-0.52}$	$\sim 10^{22}$	$1.22^{+0.14}_{-0.39}$	[1.0-1.2]	...	[0.7-0.8]	15.66/17
NGC 5846	SB	ME+PL	$0.12^{+0.35}_{-0.12}$	...	$1.65^{+0.95}_{-0.67}$	[0.8-1.2]	$0.50^{+0.11}_{-0.21}$	[0.5-0.7]	21.91/25
NGC 5866	SB	...	...	...	...	...	...	...	...
NGC 6251	AGN	ME+PL	$0.44^{+0.43}_{-0.26}$	$\sim 10^{22}$	$1.60^{+0.29}_{-0.22}$	[1.0-1.4]	$0.26^{+0.34}_{-0.09}$	[0.4-0.6]	65.27/62
NGC 6240	AGN	RS+PL	$1.11^{+0.10}_{-0.10}$	$\sim 10^{22}$	$1.03^{+0.14}_{-0.15}$	[0.8-1.0]	$0.76^{+0.06}_{-0.06}$	[0.7-0.8]	126.79/112
IRAS 17208-0014	AGN	...	...	$\sim 10^{22}$	...	[1.6-2.0]	...	[0.6-0.8]	...
NGC 6482	SB	ME	$0.31^{+0.10}_{-0.18}$	...	...	...	$0.68^{+0.13}_{-0.07}$	...	16.41/18
NGC 7130	AGN	RS+PL	$0.06^{+0.04}_{-0.04}$	...	$2.51^{+0.41}_{-0.22}$	[1.2-1.4]	$0.82^{+0.03}_{-0.05}$	[0.7-0.8]	81.43/57
NGC 7331	SB	...	...	...	...	[2.2-2.6]	...	[0.6-0.8]	...
IC 1459	AGN	ME+PL	$0.28^{+0.15}_{-0.02}$	...	$1.89^{+0.10}_{-0.11}$	[1.8-2.0]	$0.30^{+0.25}_{-0.06}$	[0.7-0.9]	189.47/166

NOTES.- (*) Off of any grid. UGC 08696 has been fitted including a Gaussian model where the best fit is centered on 5.93 keV with a weight of 1.22 keV.

Table 2.7: *Soft (Q_A), medium (Q_B) and hard (Q_C) hardness ratios for the whole sample.*

Name	Q_A	Q_B	Q_C
NGC 0315	-0.06 ±0.05	-0.05 ±0.04	-0.59 ±0.03
ARP 318A	-0.20 ±0.11	-0.45 ±0.14	-0.74 ±0.17
ARP 318B	0.04 ±0.18	-0.09 ±0.22	-0.88 ±0.10
NGC 1052	-0.13 ±0.21	0.03 ±0.23	-0.37 ±0.13
NGC 2681	-0.09 ±0.06	-0.27 ±0.11	-0.67 ±0.13
UGC 05101	-0.03 ±0.13	-0.05 ±0.14	-0.41 ±0.14
NGC 3226	0.58 ±0.13	0.09 ±0.14	-0.49 ±0.08
NGC 3245	-0.19 ±0.26	-0.35 ±0.29	-0.78 ±0.20
NGC 3379	0.18 ±0.22	-0.34 ±0.28	... ...
NGC 3507	-0.36 ±0.08	-0.40 ±0.20	... ...
NGC 3607	0.25 ±0.17	-0.38 ±0.24	... ...
NGC 3608	0.47 ±0.22	-0.69 ±0.17	-0.75 ±0.23
NGC 3628	0.46 ±0.26	0.10 ±0.17	-0.60 ±0.17
NGC 3690B	0.39 ±0.12	-0.25 ±0.09	-0.48 ±0.10
NGC 4111	-0.26 ±0.08	-0.38 ±0.18	-0.45 ±0.17
NGC 4125	-0.18 ±0.16	-0.32 ±0.19	-0.68 ±0.21
NGC 4261	-0.37 ±0.03	-0.36 ±0.07	-0.33 ±0.06
NGC 4314	-0.22 ±0.16	-0.35 ±0.29	... ...
NGC 4374	-0.07 ±0.08	-0.22 ±0.09	-0.75 ±0.08
NGC 4395	-0.20 ±0.12	0.34 ±0.06	-0.52 ±0.03
NGC 4410A	-0.07 ±0.06	-0.27 ±0.08	-0.67 ±0.07
NGC 4438	-0.05 ±0.05	-0.41 ±0.09	-0.75 ±0.13
NGC 4457	-0.17 ±0.07	-0.25 ±0.12	-0.70 ±0.14
NGC 4459	-0.13 ±0.25	0.00 ±0.43	... ...
NGC 4486	-0.04 ±0.01	-0.21 ±0.02	-0.64 ±0.01
NGC 4494	-0.02 ±0.12	-0.16 ±0.16	-0.87 ±0.08
NGC 4552	-0.01 ±0.05	-0.20 ±0.07	-0.69 ±0.07
NGC 4579	-0.08 ±0.02	-0.15 ±0.02	-0.61 ±0.02
NGC 4594	0.15 ±0.05	-0.14 ±0.05	-0.65 ±0.04
NGC 4596	-0.42 ±0.37	-0.35 ±0.56	... ...
NGC 4636	-0.12 ±0.03	-0.50 ±0.06	-0.73 ±0.11
NGC 4676A	0.07 ±0.25	-0.10 ±0.29	-0.53 ±0.40
NGC 4676B	-0.21 ±0.18	-0.16 ±0.25	... ...
NGC 4696	-0.17 ±0.11	0.00 ±0.33	... ...
NGC 4698	-0.06 ±0.17	-0.20 ±0.22	-0.63 ±0.25
NGC 4736	-0.15 ±0.04	-0.23 ±0.05	-0.68 ±0.06
NGC 5055	0.03 ±0.14	-0.28 ±0.15	-0.73 ±0.13
NGC 5194	-0.25 ±0.03	-0.42 ±0.07	-0.45 ±0.17
MRK 0266NE	-0.01 ±0.13	0.13 ±0.19	-0.34 ±0.14
UGC 08696	0.00 ±0.10	-0.14 ±0.11	0.12 ±0.08
CGCG 162-010	0.09 ±0.07	-0.22 ±0.12	... ...
NGC 5746	0.58 ±0.18	-0.01 ±0.12	-0.51 ±0.08
NGC 5846	-0.35 ±0.05	-0.35 ±0.12	-0.57 ±0.26
NGC 5866	-0.23 ±0.21	-0.63 ±0.29	-0.52 ±0.24
NGC 6251	0.19 ±0.07	-0.21 ±0.06	-0.55 ±0.05
NGC 6240	0.52 ±0.05	0.01 ±0.05	-0.48 ±0.05
IRAS 17208-0014	0.44 ±0.18	0.01 ±0.15	-0.67 ±0.12
NGC 6482	0.10 ±0.08	-0.38 ±0.14	-0.83 ±0.15
NGC 7130	-0.12 ±0.04	-0.33 ±0.06	-0.61 ±0.09
NGC 7331	-0.16 ±0.21	-0.35 ±0.22	-0.81 ±0.14
IC 1459	0.00 ±0.03	-0.19 ±0.03	-0.72 ±0.03

Bibliography

Balucinska-Church, M. and McCammon, D.: 1992, *Astrophysical Journal* **400**, 699

Barth, A. J.: 2002, in *Issues in Unification of Active Galactic Nuclei*, Vol. 258, p. 147

Barth, A. J., Ho, L. C., Filippenko, A. V., and Sargent, W. L. W.: 1998, *Astrophysical Journal* **496**, 133

Barth, A. J., Sarzi, M., Rix, H.-W., Ho, L. C., Filippenko, A. V., and Sargent, W. L. W.: 2001, *Astrophysical Journal* **555**, 685

Barth, A. J. and Shields, J. C.: 2000, *Publications of the Astronomical Society of the Pacific* **112**, 753

Boller, T., Gallo, L. C., Lutz, D., and Sturm, E.: 2002, *Monthly Notices of the Royal Astronomical Society* **336**, 1143

Braatz, J. A., Wilson, A. S., and Henkel, C.: 1997, *Astrophysical Journal Supplement Series* **110**, 321

Cappi, M., Panessa, F., Bassani, L., Dadina, M., Dicocco, G., Comastri, A., della Ceca, R., Filippenko, A. V., Gianotti, F., Ho, L. C., Malaguti, G., Mulchaey, J. S., Palumbo, G. G. C., Piconcelli, E., Sargent, W. L. W., Stephen, J., Trifoglio, M., and Weaver, K. A.: 2006, *Astronomy and Astrophysics* **446**, 459

Carrillo, R., Masegosa, J., Dultzin-Hacyan, D., and Ordonez, R.: 1999, *Revista Mexicana de Astronomia y Astrofisica* **35**, 187

Ceballos, M. T. and Barcons, X.: 1996, *Monthly Notices of the Royal Astronomical Society* **282**, 493

Chiaberge, M., Capetti, A., and Macchetto, F. D.: 2005, *Astrophysical Journal* **625**, 716

Cowan, J. J., Romanishin, W., and Branch, D.: 1994, *Astrophysical Journal* **436**, L139

Delgado, R. M. G., Fernandes, R. C., Perez, E., Martins, L. P., Storchi-Bergmann, T., Schmitt, H., Heckman, T., and Leitherer, C.: 2004, *Astrophysical Journal* **605**, 127

Dickey, J. M. and Lockman, F. J.: 1990, *Annual Review of Astronomy and Astrophysics* **28**, 215

Donato, D., Sambruna, R. M., and Gliozzi, M.: 2004, *Astrophysical Journal* **617**, 915

Dopita, M. A., Koratkar, A. P., Evans, I. N., Allen, M., Bicknell, G. V., Sutherland, R. S., Hawley, J. F., and Sadler, E.: 1996, Vol. 103, p. 44

Dudik, R. P., Satyapal, S., Gliozzi, M., and Sambruna, R. M.: 2005, *Astrophysical Journal* **620**, 113

Eracleous, M., Shields, J. C., Chartas, G., and Moran, E. C.: 2002, *Astrophysical Journal* **565**, 108

Fabbiano, G.: 2006, Vol. 230, pp 180–184

Fabian, A. C.: 1979, *Royal Society of London Proceedings Series A* **366**, 449

Falcke, H., Nagar, N. M., Wilson, A. S., and Ulvestad, J. S.: 2000, *Astrophysical Journal* **542**, 197

Ferland, G. J. and Netzer, H.: 1983, *Astrophysical Journal* **264**, 105

Fernandes, R. C., Delgado, R. M. G., Schmitt, H., Storchi-Bergmann, T., Martins, L. P., Perez, E., Heckman, T., Leitherer, C., and Schaerer, D.: 2004, *Astrophysical Journal* **605**, 105

Ferrarese, L. and Merritt, D.: 2000, *Astrophysical Journal* **539**, L9

Filho, M. E., Barthel, P. D., and Ho, L. C.: 2000, *Astrophysical Journal Supplement Series* **129**, 93

Filho, M. E., Barthel, P. D., and Ho, L. C.: 2002, *Astrophysical Journal Supplement Series* **142**, 223

Filho, M. E., Fraternali, F., Markoff, S., Nagar, N. M., Barthel, P. D., Ho, L. C., and Yuan, F.: 2004, *Astronomy and Astrophysics* **418**, 429

Filippenko, A. V. and Halpern, J. P.: 1984, *Astrophysical Journal* **285**, 458

Filippenko, A. V. and Terlevich, R.: 1992, *Astrophysical Journal* **397**, L79

Flohic, H. M. L. G., Eracleous, M., Chartas, G., Shields, J. C., and Moran, E. C.: 2006, *Astrophysical Journal* **647**, 140

Fosbury, R. A. E., Mebold, U., Goss, W. M., and Dopita, M. A.: 1978, *Monthly Notices of the Royal Astronomical Society* **183**, 549

Gallo, L. C., Lehmann, I., Pietsch, W., Boller, T., Brinkmann, W., Friedrich, P., and Grupe, D.: 2006, *Monthly Notices of the Royal Astronomical Society* **365**, 688

Granato, G. L., Danese, L., and Franceschini, A.: 1997, *Memorie della Societa Astronomica Italiana* **68**, 39

Griffiths, R. E., Ptak, A., Feigelson, E. D., Garmire, G., Townsley, L., Brandt, W. N., Sambruna, R., and Bregman, J. N.: 2000, *Science* **290**, 1325

Grimes, J. P., Heckman, T., Strickland, D., and Ptak, A.: 2005, *Astrophysical Journal* **628**, 187

Grimm, H.-J., McDowell, J., Zezas, A., Kim, D.-W., and Fabbiano, G.: 2005, *Astrophysical Journal Supplement Series* **161**, 271

Guainazzi, M., Matt, G., and Perola, G. C.: 2005, *Astronomy and Astrophysics* **444**, 119

Halpern, J. P. and Steiner, J. E.: 1983, *Astrophysical Journal* **269**, L37

Hasinger, G., Altieri, B., Arnaud, M., Barcons, X., Bergeron, J., Brunner, H., Dadina, M., Dennerl, K., Ferrando, P., Finoguenov, A., Griffiths, R. E., Hashimoto, Y., Jansen, F. A., Lumb, D. H., Mason, K. O., Mateos, S., McMahon, R. G., Miyaji, T., Paerels, F., Page, M. J., Ptak, A. F., Sasseen, T. P., Schartel, N., Szokoly, G. P., Tromper, J., Turner, M., Warwick, R. S., and Watson, M. G.: 2001, *Astronomy and Astrophysics* **365**, L45

Hawley, S. A. and Phillips, M. M.: 1980, *Astrophysical Journal* **235**, 783

Heckman, T. M.: 1980, *Astronomy and Astrophysics* **87**, 152

Heckman, T. M., Crane, P. C., and Balick, B.: 1980, *Astronomy and Astrophysics Supplement Series* **40**, 295

Heinke, C. O., Grindlay, J. E., Edmonds, P. D., Cohn, H. N., Lugger, P. M., Camilo, F., Bogdanov, S., and Freire, P. C.: 2005, *Astrophysical Journal* **625**, 796

Ho, L. C., Feigelson, E. D., Townsley, L. K., Sambruna, R. M., Garmire, G. P., Brandt, W. N., Filippenko, A. V., Griffiths, R. E., Ptak, A. F., and Sargent, W. L. W.: 2001, *Astrophysical Journal* **549**, L51

Ho, L. C., Filippenko, A. V., and Sargent, W. L. W.: 1997, *Astrophysical Journal* **487**, 568

Ishisaki, Y., Makishima, K., Iyomoto, N., Hayashida, K., Inoue, H., Mitsuda, K., Tanaka, Y., Uno, S., Kohmura, Y., Mushotzky, R. F., Petre, R., Serlemitsos, P. J., and Terashima, Y.: 1996, *Publications of the Astronomical Society of Japan* **48**, 237

Iyomoto, N., Makishima, K., Fukazawa, Y., Tashiro, M., Ishisaki, Y., Nakai, N., and Taniguchi, Y.: 1996, *Publications of the Astronomical Society of Japan* **48**, 231

Jimenez-Bailon, E., Piconcelli, E., Guainazzi, M., Schartel, N., Rodriguez-Pascual, P. M., and Santos-Lleo, M.: 2005, *Astronomy and Astrophysics* **435**, 449

Karachentsev, I. D. and Drozdovsky, I. O.: 1998, *Astronomy and Astrophysics Supplement Series* **131**, 1

Keel, W. C.: 1980, *Astronomical Journal* **85**, 198

Laine, S., Knapen, J. H., Perez-Ramirez, D., Doyon, R., and Nadeau, D.: 1999, *Monthly Notices of the Royal Astronomical Society* **302**, L33

Lawrence, A. and Elvis, M.: 1982, *Astrophysical Journal* **256**, 410

Leighly, K. M.: 1999, *Astrophysical Journal Supplement Series* **125**, 297

Maiolino, R.: 2001, *X-ray Astronomy: Stellar Endpoints, AGN, and the Diffuse X-ray Background* **599**, 199

Maoz, D., Nagar, N. M., Falcke, H., and Wilson, A. S.: 2005, *Astrophysical Journal* **625**, 699

Marquez, I., Masegosa, J., Durret, F., Delgado, R. M. G., Moles, M., Maza, J., Perez, E., and Roth, M.: 2003, *Astronomy and Astrophysics* **409**, 459

Marquez, I. and Moles, M.: 1996, *Astronomy and Astrophysics Supplement Series* **120**, 1

Masegosa, J. and Marquez, I.: 2003, *Astrophysics and Space Science* **284**, 483

Mateos, S., Barcons, X., Carrera, F. J., Ceballos, M. T., Hasinger, G., Lehmann, I., Fabian, A. C., and Streblyanska, A.: 2005, *Astronomy and Astrophysics* **444**, 79

Nagar, N. M., Falcke, H., and Wilson, A. S.: 2005, *Astronomy and Astrophysics* **435**, 521

Nagar, N. M., Falcke, H., Wilson, A. S., and Ho, L. C.: 2000, *Astrophysical Journal* **542**, 186

Nagar, N. M., Falcke, H., Wilson, A. S., and Ulvestad, J. S.: 2002, *Astronomy and Astrophysics* **392**, 53

Ott, J., Martin, C. L., and Walter, F.: 2003, *Astrophysical Journal* **594**, 776

Ott, J., Walter, F., and Brinks, E.: 2005, *Monthly Notices of the Royal Astronomical Society* **358**, 1453

Pogge, R. W., Maoz, D., Ho, L. C., and Eracleous, M.: 2000, *Astrophysical Journal* **532**, 323

Ptak, A., Heckman, T., Levenson, N. A., Weaver, K., and Strickland, D.: 2003, *Astrophysical Journal* **592**, 782

Ptak, A., Serlemitsos, P., Yaqoob, T., and Mushotzky, R.: 1999, *Astrophysical Journal Supplement Series* **120**, 179

Raymond, J. C. and Smith, B. W.: 1977, *Astrophysical Journal Supplement Series* **35**, 419

Rinn, A. S., Sambruna, R. M., and Gliozzi, M.: 2005, *Astrophysical Journal* **621**, 167

Roberts, T. P. and Warwick, R. S.: 2000, *Monthly Notices of the Royal Astronomical Society* **315**, 98

Roberts, T. P., Warwick, R. S., and Ohashi, T.: 1999, *Monthly Notices of the Royal Astronomical Society* **304**, 52

Sarzi, M., Rix, H.-W., Shields, J. C., Rudnick, G., Ho, L. C., McIntosh, D. H., Filippenko, A. V., and Sargent, W. L. W.: 2001, *Astrophysical Journal* **550**, 65

Satyapal, S., Dudik, R. P., O'Halloran, B., and Gliozzi, M.: 2005, *Astrophysical Journal* **633**, 86

Shields, J. C.: 1992, *Astrophysical Journal* **399**, L27

Sofue, Y., Yoshida, S., Aoki, T., Soyano, T., Tarusawa, K., Hamabe, M., and Wakamatsu, K.-I.: 1994, *Publications of the Astronomical Society of Japan* **46**, 1

Soria, R., Fabbiano, G., Graham, A. W., Baldi, A., Elvis, M., Jerjen, H., Pellegrini, S., and Siemiginowska, A.: 2006a, *Astrophysical Journal* **640**, 126

Soria, R., Graham, A. W., Fabbiano, G., Baldi, A., Elvis, M., Jerjen, H., Pellegrini, S., and Siemiginowska, A.: 2006b, *Astrophysical Journal* **640**, 143

Soria, R. and Motch, C.: 2004, *Astronomy and Astrophysics* **422**, 915

Stauffer, J. R.: 1982, *Astronomical Journal* **87**, 1507

Streblyanska, A., Hasinger, G., Finoguenov, A., Barcons, X., Mateos, S., and Fabian, A. C.: 2005, *Astronomy and Astrophysics* **432**, 395

Strickland, D. K., Heckman, T. M., Colbert, E. J. M., Hoopes, C. G., and Weaver, K. A.: 2004, *Astrophysical Journal Supplement Series* **151**, 193

Teng, S. H., Wilson, A. S., Veilleux, S., Young, A. J., Sanders, D. B., and Nagar, N. M.: 2005, *Astrophysical Journal* **633**, 664

Terashima, Y.: 1999, *Advances in Space Research* **23**, 851

Terashima, Y., Ho, L. C., Ptak, A. F., Mushotzky, R. F., Serlemitsos, P. J., Yaqoob, T., and Kunieda, H.: 2000, *Astrophysical Journal* **533**, 729

Terashima, Y., Kunieda, H., Serlemitsos, P. J., and Ptak, A.: 1998, in *The Hot Universe*, Vol. 188, p. 444

Terlevich, R. and Melnick, J.: 1985, *Monthly Notices of the Royal Astronomical Society* **213**, 841

Tonry, J. L., Dressler, A., Blakeslee, J. P., Ajhar, E. A., Fletcher, A. B., Luppino, G. A., Metzger, M. R., and Moore, C. B.: 2001, *Astrophysical Journal* **546**, 681

Tully, R.: 1998, *Cambridge: Cambridge Univ. Press* 1

Veilleux, S.: 1987, Vol. 19, p. 695

Veilleux, S., Sanders, D. B., and Kim, D.-C.: 1999, *Astrophysical Journal* **522**, 139

Veron, P., Veron, M. P., Bergeron, J., and Zuidervijk, E. J.: 1981, *Astronomy and Astrophysics* **97**, 71

Vignati, P., Molendi, S., Matt, G., Guainazzi, M., Antonelli, L. A., Bassani, L., Brandt, W. N., Fabian, A. C., Iwasawa, K., Maiolino, R., Malaguti, G., Marconi, A., and Perola, G. C.: 1999, *Astronomy and Astrophysics* **349**, L57

Wrobel, J. M. and Heeschen, D. S.: 1991, *Astronomical Journal* **101**, 148

Zezas, A., Fabbiano, G., Rots, A. H., and Murray, S. S.: 2002, *Astrophysical Journal Supplement Series* **142**, 239

Chapter 3

AN X-RAY VIEW OF 82 LINERs WITH *Chandra* AND *XMM-Newton*

O. González-Martín[♠], J. Masegosa[♠], I. Márquez[♠], M. Guainazzi[♠♠] and E. Jiménez-Bailón[♠♠♠]
[♠] Instituto de Astrofísica de Andalucía, Granada (SPAIN)
[♠♠] ESAC, Madrid (SPAIN)
[♠♠] UNAM, Mexico D.F. (MEXICO)

We present the results of an homogeneous X-ray analysis of 82 LINERs selected from the catalogue by Carrillo et al. (1999) with available Chandra (68 sources) and XMM-Newton (55 sources) observations. Both together comprise the largest sample of LINERs with X-ray spectral fit ever analysed (60 out of the 82 objects). Information from the literature on the black hole masses, optical morphology, optical emission lines, radio compactness and stellar populations have been added for the analysis. The nuclear X-ray morphology has been classified according to the compactness of the detected nuclear source in the hard band (4.5-8.0 keV). 60% of the sample shows such a compact nuclear source. The analysis of their spectra has shown that best is a composite model (a combination of a thermal and a power law component with two absorbers, MEPL and ME2PL). The resulting median spectral parameters are: $<\Gamma>$*=2.11± 0.52 ,* $<\mathrm{kT}>$*=0.54± 0.30 keV,* $<\log(\mathrm{NH1})>$*=21.32± 0.71 and* $<\log(\mathrm{NH2})>$*=21.93± 1.36 . The Compton-thickness nature of the LINER nuclei in our sample has been investigated by means of the FeK iron emission line (detected in 13 galaxies) and the* $\mathrm{F_X}(2-10\mathrm{keV})/\mathrm{F}([\mathrm{OIII}])$ *ratios. 58% of the LINER sample are found to be Compton-thick candidates. After Compton-thickness correction, they have quite large median soft and hard luminosities,* $<\log(\mathrm{L}(0.5-2\ \mathrm{keV}))>=$ *40.51± 1.41 and* $<\log(\mathrm{L}(2-10\ \mathrm{keV}))>=$ *40.87± 1.38 , respectively, pretty similar to the ranges found for nearby low luminosity Seyferts. The investigation of the origin of the obscuring material allows us to conclude that, whereas the column density NH1 reflects what is found with the optical extinction, the column density NH2 seems to be most probably associated to the inner parts of the central source. The calculated*

Eddington ratios cover the range from 10^{-2} to 10^{-6}, unexpectedly overlapping with those reported for Seyfert 2 galaxies. Finally, adding all the multiwavelenght existing data, we conclude that evidences do exist supporting the AGN nature of their nuclear engine for 90% of the sample (74 out of 82 objects). However, there is a mismatch between multiwavelength information in order to determine the AGN nature. Therefore, the main contributions in this paper have been, first to illustrate that AGNs are much more frequent among LINERs than previously reported and, second, that the reason for the differences between LINERs and Seyferts 2 are not due to different accretion rates as claimed before. Clumpy dusty models need to be further investigated for an eventual explanation of the nature of different AGN populations.

3.1 Introduction

The cmpactness, high luminosity, temporal variability and spectral features of active galactic nuclei (AGN) are best explained as a consequence of disk accretion onto a supermassive blck hole (SMBH). Under the Unified Model proposed by Antonucci (1993), this central engine is surrounded by a dusty toroidal structure so that the observed diversity simply reflects different viewing angles of an axisymmetric geometry.

Observationally, type 1 AGNs are have soft X-ray spectra (below ≈ 10 keV) and both narrow and broad optical emission lines, where as type 2 AGNs show harder X-ray spectra and only narrow optical emission lines. The torus provides anisotropic obscuration of the center, so both broad emission lines and X-ray emission, that comes from the inner part of the AGN, are seen when the source is seen face-on (type 1) and are obscured when it is seen edge-on (type 2).

Evidences have been accumulated from many different observations in the infrared, optical, and X-ray bands supporting the unification model. Despite this progress, no physically consistent model is currently available to account for the formation and evolution of the dusty torus, which may provide the crucial link between the galactic structure at larger scales and the accretion disk that fuels the SMBHs.

X-rays have been used as a powerful measure of the AGN power through the 2-10 keV luminosity, to quantify the absorbing material (up to $10^{24}\mathrm{cm}^{-2}$ with the current missions), i.e. the dusty torus, and to derive information about the central engine from the spectral fit model. The large progress on X-ray background investigations has proven a larger number of AGNs than those observed at optical wavelengths (Comastri and Brusa, 2008). Such a high percentage of AGNs at X-

ray frequencies can be interpreted as due to large amounts of obscuration (Maiolino et al., 1998). In the nearby Universe a full characterization of large samples of AGNs have been possible at X-ray frequencies during the last decade. Several families of AGNs have been studied: Seyfert 2 (Maiolino et al., 1998; Risaliti et al., 1999; Cappi et al., 2006; Panessa et al., 2006), Seyfert 1 (Nandra et al., 2007) or PG-QSOs (Jimenez-Bailon et al., 2006). Moreover, the X-ray regime has been used to look for AGNs in objects otherwise obscured. This is the case of high redshift surveys (Comastri and Brusa, 2008) or Starburst samples (Tzanavaris and Georgantopoulos, 2007).

These studies are specially important in low luminosity AGNs (LLAGNs), with bolometric luminosities $L_B < 10^{44} \mathrm{erg\ s^{-1}}$, since over 40% of nearby galaxies contain such low-power AGNs (see the review by Ho, 2008). We have focused our attention in low ionization narrow emission-line regions (LINERs). They were originally defined as a subclass of LLAGNs by Heckman (1980) and are characterized by optical spectra dominated by emission lines of moderate intensities arising from gas in lower ionization states than classical AGNs. LINERs where defined as galaxies whose spectra satisfy $[\mathrm{OII}]\lambda3727/[\mathrm{OIII}]\lambda5007 \geq 1$ and $[\mathrm{OI}]\lambda6300/[\mathrm{OIII}]\lambda5007 \geq 1/3$ (Heckman 1980). Previous studies on LINERs showed much dispute on the ionisation mechanism of these objects. Shock heating (Dopita and Sutherland, 1995), Wolf-Rayet or OB stars in a compact, young star clusters in the nucleus of the host galaxy (Terlevich and Melnick, 1985; Filippenko and Terlevich, 1992) or low luminosity AGNs (Ho et al., 1997; Eracleous and Halpern, 2001) mechanisms have been discussed since LINERs were discovered. Ho (2008) has concluded, based in the nowadays accumulated set of data, that stellar photoionization by young or intermediate stars and shock heating can be ruled out as the excitation mechanisms for LINERs.

Thus it will be of large importance to isolate and study the nature of the AGN hosted by most of the LINERs. Satyapal et al. (2005) (see also Ho et al., 2001; Satyapal et al., 2004; Dudik et al., 2005) estimated the 2-10 keV luminosities of a sample of LINERs with *Chandra* data. They found that AGNs are very frequent among the LINER population and by means of the Eddington ratio, they conclude that LINERs are the faintest end of the fundamental correlation between mass accretion rate and star formation rates, being very inefficient systems in the accretion process onto the putative nuclear black hole. Flohic et al. (2006) studied a sample of 19 LINERs through archival *Chandra* data to investigate the presence of an AGN. They found that AGNs contribute in median 60% to the 0.5-10 keV luminosity although they suggest that the AGN power is not enough to produce the observed optical emission lines, invoking shocks or stellar processes. Our previous analysis (Gonzalez-Martin et al., 2006b, discussed in Chapter 2, hereinafter GM+06) presented the results from a homogeneous analysis of a sample of 51 LINER galaxies observed with

Chandra/ACIS. The morphological classification toghether with the spectral analysis, when possible, allowed us to conclude that al least 60% of LINERs can host an AGN. It is then worthwhile to fully characterize the spectral energy distribution at X-ray frequencies in order to investigate the frequency of AGN amongst LINER population and its nature. On the other hand, it is also important to measure the population of obscured AGNs in them, before drawing a more general conclusion on AGN population and its relation to higher luminosity AGNs.

In this paper we compile a sample of 82 LINERs, the largest sample of LINERs ever analysed at X-ray frequencies with *Chandra* (68 objects) and *XMM-Newton* (55 objects) data. The addition of *XMM-Newton* data gives us the opportunity to perform the spectral analysis in 60 out of the 82 objects, otherwise small number since *Chandra* data has a lower sensitivity. In the other hand, *Chandra* data includes an important advantage for the image analysis since it has a high spatial resolution, which is very important because the X-ray morphology of LINERs has been demonstrated to be very complex (GM+06). We present a detailed study of the X-ray properties: soft (0.5-2 keV) and hard (2-10 keV) luminosities, spectral index, temperature, hydrogen column densities and spectral fittings. *HST* data were taken to add morphological information at optical wavelengths and *2MASS* data to obtain NIR morphology. Black hole masses were estimated, radio, and UV information and optical emission lines were also compiled.

Section 3.2 presents the sample and describes the data, Section 3.3 shows the details on the data reduction, Section 3.4 includes the data analysis, Section 3.5 presents *Chandra* results, Section 3.6 compares with previous GM+06 analysis, Section 3.7 presents *XMM-Newton* results, Section 3.8 shows the X-ray (both *Chandra* and *XMM-Newton*) LINER sample results, Section 3.9 discusses the nature of LINERs and finally in Section 3.10 we present the summary of our results.

3.2 The sample and the data

The sample analysed in this work has been extracted from the multi-wavelength catalogue of LINERs compiled by Carrillo et al. (1999) (hereinafter MCL). MCL includes most of the LINER galaxies known until 1999. It provides information on broad band and monochromatic emission from the radio frequencies to X-ray for 476 objects classified as LINERs. We have selected all the galaxies compiled in MCL with available *Chandra* data until 2007-06-30 and *XMM-Newton* data until 2007-04-30. The search has been done by using HEASARC archive[1].

[1] $http://heasarc.gsfc.nasa.gov/$

The amount of LINERs is 108 with *Chandra* data and 107 with *XMM-Newton* data. 76 objects are present in both archives, so the sample comprises 139 LINERs.

The LINER identification was done using standard diagnostic diagrams (Baldwin et al., 1981; Veilleux, 1987). The optical spectroscopic classification was reanalyzed by using three diagnostic diagrams: 1) log([OIII] 5007Å/Hβ) versus log([NII] 6584Å/Hα); 2) log([OIII]5007Å/Hβ) versus log([SII]6584Å/Hα) and 3) log([OIII] 5007Å/Hβ) versus log([OI]6300Å/Hα). The regions in these diagrams occupied by LINERs are characterized by log([OIII] /Hβ) $<$ 0.5, log([NII] /Hα) $>$ -0.2, log([SII] /Hα) > -0.4 and log([OI] /Hα) > -1.1.

We have obtained the emission line fluxes for all but 18 objects from the literature (Ho et al., 2001; Veilleux et al., 1995; Moustakas and Kennicutt, 2006; Wu et al., 1998). These 18 objects have been excluded from the sample in order to ensure a sample of bona-fide LINERs. In the same vein, another four objects, lacking [OIII] measured fluxes (NGC 3189, NGC 4414, NGC 5350 and NGC 6503) have been excluded from the sample. NGC 4013 was also rejected because it has 100% error in its measurements. 51 out of the 116 objects were already classified as LINERs in our previous work GM+06. However, we have detected that the nuclei of NGC 4395 and NGC 5194 were misclassified as LINERs, belonging to the Seyfert class. We have therefore excluded these two objects from the final sample as well.

Eight of the remaining 65 objects were already excluded from the group of LINERs since they were classified as Starburst, Seyferts or Transition objects in GM+06. Then, the remaining 57 objects have been reclassified in this paper, finding that 18 are Starbursts (NGC 660, IRAS 08572+3915, IRAS 09111-1007, IRAS 10565+2448, NGC 3921, NGC 4435, NGC 4651, NGC 4666, UGC 08335, IC 0883, IRAS 15250-3609, NGC 5953, CGCG 463-030, MRK 0883, NGC 6285, NGC 6286, MRK 507 and NGC 7769), 5 are Seyferts (NGC 3031, NC 3312, IRAS 14348-1447SW, NGC 6951 and NGC 7479) and 34 LINERs.

Adding these 34 new LINERs to our previous sample of 49 LINERs, it ends up in a final sample of 83 objects, 68 observed with *Chandra* and 55 with *XMM-Newton* data, 40 of them in both datasets.

Table 3.1 includes the properties of the host galaxies[2]: Col. (1) Label number; Col. (2) source common name; Col. (3) R.A. 2000 position; Col. (4) Dec. 2000 position; Col. (5) redshift; Col. (6) distance; Col. (7) reference for the distance; Col. (8) B magnitude; Col. (9) E(B-V)and Col. (10) morphological type. Distances have been chosen first from Tonry et al. (2001) if available, second from Ferrarese et al. (2000), third from Tully (1998) and otherwise assuming H_0= 75 km s^{-1}Mpc.

Fig. 3.1 shows, from top to bottom, the redshift, morphological type, absolute B magnitude and apparent magnitude distributions. The distributions for the 476

[2]Main properties extracted from the RC3 catalogue

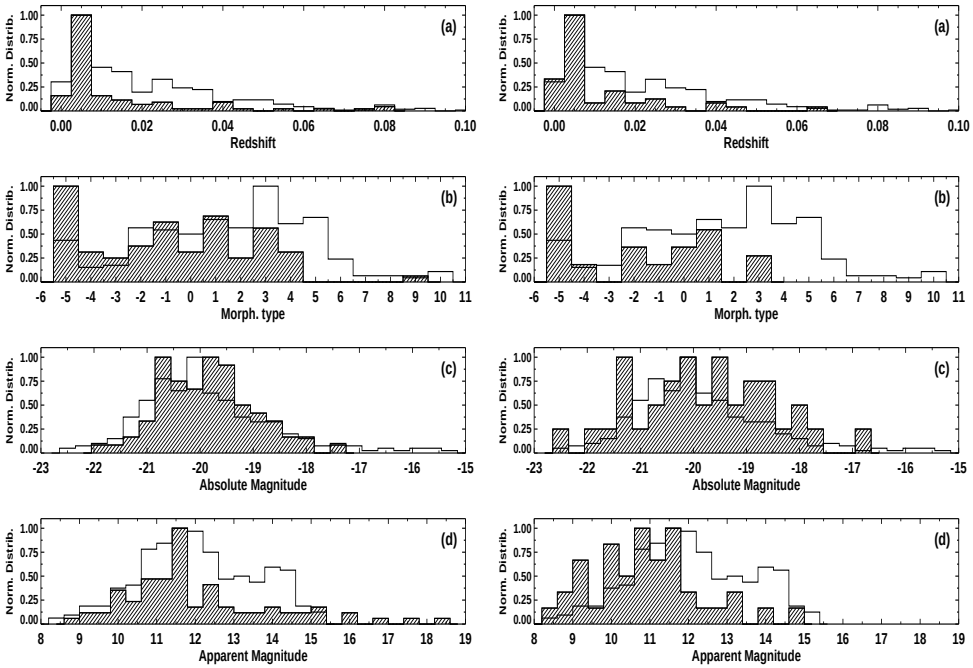

Figure 3.1: *(*Left*): total sample of LINERs in MCL (empty histogram) versus X-Ray sample (dashed histogram), normalized to the peak. (*Right*): X-Ray sample (empty histogram) versus the sample reported by GM+06, normalized to the peak. (a) Redshift, (b) morphological types (from the RC3 catalog: t<0 are for ellipticals, t=0 for S0, t=1 for Sa, t=3 for Sb, t=5 for Sc, t=7 for Sd, and t>8 for Irregulars), (c) absolute magnitudes, and (d) apparent magnitudes distribution.*

LINERs in the MCL catalogue are shown with empty histograms. To the left (right) pannels, the corresponding distribution for our final (GM+06) sample are shown with dashed histograms. All distributions are normalised to their maximum values.

Comparing with our previous work on a smaller sample of 51 objets (GM+06) we now have later morphological types. However, there still exists a lack of later morphological types (t>4) compared to the whole MCL catalogue. It seems that the lack of faint LINERs present in our previous analysis (GM+06) now dissapears. The median total absolute magnitude is now -19.9±0.9 which is consistent with that in the MCL catalogue (-20.0±1.5). The median redshift is z = 0.059±0.018, higher to that for MCL (z =0.015±0.040) but still within one sigma deviation.

Table 3.2 provides the observational details for each source: Col. (1) label num-

ber; Col. (2) source name; Col. (3) galactic column density[3]; Col. (4) spatial scale (parsecs per arcsec); Col. (5) the observational identifier for *Chandra* data; Col. (6) Net exposure time of the *Chandra* observation; Col. (7) *Chandra* R.A.; Col. (8) *Chandra* Dec.; Cols. (9) and (10) radii of the extracted regions in parsecs and arcsecs units, respectively; Col. (11) offset between the *Chandra* position and the nuclear position from 2MASS; Col. (12) pileup percentage in *Chandra* data; Col. (13) the observational identifier for *XMM-Newton* data; Col. (14) net exposure time of the *XMM-Newton* observation; Col. (15) pileup percentage in *XMM-Newton* data; Col. (16) *HST* filter; Col. (17) observing *HST* identifier and Col. (18) *HST* exposure time.

3.3 Data reduction

Level 2 event data from ACIS instrument have been extracted from *Chandra* archive. The data products have been analysed in an uniform, self-consistent manner using *CXC Chandra Interactive Analysis of Observations* (CIAO) software version 3.4. *Chandra* data have been reduced following the prescriptions in GM+06. In the following subsections we include the details on *Chandra* reduction only if different to that reported in GM+06.

XMM-Newton data have been reduced with SAS v7.0.0, using the most updated calibration files available. In this paper, only data from the EPIC pn camera (Struder et al., 2001) will be discussed. The spectral analysis has been performed with *XSPEC* (version 12.3.1).

Images could be dominated by the background if time intervals affected by "flares" are not excluded. In *XMM-Newton* data high-background particle "flares" were removed by applying fixed thresholds on the single-event, E>10 keV and Δt=10s light-curves by using the SAS task EVSELECT.

Pileup affects both flux measurements and spectral characterisation of bright sources (Ballet, 2001). The pileup estimation has been performed using PIMMS software. To evaluate the importance of pileup for each source we have used the 2-10 keV flux, the spectral index, the column densities both galactic and that estimated from the spectral analysis and the redshift. In the case of *Chandra* data the frame time of the observation was also needed. The resulting percentage of pileup is reported Cols. (12) and (15) in Table 3.2.

We notice that pileup effects are unimportant in our sample, being in most cases below 10%. For *Chandra* data only three galaxies, NGC 4486, NGC 4579 and NGC 4594, show pileup fractions larger than 10%. For NGC 3998 the pileup is 7%, and for NGC 4278 it is 5%. All the remaining observations show pileups below 4%. For

[3]The galactic column density has been obtained through the task NH within HEASARC software.

XMM-Newton data, only MCG -5-23-16, NGC 4486 and NGC 4696 show pileup fractions higher or around 10%. 3C 218, NGC 3998, NGC 4278, NGC 4736, CGCG 162-010 and NPM1G -12.0625 show a fraction from 4 to 9%. All the other observations show pileups below 2%. We have hence decided not to use the *XMM-Newton* data with pileup fractions larger than 10% (MCG 5-23-16, NGC 4486 and NGC 4696) what results in a final sample of 82 galaxies. Note that since MCG -5-23-16 is the only case with *XMM-Newton* data strongly affected by pileup wihout *Chandra* data. We keep the remaining *XMM-Newton* and *Chandra* data since the pileup effects have been proven to be negligible.

3.3.1 Image data reduction

For the *Chandra* data presented here the image quality has been improved with respect to that in GM+06, with the aim of enhancing the detection of substructures. We have used CSMOOTH task with a minimum and maximum significance signal-to-noise ratio between 3 and 4, respectively, smaller than the value used by GM+06. Only in a few cases differences on the morphological classification are found due to this improvement (see Appendix B, for a discussion of the particular cases).

XMM-Newton smoothed images have been generated using the ASMOOTH SAS task applied to the pn images. We have applied the adaptive convolution technique, designed for Poissonian images, with $S/N \geq 5$. *XMM-Newton* images have been used only when *Chandra* data were not available, i.e., in 14 cases (see below, Section 3.4.1).

3.3.2 Nuclear identification and extraction region

From our previous paper (GM+06) we know that most objects show a complex morphology, with several sources surrounded by diffuse emission. This complex structure makes the nuclear identification a decisive issue.

The use of the excellent spatial resolution data provided by *Chandra* allows us to extract regions with radii lower than 100 pc in 5 cases (NGC 2787, NGC 2841, NGC 4594, NGC 4736 and NGC 5055) with a median value of 300 pc for the assumed distances of our sample. For most of the sources, the extraction region is so small that we can rule out the possibility that additional X-ray emitting sources are contributing significantly to the observed emission, eventually provoking a missclassification of the nuclear source as an AGN .

The nuclear position was retrieved from the 2MASS catalogue and we have identified as the X-ray nucleus the source closest to that 2MASS position. These X-ray positions are tabulated in columns 6 and 7 in Table 3.2. Nuclear spectra were ex-

tracted from a circular region centred in the object using regions defined to include as many of the source photons as possible, but at the same time to minimize the contamination from nearby sources and background. Col. 8 shows the extraction radius and Col. 9 shows the X-ray to optical offset of the nuclei. The extraction region is in most of the cases around 2″, always smaller than 8″. All but two sources are within the extraction region, namely NGC 4696 and MRK 0848. NGC 4696 was already reported as having extended morphology without a nuclear component in GM+06.

For *XMM-Newton* data, the nuclear positions have been retrieved from NED and automatically circular regions with 25″ radii (500 pixels) have been selected as the extraction regions. This 25″ radius is between 80% (85%) of the PSF at 1.5 keV (9.0 keV) for an on-axis source with EPIC pn instrument. These extraction regions range between 630 pc (NGC 4736) and 40 kpc (IRAS 14348-1447) at the distances of our sample. The extraction radius is hence large enough to include de nucleus together with the central region of the galaxy, so this radius guarantees that the nucleus is always within the extraction region centered at the optical position.

3.3.3 Spectral data reduction

Only the objects with more than 200 counts in the 0.5-10 keV energy range have been used to perform the spectral fitting. The number of counts have been computed by using DMEXTRACT and DMLIST tasks within CIAO package for *Chandra* data and EVSELECT for *XMM-Newton* data. They are tabulated in Cols. (6) and (14) in Table 3.2 for *Chandra* and *XMM-Newton* data, respectively.

The nuclear positions have been defined as explained in Section 3.3.2. In order to determine appropiate source extraction, the aperture radius for each source on the detector was estimated as follows: (1) 4-6 pixels for a single source, (2) 3-4 pixels for objects with few knots close to the nucleus to exclude nearby sources, and (3) ≥ 6 pixels for sources dominated by diffuse emission, since a good S/N is required for extracting the spectra. The background region is defined as either a source-free circular annulus centred in the nucleus or a circular region close to the nucleus. Response and ancillary response files were created using the CIAO MKACISRMF and MKWARF tools.

In *XMM-Newton* data the background was extracted from a circular region in the same chip as for the source region. The regions were extracted by using EVSELECT and pn redistribution matrix and effective areas were calculated with RMFGEN and ARFGEN tasks, respectively.

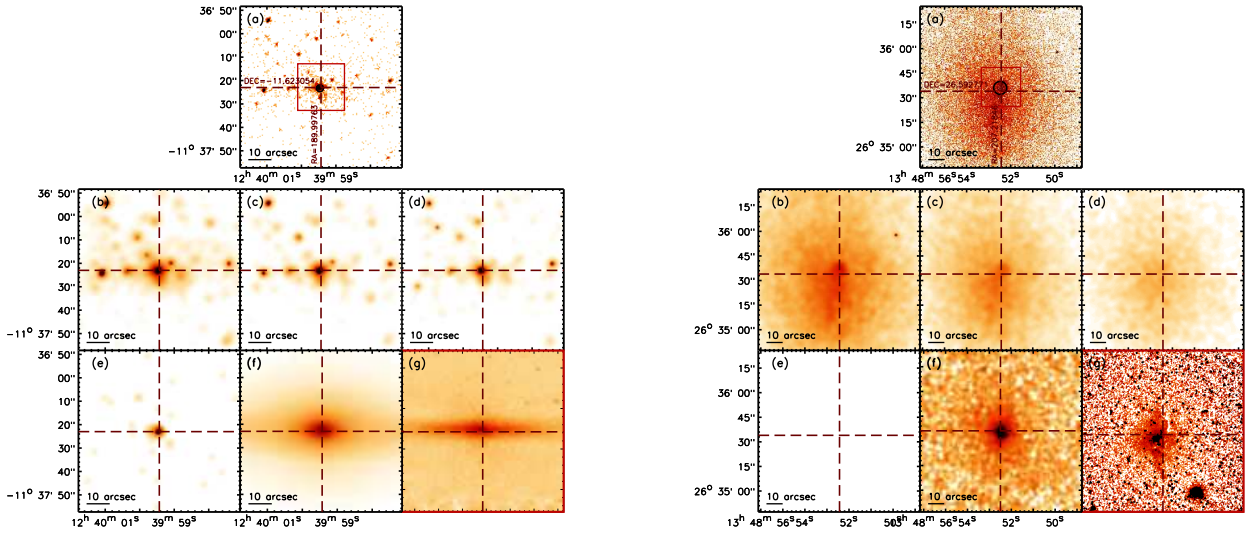

(i) NGC 4594 (ii) CGCG 162-010

Figure 3.2: *Images for (i) the AGN candidate NGC 4594 and (ii) for the SB candidate CGCG 162-010. The top image corresponds to the 0.6-8.0 keV band without smoothing. The following 4 images correspond to the X-ray bands 0.6–0.9 (*Centre-left*), 1.6–2.0 (*Centre-Centre*), 4.5–8.0* (*Centre-Right*) and 6.0–7.0 keV (*Bottom-Left*). The 2MASS image in Ks band is plotted in the* Center-Bottom *box. The enlarged view of the region marked as a rectangle in the top image is the sharp-divided HST optical image in the filter F814W (*Bottom-Right*). Note that this figure plots the same example than that reported in GM+06. However the smoothing treat is different (3-4 significant signal-to-noise ratio).*

3.4 Data analysis

3.4.1 Imaging analysis

In order to gain insight into the emission mechanisms for the whole sample of LINERs, we have studied the X-ray morphology of the sources in six energy bands: 0.6–0.9, 0.9–1.2, 1.2–1.6, 1.6–2.0, 2.0–4.5, and 4.5–8.0 keV. The bands were chosen to maximize the detection, as well as to obtain a good characterisation of the spectra, as illustrated in the next section (same as GM+06). In the last energy band (4.5–8.0 keV), the range from 6.0 to 7.0 keV was excluded to avoid possible contamination due to the FeK emission line[4] (the corresponding band will be called (4.5–8.0)* keV hereafter). *Chandra* data have been used for image analysis when available; *XMM-Newton* data have been used otherwise. Fourteen *XMM-Newton* images have been included in the image catalogue, namely NGC 0410, NGC 2639, NGC 2655, NGC 2685, NGC 3185, NGC 3226, NGC 3623, NGC 3627, IRAS 12112+0305, NGC 5005, NGC 5363, IC 4395, NGC 7285 and NGC 7743.

Adaptively smoothed images were not used for any quantitative analysis, but only for a morphological classification. An example of the images in the four bands 0.6–0.9, 1.6–2.0, 4.5–8.0*, and 6–7 keV are given in Fig. 3.2. See Appendix C on the catalogue of images that provides this information for the whole sample. The extraction region is plotted with a black circle in the *Top-Centre* figure. We have added the 2MASS IR Ks band (*Bottom-centre*) and the optical *HST* F814W[5] band (*Bottom-right*) when available. *HST* data have been processed following the sharp dividing method (Sofue et al., 1994; Marquez and Moles, 1996; Laine et al., 1999; Marquez et al., 2003, and references therein) in order to better show the internal structure of the galaxy. The observational details of the *HST* data are included in Table 3.2 (Cols. 16, 17 and 18).

Since we focus our attention on the nuclear sources, no attempt has been made to fully characterise the flux and the spectral properties (when possible) of extranuclear sources, whose study is beyond the scope of this paper. As a first insight into the nature of LINERs, we have taken the presence of an unresolved compact nuclear source in the hard band (4.5–8.0* keV) as evidence of an AGN. Note that due to the better resolution of *Chandra* data the detection of a point-like source in the 68 objects with *Chandra* data is a stronger argument pointing to their AGN nature. We also give the results for the whole sample for completeness. Of course, multiwavelength observations will be needed to assess their nature (See Sect. 3.9). The sample has been grouped into 2 main categories (same as GM+06):

[4]The most common emission features in the 2-10 keV band of AGN spectra are those of iron between 6.4–6.97 keV (depending on the ionisation state of Fe), related to the reflexion in the accretion disk.

[5]Or the availabe HST image with closest broad band to this one.

- **AGN candidates:** We include all the galaxies with a clearly identified, unresolved nuclear source in the hard band (4.5–8.0)* keV. In Fig. 3.2a we show NGC 4594, as an example of AGN candidate, where a clear point-like source exists in the hardest band (*centre-right*). Almost sixty percent (48/82) of our sample galaxies have been classified as AGN-like nuclei and 63% (43/68) with *Chandra* imaging data.

- **Starburst candidates (hereinafter SB):** Here we include all the objects without a clearly identifiable nuclear source in the hard band. To call Starburst candidates as those without nuclear source at hard energies is, in some way, an abuse of the language, as we are refering to any process that does not have an AGN (star-formation, globular clusters, etc.) or is suficiently obscured (as Compton-thick object). In Fig. 3.2b we show the images of CGCG 162-010 as an example of these systems. Note that there does not appear to be a nuclear source in the hardest energy band (centre-left). Forty percent (34/82) of the sample of LINERs falls into this category and 57% (25/68) within the sub-sample with *Chandra* imaging data.

3.4.2 Spectral modelling

The spectra have been fitted in the 0.5-8.0 keV energy range using XSPEC v12.3.1. To be able to use the χ^2 statistics, the spectra were binned in order to obtain a minimum of 20 counts per spectral bin before background subtraction. The task GRPPHA included in the software FTOOLS has been used for this purpose.

To discriminate which emission mechanisms are involved in these objects and at the same time to get a good estimation of the X-ray luminosities, a careful analysis of the X-ray spectra must be done. Since our aim is to try to disentangle whether the emission mechanism might be due to an AGN or to thermal emission, two models have been used: a single power-law and a single-temperature optically-thin plasma emission model. With respect to GM+06, here Raymond-Smith models (Raymond and Smith, 1977) have been removed and MEKAL models are used instead since both represent the same physical mechanism (emission by a hot thermal plasma) but MEKAL is a better representation because it is more sensitive to chemical abundances. GM+06 did not find differences between the temperatures reported by the two models and needed the inclusion of MEKAL model in eight cases.

We also test the combination of MEKAL plus power-law model. This model is similar to that reported in GM+06, but now two absorptions have been included to describe the most general scenario of obscuring matter, in which the one coming from a thermal region can be located at a different locus from the obscured matter around the AGN. Moreover, galactic absorption has been fixed to the predicted

value (Col. (3) in Table 3.2) using NH tool within FTOOLS.

GM+06 obtained that the most plausible scenario for LINER nuclei is the combination of a thermal model (MEKAL or Raymond Smith models) with a primary power law continuum (described by the spectral index) responsible for the bunch of the hard X-rays. However, it has to be noticed that some objects do not fit into the proposed scenarios described in GM+06. This is the case, e.g., of UGC 08696, which was fitted in our previous analysis adding a Gaussian to the best-fit centered at 5.93 keV with a width of 1.22 keV. Xia et al. (2002) found that the 10″ central region is clearly complex and consists of at least three components: at energies above 3 keV, there is a heavily absorbed power law plus a narrow 6.4 keV FeKα line, and at soft energies a less absorbed power-law and a MEKAL thermal plasma reproduce the emission with many evident line features, in particular FeL and Ne line complexes and other α element emission lines (such as Mg Kα, Si Kα lines, O_{VII} and O_{VIII} lines). In the analysis presented here we have decided to use a more general framework, as explained below.

Cappi et al. (1999) found that the general picture for an AGN in X-rays can be modelled by the so-called *Baseline* model for AGNs. This *Baseline* model includes the following components: (a) The primary continuum described by a power law; (b) a Compton reflection component from cold matter; (c) a narrow Kα iron line modelled with a Gaussian profile; and (d) for the soft X-ray spectrum (< 2 keV), a combination of a thermal component model (MEKAL) and a scattering component by ionised material (power-law model with the same slope that the primary continuum).

We will prove the goodness of this model when applied to LINERs with the following simplifications. (1) The reflection component is seen at high energies (> 8 keV), so we have removed this component for simplicity. (2) The iron emission line will be studied independently. Therefore, the final model is a lineal combination of a soft component (abs(MEKAL+power-law)) and a hard component (abs(power-law)).

One of the objectives of our analysis is to study the importance of the thermal emission in our LINER sample. We have included a modification of the *Baseline* model to allow this analysis by the exclusion of the thermal component. Our last model is the combination of a primary continuum described by a power-law with a soft spectrum fitted with a scattering component (abs(power-law)+abs(power-law)).

To summarise, we have selected five models in order to parametrise five emission mechanism scenarios (the first is the simplest scenario and the last the most complex one):

1. *Power-law model*: (for simplicity hereinafter **PL**). This is the simplest scenario in which an AGN-like object is dominating the emission mechanisms throughout the whole X-ray range. The free parameters are the spectral index Γ and the

normalisation[6]. The column density is added as a free parameter, to take into account the absorption by matter between our galaxy and the target nucleus.

2. *MEKAL model*: (for simplicity hereinafter **ME**). In this case the thermal emission is the responsible for the bunch of the X-ray energy distribution. Temperature and normalisation are free parameters. Also an absorption in addition to the galactic value is included with column density as the free parameter, in order to take into account the matter between our galaxy and the nucleus.

3. *MEKAL plus power-law model*: (for simplicity hereinafter **MEPL**). The AGN dominates the hard X-rays although it cannot explain the soft X-rays (< 2 keV) that require an additional thermal contribution. The four parameters explained in ME and PL models are considered together.

4. *Power-law plus power-law model*: (for simplicity hereinafter **2PL**). This is the general scenario for which the bunch of the hard X-rays is due to a primary continuum described by a power-law and the soft X-ray spectrum is due to a scattering component also described by a power-law with the same spectral index. Therefore, the free parameters are Γ and two normalisations.

5. *MEKAL plus power-law and power-law model*: (for simplicity hereinafter **ME2PL**). As the model explained before, but including the plausible contribution of thermal emission at soft X-rays. This is the Compton-thin Seyfert 2 *baseline* model used by Guainazzi et al. (2005). The free parameters are Γ, temperature (kT) and three normalisations.

For models 3, 4 and 5, two absorbing column densities are used, which will be called hereinafter NH1 and NH2. Tables 3.3 and 3.13 give the spectral parameters and statistics for the PL model in *Chandra* and *XMM-Newton* data, respectively. The columns correspond to Col. (1) label number, Col. (2) name, Col. (3) column density (NH1) in units of 10^{22} cm^{-2}, Col. (4) the spectral index and Cols. (5), (6) and (7) χ^2, degree of freedom and reduced χ^2, respectively.

Tables 3.4 and 3.14 give the spectral parameters and statistics for the ME model in *Chandra* and *XMM-Newton* data, respectively, where Col. (1) label number, Col. (2) name, Col. (3) column density (NH1) in units of 10^{22} cm^{-2}, Col. (4) temperature and Cols. (5), (6) and (7) χ^2, degree of freedom and reduced χ^2, respectively.

Tables 3.6 and 3.16 give the spectral parameters and statistics for the MEPL model in *Chandra* and *XMM-Newton* data, respectively, with Col. (1) label number,

[6]Normalisations are shown in Tables 3.5, 3.6 and 3.7 for *Chandra* data and Tables 3.15, 3.16, and 3.17 for *XMM-Newton* data, only where two additives models are involved; otherwise they are directly related to the computed flux.

Col. (2) name, Cols. (3) and (4) the two column densities (NH1 and NH2) in units of 10^{22} cm^{-2}, Col. (5) spectral index, Col. (6) temperature, Cols. (6) and (7) normalisations for the two components and Cols. (8), (9) and (10) χ^2, degree of freedom and reduced χ^2, respectively.

Tables 3.5 and 3.15 give the spectral parameters and statistics for the 2PL model in *Chandra* and *XMM-Newton* data, respectively, with Col. (1) label number, Col. (2) name, Cols. (3) and (4) the two column densities (NH1 and NH2) in units of 10^{22} cm^{-2}, Col. (5) spectral index, Cols. (6) and (7) normalisations for the two components and Cols. (8), (9) and (10) χ^2, degree of freedom and reduced χ^2, respectively.

Tables 3.7 and 3.15 give the spectral parameters and statistics for the ME2PL model in *Chandra* and *XMM-Newton* data, respectively, with Col. (1) label number, Col. (2) name, Cols. (3) and (4) NH1 and NH2 in units of 10^{22} cm^{-2}, Col. (5) spectral index, Col. (6) temperature, Cols. (7), (8) and (9) normalisations for the three components and Cols. (10), (11) and (12) χ^2, degree of freedom and reduced χ^2, respectively.

3.4.3 Best-fit selection criteria

We have chosen the best fit model as the simplest model that gives a good fit with acceptable parameters.

To estimate whether the inclusion of a more complex model improves significantly the fit, the F-statistics test (F-test task within XSPEC software) has been applied. The F-test is a model comparison test which is used to select, from two competing models, which is the best fit describing a particular data-set. A standard threshold for selecting the more complex model is a significance lower than 0.05 (95% confidence). Tables 3.8 and 3.18 show the F-test results for *Chandra* and *XMM-Newton* data, respectively, with Col. (1) label number, Col. (2) name, Cols. from (3) to (7) significance for 2PL versus PL, MEPL versus ME, MEPL versus PL, ME2PL versus MEPL and ME2PL versus 2PL, respectively. Col. (11) shows the final best-fit.

In practise, the used methodology can be summarised as follows:

- *Reliable model.* We have considered a model as an acceptable spectral fit when χ^2_r is in the range from 0.6 to 1.5 and the resulting parameters are within an acceptable range of values, that we consider T$\sim$0-2 keV or Γ $\sim$1-3. The highest values of expected temperatures (1-2 keV) is for the central galaxies in clusters (Kaastra et al., 2008, and references therein). Those values corresponding to unphysical parameters and/or with a bad χ^2_r are marked with 'U' in Tables 3.8 and 3.18 for *Chandra* and *XMM-Newton* data, respectively. When the range of values provided for a parameter is not constrained, the resulting fit is also

considered as bad, and consequently marked with "U" in the corresponding table.

- *Simplest model.*We have defined whether ME or PL are a better description of the data by using the χ^2_r. The two possibilities were included when the χ^2_r are too close to discriminate between the two.

- *Composite model.* When ME is better than PL, we have used the F-test to know whether MEPL improves the results provided by ME (Cols. (4) in Tables 3.8 and 3.18 for *Chandra* and *XMM-Newton* data, respectively). When PL is better than ME, 2PL and MEPL were tried as a complication of PL (Cols. (3) and (5) in Tables 3.8 and 3.18 for *Chandra* and *XMM-Newton* data, respectively). When none of the two simple models are good enough we tested 2PL vs. PL, MEPL vs. ME and MEPL vs. PL to know if 2PL or MEPL are good representations by using the F-test. In the case that after this selection the two composite models, MEPL and 2PL, are reliable, we have compared again the χ^2_r to select the better description (χ^2_r closer to unity).

- *ME2PL model.* When the best-fit is MEPL or 2PL, we have used the F-test (Cols. (6) or (7) in Tables 3.8 and 3.18) to test whether the inclusion of ME2PL results in a statistically significant improvement.

To clarify the methodology, we present a couple of examples: NGC 4261 for *Chandra* data and NGC 0410 for *XMM-Newton* data. In the case of NGC 4261, neither PL nor ME models show a statistically acceptable fit ($\chi^2_r = 4.92$ and $\chi^2_r = 6.89$, respectively). 2PL also shows an unacceptable χ^2_r=3.59. MEPL has a reasonable χ^2_r, but the spectral index is too flat ($\Gamma = 0.07$). Then, the only acceptable model is the composite ME2PL that gives $\chi^2 = 1.29$ and parameters within the allowed ranges ($\Gamma = 2.37$ and kT=0.57 keV). In the case of NGC 0410, among the simplest model, only ME is a good fit because PL results in χ^2_r=5.94. The F-statistics test shows that MEPL results in an improvement in the final fit (see Col. (4) in Table 3.18) and ME2PL cannot be the final best-fit because it shows unrealistic parameters ($\Gamma = 5.72$). Then, the model selected as the best fit is MEPL ($\chi^2_r = 1.23$, $\Gamma = 2.43$ and kT=0.69 keV).

To sum up, in what follows we will talk about either reliable fits or best fits, the latter corresponding to that reliable model that better reproduces the data.

3.4.4 *Chandra* Data

For 44 out of 68 objects the spectral analysis has been possible. Fig. 3.3 shows an example of the spectrum with each model for the case of NGC 4261. The resulting

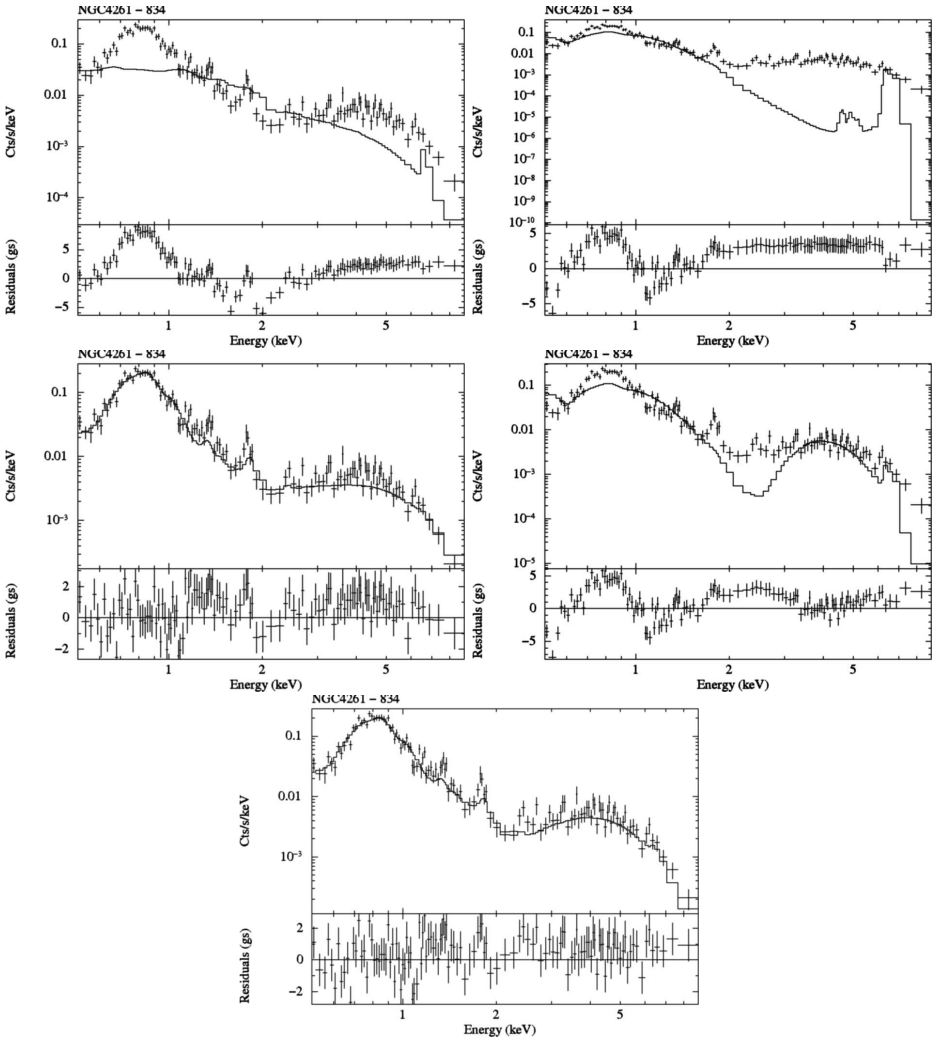

Figure 3.3: *Spectral fits of NGC 4261 (*Chandra *data). (*Top-left*): Thermal model (ME), (*Top-right*): Power-law model (PL), (*Centre-left*): Power-law plus thermal model (MEPL), (*Centre-right*): Two power-law model 2PL), (*Bottom*): Two power-law plus thermal model (ME2PL). The best-fit is ME2PL model.*

best-fit models for our sample galaxies are summarised in Table 3.9, with Col. (1) label number, Col. (2) name; Col. (3) X-ray nuclear class; Col. (4) the final fit. Resulting column densities for the best-fit are shown in Cols. (5) and (6), the spectral index and temperature are shown in Cols. (7) and (8) when PL and ME were needed

and Cols. (9), (10) and (11) show the χ^2, degree of freedom (d.o.f.) and reduced χ^2.

In order to better characterise our sources, we grouped our analysis in "Single Models" with one component (ME and PL) and "Composite Models" when more than a single component is needed (MEPL, 2PL and ME2PL).

Single Models:

PL is reliable in 25 objects, but 2PL and/or MEPL result in an improvement in all but 7 objects (NGC 2787, NGC 3414, NGC 3945, NGC 4594, NGC 5055, NGC 5746 and IRAS 17208-0014) by using the F-test statistics. Therefore, seven objects show the single PL as the best-fit.

ME is reliable in 14 objects, but PL or the inclusion of a composite model MEPL result in an improvement in all but 3 cases (NGC 3507, CGCG 162-010 and NGC 6482), which represents only 7% of the sample.

Composite Models:

When we exclude the cases in which ME or PL is the best representation, the complex model is needed in 34 out of the 44 objects (77%). The 2PL model is better than MEPL in 12 cases (NGC 0833, NGC 1052, UGC 05101, NGC 3998, NGC 4374, NGC 4486, NGC 4736, MRK 266NE, UGC 08696, NGC 6251, NGC 6240 and IC 1459) and MEPL is better than 2PL in 19 objects. Three objects (NGC 0835, NGC 4111 and NGC 4261) do not fit within neither MEPL nor 2PL because of unrealistic spectral indices. For these 12 objects reliably fitted with 2PL, the F-test demonstrates that the use of ME2PL is an improvement in all but NGC 1052 and UGC 05101. Within the 19 objects reliably fitted with MEPL, the F-test demonstrates that the use of ME2PL improves the resulting fit only in NGC 2681 and NGC 3898. Furthermore, NGC 0835, NGC 4111 and NGC 4261 only fit with the composite ME2PL model.

In summary, PL is the best-fit in 7 cases (16%) while ME is the best-fit only in 3 cases (7%). MEPL is the best-fit model in 17 out of 44 objects (39%) while 2PL is the best-fit in 2 cases (4%). ME2PL was needed in 15 cases (34%).

The median values of Γ, temperature and soft and hard column densities are $<\Gamma>$=2.05$\pm$0.42 , $<$kT$>$=0.57$\pm$0.22 keV , $<$NH1$>$=(0.28$\pm$0.72)$\times 10^{22}\,\mathrm{cm}^{-2}$ and $<$NH2$>$=(0.86$\pm$10.43) $\times\ 10^{22}\,\mathrm{cm}^{-2}$.

Luminosities

Soft (0.5-2.0 keV) and hard (2-10 keV) luminosities have been computed from the best-fit selected model for the sub-sample of 44 objects with spectral fitting. In order

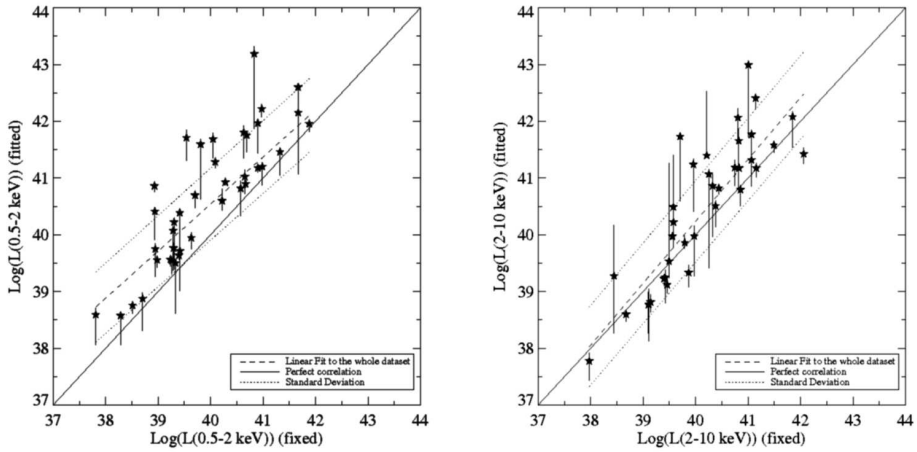

Figure 3.4: *Comparison between the luminosity obtained with the best-fit versus the estimated luminosity assuming a spectral index* Γ*=1.8 and galactic absorption.*

to get a luminosity estimation of the whole sample we have used the same procedure developed in GM+06 and based in that proposed by Ho et al. (2001). We obtained a count rate to flux conversion factor between 2.0–10.0 keV and 0.5–10.0 keV energy ranges, assuming a power-law model with a spectral index of 1.8 and the Galactic interstellar absorption (NH task within FTOOLS) when the spectral fit is not available.

Table 3.12 shows the X-ray fluxes and luminosities, with Col. (1) label number, Col. (2) name, Cols. (3) and (4) soft (0.5–2.0 keV) and hard (2–10 keV) observed fluxes in units of 10^{-13}erg s^{-1}, and Cols. (5) and (6) logarithm of soft and hard intrinsic luminosities.

To validate the approximation, we have computed the soft and hard X-ray luminosity assuming a spectral index of 1.8 and the Galactic interstellar absorption in the subsample of objects with spectral fit. The X-ray luminosities computed through the spectral fit were then plotted against the X-ray luminosities computed assuming the fixed power-law model (Fig. 3.4). The continuous line indicates the position for identity (x=y) while the dashed line is the linear fit to the data. Dotted lines correspond to 3-sigma deviation, above and below the fit. Arrows are upper limits on the luminosity. Both soft and hard X-ray luminosities tend to be underestimated with the fixed model (slope 0.829$\pm$0.008 and zero point of 7.37$\pm$ 0.32 for the soft X-ray luminosity and slope 1.091$\pm$0.009 and zero point -3.41$\pm$ 0.36 for the hard X-ray luminosity).

NGC 0833, NGC 0835, NGC 1052, UGC 05101, UGC 08696 and NGC 6240 show high discrepancies between estimated and modelled luminosities, mainly because the spectral modelling suggests that high column densities (1-5$\times 10^{23}$ cm^{-2}) and/or strong iron emission lines are required, whereas we are assuming a galactic column density value in our estimation. In addition, 7 objects have large departures only for the soft X-ray luminosity calculated assuming a fixed power-law model (NGC 0315, NGC 3898, NGC 4111, NGC 4261, NGC 4696, NGC 5813, and NGC 7130). For NGC 0315, NGC 3898, NGC 4111 we can attribute such differences as due to the differing column densities, but this is not the case for the remaining objects. The median deviations from the expected value are 0.65 for the soft luminosity and 0.10 for the hard luminosity. It therefore appears that the estimation of the hard X-ray luminosity is reasonably good, with an exception when very obscured galaxies are analysed. Soft X-ray luminosities have to be taken with some reserves. This result appears not to be a surprise since most of the objects are better represented by a composite model and then at soft energies they are more affected by the assumed simplistic approximation of a single power law.

3.4.5 *XMM-Newton* data

In 44 out of 55 objects the spectral analysis has been possible. Fig. 3.5 shows an example of the spectrum with each model for the case of NGC 4261. The resulting best-fit models are summarised in Table 3.19, where the columns correspond to Col. (1) label number, Col. (2) name; Col. (3) X-ray nuclear class; Col. (4) final fit; Cols. (5) and (6) reported column densities (NH1 and NH2) for the best-fit, Cols. (7) and (8) spectral index and temperature when PL and ME were needed and Cols. (9), (10) and (11) χ^2, degree of freedom (d.o.f.) and reduced-χ^2. As for *Chandra* data, in the following sections we divide the analysis between "Single Models" (ME and PL) and "Composite Models" (MEPL, 2PL and ME2PL).

Single Models:

PL gives a statistically acceptable fit in 13 out of the 45 objects (NGC 2787, NGC 3226, NGC 3628, NGC 3998, NGC 4278, NGC 4321, NGC 4494, NGC 4579, NGC 4594, MRK 0848, NGC 6240, IRAS 17208-0014 and NGC 7285). However, 2PL or MEPL result in an improvement in 8 objects (NGC 2787, NGC 3226, NGC 4278, NGC 4321, NGC 4579, NGC 4594, NGC 6240 and NGC 7285) by using the F-test statistics. In the case of IRAS 17208-0014, ME is a better description of the data-set. Therefore, four objects show the single PL as the best-fit (NGC 3628, NGC 3998, NGC 4494 and MRK 0848).

ME gives a reliable fit in 7 objects (NGC 0410, NGC 2639, UGC 04881, NGC 4125, IRAS 14348-1447, IRAS 17208-0014 and NGC 6482), but the inclusion of a complex

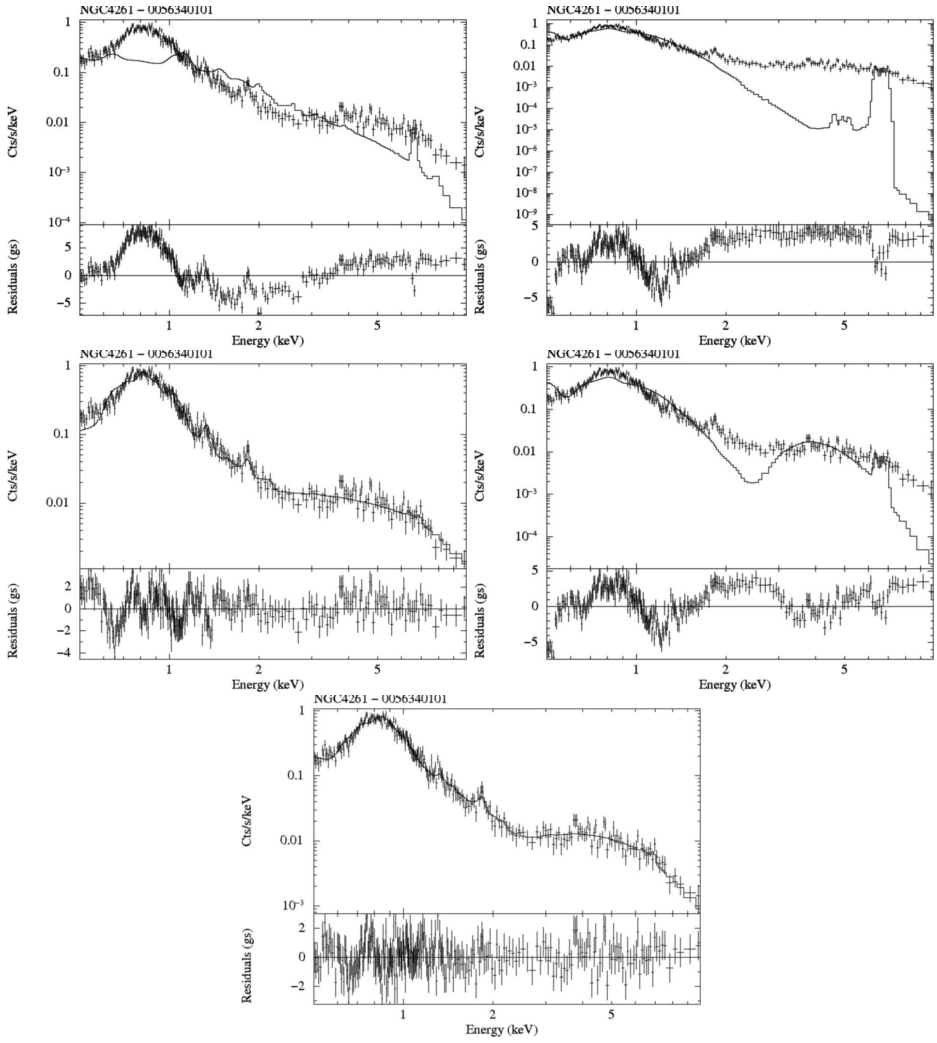

Figure 3.5: *Spectral fits of NGC 4261 (*XMM-Newton *data). (*Top-left*): Thermal model (ME), (*Top-right*): Power-law model (PL), (*Centre-left*): Power-law plus thermal model (MEPL), (*Centre-right*): Two power-law model (2PL), (*Bottom*): Two power-law plus thermal model (ME2PL). The best-fit is ME2PL model.*

model results in an improvement in NGC 0410 and NGC 4125. Hence, ME is a good representation only in 5 cases (NGC 2639, UCG 04881, IRAS 14348-1447, IRAS 17208-0014 and NGC 6482), which is the 11% of the sample.

Composite Models:

A complex model is therefore needed in 36 out of the 44 objects.

The F-test and χ^2 statistics show that 2PL is a better description only in 3 cases (NGC 1052, NGC 3226 and NGC 4594) and MEPL in 29 objects. Within these 29 objects, NGC 7743 does not show a statistically acceptable fit, being the more acceptable a MEPL fit ($\chi^2_R = 1.76$). Moreover, in UGC 05101, NGC 4261, UGC 08696 and NGC 7743 neither MEPL nor 2PL are good representations of the data-sets.

Within these objects reliably fitted by 2PL, the F-test demonstrates that the use of ME2PL is not an improvement only in NGC 3226.

Within the 29 objects reliably fitted by MEPL, the F-test demonstrates that the use of ME2PL is not an improvement in 17 objects (NGC 0410, 3C 218, NGC 3690B, NGC 4125, NGC 4278, NGC 4314, NGC 4321, NGC 4552, NGC 4636, NGC 4736, NGC 5005, CGCG 162-010, IC 4395, NGC 5813, NGC 7285, IC 1459 and NGC 7743). In UGC 05101, NGC 4261, UGC 08696 and NGC 7743 the only model that gives a satisfactory fit is ME2PL.

In summary, PL is the best-fit in 4 cases (9%) while ME is the best-fit only in 5 cases (11%). MEPL is the best-fit model in 17 out of 44 objects (39%) while 2PL was the best-fit only in 1 case (2%). ME2PL was needed in 17 objects (39%).

The median values of Γ, temperature and soft and hard column densities are $<\Gamma>$=1.99$\pm$0.37 , $<$ kT $>$=0.61$\pm$0.38 keV , $<$ NH1 $>$=(0.10$\pm$0.18) $\times 10^{22}$ cm^{-2} and $<$ NH2 $>$=(0.87$\pm$16.86) $\times 10^{22}$ cm^{-2} .

***XMM-Newton* luminosities**

Soft (0.5-2.0 keV) and hard (2-10 keV) luminosities have been computed from the best-fit selected model for the sub-sample of 44 objects with spectral fitting for *XMM-Newton* data. In order to get a luminosity estimation of the whole sample we have again used the procedure developed in GM+06 after Ho et al. (2001). We obtain a count rate to flux conversion factor between 2.0–10.0 keV and 0.5–10.0 keV energy ranges, assuming a power-law model with a spectral index of 1.8 and the Galactic interstellar absorption (NH task within FTOOLS) when the spectral fit is not available.

Table 3.22 shows the X-ray fluxes and luminosities, with Col. (1) label number, Col. (2) name, Col. (3) X-ray nuclear class; Cols. (4) and (5) soft (0.5–2.0 keV) and hard (2–10 keV) observed fluxes in units of 10^{-13}erg s^{-1}, and Cols. (6) and (7) logarithm of the soft and hard intrinsic luminosities.

To validate the aproximation, we have computed the soft and hard X-ray luminosities assuming a spectral index of 1.8 and Galactic interestellar absorption in the sub-sample of objects with spectral fit. Fig. 3.6 shows soft (*Top*) and hard (*Bottom*)

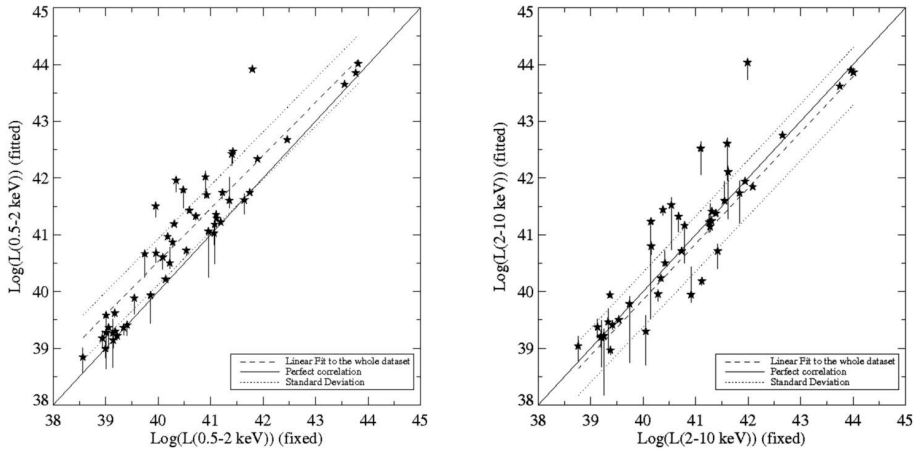

Figure 3.6: *Comparison between the luminosity obtained with the best-fit versus the estimated luminosity assuming spectral index of 1.8 and galactic absorption with* XMM-Newton.

fixed versus fitted luminosities. Continuous line indicates the position of the identity line, the dashed line is the linear fit to the data and the dotted line corresponds to 3 σ above and below the fit. Both soft and hard X-ray luminosities tend to be underestimated with slopes 0.935±0.005 and 0.983±0.006 and zero points 3.12± 0.21 and 0.56± 0.25 .

3.4.6 Iron emission lines

We have searched for the presence of the neutral iron emission line, adding a narrow gaussian centred at redshifted 6.4 keV to the best-fit selected. Two gaussians were also included to avoid contributions from FeXXV at 6.7 keV and FeXXVI at 6.95 keV.

Tables 3.10 and 3.20 show the emission line fluxes of the three emission lines for *Chandra* and *XMM-Newton* data, respectively. Col. (1) shows the object label, Col. (2) gives the name and Cols. (3), (4) and (5) show the emission line fluxes including the error bars for FeKα at 6.4 keV, FeXXV at 6.7 keV and FeXXVI at 6.95 keV, respectively.

Tables 3.11 and 3.21 show the equivalent widths of the three emission lines for *Chandra* and *XMM-Newton* spectra, respectively. Col. (1) shows the label of the object label, Col. (2) gives the name and Cols. (3), (4) and (5) show the equivalent widths, including the error bars, for FeKα at 6.4 keV, FeXXV at 6.7 keV and FeXXVI at 6.95 keV, respectively.

Within the *Chandra* sample FeKα is detected in 6 objects (NGC 0833, UGC 05101,

NGC 4486, NGC 4579, NGC 6240, UGC 08696 and NGC 7130) being three objects (NGC 0833, NGC 6240 and NGC 7130) compatible with high EW (EW>500 eV). Fe XXV is detected in NGC 4486, and NGC 6240 while FeXXVI is detected in four cases (NGC 4486, NGC 4579, NGC 4736 and NGC 6240). We present upper limits otherwise.

The *XMM-Newton* sample show FeKα emission lines in 10 objects (NGC 0315, NGC 0835, NGC 1052, UGC 05101, NGC 3690B, NGC 4579, MRK 266NE, UGC 08696, NGC 6240 and NGC 7285) being 4 objects (NGC 0835, UGC 05101, MRK 266NE and NGC 6240) compatible with high EW. Nine out of 10 cases have *Chandra* observations (excepting NGC 7285) however only in 3 objects we detected the FeKα emission lines. In these cases in which it was detected with *Chandra* data the width of the FeKα emission line is coincident with that from *XMM-Newton* data. FeXXV is detected in 11 cases (NGC 0315, NGC 0410, NGC 1052, UGC 05101, 3C 218, NGC 3690B, NGC 4579, UGC 08696, CGCG 162-010, NGC 6240 and NPM1G -12.0625).

XMM-Newton data is better suited in the range were these emission lines are placed ($\sim$ 7 keV). Then, *XMM-Newton* result is taken when available while *Chandra* was taken otherwise.

3.5 *Chandra* results

We report the results for the 68 LINERs with *Chandra* data. Within these 68 objects, 44 have more than 200 counts what makes the spectral analysis feasible.

The main results from our spectral analysis is that, using the single models, 24 of the 44 galaxies (57%) can be reproduced with a good fit with a single PL whereas only 10 out of the 44 (22%) can be reproduced with a single ME. When using 2PL, we obtained improvement from the single PL in only 2 cases. However if MEPL or ME2PL are taken instead a reliable fit is obtained for 38 out of the 44 objects (84%). The best fit model according to the methodology explained in the previous section is shown in Table 3.9.

Attending to the X-ray morphology in the $4.5 - 8.0^{*}$ keV band the nuclei have been classified according to the detection (AGN-like) or not (SB-like) of an unresolved nuclear source (see Section 3.4.1). This classification is presented in Col. (3) in Table 3.9. The main result is that 42 out of the 68 objects (62%) fall within the AGN category. This percentage increases up to an 80% when only objects with more than 200 counts are considered (35 out of the 44 objects). We note that all the objects for which the best fit is provided either by PL (7 objects) or 2PL (2 objects) are classified as AGN, whereas the three galaxies with a ME as a best fit belong to the SB group. For the cases where no spectral fitting could be done, most of them (19 out of 24)

have been classified as SB-like objects.

A deepest understanding on the nature of the SB-like galaxies can be obtained based on their spectral characteristics. Within the SB-like family, a proper spectral fitting have been possible for 9 galaxies (NGC 3507, NGC 3898, NGC 4321, NGC 4696, CGCG 162-010, NGC 5813, NGC 5846, NGC 6482 and NPM1G -12.0625). In four cases (NGC 4321, NGC 4696, CGCG 162-010 and NPM1G -12.0625) the resulting (2-10 keV) X-ray luminosities seem to be too high ($> 10^{40}$erg s^{-1}) to be interpreted as due to star forming processes; additional sources for such an excess could be either an obscured AGN or an additional component like that coming from the hot gas observed in galaxy clusters. On that respect, it is worthwhile to notice that 5 out of 9 SB galaxies (NGC 4696, CGCG 162-010, NGC 5846, NGC 6482 and NPM1G -12.0625) are confirmed brightest galaxies in clusters; all the remaining, excepting NGC 3507, are known to be members of clusters. Thus, the inclusion of cluster emission could be a possible explanation for their high luminosity. A proper modelization of the hot gas from the underlying cluster needs to be done indeed before any conclusion is drawn. Moreover, regarding their best fit spectral model, none of them need two PL components. In three cases (NGC 3507, CGCG 162-010 and NGC 6482) a single ME is the best representation of their spectra, and for the remaining 6 galaxies MEPL is shown as the best fit (see Table 3.9).

3.5.1 Obscuration

The histogram with the resulting column densities is given in Fig. 3.7 (*Top*, NH1, and *Bottom*, NH2). The empty histograms show the distribution for the whole sample with spectral fittings. We have also studied how NH values are related to the spectral model used. The dashed histograms represent the sub-sample of objects with two-powerlaws (ME2PL and 2PL) as best fit. While NH1 has a narrow distribution centred at $(0.28\pm0.72)\times10^{22}$ cm^{-2} , NH2 shows a wide range with a median value and standard deviation of $(0.86\pm10.43)\times10^{22}$ cm^{-2} . NH1 does not show any tendency with the spectral model, but the highest values of NH2 are obtained with ME2PL. The NH2 empty histogram corresponds to MEPL since single models do not include this second absorption.

We have tested how these distributions change when we take ME2PL or 2PL reliable models instead of the best fits. The result is shown in Fig. 3.8. The median values and standard deviations are $(0.20\pm1.61)\times10^{22}$ cm^{-2} and $(9.45\pm37.93)\times10^{22}$ cm^{-2} , respectively. NH1 shows a similar distribution than the best-fit results while NH2 has a narrower range of values with a median value 10 times higher than the best-fit results. Then we want to remark that the model selection is crucial in order to set the resulting column density. We note at this respect that Seyfert galaxies have

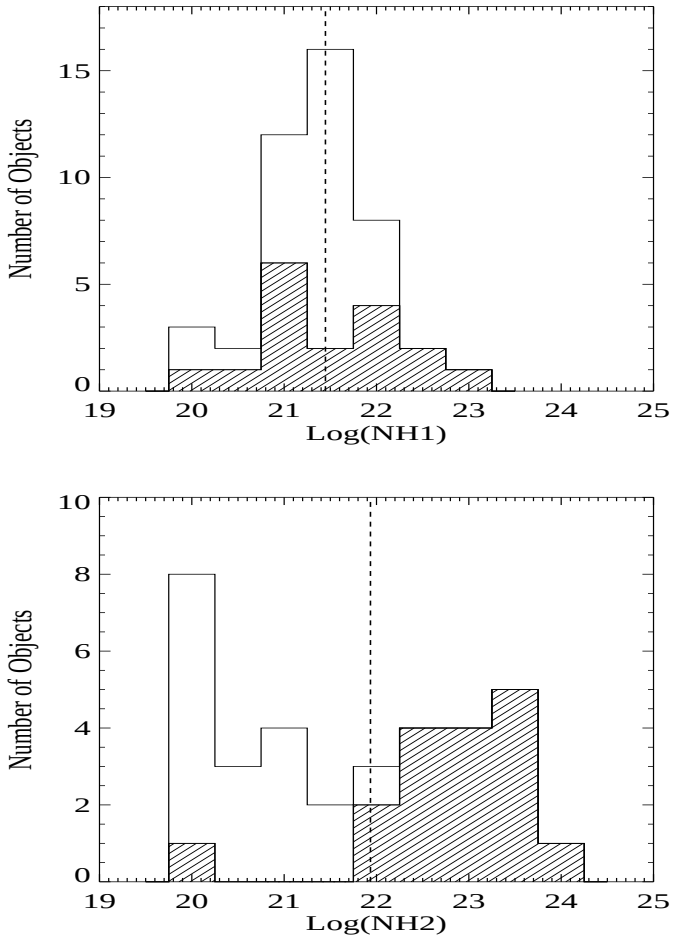

Figure 3.7: *Histogram of column densities obtained with* Chandra *data (emptied histogram). The filled histogram is the sub-sample of objects fitted to ME2PL and 2PL models. (*Top*): NH1 column density histogram and (*Bottom*): NH2 column density histogram.*

been assumed to be fitted to 2PL, whereas here we have found that MEPL is a good description, at least for LINERs, for a large percentage of the data.

In Seyfert 2 galaxies, NH2 is related to the obscuration of the primary continuum. The range this absorption covers in LINERs is compatible with the results reported for Seyfert galaxies (Bianchi et al., 2004; Guainazzi et al., 2005; Panessa et al., 2006; Cappi et al., 2006). However this does not appear to be the case for NH1.

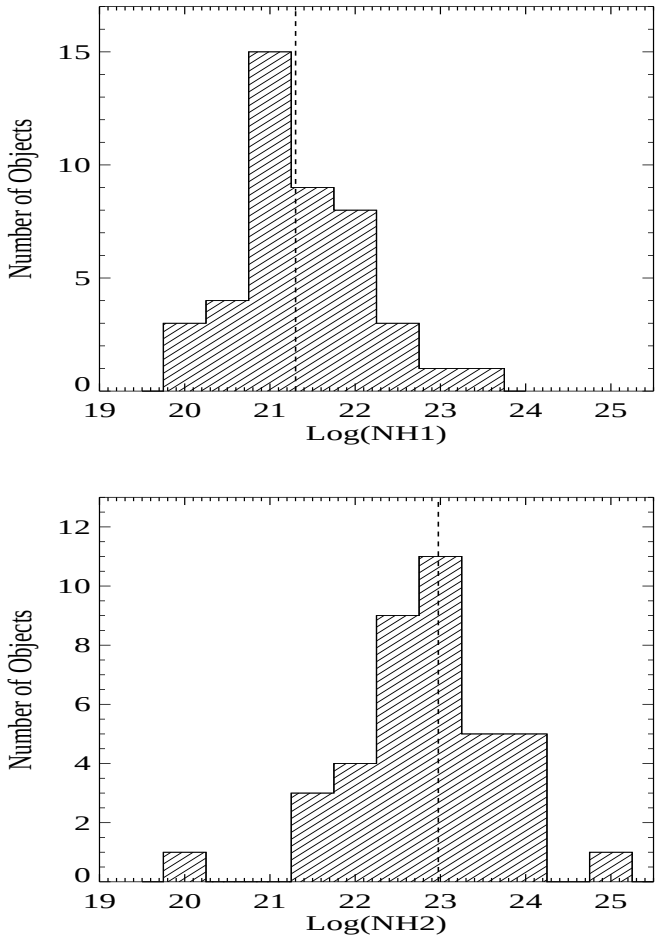

Figure 3.8: *Histogram of column densities obtained with* Chandra *data through ME2PL model. (*Top*): NH1 column density histogram and (*Bottom*): NH2 column density histogram.*

Guainazzi et al. (2005) found an NH1 around $10^{20}\mathrm{cm}^{-2}$, and related this absorption to the host galaxy. However, NH1 is one order of magnitude above the galactic value in LINERs. The fact that our column density is larger than that expected for Seyfert galaxies has opened the question of its origin. Two possibilities are plausible: (1) It is coming from the surrounding medium, making it more obscured than in Seyfert galaxies or (2) it is coming from the nucleus itself, hence a different origin

than in Seyfert galaxies.

One way to discard one of the two possibilities is through the spectral analysis of the diffuse emission around the nucleus. From the sample of objects with spectral fitting we selected those objects with more than 200 counts in the diffuse emission. To select the initial sample we have computed the number of counts in an annulus with an inner (outer) radius 1.5 (3) times the nuclear extraction regions. Twenty three sources have more than 200 counts. After this first selection we have re-examined the extracion regions to guarantee that only diffuse emission is included. In 11 objects (NGC 0315, NGC 3998, NGC 3690B, NGC 4261, NGC 4278, NGC 4321, NGC 4486, NGC 4552, NGC 4579, NGC 4594 and NGC 4736) the annulus resulted in a bad extraction region because it is contained by point-like sources (see Appendix C). In these cases the annulus has been replaced by several circles around

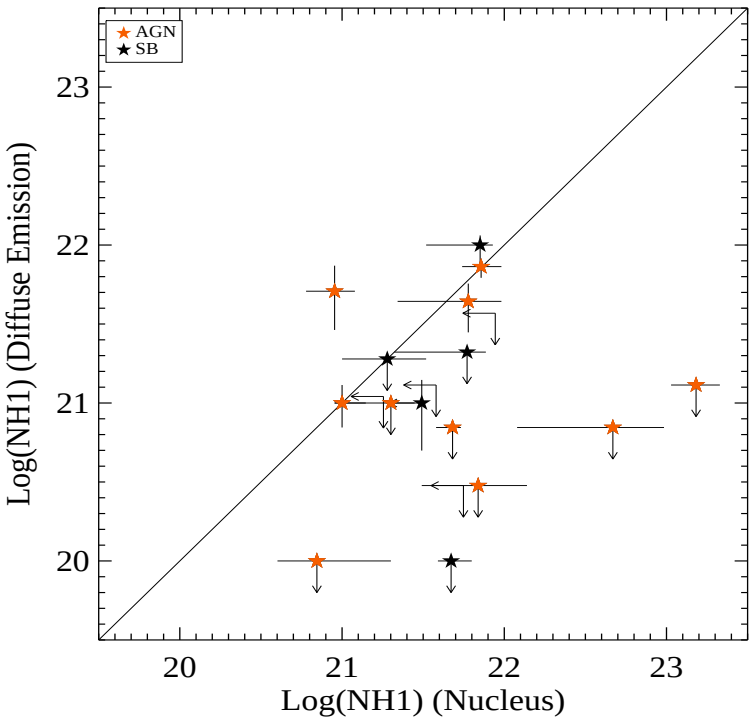

Figure 3.9: *NH1 column density of the diffuse emission versus the NH1 column density of the nuclear emission. Arrows are upper limits.*

the nucleus excluding such point sources. However, in four objects (NGC 3998, NGC 3690B, NGC 4594 and NGC 4736) the emission is still too complex to select only diffuse emission, so these sources have been excluded from the sample. In NGC 3998, NGC 4594 and NGC 4736 many point sources are detected to make a clean study of the diffuse emission. NGC 3690B is strongly interacting with IC 694, showing a plethora of X-rays features that do not allow to perform the spectral analysis. Finally we have a clean sample of 19 objects for which the spectral analysis on the diffuse emission has been possible.

We have investigated ME, PL and MEPL. ME is the expected result for thermal emission. PL is considered to take into account the eventual contamination of additional, unresolved point-like sources. MEPL is included to add the possibility that we have a number of unresolved point-like sources with thermal emission. 2PL and ME2PL were not tried since they have not a physical correspondence in the modelization of the diffuse emission.

The resulting best-fit models for the diffuse emission are summarised in Table 3.23, with Col. (1) label number, Col. (2) name; Col. (3) final fit; Cols. (4) and (5) column densities for the best-fit; Cols. (6) and (7) spectral index and temperature when PL and MEKAL were needed and Cols. (8), (9) and (10) χ^2, degree of freedom (d.o.f.) and reduced χ^2.

To study whether the nuclear NH1 column density is coming from the diffuse emission or from the AGN itself, Fig. 3.9 shows the diffuse NH1 versus the nuclear NH1. The two quantities are not compatible, including the error bars, in seven cases (37%). Six of them (NGC 0315, 3C 218, NGC 4111, NGC 4261, NGC 4579 and CGCG 162-010) show that for the diffuse emission NH1 is compatible with the galactic value, whereas the nuclear NH1 is larger. In all these we can safely conclude that our measured NH1 is not due to the emission from the host galaxy and its origin needs to be found in the inner nuclear region. In the case of NGC 4278, the absorption in the diffuse emission is found to be larger than in the nucleus. It is worthwhile to notice that in addition to these, in other six galaxies (NGC 4125, NGC 4321, NGC 4374, NGC 4552, NGC 4696 and IC 1459) only upper limits for NH1 have been obtained and, thus, we can not asses whether both nuclear and diffuse NH1 have the same origin. All together it seems that we can conclude that for 6 galaxies, nuclear and diffuse NH1 have the same origin, i.e. most probably related to the physical conditions of the material in the host galaxy. For another 6 galaxies, the origin of the absorption observed in the nuclear emission is related to the inner conditions closer to the AGN and not to the host. For the remaining galaxies, a firm conclusion can not be drawn based on the present data.

3.5.2 Luminosities

Fig. 3.10 shows the (0.5-2.0) keV (*Top*) and (2-10) keV (*Bottom*) luminosity histograms. The filled histograms correspond to the sub-sample of objects with spectral fit and the empty histograms contain the whole sample, adding a luminosity estimation for the cases in which the spectral analysis was not possible (see Sections 3.4.4 and 3.4.5). The median values and standard deviations for the whole sample (continuous lines) are 39.95$\pm$1.19 and 39.85$\pm$1.17 for the soft and hard luminosities, respectively. The objects with spectral fit tend to be located at higher luminosities ($> 1 \times 10^{39}$erg s^{-1}) in both histograms (median values of 40.86$\pm$0.99 and 40.51$\pm$1.13 , dashed lines in Fig. 3.10).

Hard X-ray luminosities show a bimodal distribution centered around 1 $\times 10^{39}$ erg s^{-1} and 1 $\times$ 10^{41}erg s^{-1}, indicating a plausible distinction between two populations of LINERs. A hint of such a dual behaviour is also seen for soft luminosities.

Fig. 3.11 shows the whole sample with spectral fitting luminosity histograms and the sub-sample of objects with ME2PL or 2PL as best fits. As a consequence of the high obscuration in these spectral fittings (see Fig. 3.7), the unabsorbed X-ray luminosities are among the highest values of the sample when ME2PL or 2PL models are the best fit.

To illustrate the relationship between this obscuration and the luminosity Fig. 3.12 shows NH1 and NH2 versus soft (0.5-2.0keV) and hard (2-10 keV) X-ray luminosities. Note that upper limits are not included in the plots for clarity. The NH1 column density only shows a trend with luminosities while both soft and hard X-ray luminosities increase with NH2 column density.

3.5.3 Temperature and spectral index

Fig. 3.13 shows the histograms of temperature, kT (*Top*) and spectral index, Γ (*Bottom*). The whole sample distributions are shown with the empty histogram while the dashed histograms show the sub-sample of objects best fitted with 2PL or ME2PL models. The median value and standard deviation of the temperature is $< kT >=$ 0.57$\pm$0.22 keV (shown as a dashed line in Fig. 3.13 *Top*). kT values are distributed around an asymmetrical, bimodal distribution centered at 0.25 keV and 0.65 keV. The first peak is more representative of the value obtained for Seyfert 1 galaxies (Teng et al., 2005; Panessa et al., 2008) while the second peak is close to that obtained in starburst galaxies (Strickland et al., 2002; Grimes et al., 2005). The spectral indices (Fig. 3.13 *Bottom*) show an asymmetrical distribution with a median value and standard deviation of 2.05$\pm$0.42 (displayed as a dashed line in Fig. 3.13 *Bottom*).

Since both hard luminosities and temperatures show a bimodal distribution, we have attempted to analyse whether a connection exists between L(2-10 keV) and

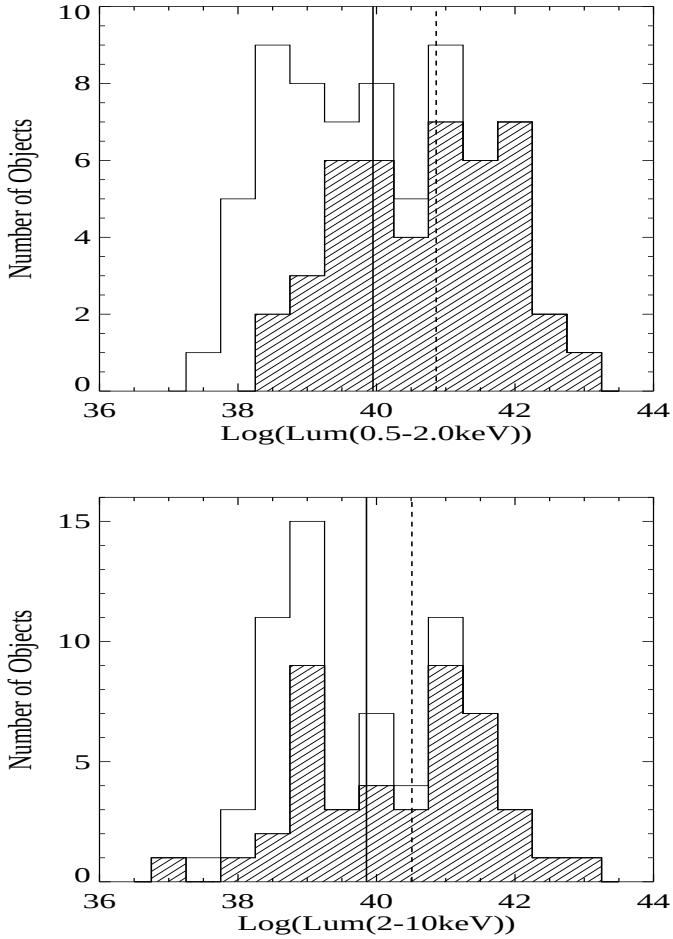

Figure 3.10: *Histogram of soft (*Top*) and hard (*Bottom*) X-ray luminosity obtained with* Chandra *data (emptied histogram). The filled histograms are made with the sub-sample of objects with spectral fittings. The continuous and dashed lines are the median value for the whole sample and the sub-sample of objects with spectral fitting.*

kT. Fig. 3.14 compares these two quantities. Dashed lines correspond to the values where the histograms reach the minimun between the two peaks: 0.45 keV and 1×10^{40}erg s^{-1}, respectively. All the objects but one (NGC 4457[7]) with low tempera-

[7]Note that its temperature range falls within the range of high temperature objects.

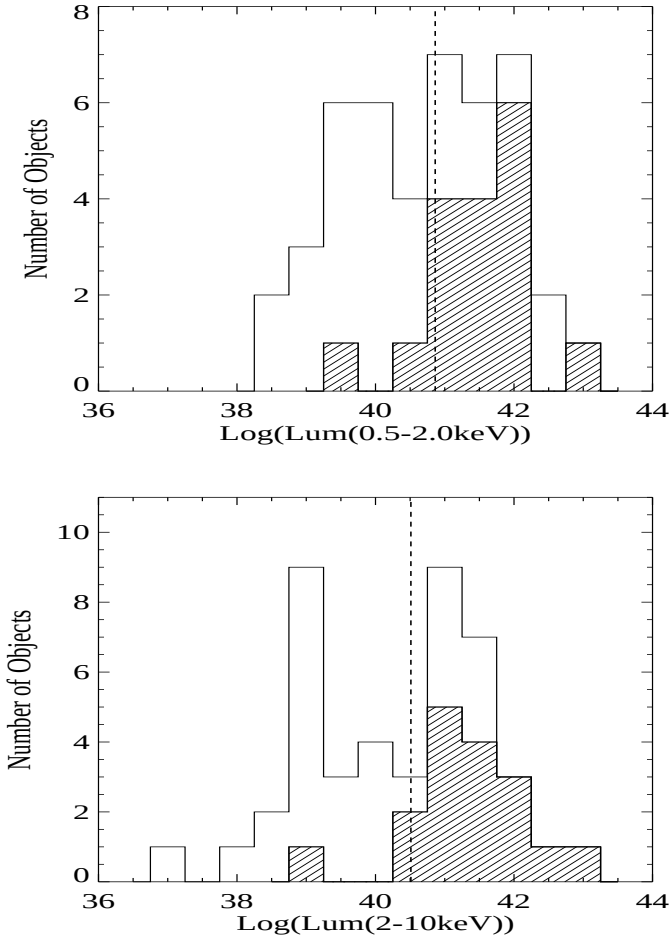

Figure 3.11: *Histogram of soft (*Top*) and hard (*Bottom*) X-ray luminosity obtained with* Chandra *data (emptied histogram) with spectral fittings. The filled histogram is the subsample of objects fitted to ME2PL and 2PL models.*

tures (< 0.45 keV) are in the group of high luminosities ($> 10^{40}$erg s^{-1}) (NGC 3690B, NGC 3998, NGC 4321, NGC 4410, NGC 4579 and NGC 6251). Also all the objects but NGC 4457 in the low luminosity range ($< 10^{40}$erg s^{-1}) show a temperature above 0.45 keV. There is also a mixed group of objects with high temperature and high luminosity. The same trend is found with the soft luminosity.

Again, to understand the nature of the thermal component, we have used the

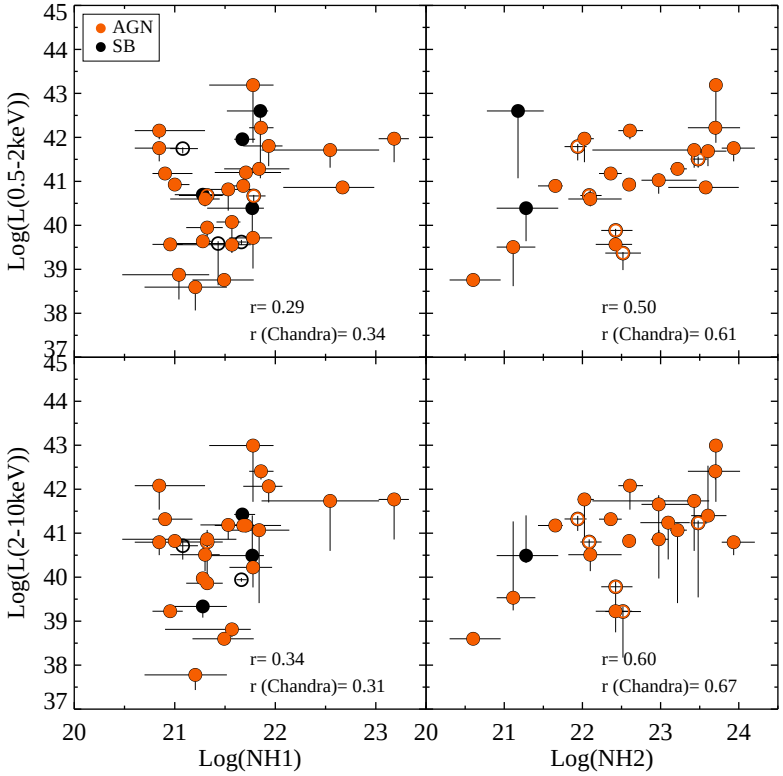

Figure 3.12: *Comparison between NH column densities and luminosities.* Top-left: *Soft (0.5-2.0 keV) luminosity versus NH1;* Top-right: *Soft (0.5-2.0 keV) luminosity versus NH2;* Bottom-left: *Hard (2-10 keV) luminosity versus NH1 and ;* Bottom-right: *Hard (2-10 keV) luminosity versus NH2.* XMM-Newton *data are plotted with open circles. For clarity upper limits are not included in the plot.*

spectral analysis of the diffuse emission to compare it with that obtained for the nuclear emission. Fig. 3.15 shows the temperatures of the diffuse emission versus that of the nucleus. 3C 218 and CGCG 162-010 are out of the plot. 3C 218, NGC 4486 and CGCG 162-010 have temperatures higher in the surrounding medium than in the nucleus and NGC 6240 shows a lower temperature than in the nucleus. In spite of these 3 points, for the remaining nuclei we get the same temperature for nuclear and diffuse thermal components. Thus, these results may suggest that the thermal

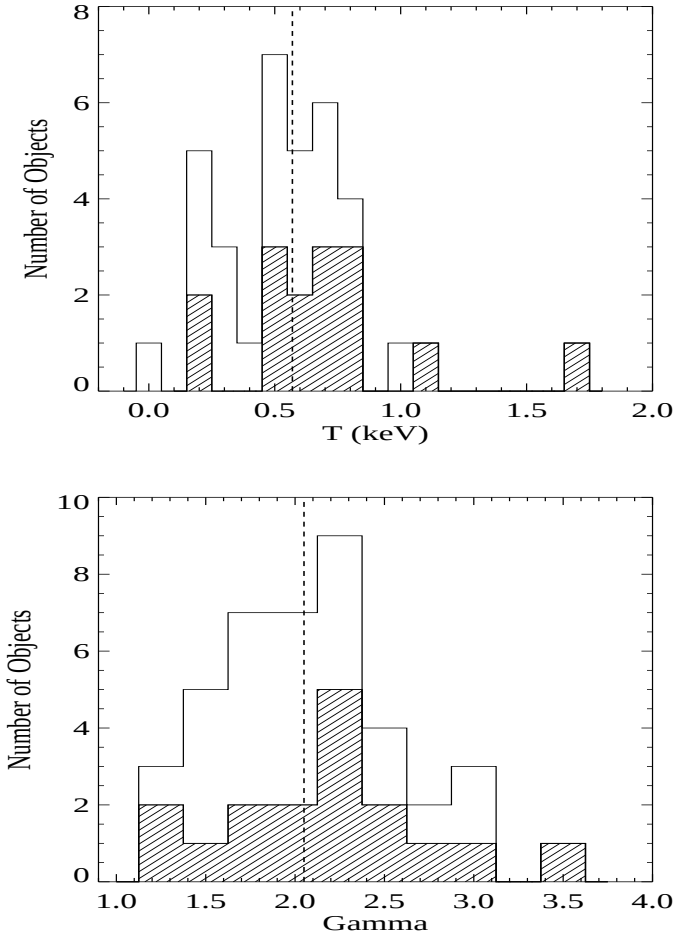

Figure 3.13: *Histogram of temperature (*Top*) and spectral index (*Bottom*) obtained with* Chandra *data (emptied histogram). The filled histogram is the sub-sample of objects fitted to ME2PL and 2PL models.*

nuclear component is fully related to the surrounding medium.

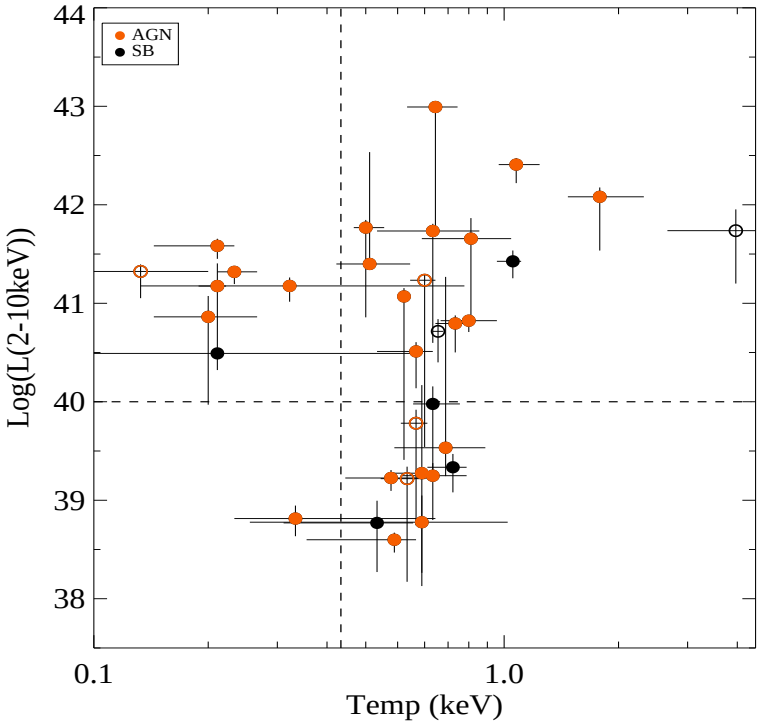

Figure 3.14: *Hard (2-10 keV) luminosity versus temperature. The* XMM-Newton *data are plotted with open cicles. Dashed lines divide between the two populations found with the temperature (0.45 keV) and hard luminosity (*1×10^{40} erg s^{-1}*) histograms.*

3.6 GM+06 comparison

GM+06 analysed a sample of 51 objects giving the spectral information in the 23 cases with high signal-to-noise (see below). From these 51 objects, NGC 0833, NGC 0835, NGC 3226, NGC 4395 and NGC 5194 cannot be used for comparison purposes for different reasons: NGC 0833 and NGC 0835 were misclassified as NGC 0838 and NGC 0839 in the Hickson compact group Hck 16. NGC 4395 and NGC 5194 have been re-classified as Seyfert galaxies and then, excluded from the sample (see Section 3.2). For NGC 3226 strong difficulties have been found on data calibration due to the lost of the adequate calibration files to this observation. Then 46 objects remain for comparison purposes. The observations, source and background extraction regions are the same in both studies.

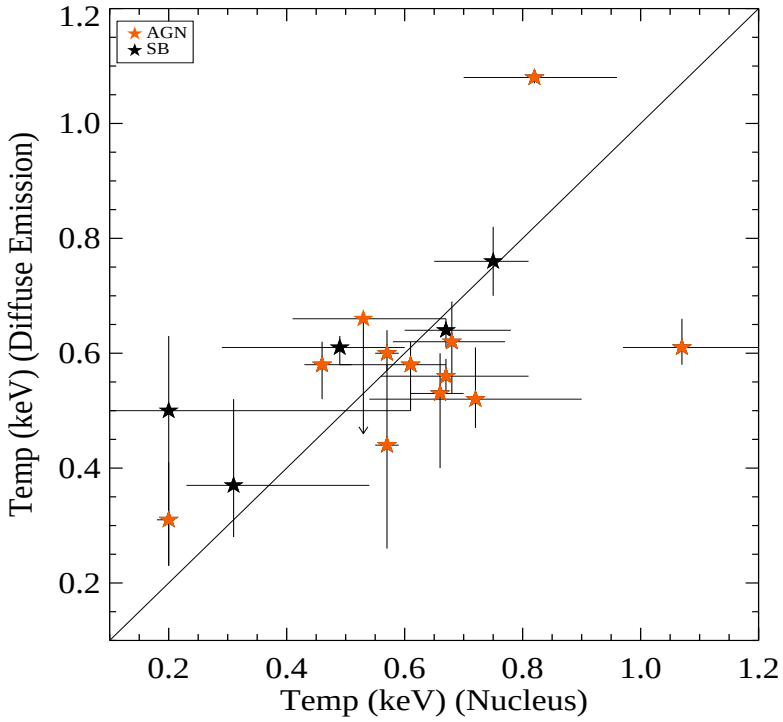

Figure 3.15: *Temperature of the diffuse emission versus the temperature of the nuclear emission. 3C 218 and CGCG 162-010 are out of the plot with coordinates (x,y)=[1.71 keV, 3.00 keV] and (x,y)=[1.05 keV, 4.09 keV], respectively.*

From this sample of 46 galaxies, we have performed the spectral analysis for 32 objects, while GM+06 presented the spectral analysis only for 21 objects. The spectral analysis was performed by GM+06 when the resulting spectrum, had grouping per bin of at least 20 counts. In the present paper all the sources with more than 200 counts are used instead. Then we include objects that might have low count in a specific energy range but with a total number of counts higher than 200. This is specially importat in the hard energy range where we can report spectral fitting for sources with a poor spectrum at high energies that were excluded in GM+06.

Regarding spectral fitting, the sample in GM+06 is smaller but with higher quality data. Here we believe that the sample is less biased to brighter sources resulting in a more homogeneous analysis. To get insight into the differences in both studies

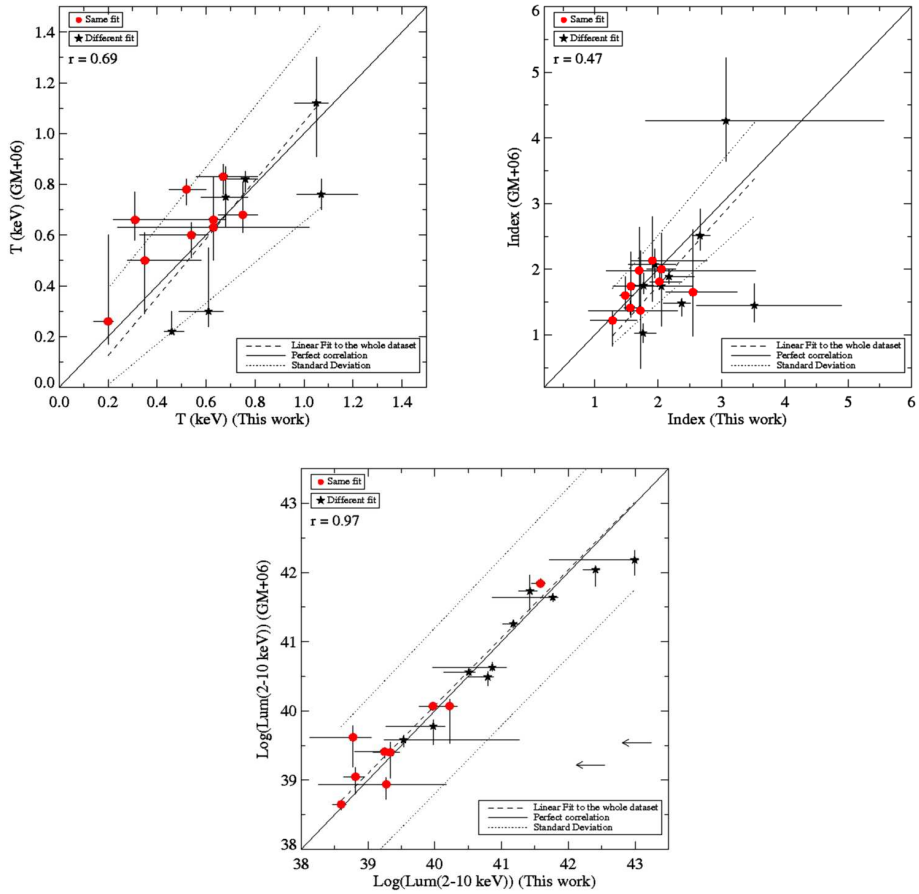

Figure 3.16: *Comparison between* Chandra *results here and those reported in GM+06. Previous and actual temperature (*Top-Left*), spectral index (*Top-Right*) and hard (2-10 keV) luminosity (*Bottom*) are compared. Objects with similar model than GM+06 are marked as red circles; black stars shows objects fitted with different models. Objects showing upper limits are excluded from the comparisons. The solid line shows the linear correlation with zero point equal to zero and slope unity. The dashed line is the linear fit to the data while the dotted lines compared to one standard deviation above and bellow the linear fit.*

we have still 21 galaxies in common for comparison purposes.

3.6.1 Image Classification

The differences in the smoothing proccess used in this paper with respect to GM+06 lead to a different morphological classification on a few sources. NGC 3245, NGC 4438 and NGC 4676B have been changed from SB-like to AGN-candidate and NGC 3628 from AGN-like to SB-like. For NGC 3628 we have revised the classification since, although a source is present in the hard band, it is not point-like as required for the AGN-like classification (see Appendix C). We have classified as AGN candidates 30 out of the 46 objects whereas GM+06 classified as such 27 out of the 46 objects, which does not mean much difference anyway.

3.6.2 Best-fit

We have compared the new resulting best-fits with those previously obtained by GM+06 for the 21 objects with spectral fittings in common. Note that there are some differences between the spectral analysis: (1) The Raymond-Smith model (RS) has not been tried in our analysis (see Sect. 3.4.2) and (2) the current composite models include two absorptions instead of the one used in GM+06. Therefore, RS used in GM+06 is similar to ME and, RS+PL and ME+PL are similar to MEPL. Finally, 2PL and ME2PL were not tried in GM+06.

The final best-fit agrees with that obtained by GM+06 in all but 10 cases (NGC 0315, NGC 3690B, NGC 4374, NGC 4410A, NGC 4696, UGC 08696, CGCG 162-010, NGC 6240, NGC 7130 and IC 1459). NGC 0315, NGC 3690B, UGC 08696, NGC 6240, NGC 7130 and IC 1459 are better fitted now with a more complex model (ME2PL) than that proposed by GM+06. NGC 4374, NGC 4410A and NGC 4696 are better fitted with MEPL instead of PL. This can be explained for the inclusion of two absorptions. CGCG 162-010 is better modelled with ME, instead of RS+PL by GM+06. Statistically speaking, the reduced χ^2 for the objects in common shows a median value and standard deviation $< \chi^2_r > = 0.88 \pm 0.13$ in this paper and $< \chi^2_r >= 1.04 \pm 0.21$ in GM+06. The median value is higher in GM+06 than in this work because more complicated models with a large set of free parameters have been used. However, the standard deviation is lower than in GM+06, indicating that we have found a better fit in more cases than GM+06.

3.6.3 Spectral parameters

Fig. 3.16 compares the temperature (*Left*), spectral index (*Centre*) and hard (2-10 keV) luminosity (*Right*) reported here versus those obtained by GM+06. The linear fit is shown as the dashed line while the solid line indicates identity (slope one and zero offset). Dotted lines correspond to one standard deviation above and below that

line. Objects with similar model than GM+06 are plotted as red circles and those with different models, as black stars. Upper limits are excluded from the plots, excepting for luminosities (showed as arrows).

Temperature and spectral index seem to correspond to the reported values in GM+06 (see Fig. 3.16 *Left* and *Centre*).

Temperatures show a correlation (r=0.69) with slope 1.15± 0.20 and zero point -0.10± 0.15 . Within one standard deviation (dotted lines) the linear fit is consistent with identity. All the derived values are consistent with those reported in GM+06 including error bars. There is a trend towards lower temperatures here than in GM+06.

Spectral indices show slope 1.07± 0.13 and zero point -0.38± 0.26 with a correlation coefficient r=0.47. All the points, with the exception of NGC 3690B, NGC 4696 and NGC 6240, are consistent with those reported in GM+06 including error bars. But notice that these sources were fitted with different models in GM+06.

In our current baseline model, NH1 is related to the soft component while NH2 is related to the hard power-law. However, GM+06 used just one absorber, NH. The median and standard deviations are $0.31\pm\ 0.33\times10^{22}\mathrm{cm}^{-2}$, $0.37\pm\ 4.70\times10^{22}\mathrm{cm}^{-2}$ and $1.06\pm31.46\times10^{22}\mathrm{cm}^{-2}$, for NH, NH1 and NH2, respectively. Then, NH appears to be more closely related to NH1 than to NH2.

In summary, our estimation of temperatures and spectral indices seems to be the same than that reported in GM+06. NH1 and NH2 show high values of column densities that have no counterpart in the scheme proposed by GM+06. In all the figures we donot find any special trend among the objects with the same spectral fit (marked as red circles in Fig. 3.16).

3.6.4 Luminosities

Fig. 3.16 (*Top-Right*) compares the 2-10 keV luminosity reported by GM+06 versus the one calculated here. All the luminosities are consistent with those in GM+06 excepting NGC 4494, NGC 6251 and NGC 6240. The slope of the linear fit is 0.98± 0.01 with zero point 0.85± 0.61 and a correlation coefficient 0.97. All the objects are within one standard deviation of this fit. No special trend among the objects with the same fit was found. Then, we conclude that the hard (2-10 keV) luminosity is independent of the spectral fit and is therefore a robust parameter.

3.7 *XMM-Newton* results

We have added *XMM-Newton* data in an attempt to achieve three main objectives: (1) to enlarge the sample with spectral fits; (2) to obtain more accurate spectral anal-

ysis since *XMM-Newton* data have higher sensitivity than *Chandra* data; and (3) to get information about the iron FeKα line due to the superb sensitivity of the *XMM-Newton*/EPIC camera at such energies.

Results for 55 LINERs with *XMM-Newton* data are reported. Within the 55 LINERs, 44 have more than 200 counts what makes the spectral analysis feasible. This implies 15 new objects and 16 new spectra compared to the *Chandra* sample.

MEPL and ME2PL appear to be the best-fit representation for most of the sources, 78% (17 objects with MEPL and 17 with ME2PL). 2PL was only needed in one object, PL is the best-fit in 4 cases (9%) and ME is the best-fit in 5 cases (11%).

Note that the *XMM-Newton* images were used only when *Chandra* data was not available, i.e., in 14 cases (NGC 0410, NGC 2639, NGC 2655, NGC 2685, NGC 3185, NGC 3226, NGC 3623, NGC 3627, IRAS 12112+0305, NGC 5005, NGC 5363, IC 4395, NGC 7285 and NGC 7743). Six objects (NGC 2655, NGC 2685, NGC 3226, NGC 5005, NGC 5363 and NGC 7285) are classified as AGN-like objects. However, let us notice that NGC 3226 HETG *Chandra* data have been reported by George et al. (2001) and a nuclear point source has been detected by using the zero order data; for NGC 3623, NGC 3627 and NGC 5005 snapshot ACIS-S data have been shown in Dudik et al (2005) and they classified these galaxies as class IV (objects displaying no nuclear source) the two first and III (objects reveal a hard nuclear point source embedded in soft diffuse emission) the last one following Ho et al. (2001) classification scheme. All agree with our classification. Then, even if the *XMM-Newton* classification needs to be taken with care, the X-ray morphology in the 4.5–8.0* keV band shows that 30/55 objects (54%) are classified as AGN-like sources. Within the objects with spectral fits 27/44 are classified AGN-like sources (61%).

The high spatial resolution of *Chandra* data have demostrated that LINERs present complex morphologies with point-like sources close to the nucleus and diffuse emission contaminating the nuclear extraction apertures of *XMM-Newton* data. Then the morphological classification based on *XMM-Newton* data is included for completeness but their low resolution does not allow to extract any conclusion based on these data.

The addition of some extranuclear sources or diffuse emission can also contribute to the spectra. Thus a careful analysis of the limitation of *XMM-Newton* data must be done to fully understand in which cases *XMM-Newton* data are still valid for our purposes. We have followed three approaches: (1) Comparison with *Chandra* data for the objects in common, (2) Re-analysis of *Chandra* data for these objects in common with the same aperture (25 arcsecs) and (3) statistical comparison between the 68 objects observed with *Chandra* and the 55 objects observed with *XMM-Newton*. These three steps will be discussed in the following subsections.

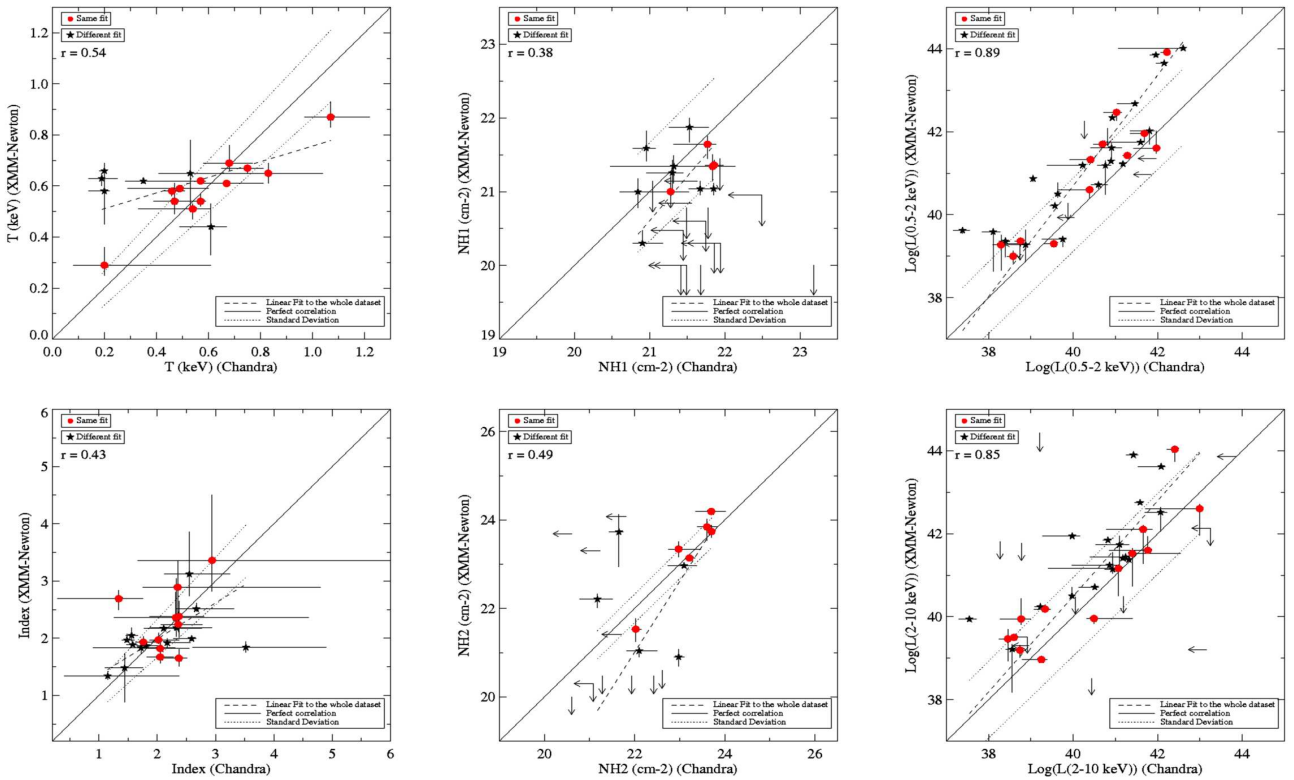

Figure 3.17: *Comparison between* Chandra *and* XMM-Newton *data. Temperature (*Top-Left*), spectral index (*Bottom-Left*), NH1 column density (*Top-Right*), NH2 column density (*Bottom-Right*), soft (0.5-2 keV) luminosity (*Top-Right*) and hard (2-10 keV) luminosity (*Bottom-Right*). The solid line shows the linear correlation with zero point equal to zero and the slope equal to one. The dashed line is the linear fit to the data while the dotted lines are one standard deviation above an bellow the linear fit. There are three objects out of the temperature plot: 3C 218 [1.71, 2.77]keV, CGCG 162-010 [1.05, 3.26]keV and NPM1G -12.0625 [0.31, 2.69]keV.*

3.7.1 Comparison with *Chandra* data

There are 40 objects with *Chandra* and *XMM-Newton* data and 28 with spectral fits. It has to be noticed that about half of them (12 cases) shows the same spectral fit (NGC 0315, NGC 0835, NGC 4125, NGC 4261, NGC 4321, NGC 4552, NGC 4736, MRK 0266NE, UGC 08696, NGC 5813, NGC 6240 and NGC 6482). Nine objects have a more complex model in *XMM-Newton* data than in *Chandra* data (NGC 1052, NGC 2787, UGC 05101, NGC 4579, NGC 4594, CGCG 162-010, NGC 5846, NGC 6251 and NPM1G -12.0625), five have a more complex model with *Chandra* data (3C 218, NGC 3690B, NGC 4278, NGC 4494 and IC 1459) and IRAS 17208-0014 appear as a ME with *XMM-Newton* data and as PL with *Chandra* data.

The explanation for these differences is mainly due to aperture effects, as we will demostrate below. A number of objects are surrounded by soft emission which adds a thermal component to the final spectra in *XMM-Newton* data (e.g. NGC 5846), or point-like sources associated with ULXs can contribute to the total spectrum of some sources (e.g NGC 2787). But this cannot be the full story since in 6 cases *XMM-Newton* data show a more simple model (see Appendix B on individual sources for a detail information in each object). Statistically speaking, the reduced χ^2 shows median value and standard deviation $< \chi^2_r >= 0.91 \pm 0.18$ and $< \chi^2_r >= 1.07 \pm 0.21$ for the objects in common between *Chandra* and *XMM-Newton* samples, respectively. *XMM-Newton* median value is larger than in *Chandra* data most probably because of its higher sensitivity. However, the standard deviation is similar for both datasets.

Fig. 3.17 compares the temperature (*Top-Left*), spectral index (*Bottom-Left*), NH1 (*Top-Right*), NH2 (*Bottom-Right*), soft (0.5-2 keV) luminosity (*Top-Right*) and hard (2-10 keV) luminosity (*Bottom-Right*) obtained with *XMM-Newton* versus those with *Chandra* data. The linear fit is shown as a dashed line while solid line indicates identity (slope one and zero offset). Dotted lines correspond to one standard deviation error above and below that line. Again, objects with the same model for both instruments are marked as red circles, those with different models are marked as black stars. Upper limits, marked as arrows, are not used for the linear fit.

Note that three objects are out of the temperature plot in Fig. 3.17 (*Top-Left*) (3C 218, CGCG 162-010 and NPM1G -12.0625). They have a much higher temperature with *XMM-Newton* than with *Chandra* data. They are the central galaxies of the clusters Abell 780, Abell 1795 and Abell 2597 and thus a strong thermal emission from the cluster might be included in the *XMM-Newton* aperture. For *XMM-Newton* data the aperture is 25 arcsec in comparison with the *Chandra* apertures of 2.2, 3.9 and 1.8 arcsecs, respectively. For the remaining objects the temperature shows slope 0.31 ± 0.08 and zero point 0.45 ± 0.05 with correlation coefficient 0.54. The resulting *XMM-Newton* and *Chandra* temperatures have larger departures when different

best-fits (black stars in Fig. 3.17) are selected. *XMM-Newton* resulting temperatures seem to be less spread, concentrated to a narrower range of values, locating low temperature ($\leq$ 0.2 keV in *Chandra* data) objects to higher values in the *XMM-Newton* estimation (kT $\sim$ 0.6 keV). It has to be noticed that three objects depart from the quoted correlation, NGC 3690B, NGC 4579 and NGC 6251, all with different fits.

The comparison between *Chandra* and *XMM-Newton* spectral indices (Fig. 3.17, *Bottom-Left*) shows slope 0.63$\pm$ 0.08 and zero point 0.73$\pm$ 0.16 with correlation coefficient 0.43. Two objects are out of the identity line, including error bars (NGC 3690B and UGC 05101). Again, no special trend has been found for the objects with the same spectral fit.

The comparison between *Chandra* and *XMM-Newton* NH1 values (Fig. 3.17, *Top-Center*) shows slope 1.20$\pm$ 0.02 and zero point -4.55$\pm$ 0.35 with a poor correlation coefficient (r=0.38). All the points are nevertheless placed in the region compatible with identity. No special trend has been found among the objects with the same spectral fit.

The comparison between *Chandra* and *XMM-Newton* NH2 values (Fig. 3.17, *Bottom-Center*) shows slope 1.60$\pm$ 0.01 and zero point -14.24$\pm$ 0.17 with correlation coefficient 0.49. Objects with the same best-fit tend to be located close to the identity line. Four objects are far from the perfect correlation (NGC 3690B, NGC 4579, IC 1459 and NPM1G -12.0625), all of them with different fits.

L(0.5-2keV) and L(2-10keV) are the best correlated (r=0.85 and r=0.87, respectively) with slopes 1.34$\pm$ 0.01 and 1.15$\pm$ 0.01 and zero points -12.72$\pm$ 0.44 and -5.63$\pm$ 0.49 . However, both *XMM-Newton* luminosities tend to be larger than those calculated with *Chandra* data, a median factor around of 6.0 and 2.4 dex in the energy ranges (0.5-2.0 keV) and (2-10 keV), respectively.

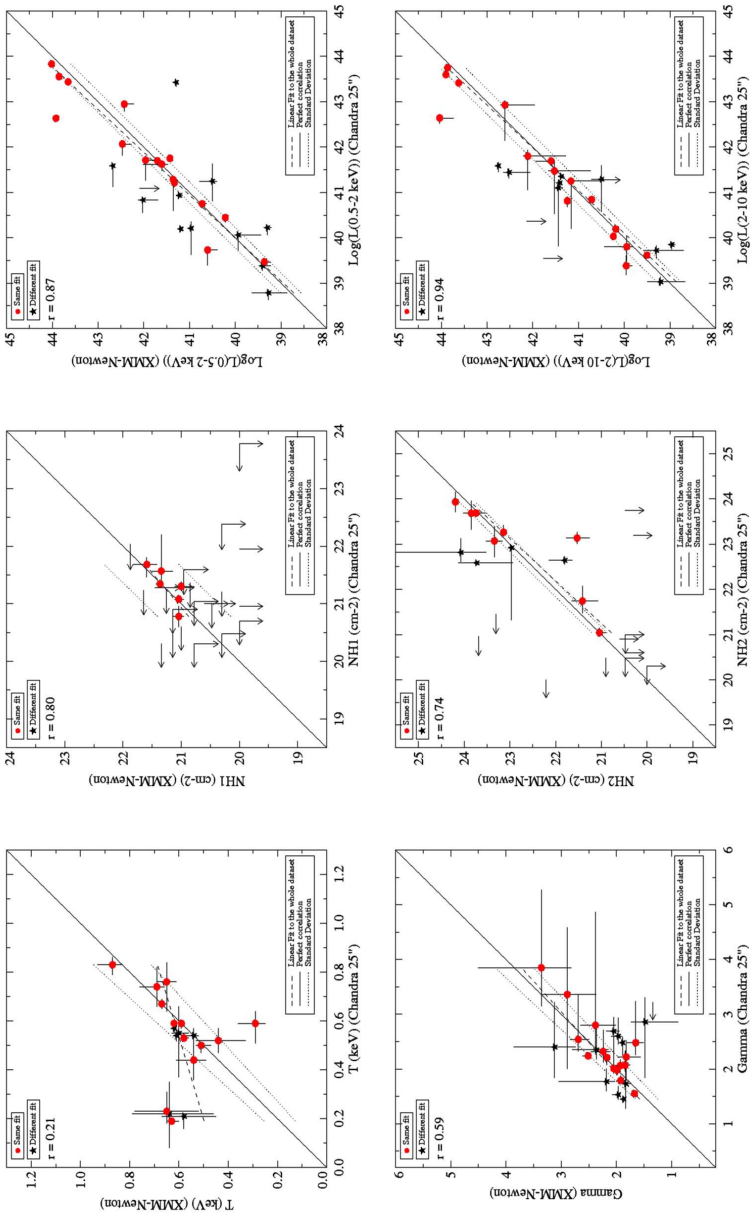

Figure 3.18: *Comparison between large aperture* Chandra *(Chandra 25″) vs* XMM-Newton *results. Temperature (Top-Left), spectral index (Bottom-Left), NH1 column density (Top-Right), NH2 column density (Bottom-Right), soft (0.5-2 keV) luminosity (Top-Right) and hard (2-10 keV) luminosity (Bottom-Right). The solid line shows the linear correlation with zero point equal to zero and the slope equal to one. The dashed line is the linear fit to the data while the dotted lines are one standard deviation above an bellow the linear fit. Three objects are out of the temperature plot: 3C 218 [0.47, 2.77] keV, CGCG 162-010 [3.25, 3.26] keV and NPM1G -12.0625 [2.72, 2.69] keV.*

Aperture effects. *Chandra* 25″ aperture data versus *XMM-Newton* data

The finding of higher luminosities, both soft and hard, and the discrepancies in temperatures point to the idea that these effects might be due to the difference in aperture radius. The *XMM-Newton* data extraction radius is 25″ for all objects whereas the extraction region in *Chandra* data, shown in Table 3.2, is always smaller than 3″ radius. To test such a possibility we have performed a new spectral analysis on *Chandra* data using a fixed 25″ radius for the extraction region (*Chandra 25″* hereinafter), identical to that used in *XMM-Newton* data, for the 28 objects in common. The process has been the same than in the previous analysis and the best fit results are shown in Table 3.24. Col. (1) gives the label number; Col. (2) shows the name; Col. (3) presents the final fit; calculated column densities for the best-fit are shown in Cols. (4) and (5), spectral index and temperature are shown in Cols. (6) and (7) when PL and ME model were needed and Cols. (8) and (9) show the χ^2 and degree of freedom (d.o.f.), and Col. (10) provides the reduced χ^2.

Sixteen out of the 28 objects show the same spectral model when it is compared to *XMM-Newton* data (NGC 0315, NGC 0835, 3C 218, NGC 3690B, NGC 4261, NGC 4278, NGC 4321, NGC 4736, MRK 0266NE, UGC 08696, CGCG 162-010, NGC 5813, NGC 6240, NGC 6482, IC 1459 and NPM1G -12.0625). It has to be noticed that among them, in ten cases (NGC 0315, NGC 0835, NGC 4261, NGC 4321, NGC 4736, MRK 0266NE, UGC 08696, NGC 5813, NGC 6240, and NGC 6482) the small aperture *Chandra* data also show the same spectral model indicating the dominance of the nuclear source over the surrounding medium. For the other six galaxies (3C 218, NGC 3690B, NGC 4278, CGCG 162-010, IC 1459 and NPM1G -12.0625), the best-fit model changes from ME2PL with *Chandra* small aperture to MEPL with *Chandra* 25″ and *XMM-Newton* data in four objects. Then, it seems that the large aperture tends to dilute the final best-fit to a simplified model.

For the remaining galaxies, the comparison is a rather confusing. Six of them (NGC 1052, NGC 2787, UGC 05101, NGC 4494, NGC 5846 and NGC 6251) show a coincident spectral model for *Chandra* small and large apertures, but it is different to that from *XMM-Newton* data analysis. The discrepancy with *XMM-Newton* spectral fit has to be found in the poor quality data for these *Chandra* observations (see for instance Appendices D and E, for *Chandra* and *XMM-Newton* spectral fits for NGC 1052). Another two galaxies (NGC 4125 and NGC 4552) are fitted with the same best-fit in *Chandra* small aperture and *XMM-Newton* data (MEPL) while *Chandra* 25″ data reports a different model (ME2PL). Finally, there are four cases (NGC 3998, NGC 4579, NGC 4594 and IRAS 17208-0014) showing different best-fits for the three datasets.

Fig. 3.18 compares temperature (*Top-Left*), spectral index (*Bottom-Left*), NH1

Top-Center), NH2 (*Bottom-Center*), soft (0.5-2 keV) luminosity (*Top-Right*) and hard (2-10 keV) luminosity (*Bottom-Right*) between *Chandra* 25" and *XMM-Newton* data. Again, red circles (black stars) represent objects fitted with (without) the same best-fit model and upper limits are plotted as arrows but not used in the linear fit. The solid line shows identity, the dotted lines show one standard deviation bellow and above that line and the black dashed line shows the linear fit to the data.

The temperatures (Fig. 3.18, *Top-Left*) show again a similar trend than that found for the small aperture *Chandra* best-fits, with slope 0.30± 0.08 , zero point 0.44± 0.05 and correlation coefficient 0.21, now with a larger spread for the points with similar fits. Three objects are out of the plot (3C 218 [0.47, 2.77] keV, CGCG 162-010 [3.25, 3.26] keV and NPM1G -12.0625 [2.72, 2.69] keV). CGCG 162-010 and NPM1G -12.0625 recover the *XMM-Newton* temperature with the same fit when we use *Chandra* 25" data, whereas 3C 218 results in a lower temperature and a different model with the larger aperture. It then appears that the differences between *Chandra* and *XMM-Newton* temperatures do not seem to be due to aperture effects. The objects with rather low temperatures (around 0.2 keV) show again a lower temperature with the large aperture (NGC 3690B, NGC 4278, NGC 6251, IRAS 17208-0014). We think that the only explanation for this effect has to be ralated to the lower sensitivity of *XMM-Newton* data at low energies.

The comparison of the spectral indices (Fig. 3.18, *Bottom-Left*) shows a slightly better correlation (r=0.59 now, against r=0.57 before) with slope 0.89± 0.06 and zero point 0.28± 0.12 . The points with two different models (black stars) have higher discrepancies than those with the same fit (red circles), suggesting that the differences in the spectral indices from *Chandra* and *XMM-Newton* data may be more related to the selection of the best-fit model than to aperture effects.

No strong results can be derived from NH1 and NH2 since the number of objects without upper limits is small. For NH1, the linear fit slope is 0.83± 0.01 and the zero point is 3.64± 0.32 (r=0.80). For NH2, the linear fit slope is 1.06± 0.00 and the zero point is -1.62± 0.09 (r=0.74). NH1 values show a much better correlation (r=0.80) than with *Chandra* small aperture (r=0.38). Then, the discrepancies in NH1 values seem to be related to aperture effects. NH2 derived from different spectral fits seem to show larger departures. Then the selected model may be crucial to derive NH2, as we already knew from the *Chandra* results (Sect. 3.5).

Regarding luminosities, both L(0.5-2keV) and L(2-10keV) are well correlated (with correlation coefficients r=0.87 and r=0.94, respectively), showing slopes 1.06± 0.00 and 1.06± 0.00 and zero points -2.34± 0.13 and -2.58± 0.16 , respectively. Then, it seems that the difference in luminosities can be entirely attibuted to aperture effects. However, the effect is smaller for the harder luminosity, since there is only a factor of 2.4 dex between *Chandra* small aperture and *XMM-Newton* data in L(2-10 keV).

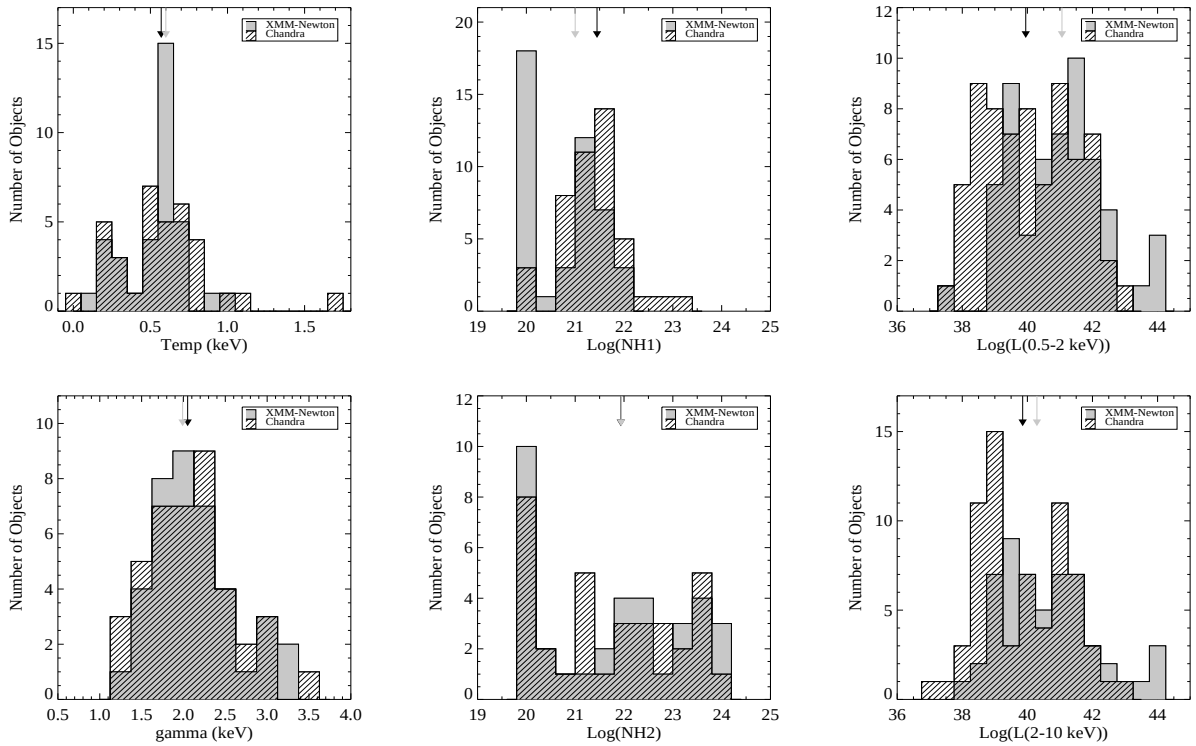

Figure 3.19: *Temperature (*Top-Left*), spectral index (*Bottom-Left*), NH1 (*Top-Centre*), NH2 (*Bottom-Centre*), soft (0.5-2 keV) luminosity (*Top-Right*) and hard (2-10 keV) luminosity (*Bottom-Right*) histograms . The* Chandra *data is shown as dashed histogram while the grey histogram plots the* XMM-Newton *data. The median value for* Chandra *and* XMM-Newton *data are marked as black and grey arrows, respectively. Four objects (3C 218, CGCG 162-010, IRAS 14348-1447 and NPM1G -12.0625) have been excluded from the* XMM-Newton *temperature histograms because they show a temperature above 2 keV.*

Statistical comparison between *Chandra* small aperture and *XMM-Newton* samples

A reliable comparison between the fitting parameters from the two sets of data is difficult because of the small number of objects in common. Then, the statistical comparison of the two samples is important to ensure the final conclusions about the utility of the *XMM-Newton* sample.

In statistical terms, PL and ME are worse representations (low number of best-fits) of the data with *XMM-Newton* than with *Chandra*. Also 2PL is a worse representation of the whole sample than in *Chandra* data. However, MEPL is equally good and ME2PL increases its percentage in more than 10%. These changes are easily explained because of the large extraction region used in *XMM-Newton*. The main effect is that additional thermal components are required for the spectral fitting. Then the simplest models (PL and ME) and 2PL decrease its percentage and increasing the preponderance of ME2PL model.

The resulting reduced χ^2 are $< \chi^2_r >= 0.90 \pm 0.20$ and $< \chi^2_r >= 1.07 \pm 0.23$ for *Chandra* and *XMM-Newton* samples, respectively. The median value is higher for *XMM-Newton* than for *Chandra* data because of the higher sensitivity of *XMM-Newton* data. However, both standard deviations are similar. This confirms the results reported for the subsample of objects with both *Chandra* and *XMM-Newton* data (see Section 3.5).

Fig. 3.19 shows the histograms for the temperature (*Top-Left*), spectral index (*Bottom-Left*), NH1 (*Top-Centre*), NH2 (*Bottom-Centre*), soft (0.5-2 keV) luminosity (*Top-Right*) and hard (2-10 keV) luminosity (*Bottom-Right*). The results for *Chandra* data are shown as dashed histograms while grey histograms plot the *XMM-Newton* results. The median values for *Chandra* and *XMM-Newton* data are marked as black and grey arrows, respectively. The Kolmogorov-Smirnov (K-S) test has been applied in all cases to quantify the probability that both sets of data are drawn from the same distribution.

Temperatures (Fig. 3.19, *Top-Left*) show median values compatible within one standard deviation (0.60$\pm$0.20 for *XMM-Newton* and 0.57$\pm$0.31 for *Chandra* data). The two peaks around 0.25 keV and 0.65 keV are also found in *XMM-Newton* data. The main differences are: (1) Four objects, all located at the centre of a galaxy cluster, show values larger than 2 keV (3C 218, CGCG 162-010, IRAS 14348-1447 and NPM1G -12.0625), and (2) The peak at 0.60 keV is much stronger than the same peak in *Chandra* data. The K-S test results in a 33.3% probability for these two distributions to be the same. When the test is performed taking out all the sources with temperatures larger than 2 keV, a higher probability is found (44%).

The first difference is easily explained because of the large aperture used for

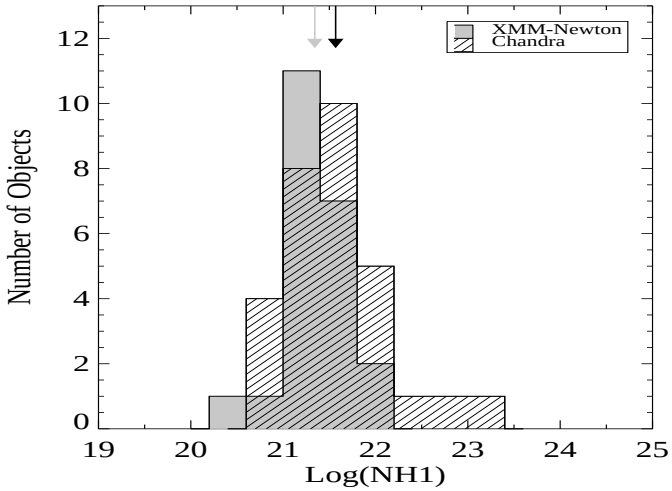

Figure 3.20: *NH1 column density histograms. The* Chandra *data is shown as dashed histogram while the grey histogram plots the* XMM-Newton *data. The median value for* Chandra *and* XMM-Newton *data are marked as black and grey arrows, respectively.*

XMM-Newton spectra. The centres of clusters show a strong thermal contribution that can be described by a thermal model with temperatures around 2-3 keV (Kaastra et al., 2008). The large aperture of *XMM-Newton* spectra includes a substantial amount of cluster contribution which is more easily removed in *Chandra* data. In fact, *Chandra 25″* data recovers the *XMM-Newton* temperature in two of the three galaxies (CGCG 162-010 and NPM1G 12.0625) that are in both samples.

The soft, diffuse observed emission can contribute as a thermal component at around 0.6-0.7 keV, which is the case for most of the galaxies (see figures in Appendix C). Regarding the differences found at low energies, temperatures around 0.1-0.2 keV seem to be most probably related with diferences in sensitivity between both datasets at low energies, with *XMM-Newton*data worse suited to trace it.

The spectral indices (Fig. 3.19, *Bottom-Left*) show a very similar distributions with median values 2.05±0.53 and 1.99±0.49 for *Chandra* and *XMM-Newton* data, respectively. The K-S test shows that spectral index has a 83.2% probability that these two distributions are drawn from the same population. Then the intrinsic spectral index seems to be equally derived from both sets of data.

The logarithms of NH1 (Fig. 3.19, *Top-Center*) show median values 21.4±0.6 and 21.0±0.7 for *Chandra* and *XMM-Newton* data, respectively. The K-S test results in

a 0.4% probability for these two distributions to be the same. Both samples show a peak around 3×10^{21} cm^{-2} but *XMM-Newton* data show an additional peak compatible with the value of galactic absorption. From our previous analysis we have learnt that the correlation between NH1 for *Chandra* and *XMM-Newton* data is improved when using *Chandra 25"* data.

The K-S test shows that neither NH1 nor NH2 are drawn from the same distribution. For the case of NH1, two effects have to be taken into account, aperture effects and lower sensitivity at soft energies. However, the median values are not too far, 21.6±0.5 and 21.3±0.4 for *Chandra* and *XMM-Newton*, respectively. NH2 shows the same median values for both *Chandra* and *XMM-Newton* data (21.9±1.4) with similar distributions (Fig. 3.19 *Centre-Bottom*). Then *XMM-Newton* resulting NH2 column densities seem to be as good as *Chandra* NH2 column densities, even if a low probability (25.8%) is obtained with the K-S test.

The largest discrepancies between both sets of data are found in the soft (0.5-2 keV) and hard (2-10 keV) luminosities. The median values of the soft (hard) luminosities are 39.9±1.4 (39.9±1.3) and 41.1±1.4 (40.3±1.5) for *Chandra* and *XMM-Newton* samples. Then *XMM-Newton* data result in soft (hard) luminosities around 10 (2.5) times brighter than with *Chandra* data. These two quantities are compatible with that derived from the linear fit for the data in common (see Section 3.7.1). Then the soft luminosity appears to be highly contaminated by the surrounding medium whereas the hard luminosity seems to be only twice *Chandra* luminosity, which is within the error bars. Moreover, the 2-peaks in hard X-ray luminosity distribution for *Chandra* values are not seen in *XMM-Newton* values. The soft (0.5-2.0 keV) luminosity shows a similar bimodal distribution at 10^{40}erg s^{-1}. The K-S test shows that (0.5-2.0 keV) and (2-10 keV) luminosities have a 1.2% and 1.0% of probability that these two distributions are the same. In fact, when we make the offset proposed in the previous section the K-S test shows that (0.5-2.0 keV) and (2-10 keV) luminosities have 50% and 53% probabilities that these two distributions are the same (offsets 1.13 and 0.44 dex, respectively).

In summary, the differences in luminosities, both soft and hard are a factor of ∼5-10 and ∼2.5 times the *Chandra* luminosity, respectively. The discrepancies in NH1 and temperature might be due to different sensitivity between the two instruments. The discrepances in NH1 also seem to be related to aperture effects. NH2 is strongly linked to the best-fit model selected and independent on the selected aperture or sensitivity. Finally, the spectral index has shown to be the most robust parameter.

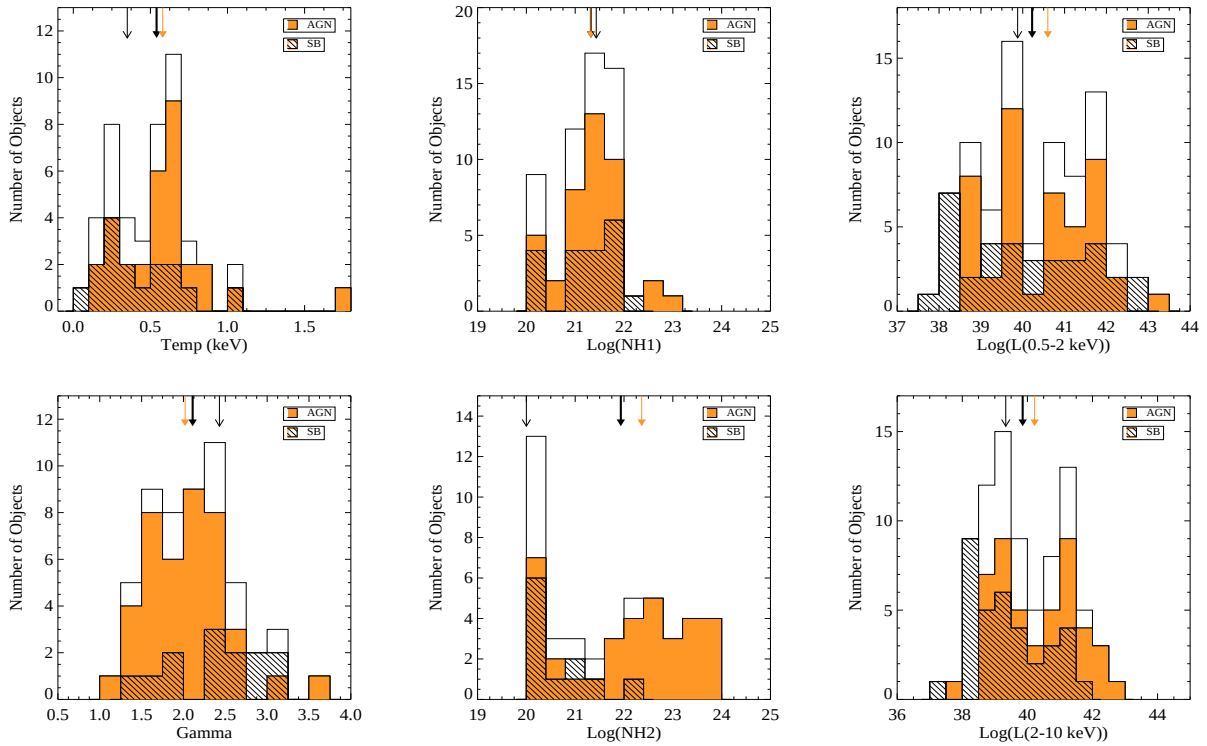

Figure 3.21: *Temperature (*Top-Left*), spectral index (*Bottom-Left*), NH1 (*Top-Centre*), NH2 (*Bottom-Centre*), soft (0.5-2 keV) luminosity (*Top-Right*) and hard (2-10 keV) luminosity (*Bottom-Right*) histograms. The median values are marked with arrows. IRAS 14348-1447 has been excluded from the temperature histogram because it shows a temperature above 2 keV.*

3.8 X-ray results on the final LINER sample

A total sample of 82 LINERs is presented in this paper, 68 of them observed with *Chandra* and 55 with *XMM-Newton*. The spectral analysis has been possible for 60 out of the 82 objects (16 with *Chandra* data, 16 with *XMM-Newton* data and 28 objects with both datasets).

Having in mind all the limitations considered above when comparing *Chandra* and *XMM-Newton* data, we have constructed the final sample by using *XMM-Newton* data only when *Chandra* data are not available.

The resulting best-fit models for our final sample galaxies are summarised in Table 3.26. Col. (1) gives the label number, Col. (2) the name; Col. (3) the morphological classification; Col. (4) the selected instrument; Col. (5) presents the final fit; reported column densities for the best-fit are shown in Cols. (6) and (7), the spectral index and temperature are shown in Cols. (8) and (9) when PL and ME model were needed and Col. (10) shows the reduced χ^2.

Table 3.27 shows the X-ray fluxes and luminosities. Col. (1) shows the label number, Col. (2) the name of the object, Col. (3) the morphological classification, Col. (4) the selected instrument; Cols. (5) and (6) give the soft (0.5–2.0 keV) and hard (2–10 keV) observed fluxes in units of 10^{-13}erg s^{-1}, and Cols. (7) and (8) give the logarithm of the soft and hard intrinsic luminosities.

Almost sixty percent (48/82) of our final galaxy sample have been classified as AGN-like nuclei. Forty percent (34/82) of the final sample of LINERs falls into SB-like nuclei category. 41 out of the 60 objects with spectral fit (68%) are classified as AGN-like, while 19 out of the 60 (32%) are classified as SB-like objects.

MEPL or ME2PL are the best representation for 70 % of the sample (24 galaxies have been fitted with MEPL and 18 with ME2PL). 2PL is a good fit only for 3 cases and single models PL and ME are the best fits in 9 and 6 cases, respectively.

Within our expectations for the AGN-like population, a thermal ME model is not found as a good fit for any of the galaxies. All the LINERs best fitted with ME2PL have been classified as AGN-like objects. Within the 19 objects classified as SB-like objects, 6 have been fitted with ME model (NGC 2639, UGC 04881, NGC 3507, CGCG 162-010, IRAS 14348-1447 and NGC 6482). However, CGCG 162-010 and IRAS 14348-1447 show luminosities higher than 10^{41} erg s^{-1}, indicating a mechanism more efficient than thermal proccesses, or some additional contribution for unresolved sources.

Fig. 3.21 shows distributions for temperature (*Top-Left*), spectral index (*Bottom-Left*), NH1 (*Top-Centre*), NH2 (*Bottom-Centre*), soft (0.5-2 keV) luminosity (*Top-Right*) and hard (2-10 keV) luminosity (*Bottom-Right*). The final median values and standard deviation describing the main X-ray properties of our final LINER sample

(plotted as arrows in Fig. 3.21) are reported in Table 3.28.

The temperature (Fig. 3.21, *Top-Left*) shows a bimodal distribution centered at kT=0.2 keV and kT=0.6 keV. Only IRAS 14348-0014 shows a temperature larger than 2 keV. NH1 (Fig. 3.21, *Top-Center*) shows a narrow distribution centred at $2.1 \pm 5.2 \times 10^{21}$ cm^{-2}. Again the median value for NH1 is higher in our LINERs than that reported for Seyfert 2 galaxies (Guainazzi and Bianchi, 2007). NH2 shows a broader distribution centred at $8.5 \pm 22.9 \times 10^{21}$ cm^{-2}. The hard (2-10 keV) luminosity shows also a bimodal distribution centred at 10^{39} erg s^{-1} and 3×10^{41} erg s^{-1}. A similar trend, but less clear, is found in the soft (0.5-2 keV) luminosity.

Open circles in Figs. 3.12 and 3.14 are the *XMM-Newton* results. The main results obtained with *Chandra* data are corroborated with the addition of *XMM-Newton* data. *XMM-Newton* data confirm that all the objects with low temperatures (< 0.45 keV) but one (NGC 4457[8]) are in the group of high luminosities ($> 10^{40}$ erg s^{-1}) (NGC 3690B, NGC 3998, NGC 4321, NGC 4410A, NGC 4579, NGC 6251 and NGC 7285). Also all the objects with low luminosities ($< 10^{40}$erg s^{-1}) but NGC 4457 show temperatures above 0.45 keV (NGC 2681, NGC 2841, NGC 4278, NGC 4374, NGC 4494, NGC 4552, NGC 4696, NGC 4736, NGC 5363, NGC 5813 and NGC 6482). There is also a mixed group of objects with high temperature and high luminosity. Temperatures above 0.45 keV are related to strong thermal proccesses (Strickland et al., 2002) whereas temperatures around 0.2 keV are known for Seyfert 1 objects (Teng et al., 2005; Panessa et al., 2008). The fact that the objects with a low temperature are high luminosity objects seems to be very suggestive. We wonder if all of them are related to Seyfert type 1 objects. Then, it seems that a connection between the AGN and the thermal population does exists, since high-power sources do not show evidence of thermal processes and low-power sources do show these evidences.

3.9 Discussion

3.9.1 LINERs Obscuration

The main characteristics of the X-ray spectrum of an AGN were described in Section 3.4 as the composition of several mechanisms: (1) A primary power-law continuum from the inner parts of the AGN; (2) a reflection component due to the reflection of the previous, primary continuum in the so-called torus; and (3) the soft spectrum (below 2 keV) described by a scattering plus a thermal component related to both internal and external contributions. In this scenario, the column densities provide information on the location of the absorbing material. Whereas NH1 is mostly

[8]Note that its temperature range falls within the range of high temperature objects.

related to the scattering and/or thermal components, NH2 must be related to the inner parts of the AGN.

Nevertheless, the absorbing column densities can be so high that the emission coming from the central engine is completely absorbed below 10 keV. Obscured AGNs may be classified at X-ray frequencies as *Compton-thick* ($N_H \simeq 1.5 \times 10^{24} cm^{-2}$) and *Compton-thin* (for smaller column densities, but still in excess of the Galactic one). In these obscured AGNs the reflection components can be missinterpreted as a primary continuum and consequently might be misclassified as *Compton-thin* AGNs. In practise, in this scenario the value obtained for NH2 in the spectral fit gives information about the reflection component instead of the primary continuum.

GM+06 pointed out a very likely possibility that LINERs are significantly obscured, specially those objects classified as SB candidates. However, the use of a single column density in those models (NH) did not allow to perform a detailed analysis of obscuration in LINERs. The new fitting procedure used here gives an unique opportunity to study such an effect.

Compton-thick tracers: $F_X(2-10\ keV)/F_{[OIII]}$ ratio

Maiolino and Rieke (1995) showed that the [OIII] emission line luminosity can be considered as one of the best indicators of nuclear activity in galaxies. On the other side, the X-ray emission at 2-10 keV should be an intrinsic property of the AGN in the case that the primary continuum is not suppressed by a highly obscuring material. When the primary continuum is suppressed due to heavy absorption ($N_H > 10^{24} cm^{-2}$), the ratio between hard X-rays and [OIII] lowers because the computed X-ray luminosity is underestimated. For a large sample of Seyfert 2 galaxies it has been shown that the ratio $L_{2-10keV}/L_{[OIII]}$ can be used as good diagnostics to discriminate between *Compton-thick* and *Compton-thin* sources (Bassani et al., 1999; Panessa and Bassani, 2002; Maiolino et al., 2003; Panessa et al., 2005, 2006). In this section, we attempt to use this ratio to evaluate the possibility, for a number of our LINER sources, to be *Compton-thick*.

We have searched in the literature for [OIII] fluxes and $H\alpha/H\beta$ ratios (Ho et al., 2001; Moustakas and Kennicutt, 2006; Veilleux et al., 1995; Keel et al., 1985; Keel, 1983; Koski, 1978; Greenawalt et al., 1997; Duc et al., 1997) and found them for 79 out of the 82 objects (excepting for NGC 835, CGCG 162-010 and IC 1459). The reddening-corrected [OIII] fluxes are reported in Table 3.30: Col. (1) label number; Col. (2) name; Col. (3) our measured $EW(FeK\alpha)$; Col. (4) log(L[OIII]) from the literature; Col. (5) our calculated log(L(0.5-2 keV); Col. (6) our calculated log(L(2-10 keV); Col. (7) L(2-10 keV)/L[OIII]; Col. (8) log (M_{BH}) (see below) and Col. (9) reference for the velocity dispersion used to calculate M_{BH}.

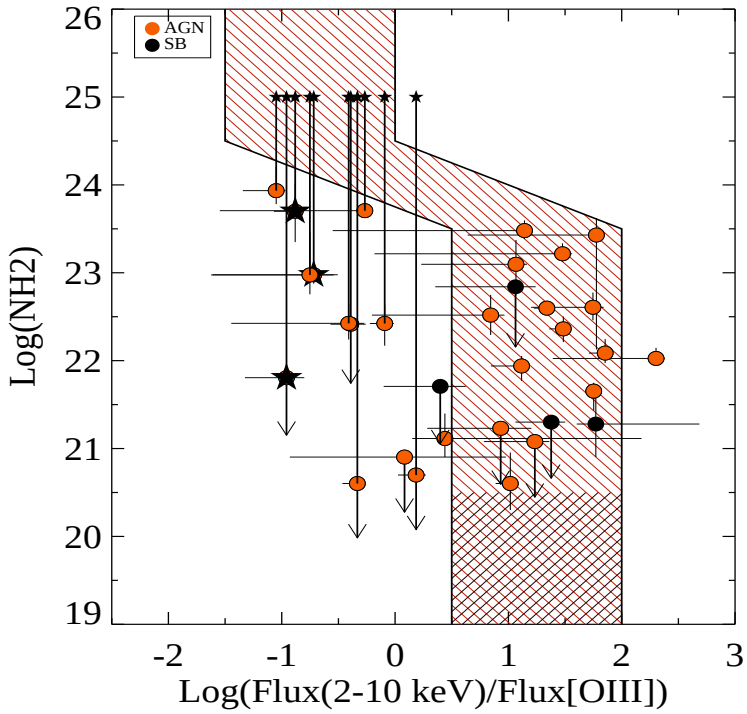

Figure 3.22: *Diagram of absorbing column density NH2 versus the ratio between the observed 2-10 keV flux and the reddening corrected [OIII] fluxes. Red circles are AGN candidates and black circles, SB candidates. Black stars correspond to confirmed Compton-thick sources. A continuous black line ended in a small star shows the location where Compton-thick candidates must be located once corrected for obscuration. The double-dashed region indicates the expected locus from the average ratio observed in type 1 Seyfert galaxies (Heckman et al., 2005). The dashed region has been computed assuming that L(2-10 keV) is absorbed by the NH reported in the ordinate (see Maiolino et al., 1998).*

Fig. 3.22 shows the diagram of the absorbing column density NH2 versus the ratio between observed 2-10 keV and reddening corrected [OIII] fluxes. Black circles are the SB candidates, red circles are the AGN candidates and stars are already known *Compton-thick* sources UGC 05101, NGC 3690B and NGC 6240 (see Comastri and Fiore, 2004, and references therein).

The double-dashed region indicates the expected locus from the average ratio observed in type 1 Seyfert galaxies ($< \log(F_X(2-10\ \mathrm{keV})/F_{[OIII]}) >= 1.59 \pm 0.48$

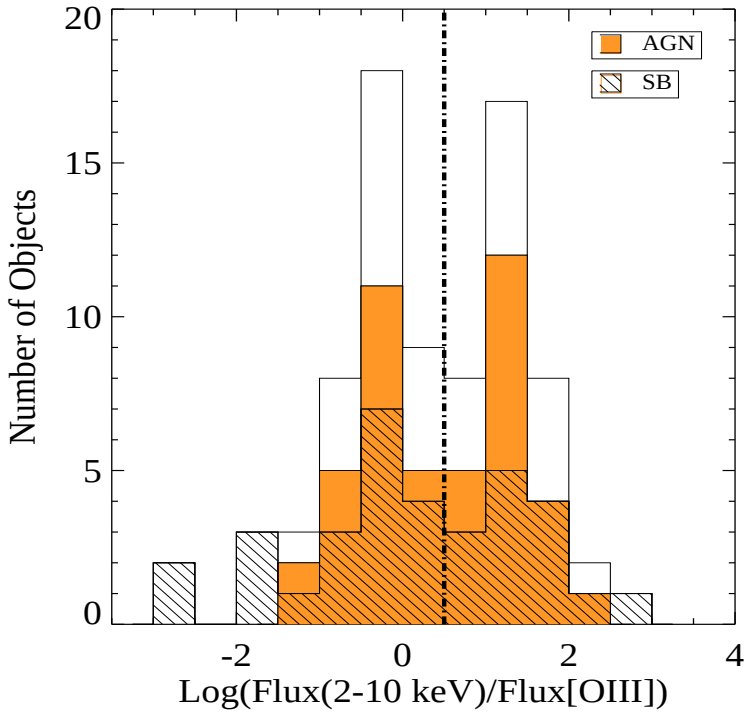

Figure 3.23: *Histogram for the ratio between 2-10 keV and reddening-corrected [OIII] fluxes, for the whole sample (empty histogram), the sub-sample of objects classified as SB (dashed histogram) and the sub-sample of objects classified as AGN candidates (orange-filled histogram).*

Heckman et al., 2005). The dashed region has been computed assuming that L(2-10 keV) is absorbed by NH reported in the ordinate (see Maiolino et al., 1998). This diagram is interpreted as that the objects out of such region might be obscured with column densities higher than $10^{24}\mathrm{cm}^{-2}$ and they should be in the upper region of the diagram, as it is shown by the straight lines. It has to be noticed that the three known *Compton-thick* sources fall out of the dashed region. In addition to them, we have found seven new candidates (NGC 4278, NGC 4410A, NGC 4457, MRK 266NE, NGC 5363, NGC 6251 and NGC 7130).

Fig. 3.23 shows the $F_X(2-10\ \mathrm{keV})/F_{[OIII]}$ distributions for the whole sample (empty histogram), for AGN candidates (orange-filled histogram) and for SB candidates (dashed histogram). The distribution is similar to that found by Maiolino

et al. (1998) for a sample of Seyferts. It shows two peaks centered at -0.5 and 1.0, with the latter value corresponding to the ratios found for type 1 Seyfert galaxies and the former to *Compton-thick* objects. Also note that the minimum of the distribution falls in the limit where Maiolino et al. (1998) found the distinction between *Compton-thick* and *Compton-thin* objects. We have hence defined two regimes to ensure the classification: (1) $\log(F_X(2-10\ \mathrm{keV})/F_{[OIII]}) < -0.15$ for secure *Compton-thick* objects ('CT' in Table 3.31) and (2) $-0.15 < \log(F_X(2-10\ \mathrm{keV})/F_{[OIII]}) < 0.5$ for doubtful *Compton-thick* candidates ('CT?' in Table 3.31). The value $\log(F_X(2-10\ \mathrm{keV})/F_{[OIII]}) < 0.5$ corresponds to the limit reported by Maiolino et al. (1998) between Seyfert 1 and Seyfert 2 galaxies. The ratio $\mathrm{Log}(F_X(2-10\ \mathrm{keV})/F_{[OIII]}) < -0.15$ is the conservative limit of the value assumed by Bassani et al. (1999).

Twenty five out of the 79 galaxies (31.6%) result to be *Compton-thick* candidates following this criterium. Eighteen objects (NGC 0474, NGC 2681, NGC 2685, NGC 3379, NGC 3608, NGC 3627, NGC 3898, NGC 4036, NGC 4125, IRAS 12112+0305, NGC 4278, NGC 4374, NGC 4410A, NGC 4698, NGC 5005, NGC 5813, NGC 7331 and NPM 1G -12.0625) show ratios from -0.15 to 0.5, so they are doubtful *Compton-thick* candidates ('CT?' in Table 3.31). The percentage of *Compton-thick* candidates increases to 53.2% (42/79) when doubtful *Compton-thick* objects are included.

UGC 05101, NGC 3690B, NGC 5005 and NGC 6240 are known *Compton-thick* sources (Ptak et al., 2003; Ceca et al., 2002; Risaliti et al., 1999; Vignali et al., 1999). NGC 6240 and NGC 3690B were confirmed *Compton-thick* sources in *BeppoSAX* data (at energies up to 300 keV) while UGC 05101 and NGC 5005 show *Compton-thick* evidences throught the detection of a high upper limit for the $EW(FeK\alpha)$ through *ASCA* data (Risaliti et al., 1999). In this work we have classified UGC 05101, NGC 3690B, NGC 6240 as *Compton-thick* sources but NGC 5005 can not be confirmed with our data because it only has an upper limit on the hard X-ray luminosity and the $H\alpha/H\beta$ ratio is not available.

However, there are two points to stress with respect to the use of this indirect method to find *Compton-thick* objects. First, we want to note that 21 sources have an unrealistic ratio of $H\alpha/H\beta$ below 3.10, the assumed ratio for AGNs (Osterbrock and Ferland, 2006). This can be due to the presence of absorptions contaminating the emission lines or to a complex continuum subtraction. In these cases we have assumed a minimum value of 3.10 which means that not correction is made. The [OIII] emission line flux might be therefore underestimated, so the number of *Compton-thick* objects would be a lower limit. In fact, only 1 out of these 21 objects is classified as *Compton-thick* and seven are doubtful *Compton-thick* objects.

The second comment is about the host galaxy. Objects with a disrupted morphology, like merger candidates, can have an such an enhancement of star formation processes that they overwhelm the host galaxy emision. This implies that a

large percentage of the measured [OIII] line flux would come from star-forming processes and therefore the nuclear [OIII] luminosity could be overestimated. This perturbed morphology is present in 7 cases (IIIZW 035, UGC 4881, NGC 3690B, IRAS 12112+0305, NGC 4410A, MRK 266NE and NGC 6240, see Appendix F), all of them *Compton-thick* candidates. As mentioned above, NGC 3690B and NGC 6240 are true *Compton-thick* sources, so there remain 5 cases in which the classification might be taken with caution.

Cappi et al. (2006) reported a sub-sample of 27 distance-limited Seyfert galaxies, 5 of them *Compton-thick* (18.5%). However, four of their objects are in our LINER sample (NGC 2685, NGC 3185, NGC 4579 and NGC 4698). Excluding these four objects, 4 out of the remaining 23 objects are classified as *Compton-thick* candidates (17.4%). Panessa et al. (2006) found arguments favouring the Compton-thickness nature in 11 out of their 47 Seyfert 2 analyzed (23%); however, among them 10 objects are confirmed LINERs in our sample (NGC 2639, NGC 2655, NGC 2685, NGC 3185, NGC 3608, NGC 3627, NGC 4579, NGC 4698, NGC 6482 and NGC 7743). Excluding these objects, 9 out of the 37 Seyfert 2 galaxies in Panessa et al. (2006) are *Compton-thick* (24%). For the 10 objects in common, they classified as *Compton-Thick* NGC 3185 and NGC 7743, in agreement with our classification. However, we also classified NGC 2639, NGC 2685, NGC 3608, NGC 3627 and NGC 4698. All these 5 objects show a ratio above -0.15 excepting NGC 2639, that they classified as a doubtful object.

Considering separately AGN and SB candidates in our sample, 51.1% (23/45) of the former are *Compton-thick* objects (14/45 or 31.1% excluiding doubtful objects). Among SB candidates the percentage of *Compton-thick* objects is 58.8% (20/43) (11/34 or 32.4% excluiding doubtful objects), slightly higher than for AGN candidates. Then, for both cases the percentage of *Compton-thick* objects is larger that for Seyfert galaxies in Cappi et al. (2006) and Panessa et al. (2006) .

Assuming that all the candidates are actually *Compton-thick*, then their intrinsic column densities should be higher than $10^{24}\mathrm{cm}^{-2}$. Their X-ray luminosities are underestimated since the column density correction is wrong. We separated our objects considering the two groups with $\mathrm{F_X}$ /F([OIII]) > 0.5 (*Compton-thin*) and $\mathrm{F_X}$ /F([OIII]) < 0.5 (*Compton-thick*), respectively. ($< \mathrm{F_X}$ /F([OIII])$_{\mathrm{thin}} >$ = 16.5 and $< \mathrm{F_X}$ /F([OIII])$_{\mathrm{thick}} >$ = 0.5). Then we consider that the ratio between these two quantities can be used as the correction factor between *Compton-thick* and *Compton-thin* sources: $< \mathrm{F_X}\ (2-10\ \mathrm{keV})/\mathrm{F}([\mathrm{OIII}])_{\mathrm{thin}} > / < \mathrm{F_X}\ (2-10\ \mathrm{keV})/\mathrm{F}([\mathrm{OIII}])_{\mathrm{thick}} >$ =33. Applying this correction factor to our *Compton-thick* sources we can obtain the corresponding corrected X-ray fluxes and luminosities, that are reported in Table 3.30.

In a similar way, Panessa et al. (2006) used Type 1 Seyferts and known *Compton-thick* objects and obtained a value of 60 for this ratio, so the double of what we get.

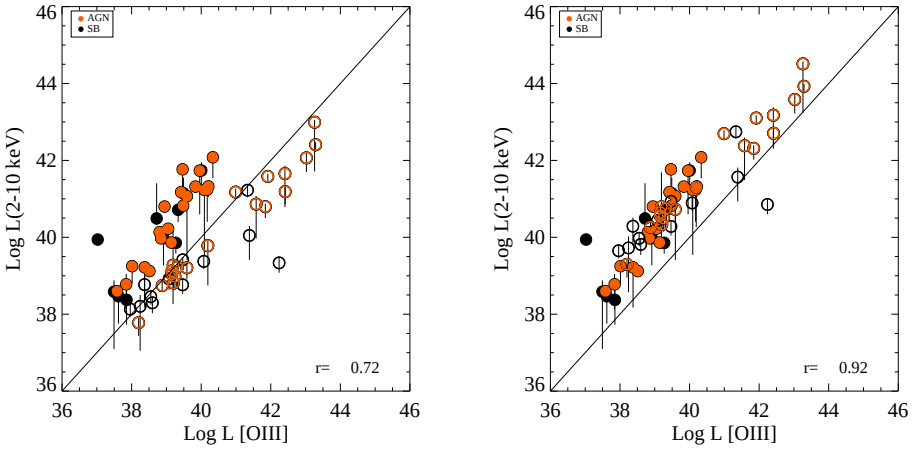

Figure 3.24: *L(2-10 keV) versus L[OIII] before (*left*) and after (*right*) the Compton-thick correction. Red circles are AGN candidates while SB are shown as SB candidates. Open circles corrrespond to Compton-thick candidates.*

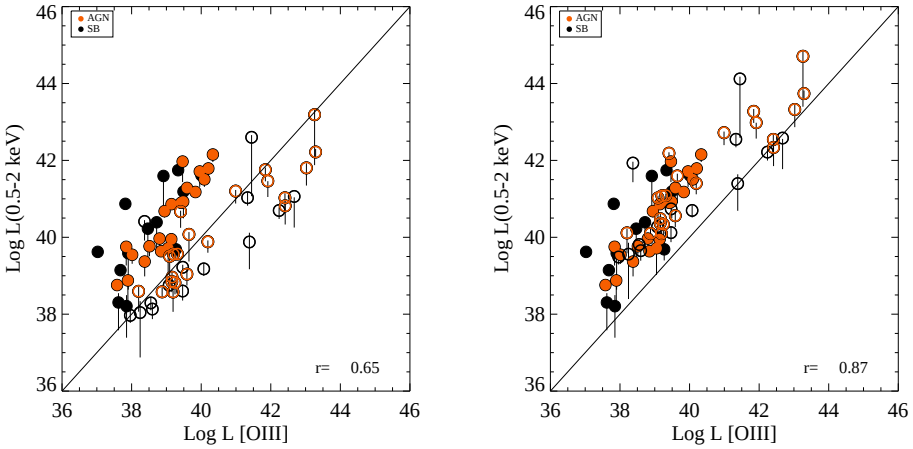

Figure 3.25: *L(0.5-2 keV) versus L[OIII] before (*left*) and after (*right*) the Compton-thick correction. Symbols as in Fig. 3.24*

The discrepancy may be due to the use of the mean instead of the median value. Indeed, we obtain 70 for this ratio if we use the mean value.

Fig. 3.24 shows the hard (2-10 keV) luminosity versus the [OIII] luminosity before (*Left*) and after (*Right*) the *Compton-thick* correction. Red circles are AGN can-

didates while SB candidates are shown as black circles. Open circles are *Compton-thick* objects. The linear correlation between these two quantities is extremely good (r=0.92) once the correction is applied. A similar correlation can be seen with L(Hα) (r=0.85, not shown). Notice that SB candidates are located at low luminosities and AGN candidates expand the whole range. Moreover, all of them populate the same location than Seyfert galaxies (Panessa et al., 2006) . The fact that the [OIII] luminosity correlates with the hard X-ray luminosity may suggest that both magnitudes are tracing the same process.

Fig. 3.25 shows the soft (0.5-2 keV) luminosity versus the [OIII] luminosity before (*Left*) and after (*Right*) the *Compton-thick* correction. Again, after the correction for *Compton-thickness*, the two magnitudes present a good correlation (r=0.88) although the dispersion is larger than for the hard X-ray luminosity. Then, it appears that the bunch of the soft luminosity seems to come from the same mechanism than the [OIII] luminosity, and some additional mechanisms are also probably contributing to the soft luminosity.

Nenkova et al. (2002) proposed that the obscuring region of AGNs is a toroidal distribution of dusty clouds. Ibar and Lira (2007) predicted an intrinsic *Compton-thick* source fraction of 58% while the 'clasical' torus produces a fraction of *Compton-thick* sources of 27%. The results on the fraction of *Compton-thick* objects within the LINERs range between 31.6% and 53.2%. Thus, the upper limit would need a clumpy torus scenario while the lower limit is consistent with a 'classical' torus.

Compton-thick tracers: The EW of the iron-line emission, $EW(FeK\alpha)$

It has been proben by Bassani et al. (1999) that the equivalent width of the iron Kα line (EW(FeKα)) is another *Compton-thick* tracer. This idea comes from the finding that EW(FeKα) for Seyfert 1 galaxies typically amounts to a few hundreds eV (Turner et al., 1998; Perola et al., 2002; Panessa et al., 2008), while when the column density increases to a few 10^{23} cm^{-2}, EW increases, since it is measured against a depressed continuum. EW(FeKα) can reach values as high as 500 eV for column densities higher than 10^{24} cm^{-2} (Matt, 1997; Bassani et al., 1999).

From a theoretical point of view, Ghisellini et al. (1994) made a Monte Carlo simulation of the X-ray spectrum. They found that at large inclination angles and for large torus column densities, the spectrum is attenuated by photoabsorption and *Compton* scattering, while the iron fluorescence line produced by the torus can have large EW(FeKα). They found that for column densities $> 10^{24}$cm^{-2}, i.e. *Compton-thick* regime, equivalent widths higher than 500 eV are found, in agreement with the observational results by Bassani et al. (1999).

For our sample of 82 LINERs, the iron emission line has been fitted for 51 ob-

jects, and detected in 13 out of these 51 (NGC 0315, NGC 0833, NGC 0835, NGC 1052, UGC 05101, NGC 3690B, NGC 4486, NGC 4579, MRK 0266NE, UGC 08696, NGC 6240, NGC 7130 and NGC 7285).

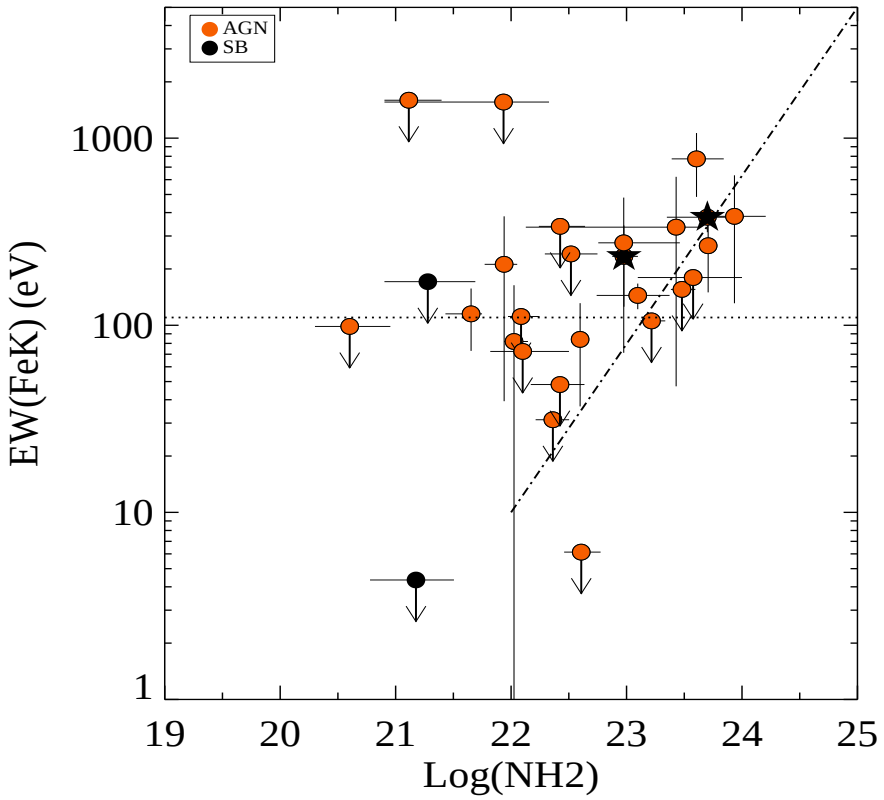

Figure 3.26: *EW of the FeKα emission line versus the NH2 column density. Red circles are AGN candidates and black circles show the SB candidates. Black stars are Compton-thick sources. The horizontal dotted line is the zero level reported by Guainazzi et al. (2005) for a sample of Seyfert 2 objects. The diagonal dotted-dashed line shows the predicted line reported by Ghisellini et al. (1994) for attenuation by photoabsorption and Compton scattering.*

In order to further explore the use of EW(FeKα) as a tracer for obscuration, we analyse whether it depends on the absorbing column density NH2 (Fig. 3.26). Upper limits on the column densities were excluded from this analysis. Again red circles are AGN candidates, black circles show SB candidates and black stars

are *Compton-thick* sources. The dotted line is the zero level reported by Guainazzi et al. (2005) for a sample of Seyfert 2 objects; the dotted-dashed line shows the predicted line reported by Ghisellini et al. (1994) for attenuation by photoabsorption and *Compton* scattering (half opening angle $\sim 30°$ and view angles around 70°).

Below 10^{23}cm^{-2}, EW(FeKα) seems to remain constant around 100 eV, as it is the case for Seyfert 1 nuclei (Nandra et al., 2007) and unobscured quasars (Jimenez-Bailon et al., 2005). For NH2$> 10^{23}$cm^{-2}, EW(FeKα) seems to increase up to $\sim$ 500 eV at 10^{24}cm^{-2}. Guainazzi et al. (2005) found a similar trend in a sample of 49 Seyfert 2 galaxies. This is an evidence of the similarities between Seyfert and LINER nuclei, that share the same scenario in which the iron line is originated in the inner wall of the torus (Fabian, 2005).

We have been able to determine the EW(FeKα) of three out of the four *Compton-thick* sources in our sample, finding 278.4 ± 178.1 keV, 233.4 ± 107.8 keV and 378.1 $\pm$63.8 keV, for UGC 05101, NGC 3690B and NGC 6240, respectively (shown as black stars in Figs. 3.26 and 3.27). These values are compatible with 410$\pm$250 eV, 422 $\pm$260 eV and 300$\pm$100 eV reported in the literature for UGC 05101 (Imanishi et al., 2003), NGC 3690B (Ballo et al., 2004) and NGC 6240 (Boller et al., 2003). These values do not agree with the expected EW(FeKα) for *Compton-thick* sources ($> 500\ eV$). However they seem to be located along the predicted line by Ghisellini et al. (1994). Note that UGC 05101 is excluded from the plot in Fig. 3.26 since only an upper limit is available for NH2.

The correlation between EW(FeKα) versus the Log(Fx/F[OIII]) was used as *Compton-thick* tracer by Bassani et al. (1999). They found that both EW(FeKα) and column density decrease when the ratio log(F(2 $-$ 10 keV)/F[OIII]) increases. They found log(Fx/F[OIII]) > 0 and EW(FeKα)$\sim$100 eV for Seyfert 1 galaxies, whereas *Compton-thick* galaxies were located at EW(FeKα) > 500 and log(Fx/F[OIII]) < 0.

Fig. 3.27 shows EW(FeKα) versus Log(Fx/F[OIII]). The black lines show the trend between this two quantities reported by Bassani et al. (2000). The red-dotted rectangle delineates the region occupied by Seyfert 1 galaxies, and the red-full lines correspond to the region where *Compton-thick* sources are placed (Bassani et al., 2000).

At least half of our objects are located in the region occupied by Seyfert 1 objects. However, neither of the known *Compton-thick* sources fall in the expected region for such sources, as reported by Bassani et al. (2000). We notice that in order to include *Compton-thick* objects, the EW(FeKα) limit should be re-defined to a lower value of EW(FeKα)$\sim$200 eV. The dashed red line is shown to include EW(FeKα)$>$ 200 eV and ratios below 0.5 (the Seyfert 1 limit). NGC 2681, UGC 05101, NGC 3690B, NGC 4374, NGC 4410A, MRK 266NE, NGC 5363, NGC 6240, IRAS 17208-0014 and NGC 7130 fall in this regime. However, such a low limit on EW(FeKα) does not allow to distinguish between type 1 Seyferts and *Compton-thick* sources.

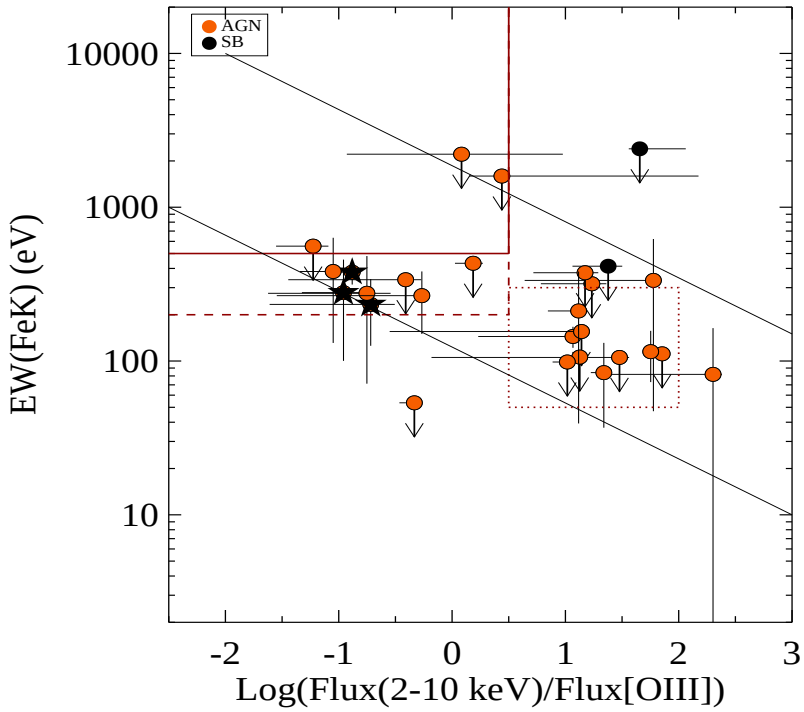

Figure 3.27: *EW of the FeKα line versus the ratio between the observed 2-10 keV flux and the dereddened [OIII] fluxes. Red circles are AGN candidates, black circles show the SB candidates and black stars are Compton-thick sources. The full lines shows the trend between this two quantities shown by Bassani et al. (2000), the dotted red line shows the region where Seyfert 1 are located while the red-continuous line shows the region where Compton-thick source are placed (Bassani et al., 2000). The red-dashed line shows the extension of the limit to include our Compton-thick nuclei.*

Then, we want to remark that further studies on the behaviour of the EW(FeKα) of the iron line are required in order to understand its usefulness as a *Compton-thick* tracer.

3.9.2 Obscuring material implications

The inclusion of objects showing *Compton-thick* signatures can induce several problems in our previous analysis because: (1) the values derived for NH2 for *Compton-*

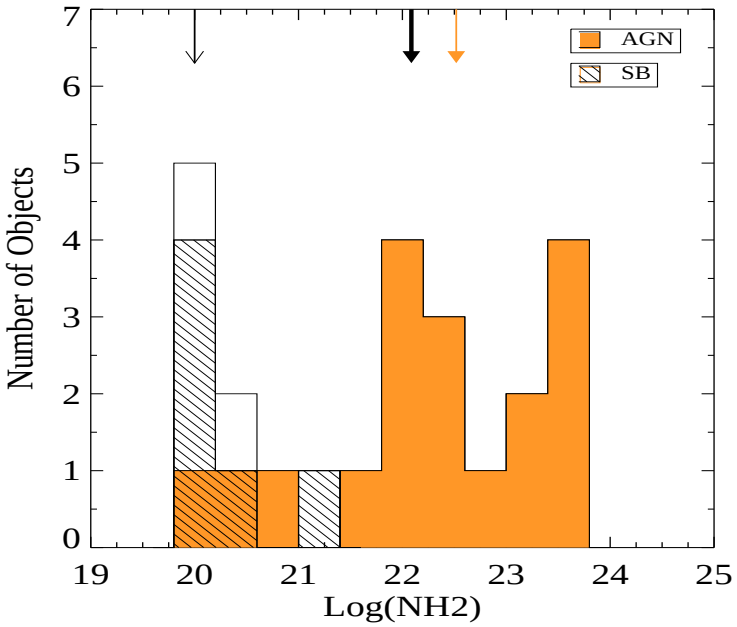

Figure 3.28: *NH2 column density histogram after Compton-thickness correction, i.e., excluding CT candidates.*

thick candidates are not correct and must be removed from the analysis and (2) the soft and hard luminosities distributions presented before must be reanalysed once the luminosities for *Compton-thick* candidates are corrected.

Fig. 3.28 shows the new distribution for NH2 after removing *Compton-thick* candidates. The fact that the new distribution is similar to that shown previously (Fig.3.21 *Bottom-Center*), reinforces the goodness of our result. SB candidates seem to be located at low NH2, mostly compatible with galactic column densities. AGN candidates expand a wide range with NH2 from 10^{20}cm^{-2} to 10^{24}cm^{-2}.

Fig. 3.29 shows the histograms for the soft (*Left*) and hard (*Right*) X-ray luminosities. The soft luminosity median values now are 41.03$\pm$ 1.30 , 40.53$\pm$ 1.46 and 40.87$\pm$ 1.38 for AGN, SB and the whole sample, respectively. The hard luminosity median values now are 40.79$\pm$ 1.42 , 39.98$\pm$ 1.21 and 40.51$\pm$ 1.41 for AGN, SB and the whole sample, respectively. All the reported values are larger than those provided in the previous section, and now closer to the luminosities for Seyfert samples (Panessa et al., 2006; Cappi et al., 2006). The two peaks found for the distribution of hard X-ray luminosities now disappear, so do the differences between SB and AGN

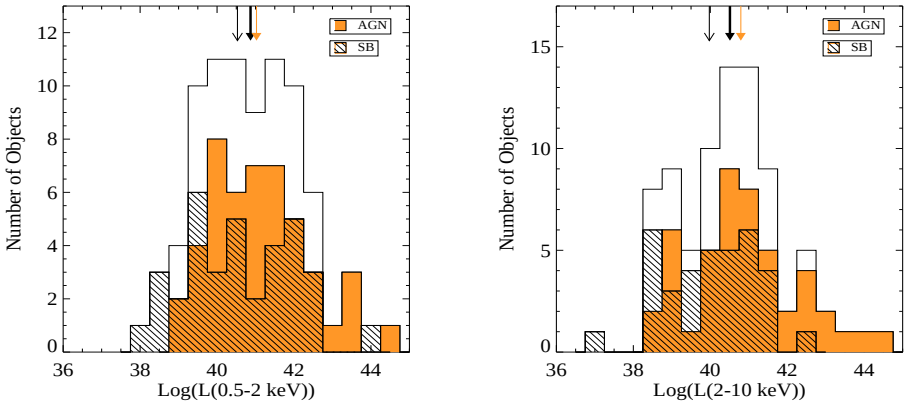

Figure 3.29: *Soft (0.5-2 keV) (*Left*) and hard (2-10 keV) (*Right*) luminosities histograms after Compton-thickness correction. Thick-black, thin-black and orange arrows indicate the median values for the whole sample, SB and AGN candidates, respectively.*

candidates in the hard luminosity.

Fig. 3.12 (Section 3.5) showed a comparison between between NH1 and NH2 column densities and both soft (0.5-2 keV) and hard (2-10 keV) luminosities. We found a correlation between hard X-ray (2-10 keV) luminosities and both NH1 and NH2 column densities. However, after the *Compton-thickness* correction, the correlation between NH2 and luminosities found before almost disappears (Fig. 3.30). The dashed line shows the region where unobscured Seyfert 2 are located (Panessa and Bassani, 2002). The dotted rectangle shows the region were luminous Seyfert 2 with $F_{[OIII]} > 4 \times 10^{-13}$erg cm^{-2} s^{-1} are placed (Risaliti et al., 1999). Then our LINER sample resembles the faint end of the distribution in the sample by Risaliti et al. (1999), being more obscured than the Seyfert 2 galaxies in Panessa and Bassani (2002). In fact, the column density reported for unobscured Seyfert 2 seems to be more related to our NH1 than to NH2.

Therefore, LINERs cover the same range in luminosities (soft X-rays, hard X-rays and [OIII] luminosities) than Seyfert galaxies. The iron emission line shows the same behaviour than in Seyfert samples (see Fig. 3.26). Although the optical spectrum shows different signatures, at X-rays frequencies LINER and Seyfert 2 nuclei are undistinguishable objects.

Since NH1 values for Seyfert 2 nuclei are consistent with galactic absorption in most cases (Guainazzi et al., 2005), but LINERs show a mean value around 10^{21}cm^{-2}, we have investigated the possibility that the differences in the optical nuclear classification come from differing obscuring material around them.

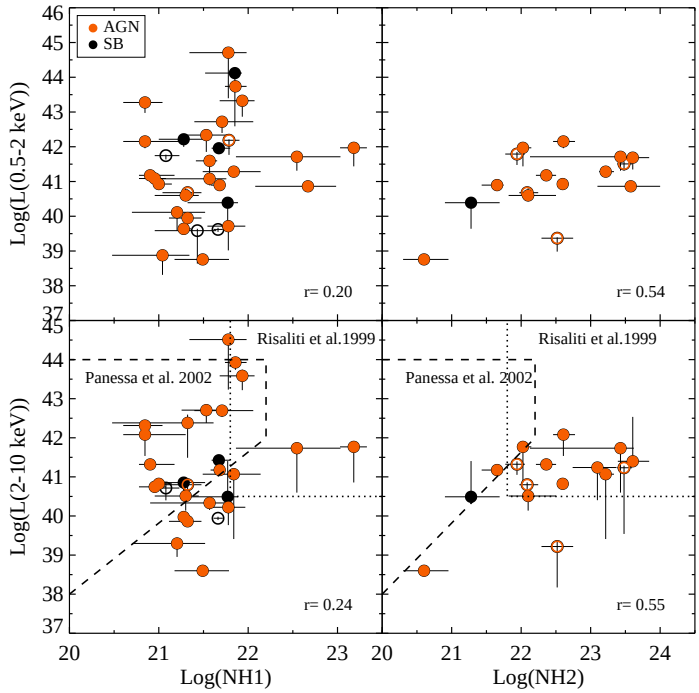

Figure 3.30: *Comparison between NH1 and NH2 column densities and luminosities corrected for Compton-thickness.* Top-left: *Soft (0.5-2.0 keV) luminosity versus NH1;* Top-right: *Soft (0.5-2.0 keV) luminosity versus NH2;* Bottom-left: *Hard (2-10 keV) luminosity versus NH1 and ;* Bottom-right: *Hard (2-10 keV) luminosity versus NH2. The* XMM-Newton *data are plotted with open circles. For clarity upper limits are not included in the plot. The dashed line shows the region where unobscured Seyfert 2 are located (Panessa and Bassani, 2002). The dotted rectangle shows the region were luminous Seyfert 2 with* $F_{[OIII]} > 4 \times 10^{-13}$erg cm^{-2} s^{-1} *are placed (Risaliti et al., 1999).*

To do so, we have computed the optical extinction by using the Hα/Hβ ratios. Objects showing a lower limit of Hα/H$\beta = 3.10$ have been removed from this analysis. Assuming a galactic ratio Av/$N_H = 5 \times 10^{-22}$cm^{-2}, we can express Av in units of cm^{-2}. Fig. 3.31 shows the histograms of the ratio between the NH1 and Av (*Left*) and NH2 and Av (*Right*). NH2 is higher than that expected from Av measurements. This result was already drawn by Maiolino (2001) for a sample of type 2 Seyfert

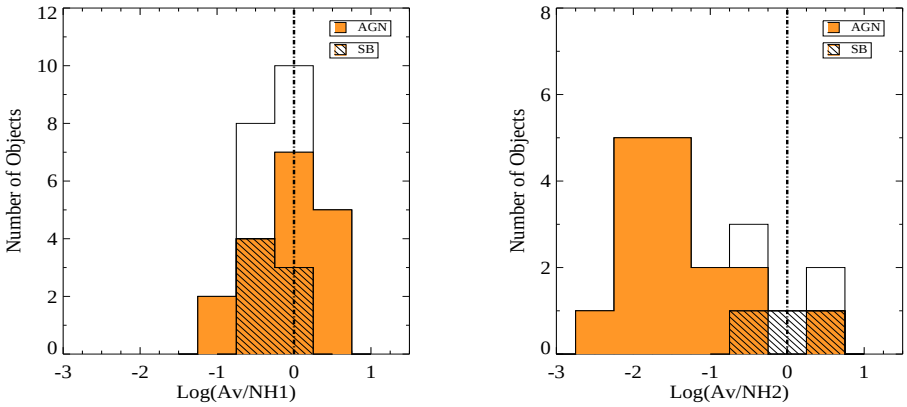

Figure 3.31: *Histograms of the ratio between the NH1 and Av (*Left*) and NH2 and Av (*Right*)*

galaxies. On the other side, NH1 seems to be consistent with Av. In fact, when we plot NH1 versus Av (Fig. 3.32), there is a clear trend between NH1 and Av, with only two objects (IRAS 17208-0014 and UGC 05101) showing large departures from the general trend.

In the sample of unobscured Seyfert 2, Panessa and Bassani (2002) found that the X-ray obscuration measured with NH at X-ray frequencies is consistent with the one measured at optical wavelengths (Av). This appears to be in good agreement with our results, since the NH measured by Panessa and Bassani (2002) is more related to our NH1 than to NH2. In fact they use only one absorber as in GM+06, also consistent with NH1 but far from the NH2 results. Then, while NH1 seems to be related to the optical extinction, NH2 appears to be much larger.

Guainazzi et al. (2001) studied the correlation among X-ray absorption, optical reddening and nuclear morphology in Seyfert 2 galaxies. They found a relation between optical extinction and *Compton-thin* Seyfert 2 galaxies, while *Compton-thick* sources do not show such dusty, nuclear environments. However, we do find a correlation between NH1 and optical extinction for both populations.

To study the relevance of dust in the nuclear region of LINERs we have investigated the optical morphological counterparts of the X-ray sources. For this goal, we have used sharp-divided images from available *HST* data (for 67 out of the 82 LINERs), mainly with the F814W filter (see Section 3.4.1). The resulting images are shown in Appendix C.

As we did in GM+06, according to the appearance of the central regions, two main groups can be distinguished:

- Galaxies with compact nuclear sources, when a knot coincident with the cen-

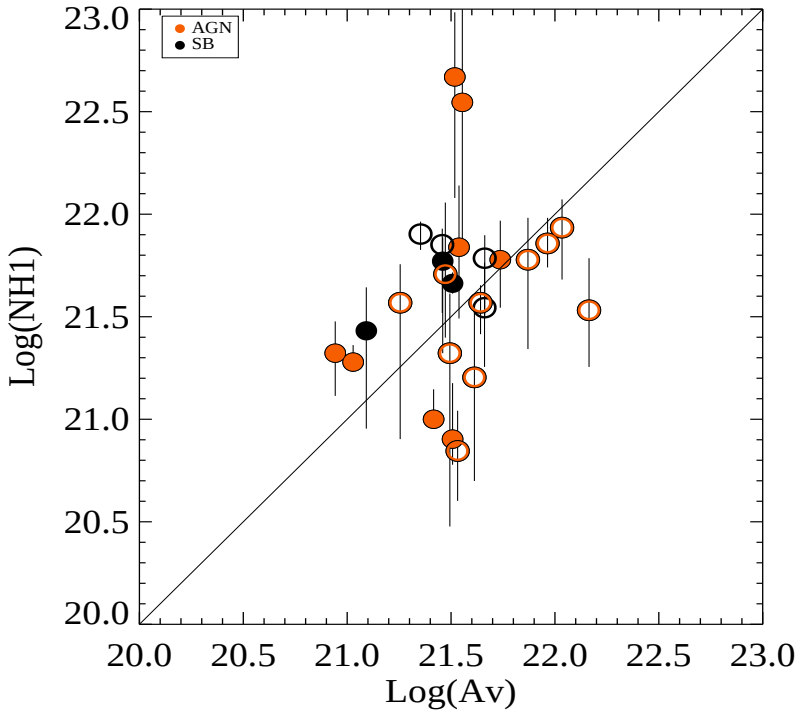

Figure 3.32: *NH1 column density versus optical extinction Av. The continuous line shows identity (zero offset and slope equal to one).*

tral X-ray source is detected in the sharp-divided image ('C' in Col. 5 in Table 3.31). 59 out of the 67 fall into this category. NGC 4111, NGC 5005 and NGC 5746 were marked as doubtful compact sources ('C?' in Col. 5 in Table 3.31) because they have strong dust lanes across their nuclear regions.

- Galaxies with dusty nuclear regions, when dust-lanes like features are seen and no central knot is detected ('D' in Col. 5 in Table 3.31). 6 sources fall into this category.

NGC 3628 and NGC 4261 were classified as undefined ('U' in Col. in Table 3.31). NGC 3628 sharp-divided image does not show any structure and NGC 4261 is saturated.

It appears that for most of the galaxies ($\sim$ 88%) a compact nucleus is found. This is consistent with the results of optical *HST* data recently published by Gonzalez-

Delgado et al. (2008) for a sample of LINERs and Transition Objects. Taking their data and reclassifying them according to our criteria we have found that only 5 out of their 34 LINERs appear not to be compact.

Looking to the coincidence between X-ray and optical compactness we found that among the 38 galaxies classified as AGN at X-ray frequencies, only NGC 4438 does not appear to be compact. The absence of an identifiable nuclear source can be mainly attributed to the large dust line crossing the nucleus (see Appendix C). For the 29 SB candidates with *HST* data, 23 are classified as compact sources at optical frequencies while 5 objects shows a dusty morphology. Among them, the population is equally distributed in *Compton-thin* and *Compton-thick* sources, at variance with what has been claimed by Guainazzi et al. (2001) for Seyferts. They found that *Compton-thin* objects prefer dustier environment whereas *Compton-thick* nucleus distribute both in dustier and dust-free regions. Based in the present data a relationship between the optical morphology and Compton-thickness is not evident, being LINERs not specially dustier objects. Thus, it appears that the Compton-thickness nature is more related to the dusty torus that to the host galaxy, in accordance with the difference we found between NH1 and NH2.

3.9.3 Galaxy environment of LINERs

To take into account the eventual influence of the environmental status in the properties of our sample galaxies, we have searched in the NED for information related to the large scale of the hosting galaxies. This information is provided in Col. (12) in Table 3.31, and an atlas of the galaxies is presented in Appendix D. We have searched for possible companions at projected distances smaller than 250 kpc. Eventual companions and their corresponding redshifts are provided in the notes, Appendix A. Galaxies have been classified in 4 groups according to their environment: 1) isolated, when no projected companions with comparable sizes and redshift difference smaller than 1000 km/s are found, 2) pairs, when only another galaxy of comparable size and close in redshift is identified (wide and close pairs together with merging systems are grouped into this cathegory), 3) group environment, for galaxies in small groups (either compact or loose), 4) cluster, for galaxies known to reside in cluster environments (in some cases, they correspond to the cluster center - see Appendix A). This classification is included in Col. (13) in Table 3.31.

In general, the environmental status does not seem to be connected with all the analysed properties, excepting in two aspects: [OIII] and hard X-ray luminosities, that are clearly enhanced in the second group, and thus modifying the Compton-thickness. A closer inspection of this result clearly indicates that the merging processes seem to be able to account for such an effect, since the galaxies with clearly

enhanced luminosities are those in merging pairs (namely UGC 05101, UGC 8696, NGC 3690, NGC 4410, NGC 6240, NGC 6251, Mrk 266, IRAS 17208-0014 and IRAS 12112+0305) some of them even belonging to the group of ultraluminous infrared galaxies. The excess in the [OIII] and hard X-ray luminosities can be most probably attibuted to the huge star formation activity that is also present in such systems.

With respect to Compton-thickness, the resulting average and sigma values for L(hard)/L[OIII] for the different environments are provided in Table 3.10, and the corresponding histograms shown in Fig. 3.33. We note that *Compton-thick* objecs are not found in cluster environments, but are relatively frequent in the group of merging systems. This could be understood by considering that a huge amount of obscuring material is being transported to the nuclear regions as a result of the merging process (for instance Mihos and Hernquist, 1994; Barnes and Hernquist, 1996). Nevertheless, a number of galaxies in the group of isolated objects, for which such an effect can not be invoked, are also *Compton-thick* candidates (NGC 2639, NGC 2685, NGC 4457, NGC 4698, NGC 7331 and NGC 7743), so the origin of the obscuring material in these systems have to be related either to intrinsic properties or to secular processes in their host galaxies.

3.9.4 Black hole Masses and Accretion rate

We have estimated the black-hole masses, from the velocity dispersions available at Hyperleda[9] for 63 out of the 82 (Table 3.30). Black hole masses were determined using the correlation between stellar velocity dispersion and black hole mass reported by Tremaine et al. (2002):

$$log(M_{BH}(M\odot)) = 8.13 + 4.02 \times log(\sigma(km\ s^{-1})/200) \quad (3.1)$$

The distribution of black hole masses is plotted in Fig. 3.34. They range from $10^6 M\odot$ to $10^{9.5} M\odot$ with median value and standard deviation of 8.22$\pm$ 0.65 . The Seyfert 2 sample observed by Panessa et al. (2006) covered the same range of black hole masses but peaking at lower values ($10^8 M\odot$). There is not distinction between SB and AGN candidates. Black hole masses show a tendency for being much larger for galaxies with larger bulges, and smaller values for later type galaxies. In fact, taking all ellipticals and lenticulars together (43 galaxies), their median black hole mass is log (M_{BH})=8.28 $\pm$ 0.61, whereas it is log (M_{BH})=7.78 $\pm$ 0.66 for spirals later than Sa (19 galaxies).

Fig. 3.35 shows L(2-10 keV) versus the black hole mass, before (*Left*) and after (*Right*) Compton-thickness correction (explained in previous Section). Red circles are AGN candidates, black circles are SB candidates. The objects classified as

[9] http://leda.univ-lyon1.fr/

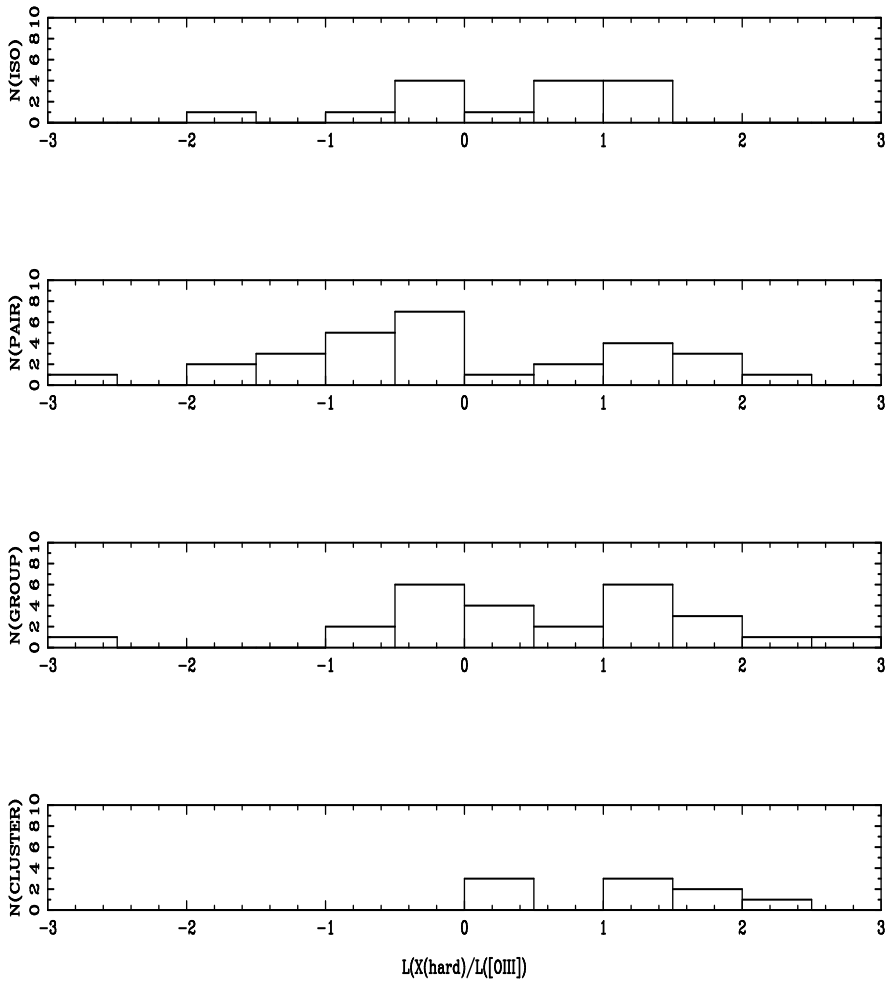

Figure 3.33: *Histogram for the L(2-10 keV)/L[OIII] for the different environments, from isolated (a), to pairs (b), groups (c) and clusters (d), from top to bottom.*

Compton-thick are shown as open circles. Black-open squares show the Seyfert samples from Cappi et al. (2006) and Panessa et al. (2006). Solid lines correspond to Eddington ratios 0.01, 10^{-4},10^{-6} (assuming $L_{bol}/L(2-10\ keV) \sim 30$, Risaliti and Elvis, 2004).

Before the Compton-thickness correction the median Eddington ratio $L_{bol}/L_{Edd} = 4.7 \times 10^{-6}$, which is consistent with the result by Dudik et al. (2005), who found a ratio $L_{bol}/L_{Edd} = 7 \times 10^{-6}$ for a sample of LINERs. Nevertheless, after such a correction this ratio increases up to $L_{bol}/L_{Edd} = 4.6 \times 10^{-5}$. The low percentages for

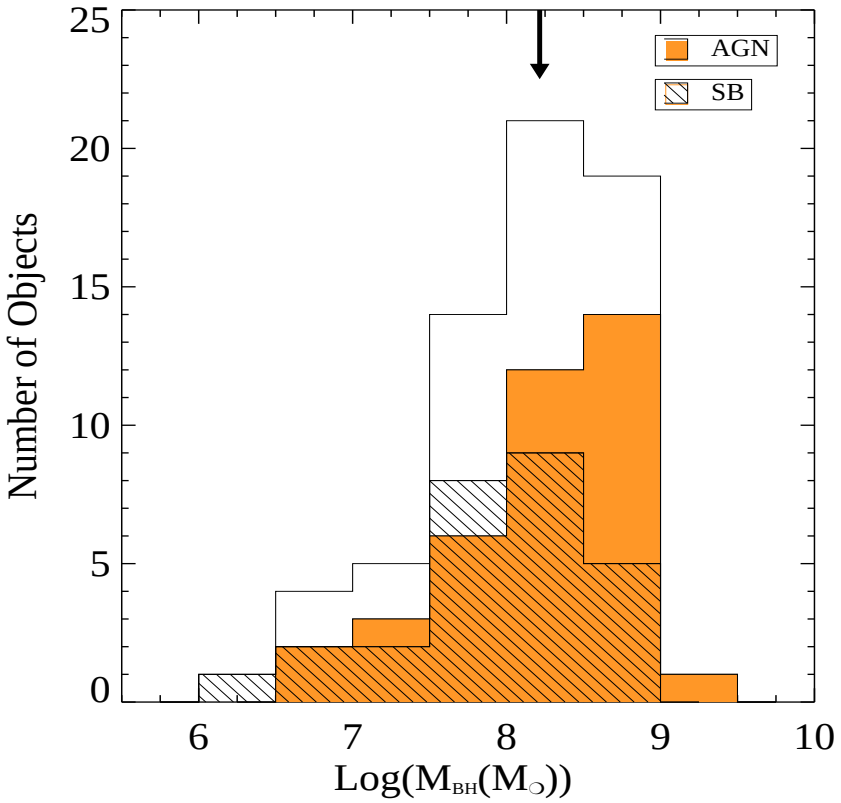

Figure 3.34: *Histogram for black hole masses.*

the accretion rate indicate an inneficient accretion flow ($< 10^{-3}$, Terashima et al., 2002). It can be seen that Seyferts expand the same range of Eddington ratios, although they tend to occupy the region close to L_{bol}/L_{Edd}=0.01, while LINERs tend to be closer to L_{bol}/L_{Edd}=0.0001.

3.9.5 Multiwavelength analysis of LINERs

In addition to X-ray signatures (e.g. hard X-ray compact nuclear source, FeKα 6.4 keV iron emission line or spectral energy distribution well fitted to the *BLM* of AGNs), independent evidence on the AGN nature of LINER nuclei can be found at other wavelengths. The last part of our study will deal with this multiwavelenght

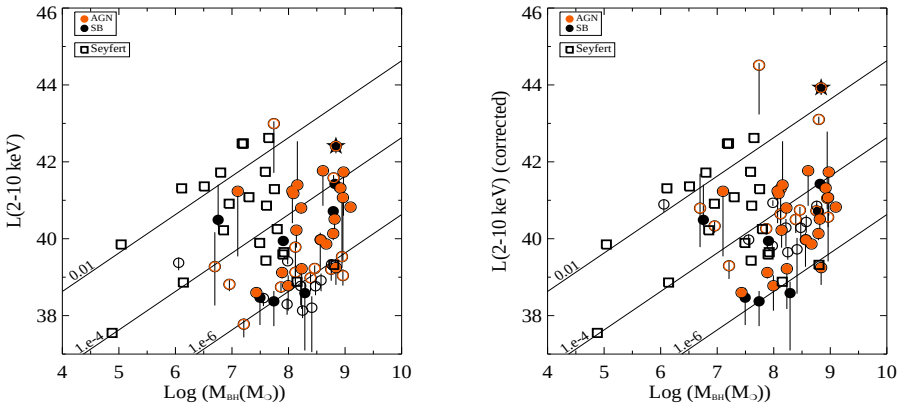

Figure 3.35: *2-10 keV luminosity versus the black hole masses, before (*Left*) and after (*Right*) Compton-thickness correction. Red circles are AGN candidates, black circles are SB candidates. The objects classified as Compton-thick were are shown as open circles. Black-open squares shows the Seyfert sample form Cappi et al. (2006) and Panessa et al. (2006). Solid lines are Eddington ratios of 0.01,* 10^{-4},10^{-6} *(assuming* $L_{bol}/L(2-10\ keV) \sim 30$*, Risaliti and Elvis (2004).*

analysis.

Before entering into it, we want to say a few words about the sometime large dispute (see Ho et al., 2008, for a full discussion) on other alternatives to the X-ray emission in LINERs, such as Starburst and/or ULX contamination. Starbust contribution has been invoked to explain the observed X ray emission for some particular cases (i.e. Eracleous et al., 2002; Jimenez-Bailon et al., 2005, on the LINER NGC 4736 and on the low luminosity AGNs NGC 1808, respectively). In these cases the contamination from high mass X-ray binaries (HMXB) can be claimed but in GM+06 we have already argued that HMXB cannot be considered as an important ingredient for most of the galaxies. By using the data from Cid-Fernandes et al. (2004) and Gonzalez-Delgado et al. (2004), we have found that for the 21 objects in common only young stellar population can be claimed in three objects, NGC 3507, NGC 3998 and NGC 4321 (see Col. (8) in Table 3.31). NGC 3998 has a broad Hα emission line (Ho et al., 1997) pointing to its AGN nature. For the other two galaxies their X-ray morphology is that of an SB candidate and a detailed analysis need to be done to evaluate the importance of HMXB in them. But for the remaining objects young stars cannot be important contributors to the observed emission.

On the other hand, Ultra-luminous X-ray sources (ULXs, see Fabbiano, 2006, for

a review) can constitute an important contribution at X-rays energies. The high X-ray luminosity found for an ULX in the star-forming galaxy NGC 7424 (Soria et al., 2006), with luminosity of 10^{40} erg s^{-1}, proves how important the contamination produced by such objects can be if they are found at nuclear locations, making this analysis extremely difficult and implying that only indirect proofs can be invoked. But it has to be taken into account that the reported high luminous ULXs are mostly asociated to young clusters where large events of star formation are occuring (see for instance data on the Antenae and NGC 1275, Wolter et al., 2006; Gonzalez-Martin et al., 2006a, respectively) which appears not to be our case. Thus it seems that neither HMXB nor ULX can be considered as serious alternatives to explain the X-rays.

Now, to get hints on the eventual presence of an AGN and to have a general view on the multiwavelength properties of LINERs we have compiled from the literature all the information available at frequencies from radio to UV. The relevant informations for our discussion on multiwavelength data are tabulated in Table 3.31, with Col. (1): label number; Col. (2): name; Col. (3): X-ray nuclear class; Col. (4): hard X-ray luminosity; Col. (5): HST nuclear class; Col. (6): Radio compactness and spectral type; Col. (7): percentage of young stars; Col. (8): UV variability; Col. (9): X-ray variability; Col. (10): UV compactness; Col. (11): Compton-thickness type; Col. (12): Environment; Col. (13): code for the environment. Under the Unified Model the main ingredients expected to be common in AGNs are: (1) a region of high velocity and high velocity dispersion, called Broad Line Region (BLR); (2) variability at UV and; (3) an unresolved radio compact core associated with a flat continuum (Nagar et al., 2005; Filho et al., 2004). The presence of any of these components will be taken as an AGN signature.

Broad Hα components has been reported in 15 cases (18%) in our sample. However, the detection of broad Hα must be taken with caution since weak broad Hα lines could exist and/or an insufficiently high spectral resolution could misclassified the blending of narrow Hα line as a broad line Hα. Excepting NGC 2639 and NGC 4636, all the 16 objects showing BLR in our sample are classified as AGN through X-ray morphology (86%). Ho et al. (2008) has shown that type 1 LINERs host a point like source in 95%, consistent with our findings. Among the type 2 LINERs, the detection rate is 50%, lower than the reported rate by Ho et al. (2008), a difference that may be related to the less homogeneous character of our sample with respect to Ho's, who only uses sources from the Palomar Sky spectroscopic survey.

In six cases (NGC 3998, NGC 4486, NGC 4552, NGC 4579, NGC 4594 and NGC 4736) UV variability has been found (Maoz et al., 2005). These UV variable objects are tabulated in Table 3.31, Col. (10); all of them compatible with the X-ray morphological classification as AGN. Interestingly, all the sources showing UV variability

appear as *Compton-thin* in X-rays. This is consistent with the idea that highly obscured objects will be lost in UV surveys.

Finally, observations at radiofrequencies do exist for 75 out of our 82 LINERs. 28 sources have not been detected at 2cm (Nagar et al., 2005, and references therein) whereas compact sources are detected in 54/75 (72%). Among the 54 compact sources, six show steep nuclear spectra while 25 are compatible with the presence of an AGN (17 show flat spectra and 8 show jet structure). Among these 25 objects, 14 have been classified as AGN candidates and 11 have been classified as SB candidates. Among the 54 sources detected at radio frequencies, 30 are detected at X-rays.

Adding together the resuls on X-rays, UV variability, radio classifications and Compton-thickness only 9 sources (12.2%) do not show any evidences of AGN nature, namely NGC 0410, NGC 0524, NGC 3623, NGC 3628, NGC 4314, NGC 4321, NGC 4459, NGC 4596, and NGC 4676A. The spectral analysis was possible for only 5 sources and it is incompatible with a thermal origin (i.e. ME model) in all cases.

Then, attending to the present X-ray analysis of this large compilation of LINERs, and adding the available radio, UV and optical information, most of the LINERs seem to host an AGN (90%).

3.10 Summary and conclusions

Along this paper the nuclear characterisation of 82 LINER galaxies in X-rays, 68 with *Chandra* and 55 with *XMM-Newton* data is presented. Both together comprise the largest sample of LINERs with X-ray spectral fit ever analysed (60 out of the 82 objects). We also use the information on the black hole masses, optical morphology with *HST* data, optical emission lines, radio compactness and stellar populations reported in the literature.

Several caveats must be considered in order to compare *Chandra* and *XMM-Newton* data. Firstly, the LLAGNs features responsible for their complex morphology, at least LINERs, contribute to the whole X-ray energy range. This is specilly relevant at soft X-rays (0.5-2 keV) where it can be more than an order of magnitude higher. Secondly, the spectral model selection is a crucial step. NH2 column density is the most affected parameter, showing higher values when two power-laws are imposed for the spectral fit. Luminosity is a robust parameter since it is independent on the fit. In fact, the assumption of a power law model with spectral index 1.8 and galactic absorption provides a good estimation of hard luminosities. Finally, the $\mathsf{EW}(\mathsf{FeK}\alpha)$ of the FeK emission line does not seem to be a good tracer of the *Compton-thickness* because confirmed *Compton-thick* objects do not fix within the sce-

nario previously proposed. A study of the $\mathsf{EW(FeK}\alpha)$ of *Compton-thick* candidates with the current instrumentation must be done.

To summarise, we present the most important conclusions in this paper:

1. ***X-ray Imaging:*** 60% (49/82) of the sample shows a compact nuclear source at 4.5-8 keV band (the so-called AGN candidates), 68% (41/60) within the sample with spectral fit.

2. ***X-ray spectroscopy:*** MEPL and ME2PL are the best representation of the data in 70% (42/60) of the sample. 2PL was good enough only in three cases (5%) while single models (ME or PL) were needed in 15 cases (25%). The median spectral parameters are: $<\Gamma>$=2.11$\pm$ 0.52 , $<$ kT $>$=0.54$\pm$ 0.30 keV, $<\log(\mathsf{NH1})>$=21.32$\pm$ 0.71 and $<\log(\mathsf{NH2})>$=21.93$\pm$ 1.36 . The FeK iron emission line was detected in 13 cases and upper limits are reported for 51 LINERs. The distribution of $\mathsf{EW(FeK}\alpha)$ versus NH2 is consistent with Seyfert samples.

3. ***Compton-thickness:*** 53% of the sample show indications of Compton-thickness through $\mathsf{F_X(2-10keV)/F([OIII])}$ ratios.

4. ***Luminosities:*** Soft and hard luminosities range between log(L(0.5-2 keV)) = 37.5-43.5 and log(L(2-10 keV)) = 37-43, respectively with median values (in logaritmic scale) of $\mathsf{L(0.5-2\ keV)}$ = 40.22$\pm$ 1.33 and $\mathsf{L(2-10\ keV)}$ = 39.85$\pm$ 1.26 . The 2-10 keV luminosity shows a bimodal distribution centred at 39 and 41.5. After *Compton-thick* correction both, soft and hard luminosities, range from log($\mathsf{L_X}$)=38-45 and the median values are $<\log(\mathsf{L(0.5-2\ keV)})>$= 40.51$\pm$ 1.41 and $<\log(\mathsf{L(2-10\ keV)})>$= 40.87$\pm$ 1.38 . The bimodal distribution almost disappears after the Compton-thickness correction.

5. ***The origin of the obscured matter:*** NH1 column density of LINERs correlates with the optical extinction while a deficit is found when the latter is compared to NH2. This is interpreted as NH1 tracing the optical extinction while NH2 is coming from inner parts of the AGN, where the radiation at optical wavelengths cannot penetrate.

6. ***LINERs/Seyferts:*** After *Compton-thick* correction there are not differences between AGN-like and SB-like objects. This implies that only image analysis is not enough to determine the presence of an AGN, being the X-ray spectral analysis complemented with needed multiwavelength information. [OIII], (0.5-2 keV) and (2-10 keV) luminosities correlate, indicating that they are originated by the same mechanism. Moreover the distribution is in the same range

of luminosities (Eddington rates $\sim 10^{-(2-6)}$) than Seyfert 2 reported previously.

7. ***AGN nature:*** Adding up the multiwavelength information discussed throughout this paper, at least 74 out of the 82 objects (90%) show evidences of harbouring an AGN.

All the properties in the present paper, indicate that LINERs are *not* the faint tail of the AGN population, showing the same range of properties than type 2 Seyferts.

The large percentage of *Compton-thick* candidates found in LINERs and its implication on the Eddington rates rise the question of whether such an effect could be extrapolated to the X-ray background and then, to the amount of obscured LLAGNs in the high redshift Universe. The determination of the truly obscured AGNs within *Compton-thick* candidates, through observations above 10 keV, is still open. Unfortunately, such a question needs instrumentation with high sensitivity to the range above 10 keV, including high spatial resolution to detect sources as LINERs. We hope that future missions like *Simbol-X*, *XEUS* and/or *Constellation-X* will help to verify this possibility.

Acknowledgements

We gratefully acknowlegde the useful comments from R. Rupke. This work was financed by DGICyT grants AYA 2003-00128, AYA 2006-01325, AYA 2007-62190 and the Junta de Andalucía TIC114. OGM acknowledges financial support by the Ministerio de Educación y Ciencia through the Spanish grant FPI BES-2004-5044. This research has made use of data obtained from the *Chandra* Data Archive provided by the *Chandra* X-ray Center (CXC). This research has made use of data obtained from the *XMM-Newton* Data Archive provided by the *XMM-Newton* Science Archive (XSA). The NRAO is a facility of the National Science Foundation operated under cooperative agreement by Associated Universities, Inc. This research made use of the NASA/IPAC extragalactic database (NED), which is operated by the Jet Propulsion Laboratory under contract with the National Aeronautics and Space Administration. This publication makes use of data products from the Two Micron All Sky Survey, which is a joint project of the University of Massachusetts and the Infrared Processing and Analysis Center/California Institute of Technology, funded by the National Aeronautics and Space Administration and the National Science Foundation. We acknowledge the usage of the Hyperleda database.

Table 3.1: Summary of the general properties of our LINER sample

Num	Name	Other Name	RA	Dec	Redshift	Dist. (Mpc)	Ref.	B	E(B-V)	Morph. Type
(1)	(2)	(3)	(4)	(5)	(6)	(7)	(8)	(9)	(10)	(11)
1	NGC 0315.....	UGC 0597	00 57 48.88	+00 21 08.8	0.01646	68.11	(b)	12.202	0.065	E
2	NGC 0410.....	UGC 0735	01 10 58.87	+03 09 08.3	0.01765	71.87	(b)	12.519	0.059	E(s)
3	NGC 0474.....		01 20 06.70	+00 24 55.0	0.00775	32.51	(d)	12.382	0.035	S0(r)
4	IIIZW 035		01 44 30.50	+17 06 05.0	0.02743	109.67	(b)		0.063	
5	NGC 0524.....	UGC 0968	01 24 47.72	+00 32 19.8	0.00793	23.99	(c)	11.381	0.082	S0-a
6	NGC 0833.....	ARP 318B	02 09 20.88	+10 08 00.3	0.01357	49.74	(b)	13.697	0.025	Sa
7	NGC 0835.....	ARP 318A	02 09 24.69	−10 08 10.5	0.01357	50.45	(b)	13.159	0.025	Sab(sr)
8	NGC 1052.....		02 41 04.80	+08 15 20.8	0.0049	19.41	(c)	11.436	0.027	E
9	NGC 2639.....	UGC 4544	08 43 38.08	+50 12 20.0	0.01112	45.45	(b)	12.596	0.024	Sa(r)
10	NGC 2655.....	UGC 4637	08 55 37.73	+78 13 23.1	0.00467	24.43	(d)	10.98	0.031	S0-a(s)
11	NGC 2681.....	UGC 4645	08 53 32.73	+51 18 49.3	0.00230	17.22	(c)	11.148	0.023	S0-a(s)
12	NGC 2685.....	UGC 4666	08 55 34.75	+58 44 03.9	0.00294	16.22	(d)	12.16	0.062	S0-a(s)
13	UGC 4881.....		09 15 55.10	+44 19 55.0	0.03930	157.09	(b)		0.017	
14	3C 218	Hydra A	09 18 05.67	−12 05 44.0	0.05487	218.04	(b)	14.296	0.041	E-SO
15	NGC 2787.....	UGC 4914	09 19 18.56	+69 12 12.0	0.00232	7.48	(c)	11.602	0.133	S0-a(sr)
16	NGC 2841.....	UGC 4966	09 22 02.63	+50 58 35.5	0.00212	11.97	(d)	10.063	0.015	Sb(r)
17	UGC 05101.....		09 35 51.65	+61 21 11.3	0.03939	157.3	(b)	15.278	0.033	
18	NGC 3185.....		10 17 38.57	+21 41 17.7	0.00406	21.28	(d)	12.936	0.027	Sa(sr)
19	NGC 3226.....	UGC 5617	10 23 27.01	+19 53 54.7	0.0059	23.55	(c)	12.339	0.023	E
20	NGC 3245.....	UGC 5663	10 27 18.39	+28 30 26.6	0.00522	20.89	(c)	11.655	0.025	S0(r)
21	NGC 3379.....	M 105	10 47 49.60	+12 34 53.9	0.00265	10.57	(c)	10.218	0.024	E
22	NGC 3414.....	UGC 5959	10 51 16.23	+27 58 30.0	0.00471	25.23	(c)	12.055	0.025	S0(s)
23	NGC 3507.....	UGC 6123	11 03 25.39	+18 08 07.4	0.00495	19.77	(d)	12.084	0.024	SBb(s)
24	NGC 3607.....	UGC 6297	11 16 54.66	+18 03 06.5	0.0057	22.80	(c)	10.933	0.021	E-SO
25	NGC 3608.....	UGC 6299	11 16 58.96	+18 08 54.9	0.00572	22.91	(c)	11.567	0.021	E
26	NGC 3623.....	M 65	11 18 55.96	+13 05 32.0	0.00269	7.28	(d)	10.139	0.025	SABa(s)
27	NGC 3627.....	M 66	11 20 15.03	+12 59 29.6	0.00242	10.28	(a)	9.735	0.033	SABb(s)
28	NGC 3628.....	UGC 6350	11 20 17.01	+13 35 22.9	0.00192	7.73	(d)	9.972	0.027	Sb
29	NGC 3690B	MRK 171	11 28 32.20	+58 33 44.0	0.0104	41.60	(b)	13.369	0.017	SBm(s)
30	NGC 3898.....	UGC 6787	11 49 15.37	+56 05 03.7	0.00392	21.98	(d)	11.257	0.020	Sab
31	NGC 3945.....	UGC 6860	11 53 13.73	+60 40 32.0	0.0042	22.49	(d)	11.7	0.028	S0-a(sr)
32	NGC 3998.....	UGC 6946	11 57 56.12	+55 27 12.7	0.00346	14.13	(c)	11.409	0.016	S0(r)
33	NGC 4036.....	UGC 7005	12 01 26.75	+61 53 44.8	0.00482	24.55	(d)	11.536	0.024	E-SO
34	NGC 4111.....	UGC 7103	12 07 03.13	+43 03 55.4	0.00375	15.00	(c)	11.67	0.014	S0-a(r)

Table 3.1: Continuation

Num	Name	Other Name	RA	Dec	Redshift	Dist. (Mpc)	Ref.	B	E(B-V)	Morph. Type
(1)	(2)	(3)	(4)	(5)	(6)	(7)	(8)	(9)	(10)	(11)
35	NGC 4125.....	UGC 7118	12 08 06.02	+65 10 26.9	0.00597	23.88	(c)	10.633	0.019	E
36	IRAS 12112+0305		12 13 46.00	+02 48 38.0	0.07331	291.12	(b)	18.272	0.021	S?
37	NGC 4261.....	UGC 7360	12 19 23.22	+05 49 30.8	0.00737	31.62	(c)	11.35	0.018	E
38	NGC 4278.....	M 98	12 20 06.83	+29 16 50.7	0.00216	16.07	(c)	11.042	0.029	E
39	NGC 4314.....	UGC 7443	12 22 31.99	+29 53 43.3	0.00242	9.68	(d)	11.416	0.025	Sa(sr)
40	NGC 4321.....	M 100	12 22 54.90	+15 49 20.6	0.00524	16.14	(a)	10.022	0.026	SABb(s)
41	NGC 4374.....	M 84	12 25 03.74	+12 53 13.1	0.0046	18.37	(c)	10.114	0.041	E
42	NGC 4410A.....	UGC 7535	12 26 28.86	+09 01 10.8	0.02512	100.30	(d)	13.948	0.025	Sab
43	NGC 4438.....	UGC 7574	12 27 45.59	+13 00 31.8	0.0042	16.83	(d)	10.927	0.028	Sa
44	NGC 4457.....	UGC 7609	12 28 59.01	+03 34 14.1	0.00435	17.38	(d)	11.711	0.022	S0-a(sr)
45	NGC 4459.....	UGC 7614	12 29 00.03	+13 58 42.8	0.00402	16.14	(c)	11.454	0.045	S0-a(r)
46	NGC 4486.....	M 87	12 30 49.42	+12 23 28.0	0.00402	16.07	(c)	9.587	0.023	E
47	NGC 4494.....	UGC 7662	12 31 24.03	+25 46 29.9	0.00427	17.06	(c)	10.681	0.021	E
48	NGC 4552.....	M 89	12 35 39.81	+12 33 22.8	0.0038	15.35	(c)	10.67	0.041	E
49	NGC 4589.....	UGC 7796	12 37 25.03	+74 11 30.8	0.00660	21.98	(c)	11.703	0.028	E
50	NGC 4579.....	M 58	12 37 43.52	+11 49 05.5	0.0042	16.83	(d)	10.478	0.041	SABb(s)
51	NGC 4596.....	UGC 7828	12 39 55.94	+10 10 33.9	0.0042	16.83	(d)	11.437	0.022	S0-a(sr)
52	NGC 4594.....	M 104	12 39 59.43	−11 37 23.0	0.00245	9.77	(c)	9.155	0.051	Sa
53	NGC 4636.....	UGC 7878	12 42 49.87	+02 41 16.0	0.00365	14.66	(c)	10.429	0.029	E
54	NGC 4676A.....		12 46 10.08	+30 43 55.2	0.022	88.00	(b)	14.4	0.016	S0-a(s)
55	NGC 4676B.....		12 46 11.23	+30 43 21.6	0.022	88.00	(b)	14.954	0.016	S0-a(s)
56	NGC 4698.....	UGC 7970	12 48 22.92	+08 29 14.3	0.0042	16.83	(d)	11.554	0.026	Sa
57	NGC 4696.....	Abell 3526	12 48 49.28	−41 18 40.0	0.00887	35.48	(c)	11.684	0.112	E
58	NGC 4736.....	M 94	12 50 53.06	+41 07 13.6	0.0013	5.20	(c)	8.707	0.018	Sab(r)
59	NGC 5005.....	UGC 8256	13 10 56.23	+37 03 33.1	0.00315	21.28	(d)	10.539	0.014	SABb(s)
60	NGC 5055.....	M 63	13 15 49.33	+42 01 45.4	0.0018	7.14	(d)	9.323	0.018	Sbc
61	MRK 266NE	NGC 5256	13 38 17.80	+48 16 41.2	0.02805	112.0	(b)	14.10	0.013	
62	UGC 08696.....	MRK 273	13 44 42.11	+55 53 12.7	0.03778	150.9	(b)	15.106	0.008	
63	CGCG 162-010 ..	Abell 1795	13 48 52.43	+26 35 34.0	0.06315	252.6	(b)	15.197	0.013	
64	NGC 5363.....		13 56 07.24	+05 15 17.0	0.00379	22.39	(d)	11.084	0.027	S0-a
65	IC 4395	UGC 9141	14 17 21.08	+26 51 26.7	0.03651	148.50	(b)	14.698	0.017	Sb
66	IRAS 14348-1447		14 37 38.37	−15 00 22.8	0.08273	329.65	(b)	16.623	0.123	S?
67	NGC 5746.....	UGC 9499	14 44 55.92	+01 57 18.0	0.00735	29.38	(d)	11.342	0.040	SABb(s)
68	NGC 5813.....		15 01 11.26	+01 42 07.1	0.00657	32.21	(c)	11.483	0.057	E
69	NGC 5838.....	UGC 9692	15 05 26.26	+02 05 57.6	0.00453	28.44	(d)	11.785	0.053	E-SO

Table 3.1: Continuation

Num	Name	Other Name	RA	Dec	Redshift	Dist. (Mpc)	Ref.	B	E(B-V)	Morph. Type
(1)	(2)	(3)	(4)	(5)	(6)	(7)	(8)	(9)	(10)	(11)
70	NGC 5846.....	UGC 9705	15 06 29.29	+01 36 20.2	0.00622	24.89	(c)	11.074	0.056	E
71	NGC 5866.....	UGC 9723	15 06 29.50	+55 45 47.6	0.00385	15.35	(c)	10.73	0.013	S0-a
72	MRK 0848	IZW 107	15 18 06.35	+42 44 36.7	0.04019	164.48	(b)	15.99	0.026	S0
73	NGC 6251.....	UGC 10501	16 32 31.97	+82 32 16.4	0.02297	91.90	(b)	13.768	0.087	E
74	NGC 6240.....	UGC 10592	16 52 58.89	+02 24 03.4	0.02445	97.80	(b)	13.816	0.076	S0-a
75	IRAS 17208-0014		17 23 21.96	+00 17 00.9	0.04275	171.0	(b)	17.53	0.344	S?
76	NGC 6482.....	UGC 11009	17 51 48.81	+23 04 19.0	0.01315	52.60	(b)	12.225	0.101	E
77	NGC 7130.....	IC 5135	21 48 19.50	−34 57 04.7	0.01612	64.50	(b)	12.927	0.029	Sa
78	NGC 7285.....		22 28 38.00	−24 50 26.8	0.01442	57.54	(b)	12.963	0.025	SBa(s)
79	NGC 7331.....	UGC 12113	22 37 04.09	+34 24 56.3	0.00377	13.12	(c)	10.199	0.091	Sbc
80	IC 1459	IC 5265	22 57 10.60	−36 27 44.0	0.0055	29.24	(c)	10.961	0.016	E
81	NPM1G -12.0625	Abell 2567	23 25 19.82	−12 07 26.4	0.08299	327.93	(b)	16.177	0.030	S?
82	NGC 7743.....	UGC 12759	23 44 21.14	+09 56 02.7	0.00570	20.70	(c)	12.392	0.068	S0-a(s)

NOTES.–Distances from the following references: (a) Ferrarese et al. (2000); (b) from cosmology assuming $H_o = 75 Km\ Mpc^{-1}\ s^{-1}$; (c) Tonry et al. (2001); and (d) Tully (1998)

Table 3.2: Observational details*

				Chandra data								*XMM-Newton* data			*HST* data		
Num	Name	NHgal (cm^{-2})	Scale (pc/″)	ObsID	Expt. (ks)	RA	Dec	Radii (pc)	Radii (arcs)	Offset (arcs)	Pileup (%)	ObsID	Expt. (ksec)	Pileup (%)	Filter	ObsID	Expt. (sec)
(1)	(2)	(3)	(4)	(5)	(6)	(7)	(8)	(9)	(10)	(11)	(12)	(13)	(14)	(15)	(16)	(17)	(18)
1	NGC 0315.....	0.0588	330.2	4156	52.3	00 57 48.870	+30 21 08.75	649.8	1.968	0.271	1.295	305290201	43.7	0.052	F814W	6673	230
2	NGC 0410.....	0.0540	348.4	...	...	...	...	...	...	...	...	203610201	19.6	0.012	...	...	...
3	NGC 0474.....	0.0332	157.6	7144	14.9	01 20 06.799	+03 24 57.06	897.7	5.696	2.217	0.078	200780101	16.3	0.001	...	...	...
4	IIIZW 035	0.0505	531.7	6855	14.5	01 24 47.751	+09 32 19.71	1129.3	2.124	0.593	0.209	203390201	13.8	0.001	F814W	10592	720
5	NGC 0524.....	0.0485	116.3	6778	13.7	01 44 30.500	+17 06 07.53	295.2	2.538	2.520	0.015	...	...	...	F814W	5999	160
6	NGC 0833.....	0.0221	241.1	923	12.2	02 09 24.662	-10 08 10.44	1897.9	7.872	0.746	1.549	115810301	44.8	0.306	...	...	...
7	NGC 0835.....	0.0221	244.6	923	12.1	02 09 20.797	-10 07 58.62	1684.8	6.888	1.017	0.298	115810301	44.8	0.306	...	...	...
8	NGC 1052.....	0.0307	94.1	385	10.9	02 41 04.833	-08 15 20.57	138.9	1.476	1.552	2.920	306230101	47.2	0.910	F555W	3639	500
9	NGC 2639.....	0.0304	220.3	...	...	...	...	...	...	...	...	301651101	7.4	0.001	F606W	5479	500
10	NGC 2655.....	0.0209	118.4	...	...	...	...	...	...	...	...	301650301	8.9	0.995	F547M	5419	300
11	NGC 2681.....	0.0245	83.5	2060	70.7	08 53 32.783	+51 18 48.85	205.4	2.46	0.770	0.353	...			F555W	4854	500
12	NGC 2685.....	0.0414	78.6	...		...	...	...	...	...	...	085030101	8.6	0.002	...	...	...
13	UGC 4881.....	0.0153	761.6	6857	14.6	09 15 55.556	+44 19 57.90	2421.1	3.179	0.554	0.278	203390401	19.0	0.002	F814W	10592	760
14	3C 218	0.0494	1057.1	4969	79.9	09 18 05.675	-12 05 44.06	2323.5	2.198	0.672	1.011	109980301	24.0	4.732	...	...	...
15	NGC 2787.....	0.0432	36.3	4689	29.4	09 19 18.570	+69 12 11.59	95.8	2.639	0.388	2.931	200250101	32.9	0.049	F814W	6633	365
16	NGC 2841.....	0.0145	58.0	6096	26.7	09 22 02.687	+50 58 35.89	99.4	1.714	0.267	0.688	201440101	29.9	0.064	F814W	9788	120
17	UGC 05101.....	0.0267	762.6	2033	48.2	09 35 51.676	+61 21 11.06	2251.2	2.952	1.322	0.874	085640201	26.5	0.043	F814W	6346	400
18	NGC 3185.....	0.0212	103.2	...	...	...	...	...	...	...	...	112552001	8.4	0.003	F814W	9042	160
19	NGC 3226.....	0.0214	114.2	...	...	...	...	...	...	...	...	101040301	30.9	0.402	...	...	...
20	NGC 3245.....	0.0208	101.3	2926	9.6	10 27 18.339	+28 30 27.21	199.4	1.968	1.031	0.573	...	...	...	F702W	7403	140
21	NGC 3379.....	0.0275	51.2	1587	31.3	10 47 49.611	+12 34 53.75	100.8	1.968	0.367	0.310	...	...	...	F814W	5512	335
22	NGC 3414.....	0.0212	122.3	6779	13.5	10 51 16.216	+27 58 30.14	240.7	1.968	0.133	2.892	...	...	...	...	...	...
23	NGC 3507.....	0.0163	95.8	3149	38.0	11 03 25.313	+18 08 07.32	235.7	2.46	0.845	0.042	...	...	...	F606W	5446	80
24	NGC 3607.....	0.0148	110.5	2073	38.4	11 16 54.612	+18 03 04.39	326.2	2.952	2.119	0.297	...	...	...	F814W	5999	160
25	NGC 3608.....	0.0149	111.1	2073	38.4	11 16 58.891	+18 08 53.71	218.6	1.968	1.840	0.083	...	...	...	F814W	5454	230
26	NGC 3623.....	0.0216	35.3	...	...	...	...	...	...	...	...	082140301	28.9	0.030	F814W	9042	230
27	NGC 3627.....	0.0243	49.8	...	...	...	...	...	...	...	...	093641101	5.3	0.038	F814W	8602	350
28	NGC 3628.....	0.0222	37.5	2039	54.7	11 20 16.919	+13 35 22.75	110.7	2.952	1.381	0.154	110980101	41.6	0.110	F606W	5446	80
29	NGC 3690B.....	0.0098	201.7	1641	24.3	11 28 30.946	+58 33 40.46	645.0	3.198	1.177	0.456	112810101	15.5	0.395	F814W	8602	350
30	NGC 3898.....	0.0108	106.6	4740	56.9	11 49 15.353	+56 05 03.62	494.4	4.638	1.364	0.224	...	...	...	F814W	9042	230
31	NGC 3945.....	0.0166	109.0	6780	13.8	11 53 13.647	+60 40 32.17	254.6	2.336	0.652	0.382	...	...	...	F814W	6633	425
32	NGC 3998.....	0.0122	68.5	6781	13.6	11 57 56.123	+55 27 13.37	123.9	1.809	0.577	7.333	090020101	9.0	6.680	F658N	5924	553
33	NGC 4036.....	0.0189	119.0	6783	13.7	12 01 26.787	+61 53 44.33	189.9	1.596	0.818	0.066	...	...	...	F702W	6785	400
34	NGC 4111.....	0.0140	72.7	1578	14.8	12 07 03.142	+43 03 57.34	214.6	2.952	1.000	0.523	...	...	...	F702W	6785	600
35	NGC 4125.....	0.0184	115.8	2071	61.9	12 08 05.990	+65 10 27.60	284.9	2.46	1.703	0.144	141570201	35.3	0.023	F814W	6587	700
36	IRAS 12112+0305	0.0179	1411.4	...	...	...	...	...	...	...	...	081340801	18.0	0.001	...	...	...
37	NGC 4261.....	0.0155	153.3	834	31.3	12 19 23.235	+05 49 30.39	528.0	3.444	0.897	0.868	056340101	27.0	0.931	F702W	5476	140
38	NGC 4278.....	0.0177	77.9	7077	11.0	12 20 06.850	+29 16 50.64	216.3	2.777	0.450	5.087	205010101	30.5	2.391	F814W	5454	230
39	NGC 4314.....	0.0178	46.9	2062	14.5	12 22 32.122	+29 53 44.76	276.9	5.904	2.076	0.534	201690301	22.3	0.002	F814W	6265	300
40	NGC 4321.....	0.0239	78.2	6727	37.6	12 22 54.820	+15 49 17.34	384.7	4.92	3.387	1.591	106860201	26.9	0.091	F814W	9776	100
41	NGC 4374.....	0.0260	89.1	0803	28.2	12 25 03.719	+12 53 13.24	131.5	1.476	0.386	2.285	...	...	...	F814W	6094	260
42	NGC 4410A.....	0.0170	486.3	2982	34.8	12 26 28.236	+09 01 10.81	957.0	1.968	1.079	0.288	...	...	...	F606W	5479	500
43	NGC 4438.....	0.0266	81.6	2883	24.6	12 27 45.592	+13 00 33.01	240.9	2.952	1.786	1.465	...	...	...	F814W	6791	350
44	NGC 4457.....	0.0182	84.3	3150	36.1	12 28 59.039	+03 34 14.29	248.9	2.952	0.453	3.603	...	...	...	...	...	...
45	NGC 4459.....	0.0267	78.2	2927	9.8	12 29 00.038	+13 58 41.73	153.9	1.968	1.046	0.228	...	...	...	F814W	5999	160

Table 3.2: Continuation

				Chandra data								*XMM-Newton* data			*HST* data		
Num	Name	NHgal (cm^{-2})	Scale (pc/")	ObsID	Expt. (ks)	RA	Dec	Radii (pc)	Radii (arcs)	Offset (arcs)	Pileup (%)	ObsID	Expt. (ksec)	Pileup (%)	Filter	ObsID	Expt. (sec)
(1)	(2)	(3)	(4)	(5)	(6)	(7)	(8)	(9)	(10)	(11)	(12)	(13)	(14)	(15)	(16)	(17)	(18)
46	NGC 4486.....	0.0254	77.9	2707	98.7	12 30 49.423	+12 23 28.31	191.6	2.46	0.439	10.841	200920101	72.9	>10	F814W	6775	246
47	NGC 4494.....	0.0152	82.7	2079	12.7	12 31 24.098	+25 46 29.80	162.8	1.968	0.913	0.273	071340301	24.5	0.020	F814W	6554	900
48	NGC 4552.....	0.0257	74.4	2072	54.3	12 35 39.813	+12 33 23.35	183.0	2.46	0.689	1.282	141570101	32.1	0.139	F814W	6099	500
49	NGC 4589.....	0.0199	106.6	6785	13.5	12 37 24.832	+74 11 30.62	251.6	2.360	2.118	0.039	...	...	...	F814W	5454	230
50	NGC 4579.....	0.0247	81.6	0807	29.8	12 37 43.498	+11 49 05.49	160.6	1.968	0.363	11.984	112840101	19.6	2.079	F791W	6436	300
51	NGC 4596.....	0.0198	81.6	2928	9.2	12 39 55.971	+10 10 35.04	301.1	3.69	0.698	0.273	...	...	...	F606W	5446	80
52	NGC 4594.....	0.0377	47.4	1586	18.5	12 39 59.447	-11 37 23.05	70.0	1.476	0.497	11.946	084030101	15.8	0.790	F814W	5512	245
53	NGC 4636.....	0.0181	71.1	4415	73.8	12 42 49.822	+02 41 15.87	909.4	12.79	0.657	1.951	111190201	16.4	0.528	F814W	8686	100
54	NGC 4676A.....	0.0128	426.6	2043	27.9	12 46 10.118	+30 43 55.61	1679.1	3.936	1.018	0.245	...	...	...	F814W	8669	160
55	NGC 4676B.....	0.0128	426.6	2043	27.9	12 46 11.147	+30 43 23.13	1679.1	3.936	2.044	0.468	...	...	...	F814W	8669	160
56	NGC 4698.....	0.0187	81.6	3008	29.4	12 48 22.908	+08 29 14.63	180.7	2.214	0.243	0.291	112551101	10.3	0.004	F814W	9042	230
57	NGC 4696.....	0.0806	172.0	1560	54.6	12 48 48.830	-41 18 43.30	677.0	3.936	7.450	0.711	046340101	40.2	>10	F814W	8683	500
58	NGC 4736.....	0.0144	25.2	808	46.3	12 50 53.120	+41 07 13.23	37.2	1.476	0.748	0.776	094360601	16.8	6.169	F814W	9042	230
59	NGC 5005.....	0.0108	103.2	...	...	...	...	...	...	...	...	110930501	8.5	0.060	F814W	9042	230
60	NGC 5055.....	0.0132	34.6	2197	27.7	13 15 49.244	+42 01 45.86	51.1	1.476	0.440	0.348	...	...	...	F814W	9042	230
61	MRK 266NE	0.0168	543.0	2044	17.4	13 38 17.881	+48 16 40.82	1068.6	1.968	1.216	0.720	055990501	16.2	0.741	F606W	5479	500
62	UGC 08696.....	0.0109	731.6	809	41.5	13 44 42.112	+55 53 13.13	1439.8	1.968	0.453	1.001	101640401	18.0	0.129	F814W	6346	400
63	CGCG 162-010 ..	0.0119	1224.6	493	19.6	13 48 52.461	+26 35 36.26	4820.0	3.936	2.333	0.395	097820101	42.3	8.109	F814W	7281	300
64	NGC 5363.....	0.0209	108.5	...	...	...	...	...	...	...	...	201670201	19.3	0.087	...	...	...
65	IC 4395	0.0155	719.9	...	...	...	...	...	...	...	...	150480401	18.3	0.001	...	...	...
66	IRAS 14348-1447	0.0783	1598.2	6861	14.7	14 37 38.324	-15 00 24.88	3711.0	2.322	0.992	0.211	081341401	18.0	0.010	F814W	6346	400
67	NGC 5746.....	0.0327	142.4	3929	36.8	14 44 55.995	+01 57 18.11	210.2	1.476	0.549	1.342	...	...	...	F814W	9046	400
68	NGC 5813.....	0.0421	156.2	5907	48.4	15 01 11.195	+01 42 07.24	646.0	4.136	0.553	0.331	302460101	28.1	0.335	F814W	5454	230
69	NGC 5838.....	0.0419	137.9	6788	13.6	15 05 26.268	+02 05 57.92	286.3	2.076	0.402	0.050	...	...	...	F814W	7450	140
70	NGC 5846.....	0.0426	120.7	4009	23.0	15 06 29.190	+01 36 19.65	593.8	4.92	1.283	1.622	021540101	25.2	0.408	F814W	5920	1150
71	NGC 5866.....	0.0146	74.4	2879	31.9	15 06 29.477	+55 45 46.08	329.4	4.428	1.563	0.224	...	...	...	...	...	...
72	MRK 0848	0.0190	797.4	6858	14.5	15 18 06.109	+42 44 44.94	2019.0	2.532	8.980	0.783	203390601	19.8	0.013	F814W	10592	760
73	NGC 6251.....	0.0549	445.5	847	25.4	16 32 31.850	+82 32 15.67	876.7	1.968	1.948	0.422	056340201	41.1	1.788	F814W	6653	500
74	NGC 6240.....	0.0578	474.1	1590	36.7	16 52 58.905	+02 24 03.27	1516.2	3.198	0.455	1.770	147420201	20.0	0.891	F814W	6430	400
75	IRAS 17208-0014	0.0999	829.0	2035	48.4	17 23 22.008	-00 17 00.64	2039.3	2.46	0.682	0.564	081340601	13.9	0.001	F814W	6346	400
76	NGC 6482.....	0.0788	255.0	3218	19.1	17 51 48.831	+23 04 18.92	627.3	2.46	0.000	0.094	304160401	6.7	0.001	...	...	...
77	NGC 7130.....	0.0198	312.7	2188	36.9	21 48 19.532	-34 57 05.04	615.4	1.968	0.431	0.081	...	...	...	F606W	5479	500
78	NGC 7285.....	0.0179	279.0	...	29.5	...	...	...	...	...	...	206490301	17.2	0.104	...	...	...
79	NGC 7331.....	0.0861	63.6	2198	...	22 37 04.027	+34 24 55.96	125.2	1.968	0.945	0.202	103861301	0.8	0.012	F814W	7450	85
80	IC 1459	0.0118	141.8	2196	53.5	22 57 10.604	-36 27 43.57	418.6	2.952	0.604	3.671	135980201	26.9	0.385	F814W	5454	230
81	NPM1G -12.0625	0.0249	1589.8	7329	58.9	23 25 19.726	-12 07 27.11	2953.8	1.858	0.153	1.326	147330101	89.6	7.767	F702W	6228	1050
82	NGC 7743.....	0.0525	100.4	...	...	...	...	...	...	...	...	301651001	9.6	0.022	F606W	8597	280

(*)Column density NHgal in units of 10^{22} cm^{-2}.

Table 3.3: *Power-Law model applied to* Chandra *spectra*

Num	Name	N_H (10^{22} cm^{-2})	Γ	χ^2	d.o.f	χ^2_r
(1)	(2)	(3)	(4)	(5)	(6)	(7)
1	NGC 0315	0.18 [0.15,0.21]	1.29 [1.21, 1.37]	479.69	366	1.31
6	NGC 0833 . . . . . U	0.00 [0.00,0.72]	-1.45 [-2.10,-1.16]	61.29	58	1.06
7	NGC 0835 . . . . . U	0.79 [0.44,1.09]	7.85 [5.09, 9.96]	91.18	57	1.60
8	NGC 1052 . . . . . U	0.00 [0.00,0.08]	0.05 [-0.14, 0.43]	51.44	59	0.87
11	NGC 2681 . . . . . U	0.43 [0.37,0.59]	4.69 [3.74, 6.68]	147.51	106	1.39
14	3C 218	0.02 [0.00,0.05]	1.57 [1.46, 1.66]	298.68	265	1.13
15	NGC 2787	0.11 [0.03,0.22]	2.33 [1.87, 2.94]	21.01	16	1.31
17	UGC 05101	0.04 [0.00,0.10]	1.29 [0.96, 1.49]	89.14	93	0.96
22	NGC 3414	0.21 [0.13,0.30]	2.02 [1.70, 2.48]	118.01	129	0.91
23	NGC 3507 . . . . . U	1.06 [0.81,1.11]	9.18 [0.00, 0.00]	77.38	44	1.76
29	NGC 3690B	0.00 [0.00,0.01]	2.05 [1.79, 2.33]	185.45	152	1.22
30	NGC 3898 . . . . . U	0.00 [0.00,0.06]	2.37 [2.16, 2.81]	18.59	11	1.69
31	NGC 3945	0.04 [0.00,0.17]	2.60 [2.32, 3.22]	56.82	83	0.68
32	NGC 3998	0.00 [0.00,0.01]	1.37 [1.34, 1.42]	534.03	458	1.17
34	NGC 4111 . . . . . U	1.00 [0.83,1.04]	-2.50 [0.00, 0.00]	126.79	69	1.84
35	NGC 4125	0.12 [0.00,0.25]	2.48 [1.82, 2.86]	41.07	61	0.67
37	NGC 4261 . . . . . U	1.20 [1.18,1.21]	9.91 [9.03, 0.00]	1209.62	246	4.92
38	NGC 4278	0.07 [0.05,0.08]	2.47 [2.40, 2.53]	316.12	297	1.06
40	NGC 4321	0.17 [0.11,0.24]	2.80 [2.55, 3.17]	154.79	123	1.26
41	NGC 4374	0.16 [0.11,0.21]	2.26 [2.08, 2.50]	106.00	125	0.85
42	NGC 4410A	0.00 [0.00,0.03]	1.86 [1.77, 2.03]	136.56	158	0.86
43	NGC 4438 . . . . . U	1.20 [0.98,1.24]	9.45 [8.54, 9.91]	225.31	100	2.25
44	NGC 4457 . . . . . U	0.42 [0.33,0.50]	4.56 [3.91, 5.14]	128.10	85	1.51
46	NGC 4486 . . . . . U	0.00 [0.00,0.00]	1.30 [1.28, 1.32]	875.51	433	2.02
47	NGC 4494	0.21 [0.03,0.34]	2.98 [1.68, 3.73]	47.30	59	0.80
48	NGC 4552	0.14 [0.11,0.18]	2.71 [2.57, 2.94]	193.61	165	1.17
50	NGC 4579	0.00 [0.00,0.01]	1.25 [1.23, 1.29]	553.24	419	1.32
52	NGC 4594	0.19 [0.17,0.23]	1.56 [1.46, 1.67]	300.39	281	1.07
57	NGC 4696 . . . . . U	0.00 [0.00,0.17]	4.27 [4.01, 5.18]	82.15	77	1.07
58	NGC 4736	0.14 [0.11,0.17]	2.60 [2.48, 2.87]	220.73	190	1.16
60	NGC 5055	0.16 [0.05,0.33]	2.30 [1.85, 3.16]	42.78	62	0.69
61	MRK 266NE . . . . U	0.00 [0.00,0.03]	0.86 [0.53, 1.13]	98.04	81	1.21
62	UGC 08696 . . . . . U	0.00 [0.00,0.02]	0.61 [0.44, 0.76]	417.44	233	1.79
63	CGCG 162-010 . . U	0.49 [0.38,0.61]	4.51 [4.06, 5.24]	167.55	154	1.10
67	NGC 5746	0.60 [0.35,0.93]	1.28 [0.93, 1.67]	87.71	112	0.78
68	NGC 5813 . . . . . U	1.11 [1.08,1.15]	9.95 [-3.00, 0.00]	92.18	33	2.79
70	NGC 5846 . . . . . U	1.17 [1.14,1.19]	9.87 [-2.95, 0.00]	190.07	88	2.16
73	NGC 6251	0.00 [0.00,0.00]	1.93 [1.76, 2.01]	343.88	253	1.36
74	NGC 6240	0.32 [0.27,0.38]	1.45 [1.37, 1.51]	425.89	356	1.20
75	IRAS 17208-0014 .	0.34 [0.18,0.61]	1.63 [1.34, 1.86]	48.01	63	0.76
76	NGC 6482 . . . . . U	1.32 [1.26,1.37]	9.99 [-3.00, 0.00]	109.35	68	1.61
77	NGC 7130 . . . . . U	0.29 [0.24,0.35]	4.04 [3.82, 4.51]	280.87	160	1.76
80	IC 1459	0.17 [0.15,0.18]	2.00 [1.93, 2.07]	343.85	338	1.02
81	NPM1G -12.0625U	0.32 [0.22,0.42]	3.81 [3.30, 4.39]	140.00	141	0.99

Table 3.4: *MEKAL model applied to* Chandra *spectra*

Num	Name	N_H (10^{22} cm^{-2})	kT (keV)	χ^2	d.o.f	χ^2_r
(1)	(2)	(3)	(4)	(5)	(6)	(7)
1	NGC 0315 . . . . . U	0.17 [0.15, 0.19]	56.99 [36.16, 0.00]	480.84	369	1.30
6	NGC 0833 . . . . . U	17.73 [12.80,23.68]	13.98 [7.62, 0.00]	77.53	61	1.27
7	NGC 0835 . . . . . U	0.39 [0.19, 0.53]	0.36 [0.22, 0.49]	98.78	60	1.65
8	NGC 1052 . . . . . U	0.30 [0.13, 0.93]	70.00 [32.09, 0.00]	83.54	62	1.35
11	NGC 2681 . . . . . U	0.00 [0.00, 0.01]	2.80 [2.01, 3.34]	219.16	109	2.01
14	3C 218 . . . . . U	0.00 [0.00, 0.01]	8.85 [6.63,11.45]	306.10	268	1.14
15	NGC 2787 . . . . . U	0.00 [0.00, 0.02]	4.68 [3.52, 6.23]	31.25	19	1.64
17	UGC 05101 . . . . . U	0.04 [0.00, 0.10]	64.10 [16.41, 0.00]	100.99	96	1.05
22	NGC 3414 . . . . . U	0.08 [0.04, 0.14]	5.31 [4.00, 7.98]	123.33	132	0.93
23	NGC 3507	0.08 [0.00, 0.39]	0.51 [0.28, 0.64]	60.92	47	1.30
29	NGC 3690B . . . . . U	0.00 [0.00, 0.01]	8.46 [5.08,33.11]	209.57	155	1.35
30	NGC 3898 . . . . . U	0.00 [0.00, 0.01]	4.40 [3.20, 5.70]	64.29	14	4.59
31	NGC 3945	0.00 [0.00, 0.01]	2.91 [2.40, 3.56]	98.70	86	1.15
32	NGC 3998 . . . . . U	0.00 [0.00, 0.00]	21.87 [17.68,27.46]	577.49	461	1.25
34	NGC 4111 . . . . . U	1.22 [1.06, 1.36]	0.09 [0.07, 0.09]	147.54	72	2.05
35	NGC 4125	0.00 [0.00, 0.05]	3.56 [2.45, 6.34]	45.00	64	0.70
37	NGC 4261 . . . . . U	0.00 [0.00, 0.00]	5.32 [4.29, 6.55]	1716.10	249	6.89
38	NGC 4278 . . . . . U	0.00 [0.00, 0.00]	2.98 [2.90, 3.16]	972.34	300	3.24
40	NGC 4321 . . . . . U	0.00 [0.00, 0.01]	2.84 [2.50, 3.30]	202.14	126	1.60
41	NGC 4374 . . . . . U	0.02 [0.00, 0.05]	4.30 [3.55, 5.33]	119.13	128	0.93
42	NGC 4410A . . . . U	0.00 [0.00, 0.00]	4.60 [3.92, 5.80]	170.46	161	1.06
43	NGC 4438	0.41 [0.37, 0.49]	0.53 [0.47, 0.59]	139.28	103	1.35
44	NGC 4457 . . . . . U	0.00 [0.00, 0.01]	2.72 [2.16, 3.63]	177.85	88	2.02
46	NGC 4486 . . . . . U	0.00 [0.00, 0.00]	41.90 [36.43,59.83]	915.53	436	2.10
47	NGC 4494	0.00 [0.00, 0.05]	4.04 [2.65, 7.03]	47.95	62	0.77
48	NGC 4552 . . . . . U	0.00 [0.00, 0.00]	2.98 [2.68, 3.40]	283.97	168	1.69
50	NGC 4579 . . . . . U	0.00 [0.00, 0.00]	70.00 [50.89, 0.00]	559.41	422	1.33
52	NGC 4594 . . . . . U	0.15 [0.12, 0.17]	12.42 [9.38,17.95]	300.38	284	1.06
57	NGC 4696	0.22 [0.10, 0.33]	0.63 [0.58, 0.69]	74.50	80	0.93
58	NGC 4736 . . . . . U	0.00 [0.00, 0.00]	3.36 [3.12, 3.77]	386.25	196	1.97
60	NGC 5055 . . . . . U	0.00 [0.00, 0.06]	4.98 [3.44, 8.55]	48.02	65	0.74
61	MRK 266NE . . . . U	0.00 [0.00, 0.05]	70.00 [30.59, 0.00]	108.92	84	1.30
62	UGC 08696 . . . . . U	0.11 [0.08, 0.16]	69.98 [46.46, 0.00]	507.30	236	2.15
63	CGCG 162-010 . . .	0.47 [0.39, 0.63]	1.05 [0.96, 1.10]	142.58	141	1.01
67	NGC 5746 . . . . . U	0.60 [0.45, 0.82]	54.97 [15.54, 0.00]	87.55	115	0.76
68	NGC 5813 . . . . . U	0.24 [0.17, 0.30]	0.50 [0.47, 0.54]	71.01	36	1.97
70	NGC 5846	0.00 [0.00, 0.02]	0.60 [0.57, 0.63]	110.56	91	1.21
73	NGC 6251 . . . . . U	0.00 [0.00, 0.00]	9.26 [6.73,11.88]	402.29	256	1.57
74	NGC 6240 . . . . . U	0.29 [0.24, 0.36]	17.21 [9.40,30.95]	551.31	359	1.54
75	IRAS 17208-0014U	0.27 [0.18, 0.46]	11.46 [6.17, 0.00]	52.26	66	0.79
76	NGC 6482	0.19 [0.10, 0.33]	0.75 [0.65, 0.81]	60.72	71	0.86
77	NGC 7130 . . . . . U	0.56 [0.52, 0.62]	0.53 [0.48, 0.56]	452.50	163	2.78
80	IC 1459 . . . . . U	0.05 [0.04, 0.06]	6.74 [6.17, 7.32]	503.73	341	1.48
81	NPM1G -12.0625 .	0.00 [0.00, 0.01]	1.88 [1.65, 2.24]	184.44	144	1.28

Table 3.5: Power-Law plus Power-Law model applied to *Chandra* spectra

Num	Name	N_{H1} (10^{22} cm^{-2})	N_{H2} (10^{22} cm^{-2})	Γ	A_{PL1}	A_{PL2}	χ^2	d.o.f	χ^2_r
(1)	(2)	(3)	(4)	(5)	(6)	(7)	(8)	(9)	(10)
1	NGC 0315	$0.20^{0.24}_{0.17}$	$2.15^{3.27}_{1.55}$	$1.64^{2.00}_{1.54}$	1.01e-04 $^{1.19e-04}_{9.18e-05}$	9.37e-05 $^{1.62e-04}_{3.94e-05}$	470.83	364	1.29
6	NGC 0833	$0.00^{0.15}_{0.00}$	$22.67^{34.19}_{17.18}$	$2.44^{3.74}_{1.66}$	4.59e-06 $^{1.14e-05}_{3.25e-06}$	1.06e-03 $^{7.00e-02}_{2.62e-04}$	43.95	56	0.78
7	NGC 0835 ..... U	$0.78^{1.10}_{0.55}$	$69.73^{103.09}_{49.47}$	$7.76^{9.76}_{5.87}$	1.73e-04 $^{4.15e-04}_{7.51e-05}$	8.90e+00 $^{4.53e+01}_{1.91e-01}$	68.47	55	1.24
8	NGC 1052	$0.04^{0.26}_{0.00}$	$12.50^{23.58}_{5.51}$	$1.15^{2.37}_{0.41}$	5.48e-05 $^{1.19e-04}_{3.73e-05}$	2.73e-04 $^{6.63e-04}_{7.36e-05}$	44.79	57	0.79
11	NGC 2681 ..... U	$0.91^{1.05}_{0.83}$	$12.95^{17.42}_{10.06}$	$8.02^{8.44}_{7.09}$	1.56e-04 $^{1.93e-04}_{4.49e-05}$	4.55e-02 $^{5.62e-02}_{1.96e-02}$	99.84	104	0.96
14	3C 218.....	$0.20^{0.25}_{0.16}$	$6.18^{7.79}_{4.93}$	$2.75^{3.15}_{2.31}$	5.30e-05 $^{6.40e-05}_{4.87e-05}$	1.92e-04 $^{2.22e-04}_{1.09e-04}$	281.21	263	1.07
15	NGC 2787 ..... U	$0.12^{0.49}_{0.03}$	$8.61^{0.00}_{0.00}$	$2.45^{4.59}_{1.99}$	3.27e-05 $^{4.62e-05}_{2.15e-05}$	1.58e-05 $^{1.66e-04}_{0.00e+00}$	20.70	14	1.48
17	UGC 05101	$0.07^{0.22}_{0.00}$	$122.65^{304.92}_{63.65}$	$1.44^{1.75}_{1.10}$	6.62e-06 $^{9.83e-06}_{3.58e-06}$	1.57e-04 $^{5.80e-04}_{1.65e-05}$	81.79	91	0.90
22	NGC 3414 ..... U	$0.31^{0.46}_{0.00}$	$5.44^{0.00}_{0.00}$	$2.60^{3.79}_{1.81}$	1.03e-04 $^{1.62e-04}_{0.00e+00}$	1.08e-04 $^{6.79e-04}_{0.00e+00}$	117.50	127	0.93
23	NGC 3507 ..... U	$1.09^{1.15}_{0.82}$	$5000.00^{0.00}_{0.00}$	$9.73^{0.00}_{8.22}$	1.75e-04 $^{2.14e-04}_{1.41e-04}$	3.93e-08 $^{0.00e+00}_{0.00e+00}$	77.20	42	1.84
29	NGC 3690B.....	$0.13^{0.19}_{0.05}$	$9.52^{12.07}_{7.76}$	$3.39^{3.91}_{2.89}$	5.30e-05 $^{7.55e-05}_{4.05e-05}$	1.17e-03 $^{1.80e-03}_{9.17e-04}$	125.35	150	0.84
30	NGC 3898 ..... U	$0.29^{0.52}_{0.25}$	$5.37^{8.07}_{3.90}$	$4.79^{5.12}_{4.17}$	2.93e-05 $^{5.20e-05}_{1.40e-05}$	1.69e-03 $^{3.65e-03}_{5.85e-04}$	7.65	9	0.85
31	NGC 3945	$0.07^{0.16}_{0.00}$	$158.54^{3796.92}_{92.81}$	$2.73^{3.22}_{2.37}$	5.11e-05 $^{6.72e-05}_{2.68e-05}$	7.97e-03 $^{7.98e+00}_{2.44e-05}$	54.00	81	0.67
32	NGC 3998	$0.00^{0.00}_{0.00}$	$1426.35^{0.00}_{997.87}$	$1.37^{1.40}_{1.35}$	1.41e-03 $^{1.44e-03}_{1.40e-03}$	2.53e+01 $^{7.26e+06}_{0.00e+00}$	534.08	456	1.17
34	NGC 4111 ..... U	$1.03^{1.09}_{0.97}$	$13.12^{18.38}_{10.50}$	$10.00^{0.00}_{-3.00}$	4.77e-04 $^{5.89e-04}_{4.05e-04}$	6.11e-01 $^{1.08e+00}_{2.21e-01}$	104.62	67	1.56
35	NGC 4125 ..... U	$0.41^{0.63}_{0.07}$	$5.97^{10.72}_{2.54}$	$4.62^{6.99}_{2.21}$	1.11e-05 $^{3.78e-05}_{0.00e+00}$	1.30e-04 $^{5.14e-04}_{0.00e+00}$	38.59	59	0.65
37	NGC 4261 ..... U	$1.02^{1.14}_{0.90}$	$48.55^{56.54}_{41.80}$	$8.77^{9.67}_{8.00}$	1.35e-03 $^{1.84e-03}_{9.75e-04}$	6.31e+01 $^{2.71e+02}_{1.46e+01}$	876.03	244	3.59
38	NGC 4278 ..... U	$0.20^{0.26}_{0.17}$	$4.34^{5.06}_{3.78}$	$3.42^{3.91}_{3.24}$	1.78e-04 $^{2.17e-04}_{1.68e-04}$	4.40e-04 $^{1.01e-03}_{3.05e-04}$	280.69	295	0.95
40	NGC 4321 ..... U	$0.50^{0.66}_{0.42}$	$7.71^{10.09}_{6.11}$	$5.06^{6.08}_{4.24}$	1.13e-04 $^{1.74e-04}_{7.97e-05}$	1.93e-03 $^{5.99e-03}_{5.75e-04}$	132.69	121	1.10
41	NGC 4374	$0.23^{0.44}_{0.14}$	$9.31^{45.25}_{0.00}$	$2.64^{2.74}_{2.20}$	5.07e-05 $^{9.55e-05}_{2.50e-05}$	7.37e-05 $^{1.78e-04}_{0.00e+00}$	103.67	123	0.84
42	NGC 4410A	$0.07^{0.10}_{0.04}$	$14.85^{43.48}_{6.43}$	$2.32^{2.44}_{1.93}$	4.36e-05 $^{5.59e-05}_{3.56e-05}$	8.67e-05 $^{1.99e-04}_{2.19e-05}$	129.62	156	0.83
43	NGC 4438 ..... U	$1.27^{1.30}_{1.14}$	$9.19^{10.91}_{8.32}$	$9.99^{0.00}_{9.41}$	1.79e-03 $^{1.97e-03}_{1.64e-03}$	2.40e-01 $^{3.94e-01}_{1.33e-01}$	175.75	98	1.79
44	NGC 4457 ..... U	$1.06^{1.16}_{0.78}$	$9.82^{11.99}_{7.60}$	$9.00^{0.00}_{7.32}$	3.31e-04 $^{4.75e-04}_{1.37e-04}$	7.70e-02 $^{1.78e-01}_{2.77e-02}$	95.70	83	1.15
46	NGC 4486	$0.16^{0.17}_{0.13}$	$4.75^{4.97}_{4.38}$	$2.72^{2.83}_{2.53}$	3.67e-04 $^{3.86e-04}_{3.36e-04}$	2.11e-03 $^{2.48e-03}_{1.55e-03}$	584.94	431	1.36
47	NGC 4494 ..... U	$0.55^{0.83}_{0.28}$	$8.15^{14.21}_{5.39}$	$4.38^{6.37}_{2.26}$	9.05e-05 $^{1.11e-04}_{5.51e-05}$	2.77e-03 $^{9.56e-03}_{6.40e-04}$	40.04	57	0.70
48	NGC 4552 ..... U	$0.44^{0.49}_{0.34}$	$7.19^{9.81}_{5.56}$	$4.72^{5.03}_{3.94}$	1.25e-04 $^{1.61e-04}_{6.92e-05}$	9.34e-04 $^{3.11e-03}_{4.44e-04}$	170.11	163	1.04
50	NGC 4579 ..... U	$0.00^{0.01}_{0.00}$	$644.93^{0.00}_{395.97}$	$1.26^{1.28}_{1.23}$	5.60e-04 $^{5.88e-04}_{5.51e-04}$	4.17e-01 $^{2.24e+01}_{0.00e+00}$	553.22	417	1.33
52	NGC 4594	$0.24^{0.41}_{0.00}$	$3.47^{44.74}_{0.00}$	$1.94^{2.57}_{1.53}$	1.91e-04 $^{2.93e-04}_{0.00e+00}$	1.26e-04 $^{6.13e-04}_{0.00e+00}$	298.21	279	1.07
57	NGC 4696 ..... U	$0.90^{0.98}_{0.75}$	$9.13^{11.27}_{7.01}$	$9.73^{0.00}_{6.84}$	1.87e-03 $^{2.19e-03}_{5.89e-04}$	3.72e-01 $^{6.62e-01}_{1.33e-01}$	69.76	75	0.93
58	NGC 4736 ..... U	$0.28^{0.37}_{0.25}$	$9.12^{11.49}_{6.32}$	$3.62^{4.12}_{3.39}$	1.33e-04 $^{1.79e-04}_{1.14e-04}$	6.44e-04 $^{1.77e-03}_{3.41e-04}$	192.53	191	1.01
60	NGC 5055	$0.16^{0.31}_{0.11}$	$180.58^{0.00}_{116.74}$	$2.32^{6.57}_{1.89}$	1.38e-05 $^{2.12e-05}_{1.03e-05}$	1.38e+00 $^{9.10e+02}_{0.00e+00}$	42.29	60	0.70

Table 3.5: Continuation

Num	Name	N_{H1} (10^{22} cm^{-2})	N_{H2} (10^{22} cm^{-2})	Γ	A_{PL1}	A_{PL2}	χ^2	d.o.f	χ^2_r
(1)	(2)	(3)	(4)	(5)	(6)	(7)	(8)	(9)	(10)
61	MRK 266NE.....	$0.02^{0.14}_{0.00}$	$15.14^{27.99}_{8.79}$	$1.80^{2.82}_{1.38}$	1.21e-05 $^{1.45e-05}_{9.89e-06}$	1.05e-04 $^{1.64e-04}_{4.23e-05}$	75.01	79	0.95
62	UGC 08696.....	$0.35^{0.42}_{0.24}$	$50.79^{55.39}_{42.41}$	$2.56^{2.85}_{2.34}$	2.79e-05 $^{3.42e-05}_{1.83e-05}$	3.16e-03 $^{3.78e-03}_{2.83e-03}$	217.95	231	0.94
63	CGCG 162-010..U	$0.64^{1.09}_{0.47}$	$5000.00^{0.00}_{0.00}$	$4.95^{6.94}_{4.40}$	2.73e-04 $^{7.88e-04}_{1.80e-04}$	1.04e-07 $^{0.00e+00}_{0.00e+00}$	151.90	136	1.12
67	NGC 5746..... U	$0.13^{0.00}_{0.00}$	$0.80^{10.49}_{0.00}$	$1.29^{3.58}_{1.00}$	3.47e-06 $^{1.47e-04}_{0.00e+00}$	1.91e-05 $^{4.68e-04}_{0.00e+00}$	87.40	110	0.79
68	NGC 5813..... U	$1.17^{1.19}_{1.14}$	$0.00^{0.29}_{0.00}$	$9.87^{0.00}_{8.84}$	9.28e-04 $^{1.03e-03}_{8.15e-04}$	1.74e-09 $^{3.06e-08}_{1.35e-10}$	190.08	86	2.48
70	NGC 5846..... U	$1.16^{1.19}_{1.02}$	$8.13^{12.23}_{6.17}$	$9.87^{0.00}_{9.50}$	8.88e-04 $^{9.75e-04}_{7.58e-04}$	1.81e-02 $^{5.04e-02}_{4.59e-03}$	177.16	76	2.21
73	NGC 6251.....	$0.00^{0.04}_{0.00}$	$4.77^{5.80}_{4.01}$	$2.87^{3.50}_{2.68}$	9.43e-05 $^{1.17e-04}_{8.82e-05}$	5.53e-04 $^{9.76e-04}_{3.89e-04}$	261.07	251	1.04
74	NGC 6240.....	$0.42^{0.52}_{0.35}$	$46.83^{104.39}_{26.92}$	$1.77^{2.08}_{1.57}$	1.66e-04 $^{2.04e-04}_{1.39e-04}$	3.82e-04 $^{9.55e-04}_{2.35e-04}$	407.88	354	1.15
75	IRAS 17208-0014 .	$0.59^{1.08}_{0.05}$	$6.74^{13.07}_{0.00}$	$2.81^{3.22}_{1.27}$	1.37e-05 $^{4.21e-05}_{7.16e-06}$	3.92e-05 $^{8.15e-04}_{0.00e+00}$	47.40	61	0.78
76	NGC 6482..... U	$1.32^{1.37}_{1.26}$	$5000.00^{0.00}_{5000.0}$	$9.99^{0.00}_{-3.00}$	1.40e-03 $^{1.62e-03}_{1.17e-03}$	1.45e-05 $^{0.00e+00}_{0.00e+00}$	109.43	66	1.66
77	NGC 7130..... U	$0.39^{0.47}_{0.34}$	$40.87^{60.33}_{28.29}$	$4.70^{5.17}_{4.37}$	2.06e-04 $^{2.67e-04}_{1.65e-04}$	1.43e-02 $^{2.10e-02}_{6.24e-03}$	235.04	158	1.49
80	IC 1459.....	$0.29^{0.34}_{0.25}$	$4.28^{5.15}_{3.63}$	$2.92^{3.21}_{2.62}$	2.98e-04 $^{3.38e-04}_{2.68e-04}$	6.43e-04 $^{1.10e-03}_{3.12e-04}$	322.67	336	0.96
81	NPM1G -12.0625U	$0.32^{0.42}_{0.22}$	$5000.00^{0.00}_{0.00}$	$3.80^{4.38}_{3.30}$	4.75e-05 $^{6.23e-05}_{3.96e-05}$	5.91e-09 $^{0.00e+00}_{0.00e+00}$	140.01	139	1.01

Table 3.6: Power-Law+MEKAL model applied to *Chandra* spectra

Num	Name	N_{H1} (10^{22} cm^{-2})	N_{H2} (10^{22} cm^{-2})	Γ	kT (keV)	A_{ME}	A_{PL}	χ^2	d.o.f	χ^2_r
(1)	(2)	(3)	(4)	(5)	(6)	(7)	(8)	(9)	(10)	(11)
1	NGC 0315	$0.01^{0.10}_{0.00}$	$0.69^{0.88}_{0.58}$	$1.63^{1.79}_{1.56}$	$0.45^{0.51}_{0.38}$	2.14e-05 $^{3.37e-05}_{1.86e-05}$	1.67e-04 $^{1.96e-04}_{1.43e-04}$	380.10	363	1.05
6	NGC 0833 .... U	$0.43^{0.84}_{0.00}$	$2.30^{13.37}_{0.00}$	-1.27 $^{0.10}_{-2.26}$	$0.36^{0.89}_{0.14}$	2.30e-05 $^{3.47e-04}_{7.95e-06}$	1.35e-06 $^{5.22e-05}_{2.58e-07}$	32.97	55	0.60
7	NGC 0835 .... U	$0.31^{0.61}_{0.09}$	$0.00^{1.24}_{0.00}$	$0.03^{1.88}_{-0.54}$	$0.33^{0.47}_{0.22}$	6.02e-05 $^{1.84e-04}_{3.24e-05}$	1.54e-06 $^{1.10e-05}_{2.48e-07}$	65.19	54	1.21
8	NGC 1052 .... U	$0.02^{0.92}_{0.00}$	$0.14^{1.75}_{0.00}$	-0.09 $^{0.58}_{-0.54}$	$0.68^{0.88}_{0.28}$	1.88e-05 $^{5.85e-03}_{4.66e-06}$	2.84e-05 $^{6.09e-05}_{1.51e-05}$	42.19	56	0.75
11	NGC 2681	$0.15^{0.28}_{0.01}$	$0.00^{0.08}_{0.00}$	$1.57^{1.89}_{1.29}$	$0.63^{0.68}_{0.54}$	1.11e-05 $^{2.26e-05}_{6.61e-06}$	4.04e-06 $^{5.87e-06}_{3.03e-06}$	66.87	103	0.65
14	3C 218	$0.00^{0.08}_{0.00}$	$0.00^{0.26}_{0.00}$	$1.33^{1.44}_{1.19}$	$1.58^{1.93}_{1.34}$	2.00e-05 $^{3.35e-05}_{1.25e-05}$	2.25e-05 $^{2.61e-05}_{1.85e-05}$	269.72	262	1.03
15	NGC 2787	$0.00^{0.00}_{0.00}$	$0.18^{0.53}_{0.12}$	$2.41^{3.62}_{1.80}$	$0.38^{10.47}_{0.19}$	4.93e-06 $^{4.27e-05}_{0.00e+00}$	3.13e-05 $^{8.11e-05}_{2.36e-05}$	18.86	13	1.45
17	UGC 05101 ... U	$0.86^{1.18}_{0.48}$	$0.00^{0.64}_{0.00}$	$0.60^{1.09}_{0.19}$	$0.47^{0.61}_{0.13}$	3.05e-05 $^{6.43e-05}_{7.07e-06}$	2.65e-06 $^{4.93e-06}_{1.50e-06}$	76.73	90	0.85
22	NGC 3414	$14.47^{82.39}_{0.00}$	$0.28^{0.49}_{0.17}$	$2.44^{3.29}_{2.00}$	$0.51^{0.00}_{0.00}$	4.77e+05 $^{4.60e+04}_{3.92e+06}$	8.96e-05 $^{1.17e-04}_{6.84e-05}$	115.38	126	0.92
23	NGC 3507 .... U	$0.09^{0.46}_{0.00}$	$746.20^{0.00}_{686.76}$	$8.80^{0.00}_{-3.00}$	$0.49^{0.63}_{0.38}$	1.09e-05 $^{2.68e-05}_{6.68e-06}$	2.13e+08 $^{0.00e+00}_{1.98e+09}$	59.05	41	1.44
29	NGC 3690B	$0.49^{0.59}_{0.30}$	$0.00^{0.17}_{0.00}$	$0.98^{1.27}_{0.83}$	$0.13^{0.15}_{0.11}$	2.94e-03 $^{6.44e-03}_{8.73e-04}$	1.46e-05 $^{1.90e-05}_{1.19e-05}$	131.60	149	0.88
30	NGC 3898 .... U	$1.39^{1.75}_{1.12}$	$0.01^{0.59}_{0.00}$	$1.81^{2.81}_{1.57}$	$0.04^{0.05}_{0.04}$	4.45e+02 $^{8.60e+02}_{6.95e+00}$	5.80e-06 $^{1.43e-05}_{4.93e-06}$	3.98	8	0.50
31	NGC 3945 .... U	$183.43^{0.00}_{2.87}$	$0.03^{0.17}_{0.00}$	$5.15^{0.00}_{2.30}$	$1.15^{0.00}_{0.00}$	4.41e-02 $^{1.05e+04}_{0.00e+00}$	4.62e-05 $^{6.92e-05}_{2.40e-05}$	55.49	80	0.69
32	NGC 3998	$0.00^{0.13}_{0.00}$	$0.09^{0.14}_{0.06}$	$1.43^{1.51}_{1.38}$	$0.08^{0.74}_{0.00}$	2.62e-04 $^{9.53e-04}_{2.34e-04}$	1.57e-03 $^{1.68e-03}_{1.49e-03}$	510.26	455	1.12
34	NGC 4111 .... U	$0.02^{0.13}_{0.00}$	$1.10^{6.57}_{0.00}$	$6.83^{0.00}_{0.00}$	$0.66^{0.71}_{0.61}$	2.43e-05 $^{3.42e-05}_{2.18e-05}$	1.51e-06 $^{3.44e-05}_{3.70e-07}$	97.49	66	1.48
35	NGC 4125	$0.53^{0.88}_{0.00}$	$0.86^{2.13}_{0.08}$	$2.32^{4.59}_{1.26}$	$0.20^{0.61}_{0.08}$	6.51e-05 $^{1.32e-03}_{2.48e-06}$	7.15e-06 $^{2.61e-05}_{2.57e-06}$	35.49	58	0.61
37	NGC 4261 .... U	$0.03^{0.07}_{0.00}$	$1.05^{2.39}_{0.01}$	$0.07^{0.63}_{-0.32}$	$0.57^{0.60}_{0.54}$	8.06e-05 $^{9.45e-05}_{7.04e-05}$	9.27e-06 $^{1.82e-05}_{5.58e-06}$	337.94	243	1.39
38	NGC 4278	$0.29^{0.67}_{0.22}$	$0.06^{0.09}_{0.03}$	$2.28^{2.39}_{2.17}$	$0.33^{0.63}_{0.18}$	5.65e-05 $^{4.60e-04}_{2.15e-05}$	1.07e-04 $^{1.17e-04}_{9.50e-05}$	269.23	294	0.92
40	NGC 4321	$0.59^{0.77}_{0.21}$	$0.19^{0.49}_{0.08}$	$2.36^{2.77}_{2.06}$	$0.21^{0.39}_{0.15}$	3.00e-04 $^{8.51e-04}_{9.84e-05}$	2.94e-05 $^{4.42e-05}_{1.85e-05}$	132.14	120	1.10
41	NGC 4374	$0.07^{0.38}_{0.00}$	$0.13^{0.25}_{0.08}$	$1.95^{2.28}_{1.53}$	$0.72^{0.90}_{0.54}$	6.32e-06 $^{5.32e-05}_{3.02e-06}$	2.87e-05 $^{3.84e-05}_{1.54e-05}$	92.38	122	0.76
42	NGC 4410A	$0.51^{1.14}_{0.25}$	$0.00^{0.05}_{0.00}$	$1.77^{1.93}_{1.63}$	$0.30^{0.80}_{0.13}$	3.07e-05 $^{2.50e-04}_{1.46e-06}$	3.18e-05 $^{3.67e-05}_{2.83e-05}$	132.47	155	0.85
43	NGC 4438	$0.37^{0.45}_{0.26}$	$0.00^{0.21}_{0.00}$	$1.91^{2.77}_{1.58}$	$0.52^{0.60}_{0.45}$	1.32e-04 $^{1.98e-04}_{5.65e-05}$	9.98e-06 $^{2.21e-05}_{6.87e-06}$	95.94	97	0.99
44	NGC 4457	$0.37^{0.57}_{0.08}$	$0.17^{2.60}_{0.00}$	$1.70^{3.54}_{1.18}$	$0.31^{0.68}_{0.22}$	6.42e-05 $^{2.18e-04}_{1.09e-05}$	8.35e-06 $^{7.06e-05}_{5.82e-06}$	68.74	82	0.84
46	NGC 4486 .... U	$1.04^{1.14}_{0.93}$	$0.00^{0.03}_{0.00}$	$1.16^{1.19}_{1.13}$	$0.08^{0.09}_{0.07}$	1.45e+00 $^{5.23e+00}_{5.47e-01}$	2.11e-04 $^{2.20e-04}_{2.06e-04}$	734.38	430	1.71
47	NGC 4494	$0.29^{0.72}_{0.00}$	$0.03^{0.17}_{0.00}$	$1.72^{2.31}_{0.90}$	$0.63^{1.02}_{0.24}$	1.54e-05 $^{1.06e-04}_{4.00e-06}$	1.34e-05 $^{3.61e-05}_{8.77e-06}$	36.50	56	0.65
48	NGC 4552	$0.35^{0.56}_{0.00}$	$0.01^{0.12}_{0.00}$	$2.02^{2.37}_{1.87}$	$0.67^{0.81}_{0.56}$	2.92e-05 $^{4.79e-05}_{1.16e-05}$	2.45e-05 $^{3.61e-05}_{2.12e-05}$	147.04	162	0.91
50	NGC 4579	$0.48^{0.54}_{0.38}$	$0.45^{0.56}_{0.27}$	$1.58^{1.66}_{1.47}$	$0.20^{0.21}_{0.18}$	5.21e-03 $^{8.63e-03}_{2.27e-03}$	8.98e-04 $^{1.01e-03}_{7.69e-04}$	506.16	416	1.22
52	NGC 4594 .... U	$17.59^{37.83}_{9.07}$	$0.20^{0.24}_{0.15}$	$1.49^{2.09}_{1.40}$	$1.78^{0.00}_{0.00}$	9.18e+02 $^{7.61e+01}_{1.70e+03}$	1.68e-04 $^{1.88e-04}_{1.47e-04}$	298.48	278	1.07
57	NGC 4696	$0.00^{0.18}_{0.00}$	$0.00^{6.93}_{0.00}$	$3.07^{5.56}_{1.80}$	$0.67^{0.78}_{0.60}$	9.27e-05 $^{1.58e-04}_{6.02e-05}$	5.91e-05 $^{3.37e-04}_{2.66e-05}$	61.63	74	0.83
58	NGC 4736	$0.31^{0.61}_{0.15}$	$0.04^{0.09}_{0.02}$	$2.05^{2.28}_{1.82}$	$0.54^{0.61}_{0.33}$	3.24e-05 $^{1.13e-04}_{1.25e-05}$	4.72e-05 $^{5.96e-05}_{3.69e-05}$	170.20	190	0.90
60	NGC 5055	$0.89^{2.44}_{0.00}$	$0.00^{0.20}_{0.00}$	$1.56^{2.75}_{1.26}$	$0.57^{1.76}_{0.00}$	2.66e-05 $^{3.69e-02}_{0.00e+00}$	5.73e-06 $^{1.41e-05}_{4.12e-06}$	40.28	59	0.68
61	MRK 266NE .. U	$0.00^{0.13}_{0.00}$	$0.00^{0.88}_{0.00}$	$-0.06^{0.30}_{-0.37}$	$0.80^{0.97}_{0.60}$	7.24e-06 $^{1.05e-05}_{5.78e-06}$	3.51e-06 $^{7.03e-06}_{2.35e-06}$	61.88	78	0.79

Table 3.6: Continuation

Num	Name	N_{H1} (10^{22} cm^{-2})	N_{H2} (10^{22} cm^{-2})	Γ	kT (keV)	A_{ME}	A_{PL}	χ^2	d.o.f	χ^2_r
(1)	(2)	(3)	(4)	(5)	(6)	(7)	(8)	(9)	(10)	(11)
62	UGC 08696	$1.14^{1.25}_{1.04}$	$29.22^{43.48}_{24.90}$	$1.12^{2.84}_{0.55}$	$0.65^{0.74}_{0.59}$	1.42e-04 $^{1.81e-04}_{1.13e-04}$	1.53e-04 $^{2.92e-03}_{4.46e-05}$	264.42	230	1.15
63	CGCG 162-010 U	$0.47^{0.63}_{0.33}$	$0.09^{1.59}_{0.00}$	$9.30^{0.00}_{0.00}$	$1.05^{1.13}_{0.95}$	1.47e-04 $^{2.07e-04}_{4.62e-05}$	1.37e-04 $^{8.34e-04}_{1.48e-06}$	141.12	135	1.05
67	NGC 5746 .... U	$0.52^{0.78}_{0.21}$	$6.61^{0.00}_{1.06}$	$3.60^{0.00}_{-2.98}$	$0.70^{0.00}_{0.00}$	1.01e-04 $^{0.00e+00}_{8.23e-01}$	2.91e-01 $^{2.02e+00}_{0.00e+00}$	86.41	109	0.79
68	NGC 5813	$0.12^{0.31}_{0.00}$	$0.15^{0.51}_{0.00}$	$2.94^{6.93}_{1.67}$	$0.49^{0.60}_{0.29}$	2.64e-05 $^{6.51e-05}_{1.99e-05}$	1.89e-05 $^{8.60e-05}_{4.91e-06}$	25.95	30	0.87
70	NGC 5846	$0.28^{0.43}_{0.00}$	$0.03^{0.17}_{0.01}$	$2.55^{3.25}_{2.12}$	$0.35^{0.58}_{0.28}$	1.04e-04 $^{1.89e-04}_{2.93e-05}$	8.85e-06 $^{1.95e-05}_{5.78e-06}$	71.90	85	0.85
73	NGC 6251	$0.00^{0.36}_{0.00}$	$0.00^{0.04}_{0.00}$	$1.48^{1.61}_{1.39}$	$0.20^{0.22}_{0.14}$	9.93e-05 $^{1.11e-03}_{8.17e-05}$	6.79e-05 $^{7.59e-05}_{6.24e-05}$	273.33	250	1.09
74	NGC 6240 .... U	$0.27^{0.32}_{0.23}$	$31.55^{140.43}_{23.35}$	$2.25^{0.00}_{0.00}$	$19.27^{39.77}_{11.88}$	4.90e-04 $^{5.32e-04}_{4.76e-04}$	8.98e-05 $^{1.17e-02}_{4.18e-06}$	428.58	353	1.21
75	IRAS 17208-0014	$1.14^{1.96}_{0.55}$	$5.00^{22.46}_{0.25}$	$1.55^{7.35}_{0.53}$	$0.67^{0.83}_{0.17}$	6.68e-05 $^{2.68e-04}_{1.94e-05}$	3.40e-05 $^{1.96e-03}_{1.06e-05}$	42.51	60	0.71
76	NGC 6482 .... U	$0.17^{0.34}_{0.11}$	$0.47^{0.00}_{0.00}$	$1.92^{0.00}_{0.00}$	$0.74^{0.81}_{0.66}$	6.04e-05 $^{9.05e-05}_{4.22e-05}$	1.93e-06 $^{4.85e-05}_{0.00e+00}$	56.51	65	0.87
77	NGC 7130	$0.45^{0.53}_{0.22}$	$0.00^{0.03}_{0.00}$	$2.43^{2.60}_{2.28}$	$0.57^{0.65}_{0.48}$	9.29e-05 $^{1.37e-04}_{5.76e-05}$	3.53e-05 $^{3.97e-05}_{3.18e-05}$	161.66	157	1.03
80	IC 1459	$0.00^{0.48}_{0.00}$	$0.21^{0.24}_{0.18}$	$1.96^{2.01}_{1.86}$	$0.53^{0.63}_{0.27}$	1.35e-05 $^{3.27e-04}_{1.03e-05}$	2.05e-04 $^{2.12e-04}_{1.86e-04}$	300.35	335	0.90
81	NPM1G -12.0625	$0.71^{0.85}_{0.33}$	$0.15^{0.32}_{0.06}$	$2.67^{3.31}_{2.34}$	$0.31^{0.54}_{0.23}$	1.37e-04 $^{2.14e-04}_{4.23e-05}$	1.84e-05 $^{3.50e-05}_{1.26e-05}$	122.36	138	0.89

Table 3.7: Power-Law plus MEKAL plus Power-law model applied to *Chandra* spectra

Num	N_{H1} (10^{22} cm^{-2})	N_{H2} (10^{22} cm^{-2})	Γ	kT (keV)	A_{PL1}	A_{PL2}	A_{ME}	χ^2	d.o.f	χ^2_r
(1)	(3)	(4)	(5)	(6)	(7)	(8)	(9)	(10)	(11)	(12)
1 ...	$15.21^{21.33}_{10.67}$	$1.06^{1.40}_{0.87}$	$2.37^{2.51}_{2.08}$	$0.46^{0.51}_{0.43}$	4.31e-04 $^{7.53e-04}_{1.41e-04}$	3.21e-04 $^{3.53e-04}_{2.41e-04}$	2.24e-05 $^{2.45e-05}_{2.03e-05}$	374.45	362	1.03
6 ...	$3.51^{10.79}_{0.73}$	$26.88^{41.78}_{1.34}$	$2.15^{5.43}_{-1.50}$	$0.67^{0.87}_{0.49}$	2.91e-05 $^{2.63e-03}_{3.96e-06}$	7.35e-04 $^{1.37e-03}_{3.69e-04}$	3.91e-06 $^{5.16e-06}_{2.72e-06}$	31.63	54	0.59
7 ...	$0.16^{3.13}_{0.00}$	$40.35^{69.46}_{24.60}$	$2.35^{4.80}_{1.75}$	$0.47^{0.59}_{0.39}$	1.24e-05 $^{2.89e-05}_{5.68e-06}$	5.83e-04 $^{6.16e-03}_{5.32e-05}$	1.20e-05 $^{1.69e-05}_{7.05e-06}$	57.38	53	1.08
8 . U	$0.36^{1.88}_{0.00}$	$12.90^{35.47}_{0.00}$	$0.61^{4.26}_{-0.02}$	$0.67^{0.83}_{0.46}$	2.54e-04 $^{1.90e-03}_{2.53e-05}$	2.97e-03 $^{7.41e-03}_{1.08e-04}$	2.17e-05 $^{3.01e-05}_{1.16e-05}$	40.87	55	0.74
11 U	$0.02^{0.19}_{0.00}$	$109.03^{0.00}_{0.00}$	$1.68^{3.64}_{1.29}$	$0.69^{0.76}_{0.64}$	4.57e-06 $^{6.95e-06}_{3.22e-06}$	1.34e-05 $^{6.06e-04}_{0.00e+00}$	6.67e-06 $^{7.63e-06}_{5.62e-06}$	68.99	102	0.68
14 ..	$0.07^{0.20}_{0.04}$	$4.05^{5.96}_{2.88}$	$2.11^{2.76}_{1.77}$	$1.71^{2.19}_{1.43}$	2.22e-05 $^{3.04e-05}_{1.68e-05}$	6.26e-05 $^{1.19e-04}_{1.76e-05}$	2.96e-05 $^{4.89e-05}_{1.48e-05}$	256.46	261	0.98
15 U	$37.27^{0.00}_{7.52}$	$0.22^{0.45}_{0.05}$	$2.22^{3.59}_{1.82}$	$0.29^{0.68}_{0.20}$	1.30e-04 $^{3.08e-02}_{0.00e+00}$	3.46e-05 $^{1.07e-04}_{2.58e-05}$	5.15e-06 $^{8.53e-06}_{3.23e-07}$	18.95	12	1.58
17 ..	$0.21^{0.66}_{0.04}$	$135.07^{380.33}_{43.51}$	$1.34^{1.75}_{1.06}$	$0.66^{1.05}_{0.47}$	6.26e-06 $^{1.37e-05}_{4.26e-06}$	1.57e-04 $^{1.30e-03}_{1.50e-05}$	1.32e-06 $^{2.46e-06}_{3.64e-07}$	76.83	89	0.86
22 U	$0.11^{61.88}_{0.00}$	$0.53^{0.00}_{0.00}$	$2.13^{3.01}_{1.68}$	$1.37^{0.00}_{0.00}$	3.23e-05 $^{2.39e-04}_{2.63e-11}$	5.45e-05 $^{4.73e-02}_{0.00e+00}$	7.37e-06 $^{7.40e-05}_{0.00e+00}$	117.05	125	0.94
23 U	$2.65^{4.40}_{0.88}$	$5000.00^{0.00}_{5000.00}$	$9.69^{0.00}_{-2.99}$	$0.50^{0.58}_{0.43}$	4.74e-04 $^{1.64e-03}_{1.21e-05}$	2.74e-06 $^{0.00e+00}_{0.00e+00}$	7.16e-06 $^{8.09e-06}_{4.79e-06}$	51.35	40	1.28
29 ..	$0.21^{0.41}_{0.03}$	$9.49^{12.54}_{7.52}$	$3.52^{4.89}_{2.61}$	$0.19^{0.25}_{0.14}$	5.37e-05 $^{1.09e-04}_{3.49e-05}$	9.71e-04 $^{1.37e-03}_{7.51e-04}$	3.24e-05 $^{5.91e-05}_{7.47e-06}$	119.66	148	0.81
30 ..	$0.06^{0.68}_{0.00}$	$3.26^{6.00}_{1.62}$	$3.35^{5.74}_{2.33}$	$0.67^{0.99}_{0.22}$	6.68e-06 $^{3.28e-05}_{0.00e+00}$	4.42e-05 $^{3.87e-03}_{2.65e-05}$	1.89e-06 $^{3.14e-06}_{0.00e+00}$	4.89	7	0.70
31 U	$0.05^{0.37}_{0.00}$	$167.99^{0.00}_{38.48}$	$2.60^{4.18}_{2.23}$	$8.02^{0.00}_{0.00}$	4.68e-05 $^{7.04e-05}_{2.93e-05}$	1.17e-02 $^{1.88e+02}_{0.00e+00}$	5.26e-06 $^{2.09e-04}_{0.00e+00}$	56.57	79	0.72
32 ..	$0.08^{0.15}_{0.06}$	$2.30^{3.18}_{1.63}$	$1.81^{2.03}_{1.65}$	$0.22^{0.25}_{0.20}$	1.57e-03 $^{1.83e-03}_{1.42e-03}$	1.25e-03 $^{1.86e-03}_{7.64e-04}$	1.49e-04 $^{2.71e-04}_{9.17e-05}$	490.35	454	1.08
34 ..	$4.67^{9.65}_{1.20}$	$37.71^{100.00}_{12.52}$	$3.04^{8.10}_{0.74}$	$0.66^{0.70}_{0.61}$	8.76e-05 $^{4.61e-04}_{3.13e-06}$	1.08e-03 $^{4.89e-03}_{0.00e+00}$	2.44e-05 $^{2.68e-05}_{2.31e-05}$	75.75	65	1.17
35 ..	$1.21^{3.44}_{0.27}$	$8.91^{1077.10}_{2.40}$	$5.39^{9.85}_{1.69}$	$0.35^{0.58}_{0.24}$	3.31e-05 $^{1.08e-03}_{0.00e+00}$	4.79e-04 $^{3.55e-03}_{0.00e+00}$	1.90e-06 $^{2.60e-06}_{1.02e-06}$	35.82	57	0.63
37 ..	$0.69^{1.38}_{0.31}$	$16.45^{21.64}_{13.25}$	$2.37^{2.80}_{1.87}$	$0.57^{0.59}_{0.55}$	3.40e-05 $^{4.98e-05}_{2.30e-05}$	7.16e-04 $^{1.17e-03}_{4.31e-04}$	7.07e-05 $^{7.42e-05}_{6.65e-05}$	313.17	242	1.29
38 ..	$0.09^{0.12}_{0.06}$	$2.65^{4.32}_{1.48}$	$2.59^{2.66}_{2.28}$	$0.53^{0.67}_{0.41}$	1.17e-04 $^{1.44e-04}_{1.09e-04}$	5.41e-05 $^{3.75e-04}_{2.70e-05}$	8.89e-06 $^{1.17e-05}_{6.07e-06}$	267.30	293	0.91
40 U	$0.60^{0.97}_{0.40}$	$7.71^{10.35}_{5.95}$	$4.97^{5.92}_{3.32}$	$0.35^{0.52}_{0.28}$	1.11e-04 $^{2.48e-04}_{5.25e-05}$	1.32e-03 $^{3.25e-03}_{1.44e-04}$	6.99e-06 $^{1.24e-05}_{1.70e-06}$	126.92	119	1.07
41 U	$0.05^{185.78}_{0.00}$	$0.36^{0.00}_{0.00}$	$1.96^{3.07}_{1.67}$	$0.73^{0.88}_{0.60}$	1.15e-05 $^{3.90e-05}_{0.00e+00}$	2.16e-05 $^{1.15e-04}_{0.00e+00}$	5.87e-06 $^{9.71e-06}_{3.03e-06}$	92.38	121	0.76
42 U	$0.03^{0.30}_{0.00}$	$15.29^{49.08}_{5.75}$	$2.13^{4.85}_{1.73}$	$1.83^{0.00}_{0.00}$	3.41e-05 $^{5.34e-05}_{1.77e-05}$	8.27e-05 $^{5.98e-04}_{1.78e-05}$	1.03e-05 $^{6.04e-05}_{0.00e+00}$	128.54	154	0.83
43 U	$0.71^{1.24}_{0.36}$	$16.20^{46.84}_{6.17}$	$4.39^{6.51}_{3.54}$	$0.65^{0.68}_{0.61}$	1.06e-04 $^{3.91e-04}_{5.27e-05}$	1.22e-03 $^{2.22e-03}_{6.04e-05}$	3.48e-05 $^{4.38e-05}_{2.93e-05}$	105.39	96	1.10
44 U	$0.22^{0.58}_{0.12}$	$9.69^{0.00}_{0.00}$	$2.41^{7.54}_{1.49}$	$0.58^{0.65}_{0.47}$	1.36e-05 $^{1.28e-04}_{0.00e+00}$	1.44e-05 $^{3.02e-04}_{0.00e+00}$	9.24e-06 $^{1.13e-05}_{7.04e-06}$	68.19	81	0.84
46 ..	$0.10^{0.14}_{0.09}$	$3.96^{4.47}_{3.66}$	$2.40^{2.52}_{2.31}$	$0.82^{0.96}_{0.70}$	2.91e-04 $^{3.09e-04}_{2.70e-04}$	1.22e-03 $^{1.80e-03}_{1.11e-03}$	1.53e-05 $^{2.03e-05}_{9.95e-06}$	567.31	429	1.32
47 ..	$0.13^{0.37}_{0.00}$	$2.65^{11.11}_{0.00}$	$2.69^{3.21}_{-0.66}$	$0.80^{1.21}_{0.61}$	1.57e-05 $^{3.31e-05}_{3.22e-06}$	4.69e-05 $^{4.83e-04}_{0.00e+00}$	6.99e-06 $^{1.09e-05}_{3.24e-06}$	35.67	55	0.65
48 ..	$0.10^{0.18}_{0.03}$	$2.93^{132.35}_{0.00}$	$2.41^{3.51}_{1.66}$	$0.80^{0.88}_{0.70}$	3.30e-05 $^{7.14e-05}_{2.18e-05}$	1.32e-05 $^{3.23e-05}_{0.00e+00}$	1.01e-05 $^{1.19e-05}_{7.29e-06}$	147.15	161	0.91
50 U	$0.16^{0.23}_{0.12}$	$586.03^{0.00}_{244.54}$	$1.39^{1.47}_{1.33}$	$0.27^{0.29}_{0.25}$	6.79e-04 $^{7.56e-04}_{6.35e-04}$	8.12e-01 $^{1.17e+01}_{0.00e+00}$	1.12e-04 $^{1.41e-04}_{9.27e-05}$	524.38	415	1.26
52 U	$0.26^{0.38}_{0.18}$	$3.07^{5.51}_{1.69}$	$1.94^{4.22}_{1.44}$	$1.82^{0.00}_{0.00}$	1.71e-04 $^{2.71e-04}_{1.11e-04}$	1.43e-04 $^{4.29e-04}_{7.15e-05}$	2.81e-05 $^{2.47e-04}_{0.00e+00}$	295.95	277	1.07
57 ..	$0.00^{0.00}_{0.00}$	$0.00^{0.00}_{0.00}$	$3.24^{4.80}_{2.67}$	$0.67^{0.78}_{0.60}$	2.91e-05 $^{0.00e+00}_{8.23e-01}$	2.92e-05 $^{0.00e+00}_{8.23e-01}$	9.31e-05 $^{1.21e-04}_{5.56e-05}$	61.71	73	0.85
58 ..	$0.14^{0.20}_{0.06}$	$12.00^{853.68}_{4.08}$	$2.54^{2.64}_{2.21}$	$0.60^{0.68}_{0.52}$	6.92e-05 $^{8.48e-05}_{4.79e-05}$	6.48e-05 $^{2.76e-04}_{6.19e-06}$	9.17e-06 $^{1.17e-05}_{6.01e-06}$	171.14	189	0.91
60 U	$0.08^{0.17}_{0.01}$	$136.99^{0.00}_{0.00}$	$1.87^{9.81}_{1.46}$	$0.78^{1.56}_{0.00}$	8.73e-06 $^{2.20e-05}_{6.19e-06}$	1.18e-01 $^{2.36e+02}_{0.00e+00}$	1.41e-06 $^{2.75e-06}_{0.00e+00}$	41.15	58	0.71

Table 3.7: Continuation

Num	N_{H1} (10^{22} cm^{-2})	N_{H2} (10^{22} cm^{-2})	Γ	kT (keV)	A_{PL1}	A_{PL2}	A_{ME}	χ^2	d.o.f	χ^2_r
(1)	(3)	(4)	(5)	(6)	(7)	(8)	(9)	(10)	(11)	(12)
61 ..	$0.00^{0.28}_{0.00}$	$9.45^{28.94}_{5.69}$	$1.34^{1.75}_{-0.29}$	$0.83^{1.04}_{0.63}$	6.32e-06 $^{9.63e-06}_{3.99e-06}$	1.85e-05 $^{5.99e-05}_{0.00e+00}$	5.78e-06 $^{8.34e-06}_{3.13e-06}$	61.01	77	0.79
62 ..	$0.60^{0.96}_{0.22}$	$50.91^{55.61}_{43.24}$	$2.05^{2.55}_{1.72}$	$0.68^{0.77}_{0.58}$	2.88e-05 $^{7.14e-05}_{2.00e-05}$	2.32e-03 $^{4.53e-03}_{1.58e-03}$	3.12e-06 $^{4.52e-06}_{1.28e-06}$	210.79	229	0.92
63 U	$0.51^{1.14}_{0.23}$	$5000.00^{0.00}_{5000.00}$	$4.36^{6.81}_{2.88}$	$1.37^{1.65}_{1.21}$	8.85e-05 $^{4.84e-04}_{2.44e-05}$	9.44e+00 $^{0.00e+00}_{0.00e+00}$	5.72e-05 $^{8.94e-05}_{3.13e-05}$	127.90	134	0.95
67 U	$0.20^{0.00}_{0.00}$	$1.34^{11.37}_{0.29}$	$1.65^{3.61}_{0.84}$	$0.06^{0.75}_{0.00}$	6.46e-06 $^{1.07e-03}_{0.00e+00}$	3.93e-05 $^{5.64e-04}_{0.00e+00}$	6.10e-03 $^{2.45e-01}_{0.00e+00}$	87.96	108	0.81
68 U	$0.17^{5.23}_{0.00}$	$1.25^{2.55}_{0.33}$	$9.95^{0.00}_{-3.00}$	$0.52^{0.58}_{0.46}$	5.36e-06 $^{2.05e-04}_{8.82e-08}$	2.10e-04 $^{3.14e-04}_{6.52e-06}$	2.01e-05 $^{3.43e-05}_{1.55e-05}$	24.13	28	0.86
70 U	$0.16^{0.51}_{0.07}$	$5000.00^{0.00}_{0.00}$	$2.89^{4.64}_{2.36}$	$0.53^{0.60}_{0.48}$	1.54e-05 $^{3.67e-05}_{8.53e-06}$	7.67e-07 $^{0.00e+00}_{0.00e+00}$	2.77e-05 $^{3.09e-05}_{2.37e-05}$	72.69	84	0.87
73 ..	$0.00^{0.12}_{0.00}$	$4.78^{5.34}_{4.02}$	$2.86^{3.58}_{2.64}$	$0.00^{0.01}_{0.00}$	9.47e-05 $^{1.09e-04}_{8.75e-05}$	5.47e-04 $^{1.51e-03}_{3.67e-04}$	1.10e+10 $^{0.00e+00}_{1.82e+10}$	258.63	249	1.04
74 ..	$0.72^{0.96}_{0.55}$	$50.12^{103.79}_{22.34}$	$1.76^{1.97}_{1.63}$	$1.07^{1.22}_{0.97}$	2.01e-04 $^{2.69e-04}_{1.18e-04}$	5.60e-04 $^{1.37e-03}_{1.67e-04}$	2.16e-05 $^{2.85e-05}_{1.50e-05}$	380.08	352	1.08
75 ..	$1.46^{3.10}_{0.73}$	$12.49^{25.33}_{4.59}$	$3.79^{5.93}_{1.26}$	$0.88^{1.13}_{0.56}$	4.05e-05 $^{4.81e-04}_{2.04e-05}$	2.54e-04 $^{1.14e-02}_{5.31e-06}$	1.22e-06 $^{2.06e-06}_{1.43e-07}$	45.24	59	0.77
76 U	$0.82^{10.06}_{0.14}$	$5000.00^{0.00}_{0.00}$	$4.06^{0.00}_{1.84}$	$0.80^{0.85}_{0.73}$	1.09e-04 $^{8.68e-04}_{2.12e-06}$	2.43e-05 $^{0.00e+00}_{0.00e+00}$	3.37e-05 $^{3.99e-05}_{2.68e-05}$	63.62	64	0.99
77 ..	$0.07^{0.11}_{0.04}$	$86.01^{160.48}_{60.51}$	$2.66^{2.82}_{2.54}$	$0.76^{0.81}_{0.68}$	4.96e-05 $^{6.60e-05}_{4.01e-05}$	1.52e-03 $^{5.65e-03}_{3.80e-04}$	2.58e-05 $^{2.99e-05}_{2.08e-05}$	155.74	156	1.00
80 ..	$0.20^{0.28}_{0.09}$	$1.26^{3.17}_{0.66}$	$2.17^{2.57}_{2.12}$	$0.61^{0.67}_{0.49}$	1.73e-04 $^{2.53e-04}_{2.86e-05}$	1.13e-04 $^{2.46e-04}_{4.03e-05}$	1.66e-05 $^{2.30e-05}_{1.03e-05}$	294.41	334	0.88
81 U	$0.30^{0.45}_{0.18}$	$5000.00^{0.00}_{0.00}$	$3.17^{3.68}_{2.75}$	$0.62^{0.81}_{0.51}$	3.21e-05 $^{4.43e-05}_{2.38e-05}$	4.06e-08 $^{0.00e+00}_{0.00e+00}$	5.85e-06 $^{8.46e-06}_{3.54e-06}$	125.45	137	0.92

Table 3.8: *F-test applied to the* Chandra *data fits.*

Num	Name	(2PL)vs(PL)	(MEPL)vs(ME)	(MEPL)vs(PL)	(ME2PL)vs(MEPL)	(ME2PL)vs(2PL)	Final Class.
(1)	(2)	(3)	(4)	(5)	(6)	(7)	(8)
1	NGC 0315	0.034	2.2e-16 U	3.2e-18	0.020	9.9e-19	ME2PL
6	NGC 0833	9.0e-05 U	9.0e-09 U	1.6e-07 U	0.14 U	1.4e-04	ME2PL
7	NGC 0835	3.8e-04 U	7.2e-04 U	3.8e-04 U	9.6e-3 U	9.2e-03 U	ME2PL
8	NGC 1052	0.019 U	5.6e-07 U	0.011 U	0.19 U	0.080 U	2PL
11	NGC 2681	1.5e-09 U	1.9e-24 U	1.2e-17 U	1	6.5e-09 U	MEPL
14	3C 218.....	3.6e-04	8.8e-06 U	6.6e-06	2.90e-04	6.0e-06	ME2PL
15	NGC 2787	0.901	0.28 U	0.692	1 U	0.589 U	PL
17	UGC 05101	0.020	3.1e-04 U	3.5e-03 U	1 U	0.062	2PL
22	NGC 3414	0.76 U	0.20 U	0.415	1 U	0.787 U	PL
23	NGC 3507	0.95 U	0.97 U	0.010 U	0.019 U	2.8e-04 U	ME
29	NGC 3690B.....	1.75e-13	3.7e-13 U	4.3e-11	1.80e-4	0.032	ME2PL
30	NGC 3898	0.018 U	2.0e-04 U	4.7e-03 U	1 U	0.21 U	MEPL
31	NGC 3945	0.127	1.7e-08 U	0.592 U	1 U	1. U	PL
32	NGC 3998	0.	2.2e-10 U	1.2e-04	2.15e-05	3.79e-09	ME2PL
34	NGC 4111	1.6e-03 U	8.8e-05 U	5.6e-04 U	5.47e-05 U	2.77e-05 U	ME2PL
35	NGC 4125	0.16 U	0.03	0.036	1	0.120 U	MEPL
37	NGC 4261	0. U	5.1e-37 U	5.5e-67 U	1.81e-05 U	8.8e-55 U	ME2PL
38	NGC 4278	2.43e-08U	6.0e-79 U	3.0e-10	0.15	7.7e-04 U	ME2PL
40	NGC 4321	8.96e-05U	2.0e-09 U	2.6e-04	0.029 U	0.071 U	MEPL
41	NGC 4374	0.25	2.0e-05 U	7.6e-04	1 U	9.3e-04 U	MEPL
42	NGC 4410A	0.017	5.5e-07 U	0.193	0.0315483 U	0.525 U	ME2PL
43	NGC 4438	5.17e-06U	1.9e-06	6.3e-18 U	1 U	2.2e-11 U	MEPL
44	NGC 4457	5.55e-06U	4.1e-15 U	4.1e-11 U	0.42 U	1.1e-06 U	MEPL
46	NGC 4486	1.80e-38U	2.5e-18 U	2.6e-16 U	7.2e-26 U	1.4e-03	ME2PL
47	NGC 4494	8.7e-03 U	0.017	2.1e-03	0.26	0.042 U	MEPL
48	NGC 4552	2.6e-05 U	5.7e-21 U	1.1e-09	1	8.53e-06 U	MEPL
50	NGC 4579	0.99 U	2.0e-07 U	4.5e-08	1 U	1.50e-05 U	MEPL
52	NGC 4594	0.36	0.939 U	0.620 U	0.12 U	0.348 U	PL
57	NGC 4696	2.2e-03 U	0.025	8.7e-05 U	1	0.011 U	MEPL
58	NGC 4736	0. U	2.3e-31 U	0.	1	1.47e-05 U	MEPL
60	NGC 5055	0.71	0.098 U	0.310	1 U	0.453 U	PL
61	MRK 266NE	2.55e-05U	4.3e-08 U	7.1e-08 U	0.30 U	3.5e-04	ME2PL
62	UGC 08696	2.52e-33U	4.5e-30 U	1.2e-22 U	6.1e-13	0.022	ME2PL
63	CGCG 162-010..	0.72 U	0.965 U	0.174 U	2.9e-04 U	9.9e-06 U	ME
67	NGC 5746	0.82 U	0.962 U	0.651 U	1 U	1. U	PL
68	NGC 5813	0. U	1.6e-05 U	2.1e-08 U	0.36 U	4.5e-04 U	MEPL
70	NGC 5846	0.93 U	1.5e-06	6.7e-18 U	1 U	U	MEPL
73	NGC 6251	9.64e-16	8.9e-19 U	2.0e-12	2.1e-04	0.31	MEPL
74	NGC 6240	4.8-04	4.1e-17 U	0. U	8.2e-11 U	4.02e-06	ME2PL
75	IRAS 17208-0014	0.68	0.046 U	0.061	1	0.253	PL
76	NGC 6482	1. U	0.568	2.2e-09 U	1 U	2.9e-08 U	ME
77	NGC 7130	7.73e-07U	1.1e-32 U	9.7e-19 U	0.016	1.1e-14 U	ME2PL
80	IC 1459	2.30e-05	5.7e-35 U	7.7e-10	9.85e-4	2.25e-07	ME2PL
81	NPM1G -12.0625	1. U	1.5e-10	3.2e-04 U	1 U	5.4e-04 U	MEPL

Table 3.9: Bestfit model applied to *Chandra* data fits

Num	Name	Type	Bestfit	N_{H1} (10^{22} cm^{-2})	N_{H2} (10^{22} cm^{-2})	Γ	kT (keV)	χ^2	d.o.f	χ^2_r
(1)	(2)	(3)	(4)	(5)	(6)	(7)	(8)	(9)	(10)	(11)
1	NGC 0315	AGN	ME2PL	$15.21^{21.33}_{10.67}$	$1.06^{1.40}_{0.87}$	$2.37^{2.51}_{2.08}$	$0.46^{0.51}_{0.43}$	374.45	362	1.03
3	NGC 0474	SB	–	...	...	...	...	...	...	...
4	IIIZW 035	SB	–	...	...	...	...	...	...	...
5	NGC 0524	SB	–	...	...	...	...	...	...	...
6	NGC 0833	AGN	ME2PL	$3.51^{10.79}_{0.73}$	$26.88^{41.78}_{1.34}$	$2.15^{5.43}_{-1.50}$	$0.67^{0.87}_{0.49}$	31.63	54	0.59
7	NGC 0835	AGN	ME2PL	$0.16^{3.13}_{0.00}$	$40.35^{69.46}_{24.60}$	$2.35^{4.80}_{1.75}$	$0.47^{0.59}_{0.39}$	57.38	53	1.08
8	NGC 1052	AGN	2PL	$0.04^{0.26}_{0.00}$	$12.50^{23.58}_{5.51}$	$1.15^{2.37}_{0.41}$	...	44.79	57	0.79
11	NGC 2681	AGN	MEPL	$0.15^{0.28}_{0.01}$	$0.00^{0.08}_{0.00}$	$1.57^{1.89}_{1.29}$	$0.63^{0.68}_{0.54}$	66.87	103	0.65
13	UGC 4881	SB	–	...	...	...	...	...	...	...
14	3C 218	AGN	ME2PL	$0.07^{0.20}_{0.04}$	$4.05^{5.96}_{2.88}$	$2.11^{2.76}_{1.77}$	$1.71^{2.19}_{1.43}$	256.46	261	0.98
15	NGC 2787	AGN	PL	$0.11^{0.22}_{0.03}$	...	$2.33^{2.94}_{1.87}$	...	21.01	16	1.31
16	NGC 2841	AGN	–	...	...	...	...	...	...	...
17	UGC 05101	AGN	2PL	$0.86^{1.18}_{0.48}$	$0.00^{0.64}_{0.00}$	$1.44^{1.75}_{1.10}$	...	81.79	91	0.90
20	NGC 3245	AGN	–	...	...	...	...	...	...	...
21	NGC 3379	SB	–	...	...	...	...	...	...	...
22	NGC 3414	AGN	PL	$0.21^{0.30}_{0.13}$	...	$2.02^{2.48}_{1.70}$	...	118.01	129	0.91
23	NGC 3507	SB	ME	$0.08^{0.39}_{0.00}$	...	...	$0.51^{0.64}_{0.28}$	60.92	47	1.30
24	NGC 3607	SB	–	...	...	...	...	...	...	...
25	NGC 3608	SB	–	...	...	...	...	...	...	...
28	NGC 3628	SB	–	...	...	...	...	...	...	...
29	NGC 3690B	AGN	ME2PL	$0.21^{0.41}_{0.03}$	$9.49^{12.54}_{7.52}$	$3.52^{4.89}_{2.61}$	$0.19^{0.25}_{0.14}$	119.66	148	0.81
30	NGC 3898	SB	MEPL	$1.39^{1.75}_{1.12}$	$0.01^{0.59}_{0.00}$	$1.81^{2.81}_{1.57}$	$0.04^{0.05}_{0.04}$	3.98	8	0.50
31	NGC 3945	AGN	PL	$0.04^{0.17}_{0.00}$	...	$2.60^{3.22}_{2.32}$	...	56.82	83	0.68
32	NGC 3998	AGN	ME2PL	$0.08^{0.15}_{0.06}$	$2.30^{3.18}_{1.63}$	$1.81^{2.03}_{1.65}$	$0.22^{0.25}_{0.20}$	490.35	454	1.08
33	NGC 4036	AGN	–	...	...	...	...	...	...	...
34	NGC 4111	AGN	ME2PL	$4.67^{9.65}_{1.20}$	$37.71^{100.00}_{12,52}$	$3.04^{8.10}_{0.74}$	$0.66^{0.70}_{0.61}$	75.75	65	1.17
35	NGC 4125	AGN	MEPL	$0.53^{0.88}_{0.00}$	$0.86^{2.13}_{0.08}$	$2.32^{4.59}_{1.26}$	$0.57^{0.59}_{0.55}$	35.49	58	0.61
37	NGC 4261	AGN	ME2PL	$0.69^{1.38}_{0.31}$	$16.45^{21.64}_{13.25}$	$2.37^{2.80}_{1.87}$	$0.57^{0.59}_{0.55}$	313.17	242	1.29
38	NGC 4278	AGN	ME2PL	$0.09^{0.12}_{0.06}$	$2.65^{4.32}_{1.48}$	$2.59^{2.66}_{2.28}$	$0.53^{0.67}_{0.41}$	267.30	293	0.91
39	NGC 4314	SB	–	...	...	...	...	...	...	...
40	NGC 4321	SB	MEPL	$0.59^{0.77}_{0.21}$	$0.19^{0.49}_{0.08}$	$2.36^{2.77}_{2.06}$	$0.20^{0.61}_{0.08}$	132.14	120	1.10
41	NGC 4374	AGN	MEPL	$0.07^{0.38}_{0.00}$	$0.13^{0.25}_{0.08}$	$1.95^{2.28}_{1.53}$	$0.72^{0.90}_{0.54}$	92.38	122	0.76
42	NGC 4410A	AGN	MEPL	$0.51^{1.14}_{0.25}$	$0.00^{0.05}_{0.00}$	$1.77^{1.93}_{1.63}$	$0.30^{0.80}_{0.13}$	132.47	155	0.85
43	NGC 4438	AGN	MEPL	$0.37^{0.45}_{0.26}$	$0.00^{0.21}_{0.00}$	$1.91^{2.77}_{1.58}$	$0.52^{0.60}_{0.45}$	95.94	97	0.99
44	NGC 4457	AGN	MEPL	$0.37^{0.57}_{0.08}$	$0.17^{2.60}_{0.00}$	$1.70^{3.54}_{1.18}$	$0.31^{0.68}_{0.22}$	68.74	82	0.84

Table 3.9: Continuation

Num	Name	Type	Bestfit	N_{H1} (10^{22} cm^{-2})	N_{H2} (10^{22} cm^{-2})	Γ	kT (keV)	χ^2	d.o.f	χ^2_r
(1)	(2)	(3)	(4)	(5)	(6)	(7)	(8)	(9)	(10)	(11)
45	NGC 4459	SB	–	...	...	...	...	...	...	...
46	NGC 4486	AGN	ME2PL	$0.10^{0.14}_{0.09}$	$3.96^{4.47}_{3.66}$	$2.40^{2.52}_{2.31}$	$0.82^{0.96}_{0.70}$	567.31	429	1.32
47	NGC 4494	AGN	MEPL	$0.29^{0.72}_{0.00}$	$0.03^{0.17}_{0.00}$	$1.72^{2.31}_{0.90}$	$0.63^{1.02}_{0.24}$	36.50	56	0.65
48	NGC 4552	AGN	MEPL	$0.35^{0.56}_{0.00}$	$0.01^{0.12}_{0.00}$	$2.02^{2.37}_{1.87}$	$0.67^{0.81}_{0.56}$	147.04	162	0.91
49	NGC 4589	SB	–	...	...	...	...	...	...	...
50	NGC 4579	AGN	MEPL	$0.48^{0.54}_{0.38}$	$0.45^{0.56}_{0.27}$	$1.58^{1.66}_{1.47}$	$0.20^{0.21}_{0.18}$	506.16	416	1.21
51	NGC 4596	SB	–	...	...	...	...	...	...	...
52	NGC 4594	AGN	PL	$0.19^{0.23}_{0.17}$	...	$1.56^{1.67}_{1.46}$	...	300.39	281	1.07
53	NGC 4636	SB	–	...	...	...	...	...	...	...
54	NGC 4676A	SB	–	...	...	...	...	...	...	...
55	NGC 4676B	SB	–	...	...	...	...	...	...	...
56	NGC 4698	SB	–	...	...	...	...	...	...	...
57	NGC 4696	SB	MEPL	$0.00^{0.18}_{0.00}$	$0.00^{6.93}_{0.00}$	$3.07^{5.56}_{1.80}$	$0.67^{0.78}_{0.60}$	61.63	74	0.83
58	NGC 4736	AGN	MEPL	$0.31^{0.61}_{0.15}$	$0.04^{0.09}_{0.02}$	$2.05^{2.28}_{1.82}$	$0.54^{0.61}_{0.33}$	170.20	190	0.90
60	NGC 5055	AGN	PL	$0.16^{0.33}_{0.05}$	...	$2.30^{3.16}_{1.85}$	...	42.78	62	0.69
61	MRK 266NE	AGN	ME2PL	$0.00^{0.28}_{0.00}$	$9.45^{28.94}_{5.69}$	$1.34^{1.75}_{-0.29}$	$0.83^{1.04}_{0.63}$	61.01	77	0.79
62	UGC 08696	AGN	ME2PL	$0.60^{0.96}_{0.22}$	$50.91^{55.61}_{43.24}$	$2.05^{2.55}_{1.72}$	$0.68^{0.77}_{0.58}$	210.79	229	0.92
63	CGCG 162-010 ..	SB	ME	$0.47^{0.63}_{0.39}$	...	...	$1.05^{1.10}_{0.96}$	142.58	141	1.01
66	IRAS 14348-1447	SB	–	...	...	...	...	...	...	...
67	NGC 5746	AGN	PL	$0.60^{0.93}_{0.35}$	...	$1.28^{1.67}_{0.93}$	...	87.71	112	0.78
68	NGC 5813	SB	MEPL	$0.12^{0.31}_{0.00}$	$0.15^{0.51}_{0.00}$	$2.94^{6.9}_{1.67}$	$0.49^{0.60}_{0.29}$	25.95	30	0.86
69	NGC 5838	AGN	–	...	...	...	...	...	...	...
70	NGC 5846	SB	MEPL	$0.28^{0.43}_{0.00}$	$0.03^{0.17}_{0.01}$	$2.55^{3.25}_{2.12}$	$0.35^{0.58}_{0.28}$	71.90	85	0.85
71	NGC 5866	SB	–	...	...	...	...	...	...	...
72	MRK 0848	SB	–	...	...	...	...	...	...	...
73	NGC 6251	AGN	MEPL	$0.00^{0.36}_{0.00}$	$0.00^{0.04}_{0.00}$	$1.48^{1.61}_{1.39}$	$0.20^{0.22}_{0.14}$	273.33	250	1.09
74	NGC 6240	AGN	ME2PL	$0.72^{0.96}_{0.55}$	$50.12^{103.79}_{22.34}$	$1.76^{1.97}_{1.63}$	$1.07^{1.22}_{0.97}$	380.08	352	1.08
75	IRAS 17208-0014	AGN	PL	$0.34^{0.61}_{0.18}$	...	$1.63^{1.86}_{1.34}$	...	48.01	63	0.76
76	NGC 6482	SB	ME	$0.19^{0.33}_{0.10}$	...	...	$0.75^{0.81}_{0.65}$	60.72	71	0.85
77	NGC 7130	AGN	ME2PL	$0.07^{0.11}_{0.04}$	$86.01^{160.48}_{60.51}$	$2.66^{2.82}_{2.54}$	$0.76^{0.81}_{0.68}$	155.74	156	1.00
79	NGC 7331	SB	–	...	...	...	...	...	...	...
80	IC 1459	AGN	ME2PL	$0.20^{0.28}_{0.09}$	$1.26^{3.17}_{0.66}$	$2.17^{2.57}_{2.12}$	$0.61^{0.67}_{0.49}$	294.41	334	0.88
81	NPM1G -12.0625	SB	MEPL	$0.71^{0.85}_{0.33}$	$0.15^{0.32}_{0.06}$	$2.67^{3.31}_{2.34}$	$0.31^{0.54}_{0.23}$	122.36	138	0.89

Table 3.10: FeKα, FeXV and FeXVI emission line fluxes with *Chandra* data.

Num	Name	Flux(FeKα) (erg s^{-1} cm^{-2})	Flux(FeXXV) (erg s^{-1} cm^{-2})	Flux(FeXXVI) (erg s^{-1} cm^{-2})
(1)	(2)	(3)	(4)	(5)
1	NGC 0315	6.99e-07 $^{1.63e-06}_{0.00e+00}$	6.00e-07 $^{1.66e-06}_{0.00e+00}$	6.39e-07 $^{1.82e-06}_{0.00e+00}$
3	NGC 0474	...	...	...
4	IIIZW 035	...	...	...
5	NGC 0524	...	...	...
6	NGC 0833	4.04e-06 $^{7.52e-06}_{5.70e-07}$	1.62e-06 $^{4.70e-06}_{0.00e+00}$	3.55e-06 $^{7.80e-06}_{0.00e+00}$
7	NGC 0835	1.49e-06 $^{3.57e-06}_{0.00e+00}$	3.26e-16 $^{2.17e-06}_{0.00e+00}$	2.29e-07 $^{2.96e-06}_{0.00e+00}$
8	NGC 1052	2.93e-06 $^{1.45e-05}_{0.00e+00}$	5.65e-06 $^{2.14e-05}_{0.00e+00}$	2.33e-17 $^{1.02e-05}_{0.00e+00}$
11	NGC 2681	2.01e-07 $^{4.78e-07}_{0.00e+00}$	5.31e-11 $^{3.25e-07}_{0.00e+00}$	3.05e-08 $^{4.23e-07}_{0.00e+00}$
13	UGC 4881	...	...	...
14	3C 218	1.92e-08 $^{3.50e-07}_{0.00e+00}$	8.09e-08 $^{4.72e-07}_{0.00e+00}$	3.69e-08 $^{4.14e-07}_{0.00e+00}$
15	NGC 2787	...	...	...
16	NGC 2841	...	...	...
17	UGC 05101	1.72e-07 $^{7.22e-07}_{0.00e+00}$	4.78e-07 $^{1.19e-06}_{0.00e+00}$	2.45e-19 $^{6.80e-07}_{0.00e+00}$
20	NGC 3245	...	...	...
21	NGC 3379	...	...	...
22	NGC 3414	0.00e+00 $^{1.09e-06}_{0.00e+00}$	0.00e+00 $^{7.45e-07}_{0.00e+00}$	0.00e+00 $^{6.48e-07}_{0.00e+00}$
23	NGC 3507	...	...	...
24	NGC 3607	...	...	...
25	NGC 3608	...	...	...
28	NGC 3628	...	...	...
29	NGC 3690B	2.72e-07 $^{1.13e-06}_{0.00e+00}$	4.35e-22 $^{1.40e-06}_{0.00e+00}$	2.40e-07 $^{1.16e-06}_{0.00e+00}$
30	NGC 3898	1.10e-18 $^{0.00e+00}_{0.00e+00}$	1.57e-20 $^{0.00e+00}_{0.00e+00}$	8.49e-26 $^{0.00e+00}_{0.00e+00}$
31	NGC 3945	0.00e+00 $^{4.23e-08}_{0.00e+00}$	0.00e+00 $^{6.12e-08}_{0.00e+00}$	0.00e+00 $^{7.72e-08}_{0.00e+00}$
32	NGC 3998	1.25e-06 $^{6.94e-06}_{0.00e+00}$	4.36e-07 $^{6.07e-06}_{0.00e+00}$	9.81e-07 $^{7.16e-06}_{0.00e+00}$
33	NGC 4036	...	...	...
34	NGC 4111	0.00e+00 $^{4.18e-07}_{0.00e+00}$	0.00e+00 $^{5.17e-07}_{0.00e+00}$	0.00e+00 $^{7.78e-07}_{0.00e+00}$
35	NGC 4125	0.00e+00 $^{5.46e-08}_{0.00e+00}$	0.00e+00 $^{5.49e-08}_{0.00e+00}$	0.00e+00 $^{1.01e-07}_{0.00e+00}$
37	NGC 4261	4.58e-07 $^{1.58e-06}_{0.00e+00}$	7.54e-07 $^{2.05e-06}_{0.00e+00}$	9.17e-29 $^{7.58e-07}_{0.00e+00}$
38	NGC 4278	1.65e-07 $^{4.70e-07}_{0.00e+00}$	9.02e-08 $^{4.00e-07}_{0.00e+00}$	2.90e-07 $^{7.05e-07}_{0.00e+00}$
39	NGC 4314	...	...	...
40	NGC 4321	0.00e+00 $^{2.35e-07}_{0.00e+00}$	0.00e+00 $^{2.93e-07}_{0.00e+00}$	0.00e+00 $^{8.15e-07}_{0.00e+00}$
41	NGC 4374	5.19e-07 $^{1.25e-06}_{0.00e+00}$	1.32e-14 $^{6.90e-07}_{0.00e+00}$	9.28e-21 $^{8.51e-07}_{0.00e+00}$
42	NGC 4410A	2.40e-07 $^{8.85e-07}_{0.00e+00}$	4.89e-07 $^{1.19e-06}_{0.00e+00}$	3.49e-07 $^{1.07e-06}_{0.00e+00}$
43	NGC 4438	7.72e-08 $^{8.56e-07}_{0.00e+00}$	4.16e-08 $^{1.06e-06}_{0.00e+00}$	5.07e-08 $^{0.00e+00}_{8.22e-01}$
44	NGC 4457	0.00e+00 $^{2.05e-08}_{0.00e+00}$	0.00e+00 $^{3.00e-08}_{0.00e+00}$	0.00e+00 $^{5.54e-08}_{0.00e+00}$
45	NGC 4459	0.00e+00 $^{1.70e-07}_{0.00e+00}$	0.00e+00 $^{2.56e-07}_{0.00e+00}$	0.00e+00 $^{3.21e-07}_{0.00e+00}$
46	NGC 4486	1.80e-06 $^{2.81e-06}_{7.89e-07}$	2.92e-06 $^{4.16e-06}_{1.68e-06}$	2.51e-06 $^{3.82e-06}_{1.21e-06}$
47	NGC 4494	0.00e+00 $^{4.60e-08}_{0.00e+00}$	0.00e+00 $^{7.00e-08}_{0.00e+00}$	0.00e+00 $^{9.39e-08}_{0.00e+00}$
48	NGC 4552	1.83e-07 $^{5.93e-07}_{0.00e+00}$	2.06e-07 $^{6.14e-07}_{0.00e+00}$	1.22e-17 $^{5.26e-07}_{0.00e+00}$
49	NGC 4589	...	...	...
50	NGC 4579	8.44e-06 $^{1.19e-05}_{4.98e-06}$	3.07e-06 $^{6.34e-06}_{0.00e+00}$	6.18e-06 $^{1.00e-05}_{2.31e-06}$
51	NGC 4596	...	...	...
52	NGC 4594	2.93e-16 $^{1.54e-06}_{0.00e+00}$	7.80e-07 $^{3.03e-06}_{0.00e+00}$	2.65e-06 $^{5.33e-06}_{0.00e+00}$
53	NGC 4636	...	...	...
54	NGC 4676A	...	...	...
55	NGC 4676B	...	...	...
56	NGC 4698	...	...	...
57	NGC 4696	...	...	...

Table 3.10: Continuation

Num	Name	Flux(FeKα) (erg s^{-1} cm^{-2})	Flux(FeXXV) (erg s^{-1} cm^{-2})	Flux(FeXXVI) (erg s^{-1} cm^{-2})
(1)	(2)	(3)	(4)	(5)
58	NGC 4736	4.99e-07 $^{1.05e-06}_{0.00e+00}$	1.92e-07 $^{7.30e-07}_{0.00e+00}$	1.97e-06 $^{3.11e-06}_{8.32e-07}$
60	NGC 5055	0.00e+00 $^{6.76e-09}_{0.00e+00}$	0.00e+00 $^{9.13e-09}_{0.00e+00}$	0.00e+00 $^{1.70e-08}_{0.00e+00}$
61	MRK 266NE	5.94e-07 $^{1.94e-06}_{0.00e+00}$	9.55e-23 $^{9.94e-07}_{0.00e+00}$	2.11e-08 $^{1.74e-06}_{0.00e+00}$
62	UGC 08696	2.28e-06 $^{3.74e-06}_{8.18e-07}$	8.20e-33 $^{3.01e-07}_{0.00e+00}$	7.72e-07 $^{2.22e-06}_{0.00e+00}$
63	CGCG 162-010..	...	...	...
66	IRAS 14348-1447	...	...	...
67	NGC 5746	7.86e-08 $^{7.63e-07}_{0.00e+00}$	0.00e+00 $^{4.62e-07}_{0.00e+00}$	1.30e-07 $^{1.03e-06}_{0.00e+00}$
68	NGC 5813	0.00e+00 $^{3.38e-08}_{0.00e+00}$	0.00e+00 $^{3.31e-08}_{0.00e+00}$	0.00e+00 $^{4.43e-08}_{0.00e+00}$
69	NGC 5838	...	...	...
70	NGC 5846	2.97e-23 $^{1.21e-06}_{0.00e+00}$	2.32e-32 $^{1.49e-06}_{0.00e+00}$	7.11e-07 $^{1.85e-06}_{0.00e+00}$
71	NGC 5866	...	...	...
72	MRK 0848	...	...	...
73	NGC 6251	5.44e-07 $^{1.85e-06}_{0.00e+00}$	0.00e+00 $^{8.72e-07}_{0.00e+00}$	3.87e-07 $^{1.82e-06}_{0.00e+00}$
74	NGC 6240	1.59e-05 $^{1.88e-05}_{1.30e-05}$	5.63e-06 $^{7.89e-06}_{3.38e-06}$	3.34e-06 $^{5.47e-06}_{1.21e-06}$
75	IRAS 17208-0014	2.52e-07 $^{6.47e-07}_{0.00e+00}$	5.56e-07 $^{1.12e-06}_{0.00e+00}$	4.67e-07 $^{1.051e-06}_{0.00e+00}$
76	NGC 6482	...	...	...
77	NGC 7130	1.56e-06 $^{2.58e-06}_{5.34e-07}$	8.00e-07 $^{1.80e-06}_{0.00e+00}$	1.65e-07 $^{1.12e-06}_{0.00e+00}$
79	NGC 7331	...	...	...
80	IC 1459	2.27e-07 $^{9.04e-07}_{0.00e+00}$	1.60e-07 $^{8.85e-07}_{0.00e+00}$	8.61e-07 $^{1.88e-06}_{0.00e+00}$
81	NPM1G -12.0625	0.00e+00 $^{0.00e+00}_{8.22e-01}$	0.00e+00 $^{1.11e-07}_{0.00e+00}$	0.00e+00 $^{1.29e-07}_{0.00e+00}$

Table 3.11: FeKα, FeXV and FeXVI emission line equivalent widths with *Chandra* data.

Num	Name	EW(FeKα) (eV)	EW(FeXXV) (eV)	EW(FeXXVI) (eV)
(1)	(2)	(3)	(4)	(5)
1	NGC 0315	75.19 $^{175.71}_{0.00}$	63.06 $^{172.89}_{0.00}$	82.81 $^{234.12}_{0.00}$
3	NGC 0474	...	...	...
4	IIIZW 035	...	...	...
5	NGC 0524	...	...	...
6	NGC 0833	334.40 $^{621.63}_{47.17}$	78.79 $^{228.90}_{0.00}$	335.18 $^{736.92}_{0.00}$
7	NGC 0835	554.50 $^{1327.41}_{0.00}$	0.00 $^{420.73}_{0.00}$	0.00 $^{1207.86}_{0.00}$
8	NGC 1052	73.58 $^{348.54}_{0.00}$	148.71 $^{571.44}_{0.00}$	0.00 $^{258.43}_{0.00}$
11	NGC 2681	929.23 $^{2211.99}_{0.00}$	19.65 $^{593.19}_{0.00}$	301.86 $^{2219.93}_{0.00}$
13	UGC 4881	...	...	...
14	3C 218	7.90 $^{164.65}_{0.00}$	78.67 $^{245.51}_{0.00}$	33.82 $^{232.56}_{0.00}$
15	NGC 2787	...	...	...
16	NGC 2841	...	...	...
17	UGC 05101	63.66 $^{266.95}_{0.00}$	209.41 $^{490.91}_{0.00}$	0.00 $^{249.61}_{0.00}$
20	NGC 3245	...	...	...
21	NGC 3379	...	...	...
22	NGC 3414	0.00 $^{588.89}_{0.00}$	0.00 $^{442.41}_{0.00}$	0.00 $^{416.08}_{0.00}$
23	NGC 3507	...	...	...
24	NGC 3607	...	...	...
25	NGC 3608	...	...	...
28	NGC 3628	...	...	...
29	NGC 3690B	205.29 $^{851.84}_{0.00}$	1.80 $^{731.19}_{0.00}$	60.45 $^{845.33}_{0.00}$

Table 3.11: Continuation

Num	Name	EW(FeKα) (eV)	EW(FeXXV) (eV)	EW(FeXXVI) (eV)
(1)	(2)	(3)	(4)	(5)
30	NGC 3898	$0.00^{0.00}_{0.00}$	$0.00^{0.00}_{0.00}$	$0.00^{0.00}_{0.00}$
31	NGC 3945	$0.00^{109.52}_{0.00}$	$0.00^{178.38}_{0.00}$	$0.00^{248.41}_{0.00}$
32	NGC 3998	$12.76^{70.76}_{0.00}$	$7.77^{64.55}_{0.00}$	$17.61^{84.89}_{0.00}$
33	NGC 4036	...	...	...
34	NGC 4111	$0.00^{179.91}_{0.00}$	$0.00^{237.77}_{0.00}$	$0.00^{414.51}_{0.00}$
35	NGC 4125	$0.00^{948.66}_{0.00}$	$0.00^{1072.28}_{0.00}$	$0.00^{2174.49}_{0.00}$
37	NGC 4261	$53.31^{182.56}_{0.00}$	$101.90^{268.55}_{0.00}$	$0.00^{103.20}_{0.00}$
38	NGC 4278	$108.77^{307.65}_{0.00}$	$62.31^{207.28}_{0.00}$	$268.56^{597.75}_{0.00}$
39	NGC 4314	...	...	...
40	NGC 4321	$0.00^{623.63}_{0.00}$	$0.00^{867.46}_{0.00}$	$0.00^{2638.45}_{0.00}$
41	NGC 4374	$661.31^{1595.10}_{0.00}$	$0.00^{461.28}_{0.00}$	$0.00^{1260.98}_{0.00}$
42	NGC 4410A	$117.55^{432.16}_{0.00}$	$245.40^{583.21}_{0.00}$	$205.63^{594.11}_{0.00}$
43	NGC 4438	$222.32^{2462.99}_{0.00}$	$13.82^{2245.79}_{0.00}$	$2.51^{0.00}_{0.00}$
44	NGC 4457	$0.00^{61.92}_{0.00}$	$0.00^{98.06}_{0.00}$	$0.00^{192.89}_{0.00}$
45	NGC 4459	$0.00^{1090710.00}_{0.00}$	$0.00^{}_{0.002388190.0}$	$0.00^{}_{0.006217140.00}$
46	NGC 4486	$84.04^{131.24}_{36.85}$	$134.79^{192.02}_{77.57}$	$139.92^{212.67}_{67.17}$
47	NGC 4494	$0.00^{80.14}_{0.00}$	$0.00^{132.01}_{0.00}$	$0.00^{188.95}_{0.00}$
48	NGC 4552	$201.92^{653.93}_{0.00}$	$409.68^{809.03}_{0.00}$	$0.00^{698.77}_{0.00}$
49	NGC 4589	...	...	...
50	NGC 4579	$158.75^{223.78}_{93.73}$	$45.85^{94.76}_{0.00}$	$132.15^{214.78}_{49.51}$
51	NGC 4596	...	...	...
52	NGC 4594	$0.00^{146.01}_{0.00}$	$61.70^{239.08}_{0.00}$	$285.41^{574.59}_{0.00}$
53	NGC 4636	...	...	...
54	NGC 4676A	...	...	...
55	NGC 4676B	...	...	...
56	NGC 4698	...	...	...
57	NGC 4696	...	...	...
58	NGC 4736	$369.76^{775.17}_{0.00}$	$35.41^{156.34}_{0.00}$	$1537.52^{2426.11}_{648.72}$
60	NGC 5055	$0.00^{35.22}_{0.00}$	$0.00^{52.90}_{0.00}$	$0.00^{107.18}_{0.00}$
61	MRK 266NE	$163.82^{518.66}_{0.00}$	$0.00^{218.47}_{0.00}$	$11.98^{501.42}_{0.00}$
62	UGC 08696	$169.48^{278.15}_{60.89}$	$0.00^{16.31}_{0.00}$	$73.53^{189.80}_{0.00}$
63	CGCG 162-010 ..	...	...	...
66	IRAS 14348-1447	...	...	...
67	NGC 5746	$41.46^{375.02}_{0.00}$	$0.00^{213.71}_{0.00}$	$129.20^{563.96}_{0.00}$
68	NGC 5813	$0.00^{1433.21}_{0.00}$	$0.00^{1656.42}_{0.00}$	$0.00^{2555.05}_{0.00}$
69	NGC 5838	... ...	...	...
70	NGC 5846	$0.00^{14895.70}_{0.00}$	$0.00^{1705.86}_{0.00}$	$231.80^{3008.03}_{0.00}$
71	NGC 5866	...	...	...
72	MRK 0848	...	...	...
73	NGC 6251	$117.80^{401.03}_{0.00}$	$0.00^{149.01}_{0.00}$	$110.50^{447.94}_{0.00}$
74	NGC 6240	$708.49^{839.10}_{577.87}$	$134.68^{188.49}_{80.88}$	$166.86^{273.14}_{60.58}$
75	IRAS 17208-0014	$217.03^{558.42}_{0.00}$	$427.05^{851.02}_{0.00}$	$462.96^{1020.93}_{0.00}$
76	NGC 6482	...	...	...
77	NGC 7130	$382.06^{633.04}_{131.08}$	$147.04^{333.58}_{0.00}$	$34.44^{307.20}_{0.00}$
79	NGC 7331	...	...	...
80	IC 1459	$42.17^{168.17}_{0.00}$	$31.13^{142.23}_{0.00}$	$194.83^{425.46}_{0.00}$
81	NPM1G -12.0625	$0.00^{0.00}_{0.00}$	$0.00^{715.42}_{0.00}$	$0.00^{925.38}_{0.00}$

Table 3.12: Observed fluxes and absorption corrected luminosities with *Chandra* data*.

Num	Name	Flux(0.5-2.0keV) (10^{-13} erg s^{-1})	Flux(2.0-10.0keV) (10^{-13} erg s^{-1})	Log(Lum(0.5-2.0keV))	Log(Lum(2.0-10.0keV))
(1)	(2)	(3)	(4)	(5)	(6)
1	NGC 0315	1.525 [0.456 , 1.802]	6.498 [0.227 , 7.755]	41.970 [41.436 , 42.041]	41.768 [40.857 , 41.846]
3	NGC 0474 ..... (*)	0.015 [0.000 , 0.037]	0.023 [0.000 , 0.060]	38.314 [0.000 , 38.745]	38.478 [0.000 , 38.916]
4	IIIZW 035 ..... (*)	0.044 [0.008 , 0.078]	0.073 [0.018 , 0.129]	39.878 [39.170 , 40.119]	40.048 [39.413 , 40.296]
5	NGC 0524 ..... (*)	0.033 [0.002 , 0.064]	0.055 [0.000 , 0.110]	38.423 [36.084 , 38.711]	38.586 [37.093 , 38.881]
6	NGC 0833	0.109 [0.045 , 0.154]	5.516 [0.424 , 6.417]	41.712 [41.311 , 41.849]	41.734 [40.598 , 41.807]
7	NGC 0835	0.411 [0.196 , 0.525]	1.365 [1.206 , 17.577]	41.687 [41.346 , 41.794]	41.399 [41.368 , 42.535]
8	NGC 1052	1.035 [0.000 , 1.445]	14.346 [2.228 , 18.071]	41.677 [0.000 , 41.843]	41.240 [40.404 , 41.337]
11	NGC 2681	0.238 [0.072 , 0.265]	1.846 [0.170 , 14.065]	38.577 [38.061 , 38.622]	39.275 [38.263 , 40.169]
13	UGC 4881 ..... (*)	0.056 [0.011 , 0.103]	0.085 [0.015 , 0.152]	40.262 [39.659 , 40.513]	40.436 [39.838 , 40.678]
14	3C 218	0.617 [0.412 , 0.726]	1.464 [0.399 , 1.818]	42.153 [41.958 , 42.219]	42.081 [41.535 , 42.176]
15	NGC 2787	0.449 [0.117 , 0.566]	0.749 [0.000 ,13898.999]	38.877 [38.314 , 38.981]	38.805 [0.000 , 43.160]
16	NGC 2841 ..... (*)	0.139 [0.099 , 0.177]	0.210 [0.148 , 0.269]	38.396 [38.249 , 38.501]	38.558 [38.410 , 38.674]
17	UGC 05101	0.121 [0.045 , 0.158]	0.810 [0.334 , 1.167]	41.805 [41.346 , 41.925]	42.066 [41.699 , 42.223]
20	NGC 3245 ..... (*)	0.118 [0.054 , 0.181]	0.182 [0.085 , 0.280]	38.819 [38.516 , 38.998]	38.982 [38.628 , 39.159]
21	NGC 3379 ..... (*)	0.064 [0.040 , 0.087]	0.101 [0.063 , 0.137]	37.969 [37.774 , 38.114]	38.131 [37.935 , 38.263]
22	NGC 3414	0.950 [0.613 , 1.170]	1.633 [1.236 , 2.217]	39.949 [39.753 , 40.041]	39.863 [39.761 , 39.988]
23	NGC 3507	0.179 [0.000 , 0.231]	0.003 [0.000 , 0.005]	39.072 [0.000 , 39.177]	37.204 [0.000 , 37.367]
24	NGC 3607 ..... (*)	0.061 [0.035 , 0.088]	0.093 [0.051 , 0.137]	38.602 [38.355 , 38.770]	38.765 [38.530 , 38.929]
25	NGC 3608 ..... (*)	0.017 [0.001 , 0.033]	0.025 [0.001 , 0.049]	38.042 [36.875 , 38.339]	38.205 [37.051 , 38.502]
28	NGC 3628 ..... (*)	0.032 [0.018 , 0.045]	0.049 [0.027 , 0.070]	37.384 [37.157 , 37.551]	37.546 [37.292 , 37.713]
29	NGC 3690B	0.947 [0.000 , 1.422]	1.293 [0.143 , 2.030]	41.772 [0.000 , 41.961]	40.862 [39.970 , 41.074]
30	NGC 3898	0.191 [0.015 , 0.268]	0.201 [1119.260 ,10468.500]	42.696 [41.538 , 42.853]	38.776 [0.000 , 43.475]
31	NGC 3945	0.793 [0.437 , 0.984]	0.376 [0.267 , 0.487]	39.767 [39.507 , 39.860]	39.121 [38.966 , 39.232]
32	NGC 3998	31.270 [25.732 , 34.339]	82.463 [60.296 , 91.311]	41.178 [41.100 , 41.220]	41.319 [41.195 , 41.364]
33	NGC 4036 ..... (*)	0.120 [0.071 , 0.175]	0.183 [0.103 , 0.266]	38.962 [38.738 , 39.116]	39.126 [38.898 , 39.298]
34	NGC 4111	0.592 [0.463 , 0.701]	3.391 [0.018 , 104.038]	40.862 [40.758 , 40.937]	40.364 [0.000 , 41.864]
35	NGC 4125	0.074 [0.000 , 0.088]	0.069 [0.000 , 0.118]	39.938 [0.000 , 40.023]	38.730 [0.000 , 38.958]
37	NGC 4261	1.876 [1.496 , 2.070]	4.318 [0.078 , 5.239]	41.284 [41.181 , 41.330]	41.069 [39.410 , 41.154]
38	NGC 4278	2.097 [1.517 , 2.385]	1.711 [1.188 , 2.067]	39.567 [39.444 , 39.619]	39.226 [39.095 , 39.307]
39	NGC 4314 ..... (*)	0.109 [0.057 , 0.157]	0.166 [0.094 , 0.240]	38.108 [37.849 , 38.273]	38.270 [37.993 , 38.425]
40	NGC 4321	0.546 [0.074 , 0.637]	5.863 [3.477 , 45.585]	40.390 [39.640 , 40.454]	40.491 [40.322 , 41.405]
41	NGC 4374	0.526 [0.068 , 0.611]	0.811 [0.411 , 44.306]	39.506 [38.617 , 39.564]	39.533 [39.245 , 41.268]
42	NGC 4410A.....	0.745 [0.337 , 0.805]	1.179 [0.819 , 1.432]	41.201 [40.878 , 41.231]	41.176 [41.016 , 41.262]
43	NGC 4438	1.105 [0.315 , 1.261]	0.322 [0.000 , 990.000]	40.076 [39.371 , 40.135]	39.047 [0.000 , 42.546]
44	NGC 4457	0.372 [0.014 , 0.437]	0.174 [0.119 , 0.240]	39.559 [39.422 , 39.613]	38.814 [38.635 , 38.946]
45	NGC 4459 ..... (*)	0.048 [0.005 , 0.090]	0.075 [0.008 , 0.139]	38.209 [37.389 , 38.496]	38.372 [37.727 , 38.641]

Table 3.12: Continuation

Num	Name	Flux(0.5-2.0keV) (10^{-13} erg s^{-1})	Flux(2.0-10.0keV) (10^{-13} erg s^{-1})	Log(Lum(0.5-2.0keV))	Log(Lum(2.0-10.0keV))
(1)	(2)	(3)	(4)	(5)	(6)
46	NGC 4486	5.146 [4.585 , 5.521]	16.433 [11.867 , 18.328]	40.927 [40.878 , 40.957]	40.823 [40.708 , 40.867]
47	NGC 4494	0.423 [0.122 , 0.528]	0.162 [0.035 , 0.304]	39.753 [39.266 , 39.843]	38.777 [38.129 , 39.048]
48	NGC 4552	0.724 [0.424 , 0.809]	0.633 [0.191 , 0.848]	39.545 [39.311 , 39.594]	39.249 [38.799 , 39.377]
49	NGC 4589 ..... (*)	0.092 [0.048 , 0.138]	0.141 [0.068 , 0.216]	38.754 [38.460 , 38.933]	38.917 [38.635 , 39.094]
50	NGC 4579	12.384 [10.648 , 12.375]	43.878 [41.562 , 45.853]	40.897 [40.836 , 40.895]	41.175 [41.148 , 41.193]
51	NGC 4596 ..... (*)	0.056 [0.012 , 0.100]	0.086 [0.021 , 0.152]	38.305 [37.581 , 38.546]	38.467 [37.755 , 38.724]
52	NGC 4594	2.252 [1.898 , 2.529]	8.018 [7.219 , 8.915]	39.637 [39.565 , 39.690]	39.973 [39.921 , 40.019]
53	NGC 4636 ..... (*)	0.414 [0.360 , 0.467]	0.632 [0.549 , 0.719]	39.051 [38.990 , 39.107]	39.214 [39.150 , 39.269]
54	NGC 4676A .... (*)	0.049 [0.025 , 0.073]	0.074 [0.035 , 0.110]	39.687 [39.398 , 39.855]	39.855 [39.577 , 40.017]
55	NGC 4676B..... (*)	0.094 [0.063 , 0.123]	0.141 [0.093 , 0.187]	39.967 [39.789 , 40.081]	40.135 [39.962 , 40.255]
56	NGC 4698 ..... (*)	0.106 [0.074 , 0.140]	0.162 [0.112 , 0.216]	38.581 [38.432 , 38.704]	38.744 [38.589 , 38.864]
57	NGC 4696	2.436 [0.223 , 3.070]	0.412 [0.102 , 0.632]	41.595 [40.626 , 41.690]	39.978 [39.270 , 40.156]
58	NGC 4736	1.166 [0.832 , 1.295]	1.317 [0.955 , 1.545]	38.758 [38.617 , 38.803]	38.599 [38.469 , 38.671]
60	NGC 5055	0.184 [0.041 , 0.241]	0.091 [0.043 , 0.130]	38.595 [38.065 , 38.712]	37.778 [37.434 , 37.925]
61	MRK 266NE	0.249 [0.114 , 0.330]	2.154 [0.242 , 3.479]	41.026 [40.719 , 41.144]	41.656 [40.784 , 41.865]
62	UGC 08696	0.251 [0.000 , 0.337]	5.366 [0.287 , 6.197]	43.189 [41.877 , 43.318]	42.993 [41.713 , 43.052]
63	CGCG 162-010	0.867 [0.459 , 1.125]	0.274 [0.184 , 0.362]	41.958 [41.813 , 42.014]	41.426 [41.254 , 41.536]
66	IRAS 14348-1447(*)	0.045 [0.012 , 0.078]	0.081 [0.026 , 0.139]	40.910 [40.419 , 41.149]	41.097 [40.529 , 41.329]
67	NGC 5746	0.184 [0.044 , 0.239]	1.528 [0.499 , 2.006]	39.715 [39.018 , 39.828]	40.223 [39.767 , 40.340]
68	NGC 5813	0.614 [0.196 , 0.716]	0.043 [0.012 , 0.073]	40.412 [39.914 , 40.446]	38.770 [38.271 , 38.995]
69	NGC 5838 ..... (*)	0.100 [0.051 , 0.148]	0.163 [0.084 , 0.237]	39.042 [38.747 , 39.207]	39.206 [38.907 , 39.381]
70	NGC 5846	0.772 [0.047 , 0.899]	9.440 [0.000 , 2306.310]	40.224 [39.389 , 40.292]	40.814 [0.000 , 43.243]
71	NGC 5866 ..... (*)	0.046 [0.026 , 0.068]	0.070 [0.036 , 0.102]	38.133 [37.872 , 38.296]	38.296 [38.023 , 38.461]
72	MRK 0848 ..... (*)	0.160 [0.105 , 0.216]	0.246 [0.162 , 0.335]	40.763 [40.575 , 40.895]	40.938 [40.747 , 41.064]
73	NGC 6251	2.168 [0.890 , 2.144]	3.618 [2.702 , 4.271]	41.463 [41.048 , 41.460]	41.583 [41.451 , 41.655]
74	NGC 6240	1.447 [1.044 , 1.719]	10.400 [7.106 , 12.029]	42.219 [42.070 , 42.298]	42.408 [42.220 , 42.473]
75	IRAS 17208-0014 ..	0.073 [0.007 , 0.100]	0.396 [0.207 , 0.529]	40.817 [40.333 , 40.947]	41.188 [40.861 , 41.323]
76	NGC 6482	0.684 [0.408 , 0.829]	0.055 [0.030 , 0.073]	40.697 [40.477 , 40.781]	39.335 [39.080 , 39.470]
77	NGC 7130	1.348 [0.699 , 1.555]	0.927 [0.462 , 1.101]	41.756 [41.455 , 41.817]	40.795 [40.501 , 40.877]
79	NGC 7331 ..... (*)	0.075 [0.048 , 0.103]	0.137 [0.087 , 0.192]	38.294 [38.102 , 38.426]	38.456 [38.249 , 38.595]
80	IC 1459	2.921 [2.072 , 4.829]	5.208 [2.485 , 6.574]	40.599 [40.431 , 40.809]	40.511 [40.137 , 40.605]
81	NPM1G -12.0625 ..	0.415 [0.050 , 0.479]	0.176 [0.000 , 46.655]	42.601 [41.070 , 42.658]	41.463 [0.000 , 43.852]

(*) Fluxes and luminosities assuming a power-law model with an index of 1.8 and galactic absorption.

Table 3.13: *Power-Law model applied to* XMM-Newton *spectra*

Num	Name	N_H (10^{22} cm^{-2})	Γ	χ^2	d.o.f	χ^2_r
(1)	(2)	(3)	(4)	(5)	(6)	(7)
1	NGC 0315 ..... U	0.09 [0.07, 0.10]	2.19 [2.13, 2.23]	1965.49	393	5.00
2	NGC 0410 ..... U	1.24 [1.23, 1.25]	10.00 [9.90, 0.00]	1075.43	181	5.94
7	NGC 0835 ..... U	0.78 [0.64, 0.88]	8.08 [6.92, 8.78]	222.00	117	1.90
8	NGC 1052 ..... U	0.00 [0.00, 0.00]	0.31 [0.29, 0.34]	2880.72	745	3.87
9	NGC 2639 ..... U	0.72 [0.45, 1.14]	5.93 [4.60, 0.00]	181.12	145	1.25
10	NGC 2655 ..... U	0.67 [0.48, 0.83]	6.93 [5.57, 8.07]	317.76	115	2.76
13	UGC 4881 ..... U	0.99 [0.90, 1.11]	10.00 [0.00, 10.00]	22.45	16	1.40
14	3C 218 ..... U	0.12 [0.11, 0.12]	2.31 [2.29, 2.33]	1662.44	842	1.97
15	NGC 2787	0.04 [0.01, 0.08]	1.96 [1.81, 2.17]	152.15	102	1.49
16	NGC 2841 ..... U	0.00 [0.00, 0.04]	2.19 [2.10, 2.39]	227.60	143	1.59
17	UGC0 5101 ..... U	0.00 [0.00, 0.05]	1.16 [1.04, 1.35]	64.70	25	2.59
19	NGC 3226	0.44 [0.38, 0.47]	1.58 [1.48, 1.65]	213.57	181	1.18
28	NGC 3628	0.46 [0.41, 0.52]	1.61 [1.53, 1.68]	264.36	247	1.07
29	NGC 3690B ..... U	0.18 [0.17, 0.20]	2.65 [2.56, 2.76]	770.18	239	3.22
32	NGC 3998	0.02 [0.02, 0.03]	1.87 [1.84, 1.89]	668.69	631	1.06
35	NGC 4125 ..... U	1.07 [1.05, 1.09]	9.97 [9.47, 9.93]	680.60	394	1.73
37	NGC 4261 ..... U	1.17 [1.08, 1.18]	9.73 [9.16, 0.00]	2099.52	259	8.11
38	NGC 4278	0.03 [0.02, 0.04]	2.06 [2.04, 2.10]	625.65	577	1.08
39	NGC 4314 ..... U	0.15 [0.07, 0.30]	3.91 [3.68, 4.60]	99.53	45	2.21
40	NGC 4321	0.22 [0.17, 0.25]	3.72 [3.38, 3.93]	312.64	214	1.46
47	NGC 4494	0.00 [0.00, 0.02]	1.83 [1.73, 1.95]	55.46	51	1.09
48	NGC 4552 ..... U	0.83 [0.78, 0.89]	7.89 [7.57, 8.30]	1624.91	459	3.54
50	NGC 4579	0.00 [0.00, 0.01]	1.96 [1.93, 1.99]	822.24	609	1.35
52	NGC 4594	0.11 [0.10, 0.13]	1.90 [1.85, 1.94]	304.12	290	1.05
53	NGC 4636 ..... U	1.09 [1.09, 1.10]	10.00 [9.96, 0.00]	2947.97	244	12.08
58	NGC 4736 ..... U	0.03 [0.02, 0.05]	2.14 [2.07, 2.21]	924.17	376	2.46
59	NGC 5005 ..... U	0.20 [0.15, 0.25]	3.07 [2.84, 3.44]	227.32	75	3.03
61	MRK 266NE .... U	0.32 [0.28, 0.40]	4.78 [4.26, 5.32]	327.38	106	3.09
62	UGC 08696 ..... U	0.00 [0.00, 0.02]	2.02 [1.92, 2.24]	223.85	52	4.30
63	CGCG 162-010 .. U	0.11 [0.11, 0.12]	2.18 [2.17, 2.19]	2740.96	1190	2.30
64	NGC 5363 ..... U	0.01 [0.00, 0.05]	2.16 [2.01, 2.38]	191.60	85	2.25
65	IC 4395 ..... U	0.39 [0.27, 0.57]	5.25 [4.12, 6.79]	46.04	25	1.84
66	IRAS 14348-1447 U	0.11 [0.00, 0.25]	2.69 [1.98, 3.30]	15.08	31	0.49
68	NGC 5813 ..... U	1.14 [1.13, 1.14]	10.00 [9.97, 10.00]	3577.37	267	13.40
70	NGC 5846 ..... U	1.15 [1.14, 1.16]	10.00 [9.97, 10.00]	3228.05	229	14.10
72	MRK 0848	0.07 [0.00, 0.19]	2.26 [1.73, 2.75]	31.18	42	0.74
73	NGC 6240	0.06 [0.05, 0.06]	1.95 [1.93, 1.97]	958.27	865	1.11
74	NGC 6251 ..... U	0.16 [0.14, 0.18]	1.95 [1.87, 2.04]	722.31	328	2.20
75	IRAS 17208-0014 .	0.31 [0.03, 0.82]	3.34 [1.89, 5.70]	40.43	33	1.23
76	NGC 6482 ..... U	1.18 [1.16, 1.19]	9.99 [9.71, 9.99]	520.30	113	4.60
78	NGC 7285	0.27 [0.21, 0.37]	1.24 [1.18, 1.39]	83.27	61	1.37
80	IC 1459 ..... U	0.11 [0.10, 0.12]	2.15 [2.10, 2.19]	537.13	313	1.72
81	NPM1G -12.0625 U	0.14 [0.13, 0.14]	2.39 [2.38, 2.40]	3663.28	1220	3.00
82	NGC 7743 ..... U	0.03 [0.00, 0.15]	2.66 [2.21, 3.81]	59.37	28	2.12

Table 3.14: *MEKAL model applied to* XMM-Newton *spectra*

Num	Name	N_H (10^{22} cm^{-2})	kT (keV)	χ^2	d.o.f	χ^2_r
(1)	(2)	(3)	(4)	(5)	(6)	(7)
1	NGC 0315 ..... U	0.00 [0.00, 0.00]	5.73 [5.46, 6.46]	2523.83	396	6.37
2	NGC 0410	0.14 [0.12, 0.18]	0.68 [0.67, 0.69]	275.01	184	1.49
7	NGC 0835 ..... U	0.59 [0.56, 0.64]	0.20 [0.19, 0.21]	261.62	120	2.18
8	NGC 1052 ..... U	3.35 [3.22, 3.51]	70.00 [68.83, 0.00]	7004.56	748	9.36
9	NGC 2639	0.80 [0.67, 0.92]	0.18 [0.15, 0.24]	180.55	148	1.22
10	NGC 2655 ..... U	0.00 [0.00, 0.00]	7.80 [5.55, 10.68]	529.01	118	4.48
13	UGC 4881	0.61 [0.32, 0.79]	0.19 [0.15, 0.29]	21.71	19	1.14
14	3C 218 ..... U	0.00 [0.00, 0.00]	3.22 [3.19, 3.28]	2119.15	845	2.51
15	NGC 2787 ..... U	0.00 [0.00, 0.00]	6.35 [5.06, 7.27]	228.27	105	2.17
16	NGC 2841 ..... U	0.00 [0.00, 0.00]	4.40 [3.69, 4.78]	450.64	146	3.09
17	UGC0 5101 ..... U	1.01 [0.89, 1.12]	0.62 [0.56, 0.71]	233.11	28	8.33
19	NGC 3226 ..... U	0.29 [0.27, 0.32]	30.56 [22.41, 42.39]	249.00	184	1.35
28	NGC 3628 ..... U	0.35 [0.32, 0.39]	13.60 [10.67, 18.04]	282.57	250	1.13
29	NGC 3690B ..... U	0.00 [0.00, 0.00]	3.96 [3.55, 4.10]	1204.55	242	4.98
32	NGC 3998 ..... U	0.00 [0.00, 0.00]	4.31 [4.24, 4.42]	2830.24	634	4.46
35	NGC 4125	0.31 [0.27, 0.36]	0.31 [0.29, 0.33]	538.27	397	1.36
37	NGC 4261 ..... U	0.00 [0.00, 0.00]	2.75 [2.65, 2.89]	3971.31	262	15.16
38	NGC 4278 ..... U	0.00 [0.00, 0.00]	3.50 [3.44, 3.57]	3072.79	580	5.30
39	NGC 4314 ..... U	0.00 [0.00, 0.00]	4.21 [3.27, 5.25]	306.68	48	6.39
40	NGC 4321 ..... U	0.73 [0.70, 0.76]	0.18 [0.18, 0.19]	774.59	217	3.57
47	NGC 4494 ..... U	0.90 [0.74, 1.05]	1.29 [1.17, 1.39]	422.02	54	7.82
48	NGC 4552 ..... U	0.00 [0.00, 0.00]	2.64 [2.50, 2.71]	5105.04	462	11.05
50	NGC 4579 ..... U	0.00 [0.00, 0.00]	4.28 [4.19, 4.39]	3340.38	612	5.46
52	NGC 4594 ..... U	0.00 [0.00, 0.01]	6.83 [6.38, 7.28]	546.43	293	1.86
53	NGC 4636 ..... U	0.00 [0.00, 0.00]	0.53 [0.52, 0.54]	538.79	247	2.18
58	NGC 4736 ..... U	0.00 [0.00, 0.00]	4.19 [4.05, 4.45]	1860.58	379	4.91
59	NGC 5005 ..... U	0.00 [0.00, 0.00]	3.01 [2.69, 3.39]	368.69	78	4.73
61	MRK 266NE .... U	0.00 [0.00, 0.00]	3.13 [2.73, 3.61]	840.04	109	7.71
62	UGC 08696 ..... U	0.00 [0.00, 0.00]	8.51 [5.58, 10.44]	369.66	55	6.72
63	CGCG 162-010 .. U	0.00 [0.00, 0.00]	3.92 [3.87, 3.95]	3097.01	1193	2.60
64	NGC 5363 ..... U	0.00 [0.00, 0.00]	5.03 [4.12, 5.79]	306.42	88	3.48
65	IC 4395 ..... U	0.65 [0.58, 0.74]	0.19 [0.18, 0.24]	58.76	28	2.10
66	IRAS 14348-1447 .	0.00 [0.00, 0.04]	3.67 [2.50, 6.46]	25.23	34	0.74
68	NGC 5813 ..... U	0.01 [0.00, 0.03]	0.60 [0.59, 0.61]	454.92	270	1.68
70	NGC 5846 ..... U	0.02 [0.00, 0.03]	0.62 [0.61, 0.63]	549.38	232	2.37
72	MRK 0848 ..... U	0.72 [0.53, 0.98]	0.53 [0.42, 0.62]	74.65	45	1.66
73	NGC 6240 ..... U	0.00 [0.00, 0.00]	4.43 [4.37, 4.52]	3304.82	868	3.81
74	NGC 6251 ..... U	0.06 [0.05, 0.07]	7.15 [6.51, 7.96]	1010.60	331	3.05
75	IRAS 17208-0014 .	0.75 [0.47, 0.99]	0.64 [0.46, 0.79]	38.53	36	1.07
76	NGC 6482	0.10 [0.06, 0.13]	0.67 [0.65, 0.68]	142.04	116	1.22
78	NGC 7285 ..... U	0.28 [0.23, 0.33]	69.49 [30.44, 0.00]	85.07	64	1.33
80	IC 1459 ..... U	0.00 [0.00, 0.00]	4.13 [4.00, 4.40]	979.63	316	3.10
81	NPM1G -12.0625U	0.00 [0.00, 0.00]	3.12 [3.11, 3.16]	4624.02	1223	3.78
82	NGC 7743 ..... U	0.00 [0.00, 0.01]	4.82 [3.77, 8.99]	98.09	31	3.16

Table 3.15: Power-Law plus Power-Law model applied to *XMM-Newton* spectra.

Num	Name	N_{H1} (10^{22} cm^{-2})	N_{H2} (10^{22} cm^{-2})	Γ	A_{PL1}	A_{PL2}	χ^2	d.o.f	χ^2_r
(1)	(2)	(3)	(4)	(5)	(6)	(7)	(8)	(9)	(10)
1	NGC 0315 ..... U	$0.52^{0.56}_{0.48}$	$8.47^{8.90}_{7.96}$	$5.34^{5.64}_{5.01}$	8.97e-04 $^{1.01e-03}_{7.86e-04}$	3.47e-02 $^{4.97e-02}_{2.31e-02}$	1446.91	391	3.70
2	NGC 0410 ..... U	$1.24^{1.25}_{1.23}$	$2746.30^{0.00}_{2506.31}$	$10.00^{0.00}_{9.90}$	7.96e-03 $^{8.20e-03}_{7.64e-03}$	6.13e+15 $^{1.14e+17}_{0.00e+00}$	1075.42	179	6.01
7	NGC 0835 ..... U	$0.92^{1.00}_{0.79}$	$9.00^{11.20}_{7.17}$	$9.09^{9.98}_{8.09}$	3.95e-04 $^{4.96e-04}_{2.68e-04}$	6.71e-02 $^{1.84e-01}_{2.79e-02}$	196.39	115	1.71
8	NGC 1052	$0.00^{0.00}_{0.00}$	$11.18^{11.65}_{10.76}$	$1.59^{1.63}_{1.55}$	1.29e-04 $^{1.32e-04}_{1.27e-04}$	1.27e-03 $^{1.39e-03}_{1.18e-03}$	975.92	743	1.31
9	NGC 2639 ..... U	$1.15^{1.23}_{0.51}$	$5.74^{9.08}_{2.01}$	$9.79^{0.00}_{5.22}$	1.39e-03 $^{1.84e-03}_{0.00e+00}$	6.07e-02 $^{2.08e-01}_{6.47e-03}$	179.48	143	1.26
10	NGC 2655 ..... U	$0.51^{0.68}_{0.40}$	$56.08^{70.02}_{46.86}$	$5.72^{7.16}_{5.08}$	4.60e-04 $^{7.59e-04}_{3.35e-04}$	2.06e+00 $^{1.95e+01}_{7.34e-01}$	159.95	113	1.42
13	UGC 4881 ..... U	$0.54^{1.03}_{0.18}$	$42.82^{0.00}_{0.00}$	$4.92^{0.00}_{3.43}$	3.87e-05 $^{1.52e-04}_{1.53e-05}$	8.65e-02 $^{6.62e-01}_{0.00e+00}$	21.08	14	1.51
14	3C 218 ..... U	$0.00^{0.01}_{0.00}$	$0.33^{0.36}_{0.30}$	$2.47^{2.50}_{2.44}$	1.33e-03 $^{1.46e-03}_{1.28e-03}$	3.41e-03 $^{3.53e-03}_{3.26e-03}$	1562.84	865	1.98
15	NGC 2787	$0.20^{0.22}_{0.12}$	$4.47^{5.92}_{3.37}$	$3.14^{3.48}_{2.60}$	7.67e-05 $^{8.22e-05}_{6.10e-05}$	2.76e-04 $^{4.74e-04}_{8.73e-05}$	141.04	100	1.41
16	NGC 2841	$0.23^{0.33}_{0.20}$	$6.26^{7.70}_{5.24}$	$3.92^{4.84}_{3.66}$	1.22e-04 $^{1.73e-04}_{1.03e-04}$	1.35e-03 $^{4.35e-03}_{6.83e-04}$	185.43	141	1.32
17	UGC0 5101 ..... U	$0.15^{0.23}_{0.08}$	$54.25^{76.96}_{27.85}$	$1.99^{2.15}_{1.57}$	1.66e-05 $^{2.28e-05}_{1.33e-05}$	2.02e-04 $^{3.48e-04}_{6.79e-05}$	39.67	23	1.72
19	NGC 3226	$0.21^{0.30}_{0.11}$	$1.22^{1.76}_{0.94}$	$1.92^{2.12}_{1.80}$	7.41e-05 $^{1.18e-04}_{4.21e-05}$	2.46e-04 $^{3.43e-04}_{2.01e-04}$	169.21	179	0.95
28	NGC 3628 ..... U	$0.42^{3.45}_{0.22}$	$1.41^{0.00}_{0.00}$	$1.71^{1.89}_{1.56}$	1.08e-04 $^{2.05e-04}_{6.61e-05}$	3.51e-05 $^{1.34e-04}_{0.00e+00}$	263.04	245	1.07
29	NGC 3690B ..... U	$0.44^{0.48}_{0.40}$	$10.34^{11.76}_{9.19}$	$4.38^{4.64}_{4.12}$	1.16e-03 $^{1.30e-03}_{1.03e-03}$	1.50e-02 $^{2.19e-02}_{1.00e-02}$	542.00	237	2.29
32	NGC 3998	$0.04^{0.06}_{0.02}$	$3.48^{5.00}_{2.09}$	$1.99^{2.12}_{1.87}$	3.41e-03 $^{3.58e-03}_{3.29e-03}$	6.85e-04 $^{1.51e-03}_{3.39e-04}$	665.84	629	1.06
35	NGC 4125 ..... U	$9.99^{12.18}_{8.45}$	$1.07^{1.08}_{1.05}$	$9.98^{0.00}_{9.58}$	6.60e-01 $^{1.42e+00}_{3.05e-01}$	1.79e-03 $^{1.87e-03}_{1.62e-03}$	680.55	392	1.74
37	NGC 4261 ..... U	$1.01^{1.09}_{0.94}$	$41.94^{46.41}_{37.63}$	$8.74^{9.23}_{8.27}$	4.03e-03 $^{4.92e-03}_{3.32e-03}$	5.93e+01 $^{1.46e+02}_{2.48e+01}$	1403.70	257	5.46
38	NGC 4278	$0.06^{0.08}_{0.05}$	$7.23^{10.14}_{5.27}$	$2.28^{2.40}_{2.20}$	8.86e-04 $^{9.33e-04}_{8.50e-04}$	4.12e-04 $^{6.54e-04}_{2.47e-04}$	605.03	575	1.05
39	NGC 4314 ..... U	$0.42^{0.64}_{0.31}$	$7.55^{11.24}_{5.37}$	$6.12^{8.57}_{4.86}$	1.01e-04 $^{1.94e-04}_{3.67e-05}$	7.31e-03 $^{3.32e-02}_{2.07e-03}$	71.86	43	1.67
40	NGC 4321 ..... U	$0.42^{0.50}_{0.39}$	$7.56^{8.67}_{6.49}$	$5.25^{5.75}_{4.80}$	4.17e-04 $^{5.11e-04}_{3.45e-04}$	7.63e-03 $^{1.41e-02}_{3.86e-03}$	243.44	212	1.15
47	NGC 4494	$0.01^{0.11}_{0.00}$	$2.81^{7.93}_{1.55}$	$2.17^{2.70}_{1.87}$	2.91e-05 $^{3.48e-05}_{1.97e-05}$	2.99e-05 $^{1.03e-04}_{5.75e-06}$	51.11	49	1.04
48	NGC 4552 ..... U	$1.13^{1.14}_{1.13}$	$9.85^{10.25}_{9.23}$	$10.00^{0.00}_{9.71}$	8.17e-03 $^{8.32e-03}_{8.00e-03}$	2.83e+00 $^{3.21e+00}_{2.51e+00}$	1170.82	457	2.56
50	NGC 4579	$0.08^{0.09}_{0.06}$	$8.29^{9.92}_{7.14}$	$2.47^{2.57}_{2.37}$	1.57e-03 $^{1.64e-03}_{1.50e-03}$	2.15e-03 $^{2.73e-03}_{1.67e-03}$	690.09	607	1.14
52	NGC 4594	$0.17^{0.19}_{0.14}$	$3.38^{4.20}_{2.61}$	$2.39^{2.58}_{2.09}$	5.26e-04 $^{5.75e-04}_{4.70e-04}$	4.74e-04 $^{8.15e-04}_{1.71e-04}$	294.63	288	1.02
53	NGC 4636 ..... U	$1.09^{1.10}_{1.09}$	$10.49^{11.69}_{9.23}$	$10.00^{0.00}_{9.96}$	1.67e-02 $^{1.72e-02}_{1.63e-02}$	1.39e+00 $^{1.96e+00}_{8.44e-01}$	2947.99	2421	2.18
58	NGC 4736 ..... U	$0.59^{0.64}_{0.51}$	$2.06^{2.56}_{1.74}$	$6.37^{6.72}_{5.60}$	2.55e-03 $^{2.87e-03}_{1.99e-03}$	9.42e-04 $^{1.20e-03}_{7.05e-04}$	501.53	373	1.34
59	NGC 5005 ..... U	$0.53^{0.61}_{0.44}$	$11.98^{15.04}_{9.78}$	$5.34^{5.59}_{4.78}$	7.54e-04 $^{9.72e-04}_{5.91e-04}$	2.93e-02 $^{6.46e-02}_{1.95e-02}$	121.14	73	1.66
61	MRK 266NE .... U	$0.38^{0.44}_{0.29}$	$27.97^{39.74}_{20.12}$	$4.78^{5.59}_{4.56}$	2.56e-04 $^{3.19e-04}_{2.08e-04}$	4.44e-02 $^{5.99e-02}_{2.70e-02}$	213.26	104	2.05
62	UGC 08696 ..... U	$0.13^{0.17}_{0.06}$	$65.44^{83.07}_{49.97}$	$2.98^{3.19}_{2.61}$	6.40e-05 $^{7.97e-05}_{5.17e-05}$	4.69e-03 $^{6.29e-03}_{1.94e-03}$	98.76	50	1.98
63	CGCG 162-010 .. U	$0.00^{0.01}_{0.00}$	$0.31^{0.32}_{0.29}$	$2.29^{2.30}_{2.27}$	1.58e-03 $^{1.71e-03}_{1.55e-03}$	3.65e-03 $^{3.73e-03}_{3.51e-03}$	2425.64	1188	2.04
64	NGC 5363 ..... U	$0.35^{0.55}_{0.30}$	$7.13^{8.77}_{6.04}$	$4.66^{6.17}_{4.30}$	1.67e-04 $^{3.04e-04}_{1.38e-04}$	8.82e-03 $^{2.19e-02}_{7.53e-03}$	136.99	83	1.65

Table 3.15: Continuation

Num	Name	N_{H1} (10^{22} cm^{-2})	N_{H2} (10^{22} cm^{-2})	Γ	A_{PL1}	A_{PL2}	χ^2	d.o.f	χ^2_r
(1)	(2)	(3)	(4)	(5)	(6)	(7)	(8)	(9)	(10)
65	IC 4395 . . . . . U	$1.62^{1.64}_{1.61}$	$0.18^{0.18}_{0.17}$	$10.00^{0.00}_{9.97}$	3.72e-02 $^{3.86e-02}_{3.49e-02}$	1.25e-03 $^{1.34e-03}_{1.22e-03}$	4352.93	507	1.54
66	IRAS 14348-1447 U	$0.24^{0.91}_{0.00}$	$4.06^{0.00}_{0.00}$	$3.75^{7.91}_{1.71}$	2.48e-05 $^{1.09e-04}_{0.00e+00}$	8.62e-05 $^{4.67e-04}_{0.00e+00}$	13.96	29	0.48
68	NGC 5813 . . . . . U	$1.13^{1.14}_{1.13}$	$11.18^{12.34}_{10.34}$	$10.00^{10.00}_{9.99}$	1.51e-02 $^{1.55e-02}_{1.49e-02}$	1.45e+00 $^{2.01e+00}_{1.04e+00}$	3454.26	2651	3.03
70	NGC 5846 . . . . . U	$1.15^{1.15}_{1.14}$	$11.95^{12.77}_{11.34}$	$10.00^{0.00}_{9.98}$	1.36e-02 $^{1.39e-02}_{1.34e-02}$	2.17e+00 $^{2.64e+00}_{1.70e+00}$	2942.86	2271	2.96
72	MRK 0848	$0.11^{0.21}_{0.00}$	$262.62^{9419.50}_{169.53}$	$2.52^{3.03}_{2.11}$	2.29e-05 $^{2.82e-05}_{1.56e-05}$	6.21e-03 $^{2.52e-02}_{1.13e-05}$	29.22	40	0.73
73	NGC 6240	$0.08^{0.09}_{0.07}$	$13.54^{36.22}_{9.51}$	$2.09^{2.16}_{2.07}$	1.37e-03 $^{1.41e-03}_{1.33e-03}$	4.81e-04 $^{6.64e-04}_{3.22e-04}$	927.73	863	1.08
74	NGC 6251 . . . . . U	$0.22^{0.25}_{0.20}$	$144.09^{166.26}_{122.40}$	$2.31^{2.41}_{2.20}$	4.59e-04 $^{4.96e-04}_{4.26e-04}$	1.81e-02 $^{2.54e-02}_{1.19e-02}$	542.38	326	1.66
75	IRAS 17208-0014 U	$0.53^{0.95}_{0.16}$	$38.35^{96.50}_{21.98}$	$4.65^{7.39}_{3.48}$	5.35e-05 $^{1.26e-04}_{2.11e-05}$	8.02e-03 $^{2.96e-02}_{6.78e-04}$	36.93	31	1.19
76	NGC 6482 . . . . . U	$1.17^{1.18}_{1.15}$	$9.25^{10.90}_{7.99}$	$10.00^{9.99}_{9.88}$	1.22e-02 $^{1.27e-02}_{1.15e-02}$	6.60e-01 $^{1.04e+00}_{3.48e-01}$	471.82	111	4.25
78	NGC 7285	$0.08^{0.19}_{0.00}$	$1.33^{2.39}_{0.76}$	$1.69^{1.78}_{1.55}$	2.58e-05 $^{4.47e-05}_{1.72e-05}$	9.51e-05 $^{1.67e-04}_{6.41e-05}$	60.07	59	1.02
80	IC 1459	$0.30^{0.33}_{0.26}$	$6.61^{7.30}_{5.98}$	$3.52^{3.69}_{3.27}$	5.62e-04 $^{6.11e-04}_{5.03e-04}$	3.02e-03 $^{4.07e-03}_{1.97e-03}$	414.15	311	1.33
81	NPM1G -12.0625 U	$0.00^{0.00}_{0.00}$	$0.33^{0.35}_{0.32}$	$2.53^{2.55}_{2.51}$	9.09e-04 $^{9.58e-04}_{8.96e-04}$	2.77e-03 $^{2.82e-03}_{2.71e-03}$	3226.58	1218	2.65
82	NGC 7743 . . . . . U	$0.39^{0.58}_{0.14}$	$7.88^{13.01}_{4.05}$	$5.61^{8.35}_{3.53}$	7.71e-05 $^{1.35e-04}_{3.79e-05}$	5.03e-03 $^{6.17e-02}_{2.43e-03}$	51.82	26	1.99

Table 3.16: Power-Law+MEKAL model applied to *XMM-Newton* spectra.

Num	Name	N_{H1} (10^{22} cm^{-2})	N_{H2} (10^{22} cm^{-2})	Γ	kT (keV)	A_{ME}	A_{PL}	χ^2	d.o.f	χ^2_r
(1)	(2)	(3)	(4)	(5)	(6)	(7)	(8)	(9)	(10)	(11)
1	NGC 0315	$0.00^{0.01}_{0.00}$	$0.34^{0.59}_{0.18}$	$1.65^{1.81}_{1.51}$	$0.58^{0.59}_{0.56}$	1.19e-04 $^{1.24e-04}_{1.05e-04}$	1.65e-04 $^{1.94e-04}_{1.55e-04}$	410.54	390	1.05
2	NGC 0410	$0.12^{0.17}_{0.09}$	$0.00^{0.20}_{0.00}$	$2.43^{3.17}_{1.92}$	$0.69^{0.71}_{0.67}$	3.59e-04 $^{3.79e-04}_{3.15e-04}$	2.71e-05 $^{6.25e-05}_{2.07e-05}$	218.34	178	1.23
7	NGC 0835	$0.24^{0.42}_{0.14}$	$0.00^{0.05}_{0.00}$	$1.34^{2.62}_{0.78}$	$0.24^{0.25}_{0.22}$	1.63e-05 $^{3.08e-05}_{1.48e-05}$	1.60e-05 $^{2.13e-05}_{1.37e-05}$	156.89	114	1.38
8	NGC 1052 ..... U	$0.00^{0.00}_{0.00}$	$1.06^{1.12}_{0.86}$	$0.45^{0.46}_{0.36}$	$0.62^{0.63}_{0.60}$	6.17e-05 $^{6.39e-05}_{5.21e-05}$	1.33e-04 $^{1.36e-04}_{1.16e-04}$	1681.53	742	2.27
9	NGC 2639 ..... U	$0.00^{0.16}_{0.00}$	$387.76^{0.00}_{133.65}$	$-2.25^{0.00}_{0.00}$	$0.68^{0.79}_{0.63}$	4.59e-05 $^{7.39e-05}_{4.05e-05}$	1.43e-06 $^{3.65e+02}_{0.00e+00}$	181.44	142	1.28
10	NGC 2655	$0.68^{0.74}_{0.63}$	$24.11^{37.89}_{14.08}$	$2.22^{3.55}_{1.23}$	$0.19^{0.21}_{0.18}$	5.53e-03 $^{8.70e-03}_{3.28e-03}$	1.73e-03 $^{2.45e-02}_{1.72e-04}$	118.56	112	1.06
13	UGC 4881 ..... U	$0.11^{0.79}_{0.28}$	$4.36^{7.20}_{0.98}$	$1.49^{0.00}_{-3.00}$	$0.24^{0.30}_{0.14}$	5.24e-05 $^{1.35e-03}_{3.63e-05}$	4.22e-03 $^{1.08e-02}_{2.42e-05}$	19.63	13	1.51
14	3C 218	$0.11^{0.17}_{0.06}$	$0.02^{0.03}_{0.01}$	$2.12^{2.18}_{2.08}$	$2.58^{2.81}_{2.34}$	4.24e-03 $^{4.71e-03}_{3.86e-03}$	1.88e-03 $^{2.04e-03}_{1.70e-03}$	987.17	839	1.18
15	NGC 2787	$0.00^{0.56}_{0.00}$	$0.04^{0.09}_{0.00}$	$1.77^{1.96}_{1.63}$	$0.60^{0.70}_{0.24}$	5.74e-06 $^{1.41e-04}_{3.76e-06}$	4.17e-05 $^{4.93e-05}_{3.77e-05}$	132.27	99	1.34
16	NGC 2841	$0.42^{0.50}_{0.16}$	$0.00^{0.03}_{0.00}$	$1.70^{1.93}_{1.59}$	$0.23^{0.31}_{0.19}$	1.98e-04 $^{5.50e-04}_{4.45e-05}$	4.23e-05 $^{4.76e-05}_{3.80e-05}$	161.98	140	1.16
17	UGC0 5101 ..... U	$1.17^{1.31}_{0.53}$	$0.00^{0.23}_{0.00}$	$0.58^{0.78}_{0.11}$	$0.20^{0.32}_{0.14}$	4.98e-04 $^{3.62e-03}_{5.11e-05}$	3.79e-06 $^{5.73e-06}_{2.46e-06}$	33.90	22	1.54
19	NGC 3226 ..... U	$4.55^{9.40}_{2.26}$	$0.34^{0.40}_{0.29}$	$1.87^{2.16}_{-0.21}$	$30.08^{0.00}_{19.73}$	8.59e-04 $^{5.71e-03}_{2.88e-04}$	1.49e-04 $^{1.81e-04}_{1.11e-04}$	204.22	178	1.15
28	NGC 3628 ..... U	$1.31^{12.30}_{0.00}$	$0.42^{0.65}_{0.36}$	$1.66^{2.24}_{1.40}$	$6.97^{0.00}_{0.00}$	8.50e-05 $^{2.11e-04}_{0.00e+00}$	1.09e-04 $^{1.33e-04}_{7.44e-05}$	262.97	244	1.08
29	NGC 3690B	$0.22^{0.31}_{0.13}$	$0.08^{0.12}_{0.05}$	$1.84^{1.94}_{1.75}$	$0.63^{0.65}_{0.60}$	2.29e-04 $^{3.17e-04}_{1.69e-04}$	2.32e-04 $^{2.45e-04}_{2.05e-04}$	262.18	236	1.11
32	NGC 3998	$2.10^{3.20}_{1.06}$	$0.02^{0.02}_{0.01}$	$1.84^{1.86}_{1.80}$	$0.21^{1.67}_{0.00}$	3.32e+03 $^{1.64e+03}_{4.34e+05}$	3.19e-03 $^{3.28e-03}_{3.09e-03}$	666.43	628	1.06
35	NGC 4125	$0.00^{0.02}_{0.00}$	$0.00^{0.03}_{0.00}$	$2.36^{2.80}_{2.15}$	$0.54^{0.57}_{0.52}$	5.90e-05 $^{8.61e-05}_{5.51e-05}$	3.06e-05 $^{3.65e-05}_{2.64e-05}$	400.70	391	1.02
37	NGC 4261 ..... U	$0.43^{0.46}_{0.32}$	$0.00^{0.05}_{0.00}$	$0.68^{0.77}_{0.60}$	$0.32^{0.33}_{0.30}$	1.24e-03 $^{1.42e-03}_{1.05e-03}$	9.39e-05 $^{1.23e-04}_{5.65e-05}$	471.48	256	1.84
38	NGC 4278	$0.39^{0.67}_{0.26}$	$0.01^{0.03}_{0.00}$	$1.99^{2.04}_{1.96}$	$0.65^{0.78}_{0.52}$	8.35e-05 $^{2.17e-04}_{1.04e-05}$	7.32e-04 $^{7.94e-04}_{7.05e-04}$	605.97	574	1.06
39	NGC 4314	$0.27^{0.44}_{0.09}$	$0.00^{0.52}_{0.00}$	$1.46^{1.88}_{1.11}$	$0.24^{0.27}_{0.19}$	1.07e-04 $^{2.89e-04}_{6.71e-05}$	9.74e-06 $^{1.66e-05}_{6.80e-06}$	40.89	42	0.97
40	NGC 4321	$0.44^{0.57}_{0.28}$	$0.00^{0.03}_{0.00}$	$2.24^{2.46}_{2.11}$	$0.29^{0.36}_{0.25}$	3.08e-04 $^{1.11e-03}_{2.35e-04}$	8.27e-05 $^{1.02e-04}_{7.66e-05}$	211.88	211	1.00
47	NGC 4494 ..... U	$0.03^{0.00}_{0.00}$	$0.00^{0.02}_{0.00}$	$1.81^{1.94}_{1.72}$	$0.00^{0.01}_{0.00}$	5.74e+16 $^{1.35e+18}_{0.00e+00}$	2.98e-05 $^{3.25e-05}_{2.81e-05}$	54.78	48	1.14
48	NGC 4552	$0.01^{0.04}_{0.00}$	$0.00^{0.02}_{0.00}$	$1.97^{2.09}_{1.90}$	$0.61^{0.62}_{0.60}$	2.02e-04 $^{2.19e-04}_{1.90e-04}$	1.36e-04 $^{1.51e-04}_{1.29e-04}$	455.11	456	1.00
50	NGC 4579	$0.00^{0.19}_{0.00}$	$0.00^{0.00}_{0.00}$	$1.85^{1.87}_{1.83}$	$0.65^{0.68}_{0.61}$	1.16e-04 $^{1.31e-04}_{1.04e-04}$	1.09e-03 $^{1.11e-03}_{1.09e-03}$	593.91	606	0.98
52	NGC 4594 ..... U	$8012.11^{0.00}_{0.00}$	$0.11^{0.13}_{0.10}$	$1.89^{1.93}_{1.84}$	$7.59^{0.00}_{0.00}$	8.87e-07 $^{0.00e+00}_{0.00e+00}$	4.53e-04 $^{4.81e-04}_{4.34e-04}$	304.20	287	1.06
53	NGC 4636	$0.00^{0.01}_{0.00}$	$0.01^{0.17}_{0.00}$	$2.92^{3.91}_{2.36}$	$0.54^{0.55}_{0.53}$	6.85e-04 $^{7.04e-04}_{6.71e-04}$	1.09e-04 $^{1.90e-04}_{9.40e-05}$	355.63	241	1.48
58	NGC 4736	$0.00^{0.06}_{0.00}$	$0.00^{0.01}_{0.00}$	$1.67^{1.73}_{1.64}$	$0.51^{0.53}_{0.47}$	1.29e-04 $^{1.96e-04}_{1.21e-04}$	3.67e-04 $^{3.82e-04}_{3.55e-04}$	396.45	373	1.06
59	NGC 5005	$0.61^{0.80}_{0.52}$	$0.00^{0.07}_{0.00}$	$1.54^{1.73}_{1.42}$	$0.27^{0.30}_{0.21}$	1.28e-03 $^{3.24e-03}_{8.60e-04}$	7.25e-05 $^{9.09e-05}_{6.24e-05}$	70.67	72	0.98
61	MRK 266NE	$0.57^{0.61}_{0.56}$	$0.00^{0.05}_{0.00}$	$0.96^{1.17}_{0.80}$	$0.19^{0.20}_{0.18}$	3.38e-03 $^{4.18e-03}_{2.56e-03}$	2.10e-05 $^{2.66e-05}_{1.82e-05}$	146.46	103	1.42
62	UGC 08696 ..... U	$0.00^{0.03}_{0.00}$	$0.00^{0.05}_{0.00}$	$0.56^{0.80}_{0.48}$	$0.64^{0.67}_{0.60}$	2.64e-05 $^{3.62e-05}_{2.45e-05}$	1.01e-05 $^{1.30e-05}_{8.84e-06}$	91.17	49	1.86
63	CGCG 162-010 ...	$0.11^{0.14}_{0.09}$	$0.02^{0.03}_{0.01}$	$2.05^{2.08}_{2.01}$	$3.26^{3.38}_{2.98}$	5.98e-03 $^{6.28e-03}_{5.51e-03}$	2.06e-03 $^{2.23e-03}_{1.96e-03}$	1294.32	1187	1.09
64	NGC 5363	$0.00^{0.13}_{0.00}$	$0.00^{0.02}_{0.00}$	$1.59^{1.75}_{1.44}$	$0.53^{0.63}_{0.47}$	2.12e-05 $^{2.70e-05}_{1.80e-05}$	3.69e-05 $^{4.18e-05}_{3.23e-05}$	88.00	82	1.07

Table 3.16: Continuation

Num	Name	N_{H1} (10^{22} cm^{-2})	N_{H2} (10^{22} cm^{-2})	Γ	kT (keV)	A_{ME}	A_{PL}	χ^2	d.o.f	χ^2_r
(1)	(2)	(3)	(4)	(5)	(6)	(7)	(8)	(9)	(10)	(11)
65	IC 4395	$0.00^{0.42}_{0.00}$	$0.00^{0.17}_{0.00}$	$1.78^{4.00}_{1.24}$	$0.26^{0.60}_{0.19}$	8.48e-06 $^{1.63e-04}_{6.43e-06}$	9.98e-06 $^{1.63e-05}_{7.58e-06}$	25.54	22	1.16
66	IRAS 14348-1447U	$0.00^{0.00}_{0.00}$	$0.12^{0.55}_{0.00}$	$2.43^{3.30}_{1.62}$	$0.56^{0.00}_{0.00}$	2.37e-06 $^{4.31e-03}_{0.00e+00}$	1.62e-05 $^{5.58e-05}_{8.06e-06}$	13.66	28	0.49
68	NGC 5813	$0.00^{0.01}_{0.00}$	$0.26^{0.45}_{0.12}$	$3.36^{4.50}_{2.82}$	$0.59^{0.60}_{0.59}$	5.87e-04 $^{6.11e-04}_{5.75e-04}$	1.07e-04 $^{2.24e-04}_{7.14e-05}$	373.90	264	1.42
70	NGC 5846	$0.01^{0.02}_{0.00}$	$0.00^{0.04}_{0.00}$	$2.25^{2.41}_{2.07}$	$0.61^{0.62}_{0.61}$	5.03e-04 $^{5.18e-04}_{4.84e-04}$	5.66e-05 $^{6.70e-05}_{4.81e-05}$	273.24	226	1.21
72	MRK 0848	$0.01^{11.94}_{0.00}$	$0.04^{0.28}_{0.00}$	$2.02^{4.97}_{1.40}$	$0.31^{0.71}_{0.00}$	2.44e-06 $^{7.36e-05}_{1.60e-08}$	1.57e-05 $^{3.23e-05}_{1.11e-05}$	29.62	39	0.76
73	NGC 6240	$0.83^{0.86}_{0.74}$	$0.00^{0.02}_{0.00}$	$1.12^{1.19}_{1.06}$	$0.61^{0.63}_{0.58}$	9.70e-04 $^{1.09e-03}_{7.88e-04}$	1.25e-04 $^{1.37e-04}_{1.16e-04}$	439.23	325	1.06
74	NGC 6251	$0.63^{0.83}_{0.52}$	$0.05^{0.05}_{0.04}$	$1.89^{1.91}_{1.86}$	$0.35^{0.50}_{0.26}$	4.89e-04 $^{1.56e-03}_{1.27e-04}$	1.18e-03 $^{1.22e-03}_{1.15e-03}$	911.71	862	1.35
75	IRAS 17208-0014	$0.43^{0.77}_{0.00}$	$0.91^{40.66}_{0.00}$	$1.84^{8.21}_{0.40}$	$0.66^{0.81}_{0.19}$	2.97e-05 $^{1.26e-04}_{3.38e-06}$	1.07e-05 $^{5.54e-05}_{6.90e-07}$	33.62	30	1.12
76	NGC 6482 U	$0.00^{0.13}_{0.00}$	$1.76^{2.86}_{0.71}$	$6.33^{7.40}_{3.36}$	$0.67^{0.71}_{0.65}$	4.30e-04 $^{4.97e-04}_{4.13e-04}$	4.04e-03 $^{1.34e-02}_{9.04e-05}$	117.69	110	1.07
78	NGC 7285	$0.68^{0.78}_{0.00}$	$0.87^{1.13}_{0.59}$	$1.66^{1.76}_{1.43}$	$0.13^{0.19}_{0.07}$	2.10e-03 $^{5.28e-03}_{7.10e-04}$	1.13e-04 $^{1.47e-04}_{7.91e-05}$	59.28	58	1.02
80	IC 1459	$0.18^{0.27}_{0.10}$	$0.11^{0.13}_{0.08}$	$1.92^{1.99}_{1.82}$	$0.44^{0.53}_{0.33}$	8.71e-05 $^{2.42e-04}_{7.16e-05}$	2.53e-04 $^{2.73e-04}_{2.24e-04}$	329.27	310	1.06
81	NPM1G -12.0625	$0.14^{0.17}_{0.13}$	$0.03^{0.04}_{0.03}$	$2.28^{2.29}_{2.26}$	$2.66^{2.70}_{2.58}$	3.84e-03 $^{3.93e-03}_{3.67e-03}$	1.43e-03 $^{1.50e-03}_{1.41e-03}$	1557.44	1217	1.28
82	NGC 7743 U	$0.35^{0.58}_{0.18}$	$1.68^{3.63}_{0.81}$	$3.16^{6.47}_{1.49}$	$0.23^{0.29}_{0.18}$	1.60e-04 $^{1.16e-03}_{2.00e-05}$	1.18e-04 $^{1.32e-03}_{1.98e-05}$	43.95	25	1.76

Table 3.17: Power-Law plus MEKAL plus Power-law model applied to *XMM-Newton* spectra.

Num	N_{H1} (10^{22} cm^{-2})	N_{H2} (10^{22} cm^{-2})	Γ	kT (keV)	A_{PL1}	A_{PL2}	A_{ME}	χ^2	d.o.f	χ^2_r
(1)	(3)	(4)	(5)	(6)	(7)	(8)	(9)	(10)	(11)	(12)
1 ...	$0.00^{0.19}_{0.00}$	$0.67^{1.19}_{0.34}$	$1.81^{1.92}_{1.68}$	$0.59^{0.60}_{0.58}$	$2.47e\text{-}05^{1.74e-04}_{1.54e-05}$	$1.83e\text{-}04^{2.30e-04}_{1.37e-04}$	$1.21e\text{-}04^{1.27e-04}_{1.15e-04}$	397.66	389	1.02
2 . U	$0.93^{1.88}_{0.61}$	$12.22^{20.94}_{6.73}$	$5.72^{7.71}_{3.92}$	$0.73^{0.75}_{0.72}$	$4.34e\text{-}04^{1.54e-03}_{1.71e-04}$	$7.96e\text{-}03^{8.75e-02}_{1.14e-03}$	$2.39e\text{-}04^{2.61e-04}_{2.24e-04}$	226.04	177	1.28
7 ...	$0.04^{0.09}_{0.00}$	$69.63^{104.56}_{34.39}$	$2.89^{3.35}_{2.37}$	$0.54^{0.61}_{0.49}$	$1.87e\text{-}05^{3.10e-05}_{1.37e-05}$	$8.58e\text{-}04^{1.86e-03}_{2.28e-04}$	$1.60e\text{-}05^{1.80e-05}_{1.36e-05}$	129.49	113	1.15
8 ...	$0.00^{0.00}_{0.00}$	$9.22^{9.64}_{8.82}$	$1.34^{1.42}_{1.28}$	$0.60^{0.63}_{0.56}$	$1.01e\text{-}04^{1.04e-04}_{9.82e-05}$	$7.57e\text{-}04^{8.74e-04}_{7.02e-04}$	$2.19e\text{-}05^{2.42e-05}_{2.00e-05}$	800.07	741	1.08
9 . U	$0.20^{0.66}_{0.09}$	$999.99^{0.00}_{999.99}$	$3.30^{6.60}_{1.71}$	$0.71^{0.82}_{0.62}$	$5.85e\text{-}05^{1.71e-04}_{1.66e-05}$	$6.32e\text{-}02^{0.00e+00}_{0.00e+00}$	$2.84e\text{-}05^{3.90e-05}_{1.81e-05}$	168.98	141	1.20
10 ..	$0.00^{0.07}_{0.00}$	$30.20^{39.47}_{24.21}$	$2.48^{2.83}_{2.05}$	$0.64^{0.68}_{0.59}$	$4.76e\text{-}05^{7.00e-05}_{3.83e-05}$	$3.20e\text{-}03^{1.27e-02}_{1.69e-03}$	$4.93e\text{-}05^{5.63e-05}_{4.09e-05}$	94.67	111	0.85
13 . U	$0.01^{0.42}_{0.00}$	$1.35^{0.00}_{0.00}$	$2.40^{4.52}_{1.23}$	$0.63^{0.93}_{0.42}$	$4.15e\text{-}06^{5.88e-05}_{2.04e-08}$	$3.18e\text{-}03^{4.19e-02}_{2.31e-05}$	$5.33e\text{-}06^{7.23e-06}_{2.69e-06}$	15.91	12	1.33
14 ..	$0.00^{0.12}_{0.00}$	$0.32^{0.41}_{0.26}$	$2.28^{2.34}_{2.24}$	$2.77^{2.88}_{2.59}$	$1.02e\text{-}03^{1.35e-03}_{9.01e-04}$	$1.35e\text{-}03^{1.54e-03}_{1.04e-03}$	$3.75e\text{-}03^{4.14e-03}_{3.23e-03}$	989.98	863	1.19
15 ..	$0.01^{0.14}_{0.00}$	$1.00^{1.87}_{0.59}$	$2.18^{3.04}_{2.03}$	$0.63^{0.70}_{0.52}$	$2.54e\text{-}05^{7.14e-05}_{1.91e-05}$	$5.10e\text{-}05^{9.07e-05}_{1.76e-05}$	$8.83e\text{-}06^{1.14e-05}_{4.68e-06}$	126.64	98	1.29
16 ..	$0.00^{0.09}_{0.00}$	$3.30^{5.60}_{1.96}$	$2.20^{3.01}_{2.07}$	$0.58^{0.64}_{0.50}$	$4.55e\text{-}05^{5.78e-05}_{2.43e-05}$	$6.11e\text{-}05^{1.39e-04}_{3.02e-05}$	$1.26e\text{-}05^{1.55e-05}_{9.94e-06}$	155.16	139	1.12
17 ..	$0.12^{0.28}_{0.00}$	$118.52^{8450.86}_{33.53}$	$1.48^{1.73}_{0.88}$	$0.97^{1.29}_{0.72}$	$9.53e\text{-}06^{1.68e-05}_{5.00e-06}$	$1.56e\text{-}04^{1.23e-02}_{1.87e-05}$	$3.94e\text{-}06^{6.64e-06}_{2.94e-06}$	29.88	21	1.42
19 . U	$0.24^{0.28}_{0.11}$	$1.44^{1.79}_{0.95}$	$2.03^{2.13}_{1.79}$	$8.42^{0.00}_{0.00}$	$8.70e\text{-}05^{1.16e-04}_{4.03e-05}$	$2.63e\text{-}04^{3.27e-04}_{2.00e-04}$	$0.00e{+}00^{2.87e+16}_{0.00e+00}$	169.52	177	0.96
28 ..	$0.20^{222.58}_{0.00}$	$0.76^{1.04}_{0.47}$	$1.75^{1.91}_{1.61}$	$1.10^{1.52}_{0.85}$	$1.54e\text{-}05^{4.33e-05}_{0.00e+00}$	$1.35e\text{-}04^{1.72e-04}_{4.67e-06}$	$6.29e\text{-}06^{1.07e-05}_{2.01e-06}$	257.84	243	1.06
29 ..	$0.20^{0.25}_{0.17}$	$11.59^{37.29}_{6.84}$	$2.20^{2.63}_{2.09}$	$0.67^{0.69}_{0.65}$	$3.41e\text{-}04^{4.00e-04}_{3.08e-04}$	$2.26e\text{-}04^{5.61e-04}_{4.54e-05}$	$1.09e\text{-}04^{1.18e-04}_{9.99e-05}$	266.86	235	1.14
32 ..	$0.08^{0.11}_{0.04}$	$4.21^{5.48}_{3.28}$	$2.10^{2.32}_{2.02}$	$0.16^{0.20}_{0.02}$	$3.73e\text{-}03^{4.06e-03}_{3.46e-03}$	$1.59e\text{-}03^{3.25e-03}_{6.01e-04}$	$1.65e\text{-}04^{3.90e-03}_{8.27e-05}$	661.17	627	1.05
35 ..	$0.00^{0.14}_{0.00}$	$2.77^{3.87}_{1.93}$	$3.80^{5.33}_{3.06}$	$0.56^{0.58}_{0.54}$	$1.48e\text{-}05^{4.71e-05}_{6.76e-06}$	$3.34e\text{-}04^{1.27e-03}_{1.22e-04}$	$6.32e\text{-}05^{6.68e-05}_{5.85e-05}$	385.00	390	0.99
37 ..	$0.22^{0.32}_{0.14}$	$13.80^{16.20}_{11.73}$	$2.38^{2.65}_{2.01}$	$0.62^{0.63}_{0.61}$	$9.58e\text{-}05^{1.28e-04}_{6.37e-05}$	$7.99e\text{-}04^{1.02e-03}_{6.13e-04}$	$1.67e\text{-}04^{1.74e-04}_{1.61e-04}$	279.85	255	1.10
38 ..	$0.05^{0.07}_{0.03}$	$7.05^{10.66}_{4.55}$	$2.21^{2.32}_{2.08}$	$0.78^{1.12}_{0.57}$	$8.44e\text{-}04^{9.01e-04}_{7.73e-04}$	$2.99e\text{-}04^{5.85e-04}_{6.27e-05}$	$1.10e\text{-}05^{2.28e-05}_{2.71e-06}$	601.94	573	1.05
39 ..	$0.00^{0.05}_{0.00}$	$3.77^{13.63}_{2.41}$	$3.40^{3.72}_{2.85}$	$0.55^{0.61}_{0.48}$	$1.29e\text{-}05^{1.86e-05}_{9.68e-06}$	$1.34e\text{-}04^{3.03e-04}_{5.60e-05}$	$1.12e\text{-}05^{1.33e-05}_{8.24e-06}$	35.83	41	0.87
40 ..	$0.12^{0.16}_{0.06}$	$6.18^{11.79}_{3.56}$	$3.01^{3.42}_{2.58}$	$0.57^{0.62}_{0.49}$	$1.34e\text{-}04^{2.01e-04}_{8.13e-05}$	$2.12e\text{-}04^{1.06e-03}_{3.15e-05}$	$2.55e\text{-}05^{3.02e-05}_{2.02e-05}$	208.96	210	1.00
47 ..	$0.00^{0.06}_{0.00}$	$1.98^{3.47}_{1.12}$	$2.18^{2.85}_{1.95}$	$0.71^{0.85}_{0.58}$	$2.36e\text{-}05^{3.19e-05}_{1.93e-05}$	$3.67e\text{-}05^{8.83e-05}_{1.45e-05}$	$2.95e\text{-}06^{5.04e-06}_{1.02e-06}$	47.11	47	1.00
48 . U	$0.00^{0.13}_{0.00}$	$1.29^{0.00}_{0.00}$	$2.09^{3.01}_{1.70}$	$0.61^{0.62}_{0.60}$	$1.26e\text{-}04^{2.06e-04}_{0.00e+00}$	$4.38e\text{-}05^{2.78e-04}_{0.00e+00}$	$1.99e\text{-}04^{2.06e-04}_{1.90e-04}$	454.21	455	1.00
50 ..	$0.00^{0.00}_{0.00}$	$53.57^{132.93}_{8.74}$	$1.89^{1.93}_{1.86}$	$0.66^{0.69}_{0.63}$	$1.10e\text{-}03^{1.13e-03}_{1.08e-03}$	$6.10e\text{-}04^{2.54e-03}_{2.46e-04}$	$1.12e\text{-}04^{1.23e-04}_{9.70e-05}$	573.09	605	0.95
52 ..	$0.01^{0.16}_{0.00}$	$0.64^{1.40}_{0.43}$	$2.05^{2.18}_{1.95}$	$0.69^{0.75}_{0.65}$	$1.65e\text{-}04^{3.88e-04}_{1.32e-04}$	$4.27e\text{-}04^{5.40e-04}_{2.18e-04}$	$4.81e\text{-}05^{5.89e-05}_{3.55e-05}$	268.48	286	0.94
53 . U	$0.03^{0.07}_{0.01}$	$2525.39^{0.00}_{0.00}$	$2.92^{3.32}_{2.70}$	$0.54^{0.55}_{0.53}$	$1.23e\text{-}04^{1.47e-04}_{9.52e-05}$	$0.00e{+}00^{0.00e+00}_{2.96e+16}$	$6.82e\text{-}04^{6.97e-04}_{6.68e-04}$	355.93	240	1.48
58 ..	$0.13^{0.15}_{0.03}$	$2.12^{4.36}_{1.43}$	$2.79^{3.55}_{1.72}$	$0.53^{0.57}_{0.49}$	$5.55e\text{-}04^{7.71e-04}_{3.58e-04}$	$2.57e\text{-}04^{4.34e-04}_{3.69e-05}$	$1.09e\text{-}04^{1.21e-04}_{8.50e-05}$	390.47	371	1.05
59 ..	$0.26^{0.34}_{0.17}$	$10.74^{15.88}_{7.18}$	$3.23^{3.58}_{3.00}$	$0.64^{0.68}_{0.61}$	$2.21e\text{-}04^{2.78e-04}_{1.64e-04}$	$1.13e\text{-}03^{2.88e-03}_{2.59e-04}$	$4.93e\text{-}05^{6.07e-05}_{4.00e-05}$	69.66	71	0.98
61 ..	$0.00^{0.03}_{0.00}$	$21.97^{32.83}_{14.72}$	$2.69^{2.84}_{2.50}$	$0.65^{0.69}_{0.61}$	$5.61e\text{-}05^{6.47e-05}_{5.10e-05}$	$7.35e\text{-}04^{1.21e-03}_{4.60e-04}$	$3.76e\text{-}05^{4.21e-05}_{3.32e-05}$	111.07	102	1.09
62 ..	$0.00^{0.06}_{0.00}$	$54.73^{76.54}_{39.96}$	$1.82^{1.98}_{1.56}$	$0.69^{0.76}_{0.66}$	$2.52e\text{-}05^{3.35e-05}_{2.18e-05}$	$3.68e\text{-}04^{5.58e-04}_{2.00e-04}$	$1.79e\text{-}05^{2.11e-05}_{1.43e-05}$	45.57	48	0.95
63 ..	$0.00^{0.34}_{0.00}$	$0.24^{0.34}_{0.21}$	$2.13^{2.17}_{2.10}$	$3.39^{3.53}_{3.22}$	$9.34e\text{-}04^{1.48e-03}_{8.72e-04}$	$1.60e\text{-}03^{1.71e-03}_{1.11e-03}$	$5.05e\text{-}03^{5.44e-03}_{4.84e-03}$	1291.60	1186	1.09
64 ..	$0.00^{0.08}_{0.00}$	$2.66^{4.37}_{1.74}$	$2.14^{2.69}_{1.76}$	$0.61^{0.65}_{0.56}$	$3.29e\text{-}05^{4.24e-05}_{2.67e-05}$	$6.66e\text{-}05^{1.41e-04}_{2.60e-05}$	$2.19e\text{-}05^{2.54e-05}_{1.77e-05}$	79.70	81	0.90

Table 3.17: Continuation

Num	N_{H1} (10^{22} cm^{-2})	N_{H2} (10^{22} cm^{-2})	Γ	kT (keV)	A_{PL1}	A_{PL2}	A_{ME}	χ^2	d.o.f	χ^2_r
(1)	(3)	(4)	(5)	(6)	(7)	(8)	(9)	(10)	(11)	(12)
65 . U	$0.06^{0.23}_{0.00}$	$24.12^{0.00}_{0.00}$	$2.70^{4.12}_{1.95}$	$0.57^{0.65}_{0.44}$	1.26e-05$^{1.89e-05}_{7.91e-06}$	6.54e-05$^{7.16e-04}_{0.00e+00}$	7.87e-06$^{1.01e-05}_{5.78e-06}$	22.41	21	1.07
66 . U	$0.09^{1.65}_{0.00}$	$0.88^{11.16}_{0.00}$	$2.72^{9.31}_{1.65}$	$0.58^{0.00}_{0.00}$	1.12e-05$^{6.18e-05}_{0.00e+00}$	1.25e-05$^{8.15e-01}_{0.00e+00}$	3.08e-06$^{7.28e-06}_{0.00e+00}$	13.49	27	0.50
68 . U	$0.31^{0.46}_{0.20}$	$999.99^{0.00}_{999.99}$	$3.67^{4.47}_{2.83}$	$0.59^{0.60}_{0.59}$	1.28e-04$^{1.71e-04}_{8.99e-05}$	1.79e+11$^{0.00e+00}_{0.00e+00}$	5.86e-04$^{6.00e-04}_{5.73e-04}$	373.80	263	1.42
70 . .	$0.14^{0.22}_{0.06}$	$20.30^{33.76}_{8.93}$	$3.12^{3.86}_{2.74}$	$0.62^{0.62}_{0.61}$	1.00e-04$^{1.19e-04}_{7.54e-05}$	4.20e-04$^{5.17e-04}_{3.42e-05}$	4.83e-04$^{4.92e-04}_{4.74e-04}$	267.90	225	1.19
72 . U	$1.03^{0.21}_{1.85}$	$6.74^{5.10}_{8.38}$	$9.89^{8.14}_{1.23}$	$70.00^{0.00}_{0.60}$	1.23e-04$^{1.68e-04}_{5.68e-05}$	4.77e-02$^{0.00e+00}_{8.70e-01}$	2.54e-05$^{4.64e-05}_{2.12e-06}$	24.54	38	0.65
73 . .	$0.07^{0.07}_{0.06}$	$48.69^{107.06}_{24.96}$	$1.97^{2.07}_{1.93}$	$0.58^{0.67}_{0.45}$	1.27e-03$^{1.32e-03}_{1.24e-03}$	4.38e-04$^{8.46e-04}_{2.14e-04}$	2.58e-05$^{3.50e-05}_{1.59e-05}$	911.04	861	1.06
74 . .	$0.23^{0.27}_{0.21}$	$155.52^{179.68}_{134.03}$	$1.93^{2.03}_{1.89}$	$0.87^{0.93}_{0.83}$	3.27e-04$^{3.57e-04}_{2.98e-04}$	8.83e-03$^{1.18e-02}_{5.53e-03}$	7.05e-05$^{7.98e-05}_{6.14e-05}$	388.46	324	1.20
75 . U	$0.45^{4.96}_{0.07}$	$27.51^{0.00}_{0.00}$	$2.64^{7.39}_{1.13}$	$0.73^{0.89}_{0.60}$	2.23e-04$^{1.50e-03}_{6.56e-05}$	4.81e-02$^{1.57e-01}_{1.69e-03}$	7.53e-06$^{1.08e-05}_{4.90e-06}$	32.73	29	1.13
76 . U	$2.41^{2.90}_{1.89}$	$21.90^{0.00}_{6.20}$	$9.87^{0.00}_{6.90}$	$0.68^{0.69}_{0.67}$	1.33e-02$^{2.10e-02}_{8.35e-03}$	1.64e+00$^{5.76e+00}_{0.00e+00}$	4.35e-04$^{4.51e-04}_{4.19e-04}$	114.24	109	1.05
78 . .	$0.20^{102.99}_{0.10}$	$1.66^{12.56}_{0.89}$	$1.73^{1.86}_{1.49}$	$4.31^{14.44}_{2.93}$	1.76e-05$^{1.50e-04}_{0.00e+00}$	1.07e-04$^{1.82e-04}_{0.00e+00}$	4.23e-05$^{2.09e-04}_{0.00e+00}$	58.63	57	1.03
80 . U	$0.12^{0.14}_{0.10}$	$25950.70^{0.00}_{0.00}$	$1.95^{2.01}_{1.89}$	$0.53^{0.57}_{0.49}$	2.62e-04$^{2.71e-04}_{2.53e-04}$	1.83e-05$^{0.00e+00}_{0.00e+00}$	4.16e-05$^{4.62e-05}_{3.73e-05}$	330.55	309	1.07
81 . .	$0.11^{0.13}_{0.09}$	$1.62^{2.11}_{1.04}$	$2.51^{2.61}_{2.47}$	$2.69^{2.81}_{2.54}$	1.53e-03$^{1.64e-03}_{1.46e-03}$	8.50e-04$^{1.18e-03}_{6.42e-04}$	3.07e-03$^{3.34e-03}_{2.79e-03}$	1536.37	1216	1.26
82 . U	$0.00^{0.65}_{0.00}$	$2.26^{5.27}_{1.23}$	$3.47^{6.20}_{2.42}$	$0.56^{0.67}_{0.36}$	9.54e-06$^{3.83e-05}_{4.07e-06}$	1.49e-04$^{7.26e-04}_{2.51e-05}$	1.10e-05$^{1.52e-05}_{6.24e-06}$	41.44	24	1.73

Table 3.18: *F-test applied to the* XMM-Newton *data fits.*

Num	Name	(2PL)vs(PL)	(MEPL)vs(ME)	(MEPL)vs(PL)	(ME2PL)vs(MEPL)	(ME2PL)vs(2PL)	Final Class.
(1)	(2)	(3)	(4)	(5)	(6)	(7)	(8)
1	NGC 0315	9.8e-27 U	2.2e-150 U	3.3514e-132 U	0.000433057	7.9285e-110 U	ME2PL
2	NGC 0410	0.999 U	2.3e-07	2.25093e-61 U	1 U	1.12392e-60 U	MEPL
7	NGC 0835	8.7e-04 U	6.3e-11 U	1.20906e-08 U	3.36704e-06	6.02702e-11 U	ME2PL
8	NGC 1052	2.3e-175 U	5.1e-226 U	2.56812e-86 U	1.23584e-121 U	1.07387e-32	ME2PL
9	NGC 2639	0.522 U	1. U	1 U	0.00156872 U	0.0142645 U	ME
10	NGC 2655	1.4e-17 U	4.2e-34 U	7.13292e-24 U	6.14156e-07	2.28382e-13 U	ME2PL
13	UGC 4881	0.643 U	0.960 U	0.612912 U	0.119766 U	0.184841 U	ME
14	3C 218	1. U	1.7e-135 U	1.63611e-94 U	1	2.74591e-86 U	MEPL
15	NGC 2787	0.023	4.5e-10 U	0.00300054	0.0394571	0.00510742	ME2PL
16	NGC 2841	5.3e-07 U	8.3e-29 U	2.37058e-10 U	0.014652	4.17527e-06	ME2PL
17	UGC 05101	3.6e-03 U	3.6e-08 U	0.0022769 U	0.107604 U	0.0510086 U	ME2PL
19	NGC 3226	8.9e-10	3.2e-06 U	0.0462035 U	9.85002e-09 U	1 U	2PL
28	NGC 3628	0.542 U	0.0071 U	0.731756 U	0.0288348 U	0.0883919 U	PL
29	NGC 3690B	8.3e-19 U	3.2e-75 U	5.98702e-55 U	1	6.97257e-37 U	MEPL
32	NGC 3998	0.261	1.8e-193 U	0.546316	0.0258734	0.110081	PL
35	NGC 4125	0.986 U	1.1e-22	1.06732e-44 U	7.95789e-05	5.71656e-49 U	MEPL
37	NGC 4261	3.4e-23 U	2.3e-115 U	1.0581e-82 U	1.01793e-30 U	5.07579e-90 U	ME2PL
38	NGC 4278	6.5e-05	1.2e-198 U	0.000370466	0.0506404	0.230626	MEPL
39	NGC 4314	9.1e-04 U	8.1e-17 U	3.16209e-08 U	0.0207082	6.36901e-07 U	MEPL
40	NGC 4321	3.0e-12 U	1.2e-56 U	9.98298e-18	0.0881796	1.08512e-07 U	MEPL
47	NGC 4494	0.135	1.3e-19 U	0.896826 U	0.00808113 U	0.147323	PL
48	NGC 4552	3.0e-33 U	9.2e-236 U	1.38866e-125 U	0.342866 U	2.78222e-94 U	MEPL
50	NGC 4579	8.0e-24	1.7e-223 U	1.62225e-42	3.40852e-06	3.92122e-25	ME2PL
52	NGC 4594	0.010	6.6e-34 U	1 U	2.34672e-09 U	1.68967e-06	ME2PL
53	NGC 4636	1 U	1.6e-19 U	2.42328e-110 U	1 U	6.61654e-111 U	MEPL
58	NGC 4736	3.3e-49 U	6.5e-122 U	3.29061e-68 U	0.0596432	6.83023e-21 U	MEPL
59	NGC 5005	1.0e-10 U	6.9e-24 U	3.09291e-18 U	0.313738	2.94581e-09 U	MEPL
61	MRK 266NE	2.1e-10 U	8.3e-37 U	6.24271e-18 U	1.16548e-07	3.55677e-15 U	ME2PL
62	UGC 08696	1.3e-09 U	2.5e-13 U	1.22514e-09 U	9.39834e-09 U	8.67662e-09 U	ME2PL
63	CGCG 162-010..	3.0e-32 U	8.0e-221 U	7.98859e-193 U	0.114285	4.97625e-163 U	MEPL
64	NGC 5363	9.0e-07 U	2.8e-20 U	7.57131e-14 U	0.00474153	2.97278e-10 U	ME2PL
65	IC 4395	1 U	0.0029 U	0.004148 U	0.101511 U	3.47364e-07 U	MEPL
66	IRAS 14348-1447	0.327 U	0.0054 U	0.420636 U	0.564525 U	0.629808 U	ME
68	NGC 5813	9.7e-03 U	1.7e-09 U	4.20226e-129 U	0.791023 U	1.01949e-127 U	MEPL
70	NGC 5846	2.8e-05 U	8.9e-32 U	7.59725e-121 U	0.0352933	8.13486e-118 U	ME2PL
72	MRK 0848	0.273	1.3e-06 U	0.566814	0.00789318 U	0.0362821 U	PL
73	NGC 6240	8.5e-07	6.8e-56 U	0.999749	0.426403	0.000403526	ME2PL
74	NGC 6251	5.2e-21 U	4.3e-237 U	1. U	2.90546e-10	3.28782e-24 U	ME2PL
75	IRAS 17208-0014	0.246 U	0.629	0.13146	0.381838 U	0.173667 U	ME
76	NGC 6482	4.4e-03 U	0.0018 U	2.33206e-35 U	0.0723792 U	2.69328e-34 U	ME
78	NGC 7285	6.5e-05	0.0014 U	0.000180325	0.429946	0.500812	MEPL
80	IC 1459	2.8e-18 U	2.2e-70 U	1.00689e-32 U	1 U	7.43502e-16 U	MEPL
81	NPM1G -12.0625	2.7e-34 U	2.1e-283 U	1.95984e-225 U	4.72273e-05	1.18592e-196 U	ME2PL
82	NGC 7743	0.171 U	0.0015 U	0.0535254 U	0.239693 U	0.0684019 U	MEPL

Table 3.19: Bestfit model applied to *XMM-Newton* data fits.

Num	Name	Type	Bestfit	N_{H1} (10^{22} cm^{-2})	N_{H2} (10^{22} cm^{-2})	Γ	Temp. (keV)	χ^2	d.o.f	χ^2_r
(1)	(2)	(3)	(4)	(5)	(6)	(7)	(8)	(9)	(10)	(11)
1	NGC 0315.....	AGN	ME2PL	$0.00^{0.01}_{0.00}$	$0.34^{0.59}_{0.18}$	$1.65^{1.81}_{1.51}$	$0.58^{0.59}_{0.56}$	410.54	390	1.02
2	NGC 0410.....	SB*	MEPL	$0.12^{0.17}_{0.09}$	$0.00^{0.20}_{0.00}$	$2.43^{3.17}_{1.92}$	$0.69^{0.71}_{0.67}$	218.34	178	1.23
3	NGC 0474.....	SB	–	...	...	...	...	...	...	...
4	IIIZw 035	SB	–	...	...	...	...	...	...	...
7	NGC 0835.....	AGN	ME2PL	$0.04^{0.09}_{0.00}$	$69.63^{104.56}_{34.39}$	$2.89^{3.35}_{2.37}$	$0.54^{0.61}_{0.49}$	129.49	113	1.15
8	NGC 1052.....	AGN	ME2PL	$0.00^{0.00}_{0.00}$	$9.22^{9.64}_{8.82}$	$1.34^{1.42}_{1.28}$	$0.60^{0.63}_{0.56}$	800.07	741	1.08
9	NGC 2639.....	SB*	ME	$0.80^{0.92}_{0.67}$	...	...	$0.18^{0.24}_{0.15}$	180.55	148	1.22
10	NGC 2655.....	AGN*	ME2PL	$0.00^{0.07}_{0.00}$	$30.20^{39.47}_{24.21}$	$2.48^{2.83}_{2.05}$	$0.64^{0.68}_{0.59}$	94.67	111	0.85
12	NGC 2685.....	AGN	–	...	...	...	...	...	...	...
13	UGC 04881.....	SB	ME	$0.61^{0.79}_{0.32}$	...	...	$0.19^{0.29}_{0.15}$	21.71	19	1.14
14	3C 218	AGN	MEPL	$0.10^{0.15}_{0.06}$	$0.02^{0.04}_{0.01}$	$2.17^{2.22}_{2.14}$	$2.77^{2.88}_{2.56}$	1011.82	864	1.18
15	NGC 2787.....	AGN	ME2PL	$0.01^{0.14}_{0.00}$	$1.00^{1.87}_{0.59}$	$2.18^{3.04}_{2.03}$	$0.63^{0.70}_{0.52}$	126.64	98	1.29
16	NGC 2841.....	AGN	ME2PL	$0.00^{0.09}_{0.00}$	$3.30^{5.60}_{1.96}$	$2.20^{3.01}_{2.07}$	$0.58^{0.64}_{0.50}$	155.16	139	1.12
17	UGC 05101.....	AGN	ME2PL	$0.12^{0.28}_{0.00}$	$118.52^{8450.86}_{33.53}$	$1.48^{1.73}_{0.88}$	$0.97^{1.29}_{0.72}$	29.88	21	1.42
18	NGC 3185.....	SB*	–	...	...	...	...	...	...	...
19	NGC 3226.....	AGN	2PL	$0.21^{0.30}_{0.11}$	$1.22^{1.76}_{0.94}$	$1.92^{2.12}_{1.80}$	...	169.21	179	0.95
26	NGC 3623.....	SB*	–	...	...	...	...	...	...	...
27	NGC 3627.....	SB*	–	...	...	...	...	...	...	...
28	NGC 3628.....	SB	PL	$0.46^{0.52}_{0.41}$	...	$1.61^{1.68}_{1.53}$	...	264.36	247	1.07
29	NGC 3690B	AGN	MEPL	$0.22^{0.31}_{0.13}$	$0.08^{0.12}_{0.05}$	$1.84^{1.94}_{1.75}$	$0.63^{0.65}_{0.60}$	262.18	236	1.11
32	NGC 3998.....	SB	PL	$0.02^{0.03}_{0.02}$	...	$1.87^{1.89}_{1.84}$	...	668.69	631	1.06
35	NGC 4125.....	AGN	MEPL	$0.00^{0.02}_{0.00}$	$0.00^{0.03}_{0.00}$	$2.36^{2.80}_{2.15}$	$0.54^{0.57}_{0.52}$	400.70	391	1.02
36	IRAS 12112+0305	SB*	–	...	...	...	...	...	...	...
37	NGC 4261.....	AGN	ME2PL	$0.22^{0.32}_{0.14}$	$13.80^{16.20}_{11.73}$	$2.38^{2.65}_{2.01}$	$0.62^{0.63}_{0.61}$	279.85	255	1.10
38	NGC 4278 ... (A)	AGN	MEPL	$0.39^{0.67}_{0.26}$	$0.01^{0.03}_{0.00}$	$1.99^{2.04}_{1.96}$	$0.65^{0.78}_{0.52}$	605.97	574	1.06
			2PL	$0.06^{0.08}_{0.05}$	$7.23^{10.14}_{5.27}$	$2.28^{2.40}_{2.20}$	...	605.03	575	1.05
39	NGC 4314.....	SB	MEPL	$0.27^{0.44}_{0.09}$	$0.00^{0.52}_{0.00}$	$1.46^{1.88}_{1.11}$	$0.24^{0.27}_{0.19}$	40.89	42	0.97
40	NGC 4321.....	SB	MEPL	$0.44^{0.57}_{0.28}$	$0.00^{0.03}_{0.00}$	$2.24^{2.46}_{2.11}$	$0.29^{0.36}_{0.25}$	211.88	211	1.00
46	NGC 4486.....	AGN	–	...	...	...	...	...	...	...
47	NGC 4494.....	AGN	PL	$0.00^{0.02}_{0.00}$	...	$1.83^{1.95}_{1.73}$	...	55.46	51	1.09
48	NGC 4552.....	AGN	MEPL	$0.01^{0.04}_{0.00}$	$0.00^{0.02}_{0.00}$	$1.97^{2.09}_{1.90}$	$0.61^{0.62}_{0.60}$	455.11	456	1.00
50	NGC 4579.....	AGN	ME2PL	$0.00^{0.00}_{0.00}$	$53.57^{132.93}_{8.74}$	$1.89^{1.93}_{1.86}$	$0.66^{0.69}_{0.63}$	573.09	605	0.95
52	NGC 4594.....	AGN	ME2PL	$0.01^{0.16}_{0.00}$	$0.64^{1.40}_{0.43}$	$2.05^{2.18}_{1.95}$	$0.69^{0.75}_{0.65}$	268.48	286	0.94
53	NGC 4636.....	SB	MEPL	$0.00^{0.01}_{0.00}$	$0.01^{0.17}_{0.00}$	$2.92^{3.91}_{2.36}$	$0.54^{0.55}_{0.53}$	355.63	241	1.48
56	NGC 4698.....	AGN	–	...	...	...	...	...	...	...

Table 3.19:normalsizeContinuation

Num	Name	Type	Bestfit	N_{H1} (10^{22} cm^{-2})	N_{H2} (10^{22} cm^{-2})	Γ	Temp. (keV)	χ^2	d.o.f	χ^2_r
(1)	(2)	(3)	(4)	(5)	(6)	(7)	(8)	(9)	(10)	(11)
57	NGC 4696.....	SB	–	... $^{\cdots}_{\cdots}$	... $^{\cdots}_{\cdots}$	... $^{\cdots}_{\cdots}$	... $^{\cdots}_{\cdots}$	...	...	...
58	NGC 4736.....	AGN	MEPL	$0.00^{0.06}_{0.00}$	$0.00^{0.01}_{0.00}$	$1.67^{1.73}_{1.64}$	$0.51^{0.53}_{0.47}$	396.45	373	1.06
59	NGC 5005.....	AGN*	MEPL	$0.61^{0.80}_{0.52}$	$0.00^{0.07}_{0.00}$	$1.54^{1.73}_{1.42}$	$0.27^{0.30}_{0.21}$	70.67	72	0.98
61	MRK 0266NE ...	AGN	ME2PL	$0.00^{0.03}_{0.00}$	$21.97^{32.83}_{14.72}$	$2.69^{2.84}_{2.50}$	$0.65^{0.69}_{0.61}$	111.07	102	1.09
62	UGC 08696.....	AGN	ME2PL	$0.00^{0.06}_{0.00}$	$54.73^{76.54}_{39.96}$	$1.82^{1.98}_{1.56}$	$0.69^{0.76}_{0.66}$	45.57	48	0.95
63	CGC G162-010..	SB	MEPL	$0.11^{0.14}_{0.09}$	$0.02^{0.03}_{0.01}$	$2.05^{2.08}_{2.01}$	$3.26^{3.38}_{2.98}$	294.32	1187	1.09
64	NGC 5363.....	AGN*	ME2PL	$0.00^{0.08}_{0.00}$	$2.66^{4.37}_{1.74}$	$2.14^{2.69}_{1.76}$	$0.61^{0.65}_{0.56}$	79.70	81	0.90
65	IC 4395	SB*	MEPL	$0.00^{0.42}_{0.00}$	$0.00^{0.17}_{0.00}$	$1.78^{4.00}_{1.24}$	$0.26^{0.60}_{0.19}$	25.54	22	1.16
66	IRAS 14348-1447	SB	ME	$0.00^{0.04}_{0.00}$	... $^{\cdots}_{\cdots}$	... $^{\cdots}_{\cdots}$	$3.67^{6.46}_{2.50}$	25.23	34	0.74
68	NGC 5813.....	SB	MEPL	$0.00^{0.01}_{0.00}$	$0.26^{0.45}_{0.12}$	$3.36^{4.50}_{2.82}$	$0.59^{0.60}_{0.59}$	373.90	264	1.42
70	NGC 5846.....	SB	ME2PL	$0.14^{0.22}_{0.06}$	$20.30^{33.76}_{8.93}$	$3.12^{3.86}_{2.74}$	$0.62^{0.62}_{0.61}$	267.90	225	1.19
72	MRK 0848	SB*	PL	$0.07^{0.19}_{0.00}$	... $^{\cdots}_{\cdots}$	$2.26^{2.75}_{1.73}$	... $^{\cdots}_{\cdots}$	31.18	42	0.74
73	NGC 6251.....	AGN	ME2PL	$0.07^{0.07}_{0.06}$	$48.69^{107.06}_{24.96}$	$1.97^{2.07}_{1.93}$	$0.58^{0.67}_{0.45}$	911.04	861	1.06
74	NGC 6240.....	AGN	ME2PL	$0.23^{0.27}_{0.21}$	$155.52^{179.68}_{134.03}$	$1.93^{2.03}_{1.89}$	$0.87^{0.93}_{0.83}$	388.46	324	1.20
75	IRAS 17208-0014	AGN	ME	$0.75^{0.99}_{0.47}$	... $^{\cdots}_{\cdots}$	... $^{\cdots}_{\cdots}$	$0.64^{0.79}_{0.46}$	38.53	36	1.07
76	NGC 6482.....	SB	ME	$0.10^{0.13}_{0.06}$	... $^{\cdots}_{\cdots}$	... $^{\cdots}_{\cdots}$	$0.67^{0.68}_{0.65}$	142.04	116	1.22
78	NGC 7285 ... (A)	AGN*	MEPL	$0.68^{0.78}_{0.00}$	$0.87^{1.13}_{0.59}$	$1.66^{1.76}_{1.43}$	$0.13^{0.19}_{0.07}$	59.28	58	1.02
			2PL	$0.08^{0.19}_{0.00}$	$1.33^{2.39}_{0.76}$	$1.69^{1.78}_{1.55}$	...	60.07	59	1.02
79	NGC 7331.....	SB	–	... $^{\cdots}_{\cdots}$	... $^{\cdots}_{\cdots}$	... $^{\cdots}_{\cdots}$	... $^{\cdots}_{\cdots}$	...	...	...
80	IC 1459	AGN	MEPL	$0.18^{0.27}_{0.10}$	$0.11^{0.13}_{0.08}$	$1.92^{1.99}_{1.82}$	$0.44^{0.53}_{0.33}$	329.27	310	1.06
81	NPM1G -12.0625	SB	ME2PL	$0.11^{0.13}_{0.09}$	$1.62^{2.11}_{1.04}$	$2.51^{2.61}_{2.47}$	$2.69^{2.81}_{2.54}$	1536.37	1216	1.26
82	NGC 7743.....	SB*	MEPL	$0.35^{0.58}_{0.18}$	$1.68^{3.63}_{0.81}$	$3.16^{6.47}_{1.49}$	$0.23^{0.29}_{0.18}$	43.95	25	1.76

(A) NGC 4278 and NGC 7285 do not show statistically significant differences between 2PL and MEPL. We show the resulting parameters for both models although they have been considered as fitted with MEPL in the text.

Table 3.20: FeKα, FeXV and FeXVI emission line fluxes with *XMM-Newton* data.

Num	Name	Flux(FeKα) (erg s^{-1} cm^{-2})	Flux(FeXXV) (erg s^{-1} cm^{-2})	Flux(FeXXVI) (erg s^{-1} cm^{-2})
(1)	(2)	(3)	(4)	(5)
1	NGC 0315.....	7.67e-07 $^{1.53e-06}_{8.32e-10}$	1.16e-06 $^{1.92e-06}_{4.01e-07}$	2.59e-07 $^{9.67e-07}_{0.00e+00}$
2	NGC 0410.....	9.07e-08 $^{7.80e-07}_{0.00e+00}$	9.59e-07 $^{1.74e-06}_{1.76e-07}$	5.29e-08 $^{8.00e-07}_{0.00e+00}$
3	NGC 0474.....	...	...	...
4	IIIZw 035	...	...	...
7	NGC 0835.....	1.50e-06 $^{2.06e-06}_{9.40e-07}$	0.00e+00 $^{2.73e-07}_{0.00e+00}$	3.15e-07 $^{8.14e-07}_{0.00e+00}$
8	NGC 1052.....	9.39e-06 $^{1.09e-05}_{7.93e-06}$	1.66e-06 $^{2.88e-06}_{4.48e-07}$	2.54e-06 $^{3.80e-06}_{1.27e-06}$
9	NGC 2639.....	...	...	...
10	NGC 2655.....	4.81e-07 $^{3.02e-06}_{0.00e+00}$	4.43e-16 $^{2.75e-06}_{0.00e+00}$	7.51e-07 $^{3.10e-06}_{0.00e+00}$
12	NGC 2685.....	...	...	...
13	UGC 04881.....	...	...	...
14	3C 218	7.96e-24 $^{6.17e-07}_{0.00e+00}$	4.62e-06 $^{7.45e-06}_{1.70e-06}$	3.79e-06 $^{5.77e-06}_{1.85e-06}$
15	NGC 2787.....	0.00e+00 $^{3.84e-07}_{0.00e+00}$	0.00e+00 $^{4.49e-07}_{0.00e+00}$	9.67e-08 $^{5.88e-07}_{0.00e+00}$
16	NGC 2841.....	0.00e+00 $^{3.88e-07}_{0.00e+00}$	7.84e-38 $^{5.93e-07}_{0.00e+00}$	0.00e+00 $^{4.94e-07}_{0.00e+00}$
17	UGC 05101.....	1.08e-06 $^{1.77e-06}_{3.88e-07}$	7.87e-07 $^{1.36e-06}_{2.15e-07}$	3.40e-07 $^{8.90e-07}_{0.00e+00}$
18	NGC 3185.....	...	...	...
19	NGC 3226.....	3.04e-07 $^{1.01e-06}_{0.00e+00}$	0.00e+00 $^{2.85e-07}_{0.00e+00}$	3.56e-07 $^{1.06e-06}_{0.00e+00}$
26	NGC 3623.....	...	...	...
27	NGC 3627.....	...	...	...
28	NGC 3628.....	2.03e-16 $^{5.44e-07}_{0.00e+00}$	5.69e-07 $^{1.23e-06}_{0.00e+00}$	8.03e-08 $^{7.44e-07}_{0.00e+00}$
29	NGC 3690B	2.62e-06 $^{3.84e-06}_{1.41e-06}$	2.19e-06 $^{3.38e-06}_{9.96e-07}$	1.43e-06 $^{2.57e-06}_{2.89e-07}$
32	NGC 3998.....	6.37e-12 $^{3.31e-06}_{0.00e+00}$	1.67e-06 $^{5.25e-06}_{0.00e+00}$	1.21e-06 $^{4.89e-06}_{0.00e+00}$
35	NGC 4125.....	0.00e+00 $^{7.75e-07}_{0.00e+00}$	8.05e-08 $^{1.16e-06}_{0.00e+00}$	2.34e-07 $^{1.37e-06}_{0.00e+00}$
36	IRAS 12112+0305	...	...	...
37	NGC 4261.....	2.48e-07 $^{9.92e-07}_{0.00e+00}$	1.67e-07 $^{9.33e-07}_{0.00e+00}$	5.38e-07 $^{1.34e-06}_{0.00e+00}$
38	NGC 4278.....	0.00e+00 $^{8.90e-07}_{0.00e+00}$	0.00e+00 $^{4.94e-07}_{0.00e+00}$	0.00e+00 $^{4.64e-07}_{0.00e+00}$
39	NGC 4314.....	4.63e-07 $^{1.04e-06}_{0.00e+00}$	3.30e-18 $^{6.39e-07}_{0.00e+00}$	9.57e-23 $^{5.96e-07}_{0.00e+00}$
40	NGC 4321.....	2.77e-19 $^{4.20e-07}_{0.00e+00}$	6.91e-07 $^{1.45e-06}_{0.00e+00}$	5.23e-07 $^{1.26e-06}_{0.00e+00}$
46	NGC 4486.....	...	...	...
47	NGC 4494.....	0.00e+00 $^{3.96e-07}_{0.00e+00}$	0.00e+00 $^{3.81e-07}_{0.00e+00}$	0.00e+00 $^{4.04e-07}_{0.00e+00}$
48	NGC 4552.....	8.44e-08 $^{1.11e-06}_{0.00e+00}$	0.00e+00 $^{9.08e-07}_{0.00e+00}$	0.00e+00 $^{9.34e-07}_{0.00e+00}$
50	NGC 4579.....	5.18e-06 $^{7.08e-06}_{3.29e-06}$	2.32e-06 $^{4.13e-06}_{5.04e-07}$	2.95e-06 $^{4.76e-06}_{1.14e-06}$
52	NGC 4594.....	4.20e-07 $^{1.58e-06}_{0.00e+00}$	1.12e-06 $^{2.25e-06}_{0.00e+00}$	0.00e+00 $^{5.34e-07}_{0.00e+00}$
53	NGC 4636.....	2.45e-07 $^{1.67e-06}_{0.00e+00}$	2.93e-07 $^{1.73e-06}_{0.00e+00}$	2.84e-07 $^{1.86e-06}_{0.00e+00}$
56	NGC 4698.....	...	...	...
57	NGC 4696.....	...	...	...
58	NGC 4736.....	1.48e-07 $^{1.70e-06}_{0.00e+00}$	4.80e-07 $^{2.06e-06}_{0.00e+00}$	1.02e-30 $^{1.44e-06}_{0.00e+00}$
59	NGC 5005.....	...	...	...
61	MRK 0266NE ...	1.39e-06 $^{2.43e-06}_{3.61e-07}$	3.11e-07 $^{1.13e-06}_{0.00e+00}$	2.82e-32 $^{6.15e-07}_{0.00e+00}$
62	UGC 08696.....	2.32e-06 $^{3.33e-06}_{1.31e-06}$	1.47e-06 $^{2.45e-06}_{4.86e-07}$	5.74e-07 $^{1.39e-06}_{0.00e+00}$
63	CGC G162-010 ..	0.00e+00 $^{6.88e-07}_{0.00e+00}$	1.41e-05 $^{1.67e-05}_{1.16e-05}$	2.45e-06 $^{4.03e-06}_{8.76e-07}$
64	NGC 5363.....	1.47e-07 $^{9.87e-07}_{0.00e+00}$	7.07e-07 $^{1.72e-06}_{0.00e+00}$	1.12e-07 $^{1.77e-06}_{0.00e+00}$
65	IC 4395	...	...	...
66	IRAS 14348-1447	...	...	...
68	NGC 5813.....	0.00e+00 $^{5.30e-07}_{0.00e+00}$	0.00e+00 $^{3.82e-07}_{0.00e+00}$	0.00e+00 $^{3.70e-07}_{0.00e+00}$
70	NGC 5846.....	0.00e+00 $^{2.22e-07}_{0.00e+00}$	0.00e+00 $^{2.28e-07}_{0.00e+00}$	0.00e+00 $^{2.42e-07}_{0.00e+00}$
72	MRK 0848	6.91e-08 $^{8.40e-07}_{0.00e+00}$	0.00e+00 $^{1.17e-06}_{0.00e+00}$	5.11e-07 $^{1.54e-06}_{0.00e+00}$
73	NGC 6251.....	1.03e-06 $^{2.28e-06}_{0.00e+00}$	1.26e-06 $^{2.48e-06}_{2.73e-08}$	1.49e-21 $^{7.98e-07}_{0.00e+00}$
74	NGC 6240.....	1.43e-05 $^{1.67e-05}_{1.19e-05}$	6.74e-06 $^{8.86e-06}_{4.62e-06}$	3.94e-06 $^{5.98e-06}_{1.89e-06}$

Table 3.20: Continuation

Num	Name	Flux(FeKα) (erg s^{-1} cm^{-2})	Flux(FeXXV) (erg s^{-1} cm^{-2})	Flux(FeXXVI) (erg s^{-1} cm^{-2})
(1)	(2)	(3)	(4)	(5)
75	IRAS 17208-0014	...	...	...
76	NGC 6482.....	...	...	...
78	NGC 7285.....	1.28e-06 $^{2.30e-06}_{2.37e-07}$	4.61e-07 $^{1.81e-06}_{0.00e+00}$	3.65e-07 $^{1.56e-06}_{0.00e+00}$
79	NGC 7331.....	...	...	...
80	IC 1459	0.00e+00 $^{5.24e-07}_{0.00e+00}$	0.00e+00 $^{5.41e-07}_{0.00e+00}$	2.42e-07 $^{1.07e-06}_{0.00e+00}$
81	NPM1G -12.0625	0.00e+00 $^{3.17e-07}_{0.00e+00}$	2.45e-06 $^{3.81e-06}_{1.07e-06}$	1.64e-06 $^{2.60e-06}_{6.85e-07}$
82	NGC 7743.....	3.71e-07 $^{1.77e-06}_{0.00e+00}$	1.65e-15 $^{2.24e-06}_{0.00e+00}$	0.00e+00 $^{1.32e-06}_{0.00e+00}$

Table 3.21: FeKα, FeXV and FeXVI emission line equivalent width with *XMM-Newton* data.

Num	Name	EW(FeKα) (eV)	EW(FeXXV) (eV)	EW(FeXXVI) (eV)
(1)	(2)	(3)	(4)	(5)
1	NGC 0315.....	81.89 $^{163.69}_{0.09}$	137.37 $^{227.26}_{47.46}$	27.08 $^{118.67}_{0.00}$
2	NGC 0410.....	47.02 $^{413.54}_{0.00}$	1360.47 $^{2466.75}_{249.18}$	39.11 $^{474.56}_{0.00}$
3	NGC 0474.....	...	...	...
4	IIIZw 035	...	...	...
7	NGC 0835.....	774.92 $^{1065.17}_{485.49}$	0.00 $^{59.05}_{0.00}$	0.00 $^{493.06}_{0.00}$
8	NGC 1052.....	144.40 $^{166.96}_{121.84}$	21.51 $^{37.23}_{5.79}$	43.36 $^{64.94}_{21.77}$
9	NGC 2639.....	...	...	...
10	NGC 2655.....	24.69 $^{155.51}_{0.00}$	0.00 $^{131.61}_{0.00}$	45.99 $^{189.26}_{0.00}$
12	NGC 2685.....	...	...	...
13	UGC 04881.....	...	...	...
14	3C 218	0.00 $^{6.13}_{0.00}$	51.67 $^{81.49}_{18.64}$	44.36 $^{67.29}_{21.58}$
15	NGC 2787.....	0.00 $^{291.35}_{0.00}$	0.00 $^{331.56}_{0.00}$	98.79 $^{535.73}_{0.00}$
16	NGC 2841.....	0.00 $^{240.58}_{0.00}$	0.00 $^{405.89}_{0.00}$	0.00 $^{370.30}_{0.00}$
17	UGC 05101.....	278.37 $^{456.52}_{100.22}$	151.84 $^{263.90}_{41.68}$	80.61 $^{230.46}_{0.00}$
18	NGC 3185.....	...	...	...
19	NGC 3226.....	33.67 $^{111.38}_{0.00}$	0.00 $^{30.43}_{0.00}$	47.39 $^{136.50}_{0.00}$
26	NGC 3623.....	...	...	...
27	NGC 3627.....	...	...	...
28	NGC 3628.....	0.00 $^{77.39}_{0.00}$	98.39 $^{209.02}_{0.00}$	17.14 $^{120.28}_{0.00}$
29	NGC 3690B	233.42 $^{341.24}_{125.60}$	165.42 $^{255.45}_{75.37}$	145.73 $^{262.05}_{29.41}$
32	NGC 3998.....	0.00 $^{31.26}_{0.00}$	17.29 $^{54.24}_{0.00}$	13.31 $^{53.78}_{0.00}$
35	NGC 4125.....	0.00 $^{1559.70}_{0.00}$	67.00 $^{2056.16}_{0.00}$	330.40 $^{2947.66}_{0.00}$
36	IRAS 12112+0305	...	...	...
37	NGC 4261.....	26.11 $^{105.52}_{0.00}$	21.86 $^{97.77}_{0.00}$	70.68 $^{173.30}_{0.00}$
38	NGC 4278.....	0.00 $^{48.20}_{0.00}$	0.00 $^{29.31}_{0.00}$	0.00 $^{29.63}_{0.00}$
39	NGC 4314.....	708.79 $^{1590.35}_{0.00}$	0.00 $^{492.54}_{0.00}$	204.87 $^{1029.44}_{0.00}$
40	NGC 4321.....	0.00 $^{170.94}_{0.00}$	344.52 $^{705.80}_{0.00}$	231.42 $^{584.46}_{0.00}$
46	NGC 4486.....	...	...	...
47	NGC 4494.....	0.00 $^{374.52}_{0.00}$	0.00 $^{392.19}_{0.00}$	0.00 $^{444.36}_{0.00}$
48	NGC 4552.....	24.06 $^{317.93}_{0.00}$	0.00 $^{272.73}_{0.00}$	0.00 $^{314.01}_{0.00}$
50	NGC 4579.....	115.05 $^{157.14}_{72.96}$	45.49 $^{81.07}_{9.91}$	75.31 $^{121.61}_{29.02}$
52	NGC 4594.....	28.49 $^{106.10}_{0.00}$	96.32 $^{178.57}_{0.00}$	0.00 $^{41.78}_{0.00}$
53	NGC 4636.....	296.01 $^{1753.93}_{0.00}$	346.35 $^{1171.77}_{0.00}$	550.43 $^{2472.83}_{0.00}$
56	NGC 4698.....	...	...	...
57	NGC 4696.....	...	...	...

Table 3.21: Continuation

Num	Name	EW(FeKα) (eV)	EW(FeXXV) (eV)	EW(FeXXVI) (eV)
(1)	(2)	(3)	(4)	(5)
58	NGC 4736.....	$8.71^{98.56}_{0.00}$	$56.15^{133.71}_{0.00}$	$0.00^{95.73}_{0.00}$
59	NGC 5005.....	...	...	...
61	MRK 0266NE ...	$275.72^{481.38}_{71.24}$	$47.65^{178.02}_{0.00}$	$0.00^{146.25}_{0.00}$
62	UGC 08696.....	$266.11^{382.32}_{149.90}$	$135.94^{226.84}_{45.04}$	$70.24^{173.71}_{0.00}$
63	CGC G162-010 ..	$0.00^{4.18}_{0.00}$	$105.80^{124.19}_{86.36}$	$17.29^{28.43}_{6.18}$
64	NGC 5363.....	$50.45^{337.81}_{0.00}$	$351.88^{852.44}_{0.00}$	$54.84^{700.98}_{0.00}$
65	IC 4395	...	...	...
66	IRAS 14348-1447	...	...	...
68	NGC 5813.....	$0.00^{2609.74}_{0.00}$	$0.00^{2206.17}_{0.00}$	$0.00^{2453.49}_{0.00}$
70	NGC 5846.....	$0.00^{177.73}_{0.00}$	$0.00^{204.29}_{0.00}$	$0.00^{248.38}_{0.00}$
72	MRK 0848	$196.92^{2398.18}_{0.00}$	$4.16^{916.54}_{0.00}$	$1777.01^{5307.68}_{0.00}$
73	NGC 6251.....	$24.30^{53.49}_{0.00}$	$32.90^{63.18}_{0.70}$	$0.00^{21.82}_{0.00}$
74	NGC 6240.....	$378.06^{441.86}_{314.27}$	$115.35^{151.57}_{79.14}$	$105.08^{159.76}_{50.40}$
75	IRAS 17208-0014	...	...	...
76	NGC 6482.....	...	...	...
78	NGC 7285.....	$211.68^{382.09}_{39.28}$	$59.20^{247.70}_{0.00}$	$61.49^{295.86}_{0.00}$
79	NGC 7331.....	...	...	...
80	IC 1459	$0.00^{72.47}_{0.00}$	$0.00^{76.96}_{0.00}$	$41.38^{173.16}_{0.00}$
81	NPM1G -12.0625	$0.00^{4.35}_{0.00}$	$38.34^{58.34}_{16.40}$	$26.48^{41.97}_{11.06}$
82	NGC 7743.....	$1746.22^{8337.29}_{0.00}$	$0.00^{3065.32}_{0.00}$	$0.00^{2121.33}_{0.00}$

Table 3.22: Observed fluxes and absorption corrected luminosities with *XMM-Newton* data.

Num	Name	Type	Flux(0.5-2.0keV) (10^{-13} erg s^{-1})	Flux(2.0-10.0keV) (10^{-13} erg s^{-1})	Log(Lum(0.5-2.0keV))	Log(Lum(2.0-10.0keV))
(1)	(2)	(3)	(4)	(5)	(6)	(7)
1	NGC 0315	AGN	4.051 [2.973, 9.399]	7.113 [6.455, 15.839]	41.607 [41.472, 42.019]	41.600 [41.550 ,41.939]
2	NGC 0410	SB*	5.286 [4.425, 5.667]	0.803 [0.379, 1.102]	41.745 [41.635, 41.773]	40.715 [40.400 ,40.839]
3	NGC 0474	SB	0.003 [0.000, 0.146]	0.005 [0.000, 0.256]	37.586 [00.000, 39.301]	37.781 [00.000 ,39.514]
4	IIIZw 035	SB	0.020 [0.000, 0.114]	0.037 [0.000, 0.200]	39.548 [00.000, 40.282]	39.743 [00.000 ,40.475]
7	NGC 0835	AGN	0.705 [0.443, 0.796]	1.216 [0.198, 1.664]	41.961 [41.753, 42.014]	41.526 [40.734 ,41.654]
8	NGC 1052	AGN	2.674 [2.395, 2.767]	43.488 [35.174, 48.051]	40.971 [40.921, 40.983]	41.445 [41.346 ,41.489]
9	NGC 2639	SB*	1.092 [0.000, 1.190]	0.006 [0.000, 0.007]	42.211 [00.000, 42.252]	38.277 [00.000 ,38.370]
10	NGC 2655	AGN*	2.129 [1.330, 2.426]	10.178 [0.211, 11.400]	41.506 [41.312, 41.564]	41.234 [39.541 ,41.287]
12	NGC 2685	AGN	0.197 [0.111, 0.286]	0.348 [0.189, 0.508]	38.847 [38.573, 39.011]	39.042 [38.781 ,39.209]
13	UGC 04881	SB	0.175 [0.000, 0.217]	0.000 [0.000, 0.001]	42.169 [00.000, 42.254]	38.369 [00.000 ,38.504]
14	3C 218	AGN	55.467 [54.084, 56.923]	64.110 [62.551, 66.452]	43.654 [43.641, 43.668]	43.620 [43.609 ,43.635]
15	NGC 2787	AGN	0.866 [0.373, 2.285]	1.463 [0.276, 2.876]	39.276 [38.864, 39.639]	39.208 [38.676 ,39.490]
16	NGC 2841	AGN	1.314 [0.530, 1.386]	1.624 [0.325, 2.187]	39.369 [38.983, 39.394]	39.219 [38.172 ,39.341]
17	UGC 05101	AGN	0.232 [0.104, 0.292]	1.857 [0.574, 2.623]	42.021 [41.695, 42.118]	42.521 [42.055 ,42.643]
18	NGC 3185	AGN	0.260 [0.171, 0.354]	0.434 [0.288, 0.589]	39.179 [38.995, 39.314]	39.374 [39.180 ,39.511]
19	NGC 3226	SB*	1.819 [1.230, 2.216]	8.629 [6.249, 9.889]	40.679 [40.513, 40.769]	40.800 [40.657 ,40.860]
26	NGC 3623	AGN	0.794 [0.585, 0.939]	1.726 [0.000, 48.338]	39.145 [39.003, 39.212]	39.383 [00.000 ,40.831]
27	NGC 3627	SB*	1.221 [1.023, 1.421]	2.053 [1.730, 2.387]	39.220 [39.144, 39.286]	39.415 [39.334 ,39.481]
28	NGC 3628	SB*	1.110 [0.944, 1.241]	5.571 [5.026, 6.103]	39.621 [39.551, 39.668]	39.942 [39.896 ,39.981]
29	NGC 3690B	SB	6.804 [5.727, 7.235]	8.281 [7.239, 9.050]	41.358 [41.273, 41.386]	41.244 [41.182 ,41.282]
32	NGC 3998	AGN	65.510 [64.282, 66.624]	103.012 [101.353, 105.196]	41.225 [41.217, 41.232]	41.377 [41.371 ,41.386]
35	NGC 4125	SB	2.040 [0.789, 2.021]	0.505 [0.108, 0.941]	39.934 [39.445, 39.929]	39.300 [38.703 ,39.580]
36	IRAS 12112+0305	AGN	0.091 [0.058, 0.124]	0.151 [0.096, 0.206]	41.030 [40.822, 41.172]	41.226 [41.040 ,41.363]
37	NGC 4261	SB*	5.038 [4.605, 5.344]	6.481 [1.291, 7.574]	41.429 [41.387, 41.450]	41.165 [40.501 ,41.232]
38	NGC 4278(MEPL)	AGN	15.380 [14.463, 15.942]	19.226 [18.409, 20.310]	40.216 [40.189, 40.232]	40.238 [40.219 ,40.260]
	NGC 4278 . . (2PL)		15.376 [14.691, 16.074]	18.934 [16.472, 21.119]	40.415 [40.394, 40.434]	40.297 [40.236 ,40.346]
39	NGC 4314	AGN	0.600 [0.077, 0.676]	0.629 [0.000, 343.884]	39.586 [38.638, 39.639]	39.095 [00.000 ,41.810]
40	NGC 4321	SB	2.526 [1.500, 2.787]	1.701 [1.278, 1.986]	40.604 [40.396, 40.643]	39.956 [39.831 ,40.024]
46	NGC 4486	SB	241.902 [241.349, 242.360]	189.549 [188.475, 190.567]	42.338 [42.337, 42.339]	41.847 [41.845 ,41.849]
47	NGC 4494	AGN	0.626 [0.403, 0.674]	1.042 [0.000, 154.494]	39.410 [39.226, 39.446]	39.603 [00.000 ,41.769]
48	NGC 4552	AGN	7.317 [5.796, 7.631]	3.758 [3.139, 4.416]	39.300 [39.210, 39.320]	38.967 [38.889 ,39.035]
50	NGC 4579	AGN	25.164 [23.627, 25.445]	38.261 [34.371, 40.836]	41.292 [41.265, 41.297]	41.412 [41.367 ,41.439]
52	NGC 4594	AGN	6.762 [5.460, 13.558]	13.585 [11.550, 22.447]	40.505 [40.408, 40.777]	40.504 [40.446 ,40.713]
53	NGC 4636	AGN	18.055 [15.340, 18.332]	0.417 [0.391, 0.437]	40.870 [40.801, 40.876]	39.026 [00.000 ,44.428]

Table 3.22: Continuation

Num	Name	Type	Flux(0.5-2.0keV) (10^{-13} erg s^{-1})	Flux(2.0-10.0keV) (10^{-13} erg s^{-1})	Log(Lum(0.5-2.0keV))	Log(Lum(2.0-10.0keV))
(1)	(2)	(3)	(4)	(5)	(6)	(7)
56	NGC 4698	SB	0.278 [0.187, 0.377]	0.460 [0.311, 0.612]	38.998 [38.835, 39.130]	39.193 [39.020 ,39.319]
57	NGC 4696	AGN	30.726 [30.427, 31.018]	59.942 [59.368, 93 60.508]	41.747 [41.743, 41.751]	41.942 [41.938 ,41.947]
58	NGC 4736	SB	10.983 [8.114, 11.081]	15.732 [14.749, 16.912]	39.364 [39.235, 39.368]	39.502 [39.471 ,39.531]
59	NGC 5005	AGN	3.325 [1.357, 3.513]	3.746 [0.000, 259.576]	40.668 [40.247, 40.692]	39.855 [00.000 ,41.718]
61	MRK 0266NE	AGN*	2.029 [1.280, 2.088]	2.898 [0.415, 3.622]	42.469 [42.275, 42.485]	42.108 [41.277 ,42.205]
62	UGC 08696	AGN	0.934 [0.585, 1.008]	3.894 [0.850, 5.070]	42.426 [42.220, 42.455]	42.606 [41.964 ,42.708]
63	CGC G162-010 ...	AGN	72.186 [71.022, 73.545]	91.871 [89.973, 93.815]	43.853 [43.846, 43.861]	43.899 [43.891 ,43.907]
64	NGC 5363	SB	1.266 [0.654, 1.348]	1.883 [0.186, 2.594]	39.884 [39.599, 39.919]	39.782 [38.746 ,39.919]
65	IC 4395	AGN*	0.401 [0.064, 0.378]	0.231 [0.000, 168.792]	41.062 [40.254, 41.040]	40.797 [00.000 ,43.667]
66	IRAS 14348-1447 .	SB*	0.235 [0.136, 0.320]	0.351 [0.107, 0.558]	41.614 [41.366, 41.727]	41.737 [41.200 ,41.953]
68	NGC 5813	SB	13.645 [11.492, 13.799]	0.686 [0.556, 2.255]	41.329 [41.253, 41.334]	39.945 [39.806 ,40.440]
70	NGC 5846	SB	11.648 [10.720, 12.030]	1.343 [0.000, 93.411]	41.191 [41.157, 41.205]	40.293 [00.000 ,42.135]
72	MRK 0848	SB	0.351 [0.092, 0.457]	0.420 [0.335, 1.067]	41.187 [40.493, 41.302]	41.145 [41.048 ,41.551]
73	NGC 6251	SB*	20.722 [20.160, 21.247]	36.750 [33.837, 38.867]	42.677 [42.664, 42.686]	42.755 [42.722 ,42.777]
74	NGC 6240	AGN	4.872 [4.409, 5.242]	25.206 [11.767, 27.173]	43.919 [43.877, 43.953]	44.037 [43.736 ,44.067]
75	IRAS 17208-0014 .	AGN	0.199 [0.000, 0.270]	0.035 [0.000, 0.061]	41.956 [00.000, 42.086]	40.279 [00.000 ,40.494]
76	NGC 6482	AGN	8.655 [7.607, 9.478]	0.405 [0.340, 0.461]	41.703 [41.647, 41.743]	40.185 [40.107 ,40.240]
78	NGC 7285(MEPL)	SB	0.804 [0.377, 0.937]	4.865 [2.745, 5.691]	41.790 [41.476, 41.852]	41.323 [41.052 ,41.395]
	NGC 7285 . . (2PL)		0.795 [0.240, 1.026]	4.914 [1.438, 5.919]	41.022 [40.590, 41.129]	41.332 [40.877 ,41.411]
79	NGC 7331	AGN*	0.852 [0.219, 1.469]	1.416 [0.454, 2.457]	39.271 [38.660, 39.515]	39.467 [38.927 ,39.698]
80	IC 1459	SB	5.011 [4.050, 5.321]	7.327 [6.852, 7.868]	40.725 [40.630, 40.750]	40.712 [40.684 ,40.744]
81	NPM1G -12.0625 .	AGN	45.191 [44.057, 46.127]	45.333 [43.030, 47.341]	44.016 [44.006, 44.025]	43.862 [43.838 ,43.880]
82	NGC 7743	SB	0.526 [0.000, 0.599]	0.436 [0.000, 162.682]	40.530 [00.000, 40.588]	39.548 [00.000 ,42.149]

Table 3.23: *Bestfit model applied to the diffuse emission extracted from* Chandra *data.*

Num	Name	Bestfit	N_{H1}	N_{H2}	Γ	kT (keV)	χ^2	d.o.f	χ^2_R
(1)	(2)	(3)	(4)	(5)	(6)	(7)	(8)	(9)	(10)
1	NGC 0315	ME	$0.04^{0.13}_{0.00}$	...	...	$0.58^{0.62}_{0.52}$	90.91	79	1.15
14	3C 218	ME	$0.00^{0.00}_{0.00}$	...	...	$3.00^{3.09}_{2.95}$	563.84	413	1.37
34	NGC 4111	ME	$0.00^{0.07}_{0.00}$	...	...	$0.53^{0.60}_{0.40}$	23.18	35	0.66
35	NGC 4125	ME	$0.04^{0.37}_{0.00}$	...	...	$0.44^{0.58}_{0.26}$	57.63	61	0.94
37	NGC 4261	ME	$0.00^{0.03}_{0.00}$	...	...	$0.60^{0.64}_{0.57}$	71.68	82	0.87
38	NGC 4278	ME	$0.51^{0.74}_{0.29}$	...	...	$0.54^{0.66}_{0.00}$	78.08	67	1.17
40	NGC 4321	ME	$0.06^{0.21}_{0.00}$	...	...	$0.50^{0.63}_{0.23}$	62.10	48	1.29
41	NGC 4374	MEPL	$0.00^{0.13}_{0.00}$	$0.00^{0.47}_{0.00}$	$1.93^{2.96}_{1.29}$	$0.52^{0.61}_{0.47}$	60.56	68	0.89
46	NGC 4486	MEPL	$0.10^{0.13}_{0.07}$	$0.13^{0.16}_{0.10}$	$2.70^{2.83}_{2.56}$	$1.08^{1.09}_{1.07}$	697.62	375	1.86
48	NGC 4552	ME	$0.00^{0.03}_{0.00}$	...	...	$0.56^{0.59}_{0.53}$	154.84	103	1.50
50	NGC 4579	MEPL	$0.00^{0.07}_{0.00}$	$0.00^{0.10}_{0.00}$	$1.98^{3.22}_{1.41}$	$0.31^{0.41}_{0.23}$	118.32	116	1.02
57	NGC 4696	MEPL	$0.00^{0.11}_{0.00}$	$0.00^{0.13}_{0.00}$	$3.51^{4.30}_{2.65}$	$0.64^{0.66}_{0.61}$	198.32	198	1.00
62	UGC 08696	ME	$0.44^{0.57}_{0.28}$	...	...	$0.62^{0.69}_{0.53}$	67.39	62	1.09
63	CGCG 162-010..	ME	$0.00^{0.00}_{0.00}$	...	...	$4.09^{4.23}_{3.93}$	522.95	394	1.33
68	NGC 5813	ME	$0.10^{0.14}_{0.05}$	...	...	$0.61^{0.63}_{0.58}$	150.65	127	1.19
74	NGC 6240	MEPL	$0.73^{0.80}_{0.62}$	$0.08^{0.18}_{0.00}$	$2.26^{2.61}_{1.88}$	$0.61^{0.66}_{0.58}$	174.16	175	1.00
76	NGC 6482	ME	$0.09^{0.19}_{0.01}$	...	...	$0.76^{0.82}_{0.70}$	63.62	76	0.84
80	IC 1459	ME	$0.00^{0.10}_{0.00}$	...	...	$0.58^{0.62}_{0.50}$	123.01	74	1.66
81	NPM1G -12.0625	MEPL	$1.00^{1.15}_{0.75}$	$0.23^{0.29}_{0.21}$	$2.61^{2.79}_{2.53}$	$0.37^{0.52}_{0.28}$	389.61	307	1.27

NOTES: Column density expressed in units of 10^{22} cm^{-2}

Table 3.24: *Bestfit model applied to* Chandra *data with the* XMM-Newton *extraction region (25 arcsecs).*

Num	Name	Bestfit	N_{H1}	N_{H2}	Γ	kT (keV)	χ^2	d.o.f	χ^2_r
(1)	(2)	(3)	(4)	(5)	(6)	(7)	(8)	(9)	
1	NGC 0315	ME2PL	$0.89^{1.31}_{0.65}$	$13.56^{18.62}_{10.30}$	$2.48^{3.24}_{2.26}$	$0.53^{0.55}_{0.52}$	408.66	369	1.11
7	NGC 0835	ME2PL	$0.04^{0.39}_{0.00}$	$48.03^{90.62}_{21.29}$	$3.36^{4.58}_{2.01}$	$0.44^{0.54}_{0.36}$	61.92	65	0.95
8	NGC 1052	2PL	$0.00^{59.83}_{0.00}$	$8.31^{0.00}_{0.20}$	$0.47^{3.22}_{-0.44}$	$0.55^{0.66}_{0.37}$	57.87	78	0.74
14	3C 218	MEPL	$0.00^{0.04}_{0.00}$	$0.07^{0.09}_{0.02}$	$2.21^{2.26}_{2.07}$	$0.47^{0.63}_{0.44}$	484.73	427	1.14
15	NGC 2787	PL	$0.03^{0.08}_{0.00}$	...	$1.77^{2.01}_{1.60}$	...	136.91	167	0.82
17	UGC 05101	2PL	$0.19^{0.27}_{0.10}$	$6.54^{13.46}_{4.08}$	$2.86^{3.30}_{1.84}$	...	114.29	129	0.89
29	NGC 3690B	MEPL	$0.00^{0.02}_{0.00}$	$0.00^{0.02}_{0.00}$	$2.07^{2.33}_{1.96}$	$0.19^{0.19}_{0.18}$	298.07	236	1.26
32	NGC 3998	MEPL	$0.00^{0.16}_{0.00}$	$0.08^{0.11}_{0.03}$	$1.45^{1.49}_{1.39}$	$0.23^{0.25}_{0.19}$	530.89	450	1.18
35	NGC 4125	ME2PL	$0.00^{0.03}_{0.00}$	$55.77^{179.87}_{20.79}$	$2.35^{2.76}_{2.18}$	$0.54^{0.57}_{0.51}$	192.56	194	0.99
37	NGC 4261	ME2PL	$0.37^{1.58}_{0.21}$	$18.25^{26.04}_{14.73}$	$2.80^{4.87}_{2.27}$	$0.59^{0.61}_{0.58}$	346.87	296	1.17
38	NGC 4278	MEPL	$0.48^{0.64}_{0.29}$	$0.03^{0.06}_{0.01}$	$1.98^{2.06}_{1.89}$	$0.23^{0.31}_{0.18}$	327.99	355	0.92
40	NGC 4321	MEPL	$0.00^{0.17}_{0.00}$	$0.02^{0.09}_{0.00}$	$2.32^{2.71}_{2.12}$	$0.59^{0.64}_{0.51}$	152.67	159	0.96
47	NGC 4494	MEPL	$0.00^{2.42}_{0.00}$	$0.07^{0.23}_{0.00}$	$1.73^{2.34}_{1.28}$	$0.70^{0.86}_{0.47}$	84.60	92	0.92
48	NGC 4552	ME2PL	$0.10^{0.16}_{0.05}$	$15.47^{29.23}_{10.04}$	$2.60^{2.94}_{2.45}$	$0.54^{0.56}_{0.52}$	269.34	253	1.06
50	NGC 4579	2PL	$0.09^{0.11}_{0.06}$	$3.84^{4.10}_{3.47}$	$2.48^{2.59}_{2.25}$	...	524.21	429	1.22
52	NGC 4594	2PL	$0.19^{0.23}_{0.10}$	$4.37^{5.30}_{3.52}$	$2.69^{2.95}_{2.08}$	...	283.02	308	0.92
58	NGC 4736	MEPL	$0.00^{0.02}_{0.00}$	$0.00^{0.01}_{0.00}$	$1.55^{1.59}_{1.52}$	$0.50^{0.51}_{0.47}$	386.70	384	1.01
61	MRK 266NE	ME2PL	$0.00^{0.10}_{0.00}$	$11.68^{24.59}_{5.23}$	$2.54^{3.35}_{2.33}$	$0.76^{0.84}_{0.64}$	141.49	132	1.07
62	UGC 08696	ME2PL	$0.05^{0.11}_{0.00}$	$48.66^{54.13}_{40.06}$	$2.22^{2.52}_{1.80}$	$0.74^{0.82}_{0.66}$	243.66	265	0.92
63	CGCG 162-010..	MEPL	$0.06^{0.09}_{0.04}$	$0.01^{0.02}_{0.00}$	$2.01^{2.11}_{1.92}$	$3.25^{3.43}_{2.84}$	466.00	398	1.17
68	NGC 5813	MEPL	$0.01^{0.05}_{0.00}$	$0.54^{1.17}_{0.29}$	$3.85^{5.27}_{3.15}$	$0.59^{0.60}_{0.57}$	243.38	192	1.27
70	NGC 5846	MEPL	$0.00^{0.03}_{0.00}$	$0.09^{0.27}_{0.00}$	$2.40^{3.22}_{1.84}$	$0.57^{0.59}_{0.55}$	235.55	147	1.60
73	NGC 6251	MEPL	$0.00^{0.23}_{0.00}$	$0.00^{0.08}_{0.00}$	$1.53^{1.69}_{1.44}$	$0.21^{0.22}_{0.16}$	265.07	260	1.02
74	NGC 6240	ME2PL	$0.22^{0.26}_{0.19}$	$85.75^{143.81}_{51.18}$	$2.06^{2.16}_{1.95}$	$0.83^{0.86}_{0.79}$	531.24	384	1.38
75	IRAS 17208-0014	MEPL	$0.83^{1.08}_{0.00}$	$0.05^{0.84}_{0.00}$	$1.41^{2.76}_{0.97}$	$0.22^{0.35}_{0.08}$	115.00	131	0.88
76	NGC 6482	ME	$0.20^{0.24}_{0.17}$	...	...	$0.67^{0.69}_{0.65}$	157.58	141	1.12
80	IC 1459	MEPL	$0.00^{0.18}_{0.00}$	$0.10^{0.13}_{0.08}$	$1.79^{1.88}_{1.73}$	$0.52^{0.57}_{0.47}$	323.81	364	0.89
81	NPM1G -12.0625	ME2PL	$0.12^{0.14}_{0.11}$	$0.00^{0.00}_{0.00}$	$2.24^{2.31}_{2.19}$	$2.72^{2.81}_{2.60}$	419.17	417	1.01

NOTES: Column density expressed in units of 10^{22} cm^{-2}

Table 3.25: *X-ray luminosity for* Chandra *data with the* XMM-Newton *extraction region (25″).*

Num	Name	Log(Lx(0.5-2.0 keV))	Log(Lx(2-10 keV))
(1)	(2)	(3)	(4)
1	NGC 0315	41.624 [41.482,41.650]	41.692 [41.595,41.739]
7	NGC 0835	41.711 [41.270,41.810]	41.472 [40.525,41.712]
8	NGC 1052	40.211 [39.624,40.360]	41.100 [39.818,41.282]
14	3C 218	43.438 [43.386,43.444]	43.414 [43.400,43.447]
15	NGC 2787	38.787 [38.631,38.861]	39.029 [38.949,39.133]
17	UGC 05101	40.833 [40.557,40.894]	41.443 [41.313,41.523]
29	NGC 3690B	41.284 [40.601,41.295]	40.814 [40.677,40.900]
32	NGC 3998	40.935 [40.908,40.943]	41.356 [41.347,41.371]
35	NGC 4125	40.062 [39.706,40.064]	39.720 [39.546,39.826]
37	NGC 4261	41.752 [41.680,41.779]	41.250 [40.199,41.330]
38	NGC 4278	40.445 [40.344,40.472]	40.033 [39.999,40.067]
40	NGC 4321	39.731 [39.399,39.746]	39.385 [39.184,39.602]
47	NGC 4494	39.381 [39.278,39.462]	39.543 [39.441,39.625]
48	NGC 4552	40.224 [40.065,40.228]	39.852 [39.751,39.901]
50	NGC 4579	43.428 [43.333,43.418]	41.211 [41.188,41.227]
52	NGC 4594	41.248 [40.808,41.634]	41.292 [40.582,41.599]
58	NGC 4736	39.470 [39.364,39.473]	39.615 [39.588,39.641]
61	MRK 266NE	42.068 [41.819,42.087]	41.800 [41.054,41.938]
62	UGC 08696	42.947 [42.785,43.000]	42.929 [42.141,43.019]
63	CGCG 162-010..	43.554 [43.517,43.589]	43.597 [43.579,43.676]
68	NGC 5813	41.214 [41.131,41.238]	39.804 [39.491,40.055]
70	NGC 5846	40.197 [40.158,40.231]	40.361 [40.324,40.398]
73	NGC 6251	41.588 [41.129,41.596]	41.587 [41.451,41.671]
74	NGC 6240	42.634 [42.594,42.663]	42.642 [42.525,42.693]
75	IRAS 17208-0014	41.088 [40.710,41.200]	41.273 [41.119,41.419]
76	NGC 6482	41.700 [41.648,41.739]	40.193 [40.128,40.244]
80	IC 1459	40.750 [40.655,40.761]	40.844 [40.808,40.884]
81	NPM1G -12.0625	43.833 [43.823,43.842]	43.751 [43.742,43.764]

Table 3.26: Final compilation of bestfit models for the LINER sample.

Num	Name	Type	Instrument	Bestfit	N_{H1} (10^{22} cm^{-2})	N_{H2} (10^{22} cm^{-2})	Γ	kT (keV)	χ^2_r
(1)	(2)	(3)	(4)	(5)	(6)	(7)	(8)	(9)	(10)
1	NGC 0315.....	AGN	*Chandra*	ME2PL	$15.21^{21.33}_{10.67}$	$1.06^{1.40}_{0.87}$	$2.37^{2.51}_{2.08}$	$0.46^{0.51}_{0.43}$	1.03
2	NGC 0410.....	SB*	*XMM-Newton*	MEPL	$0.12^{0.17}_{0.09}$	$0.01^{0.20}_{0.01}$	$2.43^{3.17}_{1.92}$	$0.69^{0.71}_{0.67}$	1.23
3	NGC 0474.....	SB	*Chandra*	–	...	...	...	...	...
4	IIIZW 035	SB	*Chandra*	–	...	...	...	...	...
5	NGC 0524.....	SB	*Chandra*	–	...	...	...	...	...
6	NGC 0833.....	AGN	*Chandra*	ME2PL	$3.51^{10.79}_{0.73}$	$26.88^{41.78}_{1.34}$	$2.15^{5.43}_{-1.50}$	$0.67^{0.87}_{0.49}$	0.59
7	NGC 0835.....	AGN	*Chandra*	ME2PL	$0.16^{3.13}_{0.01}$	$40.35^{69.46}_{24.60}$	$2.35^{4.80}_{1.75}$	$0.47^{0.59}_{0.39}$	1.08
8	NGC 1052.....	AGN	*Chandra*	2PL	$0.04^{0.26}_{0.01}$	$12.50^{23.58}_{5.51}$	$1.15^{2.37}_{0.41}$	...	0.79
9	NGC 2639.....	SB*	*XMM-Newton*	ME	$0.80^{0.92}_{0.67}$	...	...	$0.18^{0.24}_{0.15}$	1.22
10	NGC 2655.....	AGN*	*XMM-Newton*	ME2PL	$0.01^{0.07}_{0.01}$	$30.20^{39.47}_{24.21}$	$2.48^{2.83}_{2.05}$	$0.64^{0.68}_{0.59}$	0.85
11	NGC 2681.....	AGN	*Chandra*	MEPL	$0.15^{0.28}_{0.01}$	$0.01^{0.08}_{0.01}$	$1.57^{1.89}_{1.29}$	$0.63^{0.68}_{0.54}$	0.65
12	NGC 2685.....	AGN*	*XMM-Newton*	–	...	...	...	...	...
13	UGC 4881.....	SB	*XMM-Newton*	ME	$0.61^{0.79}_{0.32}$	...	...	$0.19^{0.29}_{0.15}$	1.14
14	3C 218	AGN	*Chandra*	ME2PL	$0.07^{0.20}_{0.04}$	$4.05^{5.96}_{2.88}$	$2.11^{2.76}_{1.77}$	$1.71^{2.19}_{1.43}$	0.98
15	NGC 2787.....	AGN	*Chandra*	PL	$0.11^{0.22}_{0.03}$	...	$2.33^{2.94}_{1.87}$	...	1.31
16	NGC 2841.....	AGN	*XMM-Newton*	ME2PL	$0.01^{0.09}_{0.01}$	$3.30^{5.60}_{1.96}$	$2.20^{3.01}_{2.07}$	$0.58^{0.64}_{0.50}$	1.12
17	UGC 05101.....	AGN	*Chandra*	2PL	$0.86^{1.18}_{0.48}$	$0.01^{0.64}_{0.01}$	$1.44^{1.75}_{1.10}$	...	0.90
18	NGC 3185.....	SB*	*XMM-Newton*	–	...	...	...	...	...
19	NGC 3226.....	AGN	*XMM-Newton*	2PL	$0.21^{0.30}_{0.11}$	$1.22^{1.76}_{0.94}$	$1.92^{2.12}_{1.80}$	...	0.95
20	NGC 3245.....	AGN	*Chandra*	–	...	...	...	...	...
21	NGC 3379.....	SB	*Chandra*	–	...	...	...	...	...
22	NGC 3414.....	AGN	*Chandra*	PL	$0.21^{0.30}_{0.13}$	...	$2.02^{2.48}_{1.70}$	...	0.91
23	NGC 3507.....	SB	*Chandra*	ME	$0.08^{0.39}_{0.01}$	...	...	$0.51^{0.64}_{0.28}$	1.30
24	NGC 3607.....	SB	*Chandra*	–	...	...	...	...	...
25	NGC 3608.....	SB	*Chandra*	–	...	...	...	...	...
26	NGC 3623.....	SB*	*XMM-Newton*	–	...	...	...	...	...
27	NGC 3627.....	SB*	*XMM-Newton*	–	...	...	...	...	...
28	NGC 3628.....	SB	*XMM-Newton*	PL	$0.46^{0.52}_{0.41}$	...	$1.61^{1.68}_{1.53}$	...	1.07
29	NGC 3690B	AGN	*Chandra*	ME2PL	$0.21^{0.41}_{0.03}$	$9.49^{12.54}_{7.52}$	$3.52^{4.89}_{2.61}$	$0.19^{0.25}_{0.14}$	0.81
30	NGC 3898.....	SB	*Chandra*	MEPL	$1.39^{1.75}_{1.12}$	$0.01^{0.59}_{0.01}$	$1.81^{2.81}_{1.57}$	$0.04^{0.05}_{0.04}$	0.50
31	NGC 3945.....	AGN	*Chandra*	PL	$0.04^{0.17}_{0.01}$	...	$2.60^{3.22}_{2.32}$	...	0.68
32	NGC 3998.....	AGN	*Chandra*	ME2PL	$0.08^{0.15}_{0.06}$	$2.30^{3.18}_{1.63}$	$1.81^{2.03}_{1.65}$	$0.22^{0.25}_{0.20}$	1.08
33	NGC 4036.....	AGN	*Chandra*	–	...	...	...	...	...

Table 3.26: Continuation

Num	Name	Type	Instrument	Bestfit	N_{H1} (10^{22} cm^{-2})	N_{H2} (10^{22} cm^{-2})	Γ	kT (keV)	χ^2_r
(1)	(2)	(3)	(4)	(5)	(6)	(7)	(8)	(9)	(10)
34	NGC 4111.....	AGN	*Chandra*	ME2PL	$4.67^{9.65}_{1.20}$	$37.71^{100.00}_{12.52}$	$3.04^{8.10}_{0.74}$	$0.66^{0.70}_{0.61}$	1.17
35	NGC 4125.....	AGN	*Chandra*	MEPL	$0.53^{0.88}_{0.01}$	$0.86^{2.13}_{0.08}$	$2.32^{4.59}_{1.26}$	$0.57^{0.59}_{0.55}$	0.61
36	IRAS 12112+0305	SB*	*XMM-Newton*	–	...	...	...	...	...
37	NGC 4261.....	AGN	*Chandra*	ME2PL	$0.69^{1.38}_{0.31}$	$16.45^{21.64}_{13.25}$	$2.37^{2.80}_{1.87}$	$0.57^{0.59}_{0.55}$	1.29
38	NGC 4278.....	AGN	*Chandra*	ME2PL	$0.09^{0.12}_{0.06}$	$2.65^{4.32}_{1.48}$	$2.59^{2.66}_{2.28}$	$0.53^{0.67}_{0.41}$	0.91
39	NGC 4314.....	SB	*XMM-Newton*	MEPL	$0.27^{0.44}_{0.09}$	$0.01^{0.52}_{0.01}$	$1.46^{1.88}_{1.11}$	$0.24^{0.27}_{0.19}$	0.97
40	NGC 4321.....	SB	*Chandra*	MEPL	$0.59^{0.77}_{0.21}$	$0.19^{0.49}_{0.08}$	$2.36^{2.77}_{2.06}$	$0.20^{0.61}_{0.08}$	1.10
41	NGC 4374.....	AGN	*Chandra*	MEPL	$0.07^{0.38}_{0.01}$	$0.13^{0.25}_{0.08}$	$1.95^{2.28}_{1.53}$	$0.72^{0.90}_{0.54}$	0.76
42	NGC 4410A.....	AGN	*Chandra*	MEPL	$0.51^{1.14}_{0.25}$	$0.01^{0.05}_{0.01}$	$1.77^{1.93}_{1.63}$	$0.30^{0.80}_{0.13}$	0.85
43	NGC 4438.....	AGN	*Chandra*	MEPL	$0.37^{0.45}_{0.26}$	$0.01^{0.21}_{0.01}$	$1.91^{2.77}_{1.58}$	$0.52^{0.60}_{0.45}$	0.99
44	NGC 4457.....	AGN	*Chandra*	MEPL	$0.37^{0.57}_{0.08}$	$0.17^{2.60}_{0.01}$	$1.70^{3.54}_{1.18}$	$0.31^{0.68}_{0.22}$	0.84
45	NGC 4459.....	SB	*Chandra*	–	...	...	...	...	...
46	NGC 4486.....	AGN	*Chandra*	ME2PL	$0.10^{0.14}_{0.09}$	$3.96^{4.47}_{3.66}$	$2.40^{2.52}_{2.31}$	$0.82^{0.96}_{0.70}$	1.32
47	NGC 4494.....	AGN	*Chandra*	MEPL	$0.29^{0.72}_{0.01}$	$0.03^{0.17}_{0.01}$	$1.72^{2.31}_{0.90}$	$0.63^{1.02}_{0.24}$	0.65
48	NGC 4552.....	AGN	*Chandra*	MEPL	$0.35^{0.56}_{0.01}$	$0.01^{0.12}_{0.01}$	$2.02^{2.37}_{1.87}$	$0.67^{0.81}_{0.56}$	0.91
49	NGC 4589.....	SB	*Chandra*	–	...	...	...	...	...
50	NGC 4579.....	AGN	*Chandra*	MEPL	$0.48^{0.54}_{0.38}$	$0.45^{0.56}_{0.27}$	$1.58^{1.66}_{1.47}$	$0.20^{0.21}_{0.18}$	1.22
51	NGC 4596.....	SB	*Chandra*	–	...	...	...	...	...
52	NGC 4594.....	AGN	*Chandra*	PL	$0.19^{0.23}_{0.17}$	...	$1.56^{1.67}_{1.46}$	...	1.07
53	NGC 4636.....	SB	*XMM-Newton*	MEPL	$0.01^{0.01}_{0.01}$	$0.01^{0.17}_{0.01}$	$2.92^{3.91}_{2.36}$	$0.54^{0.55}_{0.53}$	1.48
54	NGC 4676A.....	SB	*Chandra*	–	...	...	...	...	...
55	NGC 4676B	AGN	*Chandra*	–	...	...	...	...	...
56	NGC 4698.....	AGN	*Chandra*	–	...	...	...	...	...
57	NGC 4696.....	SB	*Chandra*	MEPL	$0.01^{0.18}_{0.01}$	$0.01^{6.93}_{0.01}$	$3.07^{5.56}_{1.80}$	$0.67^{0.78}_{0.60}$	0.83
58	NGC 4736.....	AGN	*Chandra*	MEPL	$0.31^{0.61}_{0.15}$	$0.04^{0.09}_{0.02}$	$2.05^{2.28}_{1.82}$	$0.54^{0.61}_{0.33}$	0.90
59	NGC 5005.....	AGN*	*XMM-Newton*	MEPL	$0.61^{0.80}_{0.52}$	$0.01^{0.07}_{0.01}$	$1.54^{1.73}_{1.42}$	$0.27^{0.30}_{0.21}$	0.98
60	NGC 5055.....	AGN	*Chandra*	PL	$0.16^{0.33}_{0.05}$	...	$2.30^{3.16}_{1.85}$	...	0.69
61	MRK 266NE	AGN	*Chandra*	ME2PL	$0.01^{0.28}_{0.01}$	$9.45^{28.94}_{5.69}$	$1.34^{1.75}_{0.29}$	$0.83^{1.04}_{0.63}$	0.79
62	UGC 08696.....	AGN	*Chandra*	ME2PL	$0.60^{0.96}_{0.22}$	$50.91^{55.61}_{43.24}$	$2.05^{2.55}_{1.72}$	$0.68^{0.77}_{0.58}$	0.92
63	CGCG 162-010 ..	SB	*Chandra*	ME	$0.47^{0.63}_{0.39}$	...	...	$1.05^{1.10}_{0.96}$	1.01
64	NGC 5363.....	AGN*	*XMM-Newton*	ME2PL	$0.01^{0.08}_{0.01}$	$2.66^{4.37}_{1.74}$	$2.14^{2.69}_{1.76}$	$0.61^{0.65}_{0.56}$	0.98
65	IC 4395	SB*	*XMM-Newton*	MEPL	$0.01^{0.42}_{0.01}$	$0.01^{0.17}_{0.01}$	$1.78^{4.00}_{1.24}$	$0.26^{0.60}_{0.19}$	1.16
66	IRAS 14348-1447	SB	*XMM-Newton*	ME	$0.01^{0.04}_{0.01}$	...	...	$3.67^{6.46}_{2.50}$	0.74
67	NGC 5746.....	AGN	*Chandra*	PL	$0.60^{0.93}_{0.35}$	...	$1.28^{1.67}_{0.93}$	...	0.78
68	NGC 5813.....	SB	*Chandra*	MEPL	$0.12^{0.31}_{0.01}$	$0.15^{0.51}_{0.01}$	$2.94^{6.90}_{1.67}$	$0.49^{0.60}_{0.29}$	0.87
69	NGC 5838.....	AGN	*Chandra*	–	...	...	...	...	...

Table 3.26: Continuation

Num	Name	Type	Instrument	Bestfit	N_{H1} (10^{22} cm^{-2})	N_{H2} (10^{22} cm^{-2})	Γ	kT (keV)	χ^2_r
(1)	(2)	(3)	(4)	(5)	(6)	(7)	(8)	(9)	(10)
70	NGC 5846.....	SB	*Chandra*	MEPL	$0.28^{0.43}_{0.01}$	$0.03^{0.17}_{0.01}$	$2.55^{3.25}_{2.12}$	$0.35^{0.58}_{0.28}$	0.85
71	NGC 5866.....	SB	*Chandra*	–	...	...	...	...	...
72	MRK 0848	SB	*XMM-Newton*	PL	$0.07^{0.19}_{0.01}$	...	$2.26^{2.75}_{1.73}$	...	0.74
73	NGC 6251.....	AGN	*Chandra*	MEPL	$0.01^{0.36}_{0.01}$	$0.01^{0.04}_{0.01}$	$1.48^{1.61}_{1.39}$	$0.20^{0.22}_{0.14}$	1.09
74	NGC 6240.....	AGN	*Chandra*	ME2PL	$0.72^{0.96}_{0.55}$	$50.12^{103.79}_{22.34}$	$1.76^{1.97}_{1.63}$	$1.07^{1.22}_{0.97}$	1.08
75	IRAS 17208-0014	AGN	*Chandra*	PL	$0.34^{0.61}_{0.18}$	...	$1.63^{1.86}_{1.34}$	...	0.76
76	NGC 6482.....	SB	*Chandra*	ME	$0.19^{0.33}_{0.10}$	...	...	$0.75^{0.81}_{0.65}$	0.86
77	NGC 7130.....	AGN	*Chandra*	ME2PL	$0.07^{0.11}_{0.04}$	$86.01^{160.48}_{60.51}$	$2.66^{2.82}_{2.54}$	$0.76^{0.81}_{0.68}$	1.00
78	NGC 7285.....	AGN*	*XMM-Newton*	MEPL	$0.68^{0.78}_{0.01}$	$0.87^{1.13}_{0.59}$	$1.66^{1.76}_{1.43}$	$0.13^{0.19}_{0.07}$	1.02
79	NGC 7331.....	SB	*Chandra*	–	...	...	...	...	...
80	IC 1459	AGN	*Chandra*	ME2PL	$0.20^{0.28}_{0.09}$	$1.26^{3.17}_{0.66}$	$2.17^{2.57}_{2.12}$	$0.61^{0.67}_{0.49}$	0.88
81	NPM1G -12.0625	SB	*Chandra*	MEPL	$0.71^{0.85}_{0.33}$	$0.15^{0.32}_{0.06}$	$2.67^{3.31}_{2.34}$	$0.31^{0.54}_{0.23}$	0.89
82	NGC 7743.....	SB*	*XMM-Newton*	MEPL	$0.35^{0.58}_{0.18}$	$1.68^{3.63}_{0.81}$	$3.16^{6.47}_{1.49}$	$0.23^{0.29}_{0.18}$	1.76

Table 3.27: Final compilation of observed fluxes and absorption corrected luminosities for the LINER sample.

Num	Name	Type	Instrument	Flux(0.5-2.0keV) (10^{-13} erg s^{-1})	Flux(2.0-10.0keV) (10^{-13} erg s^{-1})	Log(L(0.5-2.0keV))	Log(L(2.0-10.0keV))
(1)	(2)	(3)	(4)	(5)	(6)	(7)	(8)
1	NGC 0315.....	AGN	*Chandra*	1.525 [0.456, 1.802]	6.498 [0.227, 7.755]	41.970 [41.436, 42.041]	41.768 [40.857, 41.846]
2	NGC 0410.....	SB*	*XMM-Newton*	5.286 [4.425, 5.667]	0.803 [0.379, 1.102]	41.745 [41.635, 41.773]	40.715 [40.400, 40.839]
3	NGC 0474.....	SB	*Chandra*	0.015 [0.000, 0.037]	0.023 [0.000, 0.060]	38.314 [0.000, 38.745]	38.478 [0.000, 38.916]
4	IIIZW 035	SB	*Chandra*	0.044 [0.008, 0.078]	0.073 [0.018, 0.129]	39.878 [39.170, 40.119]	40.048 [39.413, 40.296]
5	NGC 0524.....	SB	*Chandra*	0.033 [0.002, 0.064]	0.055 [0.000, 0.110]	38.423 [36.084, 38.711]	38.586 [37.093, 38.881]
6	NGC 0833.....	AGN	*Chandra*	0.109 [0.045, 0.154]	5.516 [0.424, 6.417]	41.712 [41.311, 41.849]	41.734 [40.598, 41.807]
7	NGC 0835.....	AGN	*Chandra*	0.411 [0.196, 0.525]	1.365 [1.206, 17.577]	41.687 [41.346, 41.794]	41.399 [41.368, 42.535]
8	NGC 1052.....	AGN	*Chandra*	1.035 [0.000, 1.445]	14.346 [2.228, 18.071]	41.677 [0.000, 41.843]	41.240 [40.404, 41.337]
9	NGC 2639.....	SB*	*XMM-Newton*	1.092 [0.000, 1.190]	0.006 [0.000, 0.007]	42.211 [0.000, 42.252]	38.277 [0.000, 38.370]
10	NGC 2655.....	AGN*	*XMM-Newton*	2.129 [1.330, 2.426]	10.178 [0.211, 11.400]	41.506 [41.312, 41.564]	41.234 [39.541, 41.287]
11	NGC 2681.....	AGN	*Chandra*	0.238 [0.072, 0.265]	1.846 [0.170, 14.065]	38.577 [38.061, 38.622]	39.275 [38.263, 40.169]
12	NGC 2685.....	AGN*	*XMM-Newton*	0.197 [0.111, 0.286]	0.348 [0.189, 0.508]	38.847 [38.573, 39.011]	39.042 [38.781, 39.209]
13	UGC 4881.....	SB	*XMM-Newton*	0.175 [0.000, 0.217]	0.000 [0.000, 0.001]	42.169 [0.000, 42.254]	38.369 [0.000, 38.504]
14	3C 218	AGN	*Chandra*	0.617 [0.412, 0.726]	1.464 [0.399, 1.818]	42.153 [41.958, 42.219]	42.081 [41.535, 42.176]
15	NGC 2787.....	AGN	*Chandra*	0.449 [0.117, 0.566]	0.749 [0.000, 13898.999]	38.877 [38.314, 38.981]	38.805 [0.000, 43.160]
16	NGC 2841.....	AGN	*XMM-Newton*	1.314 [0.530, 1.386]	1.624 [0.325, 2.187]	39.369 [38.983, 39.394]	39.219 [38.172, 39.341]
17	UGC 05101.....	AGN	*Chandra*	0.121 [0.045, 0.158]	0.810 [0.334, 1.167]	41.805 [41.346, 41.925]	42.066 [41.699, 42.223]
18	NGC 3185.....	SB*	*XMM-Newton*	0.260 [0.171, 0.354]	0.434 [0.288, 0.589]	39.179 [38.995, 39.314]	39.374 [39.180, 39.511]
19	NGC 3226.....	AGN	*XMM-Newton*	1.819 [1.230, 2.216]	8.629 [6.249, 9.889]	40.679 [40.513, 40.769]	40.800 [40.657, 40.860]
20	NGC 3245.....	AGN	*Chandra*	0.118 [0.054, 0.181]	0.182 [0.085, 0.280]	38.819 [38.516, 38.998]	38.982 [38.628, 39.159]
21	NGC 3379.....	SB	*Chandra*	0.064 [0.040, 0.087]	0.101 [0.063, 0.137]	37.969 [37.774, 38.114]	38.131 [37.935, 38.263]
22	NGC 3414.....	AGN	*Chandra*	0.950 [0.613, 1.170]	1.633 [1.236, 2.217]	39.949 [39.753, 40.041]	39.863 [39.761, 39.988]
23	NGC 3507.....	SB	*Chandra*	0.179 [0.000, 0.231]	0.003 [0.000, 0.005]	39.072 [0.000, 39.177]	37.204 [0.000, 37.367]
24	NGC 3607.....	SB	*Chandra*	0.061 [0.035, 0.088]	0.093 [0.051, 0.137]	38.602 [38.355, 38.770]	38.765 [38.530, 38.929]
25	NGC 3608.....	SB	*Chandra*	0.017 [0.001, 0.033]	0.025 [0.001, 0.049]	38.042 [36.875, 38.339]	38.205 [37.051, 38.502]
26	NGC 3623.....	SB*	*XMM-Newton*	0.794 [0.585, 0.939]	1.726 [0.000, 48.338]	39.145 [39.003, 39.212]	39.383 [0.000, 40.831]
27	NGC 3627.....	SB*	*XMM-Newton*	1.221 [1.023, 1.421]	2.053 [1.730, 2.387]	39.220 [39.144, 39.286]	39.415 [39.334, 39.481]
28	NGC 3628.....	SB	*XMM-Newton*	1.110 [0.944, 1.241]	5.571 [5.026, 6.103]	39.621 [39.551, 39.668]	39.942 [39.896, 39.981]
29	NGC 3690B	AGN	*Chandra*	0.947 [0.000, 1.422]	1.293 [0.143, 2.030]	41.772 [0.000, 41.961]	40.862 [39.970, 41.074]
30	NGC 3898.....	SB	*Chandra*	0.191 [0.015, 0.268]	0.201 [1119.260, 10468.500]	42.696 [0.000, 42.853]	38.776 [0.000, 43.475]
31	NGC 3945.....	AGN	*Chandra*	0.793 [0.437, 0.984]	0.376 [0.267, 0.487]	39.767 [39.507, 39.860]	39.121 [38.966, 39.232]
32	NGC 3998.....	AGN	*Chandra*	31.270 [25.732, 34.339]	82.463 [60.296, 91.311]	41.178 [41.100, 41.220]	41.319 [41.195, 41.364]
33	NGC 4036.....	AGN	*Chandra*	0.120 [0.071, 0.175]	0.183 [0.103, 0.266]	38.962 [38.738, 39.116]	39.126 [38.898, 39.298]
34	NGC 4111.....	AGN	*Chandra*	0.592 [0.463, 0.701]	3.391 [0.018, 104.038]	40.862 [40.758, 40.937]	40.364 [0.000, 41.864]

Table 3.27: Continuation

Num	Name	Type	Instrument	Flux(0.5-2.0keV) (10^{-13} erg s^{-1})	Flux(2.0-10.0keV) (10^{-13} erg s^{-1})	Log(L(0.5-2.0keV))	Log(L(2.0-10.0keV))
(1)	(2)	(3)	(4)	(5)	(6)	(7)	(8)
35	NGC 4125.....	AGN	*Chandra*	0.074 [0.000, 0.088]	0.069 [0.000, 0.118]	39.938 [0.000, 40.023]	38.730 [0.000, 38.958]
36	IRAS 12112+0305	SB*	*XMM-Newton*	0.091 [0.058, 0.124]	0.151 [0.096, 0.206]	41.030 [40.822, 41.172]	41.226 [41.040, 41.363]
37	NGC 4261.....	AGN	*Chandra*	1.876 [1.496, 2.070]	4.318 [0.078, 5.239]	41.284 [41.181, 41.330]	41.069 [39.410, 41.154]
38	NGC 4278.....	AGN	*Chandra*	2.097 [1.517, 2.385]	1.711 [1.188, 2.067]	39.567 [39.444, 39.619]	39.226 [39.095, 39.307]
39	NGC 4314.....	SB	*XMM-Newton*	0.600 [0.077, 0.676]	0.629 [0.000, 343.884]	39.586 [38.638, 39.639]	39.095 [0.000, 41.810]
40	NGC 4321.....	SB	*Chandra*	0.546 [0.074, 0.637]	5.863 [3.477, 45.585]	40.390 [39.640, 40.454]	40.491 [40.322, 41.405]
41	NGC 4374.....	AGN	*Chandra*	0.526 [0.068, 0.611]	0.811 [0.411, 44.306]	39.506 [38.617, 39.564]	39.533 [39.245, 41.268]
42	NGC 4410A.....	AGN	*Chandra*	0.745 [0.337, 0.805]	1.179 [0.819, 1.432]	41.201 [40.878, 41.231]	41.176 [41.016, 41.262]
43	NGC 4438.....	AGN	*Chandra*	1.105 [0.315, 1.261]	0.322 [0.000, 990.000]	40.076 [39.371, 40.135]	39.047 [0.000, 42.546]
44	NGC 4457.....	AGN	*Chandra*	0.372 [0.014, 0.437]	0.174 [0.119, 0.240]	39.559 [39.422, 39.613]	38.814 [38.635, 38.946]
45	NGC 4459.....	SB	*Chandra*	0.048 [0.005, 0.090]	0.075 [0.008, 0.139]	38.209 [37.389, 38.496]	38.372 [37.727, 38.641]
46	NGC 4486.....	AGN	*Chandra*	5.146 [4.585, 5.521]	16.433 [11.867, 18.328]	40.927 [40.878, 40.957]	40.823 [40.708, 40.867]
47	NGC 4494.....	AGN	*Chandra*	0.423 [0.122, 0.528]	0.162 [0.035, 0.304]	39.753 [39.266, 39.843]	38.777 [38.129, 39.048]
48	NGC 4552.....	AGN	*Chandra*	0.724 [0.424, 0.809]	0.633 [0.191, 0.848]	39.545 [39.311, 39.594]	39.249 [38.799, 39.377]
49	NGC 4589.....	SB	*Chandra*	0.092 [0.048, 0.138]	0.141 [0.068, 0.216]	38.754 [38.460, 38.933]	38.917 [38.635, 39.094]
50	NGC 4579.....	AGN	*Chandra*	12.384 [10.648, 12.375]	43.878 [41.562, 45.853]	40.897 [40.836, 40.895]	41.175 [41.148, 41.193]
51	NGC 4596.....	SB	*Chandra*	0.056 [0.012, 0.100]	0.086 [0.021, 0.152]	38.305 [37.581, 38.546]	38.467 [37.755, 38.724]
52	NGC 4594.....	AGN	*Chandra*	2.252 [1.898, 2.529]	8.018 [7.219, 8.915]	39.637 [39.565, 39.690]	39.973 [39.921, 40.019]
53	NGC 4636.....	SB	*XMM-Newton*	18.055 [15.340, 18.332]	0.417 [0.391, 0.437]	40.870 [40.801, 40.876]	39.026 [0.000, 44.428]
54	NGC 4676A.....	SB	*Chandra*	0.049 [0.025, 0.073]	0.074 [0.035, 0.110]	39.687 [39.398, 39.855]	39.855 [39.577, 40.017]
55	NGC 4676B	AGN	*Chandra*	0.094 [0.063, 0.123]	0.141 [0.093, 0.187]	39.967 [39.789, 40.081]	40.135 [39.962, 40.255]
56	NGC 4698.....	AGN	*Chandra*	0.106 [0.074, 0.140]	0.162 [0.112, 0.216]	38.581 [38.432, 38.704]	38.744 [38.589, 38.864]
57	NGC 4696.....	SB	*Chandra*	2.436 [0.223, 3.070]	0.412 [0.102, 0.632]	41.595 [40.626, 41.690]	39.978 [39.270, 40.156]
58	NGC 4736.....	AGN	*Chandra*	1.166 [0.832, 1.295]	1.317 [0.955, 1.545]	38.758 [38.617, 38.803]	38.599 [38.469, 38.671]
59	NGC 5005.....	AGN*	*XMM-Newton*	3.325 [1.357, 3.513]	3.746 [0.000, 259.576]	40.668 [40.247, 40.692]	39.855 [0.000, 41.718]
60	NGC 5055.....	AGN	*Chandra*	0.184 [0.041, 0.241]	0.091 [0.043, 0.130]	38.595 [38.065, 38.712]	37.778 [37.434, 37.925]
61	MRK 266NE	AGN	*Chandra*	0.249 [0.114, 0.330]	2.154 [0.242, 3.479]	41.026 [40.719, 41.144]	41.656 [40.784, 41.865]
62	UGC 08696.....	AGN	*Chandra*	0.251 [0.000, 0.337]	5.366 [0.287, 6.197]	43.189 [41.877, 43.318]	42.993 [41.713, 43.052]
63	CGCG 162-010 ..	SB	*Chandra*	0.867 [0.459, 1.125]	0.274 [0.184, 0.362]	41.958 [41.813, 42.014]	41.426 [41.254, 41.536]
64	NGC 5363.....	AGN*	*XMM-Newton*	1.266 [0.654, 1.348]	1.883 [0.186, 2.594]	39.884 [39.599, 39.919]	39.782 [38.746, 39.919]
65	IC 4395	SB*	*XMM-Newton*	0.401 [0.064, 0.378]	0.231 [0.000, 168.792]	41.062 [40.254, 41.040]	40.797 [0.000, 43.667]
66	IRAS 14348-1447	SB	*XMM-Newton*	0.235 [0.136, 0.320]	0.351 [0.107, 0.558]	41.614 [41.366, 41.727]	41.737 [41.200, 41.953]
67	NGC 5746.....	AGN	*Chandra*	0.184 [0.044, 0.239]	1.528 [0.499, 2.006]	39.715 [39.018, 39.828]	40.223 [39.767, 40.340]
68	NGC 5813.....	SB	*Chandra*	0.614 [0.196, 0.716]	0.043 [0.012, 0.073]	40.412 [39.914, 40.446]	38.770 [38.271, 38.995]
69	NGC 5838.....	AGN	*Chandra*	0.100 [0.051, 0.148]	0.163 [0.084, 0.237]	39.042 [38.747, 39.207]	39.206 [38.907, 39.381]
70	NGC 5846.....	SB	*Chandra*	0.772 [0.047, 0.899]	9.440 [0.000, 2306.310]	40.224 [39.389, 40.292]	40.814 [0.000, 43.243]

Table 3.27: Continuation

Num	Name	Type	Instrument	Flux(0.5-2.0keV) (10^{-13} erg s^{-1})	Flux(2.0-10.0keV) (10^{-13} erg s^{-1})	Log(L(0.5-2.0keV))	Log(L(2.0-10.0keV))
(1)	(2)	(3)	(4)	(5)	(6)	(7)	(8)
71	NGC 5866.....	SB	*Chandra*	0.046 [0.026, 0.068]	0.070 [0.036, 0.102]	38.133 [37.872, 38.296]	38.296 [38.023, 38.461]
72	MRK 0848	SB	*XMM-Newton*	0.351 [0.092, 0.457]	0.420 [0.335, 1.067]	41.187 [40.493, 41.302]	41.145 [41.048, 41.551]
73	NGC 6251.....	AGN	*Chandra*	2.168 [0.890, 2.144]	3.618 [2.702, 4.271]	41.463 [41.048, 41.460]	41.583 [41.451, 41.655]
74	NGC 6240.....	AGN	*Chandra*	1.447 [1.044, 1.719]	10.400 [7.106, 12.029]	42.219 [42.070, 42.298]	42.408 [42.220, 42.473]
75	IRAS 17208-0014	AGN	*Chandra*	0.073 [0.007, 0.100]	0.396 [0.207, 0.529]	40.817 [40.333, 40.947]	41.188 [40.861, 41.323]
76	NGC 6482.....	SB	*Chandra*	0.684 [0.408, 0.829]	0.055 [0.030, 0.073]	40.697 [40.477, 40.781]	39.335 [39.080, 39.470]
77	NGC 7130.....	AGN	*Chandra*	1.348 [0.699, 1.555]	0.927 [0.462, 1.101]	41.756 [41.455, 41.817]	40.795 [40.501, 40.877]
78	NGC 7285.....	AGN*	*XMM-Newton*	0.804 [0.377, 0.937]	4.865 [2.745, 5.691]	41.790 [41.476, 41.852]	41.323 [41.052, 41.395]
79	NGC 7331.....	SB	*Chandra*	0.075 [0.048, 0.103]	0.137 [0.087, 0.192]	38.294 [38.102, 38.426]	38.456 [38.249, 38.595]
80	IC 1459	AGN	*Chandra*	2.921 [2.072, 4.829]	5.208 [2.485, 6.574]	40.599 [40.431, 40.809]	40.511 [40.137, 40.605]
81	NPM1G -12.0625	SB	*Chandra*	0.415 [0.050, 0.479]	0.176 [0.000, 46.655]	42.601 [41.070, 42.658]	41.463 [0.000, 43.852]
82	NGC 7743.....	SB*	*XMM-Newton*	0.526 [0.000, 0.599]	0.436 [0.000, 162.682]	40.530 [0.000, 40.588]	39.548 [0.000, 42.149]

Table 3.28: *Median and standard deviation properties for the final compilation of our LINER sample in X-rays.*

	X-ray LINER properties		
	Total	AGN	SB
Γ	2.11± 0.52	2.02± 0.48	2.43± 0.57
T(keV)	0.54± 0.30	0.58± 0.30	0.35± 0.27
Log(NH1)	21.32± 0.71	21.32± 0.71	21.43± 0.71
Log(NH2)	21.93± 1.36	22.36± 1.33	20.00± 0.77
Log(L(0.5 − 2 keV))	40.22± 1.33	40.60± 1.19	39.88± 1.47
Log(L(2 − 10 keV))	39.85± 1.26	40.22± 1.24	39.33± 1.16

Table 3.29: Final compilation of EW(FeKα) for the LINER sample

Num	Name	EW(FeKα) (eV)	EW(FeXXV) (eV)	EW(FeXXVI) (eV)
(1)	(2)	(3)	(4)	(5)
1	NGC 0315.....	$81.89^{163.69}_{0.09}$	$137.37^{227.26}_{47.46}$	$27.08^{118.67}_{0.00}$
2	NGC 0410.....	$47.02^{413.54}_{0.00}$	$1360.47^{2466.75}_{249.18}$	$39.11^{474.56}_{0.00}$
3	NGC 0474.....	...	...	...
4	IIIZW 035	...	...	...
5	NGC 0524.....	...	...	...
6	NGC 0833.....	$334.40^{621.63}_{47.17}$	$78.79^{228.90}_{0.00}$	$335.18^{}_{0.00736.92}$
7	NGC 0835.....	$774.92^{1065.17}_{485.49}$	$0.00^{59.05}_{0.00}$	$0.00^{493.06}_{0.00}$
8	NGC 1052.....	$144.40^{166.96}_{121.84}$	$21.51^{37.23}_{5.79}$	$43.36^{64.94}_{21.77}$
9	NGC 2639.....	...	...	...
10	NGC 2655.....	$24.69^{155.51}_{0.00}$	$0.00^{131.61}_{0.00}$	$45.99^{189.26}_{0.00}$
11	NGC 2681.....	$929.23^{2211.99}_{0.00}$	$19.65^{593.19}_{0.00}$	$301.86^{2219.93}_{0.00}$
12	NGC 2685.....	...	...	...
13	UGC 4881.....	...	...	...
14	3C 218	$0.00^{6.13}_{0.00}$	$51.67^{81.49}_{18.64}$	$44.36^{67.29}_{21.58}$
15	NGC 2787.....	$0.00^{291.35}_{0.00}$	$0.00^{331.56}_{0.00}$	$98.79^{535.73}_{0.00}$
16	NGC 2841.....	$0.00^{240.58}_{0.00}$	$0.00^{405.89}_{0.00}$	$0.00^{370.30}_{0.00}$
17	UGC 05101.....	$278.37^{456.52}_{100.22}$	$151.84^{263.90}_{41.68}$	$80.61^{230.46}_{0.00}$
18	NGC 3185.....	...	...	...
19	NGC 3226.....	$33.67^{111.38}_{0.00}$	$0.00^{30.43}_{0.00}$	$47.39^{136.50}_{0.00}$
20	NGC 3245.....	...	...	...
21	NGC 3379.....	...	...	...
22	NGC 3414.....	$0.00^{588.89}_{0.00}$	$0.00^{442.41}_{0.00}$	$0.00^{416.08}_{0.00}$
23	NGC 3507.....	...	...	...
24	NGC 3607.....	...	...	...
25	NGC 3608.....	...	...	...
26	NGC 3623.....	...	...	...
27	NGC 3627.....	...	...	...
28	NGC 3628.....	$0.00^{77.39}_{0.00}$	$98.39^{209.02}_{0.00}$	$17.14^{120.28}_{0.00}$
29	NGC 3690B	$233.42^{341.24}_{125.60}$	$165.42^{255.45}_{75.37}$	$145.73^{262.05}_{29.41}$
30	NGC 3898.....	...	...	...
31	NGC 3945.....	$0.00^{109.52}_{0.00}$	$0.00^{178.38}_{0.00}$	$0.00^{248.41}_{0.00}$
32	NGC 3998.....	$0.00^{31.26}_{0.00}$	$17.29^{54.24}_{0.00}$	$13.31^{53.78}_{0.00}$
33	NGC 4036.....	...	...	...
34	NGC 4111.....	$0.00^{179.91}_{0.00}$	$0.00^{237.77}_{0.00}$	$0.00^{414.51}_{0.00}$
35	NGC 4125.....	$0.00^{1559.70}_{0.00}$	$67.00^{2056.16}_{0.00}$	$330.40^{2947.66}_{0.00}$
36	IRAS 12112+0305	...	...	...
37	NGC 4261.....	$26.11^{105.52}_{0.00}$	$21.86^{97.77}_{0.00}$	$70.68^{173.30}_{0.00}$

Table 3.29: Continuation

Num	Name	EW(FeKα) (eV)	EW(FeXXV) (eV)	EW(FeXXVI) (eV)
(1)	(2)	(3)	(4)	(5)
38	NGC 4278.....	$0.00^{48.20}_{0.00}$	$0.00^{29.31}_{0.00}$	$0.00^{29.63}_{0.00}$
39	NGC 4314.....	$708.79^{1590.35}_{0.00}$	$0.00^{492.54}_{0.00}$	$204.87^{1029.44}_{0.00}$
40	NGC 4321.....	$0.00^{170.94}_{0.00}$	$344.52^{705.80}_{0.00}$	$231.42^{584.46}_{0.00}$
41	NGC 4374.....	$661.31^{1595.10}_{0.00}$	$0.00^{461.28}_{0.00}$	$0.00^{1260.98}_{0.00}$
42	NGC 4410A.....	$117.55^{432.16}_{0.00}$	$245.40^{583.21}_{0.00}$	$205.63^{594.11}_{0.00}$
43	NGC 4438.....	$222.32^{2462.99}_{0.00}$	$13.82^{2245.79}_{0.00}$	$2.51^{0.00}_{0.00}$
44	NGC 4457.....	$0.00^{61.92}_{0.00}$	$0.00^{98.06}_{0.00}$	$0.00^{192.89}_{0.00}$
45	NGC 4459.....	...	...	...
46	NGC 4486.....	$84.04^{131.24}_{36.85}$	$134.79^{192.02}_{77.57}$	$139.92^{212.67}_{67.17}$
47	NGC 4494.....	$0.00^{374.52}_{0.00}$	$0.00^{392.19}_{0.00}$	$0.00^{444.36}_{0.00}$
48	NGC 4552.....	$24.06^{317.93}_{0.00}$	$0.00^{272.73}_{0.00}$	$0.00^{314.01}_{0.00}$
49	NGC 4589.....	...	...	...
50	NGC 4579.....	$115.05^{157.14}_{72.96}$	$45.49^{81.07}_{9.91}$	$75.31^{121.61}_{29.02}$
51	NGC 4596.....	...	...	...
52	NGC 4594.....	$28.49^{106.10}_{0.00}$	$96.32^{178.57}_{0.00}$	$0.00^{41.78}_{0.00}$
53	NGC 4636.....	$296.01^{1753.93}_{0.00}$	$346.35^{1171.77}_{0.00}$	$550.43^{2472.83}_{0.00}$
54	NGC 4676A.....	...	...	...
55	NGC 4676B	...	...	...
56	NGC 4698.....	...	...	...
57	NGC 4696.....	...	...	...
58	NGC 4736.....	$8.71^{98.56}_{0.00}$	$56.15^{133.71}_{0.00}$	$0.00^{95.73}_{0.00}$
59	NGC 5005.....	...	...	...
60	NGC 5055.....	$0.00^{35.22}_{0.00}$	$0.00^{52.90}_{0.00}$	$0.00^{107.18}_{0.00}$
61	MRK 266NE	$275.72^{481.38}_{71.24}$	$47.65^{178.02}_{0.00}$	$0.00^{146.25}_{0.00}$
62	UGC 08696.....	$266.11^{382.32}_{149.90}$	$135.94^{226.84}_{45.04}$	$70.24^{173.71}_{0.00}$
63	CGCG 162-010 ..	$0.00^{4.18}_{0.00}$	$105.80^{124.19}_{86.36}$	$17.29^{28.43}_{6.18}$
64	NGC 5363.....	$50.45^{337.81}_{0.00}$	$351.88^{852.44}_{0.00}$	$54.84^{700.98}_{0.00}$
65	IC 4395	...	...	...
66	IRAS 14348-1447	...	...	...
67	NGC 5746.....	$41.46^{375.02}_{0.00}$	$0.00^{213.71}_{0.00}$	$129.20^{563.96}_{0.00}$
68	NGC 5813.....	$0.00^{2609.74}_{0.00}$	$0.00^{2206.17}_{0.00}$	$0.00^{2453.49}_{0.00}$
69	NGC 5838.....	...	...	...
70	NGC 5846.....	$0.00^{177.73}_{0.00}$	$0.00^{204.29}_{0.00}$	$0.00^{248.38}_{0.00}$
71	NGC 5866.....	...	...	...
72	MRK 0848	$196.92^{2398.18}_{0.00}$	$4.16^{916.54}_{0.00}$	$1777.01^{5307.68}_{0.00}$
73	NGC 6251.....	$24.30^{53.49}_{0.00}$	$32.90^{63.18}_{0.70}$	$0.00^{21.82}_{0.00}$
74	NGC 6240.....	$378.06^{441.86}_{314.27}$	$115.35^{151.57}_{79.14}$	$105.08^{159.76}_{50.40}$
75	IRAS 17208-0014	$217.03^{558.42}_{0.00}$	$427.05^{851.02}_{0.00}$	$462.96^{1020.93}_{0.00}$
76	NGC 6482.....	...	...	...
77	NGC 7130.....	$382.06^{633.04}_{131.08}$	$147.04^{333.58}_{0.00}$	$34.44^{307.20}_{0.00}$
78	NGC 7285.....	$211.68^{382.09}_{39.28}$	$59.20^{247.70}_{0.00}$	$61.49^{295.86}_{0.00}$
79	NGC 7331.....	...	...	...
80	IC 1459	$0.00^{72.47}_{0.00}$	$0.00^{76.96}_{0.00}$	$41.38^{173.16}_{0.00}$
81	NPM1G -12.0625	$0.00^{4.35}_{0.00}$	$38.34^{58.34}_{16.40}$	$26.48^{41.97}_{11.06}$
82	NGC 7743.....	$1746.22^{8337.29}_{0.00}$	$0.00^{3065.32}_{0.00}$	$0.00^{2121.33}_{0.00}$

Table 3.30: Relevant data for the analysis of Compton-thickness.

Num	Name	EW(FeK) (eV)	Log(L([OIII])	Log(L(0.5-2 keV)	Log(L(2-10 keV)	L(2-10keV)/L([OIII])	Log(M_{BH})	Refs.*
(1)	(2)	(3)	(4)	(5)	(6)	(7)	(8)	(9)
1	NGC 0315.....	81.89	39.47	41.97	41.77	2.30	8.61	TD81
2	NGC 0410.....	< 413.54	39.34	41.74	40.72	1.38	8.79	TD81
3	NGC 0474.....	...	38.61	40.09	<40.26	-0.13	7.93	TD81
4	IIIZW 035	...	41.39	41.66	41.83	-1.34	...	...
5	NGC 0524.....	...	37.49	38.42	38.59	1.09	8.29	TD81
6	NGC 0833.....	334.40	39.96	41.71	41.73	1.78	8.97	OFJSB
7	NGC 0835.....	774.92	...	41.69	41.40	...	8.16	TD81
8	NGC 1052.....	144.40	40.17	41.68	41.24	1.07	8.07	CDB-93
9	NGC 2639.....	...	40.04	43.99	<40.06	-1.76	7.85	S83
10	NGC 2655.....	< 155.51	40.09	41.51	41.23	1.14	7.10	OFJSB
11	NGC 2681.....	<2211.99	39.19	40.36	41.05	0.08	6.70	OFJSB
12	NGC 2685.....	...	39.16	40.63	40.82	-0.11	8.96	Din+95
13	UGC 4881.....	...	41.26	43.95	<40.15	-2.89	...	...
14	3C 218	< 6.13	40.33	42.15	42.08	1.75	...	...
15	NGC 2787.....	< 291.35	37.89	38.88	<38.81	0.91	8.11	TD81
16	NGC 2841.....	< 240.58	38.38	39.37	39.22	0.84	8.23	WRF84
17	UGC 05101.....	278.37	43.02	43.58	43.84	-0.96	...	...
18	NGC 3185.....	...	40.07	40.96	41.15	-0.70	6.06	NW95
19	NGC 3226.....	< 111.38	38.95	40.68	40.80	1.85	8.22	TD81
20	NGC 3245.....	...	39.25	40.60	40.76	-0.26	8.39	TD81
21	NGC 3379.....	...	37.96	39.75	39.91	0.17	8.25	TD81
22	NGC 3414.....	< 588.89	39.14	39.95	39.86	0.72	8.67	Din+95
23	NGC 3507.....	...	39.09	40.85	<38.98	-1.89	...	...
24	NGC 3607.....	...	39.47	40.38	40.54	-0.70	8.48	TD81
25	NGC 3608.....	...	38.24	39.82	39.98	-0.04	8.41	TD81
26	NGC 3623.....	...	37.68	39.15	<39.38	1.70	7.62	WKS
27	NGC 3627.....	...	39.47	41.00	41.19	-0.05	7.98	WKS
28	NGC 3628.....	< 77.39	37.03	39.62	39.94	2.92	7.91	WKS
29	NGC 3690B	233.42	41.58	43.55	42.64	-0.72	...	...
30	NGC 3898.....	...	38.72	44.47	<40.55	0.06	8.29	S83
31	NGC 3945.....	< 109.52	38.51	39.77	39.12	0.61	7.89	OFJSB
32	NGC 3998.....	< 31.26	39.83	41.18	41.32	1.48	8.92	TD81
33	NGC 4036.....	...	39.16	40.74	40.90	-0.03	8.12	TD81
34	NGC 4111.....	< 179.91	39.15	40.86	<40.36	1.22	7.56	OFJSB
35	NGC 4125.....	<1559.70	38.70	41.72	<40.51	0.35	8.31	TD81
36	IRAS 12112+0305	...	41.33	42.81	43.00	-0.11	...	...

Table 3.30: Continuation

Num	Name	EW(FeK) (eV)	Log(L([OIII])	Log(L(0.5-2 keV)	Log(L(2-10 keV)	L(2-10keV)/L([OIII])	Log(M_{BH})	Refs.*
(1)	(2)	(3)	(4)	(5)	(6)	(7)	(8)	(9)
37	NGC 4261.....	< 26.11	39.59	41.28	41.07	1.48	8.96	TD81
38	NGC 4278.....	< 48.20	39.32	41.35	41.00	-0.09	8.46	TD81
39	NGC 4314.....	< 708.79	37.90	39.59	<39.10	1.19	7.19	BHS02r
40	NGC 4321.....	< 170.94	38.72	40.39	40.49	1.77	6.76	WK
41	NGC 4374.....	<1595.10	39.09	41.28	41.31	0.44	8.95	TD81
42	NGC 4410A.....	< 432.16	40.99	42.98	42.95	0.19	...	...
43	NGC 4438.....	<2462.99	39.65	41.85	<40.83	-0.60	7.89	TD81
44	NGC 4457.....	< 61.92	39.20	41.34	40.59	-0.39	6.95	OFJSB
45	NGC 4459.....	...	37.85	38.21	38.37	0.52	7.74	TD81
46	NGC 4486.....	84.04	39.48	40.93	40.82	1.34	9.10	TD81
47	NGC 4494.....	< 374.52	37.84	39.75	38.78	0.93	7.99	TD81
48	NGC 4552.....	< 317.93	38.02	39.54	39.25	1.23	8.84	TD81
49	NGC 4589.....	...	39.08	40.53	40.70	-0.16	8.57	TD81
50	NGC 4579.....	115.05	39.42	40.90	41.17	1.75	8.09	WKS
51	NGC 4596.....	...	37.62	38.31	38.47	0.84	7.49	TD81
52	NGC 4594.....	< 106.10	38.85	39.64	39.97	1.13	8.57	Mar+94
53	NGC 4636.....	<1753.93	37.82	40.87	<39.03	1.21	8.29	TD81
54	NGC 4676A.....	...	39.27	39.69	39.85	0.58	...	...
55	NGC 4676B	...	38.80	39.97	40.13	1.33	8.79	WHLD
56	NGC 4698.....	...	38.88	40.36	40.52	-0.13	7.87	WK
57	NGC 4696.....	...	38.92	41.60	39.98	1.06	8.56	CDB-93
58	NGC 4736.....	< 98.56	37.58	38.76	38.60	1.02	7.43	WKS
59	NGC 5005.....	...	39.41	42.45	<41.63	0.45	...	...
60	NGC 5055.....	< 35.22	38.20	40.37	39.56	-0.42	7.21	FiBD86
61	MRK 266NE	275.72	42.41	42.80	43.43	-0.75	...	...
62	UGC 08696.....	266.11	43.26	44.97	44.77	2.19	7.74	Jam+99
63	CGCG 162-010 ..	< 4.18	...	41.96	41.43	...	8.82	OH
64	NGC 5363.....	< 337.81	40.19	41.66	41.56	-0.41	8.12	SCHL83
65	IC 4395	...	42.67	42.84	<42.58	-1.88	...	...
66	IRAS 14348-1447	...	40.00	41.61	41.74	1.73	...	...
67	NGC 5746.....	< 375.02	39.05	39.72	40.22	1.17	8.14	BRBH93
68	NGC 5813.....	<2609.74	38.37	42.19	40.55	0.40	8.22	TD81
69	NGC 5838.....	...	39.59	40.82	40.98	-0.38	8.75	DS83
70	NGC 5846.....	< 177.73	38.47	40.22	<40.81	2.35	8.49	TD81
71	NGC 5866.....	...	38.60	39.91	40.07	-0.30	7.97	TDT
72	MRK 0848	<2398.18	39.49	41.19	41.15	1.66	...	...

Table 3.30: Continuation

Num	Name	EW(FeK) (eV)	Log(L([OIII])	Log(L(0.5-2 keV)	Log(L(2-10 keV)	L(2-10keV)/L([OIII])	Log(M_{BH})	Refs.*
(1)	(2)	(3)	(4)	(5)	(6)	(7)	(8)	(9)
73	NGC 6251.....	< 53.49	41.92	43.24	43.36	-0.33	8.80	H+85
74	NGC 6240.....	378.06	43.29	44.00	44.19	-0.88	8.84	OOMM99
75	IRAS 17208-0014	< 558.42	42.41	42.60	42.97	-1.23	...	...
76	NGC 6482.....	...	42.24	42.48	41.11	-2.90	8.76	7Sam
77	NGC 7130.....	382.06	41.84	43.53	42.57	-1.05	...	...
78	NGC 7285.....	211.68	40.21	41.79	41.32	1.12	...	...
79	NGC 7331.....	...	38.55	40.07	40.23	-0.10	7.56	BRBH93
80	IC 1459	< 72.47	...	40.60	40.51	...	8.81	CDB-93
81	NPM1G -12.0625	< 4.35	41.45	44.38	<43.24	0.01	8.18	SHI90
82	NGC 7743.....	<8337.29	40.30	42.31	<41.33	-0.75	6.62	NW95

(*) Velocity dispersion taken from: TD81 (Tonry and Davis, 1981), OFJSB (Ore et al., 1991), CDB-93 (Carollo et al., 1993), S83 (Schechter, 1983), Din+95 (di Nella et al., 1995), WRF84 (Whitmore et al., 1984), NW95 (Nelson and Whittle, 1995), WKS (Whitmore et al., 1979), BHS02r (Barth et al., 2002), WK (Whitmore and Kirshner, 1981), Mar+94 (van der Marel et al., 1994), WHLD (White et al., 1983), FiBD86 (Fillmore et al., 1986), Jam+99 (James et al., 1999), OH (Oegerle and Hoessel, 1991), BRBH93 (Bower et al., 1993), DS83 (Dressler and Sandage, 1983), H+85 (Heckman et al., 1985), OOMM99 (Oliva et al., 1999), 7Sam (Faber et al., 1989), SHI90 (Smith et al., 1990).

Table 3.31: Multiwavelength properties of LINERs*.

Num	Name	X-ray Class.	Log(Lx) (2-10 keV)	*HST* Class.	Broad Hα	Radio Comp.	Stellar Pop. (%)	UV Var.	X-ray Var.	UV Comp.	*C-T**	Envir.	Env. code
(1)	(2)	(3)	(4)	(5)	(6)	(7)	(8)	(9)	(10)	(11)	(12)	(13)	(14)
1	NGC 0315	AGN	41.77	C	Yes	Yes J (1,3)	3.8	...	.....	.....	....	Cluster	20
2	NGC 0410	SB*	40.72	.....	.....	No (1,5)	2.7	...	.....	.....	....	Cluster	20
3	NGC 0474	SB	<40.26	.....	.....	No (1)	.....	...	.....	.....	CT?	Wide Pair	2.5
4	IIIZW 035	SB	41.83	C	.....	Yes F (7)	.....	...	.....	.....	CT .	Close Pair	1.5
5	NGC 0524	SB	38.59	D	.....	No (8)	.....	...	.....	.....	....	Small Group	5
6	NGC 0833	AGN	41.73	.....	.....	No (8)	.....	...	.....	.....	....	Comp. Group	4
7	NGC 0835	AGN	41.40	.....	.....	Yes S (8)	.....	...	.....	.....	— .	Comp. Group	4
8	NGC 1052	AGN	41.24	C	Yes	Yes (21)	4.0	...	.....	Yes(1)	....	Small Group	5
9	NGC 2639	SB*	<40.06	C	Yes	Yes F (9)	.....	...	.....	.....	CT .	Isolate	0
10	NGC 2655	AGN*	41.23	C	.....	Yes S (1)	.....	...	.....	.....	....	Strongly Interac.	1.5
11	NGC 2681	AGN	41.05	C	Yes	No (1)	4.2	...	.....	Yes(1)	CT?	Small Group	4
12	NGC 2685	AGN*	40.82	.....	.....	No (1)	1.4	...	.....	.....	CT?	Isolate?	0
13	UGC 4881	SB	<40.15	C	.....	.....	.....	...	.....	.....	CT .	Interact. Pair	1.5
14	3C 218	AGN	42.08	.....	.....	Yes J (10)	.....	...	.....	.....	....	Cluster	20
15	NGC 2787	AGN	<38.81	C	Yes	Yes (1)	.....	...	.....	No(1).	....	Isolate	0
16	NGC 2841	AGN	39.22	C	.....	.....	.....	...	.....	.....	....	Isolate	0
17	UGC 05101	AGN	43.84	C	.....	Yes S (7)	.....	...	.....	.....	CT .	Strongly Interac.	1.5
18	NGC 3185	SB*	41.15	C	.....	Yes marg.(9)	.....	...	.....	.....	CT .	Comp. Group	4
19	NGC 3226	AGN	40.80	.....	Yes	Yes F (5)	2.2	...	.....	.....	....	Strongly Interac.	1.5
20	NGC 3245	AGN	40.76	C	.....	No (1)	6.2	...	.....	.....	CT .	Wide Pair	2.5
21	NGC 3379	SB	39.91	C	.....	No (1)	.....	...	.....	.....	CT?	1st Leo Group	4.5
22	NGC 3414	AGN	39.86	.....	.....	Yes F (1)	.....	...	.....	.....	....	Wide Group	5
23	NGC 3507	SB	<38.98	C	.....	No (1)	32.6	...	.....	.....	CT .	Wide Pair	2.5
24	NGC 3607	SB	40.54	C	.....	Yes (1)	.....	...	.....	.....	CT .	1st Group	4.5
25	NGC 3608	SB	39.98	C	.....	No (1)	.....	...	.....	.....	CT?	Group	5
26	NGC 3623	SB*	<39.38	C	.....	No (1)	.....	...	.....	.....	....	Triplet	3
27	NGC 3627	SB*	41.19	D	.....	Yes F (2,4)	5.0(7.3)	...	.....	.....	CT?	Triplet	3
28	NGC 3628	SB	39.94	U	.....	No Ext. (1,2)	.....	...	.....	.....	....	Triplet	3
29	NGC 3690B	AGN	42.64	C	.....	Yes S (11)	.....	...	.....	.....	CT .	Strongly Interac.	1.5
30	NGC 3898	SB	<40.55	C	.....	No (1)	.....	...	.....	.....	CT?	Cluster (member)	20
31	NGC 3945	AGN	39.12	C	.....	Yes (1)	.....	...	.....	.....	....	Isolate	0
32	NGC 3998	AGN	41.32	C	Yes	Yes (1)	54.4	Yes	.....	Yes(2)	....	Group	5
33	NGC 4036	AGN	40.90	C	Yes	No (1)	.....	...	.....	.....	CT?	Wide Pair	2.5
34	NGC 4111	AGN	<40.36	C?	.....	No (1)	.....	...	.....	No(1).	....	Group	5
35	NGC 4125	AGN	<40.51	C	.....	No (1)	.....	...	.....	.....	CT?	Pair	2
36	IRAS 12112+0305	SB*	43.00	.....	.....	Yes F (7)	.....	...	.....	.....	CT?	Merger	1

Table 3.31: Continuation

Num	Name	X-ray Class.	Log(L_X) (2-10 keV)	*HST* Class.	Broad Hα	Radio Comp.	Stellar Pop. (%)	UV Var.	X-ray Var.	UV Comp.	*C-T**	Envir.	Env. code
(1)	(2)	(3)	(4)	(5)	(6)	(7)	(8)	(9)	(10)	(11)	(12)	(13)	(14)
37	NGC 4261.....	AGN	41.07.....	U....	.....	Yes J (1)	2.2	...	.....	.....	....	Group	5
38	NGC 4278.....	AGN	41.00.....	C....	Yes ..	Yes J (1)	.....	...	.....	.....	CT?	Group	5
39	NGC 4314.....	SB ...	<39.10...	C....	.....	No (1)	3.8	...	.....	No(1).	....	Group	5
40	NGC 4321.....	SB ...	40.49.....	C....	.....	No Ext. S (5)	24.7	...	.....	.....	....	Cluster Member	20
41	NGC 4374.....	AGN	41.31.....	C....	.....	Yes J (1)	.....	...	.....	.....	CT?	Cluster Center	10
42	NGC 4410A.....	AGN	42.95.....	C....	Yes ..	Yes (5)	.....	...	.....	.....	CT?	Comp. Group	4
43	NGC 4438.....	AGN	<40.83...	D....	Yes ..	No (1)	2.2	...	.....	No(1).	CT .	Pair	2
44	NGC 4457.....	AGN	40.59.....	.....	.....	No (1)	.....	...	.....	.....	CT .	Isolate?	0
45	NGC 4459.....	SB ...	38.37.....	C....	.....	No (1)	8.7	...	.....	.....	....	Group	5
46	NGC 4486.....	AGN	40.82.....	C....	Yes ..	Yes (1)	.....	Yes	Yes..	Yes(2)	....	Cluster Center	10
47	NGC 4494.....	AGN	38.78.....	C....	.....	No (1)	.....	...	.....	.....	....	Coma Cloud (Iso)	0
48	NGC 4552.....	AGN	39.25.....	C....	.....	Yes (1)	.....	Yes	Yes..	Yes(2)	....	Virgo Isolate	0
49	NGC 4589.....	SB ...	40.70.....	C....	.....	Yes (1,5)	.....	...	.....	.....	CT .	Pair	2
50	NGC 4579.....	AGN	41.17.....	C....	Yes ..	Yes (1)	.....	Yes	.....	Yes(2)	....	Small Group	5
51	NGC 4596.....	SB ...	38.47.....	C....	.....	No (1)	4.1	...	.....	.....	....	Wide Pair	2.5
52	NGC 4594.....	AGN	39.97.....	C....	.....	Yes (13)	.....	Yes	.....	Yes(2)	....	Isolate	0
53	NGC 4636.....	SB ...	<39.03...	D....	Yes ..	Yes (1)	.....	...	.....	No(1).	....	Isolate	0
54	NGC 4676A.....	SB ...	39.85.....	D....	.....	.....	.....	...	.....	.....	....	Interac. Pair	1.5
55	NGC 4676B	AGN	40.13.....	C....	.....	.....	.....	...	.....	.....	....	Interac. Pair	1.5
56	NGC 4698.....	AGN	40.52.....	C....	.....	No (1)	.....	...	.....	.....	CT?	Isolate	0
57	NGC 4696.....	SB ...	39.98.....	C....	.....	Yes F (14) ...	.....	...	.....	.....	....	Cluster Center	10
58	NGC 4736.....	AGN	38.60.....	C....	.....	Yes (1)	5.3	Yes	.....	Yes(1)	....	Isolate	0
59	NGC 5005.....	AGN*	<41.63...	C?...	Yes ..	No (1)	3.6	...	Yes..	.....	CT?	Isolate	0
60	NGC 5055.....	AGN	39.56.....	C....	.....	No (1)	5.7(14.0)	...	.....	Yes(2)	CT .	Small Comp. Group	4
61	MRK 266NE	AGN	43.43.....	C....	.....	.....	.....	...	.....	.....	CT .	Merger	1
62	UGC 08696.....	AGN	44.77.....	C....	.....	Yes F (7)	.....	...	.....	.....	....	Merger	1
63	CGCG 162-010 ..	SB ...	41.43.....	C....	.....	Yes F (15) ...	.....	...	.....	.....	— .	Cluster Center	10
64	NGC 5363.....	AGN*	41.56.....	.....	.....	Yes J (1)	.....	...	.....	.....	CT .	Group Wide Pair	2
65	IC 4395	SB* ..	<42.58...	.....	.....	.....	.....	...	.....	.....	CT .	Close Inter. Pair	1.5
66	IRAS 14348-1447	SB ...	41.74.....	C....	.....	Yes F (11) ...	.....	...	.....	.....	....	Merger	1
67	NGC 5746.....	AGN	40.22.....	C?...	.....	No (1)	.....	...	.....	.....	....	Very wide Pair	2
68	NGC 5813.....	SB ...	40.55.....	C....	.....	Yes (1)	.....	...	.....	.....	CT?	Group	5
69	NGC 5838.....	AGN	40.98.....	C....	.....	Yes F (2)	.....	...	.....	.....	CT .	Group	5
70	NGC 5846.....	SB ...	<40.81...	C....	.....	Yes J (1,2,4) .	.....	...	.....	.....	....	Group 1st	4.5
71	NGC 5866.....	SB ...	40.07.....	.....	.....	Yes F (1,2,4)	.....	...	.....	.....	CT .	Group	5
72	MRK 0848	SB ...	41.15.....	C....	.....	Yes F (16) ...	.....	...	.....	.....	....	Interact. Pair	1.5

Table 3.31: Continuation

Num	Name	X-ray Class.	Log(L_X) (2-10 keV)	*HST* Class.	Broad Hα	Radio Comp.	Stellar Pop. (%)	UV Var.	X-ray Var.	UV Comp.	*C-T**	Envir.	Env. code
(1)	(2)	(3)	(4)	(5)	(6)	(7)	(8)	(9)	(10)	(11)	(12)	(13)	(14)
73	NGC 6251.....	AGN	43.36.....	C....	.....	Yes J (17,18)	.....	...	.....	.....	CT .	Pair	2
74	NGC 6240.....	AGN	44.19.....	C....	.....	Yes (19)	.....	...	.....	.....	CT .	Merger	1
75	IRAS 17208-0014	AGN	42.97.....	C....	.....	Yes F (7)	.....	...	.....	.....	CT .	Merger	1
76	NGC 6482.....	SB ...	41.11.....	.....	.....	No (1)	1.7	...	.....	.....	CT .	Group	5
77	NGC 7130.....	AGN	42.57.....	C....	.....	Yes S (8)	.....	...	.....	.....	CT .	Interact. Pair?	1.5
78	NGC 7285.....	AGN*	41.32.....	.....	.....	.....	.....	...	.....	.....	....	Interact. Pair	1.5
79	NGC 7331.....	SB ...	40.23.....	C....	.....	Yes F (3)	1.9(2.1)	...	.....	.....	CT?	Isolate	0
80	IC 1459	AGN	40.51.....	C....	.....	Yes F (14) ...	.....	...	.....	.....	— .	Close Group	4
81	NPM1G -12.0625	SB ...	<43.24...	D....	.....	Yes S (20) ...	.....	...	.....	.....	CT?	Cluster Center	10
82	NGC 7743.....	SB* ..	<41.33...	C....	.....	Yes F (9)	.....	...	.....	.....	CT .	Isolate	0

C-T = Compton-Thick candidates. (1) Chiaberge et al. (2005); (2) Maoz et al. (2005). Col. (7) Stellar populations younger than 10^9 yr taken from Cid-Fernandes et al. (2004) and Gonzalez-Delgado et al. (2004) (within parentesis)

Col. () Broad Hα reported by Ho et al. 1997b

Col. (6) References: (1) Nagar et al. (2005); (2) Filho et al. (2000); (3) Filho et al. (2002); (4) Filho et al. (2004); (5) Filho et al. (2006); (6) Anderson and Ulvestad (2005); (7) Baan and Klockner (2006); (8) Corbett et al. (2002); (9) Ho and Ulvestad (2001); (10) Taylor et al. (1990); (11) Condon and Broderick (1991); (12) Smith (2000); (13) Bajaja et al. (1988); (14) Slee et al. (1994); (15) van Breugel et al. (1984); (16) Clemens et al. (2008); (17) Urry and Padovani (1995); (18) Jones et al. (1986); (19) Carral et al. (1990); (20) Sarazin et al. (1995); (21) Vermeulen et al. (2003) Col. (13) Interacting types: 0 = Isolate, 1 = Merger, 1.5 = Close Interacting Pair, 2 = Pair, 2.5 = Wide Pair, 3 = Triplet, 4 = Compact Group, 4.5 = 1st group, 5 = Group, 10 = Cluster Center and, 20 = Cluster Member

Table 3.32: *L(2-10 keV)/L[OIII] ratios for the LINERs grouped in different environments.*

Environment (Nr)	$L(hardX)/L[OIII]$	σ	range
ISO (15)	0.33	0.77	-1.76 to 1.23
PAIR (29)	-0.06	1.02	-2.89 to 2.19
GROUP(23)	0.43	0.91	-2.90 to 2.35
CLUSTER (9)	1.12	1.12	0.01 to 2.30

Bibliography

Anderson, J. M. and Ulvestad, J. S.: 2005, *Astrophysical Journal* **627**, 674

Antonucci, R.: 1993, *Annual Review of Astronomy and Astrophysics* **31**, 473

Baan, W. A. and Klockner, H.-R.: 2006, *Astronomy and Astrophysics* **449**, 559

Bajaja, E., Hummel, E., Wielebinski, R., and Dettmar, R.-J.: 1988, *Astronomy and Astrophysics* **202**, 35

Baldwin, J. A., Phillips, M. M., and Terlevich, R.: 1981, *Publications of the Astronomical Society of the Pacific* **93**, 5

Ballet, J.: 2001, Vol. 238, p. 381

Ballo, L., Braito, V., Ceca, R. D., Maraschi, L., Tavecchio, F., and Dadina, M.: 2004, *Astrophysical Journal* **600**, 634

Barnes, J. E. and Hernquist, L.: 1996, *Astrophysical Journal* **471**, 115

Barth, A. J., Ho, L. C., and Sargent, W. L. W.: 2002, *Astronomical Journal* **124**, 2607

Bassani, L., Dadina, M., Maiolino, R., Salvati, M., Risaliti, G., della Ceca, R., Matt, G., and Zamorani, G.: 1999, *Astrophysical Journal Supplement Series* **121**, 473

Bassani, L., Dadina, M., Maiolino, R., Salvati, M., Risaliti, G., della Ceca, R., Matt, G., and Zamorani, G.: 2000, *VizieR Online Data Catalog* **212**, 10473

Bianchi, S., Matt, G., Balestra, I., Guainazzi, M., and Perola, G. C.: 2004, *Astronomy and Astrophysics* **422**, 65

Boller, T., Keil, R., Hasinger, G., Costantini, E., Fujimoto, R., Anabuki, N., Lehmann, I., and Gallo, L.: 2003, *Astronomy and Astrophysics* **411**, 63

Bower, G. A., Richstone, D. O., Bothun, G. D., and Heckman, T. M.: 1993, *Astrophysical Journal* **402**, 76

Cappi, M., Bassani, L., Comastri, A., Guainazzi, M., Maccacaro, T., Malaguti, G., Matt, G., Palumbo, G. G. C., Blanco, P., Dadina, M., dal Fiume, D., di Cocco, G., Fabian, A. C., Frontera, F., Maiolino, R., Piro, L., Trifoglio, M., and Zhang, N.: 1999, *Astronomy and Astrophysics* **344**, 857

Cappi, M., Panessa, F., Bassani, L., Dadina, M., Dicocco, G., Comastri, A., della Ceca, R., Filippenko, A. V., Gianotti, F., Ho, L. C., Malaguti, G., Mulchaey, J. S., Palumbo, G. G. C., Piconcelli, E., Sargent, W. L. W., Stephen, J., Trifoglio, M., and Weaver, K. A.: 2006, *Astronomy and Astrophysics* **446**, 459

Carollo, C. M., Danziger, I. J., and Buson, L.: 1993, MNRAS **265**, 553

Carral, P., Turner, J. L., and Ho, P. T. P.: 1990, *Astrophysical Journal* **362**, 434

Carrillo, R., Masegosa, J., Dultzin-Hacyan, D., and Ordonez, R.: 1999, *Revista Mexicana de Astronomia y Astrofisica* **35**, 187

Ceca, R. D., Ballo, L., Tavecchio, F., Maraschi, L., Petrucci, P. O., Bassani, L., Cappi, M., Dadina, M., Franceschini, A., Malaguti, G., Palumbo, G. G. C., and Persic, M.: 2002, *Astrophysical Journal* **581**, L9

Chiaberge, M., Capetti, A., and Macchetto, F. D.: 2005, *Astrophysical Journal* **625**, 716

Cid-Fernandes, R., Delgado, R. M. G., Schmitt, H., Storchi-Bergmann, T., Martins, L. P., Perez, E., Heckman, T., Leitherer, C., and Schaerer, D.: 2004, *Astrophysical Journal* **605**, 105

Clemens, M. S., Vega, O., Bressan, A., Granato, G. L., Silva, L., and Panuzzo, P.: 2008, *Astronomy and Astrophysics* **477**, 95

Comastri, A. and Brusa, M.: 2008, *Astronomische Nachrichten* **329**, 122

Comastri, A. and Fiore, F.: 2004, *Astrophysics and Space Science* **294**, 63

Condon, J. J. and Broderick, J. J.: 1991, *Astronomical Journal* **102**, 1663

Corbett, E. A., Norris, R. P., Heisler, C. A., Dopita, M. A., Appleton, P., Struck, C., Murphy, T., Marston, A., Charmandaris, V., Kewley, L., and Zezas, A. L.: 2002, *Astrophysical Journal* **564**, 650

di Nella, H., Garcia, A. M., Garnier, R., and Paturel, G.: 1995, A&AS **113**, 151

Dopita, M. A. and Sutherland, R. S.: 1995, *Astrophysical Journal* **455**, 468

Dressler, A. and Sandage, A.: 1983, *Astrophysical Journal* **265**, 664

Duc, P.-A., Mirabel, I. F., and Maza, J.: 1997, *Astronomy and Astrophysics Supplement Series* **124**, 533

Dudik, R. P., Satyapal, S., Gliozzi, M., and Sambruna, R. M.: 2005, *Astrophysical Journal* **620**, 113

Eracleous, M. and Halpern, J. P.: 2001, *Astrophysical Journal* **554**, 240

Eracleous, M., Shields, J. C., Chartas, G., and Moran, E. C.: 2002, *Astrophysical Journal* **565**, 108

Fabbiano, G.: 2006, *Annual Review of Astronomy and Astrophysics* **44**, 323

Faber, S. M., Wegner, G., Burstein, D., Davies, R. L., Dressler, A., Lynden-Bell, D., and Terlevich, R. J.: 1989, *Astrophysical Journal Supplement Series* **69**, 763

Fabian, A. C.: 2005, *Astrophysics and Space Science* **300**, 97

Ferrarese, L., Ford, H. C., Huchra, J., Kennicutt, Jr., R. C., Mould, J. R., Sakai, S., Freedman, W. L., Stetson, P. B., Madore, B. F., Gibson, B. K., Graham, J. A., Hughes, S. M., Illingworth, G. D., Kelson, D. D., Macri, L., Sebo, K., and Silbermann, N. A.: 2000, *Astrophysical Journal Supplement Series* **128**, 431

Filho, M. E., Barthel, P. D., and Ho, L. C.: 2000, *Astrophysical Journal Supplement Series* **129**, 93

Filho, M. E., Barthel, P. D., and Ho, L. C.: 2002, *Astrophysical Journal Supplement Series* **142**, 223

Filho, M. E., Barthel, P. D., and Ho, L. C.: 2006, *Astronomy and Astrophysics* **451**, 71

Filho, M. E., Fraternali, F., Markoff, S., Nagar, N. M., Barthel, P. D., Ho, L. C., and Yuan, F.: 2004, *Astronomy and Astrophysics* **418**, 429

Filippenko, A. V. and Terlevich, R.: 1992, *Astrophysical Journal* **397**, L79

Fillmore, J. A., Boroson, T. A., and Dressler, A.: 1986, *Astrophysical Journal* **302**, 208

Flohic, H. M. L. G., Eracleous, M., Chartas, G., Shields, J. C., and Moran, E. C.: 2006, *Astrophysical Journal* **647**, 140

Ghisellini, G., Haardt, F., and Matt, G.: 1994, *Monthly Notices of the Royal Astronomical Society* **267**, 743

Gonzalez-Delgado, R. M., Fernandes, R. C., Perez, E., Martins, L. P., Storchi-Bergmann, T., Schmitt, H., Heckman, T., and Leitherer, C.: 2004, *Astrophysical Journal* **605**, 127

Gonzalez-Delgado, R. M., Perez, E., Fernandes, R. C., and Schmitt, H.: 2008, *Astronomical Journal* **135**, 747

Gonzalez-Martin, O., Fabian, A. C., and Sanders, J. S.: 2006a, *Monthly Notices of the Royal Astronomical Society* **367**, 1132

Gonzalez-Martin, O., Masegosa, J., Marquez, I., Guerrero, M. A., and Dultzin-Hacyan, D.: 2006b, *Astronomy and Astrophysics* **460**, 45

Greenawalt, B., Walterbos, R. A. M., and Braun, R.: 1997, *Astrophysical Journal* **483**, 666

Grimes, J. P., Heckman, T., Strickland, D., and Ptak, A.: 2005, *Astrophysical Journal* **628**, 187

Guainazzi, M. and Bianchi, S.: 2007, *Monthly Notices of the Royal Astronomical Society* **374**, 1290

Guainazzi, M., Fiore, F., Matt, G., and Perola, G. C.: 2001, *Monthly Notices of the Royal Astronomical Society* **327**, 323

Guainazzi, M., Matt, G., and Perola, G. C.: 2005, *Astronomy and Astrophysics* **444**, 119

Heckman, T. M.: 1980, *Astronomy and Astrophysics* **87**, 152

Heckman, T. M., Illingworth, G. D., Miley, G. K., and van Breugel, W. J. M.: 1985, *Astrophysical Journal* **299**, 41

Heckman, T. M., Ptak, A., Hornschemeier, A., and Kauffmann, G.: 2005, *Astrophysical Journal* **634**, 161

Ho, L. C.: 2008, *ArXiv e-prints* 803

Ho, L. C., Darling, J., and Greene, J. E.: 2008, *A New H I Survey of Active Galaxies*

Ho, L. C., Feigelson, E. D., Townsley, L. K., Sambruna, R. M., Garmire, G. P., Brandt, W. N., Filippenko, A. V., Griffiths, R. E., Ptak, A. F., and Sargent, W. L. W.: 2001, *Astrophysical Journal* **549**, L51

Ho, L. C., Filippenko, A. V., and Sargent, W. L. W.: 1997, *Astrophysical Journal* **487**, 568

Ho, L. C. and Ulvestad, J. S.: 2001, *Astrophysical Journal Supplement Series* **133**, 77

Ibar, E. and Lira, P.: 2007, *Astronomy and Astrophysics* **466**, 531

Imanishi, M., Terashima, Y., Anabuki, N., and Nakagawa, T.: 2003, *Astrophysical Journal* **596**, L167

James, P., Bate, C., Wells, M., Wright, G., and Doyon, R.: 1999, MNRAS **309**, 585

Jimenez-Bailon, E., Piconcelli, E., Guainazzi, M., Schartel, N., Rodriguez-Pascual, P. M., and Santos-Lleo, M.: 2005, *Astronomy and Astrophysics* **435**, 449

Jimenez-Bailon, E., Piconcelli, E., Sanchez-Portal, M., Guainazzi, M., Martocchia, A., Motch, M., Schroder, A., Bianchi, S., and Matt, G.: 2006, *Astronomische Nachrichten* **327**, 1059

Jones, D. L., Unwin, S. C., Readhead, A. C. S., Sargent, W. L. W., Seielstad, G. A., Simon, R. S., Walker, R. C., Benson, J. M., Perley, R. A., Bridle, A. H., Pauliny-Toth, I. I. K., Romney, J., Witzel, A., Wilkinson, P. N., Baath, L. B., Booth, R. S., Fort, D. N., Galt, J. A., Mutel, R. L., and Linfield, R. P.: 1986, *Astrophysical Journal* **305**, 684

Kaastra, J. S., Bykov, A. M., Schindler, S., Bleeker, J. A. M., Borgani, S., Diaferio, A., Dolag, K., Durret, F., Nevalainen, J., Ohashi, T., Paerels, F. B. S., Petrosian, V., Rephaeli, Y., Richter, P., Schaye, J., and Werner, N.: 2008, *Space Science Reviews* **134**, 1

Keel, W. C.: 1983, *Astrophysical Journal* **269**, 466

Keel, W. C., Kennicutt, R. C., Hummel, E., and van der Hulst, J. M.: 1985, *Astronomical Journal* **90**, 708

Koski, A. T.: 1978, *Astrophysical Journal* **223**, 56

Laine, S., Knapen, J. H., Perez-Ramirez, D., Doyon, R., and Nadeau, D.: 1999, *Monthly Notices of the Royal Astronomical Society* **302**, L33

Maiolino, R.: 2001, *X-ray Astronomy: Stellar Endpoints, AGN, and the Diffuse X-ray Background* **599**, 199

Maiolino, R., Comastri, A., Gilli, R., Nagar, N. M., Bianchi, S., Beker, T., Colbert, E., Krabbe, A., Marconi, A., Matt, G., and Salvati, M.: 2003, *Monthly Notices of the Royal Astronomical Society* **344**, L59

Maiolino, R. and Rieke, G. H.: 1995, *Astrophysical Journal* **454**, 95

Maiolino, R., Salvati, M., Bassani, L., Dadina, M., della Ceca, R., Matt, G., Risaliti, G., and Zamorani, G.: 1998, *Astronomy and Astrophysics* **338**, 781

Maoz, D., Nagar, N. M., Falcke, H., and Wilson, A. S.: 2005, *Astrophysical Journal* **625**, 699

Marquez, I., Masegosa, J., Durret, F., Delgado, R. M. G., Moles, M., Maza, J., Perez, E., and Roth, M.: 2003, *Astronomy and Astrophysics* **409**, 459

Marquez, I. and Moles, M.: 1996, *Astronomy and Astrophysics Supplement Series* **120**, 1

Matt, G.: 1997, *Memorie della Societa Astronomica Italiana* **68**, 127

Mihos, J. C. and Hernquist, L.: 1994, ApJL **437**, L47

Moustakas, J. and Kennicutt, R. C.: 2006, *Astrophysical Journal* **651**, 155

Nagar, N. M., Falcke, H., and Wilson, A. S.: 2005, *Astronomy and Astrophysics* **435**, 521

Nandra, K., O'Neill, P. M., George, I. M., and Reeves, J. N.: 2007, *Monthly Notices of the Royal Astronomical Society* **382**, 194

Nelson, C. H. and Whittle, M.: 1995, *Astrophysical Journal Supplement Series* **99**, 67

Nenkova, M., Ivezic, Z., and Elitzur, M.: 2002, *Astrophysical Journal* **570**, L9

Oegerle, W. R. and Hoessel, J. G.: 1991, *Astrophysical Journal* **375**, 15

Oliva, E., Origlia, L., Maiolino, R., and Moorwood, A. F. M.: 1999, A&A **350**, 9

Ore, C. D., Faber, S. M., Gonzalez, J., Stoughton, R., and Burstein, D.: 1991, *Astrophysical Journal* **366**, 38

Osterbrock, D. E. and Ferland, G. J.: 2006, *Astrophysics of gaseous nebulae and active galactic nuclei*

Panessa, F. and Bassani, L.: 2002, *Astronomy and Astrophysics* **394**, 435

Panessa, F., Bassani, L., Cappi, M., Dadina, M., Barcons, X., Carrera, F. J., Ho, L. C., and Iwasawa, K.: 2006, *Astronomy and Astrophysics* **455**, 173

Panessa, F., Bassani, L., Rosa, A. D., Bird, A. J., Dean, A. J., Fiocchi, M., Malizia, A., Molina, M., Ubertini, P., and Walter, R.: 2008, *The broad-band XMM-Newton and INTEGRAL spectra of bright type 1 Seyfert galaxies*

Panessa, F., Wolter, A., Pellegrini, S., Fruscione, A., Bassani, L., Ceca, R. D., Palumbo, G. G. C., and Trinchieri, G.: 2005, *Astrophysical Journal* **631**, 707

Perola, G. C., Matt, G., Cappi, M., Fiore, F., Guainazzi, M., Maraschi, L., Petrucci, P. O., and Piro, L.: 2002, *Astronomy and Astrophysics* **389**, 802

Ptak, A., Heckman, T., Levenson, N. A., Weaver, K., and Strickland, D.: 2003, *Astrophysical Journal* **592**, 782

Raymond, J. C. and Smith, B. W.: 1977, *Astrophysical Journal Supplement Series* **35**, 419

Risaliti, G. and Elvis, M.: 2004, Vol. 308, p. 187

Risaliti, G., Maiolino, R., and Salvati, M.: 1999, *Astrophysical Journal* **522**, 157

Sarazin, C. L., Burns, J. O., Roettiger, K., and McNamara, B. R.: 1995, *Astrophysical Journal* **447**, 559

Satyapal, S., Dudik, R. P., O'Halloran, B., and Gliozzi, M.: 2005, *Astrophysical Journal* **633**, 86

Satyapal, S., Sambruna, R. M., and Dudik, R. P.: 2004, *Astronomy and Astrophysics* **414**, 825

Schechter, P. L.: 1983, *Astrophysical Journal Supplement Series* **52**, 425

Slee, O. B., Sadler, E. M., Reynolds, J. E., and Ekers, R. D.: 1994, *Monthly Notices of the Royal Astronomical Society* **269**, 928

Smith, B. J.: 2000, *Astrophysical Journal* **541**, 624

Smith, E. P., Heckman, T. M., and Illingworth, G. D.: 1990, *Astrophysical Journal* **356**, 399

Sofue, Y., Yoshida, S., Aoki, T., Soyano, T., Tarusawa, K., Hamabe, M., and Wakamatsu, K.-I.: 1994, *Publications of the Astronomical Society of Japan* **46**, 1

Soria, R., Kuncic, Z., Broderick, J. W., and Ryder, S. D.: 2006, *Monthly Notices of the Royal Astronomical Society* **370**, 1666

Strickland, D. K., Heckman, T. M., Weaver, K. A., Hoopes, C. G., and Dahlem, M.: 2002, *Astrophysical Journal* **568**, 689

Struder, L., Briel, U., Dennerl, K., Hartmann, R., Kendziorra, E., Meidinger, N., Pfeffermann, E., Reppin, C., Aschenbach, B., Bornemann, W., Bruninger, H., Burkert, W., Elender, M., Freyberg, M., Haberl, F., Hartner, G., Heuschmann, F., Hippmann, H., Kastelic, E., Kemmer, S., Kettenring, G., Kink, W., Krause, N., Miller, S., Oppitz, A., Pietsch, W., Popp, M., Predehl, P., Read, A., Stephan, K. H., Stetter, D., Tromper, J., Holl, P., Kemmer, J., Soltau, H.,

Stetter, R., Weber, U., Weichert, U., von Zanthier, C., Carathanassis, D., Lutz, G., Richter, R. H., Solc, P., Bottcher, H., Kuster, M., Staubert, R., Abbey, A., Holland, A., Turner, M., Balasini, M., Bignami, G. F., Palombara, N. L., Villa, G., Buttler, W., Gianini, F., Laine, R., Lumb, D., and Dhez, P.: 2001, *Astronomy and Astrophysics* **365**, L18

Taylor, G. B., Perley, R. A., Inoue, M., Kato, T., Tabara, H., and Aizu, K.: 1990, *Astrophysical Journal* **360**, 41

Teng, S. H., Wilson, A. S., Veilleux, S., Young, A. J., Sanders, D. B., and Nagar, N. M.: 2005, *Astrophysical Journal* **633**, 664

Terashima, Y., Iyomoto, N., Ho, L. C., and Ptak, A. F.: 2002, *Astrophysical Journal Supplement Series* **139**, 1

Terlevich, R. and Melnick, J.: 1985, *Monthly Notices of the Royal Astronomical Society* **213**, 841

Tonry, J. L. and Davis, M.: 1981, *Astrophysical Journal* **246**, 666

Tonry, J. L., Dressler, A., Blakeslee, J. P., Ajhar, E. A., Fletcher, A. B., Luppino, G. A., Metzger, M. R., and Moore, C. B.: 2001, *Astrophysical Journal* **546**, 681

Tremaine, S., Gebhardt, K., Bender, R., Bower, G., Dressler, A., Faber, S. M., Filippenko, A. V., Green, R., Grillmair, C., Ho, L. C., Kormendy, J., Lauer, T. R., Magorrian, J., Pinkney, J., and Richstone, D.: 2002, *Astrophysical Journal* **574**, 740

Tully, R.: 1998, *Cambridge: Cambridge Univ. Press* 1

Turner, T. J., George, I. M., Nandra, K., and Mushotzky, R. F.: 1998, *Astrophysical Journal* **493**, 91

Tzanavaris, P. and Georgantopoulos, I.: 2007, *astro-ph/0703493*, A&A 468, 129-137 (2007)

Urry, C. M. and Padovani, P.: 1995, *Publications of the Astronomical Society of the Pacific* **107**, 803

van Breugel, W., Heckman, T., Butcher, H., and Miley, G.: 1984, *Astrophysical Journal* **277**, 82

van der Marel, R. P., Rix, H. W., Carter, D., Franx, M., White, S. D. M., and de Zeeuw, T.: 1994, MNRAS **268**, 521

Veilleux, S.: 1987, Vol. 19, p. 695

Veilleux, S., Kim, D.-C., Sanders, D. B., Mazzarella, J. M., and Soifer, B. T.: 1995, *Astrophysical Journal Supplement Series* **98**, 171

Vermeulen, R. C., Ros, E., Kellermann, K. I., Cohen, M. H., Zensus, J. A., and van Langevelde, H. J.: 2003, *Astronomy and Astrophysics* **401**, 113

Vignali, C., Comastri, A., Cappi, M., Palumbo, G. G. C., Matsuoka, M., and Kubo, H.: 1999, *Astrophysical Journal* **516**, 582

White, S. D. M., Davis, M., Huchra, J., and Latham, D.: 1983, MNRAS **203**, 701

Whitmore, B. C. and Kirshner, R. P.: 1981, *Astrophysical Journal* **250**, 43

Whitmore, B. C., Rubin, V. C., and Ford, Jr., W. K.: 1984, *Astrophysical Journal* **287**, 66

Whitmore, B. C., Schechter, P. L., and Kirshner, R. P.: 1979, *Astrophysical Journal* **234**, 68

Wolter, A., Trinchieri, G., and Colpi, M.: 2006, *Monthly Notices of the Royal Astronomical Society* **373**, 1627

Wu, H., Zou, Z. L., Xia, X. Y., and Deng, Z. G.: 1998, *Astronomy and Astrophysics Supplement Series* **132**, 181

Xia, X. Y., Xue, S. J., Mao, S., Boller, T., Deng, Z. G., and Wu, H.: 2002, *Astrophysical Journal* **564**, 196

Chapter 4

THE EXTENDED NARROW EMISSION LINE REGION OF NGC 4151: AN OPTICAL, RADIO AND X-RAY STUDY

O. González-Martín[♠], M. Karovska[♠♠], C. Carrasco-González[♠], M. Elvis[♠♠], I. Márquez[♠] and J. Masegosa[♠]

[♠] Instituto de Astrofísica de Andalucía, Granada (SPAIN)
[♠♠] Center for Astronomy, Cambridge MA (USA)

We present a new interpretation of archival Chandra, Hubble Space Telescope (HST), and VLA imaging observations of the circumnuclear extended emission in the nearby Type 1.5 Seyfert galaxy NGC 4151. A conical structure is seen in [SII]/Hα *and* [OIII]/Hβ *ratios, extending up to 14″. The morphological comparison between both ratios suggests photoionization from the nucleus in the Narrow Line Region (NLR) and Extended NLR (ENLR). This is confirmed by diagnostic diagrams in a number of regions along the NLR and ENLR. The resolved soft X-ray emission is spatially coincident with the* [OIII]/Hβ *ratio distribution. The X-ray spectra of the ENLR, as in the NLR, is dominated by emission lines from the photoionized medium up to 14″. We detect not only the radio jet with an overall P.A.*$\sim 77^{\circ}$*, but also a secondary jet traced by a weaker radio knots along P.A.*$\sim 53^{\circ}$*. The appearance of the radio spectral index map may be interpreted as the superposition of two linear structures along P.A.*$\sim 53^{\circ}$ *and* $\sim 77^{\circ}$*. The computed lifetime of the radio sources are larger values for the south knot located at P.A.*$\sim 53^{\circ}$*, suggesting that these secondary jet is older than the first jet. This second structure is aligned with the conical distribution as seen in X-ray and optical wavelengths. We point out to the possibility that the jet has precessed between 45° and 77° or alternatively, two jets have been ejected from the galaxy nucleus at different times.*

4.1 Introduction

The narrow line region (NLR) of active galaxies is the region of extended interstellar gas ionized by the Active Galactic Nucleus (AGN) with typical sizes of hundreds of parsecs. The NLR has the potential to provide important information onto the nature of the central energy sources, the triggering and the fueling of the activity and the dynamical evolution. In many Seyfert galaxies this ionized region extends further out to kpc scales. In these case the kpc region is called the *Extended Narrow Line Region* (ENLR, Unger et al., 1987; Penston et al., 1990).

The main suggested observational evidence of such scenario is that of the alignment between radio jets and optical emission, which extends out to distances up to tenths of kpcs from the nucleus for the most extreme cases (Gallimore et al., 1996; Capetti et al., 1997; Axon et al., 1998). The morphology of this emission resembles that of a cone with apex at the nucleus, which may suggest that nuclear outflows are the main drive mechanisms, consistent with the expectations from unified models (see Elvis, 2000, for a revised version on these models). In the Unified Model of AGN, an optically thick obscuring dust torus is envisioned to encircle the acretion disk (Antonucci, 1993), leading to a so-called *ionization cone* formed by anisotropic escape of ionizing photons (Schulz, 1988).

NGC 4151, the nearest Seyfert 1 galaxy (17 Mpc) has been extensively studied at different frequencies, and offers a unique opportunity to get insight onto the physical nature of the ENLR. Both NLR and ENLR show a biconical morphology (Penston et al., 1990; Robinson et al., 1994; Perez-Fournon and Wilson, 1990) and the kinematics of the emission line gas suggest a bidirectional outflow from the nucleus (Hutchings et al., 1999). A very simple kinematical model of biconical radial outflow can be used to explain the main features of the galaxy (Crenshaw et al., 2000; Das et al., 2005).

Soft X-ray emission adds additional hints onto the physical nature of the NLR and ENLR in Seyferts (Nazarova et al., 1998). The extended X-ray emission in NGC 4151 has been studied by Yang et al. (2001) showing a correlation between the soft X-ray emission and the ionised gas traced by [OIII]. From the spectroscopic analysis it has been shown that the main contribution to the observed soft emission can be attributed to photoionization and photoexcitation by the AGN (Ogle et al., 2000), although collisional excitation and/or on site heating by circumnuclear starbursts can not be ruled out (Armentrout et al., 2007).

A careful multiwavelength analysis of the extended emission needs to be done to separate the contribution from the quoted different components. In this paper, we present a new interpretation of the overall picture based on archival *VLA*, *Chandra* and *HST* data combined together. The detailed X-ray analysis can be performed

thanks to the high angular resolution provided by *Chandra*, that we further improved to 0.25 to the default *Chandra* pixel. This is a general treatment taking the advantage of the smaller sampling than the detector pixel scale due to the telescope dithering while moving across the detector pixels (see Karovska et al., 2007). This results in a significant improvement allowing comparison between X-ray and other wavelenghts. We constructed both [OIII]/Hα and [SII]/Hα ratio maps (presented for the first time in this paper) to investigate the ENLR ionization mechanism. *VLA* radio maps have been derived to construct a spectral index map.

Section 4.2 describes the data reduction procedures. Sections 4.3, 4.4, 4.5 and 4.6 show the *HST*, VLA, and spectra and image X-ray data anlysis, respectively. Section 4.7 discusses the main results and Section 4.8 summarise the main results.

4.2 Data reduction

4.2.1 *HST* data

We downloaded the narrow-band optical images from the MAST[1] archive for [OIII] λ5007, [SII]$\lambda\lambda 6717-6731$ doublet, [NII]+Hα triplet and continuum images. The log of *HST* observations is reported in Table 4.1. The images were retrieved after the standard OTFR[2] calibration pipeline which performs analog-to-digital conversion, bad pixel masking, bias and dark subtraction and flat field correction. The data were combined to reject cosmic rays with CR_REJECT task under IDL[3]. A crucial issue is the relative astrometry of the HST images which is accurate to 1-2 arcsec (Koekemoer et al. 2006). We decided to first match the F658N, F673N and F547M images to the F502N image. Unfortunatelly all the images are saturated in the central pixels, so instead the centroids of the saturaded region were computed. The resulting shifts for F673N and F547M were [8,11] (1pixel=0$''$.1) and [-5,25] pixels (1pixel=0$''$.045). No shift had to be applied to F658N. We also need to match the images in order to perform morphological comparisons with the X-ray and Radio maps. There are no bright stars in the WFPC field of view, so we aligned the observation with the position of the central source, taken from *VLA* 3.6cm data, since *VLA* astrometry is accurate to 0$''$.3 (see Table 4.2). At least five distinct components, C1-C5, have been identified in the radio jet (Pedlar et al., 1993). The radio spectrum of source C4 is relatively flat ($\alpha = -0.3$, $S_\nu \propto \nu^\alpha$) and thus probably contains the nucleus (Wilson and Ulvestad, 1982; Pedlar et al., 1993). The central source has been defined in the optical and X-rays by the brightest peak in each wavelength. This peak is then shifted

[1]MAST: Multi-mission archive at STScI, see http://archive.stsci.edu/
[2]OTFR: On-the-Fly Reprocessing package http://archive.stsci.edu/
[3]IDL: http://www.ittvis.com/idl/

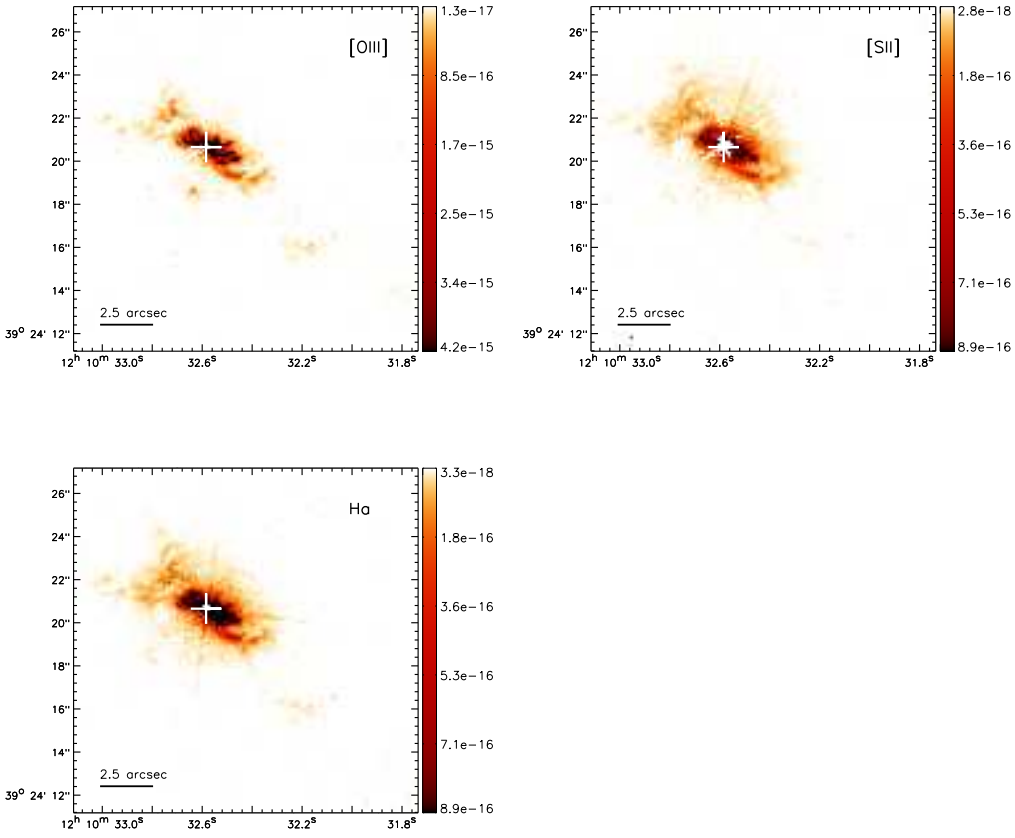

Figure 4.1: *HST narrow band continuum subtracted images. [OIII] image (*top-left*), [SII] image (*top-right*) and Hα image (*bottom*) in linear scale. Note that [SII] image has a larger pixel size because it was observed in CCD chip 3 while [OIII] and Hα were observed in the CCD chip 1.*

to the position of the VLA source C4.

Inner saturated pixels have set to zero (higher than the number of counts in SATURATE keyword in the *HST* header) in order to avoid artifact results. Note that both the innermost, saturated pixels and the linear regions corresponding to the difraction spikes are not considered in the analysis. The images were calibrated following the procedures of *HST* imaging calibration[4]. F547M filter was used for the

[4]http://www.stsci.edu/hst/wfpc2

line-free continuum subtraction in filters F502N, F658N and F673N to obtain pure line-emission images in [OIII], Hα and [SII], respectively.

The continuum is not flat in f_λ from [OIII] to [SII], so the use of F547M as the continuum for Hα and [SII] might produce incorrect line only images. Evans et al. (1993) assumed that at 6 arcsecs from the center along PA 150 and PA 330 (perpendicular to the elongated structure), the contribution of the emission line should be negligible and scaling the images accordingly. To derive the exact factor for the scaling the F547M image to the corresponding continuum three regions were defined as boxes of 50 pixels size ($\sim 2''.3$) at P.A.s 3.5°, 159° and 277° at 6″, 5″ and 7″ from the center, respectively. These regions were defined to avoid diffraction spikes. The total fluxes were computed for the emission line images and for the continuum image in each region. We then computed the scaling factor needed to completely subtract the continuum in these regions assuming there is no line emission. The correction values were 1.3, 1.7 and 1.6 for Hα, [OIII] and [SII], respectively. The total continuum flux is 7.34×10^{-14} erg s^{-1} before the correction. It implies a correction on the emission line fluxes of 1.7%, 1.3% and 4.2% of Hα, [OIII] and [SII] total fluxes, respectively. When the scaling factor is determined, imposing that the total fluxes out of the inner structure will be set to zero, this percentage increase to 2.3%, 2.2% and 6.7% for Hα, [OIII] and [SII]. [SII] had a higher increment because it is far then from the continuum filter than [OIII] and Hα.

Flux calibration was performed using the photometric calibration information in the image headers (PHOTFLAM). The calibration has been tested comparing the resulting line ratios obtained in our images with those provided by spectroscopy (Kaiser et al., 2000; Nelson et al., 2000) with the same aperture. Fluxes and radial velocities of a number of clouds within 3 arcsecs, named by Kaiser et al. (2000) as #6, #9, #19, #22 and #23, and spectroscopic measurements given by Nelson et al. (2000) for [OIII], [SII], Hα, [NII]6548Å and [NII]6584Å emission lines were used. [OIII] and [SII] do have not contamination problems as they are isolated lines. [OIII] and [SII] line fluxes computed from the spectroscopic data are consistent with our results within 10%. However, Hα is contaminated by [NII]6548Å and [NII]6584Å line emissions. The [NII]6548Å line contribution is negligible for relative velocities lower than 385 km s^{-1} whereas the [NII]6584Å line contribution ranges from 0.35 to 0.45 of the Hα+[NII]6548,6584Å flux emission. The mean value (0.40) have been adopted in order to correct from [NII]6584Å contamination.

We show the resulting continuum substracted [OIII], [SII] and Hα images in Fig. 4.1. The [OIII] and Hα images were already published (Hutchings et al., 1998) but the [SII] image is new. We note that [SII] image has a larger pixel size because it was observed in CCD chip 3 while [OIII] and Hα were observed in the CCD chip 1. Therefore, before making image ratios, all the images were smoothed to the same

angular resolution of 0″.3 (6 pixels in the [OIII] and Hα images; 3 pixels in the [SII] image).

We then constructed the [OIII]/Hβ and [SII]/Hα maps. Figs. 4.2a and 4.2b show these ratios in logarithmic scales. Pixels with signal greater than 3σ in the two input images are shown, in order to suppress spurious, noise-induced features. In order to construct the [OIII]/Hβ ratio from the [OIII]/Hα we assume the case B value of Hα/H$\beta \simeq 2.86$ (Osterbrock and Ferland, 2006). Both [SII] and [SII]/Hα images are shown in this paper for the first time.

4.2.2 VLA data

The data were taken from the VLA data archive at NRAO[5]. We selected A configuration data from the project BG070 (1998 March 27), taken at two wavelengths (3.6 cm and 6 cm). These data allow us to study NGC 4151 at similarly good resolution at both wavelengths ($\sim$0.″3 at 3.6 cm and $\sim$0.″45 at 6 cm) and so to obtain a reliable spectral index map. Both wavelengths were observed at the same epoch, and therefore we avoid spurius effects due to possible changes in the flux density of the compact sources. Total integration times were $\sim$5 h at 3.6 cm and $\sim$1 h at 6 cm. The phase calibrator was J1209+43 (located $\sim$48′ from NGC 4151), and the absolute flux calibrator was 3C286, with flux densities of $\sim$5.22 and $\sim$7.37 Jy at 3.6 and 6 cm, respectively. Model images of 3C286 at both wavelengths were used to flux calibrate the data. Data editing and calibration were carried out using the Astronomical Image Processing System (AIPS) package of NRAO, following the standard *VLA* procedures[6]. Finally, the data were self-calibrated, first in phase, and later in both amplitude and phase, using the AIPS task CALIB. The bootstrapped flux den-

[5]The NRAO is a facility of the National Science Foundation operated under cooperative agreement by Associated Universities, Inc.

[6]For a full description of the standard calibration procedures of the VLA see e.g., http://www.aoc.nrao.edu/aips

Data Set	Filter	Lines	Exp. Time (sec)
u5780203r/4r	F502N	[OIII]	860
u2i50104t/5t	F658N	Hα	860
u4230606r/7m	F673N	[SII]	1200
u2i50107t/8t	F547M	Cont.	400

Table 4.1: *HST observational details.*

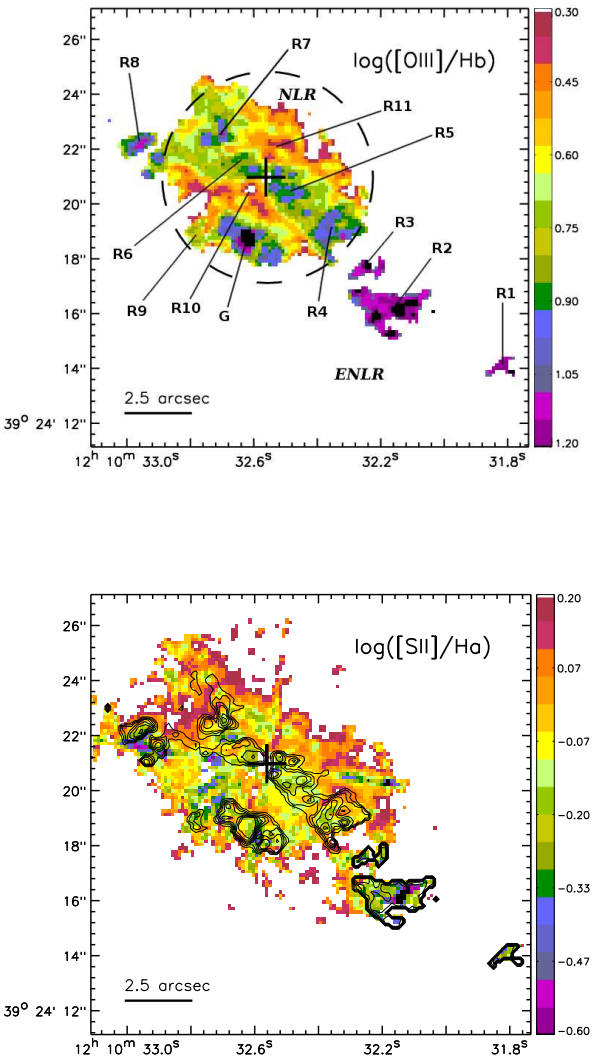

Figure 4.2: HST *image ratios.* [OIII]/Hβ *ratio image (left) and* [SII]/Hα *ratio images (right). Notice that the* [SII]/Hα *ratio image has inverse scale levels compared with* [OIII]/Hβ.Hβ *image is* 2.86^{-1} *of* $H\alpha$*. Contours on the* [SII]/Hα *image are of* [OIII]/Hβ *image. R1-R11 sources have been defined to reference them in the text. G is a ghost feature (see text). Dashed circles shows the X-ray spectral extraction regions.*

sities of the phase calibrator as well as the parameters of the synthesized beams and the rms noise of the final natural weight maps are given in Table 4.2.

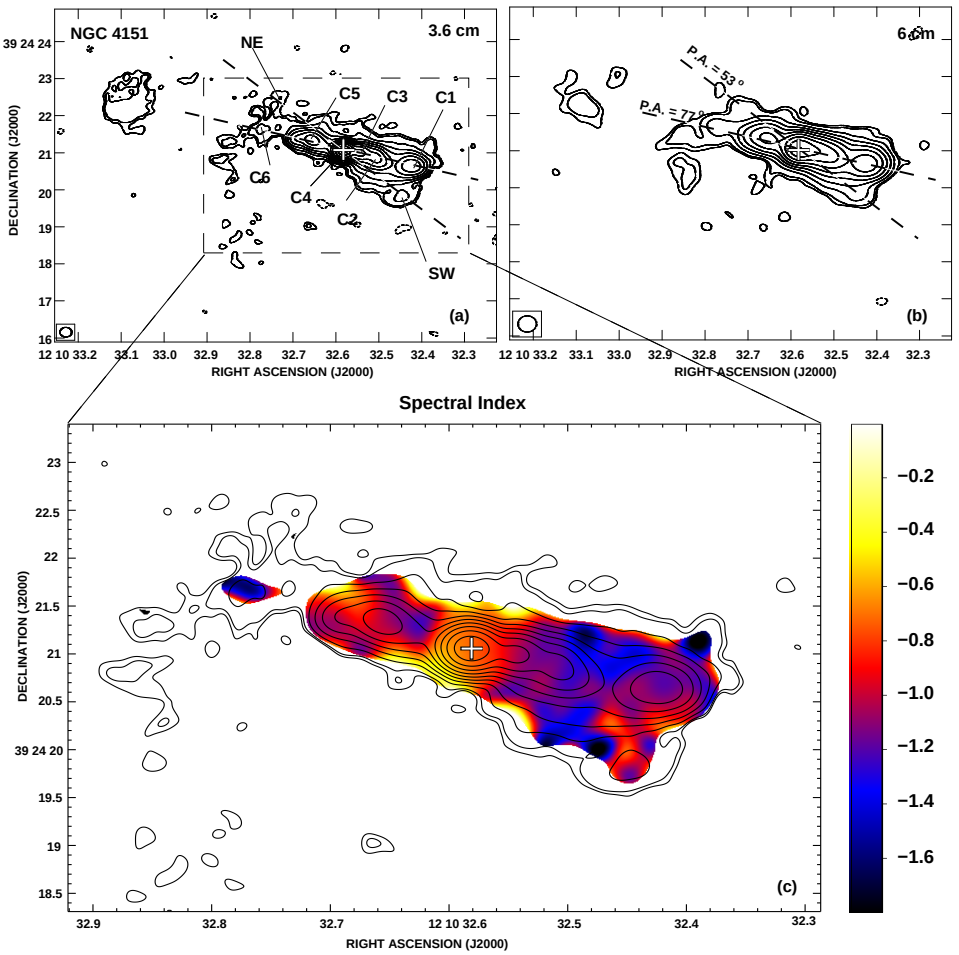

Figure 4.3: *(a) VLA radio continuum contour maps of NGC 4151 at 3.6 cm. Contour levels are −4, −3, 3, 4, 8, 16, 32, 64, 128, 256, 512, and 1024 times the rms noise of the map, 0.015 mJy/beam. The radio continuum knots C1-C6, reported by Carral et al. (1990), and the two weaker ones discussed in the text, NW and SE, are labeled. (b) VLA radio continuum contour maps of NGC 4151 at 6 cm. Contour levels are −4, −3, 3, 4, 8, 16, 32, 64, 128, 256, 512, and 1024 times the rms noise of the map, 0.046 mJy/beam. The dashed lines have the P.A.s defined by the radio continuum knots discused in the text. (c) Spectral index map performed between 3.6 cm and 6 cm of NGC 4151. Superposed are the 3.6 cm contours of figure a).*

	Bootstrapped Flux Density of Phase Calibrator (Jy)	Synthesized Beam HPBW (arcsec)	P.A. (deg)	rms Noise (μJy b^{-1})
3.6 cm	0.548 ± 0.002	0.31×0.26	87	15
6 cm	0.367 ± 0.001	0.50×0.44	-89	46

Table 4.2: *VLA radio continuum observations A-array of NGC 4151*

In order to obtain a spectral index map we made maps at 3.6 cm and 6 cm using the same (u,v) ranges, cell-size and restoring beam. We used a (u,v) range from 18.9 to 606.7 kλ, and made 6 cm uniform weight and 3.6 cm natural weight maps, obtaining the same angular resolution of $\sim$0.″34. Finally, using the task COMB in AIPS, we obtained the spectral index map for all the pixels with an intensity higher than 3σ for each map which restricts the map to the inner few arcsecs. The natural weight maps at 3.6 and 6 cm as well as the spectral index map of the inner structure are shown in Fig. 4.3.

4.2.3 *Chandra* data

The available *Chandra* data of NGC 4151 are summarized in Table 4.3. The only data sets without gratings are ObsID 347, 348 and 372. Level 1 event data of ACIS instrument were extracted from *Chandra* archive[7].

At the nucleus of NGC 4151 the source count rate is too high producing pileup[8] (Davis, 2001). We have predicted pileup fraction using the PIMMS[9] software in the 2.0-10.0 keV energy band. Table 4.3 gives our assessment of the pileup fraction for each observation. Note that in the case of grating spectra, the pileup estimated is an upper limit. The long, 3.2s frame time of the *Chandra* ObsID 348 observation is badly affected by pileup, as already reported by Yang et al. (2001) but is well-suited for the extended emission analysis as this observation has a long exposure and no gratings (which reduce the direct imaging effective area). ObsIDs 347 and 372 have frame times of 0.1s and 0.4s respectively. These shorter frame times reduce pileup. The nucleus is significantly piled up in the 0.4s, but not in the 0.1s frame time observations. Unfortunately, the 0.1 and 0.4s frame-time observations are too short to study the diffuse emission and also have reduced field-of-view. The zero-order spectrum has only modest signal-to-noise ratio as a result of the $\simeq 2$ zero-

[7] http://cda.harvard.edu/chaser/
[8] http://cxc.harvard.edu/ciao/ahelp/acis_pileup.html
[9] http://heasarc.nasa.gov/docs/software/tools/pimms.html

order transmission of the gratings. In spite of these effects, among the available data, the zero order spectra from ACIS/HETG observations will be better suited for the central 4″ region because of the lower pileup fraction (see Table 4.3). ObsID 335, 3052, 3480 and 3089 have less than 18% pileup. We decided to use ObsID 335 for the nuclear analysis since it is less affected by pileup because the short exposure time. ObsID 348 data is used for the detailed analysis of the extended diffuse emission (>4″) and ObsID 335 for the morphology study and spectral analysis of the nuclear region (<4″).

ObsID	Grating	Frame Time (s)	Expt. (ks)	Pileup (%)
335	HETG	3.2	48	<18
347*	NONE	0.4/0.1	2	11/6
348	NONE	3.2	28	83
372*	NONE	0.4/0.1	11	11/6
3052*	HETG	1.8	157	<18
3480*	HETG	1.8	93	<18
3089*	LETG	3.2	85	<18

Table 4.3: Chandra *ACIS-S observations of NGC 4151. (*) Data not used in this paper (see text for a detailed explanation).*

The data were reduced with the CIAO 3.4.0.1[10] data analysis system and the *Chandra* Calibration Database (CALDB 3.2.4[11]). We reprocessed Level 1 event data to create a new ACIS bad pixel file with ACIS_RUN_HOTPIX task to identify hot pixels and ACIS_DETECT_AFTERGLOW task to identify cosmic ray afterglows. Then we used ACIS_PROCESS_EVENTS to create a new level 2 event file. Background flares were excluded from the event file using the task LC_CLEAN.SL[12] in source-free (only background) sky regions of the same observation. The net time after flare removal is 46.9 ks in ObsID 335 and 21.9 ks in ObsID 348.

4.3 *HST* data analysis

The overall emission morphology, traced equally by [OIII], Hα and [SII] images (Fig. 4.1), is that of a bright, central elongated structure along PA=53° in the innermost 4″ radius, which extends further to the south-west with three blobbed regions at 7″,

[10]See http://asc.harvard.edu/ciao
[11]see http://cxc.harvard.edu/caldb/
[12]see http://cxc.harvard.edu/ciao/download/scripts/

8″ and 13″ (labeled as R1, R2 and R3). The elongated nature of the emission is more clearly seen in [OIII], which lacks the underlying, diffuse emission present in both in Hα and [SII] (see Fig. 4.1). Note that the emission knot labeled as G in [OIII] is a ghost (Hutchings et al., 1998).

The line ratio maps shown in Fig.4.2 trace the morphological differences and similarities between the lines and quantify the line ratios, which may determine the physical mechanisms taking place.

In [OIII]/Hβ, a beam-like structure, very narrow in the innermost 2″.5 and that gets brighter to the outskirts, can be traced continuously starting from the nuclear position and extending to the south-west up to 2″.5, where it abruptly stops and reappears again in the three knots R3, R2 and R1. While the [OIII]/Hβ structure is also seen in [SII]/Hα, the latest is broader occupying the central 6″.

Eleven regions (R1-R11, Fig. 4.2) have been defined in the [OIII]/Hβ ratio image to quantify the emission mechanism. The regions R1-R7 lie along the cone-like structure. Sources R8 and R9 are regions prominent in the [OIII] and [SII] images. Source R10 and R11, perpendicular to the cone-like structure, have been selected to search for P.A. dependent differences. For regions R1 to R9 the median value have been computed selecting contour levels higher than 0.9 in the [OIII]/Hβ ratio image. Regions R10 and R11 have been defined as rectangles. We then computed the median values for each region. The results are given in Table 4.4.

Fig. 4.4 shows the [OIII]/Hβ and [SII]/Hα ratios measurements compared with diagnostic ratios for three ionization mechanisms (Veilleux, 1987) The continuum black line plotted shows the division between ionization by HII regions and ionization by the AGN (Kewley et al., 2001). The dashed black line shows the division between AGN and shocks regions by Kewley et al. (2006) while blue dotted-dashed line is the division reported by (Veilleux, 1987). All the regions alogn the cone (R1-R7) are located in the region corresponding to ionization from the central AGN. R8 and R9 are also in the region corresponding to ionization from the ionization by the AGN, although region R9 is closer to that of ionization by star-forming processes. Regions R10 and R11 are closer to the one occupied by ionization through shock heating processes and R11 is in that region if the predicted line by Kewley et al. (2006) is taken. Changes in the [NII]6584Å contamination correction from the minimum value reported (0.35) to the maximun value (0.45) do not have any influence in the diagnostic diagram results, with all the points remaining in the region of AGN ionization.

#	RA	Dec	Log([OIII]/Hβ)	Log([SII]/Hα)
R1	182.63254	39.403879	1.18	-0.26
R2	182.63400	39.404453	1.16	-0.20
R3	182.63430	39.404893	1.13	-0.10
R4	182.63470	39.405252	1.00	-0.09
R5	182.63533	39.405737	0.97	-0.13
R6	182.63598	39.405943	0.96	-0.13
R7	182.63631	39.406277	0.99	-0.08
R8	182.63736	39.406174	1.05	-0.14
R9	182.63655	39.405219	0.96	-0.31
R10	182.63588	39.405607	0.45	-0.02
R11	182.63556	39.406159	0.44	0.01

Table 4.4: *Log([OIII]/Hβ) and Log([SII]/Hα) line ratio measurements.*

4.4 VLA data analysis

The structure of NGC 4151 is very similar at 3.6 and 6 cm (see Fig. 4.3), showing an extended knotty emission defined by the radio continuum knots C1-C6 (following the notation by Carral et al., 1990). The positions, flux densities, spectral indices α (defined as $S_\nu \propto \nu^\alpha$) between 6 and 3.6 cm, and de-convolved sizes of these knots derived from these maps are shown in Table 4.5. The radio continuum knots C1-C6 define a line with an overall P.A. $\sim 77^\circ$, in well agreement with previous findings (e.g., Pedlar et al., 1993). At a low significance level (3 and 4 rms noise of the map) we find a radio lobe 5″ from the nuclear source (C4, Ulvestad et al., 2005) to the NE along P.A.$\sim 77^\circ$ (Pedlar et al., 1993). They reported a filamentary structure between the radio lobe and the end of the main body of the radio jet (2″ in the NE direction). However, our maps only show some knots at the 3σ level coinciding with the filamentary structure seen by Pedlar et al. (1993). Furthermore, another string of knots is seen at 3 and 4σ, from the end of the main boddy of the radio jet (again 2″ in the NE direction along P.A.$\sim 77^\circ$) extending 3″ to the south.

We also detect at 3.6 cm a radio continuum knot identified as SW and a weaker extended emission identified as NE. The SW knot is also detected in our 6 cm map and in previous 3.6 cm and 2 cm radio maps by Pedlar et al. (1993). The NE knot can be seen in our 6 cm map although a clean flux measure can not be obtained because the lack of enough resolution avoids to isolate the feature from the surrounding

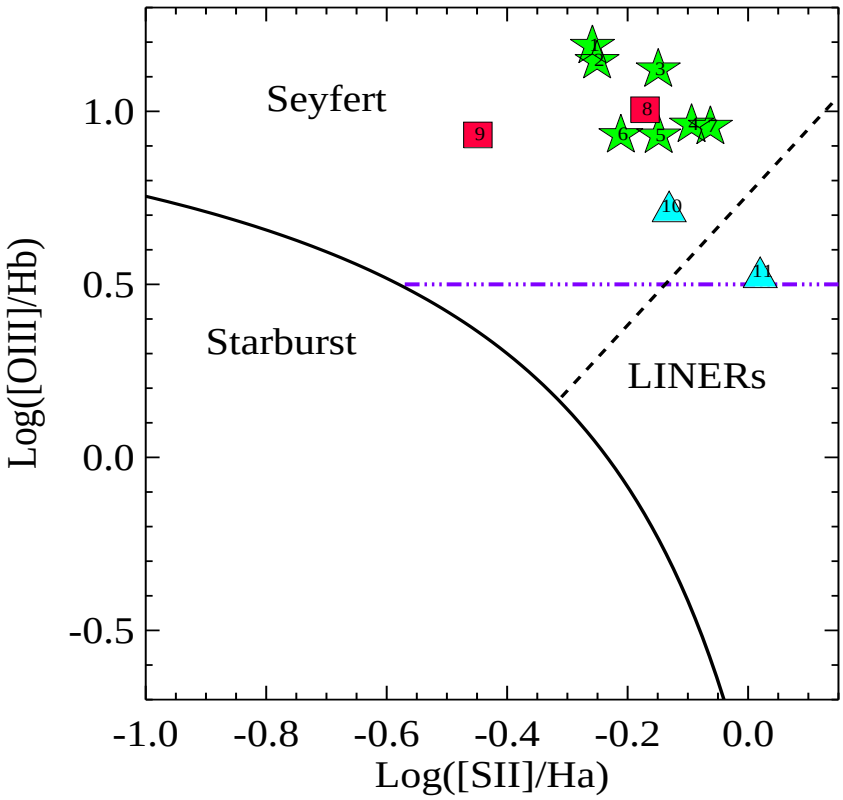

Figure 4.4: [OIII]/Hβ *vs.* [SII]/Hα *intensity ratios. R1-R7 (green stars) along the main structure; R8-R9 (red squares) prominent in emission line maps; and R10-R11 (blue triangles) are perpendicular to the main structure. The continuum black line plotted shows the division between ionization by HII regions and ionization by the AGN (Kewley et al., 2001). The dashed black line shows the division between AGN and shocks regions by Kewley et al. (2006) while blue dotted-dashed line is the division reported by (Veilleux, 1987)*

emission. We want to point out that NW, SE and knot C4 (the nucleus) are well aligned within P.A. $\sim 53°$.

The morphology of the spectral index map appears to be the result of the superposition of two linear structures along P.A.$\sim 53°$ and $\sim 77°$ that will be discussed in Section 4.7. The spectral indices are clearly non-thermal ($\alpha < -0.74$) along the

Knot	Position (J2000)		Flux Density (mJy)		Spectral	Mayor	Minor
	RA	DEC	6 cm	3.6 cm	Index	Axis	Axis
C1	12 10 32.42	39 24 20.65	17.4 ± 0.2	9.67 ± 0.03	-1.13 ± 0.02	0.33	0.33
C2	12 10 32.50	39 24 20.85	30.0 ± 0.2	15.90 ± 0.04	-1.22 ± 0.01	0.60	0.25
C3	12 10 32.55	39 24 21.00	34.5 ± 0.2	21.16 ± 0.03	-0.94 ± 0.01	0.50	0.12
C4(Nucleus)	12 10 32.58	39 24 21.05	51.1 ± 0.1	34.83 ± 0.02	-0.74 ± 0.01	0.21	0.05
C5	12 10 32.66	39 24 21.34	13.5 ± 0.2	7.99 ± 0.04	-1.01 ± 0.03	0.40	0.30
C6	12 10 32.77	39 24 21.67	0.4 ± 0.1	0.23 ± 0.04	-1.10 ± 0.60	0.34	0.34
SW	12 10 32.45	39 24 19.83	1.0 ± 0.2	0.63 ± 0.05	-0.90 ± 0.40	0.65	0.43
NE	12 10 32.74	39 24 22.31	...	0.45 ± 0.09	...	0.9	0.5

Table 4.5: *VLA flux and spectral index results for the features labeled in Fig. 4.3(a).*

jet. The flattest spectral index of ($\alpha \sim -0.74$) is found at the nuclear position and a general trend of decreasing spectral indices outwards both sides of the nucleus has been found. Knot SW shows an $\alpha = -0.9 \pm 0.4$ which is within the range of values for the other knots of the jet. In Fig. 4.3 we show the spectral index map, consistent with the spectral index determination for the main knots detected in the radio maps (see Table 4.5).

4.5 X-ray spectral analysis

The structure and kinematics of the central region of NGC 4151 were first studied with slitless optical spectra (Hutchings et al., 1998; Kaiser et al., 1999) and then with long-slit spectroscopy (Evans et al., 1993; Nelson et al., 2000; Kraemer et al., 2000). These works revealed a kinematics and ionization structure of the emission-line clouds roughly ressembling a bicone from the nucleus to a radius of 4″. These clouds, which are outflowing from the nucleus, form the NLR. Beyond the inner 4″, the emission-line clouds have lower velocities and seem to be participating in the general galaxy rotation. The later is the so called ENLR.

Based on optical analysis three regions have been selected for detailed study: (1) the nuclear region was extracted using an aperture with 2″ radius; (2) the NLR was extracted from an annulus from 2″ to 4″; and (3) the ENLR was extracted from an annulus from 4″ to 14″.

Spatial regions used through this section are shown in Figs. 4.2 and 4.9. The spectral analysis was made using ObsID 348 while that of the central emission ($<$ 2″) was performed with ObsID 335 to avoid pile-up (see Section 4.6 for a detailed explanation).

The background region since defined by source-free apertures around the soft X-ray emission regions. Counts were extracted using the CIAO tool DMEXTRACT. Response and ancillary response files were created using the CIAO MKACISRMF

and MKWARF tools. The analysis of the spectral counts was performed using the software package XSPEC (Arnaud, 1996, version 12.3.1[13]). To be able to use the χ^2 as the fit statistics, the spectra were binned to give a minimum of 20 counts per bin before background subtraction. GRPPHA task, included in FTOOLS[14]. The channels above 7 keV were ignored in the fit because the background is dominant at these energies.

4.5.1 Base Line Model (*BLM*)

The hard (2-10 keV) X-ray continuum of Seyferts is dominated by a power-law continuum, partly suppressed by photoelectric absorption at low energies(Matt et al., 2000). In Compton-thick Seyferts, the transmitted continuum is totally suppressed below 10 keV, and the X-ray continuum is accounted for by reflection of the primary nuclear emission of optically thick matter surrounding the nuclear environment (Matt et al., 2000). In the intermediate case of Compton-thin obscuration, the obscured power-law continuum and the reflection component can be equally important. Furthermore, a soft, optically thin, thermal component generally has to be included to take into account the contributions of surrounding star forming regions or ionization by the AGN (see Guainazzi et al., 2005, for a detailed description of the model).

The central NGC 4151 X-ray source has been extensively studied before, and shows a spectrum that is more complicated than this simple scheme (Schurch and Warwick, 2002; Beckmann et al., 2005; de Rosa et al., 2007). The *BeppoSAX* spectrum was characterized by a complex X-ray absorption, that is well described by a dual absorber, composed of an uniform mildly-ionized gas and cold gas partially covers the central source (Piro et al., 2005; de Rosa et al., 2007). We thus adopted a *baseline* model (*BLM*,Perola et al., 2002; Schurch and Warwick, 2002) which comprises the following components:

1. A primary power-law continuum with an exponential high energy cut-off.
2. A Compton reflection component (using PEXRAV in XSPEC, Magdziarz and Zdziarski, 1995).
3. A narrow FeKα (6.4keV) iron line fitted with a gaussian profile with the intrinsic width set to 10 eV, i.e. unresolved at ACIS spectral resolution.
4. A soft thermal component (MEKAL model in XSPEC).

[13]See http://cxc.heasarc.gsfc.nasa.gov/docs/xanadu/xspec/
[14]See http://heasarc.gsfc.nasa.gov/docs/software/ftools/ftools_menu.html

5. A scatterd component (described by a power-law with the index fixed at that of the primary power-law).

6. A dual absorber model with (a) fraction f_{cov} of the source covered by a cold column density N_{Hcold} (model ZWABS in XSPEC); (b) a mildly-ionized gas with a column density N_{Hwarm} (model ABSORI in XSPEC, Done et al., 2002)).

Additional foreground absorption from our own Galaxy is applied to all the emission components ($N_{Hgal} = 1.98 \times 10^{20}$ cm^{-2}, from Dickey and Lockman, 1990). We assume elemental abundances from Anders and Grevesse (1989). The photoionized gas is characterized by a temperature $T = 3 \times 10^4$ K. The cosine of inclination angle of the reflector was fixed to 0.95 and the reflection scaling factor was fixed to 0.1 (de Rosa et al., 2007). The iron abundance was assumed to be $(Z/Z_\odot)_{Fe} = 1.8$ and the ionization parameter $\phi = 10.3$. There are the values obtained in *BeppoSAX* observations carried out in the closest period of observations (January 1999) reported by de Rosa et al. (2007).

The parameters derived for the nuclear spectrum will be used to fix those for the contribution of the nuclear X-ray emission contamining the NLR spectrum.

We have performed a PSF analysis to determine the contribution of the point-like nuclear source to the larger NLR and ENLR regions. We used the *Chandra* PSF simulator *Chandra* Ray Tracer (ChaRT[15] Carter et al., 2003) to produce PSFs for energies 0.4, 0.8, 1.5 and 6.0 keV. Using the MARX 4.0.8[16] simulator we produced the PSF at the same focal plane position as our observations. Table 4.6 shows the percentage contribution from the nucleus due to the *Chandra* PSF for ObsID 335 and 348.

Energy	ID 335			ID 348		
(keV)	Nucl.	NLR	ENLR	Nucl.	NLR	ENLR
0.4	97.9	0.1	2.0	98.1	1.3	0.6
0.8	96.9	1.6	1.5	97.1	1.6	1.3
1.5	95.6	2.2	2.2	96.0	2.2	1.8
6.0	94.9	2.5	2.6	94.3	3.1	2.6

Table 4.6: *Percentage contribution from the nucleus due to the* Chandra *PSF.*

ObsID 335 contains 95-98% of the nuclear source within a circle with 2″ radius. The nuclear component is still a contributor at larger radii. At 6 keV the nuclear contamination due to the *Chandra* PSF is about 3.1% and 2.6% in the NLR and ENLR for ObsID 348. This model was fixed to quote the nuclear contribution in the NLR

[15]http://cxc.harvard.edu/chart/
[16]http://space.mit.edu/ASC/MARX/

and ENLR, scaled by a factor derived from Table 4.6, scaling by $0.081^{+0.008}_{-0.010}$ and $0.107^{+0.008}_{-0.008}$, respectively.

Figs. 4.5, 4.6 and 4.7 show the spectral fits of the nuclear region, NLR and ENLR, respectively, for the BLM (*top*) and for BLM+EL (*bottom*), discussed in the next section. Tables 4.7 and 4.8 include the fitted parameters obtained for BLM and BLM+EL, respectively.

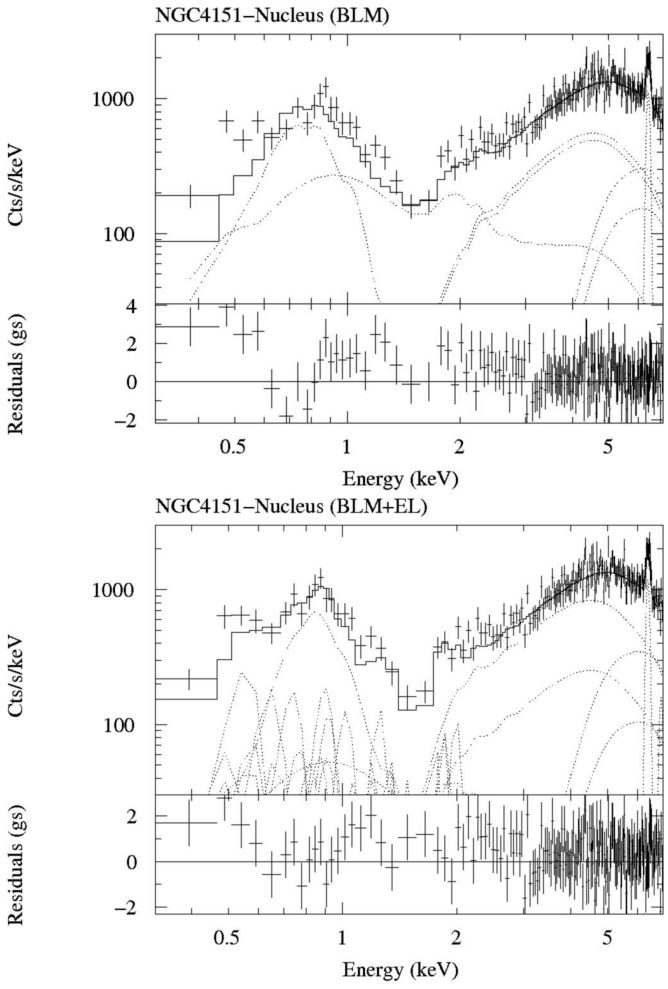

Figure 4.5: *X-ray spectral fit to the nuclear region with BLM (*Top*) and BLM+EL (*Bottom*).*

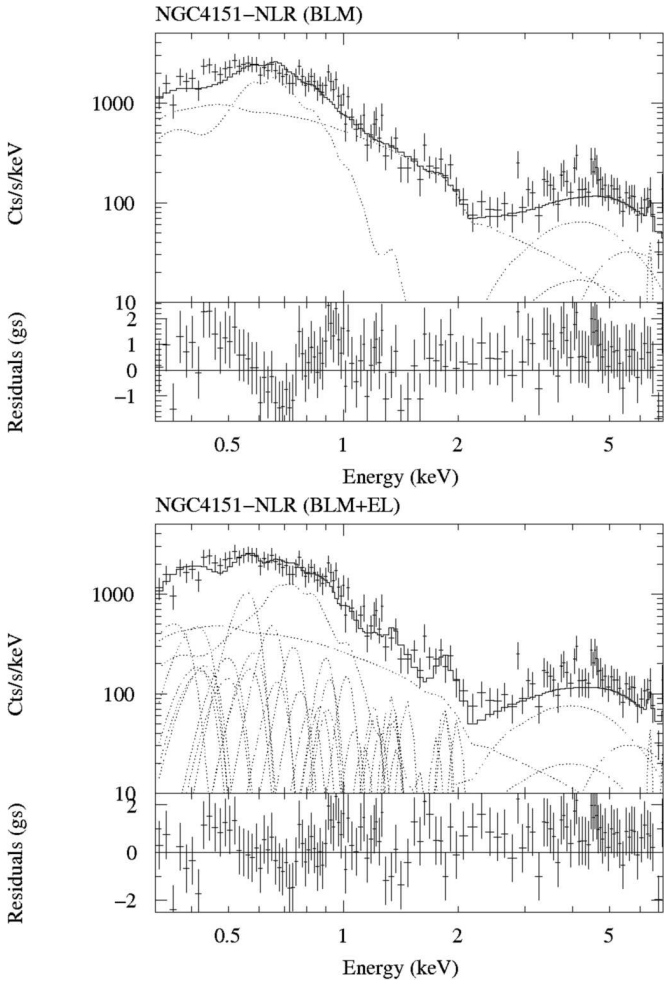

Figure 4.6: *X-ray spectral fit to the NLR with BLM (*Top*) and BLM+EL (*Bottom*).*

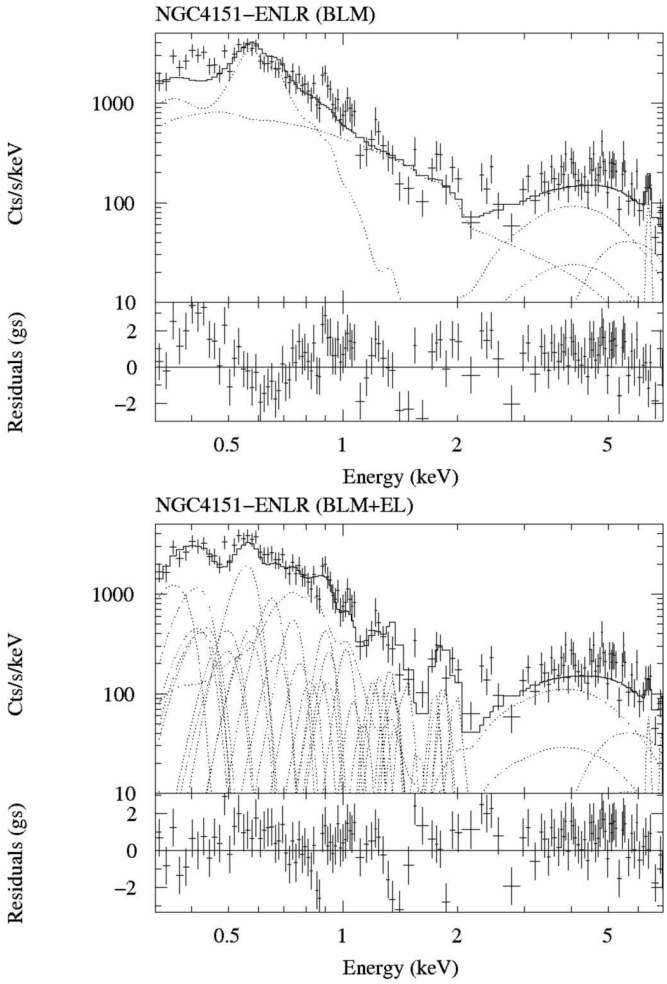

Figure 4.7: *X-ray spectral fit to the ENLR with BLM (*Top*) and BLM+EL (*Bottom*).*

Region	N_{Hcold}	f_{cold}	Γ	A_c (10^{-2})	A_{ref} (10^{-2})	N_{Hwa}	A_{sc} (10^{-5})	kT (keV)	A_{th} (10^{-5})	$EW_{FeK\alpha}$ (eV)	χ^2	d.o.f.
						BLM						
Nucleus	$7.34^{+1.55}_{-1.29}$	$0.86^{+0.02}_{-0.04}$	$1.94^{+0.17}_{-0.14}$	$7.5^{+4.4}_{-1.5}$	<2.2	$1.04^{+0.10}_{-0.10}$	$14.5^{+2.20}_{-2.30}$	$0.60^{+0.09}_{-0.12}$	$6.1^{+1.6}_{-1.6}$	197^{+38}_{-38}	472.16	430
NLR	7.34*	0.86*	1.94*	7.5*	<2.2*	$1.49^{+0.19}_{-0.17}$	$3.43^{+0.34}_{-0.28}$	$0.25^{+0.01}_{-0.01}$	$4.0^{+0.4}_{-0.4}$	<245	275.53	250
ENLR	7.34*	0.86*	1.94*	7.5*	<2.2*	$1.38^{+0.18}_{-0.12}$	$3.00^{+0.33}_{-0.35}$	$0.20^{+0.01}_{-0.01}$	$6.4^{+0.6}_{-0.4}$	<246	327.11	279

Table 4.7: *The spectral fit results of the BLM. *The intrinsic continuum added to the reflection was fixed for the NLR and ENLR according to the nucleus spectrum scaling by $0.083^{+0.009}_{-0.008}$ and $0.108^{+0.011}_{-0.009}$, respectively. N_{Hcold} and N_{Hwa} in units of 10^{23} cm^{-2}.*

Region	N_{Hcold}	f_{cold}	Γ	A_c (10^{-2})	A_{ref} (10^{-2})	N_{Hwa}	kT (keV)	A_{th} (10^{-5})	f_{Oggle}	$f_{Sch.}$	χ^2	d.o.f.
						BLM+EL						
Nucleus	$6.78^{+1.91}_{-1.64}$	$0.77^{+0.05}_{-0.21}$	$1.95^{+0.67}_{-0.19}$	$1.4^{+5.8}_{-0.3}$	$3.7^{+9.8}_{-2.9}$	$0.94^{+0.13}_{-0.25}$	$0.60^{+0.07}_{-0.09}$	$6.8^{+1.7}_{-1.7}$	$0.25^{+0.07}_{-0.05}$	$0.35^{+0.25}_{-0.25}$	437.93	426
NLR	6.78*	0.77*	1.95*	1.4*	3.7*	$1.23^{+0.19}_{-0.17}$	$0.32^{+0.05}_{-0.05}$	$2.7^{+0.5}_{-0.5}$	$0.06^{+0.02}_{-0.01}$	$0.12^{+0.02}_{-0.02}$	246.15	250
ENLR	6.78*	0.77*	1.95*	1.4*	3.7*	$1.05^{+0.10}_{-0.09}$	$0.26^{+0.03}_{-0.03}$	$4.3^{+0.5}_{-0.5}$	$0.08^{+0.01}_{-0.01}$	$0.24^{+0.03}_{-0.03}$	265.00	276

Table 4.8: *The same as before but adding ionized lines from the X-ray high resolution spectra (Ogle et al., 2000; Schurch et al., 2004). The intrinsic continuum added to the reflection was fixed for the NLR and ENLR according to the nucleus spectrum scaling by $0.081^{+0.008}_{-0.010}$ and $0.107^{+0.008}_{-0.008}$, respectively. N_{Hcold} and N_{Hwa} in units of 10^{23} cm^{-2}.*

Identification	Energy (keV)	Flux	Ref.
$C_{VI}Ly\alpha$	0.368	1.79E-04	(1)
$N_{VI}f$	0.420	1.15E-04	(1)
$N_{VI}i$	0.427	3.60E-05	(1)
$N_{VI}r$	0.431	4.50E-05	(1)
$C_{VI}Ly\beta$	0.436	3.70E-05	(1)
N_{VI}	0.498	3.9E-05	(2)
$N_{VII}Ly\alpha$	0.500	6.3E-05	(2)
$O_{VII}f$	0.560	3.1E-04	(2)
$O_{VII}i$	0.569	5.1E-05	(2)
$O_{VII}r$	0.574	6.8E-05	(2)
$O_{VIII}Ly\alpha$	0.65	1.0E-04	(2)
$N_{VII}RRC$	0.67	2.6E-05	(2)
$O_{VII}RRC$	0.74	5.2E-05	(2)
$O_{VIII}Ly\beta$	0.77	1.8E-05	(2)
$O_{VIII}Ly\gamma$	0.82	1.1E-05	(2)
$O_{VIII}RCC$	0.87	1.1E-05	(2)
$Ne_{IX}f$	0.90	3.3E-05	(2)
$Ne_{IX}i$	0.91	9.9E-06	(2)
$Ne_{IX}r$	0.92	2.0E-05	(2)
$Ne_{X}Ly\alpha$	1.02	2.0E-05	(2)
$Ne_{IX}1s3p-1s^2$	1.07	5.9E-06	(2)
$Ne_{IX}1s4p-1s^2$	1.13	3.8E-06	(2)
$Ne_{IX}RRC$	1.20	9.3E-06	(2)
$Ne_{X}Ly\beta$	1.21	7.4E-06	(2)
$Mg_{I}K\alpha$	1.25	*	
$Mg_{XI}f$	1.33	1.2E-05	(2)
$Mg_{XI}r$	1.35	9.3E-06	(2)
$Ne_{X}f$	1.36	7.2E-06	(2)
Fe_{XXII}	1.38	3.5E-06	(2)
$Mg_{XII}Ly\alpha$	1.47	1.1E-05	(2)
$Mg_{XI}1s3p-1s^2$	1.58	2.5E-06	(2)
$Si_{I}K\alpha$	1.74	*	
$Mg_{XII}Ly\beta$	1.75	5.3E-06	(2)
$Si_{XIII}f$	1.84	1.1E-05	(2)
$Si_{XIII}r$	1.87	1.1E-05	(2)
$Si_{XIV}Ly\alpha$	2.00	1.0E-05	(2)
$Fe_{I}K\alpha$	6.40	*	
Fe_{XXV}	6.93	3.3E-05	(2)

Table 4.9: *Emission lines added to BLM. References: (1) Schurch et al. (2004); (2) Ogle et al. (2000). Flux in units of photons* $s^{-1}cm^{-2}$. *(*) Emission lines allowed to vary in the spectral fit (see text).*

4.5.2 Base Line Model plus emission lines (BLM+EL)

Although the resulting NLR and ENLR best fit is formally acceptable (χ^2=275.53 for 250 d.o.f and χ^2=327.11 for 279 d.o.f, respectively), residuals show large departures from zero below 2 keV for both regions and additional components seems to be required for both NLR and ENLR.

The *Chandra* High-Energy Transmission Grating Spectrometer indeed revealed a spectrum dominated by narrow emission lines from a highly ionized nebula in the

NLR (Ogle et al., 2000). Thus, we add to the model those lines with energy fluxes obtained from that work (see Table 4.9). To complete the ionized spectrum below 0.5 keV we have also added a number of lines compiled by the RGS instruments aboard *XMM-Newton* (Schurch et al., 2004). It has to be noticed that these spectra have different extraction windows. The spectrum reported by Ogle et al. (2000) was extracted from a aperture radius of 7″.9 centered in the nucleus while the spectrum reported by Schurch et al. (2004) was extracted from an extraction window of 30″ radius. The strength of our emission lines has been scaled to those obtained by Ogle et al. (2000) and Schurch et al. (2004).

Figs. 4.5 (*bottom*), 4.6 (*bottom*), 4.7 (*bottom*) show the spectral fit of the nuclear region, NLR and ENLR with BLM+EL. Table 4.8 includes the spectral fitting parameters that were obtained. In Table 4.10 the fluxes and corrected by absorption luminosities in the soft and hard bands for the nucleus, NLR and ENLR, are shown.

In the following paragraph we discuss the spectral components of the BLM and the BLM+EL.

- **Hard-band X-ray emission:**

  The BLM described above provides a good fit to the hard energy nuclear spectrum of NGC 4151 ($\chi^2 = 472.16$ and 430 d.o.f. Table 4.7). In this energy range the inclusion of the emission lines (i.e. BLM+EL) does not provide any improvement. The entire hard energy spectrum is coming from the nucleus. The flux percentage of NLR versus the nucleus is <2.5%, below the value expected from the *Chandra* PSF.

  The reflection component is consistent with zero in the BLM ($A_{refl} < 2.2\times 10^{-3}$ ph $cm^{-2}s^{-1}keV^{-1}$) and is marginally required with BLM+EL ($A_{refl} = 3.7\times 10^{-3}$ ph $cm^{-2}s^{-1}keV^{-1}$). This agrees with *BeppoSAX* data, showing a highly variable reflection component significantly detected in 1996 and consistent with zero in 2000 and 2001. The *BeppoSAX* observations in 1999 are the closest in time to our data and showed a marginally significant reflection component ($A_{refl} \simeq 3 \times 10^{-3}$ ph $cm^{-2}s^{-1}keV^{-1}$). The iron line is fitted with a narrow line with an EW$\simeq$ 200 eV.

  In Fig. 4.8 we plot the column density of the warm absorber versus the cold absorber of the nucleus in this work (red star), Puccetti et al. (2007) (green squares) and de Rosa et al. (2007) (black triangles). It correlates (r=0.77) between the two quantities. The absorbers in our work have column densities well above those reported in the literature.

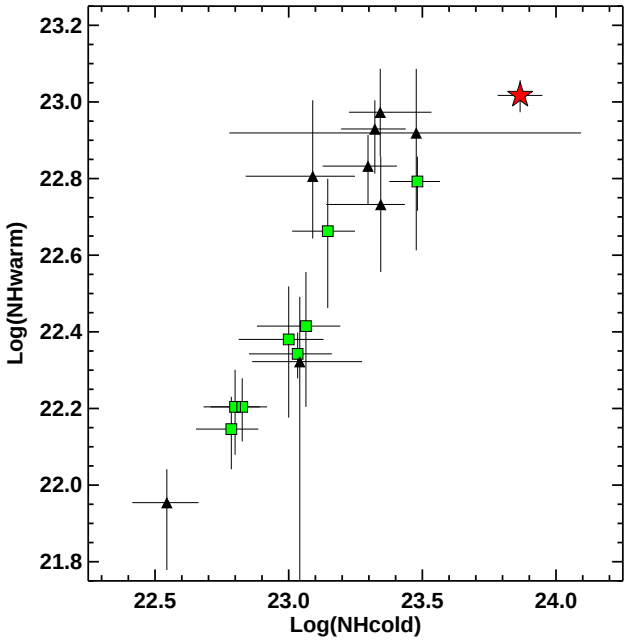

Figure 4.8: *Column density of the Warm absorber versus the Cold absorber of the nucleus in this work (Red star), Puccetti et al. (2007) (green squares) and de Rosa et al. (2007) (black triangles).*

- **Soft-band X-ray emission:**

  The *BeppoSAX* soft spectrum of NGC 4151 was well fitted with the combination of a power law continuum and a thermal plasma with kT=0.15 keV (de Rosa et al., 2007). However, although the BLM gives a formally good fit, the inclusion of the BLM+EL improved the χ^2-statistics and also minimize the residuals at low energies (see Table 4.7 and Figs. 4.6 and 4.7). The main contribution to the soft-band ($<$ 2keV) emission is coming from a ionized nebula (emission lines added to the BLM). However there are still fluctuations in the residuals, indicating that the emission line relative strengths seem to be slightly inadequate in order to get a perfect fit. Thus, it suggests that the ionized nebula has not the same properties in the NLR and ENLR.

	F_{Xobs} (0.5-2 keV)	F_{Xobs} (2-10 keV)	L_X (0.5-2 keV)	L_X (2-10 keV)
Nucl.	> 4.97	> 102.1	> 82.2	> 96.1
NLR	$1.43^{+0.12}_{-0.11}$	$7.77^{+0.52}_{-0.58}$	$2.07^{+0.39}_{-0.18}$	$3.40^{+0.20}_{-0.09}$
ENLR	$1.45^{+0.15}_{-0.12}$	$10.0^{+0.70}_{-0.49}$	$2.70^{+0.50}_{-0.30}$	$5.28^{+0.60}_{-0.53}$

Table 4.10: *Fluxes and luminosities obtained for each region. Observed flux in units of* 10^{-13}ergs^{-1}cm^{-2}. *Luminosities corrected by absorption in units of* 10^{40}ergs^{-1}

4.6 X-ray image analysis

The images in soft and hard energy (0.2-2.0 and 2.0- 7.0 keV, respectively) were adaptively smoothed (the smoothing depends on the count rate of the pixel vicinity, Ebeling et al., 2006). Smoothing algorithms are useful when the count-rate of the diffuse emission is close to the background level. The CIAO task CSMOOTH[17], using a *Fast Fourier transform* algorithm and a minimum and maximum significance S/N level of 3 and 4, and a scale maximum of 2 pixels was used.

Chandra data include information about the photon energies and positions that was used to obtain energy-filtered images, and to carry out sub-pixel resolution spatial analysis. Although the pixel size of the *Chandra*/ACIS detector is 0.492″, smaller spatial scales are accessible as the image moves across the detector pixels during the telescope dither, therefore sampling pixel scales smaller than detector. This allows sub-pixel binning of the images and a more detailed spatial analysis using PSF simulations. The PSF simulations were carried out using information on the spectral distribution and off-axis location of the system as inputs to ChaRT PSF simulator[18] (Karovska et al., 2003). Similar techniques were applied for the analysis of *Chandra* observations of e.g. several interacting binaries (Karovska et al., 2005, 2007), and the SN1987A remnant (e.g. Burrows et al., 2000; Park et al., 2002).

In addition to our high-spatial resolution analysis we applied smoothing techniques to detect the low contrast diffuse emission. For example, we applied the adaptive smoothing CIAO tool *csmooth*, based on the algorithm developed by Ebeling et al. (2006) and implemented in *asmooth*. *Csmooth* is an adaptive smoothing tool for images containing multiscale complex structures, and it preserves the spatial signatures and the associated counts as well as significance estimates (Ebeling et al., 2006, for a detailed description of this technique).

The hard (>2 keV) energy emission has already been reported as being point-like (Yang et al., 2001). The flux percentage of the NLR vs the nucleus is <2.5%, below

[17] http://cxc.harvard.edu/ciao/ahelp/csmooth.html
[18] http://asc.harvard.edu/chart/index.html

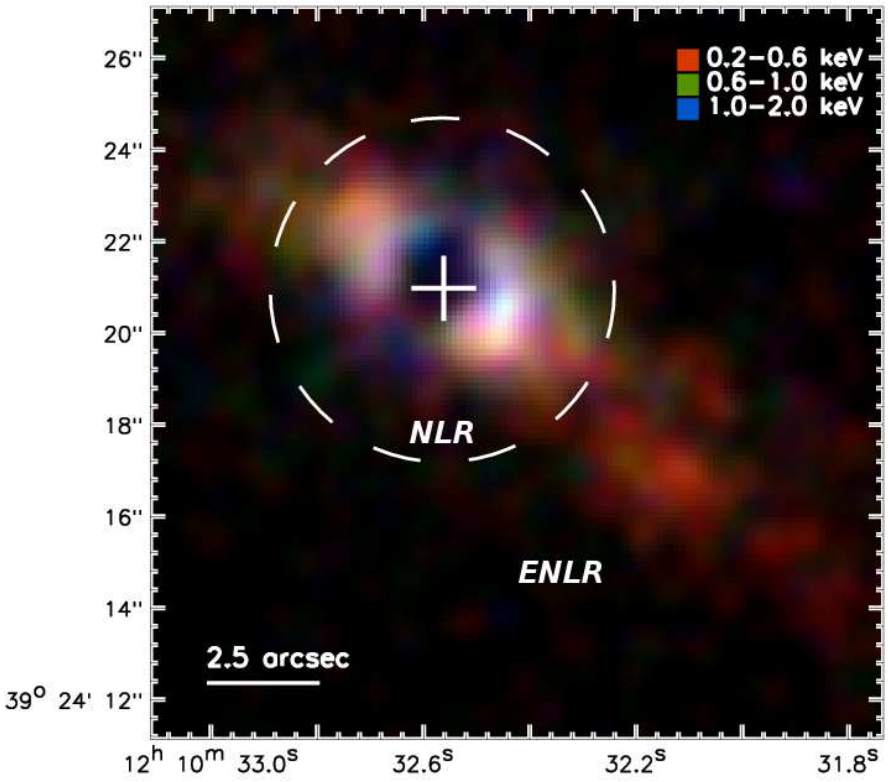

Figure 4.9: *True color image with 0.2-0.6 keV (red), 0.6-1.0 keV (green) and 1.0-2.0 keV (blue). Dashed circle shows the spectral extraction region of the NLR.*

the value expected from the PSF of *Chandra*.

In order to see the changes in the soft emission images three energy ranges have been defined: 0.2-0.6 keV, 0.6-1.0 keV and 1.0-2.0 keV (Fig. 4.9). To select the energy ranges we extracted the spectrum of R2 (see Fig. 4.10). R2 has been extracted centered in the position indicated in Table 4.4 and extrated from a circular region with a radius 1″.5, which is the minimun radius that encircles the optical region R2. After 1 keV the spectrum does not have counts so we decided to divide it into two

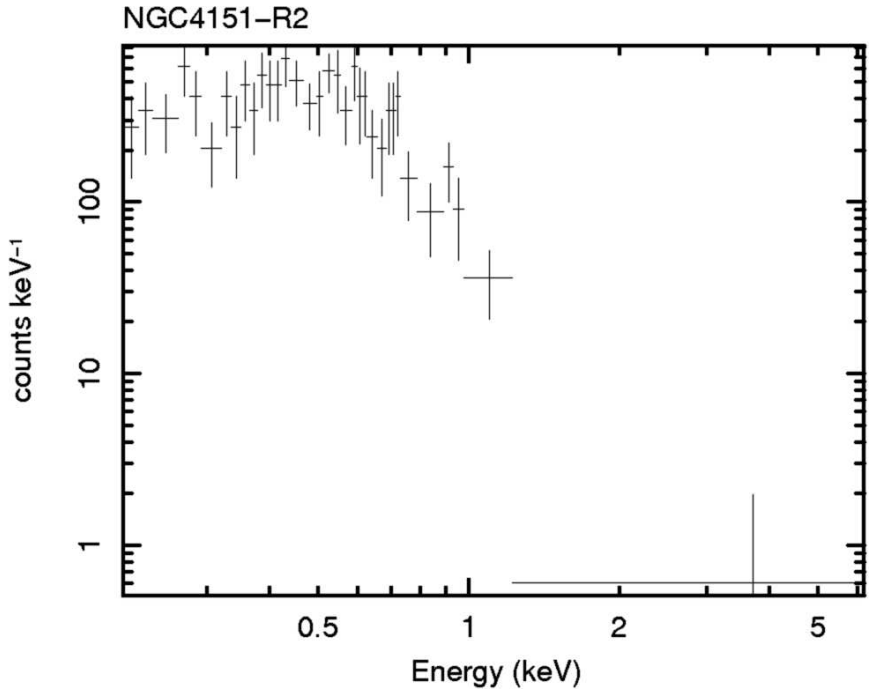

Figure 4.10: *Spectrum of the region R2.*

equal-width bands (0.2-0.6 keV and 0.6-1.0 keV) below 1 keV and complete the soft energy range (1.0-2.0 keV) with a third band image. Notice that R2 spectrum has inssufficient counts to perform the spectral analysis.

To construct the true-color image shown in Fig. 4.9 only regions above 3σ level in each band have been included. The ENLR extends up to 13″ only in 0.2-0.6 keV range. At higher energies the emission is less extended, disappearing at energies higher than 1 keV (also seen in the R2 spectrum in Fig. 4.10). The NLR is seen at energies lower than 2 keV and also at higher energies.

Fig. 4.11 shows the soft (0.2-0.6 keV) smoothed image. We find resolved soft X-ray emission up to $\sim$ 13″ ($\sim$ 780 pc) out of the nucleus, with a general spatial correlation with [OIII]/Hα emission. Yang et al. (2001) have also reported the correlation between ground based [OIII] data and soft X-rays. The cone-like NLR, as traced by the [OIII]/Hα ratio image, has a clear X-ray counterpart (P.A.$\sim$ 53°) but additional X-ray structures, not reported before, are seen with no optical correspondence and some [OIII]/Hβ structures have no X-ray counterpart. A soft X-ray structure is seen out to 7″ at P.A. $\sim$ 67° to the south-west. Moreover, an X-ray connection is clear

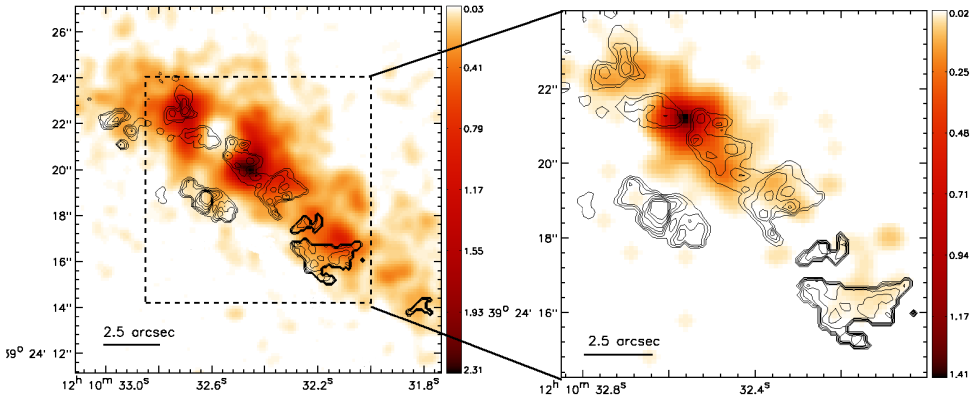

Figure 4.11: [OIII]/Hα *contours overlaid on the 0.2-0.6 keV ACIS-S image. ObsID 348 (*left*) and ObsID 335 (*right*).*

between the two blobs R1 and R2.

4.7 Discussion

The NLR and ENLR of NGC 4151 have been extensively studied; however, there are still some open questions that need to be addressed: (1) The emission mechanism of the ENLR and; (2) The misalignment between the radio jet and the optical cone like structure. Here, we have developed a multiwavelengh analysis that could help to understand this source. We have re-analyzed the *Chandra*/ACIS, *HST*/WFPC2 and *VLA* data in order to obtain information about the emission mechanism in each region and the plausible NLR/ENLR connection. Here we discuss the results and argue for a new interpretation of the data.

4.7.1 On the NLR/ENLR emission mechanisms

Evans et al. (1993) already showed the bi-conical distribution of [OIII] in NGC 4151 with *HST* images. They found opening angles projected on the plane of the sky of $75^\circ \pm 10^\circ$ with a projected axis PA $60/240^\circ$. This natural extension of the [OIII]λ5007 emission-line cones observed with HST to the emission line gas found in the near nuclear NLR and ENLR, observed from the ground, suggests that the extended

emission line gas is physically encapsulated within the volume of space generated by extending the nuclear cones to greater radii.

The comparison of the two HST images showing the structures in the ratios [OIII]/Hβ and [SII]/Hα adds some hints into the dominant physical mechanism responsible of the observed emission. From Fig. 4.2 it seems to be clear that at large scales, from the inner regions to the size of the ENLR, a general similar structure is found in both ratios. None of the regions defined in the [OIII]/Hβ image ratio (Fig. 4.2) shows that ionization by star-forming processes is the main emission mechanism (see Fig. 4.4). Only R10 and R11 (perpendicular to the conical structure) are closer to the locus of shocks ionization. Regions along the conical structure show the ionization by the AGN as the dominant emission mechanism. Nelson et al. (2000) reported the same conclusion but for the NLR by using HST long-slit spectroscopy. However here we find the same conclusion for the extended emission, pointing out to the same mechanism for both NLR and ENLR.

The NLR as traced by soft X-rays (Fig. 4.11 left), ressembles the structure seen in [OIII]/Hβ. The region R7 has a clear counterpart in X-ray and a filamentary structure links the nuclear source with this feature. Yang et al. (2001) also showed an excellent correlation between the extended soft X-ray and [OIII]λ5007 line emissions. The 0.2-0.6 keV energy range extends up to larger radii than 0.6-1.0 keV and 1.0-2.0 keV energies (see Fig. 4.9).

Yang et al. (2001) argued that the hard X-ray component was spatially unresolved and the nuclear component was described by a heavily absorbed ($N_H \simeq 3 \times 10^{22}$ cm^{-2}), hard power-law ($\Gamma \simeq 0.3$) plus a soft emission from either a power-law ($\Gamma \simeq 2.6$) or a thermal ($kT \simeq 0.6$ keV) component. The *BeppoSAX* spectra in several epochs has shown complex X-ray absorbers. The model by Yang et al. (2001) provides a good fit to our data in the hard energy range (>2 keV) but fails in the soft range, showing large residuals in the spectral fit (Fig. 4.6 and 4.7). We have included emission lines reported by high resolution spectra (Ogle et al., 2000; Schurch et al., 2004). The residuals of the spectral fit have improved (Figs. 4.6 and 4.7), even if the relative contribution of the emission lines may be slightly different from those reported before. These spectra were extracted from extraction windows larger than 8″ for *Chandra* data (30″ in the case of *XMM-Newton* data). We have enough spatial resolution to disantangle the NLR and ENLR spectra, and hints the same emission mechanism is present in both regions. This is also consistent with the result in optical bands that ionization for the central engine as the main emission mechanism for the NLR and ENLR.

4.7.2 On the radio jet misalignment

In many instances the morphology and kinematics of the NLR appear closely linked to the radio structure, particularly in Seyfert galaxies with linear or jet-like radio sources. In these objects, the line-emitting gas is often found to be co-spatial with the radio jets and there is also kinematical evidence for physical interaction between the jets and the NLR gas (Capetti et al., 1999; Whittle et al., 2005). The suggested mechanism is that the expansion of the radio plasma into the host galaxy interstellar medium produces fast shock waves that emit a hard continuum and ultimately provide the dominant source of ionizing photons (Taylor et al., 1992; Sutherland et al., 1993). The comparison of the radio jet structure and the distribution and kinematics of the ionized gas in the NLR in NGC 4151 has surprisingly revealed a misalignment of the radio jet and the NLR (Mundell et al., 2003). Such a misalignment suggests that shock excitation by passage of the radio jet is not the dominant excitation mechanism for the NLR, favoring nuclear photoionization to explain the structure of the NLR (Kaiser et al., 2000).

The most accepted explanation up to now is that the cone has a large angle that intersects with the plane of the galaxy (Pedlar et al., 1993) (See Fig. 4.12). In this case we see only the intersection with the galaxy that might not correspond to the position angle of the radio jet. The local gas velocities of the ENLR coincide with the gas velocities of the disk, indicating the that string of knots found at optical wavelengths must lie in the disk of the galaxy. Numerically, the position angle of the galaxy is 22° (Das et al., 2005), with an inclination to the line of sight of 20°, the southwest side being closer to us. The position angle of the bicone is 60°, with an inclination of 45°. The line of sight is outside of the bicone at an angle of 12° with respect to the nearest part of the bicone. Because of the large opening angle of the cone, it will intersect a sufficiently thick galactic disk ($\sim$100 pc). The northeast bicone will also intersect the northeast galactic disk because of the symmetry. This intersection produces the observed geometry of the ENLR (Pedlar et al., 1993).

Such a misalignment could be due to several kinematical components in the NLR. The whole picture shown in [OIII]/Hα line ratio could not be related to the radio jet. The kinematical components of the NLR in NGC 4151 were already analysed by Kaiser et al. (2000), suggesting at least three distinct kinematical components. One component characterized by low velocity and low velocity dispersion (radii 19″), a second cloud population characterized by high velocities and high velocity dispersions (1″.1), and an intermediate cloud population with low velocities and high velocity dispersions, which they attributed to high velocity and high velocity dispersion clouds with low velocities due to projection effects. Assuming the the outflow is traced by high velocity and high velocity dispersion regions, we ob-

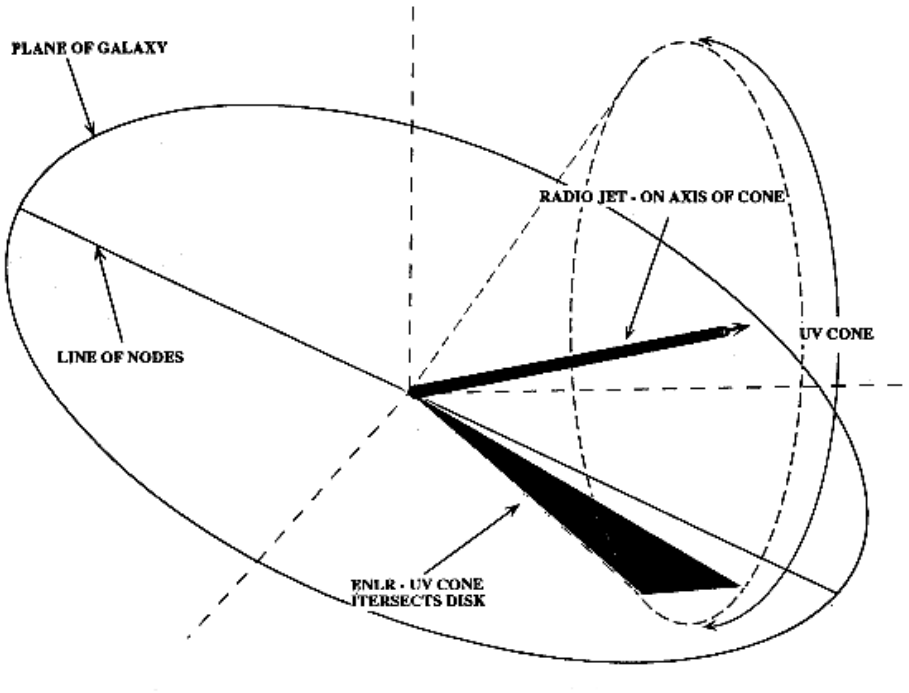

Figure 4.12: *Squeme of the scenario proposed by Pedlar et al. (1993) to explain the misalignment between the radio jet and the cone-like structure. Figure taken from Pedlar et al. (1993).*

tain that the P.A. 57° with an angular width of 60° for the NLR. Unfortunately, this does not explain the misalignment between the jet and the NLR.

The radio analysis performed here shows two jets with P.A. 52° and 77° (see Fig. 4.3). The first and faintest jet has a P.A. which is consistent with being the origin of the optical/X-ray NLR and ENLR morphologies. A cross-like structure is seen in the spectral index map through the position angles mentioned above. Thus we argue that the fainter jet is the responsible of the optical/X-ray structure seen in the NLR and ENLR. The explanation for bimodal jet feature could be: (1) Two different jets without any connection or (2) one jet that has changed the position angle with time.

In order to test our hypothesis we have computed the lifetimes of the main radio knots. In what follows, we have used the methodology by Pacholczyk (1978). The lifetime of a radio source can be obtained by assuming that its observed radio luminosity has been constant. In this case $\tau = E_e/L_R$. E_e is the relativistic particle

energy and L_R is the total radio luminosity assuming spherical geometry and that the radio continuum extends from 300 MHz top 30 GHz with the spectral indices reported in Table 4.5. We can obtain E_e by using the equation $E_e = E_{min}4/7(1+\zeta)$, that depends on the ratio of the proton energy to the electron energy (ζ) and the minimum total energy in relativistic particles and field E_{min}. χ is an unknown that could hava values between 1 and 2000. We will adopt $\zeta = 1$, i.e. assume that the protons and relativistic electrons have equal energies (see Miley 1980 for a discussion on this assumption). The value E_{min} can be computed by $E_{min} = c_{13}(1+\zeta)^{4/7}\phi^{3/7}R^{9/7}L_R^{4/7}$. c_{13} is a function that depends on the spectral index ϕ is the filling factor of fields and particles, and ranges between $\phi = 1$ for a completely filled scenario and $\phi \simeq 0$ for an empty bubble. We have estimated the implications on the selection of the two different cases $\phi = 1$ and $\phi = 0$; we find that the lifetime of the radio source τ is about 20 times larger for the bubbles with the volume filling factor is $\phi = 1$ compared with a filling factor of $\phi = 10^{-3}$. However the relative comparison between the radio sources is not affected by the chosen ϕ. Therefore, we have shown the results assuming $\phi = 1$ for simplicity. R is the characteristic linear size of the source in cm. We have taken the mean value between the minor axis and the mayor axis of the source tabulated in Table 4.5 as the knot size. Table 4.11 shows the resulting values for the different knots.

Knots along P.A. 77° (C1-C5) show $\tau \sim 0.2$ Myr whereas C6 and S knots (P.A. 53°) show higher values ($\tau > 1.$ Myr). Thus, it seems that the aged string of knots would be responsible for the extended emission observed at soft X-ray and optical wavelength. The fact that the string C1-C5 does not show such extended emission would be understood in two ways: (1) either there is not enough gas along the younger jet (P.A. 77°) to ionize the medium or (2) the jet is too young to have had enough time to interact with the medium.

	$\log(L_R)$ (ergs s^{-1})	$\log(E_{min})$ (ergs)	$\log(E_e)$ (ergs)	τ (Myr)
C1	37.96	51.36	50.81	0.22
C2	38.23	51.65	51.11	0.24
C3	38.21	51.46	50.92	0.16
C4	38.36	51.06	50.52	0.05
C5	37.82	51.31	50.76	0.28
C6	36.32	50.43	49.89	1.17
SW	36.67	50.89	50.35	1.51

Table 4.11: *Radio luminosity between 300MHz and 30GHz (L_R), minimun total energy (E_{min}), relativistic particle energy (E_e) and lifetime of the radio source (τ).*

Favouring the hyphothesis that P.A. of the jet, has changed the highest resolution 1.4 GHz *VLBI* images indicate that the average jet direction incorporates a number of sharp changes in position angle, possibly related to jet interactions with the circumnuclear environment (Mundell et al., 2003). Pedlar et al. (1993) reported significant position angle variations within two sided 3 arcsecs radio jet, suggesting a $\sim$ 1 arcsec periodicity which may have an approximate mirror symmetry about the nucleus. If indeed the oscillations of the east and west jets are coordinated, they suggest that small, systematic changes in the jet orientation have taken place with time, rather than being simply fluid instabilities. Hence, it seems plausible that the jet has precessed from 45° to 77° in a periodic way. This structure fills the wide angle seen in the NLR ([OIII]/Hα) and the second main knot at P.A. 52°, which agrees with the P.A. of the whole southwestern structure seen in the optical.

In favour of the hypothesis of two different jets, strong controversy has been reported in the literature in terms of which of these knots is the nucleus of the AGN. The component C4 is divided in four components (F, E, D and X) using *VLBA* data. Mundell et al. (2003) hypothesized that the nucleus of the active galaxy is located in *VLBA* component D whereas Ulvestad et al. (1998) suggested that *VLBA* component E, located 7 pc farther east, is the actual AGN. Ulvestad et al. (2005) reported the high-sensitivity *VLBI* imaging of NGC 4151 that identifies the flat-spectrum radio nucleus of the galaxy as component D. We would like to stress that component E has an elongated structure reported by Ulvestad et al. (2005) which has a P.A. $\sim$ 33.4° and component D3 has a P.A. 90°. Then, within 7 pc there is two elongated structures with two position angles, favouring that two jets have been ejected from the galaxy nucleus at different times.

4.8 Summary and Conclusions

We reinterpreted archival *Chandra*, *Hubble Space Telescope* (*HST*), and *VLA* observations of the circumnuclear extended emission in the nearby Type 1.5 Seyfert galaxy NGC 4151. The main results are:

- A conical structure is seen in [SII]/Hα and [OIII]/Hβ ratios, extending up to 13″. Both morphological apparience and pptical diagnostic diagrams suggest ionization from the nucleus, rather than star-formation or shock heating.

- We find resolved soft-band X-ray emission $\sim$ 14″ ($\sim$ 915 pc) out of the nucleus, which is spatially coincident with [OIII]/Hβ emission. NLR and ENLR, as seen with [OIII]/Hβ ratio, have X-ray counterpart (P.A.$\sim$ 53°) but moreover there is a second structure with P.A.$\sim$ 67° that has not optical counterpart. Soft X-ray

spectra of NLR and ENLR is consistent with ionized material for the AGN up to 14″. It is also consistent with optical diagnostics.

- We detect not only the radio jet with an overall P.A.$\sim 77^\circ$ but also a second one traced by weaker radio knots along P.A.$\sim 53^\circ$. The structures in the radio spectral index map may be interpreted as the superposition of two linear structures along P.A.$\sim 53^\circ$ and $\sim 77^\circ$. The computed lifetime of the radio sources are longer for the south knot located at P.A.$\sim 53^\circ$, suggesting that these secondary jet is older than the firt one. We interpret this result as either a jet preccesion between 45° and 77° or, alternatively, two jets that have been ejected from the galaxy nucleus at different times.

Acknowledgements

This work was financed by DGICyT grants AYA2003-00128 and the Junta de Andalucía TIC114. OGM acknowledges financial support by the Ministerio de Educación y Ciencia through the Spanish grant FPI BES-2004-5044. This research has made use of data obtained from the *Chandra* Data Archive provided by the *Chandra* X-ray Center (CXC). This research made use of the NASA/IPAC extragalactic database (NED), which is operated by the Jet Propulsion Laboratory under contract with the National Aeronautics and Space Administration. This publication makes use of data products from the Two Micron All Sky Survey, which is a joint project of the University of Massachusetts and the Infrared Processing and Analysis Center/California Institute of Technology, funded by the National Aeronautics and Space Administration and the National Science Foundation.

Bibliography

Anders, E. and Grevesse, N.: 1989, *Geochimica et Cosmochimica Acta* **53**, 197

Antonucci, R.: 1993, *Annual Review of Astronomy and Astrophysics* **31**, 473

Armentrout, B. K., Kraemer, S. B., and Turner, T. J.: 2007, *Astrophysical Journal* **665**, 237

Arnaud, K. A.: 1996, in *Astronomical Data Analysis Software and Systems V*, Vol. 101, p. 17

Axon, D. J., Marconi, A., Capetti, A., Maccetto, F. D., Schreier, E., and Robinson, A.: 1998, *Astrophysical Journal* **496**, L75

Beckmann, V., Shrader, C. R., Gehrels, N., Soldi, S., Lubinski, P., Zdziarski, A. A., Petrucci, P.-O., and Malzac, J.: 2005, *Astrophysical Journal* **634**, 939

Burrows, D. N., Michael, E., Hwang, U., McCray, R., Chevalier, R. A., Petre, R., Garmire, G. P., Holt, S. S., and Nousek, J. A.: 2000, *Astrophysical Journal* **543**, L149

Capetti, A., Axon, D. J., Macchetto, F. D., Marconi, A., and Winge, C.: 1999, *Astrophysical Journal* **516**, 187

Capetti, A., Macchetto, F. D., and Lattanzi, M. G.: 1997, *Astrophysical Journal* **476**, L67

Carral, P., Turner, J. L., and Ho, P. T. P.: 1990, *Astrophysical Journal* **362**, 434

Carter, C., Karovska, M., Jerius, D., Glotfelty, K., and Beikman, S.: 2003, in *Astronomical Data Analysis Software and Systems XII*, Vol. 295, p. 477

Crenshaw, D. M., Kraemer, S. B., Hutchings, J. B., Bradley, L. D., Gull, T. R., Kaiser, M. E., Nelson, C. H., Ruiz, J. R., and Weistrop, D.: 2000, *Astronomical Journal* **120**, 1731

Das, V., Crenshaw, D. M., Hutchings, J. B., Deo, R. P., Kraemer, S. B., Gull, T. R., Kaiser, M. E., Nelson, C. H., and Weistrop, D.: 2005, *Astronomical Journal* **130**, 945

Davis, J. E.: 2001, *Astrophysical Journal* **562**, 575

de Rosa, A., Piro, L., Perola, G. C., Capalbi, M., Cappi, M., Grandi, P., Maraschi, L., and Petrucci, P. O.: 2007, *Astronomy and Astrophysics* **463**, 903

Dickey, J. M. and Lockman, F. J.: 1990, *Annual Review of Astronomy and Astrophysics* **28**, 215

Done, C., Zycki, P. T., and Smith, D. A.: 2002, *Monthly Notices of the Royal Astronomical Society* **331**, 453

Ebeling, H., White, D. A., and Rangarajan, F. V. N.: 2006, *Monthly Notices of the Royal Astronomical Society* **368**, 65

Elvis, M.: 2000, *Astrophysical Journal* **545**, 63

Evans, I. N., Tsvetanov, Z., Kriss, G. A., Ford, H. C., Caganoff, S., and Koratkar, A. P.: 1993, *Astrophysical Journal* **417**, 82

Gallimore, J. F., Baum, S. A., O'Dea, C. P., and Pedlar, A.: 1996, *Astrophysical Journal* **458**, 136

Guainazzi, M., Matt, G., and Perola, G. C.: 2005, *Astronomy and Astrophysics* **444**, 119

Hutchings, J. B., Crenshaw, D. M., Danks, A. C., Gull, T. R., Kraemer, S. B., Nelson, C. H., Weistrop, D., Kaiser, M. E., and Joseph, C. L.: 1999, *Astronomical Journal* **118**, 2101

Hutchings, J. B., Crenshaw, D. M., Kaiser, M. E., Kraemer, S. B., Weistrop, D., Baum, S., Bowers, C. W., Feinberg, L. D., Green, R. F., Gull, T. R., Hartig, G. F., Hill, G., and Lindler, D. J.: 1998, *Astrophysical Journal* **492**, L115

Kaiser, M. E., Bradley, L. D., Hutchings, J. B., Crenshaw, D. M., Gull, T. R., Kraemer, S. B., Nelson, C. H., Ruiz, J., and Weistrop, D.: 2000, *Astrophysical Journal* **528**, 260

Kaiser, M. E., Bradley, L. D., Hutchings, J. B., Weistrop, D., Nelson, C., Kraemer, S. B., Crenshaw, D. M., Ruiz, J., and Gull, T. R.: 1999, in *Galaxy Dynamics - A Rutgers Symposium*, Vol. 182, p. 51

Karovska, M., Carilli, C. L., Raymond, J. C., and Mattei, J. A.: 2007, *Astrophysical Journal* **661**, 1048

Karovska, M., Marengo, M., Elvis, M., Fazio, G. G., Hora, J. L., Hinz, P. M., Hoffmann, W. F., Meyer, M., and Mamajek, E.: 2003, *Astrophysical Journal* **598**, L91

Karovska, M., Schlegel, E., Hack, W., Raymond, J. C., and Wood, B. E.: 2005, *Astrophysical Journal* **623**, L137

Kewley, L. J., Dopita, M. A., Sutherland, R. S., Heisler, C. A., and Trevena, J.: 2001, *Astrophysical Journal* **556**, 121

Kewley, L. J., Groves, B., Kauffmann, G., and Heckman, T.: 2006, *astro-ph/0605681*, Mon.Not.Roy.Astron.Soc. 372 (2006) 961-976

Kraemer, S. B., Crenshaw, D. M., Hutchings, J. B., Gull, T. R., Kaiser, M. E., Nelson, C. H., and Weistrop, D.: 2000, *Astrophysical Journal* **531**, 278

Magdziarz, P. and Zdziarski, A. A.: 1995, *Monthly Notices of the Royal Astronomical Society* **273**, 837

Matt, G., Fabian, A. C., Guainazzi, M., Iwasawa, K., Bassani, L., and Malaguti, G.: 2000, *Monthly Notices of the Royal Astronomical Society* **318**, 173

Mundell, C. G., Wrobel, J. M., Pedlar, A., and Gallimore, J. F.: 2003, *Astrophysical Journal* **583**, 192

Nazarova, L. S., O'Brien, P. T., Ward, M. J., and Gondhalekar, P. M.: 1998, *Astronomy and Astrophysics* **331**, 34

Nelson, C. H., Weistrop, D., Hutchings, J. B., Crenshaw, D. M., Gull, T. R., Kaiser, M. E., Kraemer, S. B., and Lindler, D.: 2000, *Astrophysical Journal* **531**, 257

Ogle, P. M., Marshall, H. L., Lee, J. C., and Canizares, C. R.: 2000, *Astrophysical Journal* **545**, L81

Osterbrock, D. E. and Ferland, G. J.: 2006, *Astrophysics of gaseous nebulae and active galactic nuclei*

Pacholczyk, A. G.: 1978, *Journal of the Royal Astronomical Society of Canada* **72**, 229

Park, S., Burrows, D. N., Garmire, G. P., Nousek, J. A., McCray, R., Michael, E., and Zhekov, S.: 2002, *Astrophysical Journal* **567**, 314

Pedlar, A., Kukula, M. J., Longley, D. P. T., Muxlow, T. W. B., Axon, D. J., Baum, S., O'Dea, C., and Unger, S. W.: 1993, *Monthly Notices of the Royal Astronomical Society* **263**, 471

Penston, M. V., Robinson, A., Alloin, D., Appenzeller, I., Aretxaga, I., Axon, D. J., Baribaud, T., Barthel, P., Baum, S. A., Boisson, C., de Bruyn, A. G., Clavel, J., Colina, L., Dennefeld, M., Diaz, A., Dietrich, M., Durret, F., Dyson, J. E., Gondhalekar, P., van Groningen, E., Jablonka, P., Jackson, N., Kollatschny, W., Laurikainen, E., Lawrence, A., Masegosa, J., McHardy, I., Meurs, E. J. A., Miley, G., Moles, M., O'Brien, P., O'Dea, C., del Olmo, A., Pedlar, A., Perea, J., Perez, E., Perez-Fournon, I., Perry, J., Pilbratt, G., Rees, M., Robson, I., Rodriguez-Pascual, P., Espinosa, J. M. R., Santos-Lleo, M., Schilizzi, R., Stasinska, G., Stirpe, G. M., Tadhunter, C., Terlevich, E., Terlevich, R., Unger, S., Vila-Vilaro, V., Vilchez, J., Wagner, S. J., Ward, M. J., and Yates, G. J.: 1990, *Astronomy and Astrophysics* **236**, 53

Perez-Fournon, I. and Wilson, A. S.: 1990, *Astrophysical Journal* **356**, 456

Perola, G. C., Matt, G., Cappi, M., Fiore, F., Guainazzi, M., Maraschi, L., Petrucci, P. O., and Piro, L.: 2002, *Astronomy and Astrophysics* **389**, 802

Piro, L., de Rosa, A., Matt, G., and Perola, G. C.: 2005, *Astronomy and Astrophysics* **441**, L13

Puccetti, S., Fiore, F., Risaliti, G., Capalbi, M., Elvis, M., and Nicastro, F.: 2007, *Monthly Notices of the Royal Astronomical Society* **377**, 607

Robinson, A., Terlevich, R., and Dyson, J.: 1994, *Astrophysics and Space Science* **222**, 265

Schulz, H.: 1988, *Astronomy and Astrophysics* **203**, 233

Schurch, N. J. and Warwick, R. S.: 2002, *Monthly Notices of the Royal Astronomical Society* **334**, 811

Schurch, N. J., Warwick, R. S., Griffiths, R. E., and Kahn, S. M.: 2004, *Monthly Notices of the Royal Astronomical Society* **350**, 1

Sutherland, R. S., Bicknell, G. V., and Dopita, M. A.: 1993, *Astrophysical Journal* **414**, 510

Taylor, D., Dyson, J. E., and Axon, D. J.: 1992, *Monthly Notices of the Royal Astronomical Society* **255**, 351

Ulvestad, J. S., Roy, A. L., Colbert, E. J. M., and Wilson, A. S.: 1998, *Astrophysical Journal* **496**, 196

Ulvestad, J. S., Wong, D. S., Taylor, G. B., Gallimore, J. F., and Mundell, C. G.: 2005, *Astronomical Journal* **130**, 936

Unger, S. W., Pedlar, A., Axon, D. J., Whittle, M., Meurs, E. J. A., and Ward, M. J.: 1987, *Monthly Notices of the Royal Astronomical Society* **228**, 671

Veilleux, S.: 1987, in *Bulletin of the American Astronomical Society*, Vol. 19, p. 695

Whittle, M., Rosario, D. J., Silverman, J. D., Nelson, C. H., and Wilson, A. S.: 2005, *Astronomical Journal* **129**, 104

Wilson, A. S. and Ulvestad, J. S.: 1982, ApJ **263**, 576

Yang, Y., Wilson, A. S., and Ferruit, P.: 2001, *Astrophysical Journal* **563**, 124

Chapter 5

THE ULTRA LUMINOUS X-RAY SOURCES IN THE HVS OF NGC 1275

We report the results of a study of X-ray point sources coincident with the High Velocity System (HVS) projected in front of NGC 1275. A very deep X-ray image of the core of the Perseus cluster made with the Chandra Observatory has been used. We find a population of Ultra-Luminous X-ray sources (ULX; 7 sources with $L_{\rm X}(0.5-7.0\,{\rm keV}) > 7\times10^{39}\,{\rm erg\,s^{-1}}$). As with the ULX populations in the Antennae and Cartwheel galaxies, those in the HVS are associated with a region of very active star formation. Several sources have possible optical counterparts found on HST images, although the X-ray brightest one does not. Absorbed power-law models fit the X-ray spectra, with most having a photon index between 2 and 3.

5.1 Introduction

The study of Ultra-Luminous X-ray sources (ULX) has been greatly expanded by the high spatial resolution and spectral grasp of the *Chandra* and *XMM-Newton* observatories, respectively. ULX sources (Fabbiano and White, 2003; Miller and Colbert, 2004) have 2–10 keV X-ray luminosities exceeding $10^{39}\,{\rm erg\,s^{-1}}$ and are found some distance from the centres of galaxies; they are not active galactic nuclei. Their luminosity exceeds that for a $10\,{\rm M_\odot}$ black hole accreting at the Eddington limit which radiates isotropically and so have created much interest in the possibility that they contain even higher mass black holes, such as InterMediate Black Holes (IMBH) of $\sim 10^3\,{\rm M_\odot}$ (Makishima et al., 2000; Miller et al., 2004). Alternatively they may appear so luminous because of beaming (Reynolds et al., 1999; King et al., 2001) or due to super Eddington accretion (Begelman, 2002).

ULX are most common in starburst galaxies and in very active star-forming regions, such as in the Antennae and the Cartwheel galaxy, where populations of tens of them are found (Zezas and Fabbiano, 2002; Wolter and Trinchieri, 2004). In some cases variability rules out the possibility that they are just clusters of lower-luminosity objects. The origin of IMBH is unclear. They may form as a result of

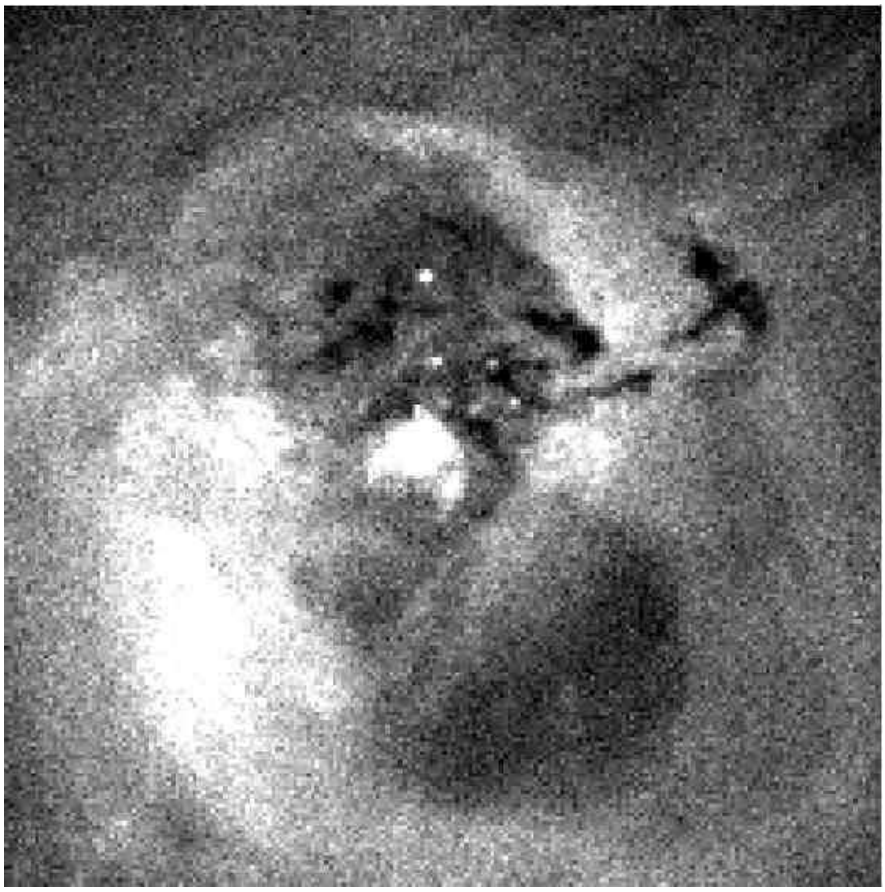

Figure 5.1: *NGC 1275 in the 0.3–7.0 keV band. Pixels are 0.49 arcsec in size and the N-S height of the image is 97 arcsec. North is to the top and east is to the left in this image. The point sources which we identify as ULX are located in the high-velocity system is seen in absorption to the north of the bright nucleus. None are seen in the south lobe*

binary interactions in dense stellar environments (Zwart and McMillan, 2002). A comparison of IMBH ULX candidates with a number of well known stellar-mass black holes candidates (BHC; Miller and Colbert, 2004) demonstrates that the ULX are more luminous but have cooler thermal disk components than standard stellar-mass BHC. Therefore, ULX in this sample are clearly different from the sample of stellar-mass BHC and are consistent with being IMBH.

Here we report on the discovery of a population of 8 point X-ray sources to the

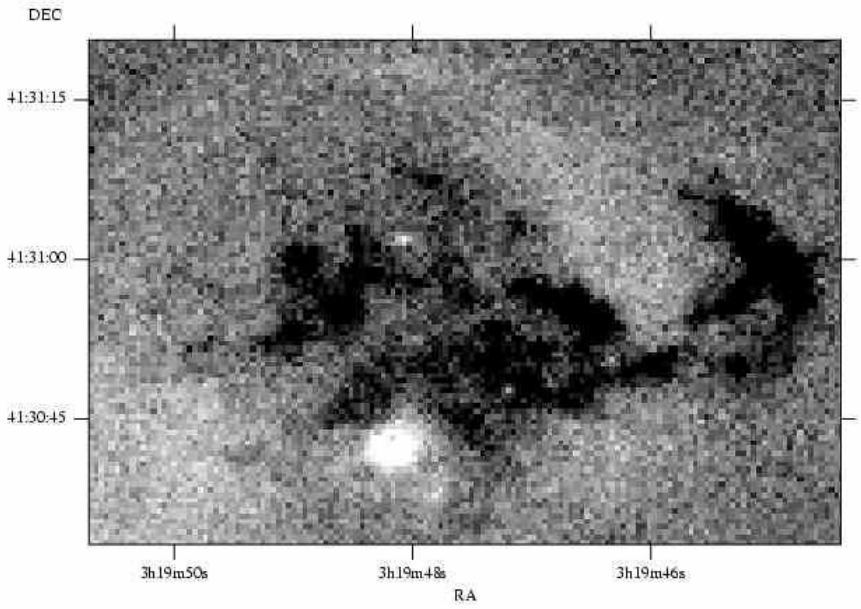

Figure 5.2: *The central region of NGC 1275 in the 0.3–0.8 keV band. Pixels are 0.49 arcsec in dimension and the entire image is* 1.77×0.89 arcmin^2. *North is to the top and east is to the left in this image. The high-velocity system is seen in absorption to the north of the bright nucleus which is at RA* $3^{\rm h}19^{\rm m}48^{\rm s}$, *Dec. +41°30′42″*

N of the nucleus of NGC 1275, which is the central galaxy in the Perseus cluster. All exceed $10^{39}\,{\rm erg\,s^{-1}}$ in X-ray luminosity, and 7 are formally ULX, if they are at the distance of the cluster. The spatial region where they lie coincides with the High Velocity System of NGC 1275. We assume that they are part of that system. We see no other point sources (apart from the nucleus) over the body of NGC 1275 (Fig. 5.1).

NGC 1275 is embedded in a complex multiphase environment. Optical imaging and spectroscopy first established the existence of two distinct emission-line system toward NGC 1275: a low-velocity component associated with the galaxy itself at 5200 km ${\rm s^{-1}}$ and a high-velocity component at 8200 km ${\rm s^{-1}}$ projected nearby on the sky (Minkowski, 1957). This latter component is associated with a small gas-rich galaxy falling into the cluster along our line of sight (Haschick et al., 1982). A merger scenario has been proposed (Minkowski, 1957). However, interaction of the low and/or high-velocity system with a third gas-rich galaxy or system of galaxies (Holtzman et al., 1992; Conselice et al., 2001), or influences from the surrounding

dense intracluster medium (ICM) (Sarazin and Surdin, 1988; Caulet et al., 1992) have been discussed.

Deep *Chandra* observations have clarified the position of the High Velocity System (HVS). The depth of the observed X-ray absorption (e.g. Fig. 5.1) is nor infilled by emission from hot gas projected along the line-of-sight so the HVS must lie well in front of NGC 1275. Gillmon et al. (2004) have estimated a lower limit on the distance of the HVS from the nucleus of 57 kpc. The low- and high-velocity system are therefore not yet directly interacting. The HVS *is* however strongly interacting with the ICM of the Perseus cluster, which has triggered strong star formation. In this paper we describe the detailed analysis of the X-ray spatial and spectral properties of the discrete sources in the high velocity system.

The paper is organized as follows: in Sect. 5.2 and 5.3 we present reduction and results from the imaging analysis and spectral analysis, respectively; in Sect. 5.4 we discuss the results; and Sect. 5.5 summarizes our findings.

Throughout this paper we use a redshift of 0.018 and $\mathrm{H}_0 = 70\ \mathrm{km\ s^{-1}\ Mpc^{-1}}$. This gives a luminosity distance to the cluster of 80 Mpc; 1 arcsec corresponds to a physical distance of 370 pc.

5.2 Imaging analysis

The *Chandra* datasets included in this analysis are listed in Table 5.1. The total exposure time, after removing periods containing flares, is 890 ks. To prepare the data for analysis, all of the datasets were reprocessed to use the latest appropriate gain file (acisD2000-01-29gain_ctiN0003). The datasets analysed each used an aimpoint on the ACIS-S3 CCD. The datasets were filtered using the lightcurve in the 2.5 to 7 keV band on ACIS-S1 CCD, which is a back-illuminated CCD like the ACIS-S3. The CIAO LC_CLEAN tool was used to remove periods 20 per cent away from the median count rate for all the lightcurves. This procedure was not used for datasets 03209 and 04289 which did not include the S1 CCD, however no flares were seen in these observations on the S3 CCD. Each of the observations was reprojected to match the coordinate system of the 04952 observation.

The 900 ks X-ray image covering the energy range $0.3 - 0.8\ \mathrm{keV}$ is shown in Fig 5.2. The bright NGC 1275 nucleus is clearly seen at RA $3^h19^m48^s$ and Dec. $+41^o30'42''$ (J2000) and the high-velocity system is seen in absorption to the north of the nucleus.

The CIAO CELLDETECT source detection routine was then used on the reprocessed level 2 event data to produce a preliminary list of point sources. The cell size ranges between 4 pixels to 8 pixels. This algorithm strongly depends on the local

Obs. ID	Seq.	Observ. date	Exp. (ks)	Nom. roll (deg)	Pointing RA (J2000)	Pointing Dec (J2000)
3209	800209	2002-08-08	95.8	101.2	3:19:46.86	+41:31:51.3
4289	800209	2002-08-10	95.4	101.2	3:19:46.86	+41:31:51.3
6139	800397	2004-10-04	51.6	125.9	3:19:45.54	+41:31:33.9
4946	800397	2004-10-06	22.7	127.2	3:19:45.44	+41:31:33.2
4948	800398	2004-10-09	107.5	128.9	3:19:44.75	+41:31:40.1
4947	800397	2004-10-11	28.7	130.6	3:19:45.17	+41:31:31.3
4949	800398	2004-10-12	28.8	130.9	3:19:44.57	+41:31:38.7
4950	800399	2004-10-12	73.4	131.1	3:19:43.97	+41:31:46.1
4952	800400	2004-10-14	143.2	132.6	3:19:43.22	+41:31:52.2
4951	800399	2004-10-17	91.4	135.2	3:19:43.57	+41:31:42.6
4953	800400	2004-10-18	29.3	136.2	3:19:42.83	+41:31:48.5
6145	800397	2004-10-19	83.1	137.7	3:19:44.66	+41:31:26.7
6146	800398	2004-10-20	39.2	138.7	3:19:43.92	+41:31:32.7

Table 5.1: Chandra *observations included in this analysis. The exposure given is the time remaining after filtering the lightcurve for flares. All observations were taken with the aimpoint on the ACIS-S3 CCD. All positions are in J2000 coordinates.*

background and the detection cell in not adjustable to the size of the source. As the X-ray diffuse emission of the NGC 1275 is very strong, the source list may well include false detections in high background level regions. Therefore problematic sources embedded in such regions have been excluded in our analysis. Moreover, as mentioned above, we only included sources associated with the HVS.

We have detected 8 bright sources close to the nucleus of NGC 1275, located in the northern inner radio lobe of 3C 84. All of these source are embedded in the same region as the HVS (see Fig. 5.1). There are no sources associated with the southern lobe (Fig. 5.1), thus we assume these sources are associated with the HVS.

Fig. 5.3 (*left*) shows the smoothed ACIS-S3 image in the 0.3–7.0 keV band, including numbered labels of all the detected sources (*top*), centred on source labelled N3 (*centre*) and centred on source N5 (*bottom*).

All the point-like sources are listed in Table 5.2, showing their positions and count rates.

We have used archival *HST* observations of NGC 1275 in order to search for optical counterparts. The galaxy was imaged with the WFPC2 camera on *HST* using the F814W ($\sim$ I, on 2001 November 6 with an exposure time of 1200 s) and F702W ($\sim$ R, on 1994 March 31 with an exposure time of 140 s) broad-band filters. Several coincidences between X-ray sources and optical knots of emission (F814W) can be

N	Position(J2000)	Count Rate (counts ks^{-1})
1....	03:19:48.736 +41:30:47.25	0.34±0.05
2....	03:19:48.166 +41:30:46.64	1.69±0.06
3....	03:19:48.090 +41:31:01.88	2.60±0.08
4....	03:19:47.994 +41:30:52.30	1.42±0.09
5....	03:19:47.925 +41:30:47.50	1.19±0.09
6....	03:19:47.602 +41:30:47.01	0.74±0.06
7....	03:19:47.422 +41:30:51.93	0.95±0.08
8....	03:19:47.214 +41:30:47.62	1.28±0.08

Table 5.2: *Positions of sources detected near the NGC 1275 centre and displayed in Fig. 5.3 (column 2) and count rate in the energy range between 0.5–7.0 keV (column 3).*

N	F_X/F_{F814W}	F_X/F_{F702W}	M_{F814W}	M_{F702W}
1....	> 26.5	> 16.2	>22.6	>22.1
2....	25.4	23.6	20.4	20.3
3....	>18800	...	>26.8	...
4....	>1081	>800	>24.5	>24.2
5....	>123	>60.6	>22.6	>21.9
6....	26.2	28.4	21.7	21.7
7....	76.7	51.4	22.3	21.9
8....	134	90.1	22.2	21.7

Table 5.3: *Optical analysis. X-ray to optical ratios (columns 2 and 3) and magnitude determinations (columns 4 and 5) for the filters F814W and F702W, respectively, with the X-ray flux between 1.0–7.0 keV.*

seen in Fig. 5.3 (right), showing the same regions as Fig. 5.3 (left).

The *HST* image shows many highly absorbed features. When we compare in detail, sources N7 and N8 are located in star forming regions, while N2 and N6 have a point-like counterpart. Sources N1, N3, N4 and N5 have no optical identification. Therefore, we have found a possible correlation between compact X-ray sources and regions of vigorous star formation. The implications are discussed later.

In order to investigate the emission mechanism of these ULX, the X-ray to optical flux ratios have been computed between the F702W and F814W *HST* broad-bands and 1.0–7.0 keV X-ray band. Preliminary processing of the raw images including corrections for the flat fielding was done remotely at the *Space Telescope Science In-*

stitute through the standard pipeline. For each frame, cosmic rays were removed by image combination, using the IMCOMBINE routine in IRAF. After cosmic ray removal, the frames were added using task WMOSAIC in STSDAS package. Photometric measurements were made with PHOT task, within the NOAO package. Finally the fluxes and magnitudes have been determined using the photometric zero-point information in the header of the calibrated image files.

These results are shown in Table 5.3, including the X-ray to optical flux ratios from the F814W and F702W broad-band filters, and the magnitude determinations from the same filters. In the cases where an optical counterpart has not been found (N1, N3, N4 and N5), the magnitudes and fluxes are just a lower limit.

5.3 Spectral analysis

We extracted spectra for all the detected sources close to the HVS, using extraction regions defined to include as many of the source photons as possible, but at the same time minimizing contamination from nearby sources and background. The background region was either a source-free circular annulus or several circles surrounding each source, in order to take into account the spatial variations of the diffuse emission and to minimize effects related to the spatial variation of the CCD response.

For each source, we extracted spectra from each of the datasets. These spectra were summed to form a total spectrum for each source. Response and ancillary response files were created for each source in each of the observations using the CIAO MKACISRMF and MKWARF tools. The responses for a particular source were summed together, weighting according to the number of counts in each observation.

The spectra were fitted using XSPEC v.11.3.2. In order to use the χ^2 statistic, we grouped the data to include at least 20 counts per spectral bin, before background subtraction. In spectral fitting we excluded any events with energies above 7.0 keV or below 0.5 keV.

Table 5.4 summarizes our spectral results in terms of the absorbing column density and photon index.

The sources have been modelled with an absorbed power law slope with photon index between Γ =[1.78-5.56] and an equivalent column density of $\mathrm{N_H} = [2.05 - 4.03]$ $\times 10^{21}$ cm^{-2}. In all the cases the single component power law give satisfactory fits. The column density of source N1 has been fixed due to the low count rate. The fitted $\mathrm{N_H}$ values are consistent with the intrinsic absorption measured e.g. in the optical band; the value of $\mathrm{A_V}$=0.54 corresponds to $\mathrm{N_H} \sim 1.1 \times 10^{21} \mathrm{cm}^{-2}$, assuming $\mathrm{A_V} = \mathrm{N_H} \times 5.3 \times 10^{-22}$ for $\mathrm{R_V} = 3.1$ (Bohlin et al., 1978). This value should be a

N	N_H ($10^{21}cm^{-2}$)	Γ	χ^2/d.o.f.
1....	$2.5^{(a)}$	$3.20^{+0.23}_{-0.37}$	112.90/101
2....	$2.72^{+1.43}_{-0.87}$	$1.78^{+0.30}_{-0.24}$	101.50/109
3....	$2.49^{+0.40}_{-0.40}$	$2.08^{+0.09}_{-0.09}$	153.86/142
4....	$2.05^{+0.91}_{-0.96}$	$2.29^{+0.44}_{-0.28}$	156.24/152
5....	$2.64^{+1.23}_{-0.93}$	$2.92^{+1.44}_{-0.36}$	124.09/139
6....	$3.74^{+1.57}_{-1.39}$	$3.51^{+0.48}_{-0.66}$	102.58/92
7....	$4.03^{+1.78}_{-1.45}$	$3.20^{+1.39}_{-0.48}$	133.69/135
8....	$2.66^{+1.00}_{-0.91}$	$2.13^{+0.52}_{-0.25}$	150.81/138

Table 5.4: *Spectral fits. (a) The column density of source N1 has been fixed due to the low count rate.*

N	F_{obs}(0.5–7.0 keV) erg cm^{-2} s^{-1}	F_{corr}(0.5–7.0 keV) erg cm^{-2} s^{-1}	log L_X (0.5–7.0 keV)
1....	2.09 $\times 10^{-15}$	4.34 $\times 10^{-15}$	39.51
2....	7.59 $\times 10^{-15}$	9.97 $\times 10^{-15}$	39.86
3....	1.64 $\times 10^{-14}$	2.28 $\times 10^{-14}$	40.22
4....	7.76 $\times 10^{-15}$	1.10 $\times 10^{-14}$	39.91
5....	5.36 $\times 10^{-15}$	1.07 $\times 10^{-14}$	39.90
6....	3.02 $\times 10^{-15}$	9.23 $\times 10^{-15}$	39.84
7....	4.28 $\times 10^{-15}$	1.18 $\times 10^{-14}$	39.95
8....	7.67 $\times 10^{-15}$	1.16 $\times 10^{-14}$	39.93

Table 5.5: *Fluxes (observed and k-corrected) and luminosities assuming a cosmological model with* $H_0 = 70\ km\ s^{-1}Mpc^{-1}$ *and z=0.018.*

lower limit to the fitted N_H value to be consistent, as is seen in Table 5.4.

As an example of our spectral fits, the brightest source, N3, has been fitted with a power-law with spectral index of 2.08 ± 0.09 and absorption of $N_H = 2.5 \pm 0.4$ $\times 10^{21}\ cm^{-2}$ (see Fig. 5.4).

In Table 5.5 we list the 0.5-7 keV flux and (absorption corrected) luminosities of the individual sources based on the best-fit power law model.

The lower limit of the luminosity of point sources in the image, if at the distance of NGC 1275, is $L_X(0.5-7.0\ keV) = 3.2 \times 10^{39} erg\ s^{-1}$, which is already well above the Eddington limit for a neutron star binary ($L_X \sim 3 \times 10^{38} erg\ s^{-1}$) and is also above the limit of canonical ULX, i.e. $\geq 10^{39} erg\ s^{-1}$.

The brightest point source has a luminosity of $L_X(0.5-7.0\ keV) = 1.67\ \times 10^{40}$

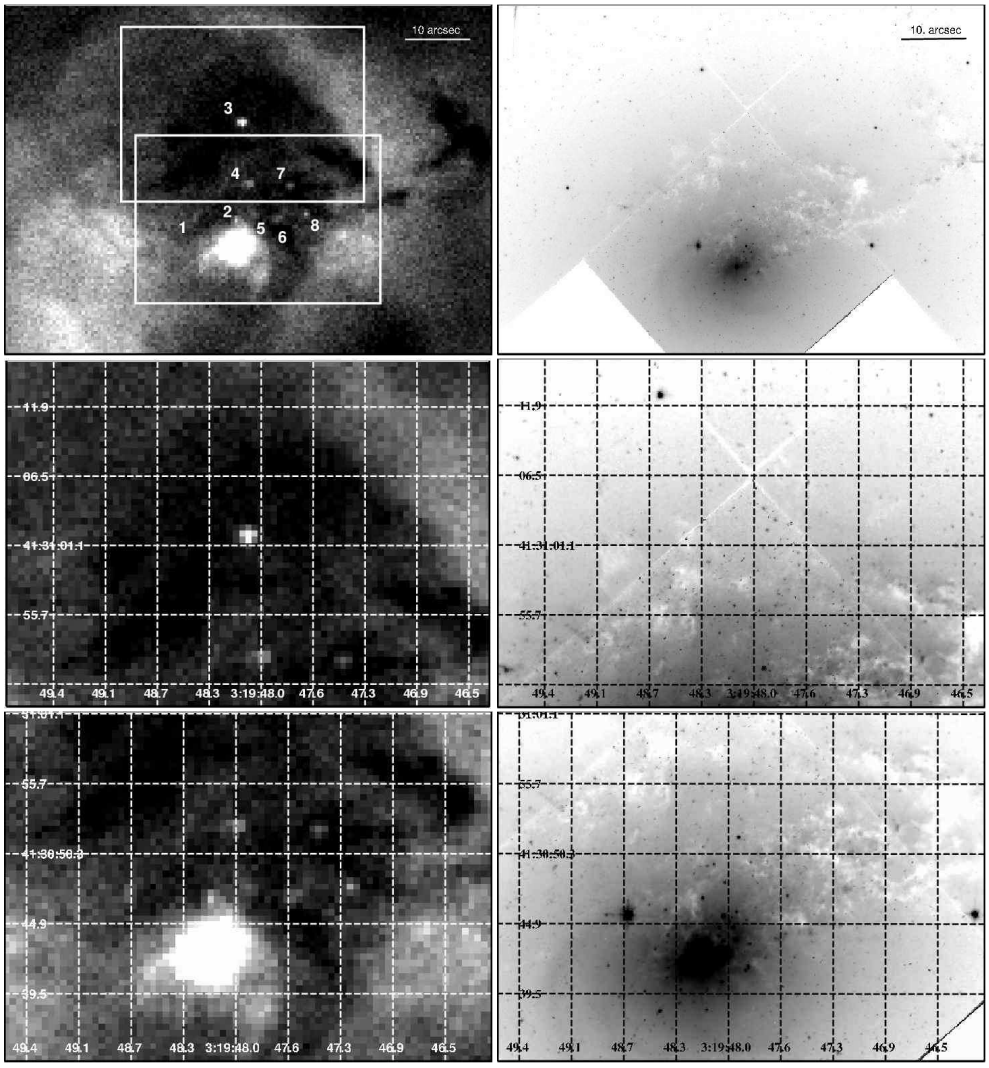

Figure 5.3: *Top-left: Broadband (0.5–7.0 keV) X-ray smoothed image with sources labelled. Top-right:* HST*/WFPC2 F814W broadband image. Centre-left: Broadband (0.5–7.0 keV) X-ray smoothed image centred in source 3. Centre-right:* HST*/WFPC2 F814W broadband image centred in source 3. Bottom-left: Broadband (0.5–7.0 keV) X-ray smoothed image centred in source 5. Bottom-left:* HST*/WFPC2 F814W broadband image centred in source 5.*

$\mathrm{erg\,s^{-1}}$, and is one of the brightest individual sources found in a galaxy. A ULX source more luminous than the entire X-ray luminosity of a normal galaxy has been

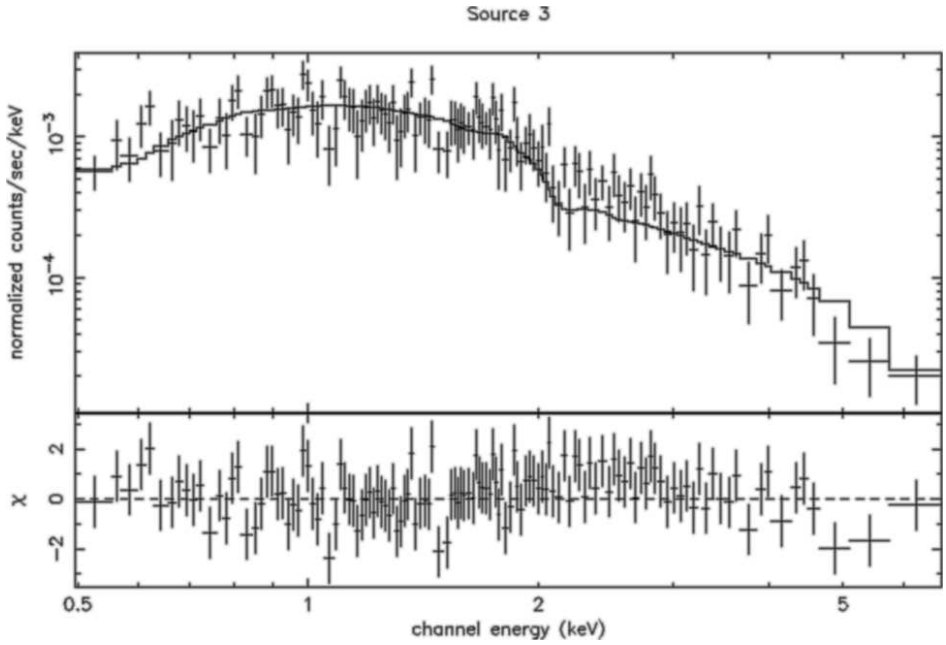

Figure 5.4: *ACIS-S spectrum of source N3. The solid line corresponds with a power law model with a spectral index of* Γ *=2.08 and absorption of* $\mathrm{N_H} = 2.5 \times 10^{21}\ \mathrm{cm}^{-2}$. *The fit residuals are presented in the lower panel.*

found in the Cartwheel system with a luminosity of at least $\mathrm{L_X} \sim 2 - 4 \times 10^{40} \mathrm{erg\ s}^{-1}$ (Gao et al., 2003; Wolter and Trinchieri, 2004). They explain this luminosity with a high-mass X-ray binary source (HMXB). The high X-ray luminosity suggests either a single extremely bright source, or a very dense collection of several high $\mathrm{L_X}$ sources, which would be even more peculiar. Evidence of time variability might suggest that is a single high $\mathrm{L_X}$ source.

Time variability analysis has been performed. The observations span about two years. Two data files were observed on 2002 August 8 and 10, and the other eleven data files were observed from 2004 October 4 to 2004 October 20, giving an almost daily coverage. The exposure times are between 22 and 143 ks. The data characteristics allows us determine short variation in 16 days (second period) and long-term variability of 2 years. Because of the low count rates of the sources in NGC 1275 (see Table 5.2), it is very hard to search for short-term variability. We extracted light-curves, using DMEXTRACT CIAO task for the two brightest sources (N3 and N4) (net count rate greater than 0.98 count s^{-1}) binned with bin sizes of 500, 1000, 2500 and 5000 s. In both cases the points were consistent with the respective mean values and variability has not been found. Furthermore, the mean values between 2002 and

2004 are the same, including errors bars. Therefore, evidence of time variability has not been found during the whole set of observations.

5.4 Discussion

Chandra has revealed significant populations of ULX in the interacting systems of the Antennae (NGC 4038/9; Zezas and Fabbiano, 2002) and the Cartwheel ring galaxy (Gao et al., 2003; Wolter and Trinchieri, 2004), where dramatic events have stimulated massive star formation. We have reported here on another example (Fig. 5.3 left) in the HVS of NGC 1275 which is interacting with the ICM of the Perseus cluster.

The sources are spatially associated with the distribution of absorbing clouds seen in soft X-ray (Fig. 5.2) and optical (Fig. 5.4) images. Two sources (N7 and N8) are directly linked with dust knots and another two (N2 and N6) have an optical point-like counterpart (Fig. 5.3 *bottom*). Similar correspondence have been found in the Cartwheel galaxy with the outer ring (Wolter and Trinchieri, 2004) and in the Antennae galaxies with 39 X-ray sources within the WFPC2 field (Zezas and Fabbiano, 2002). The optical brightness of the counterparts in the HVC are too high to be individual stars and so may be associated with young star clusters. Following the discussion of young star clusters in NCG 1275 given by Richer et al. (1993), an object of magnitude 22 corresponds to a cluster mass of about $10^6\,\mathrm{M}_\odot$ if its age is about $10^7\,\mathrm{yr}$. The HVC system travels at least 30 kpc in $10^7\,\mathrm{yr}$ so if a strong interaction with the core of the Perseus galaxy cluster has triggered star cluster formation in the HVC, then the clusters should have ages less than $\sim 10^8\,\mathrm{yr}$.

Our interpretation of the spatial correspondence with star clusters is that the regions are especially active, indicating a real link between ULX and star-forming regions, and meaning they are young objects. However the optical limits on sources N3 and 4 rule out any association with massive clusters in those cases (the limit on the absolute magnitude is about -8).

In M31 and the Milky Way (Grimm et al., 2003), XRB have luminosities consistent with the Eddington limit of a $\sim 2\mathrm{M}_\odot$ accreting object. They produce luminosities $\sim 3 \times 10^{38}\,\mathrm{erg\,s^{-1}}$, about one order of magnitude below the limiting luminosity in our sample ($3.2 \times 10^{39}\,\mathrm{erg\,s^{-1}}$). It is possible that our ULX consist of at least 15 (or 130, in the case of the brightest source found) 'normal' XRB clustered together, perhaps in a young star cluster. However in other objects we know that variability requires the presence of intrinsically luminous X-ray sources (e.g. M82; Griffiths et al., 2000; Kaaret et al., 2001). Alternative possibilities are that black hole sources, with masses in the range of galactic black hole binaries, are mildly beamed

(Reynolds et al., 1999; King et al., 2001). Spectral and timing features however rule out this possibility in some ULX (e.g. Strohmayer and Mushotzky, 2003). We note that compact supernova remnants sometimes have ULX luminosities (e.g. Fabian and Terlevich, 1996), but no recent supernovae have been reported for NGC 1275 (SN1968A was to the S of the HVS; Capetti, 2002).

Finally, we recall the IMBH model which has spectral support from some sources (Miller and Colbert, 2004, the level of absorption in NGC 1275 is too high for any soft excess to be observed). They may form in dense star clusters.

Our optical studies have clearly shown that the ULX have very high X-Ray to optical flux ratios. X-ray selected AGN from the *Rosat all sky survey* tend to have $\log(\mathrm{F_X}/\mathrm{F_{opt}}) \sim 1$. Thus the ULX do not have the optical properties expected if their were simple extensions of AGN (IMBH, as low luminosity limit). However, low mass X-ray binaries in the Milky Way have $\mathrm{F_X}/\mathrm{F_{opt}} \sim 100 - 10000$ (Mushotzky, 2004).

The results found in our system indicate that we have a mixed group of objects (see Table 5.3). At least 4 out of 8 sources (N3, N4, N5 and N8) have high X-ray to optical flux ratios. At least 3 out of 8 (N1, N2 and N6) have lower X-ray to optical ratios, possibly because they lie in star clusters.

Our data are consistent with no significant variability, similar to the result obtained on NGC 3256 by Lira et al. (2002). Time variability is frequently observed in ULX (e.g. IC 342 or M51 X-1, Sugiho et al., 2001; Liu et al., 2002, respectively), arguing that most of them are single compact objects, rather than a sum of numerous lower luminosity objects in the same object. While most ULX vary, many show low amplitude variability on long time scales (e.g. the Antennae galaxies, Zezas and Fabbiano, 2002), which is very different to galactic black holes. Zwart et al. (2004) find that a persistent bright ULX requires a doner star exceeding $15\,\mathrm{M_\odot}$. The search for characteristic frequencies is one of the most productive way of determining the nature of the ULX.

5.5 Conclusions

We have described the detailed analysis of the spatial and spectral properties of the discrete X-ray sources detected with a deep *Chandra* ACIS-S observation around NGC 1275. Our results are summarized below:

1. We have detected a total of 8 sources to the north of NGC 1275 nucleus.

2. The sources are spatially coincident with the High Velocity System and thus probably associated with it. They are therefore ULX.

3. Four of the sources have an optical counterpart in the I and R bands (from *HST* images); two of which are point-like sources and the other two are associated with star-forming regions.

4. In all the cases a single component power law gives satisfactory fits, with spectral index of Γ =[1.78-3.51] and an equivalent column density of $\mathrm{N_H}$ =[2.05 - 4.03] $\times 10^{21} \mathrm{cm}^{-2}$.

5. The minimum luminosity is $\mathrm{L_X}(0.5 - 7.0 \mathrm{keV}) = 3.2 \times 10^{39} \mathrm{erg\ s}^{-1}$ (source N1), which is already above the limit of canonical ULX.

6. No variability was detected in the two brightest sources found.

Our results add to the growing evidence that some episodes of rapid star formation lead to the production of ULX. Young, massive, star clusters may be involved in some, but not all of the sources.

Acknowledgements

OGM acknowledges the financial support by the Ministerio de Educacion y Ciencia through the program AYA2003-00128 and grant FPI BES-2004-5044. ACF thanks the Royal Society for support.

Bibliography

Begelman, M. C.: 2002, *Astrophysical Journal* **568**, L97

Bohlin, R. C., Savage, B. D., and Drake, J. F.: 1978, *Astrophysical Journal* **224**, 132

Capetti, A.: 2002, *Astrophysical Journal* **574**, L25

Caulet, A., Woodgate, B. E., Brown, L. W., Gull, T. R., Hintzen, P., Lowenthal, J. D., Oliversen, R. J., and Ziegler, M. M.: 1992, *Astrophysical Journal* **388**, 301

Conselice, C. J., Gallagher, J. S., and Wyse, R. F. G.: 2001, *Astronomical Journal* **122**, 2281

Fabbiano, G. and White, N. E.: 2003, *Compact Stellar X-ray Sources in Normal Galaxies*

Fabian, A. C. and Terlevich, R.: 1996, *Monthly Notices of the Royal Astronomical Society* **280**, L5

Gao, Y., Wang, Q. D., Appleton, P. N., and Lucas, R. A.: 2003, *Astrophysical Journal* **596**, L171

Gillmon, K., Sanders, J. S., and Fabian, A. C.: 2004, *Monthly Notices of the Royal Astronomical Society* **348**, 159

Griffiths, R. E., Ptak, A., Feigelson, E. D., Garmire, G., Townsley, L., Brandt, W. N., Sambruna, R., and Bregman, J. N.: 2000, *Science* **290**, 1325

Grimm, H.-J., Gilfanov, M., and Sunyaev, R.: 2003, *Monthly Notices of the Royal Astronomical Society* **339**, 793

Haschick, A. D., Crane, P. C., and van der Hulst, J. M.: 1982, *Astrophysical Journal* **262**, 81

Holtzman, J. A., Faber, S. M., Shaya, E. J., Lauer, T. R., Groth, J., Hunter, D. A., Baum, W. A., Ewald, S. P., Hester, J. J., Light, R. M., Lynds, C. R., O'Neil, E. J., and Westphal, J. A.: 1992, *Astronomical Journal* **103**, 691

Kaaret, P., Prestwich, A. H., Zezas, A., Murray, S. S., Kim, D.-W., Kilgard, R. E., Schlegel, E. M., and Ward, M. J.: 2001, *Monthly Notices of the Royal Astronomical Society* **321**, L29

King, A. R., Davies, M. B., Ward, M. J., Fabbiano, G., and Elvis, M.: 2001, *Astrophysical Journal* **552**, L109

Lira, P., Ward, M., Zezas, A., Alonso-Herrero, A., and Ueno, S.: 2002, *Monthly Notices of the Royal Astronomical Society* **330**, 259

Liu, J.-F., Bregman, J. N., Irwin, J., and Seitzer, P.: 2002, *Astrophysical Journal* **581**, L93

Makishima, K., Kubota, A., Mizuno, T., Ohnishi, T., Tashiro, M., Aruga, Y., Asai, K., Dotani, T., Mitsuda, K., Ueda, Y., Uno, S., Yamaoka, K., Ebisawa, K., Kohmura, Y., and Okada, K.: 2000, *Astrophysical Journal* **535**, 632

Miller, J. M., Fabian, A. C., and Miller, M. C.: 2004, *Astrophysical Journal* **614**, L117

Miller, M. C. and Colbert, E. J. M.: 2004, *International Journal of Modern Physics D* **13**, 1

Minkowski, R.: 1957, in *Radio astronomy*, Vol. 4, p. 107

Mushotzky, R.: 2004, *Progress of Theoretical Physics Supplement* **155**, 27

Reynolds, C. S., Heinz, S., Fabian, A. C., and Begelman, M. C.: 1999, *Astrophysical Journal* **521**, 99

Richer, H. B., Crabtree, D. R., Fabian, A. C., and Lin, D. N. C.: 1993, *Astronomical Journal* **105**, 877

Sarazin, C. L. and Surdin, V. G.: 1988, *Soviet Astronomy* **32**, 581

Strohmayer, T. E. and Mushotzky, R. F.: 2003, *Astrophysical Journal* **586**, L61

Sugiho, M., Kotoku, J., Makishima, K., Kubota, A., Mizuno, T., Fukazawa, Y., and Tashiro, M.: 2001, *Astrophysical Journal* **561**, L73

Wolter, A. and Trinchieri, G.: 2004, *Astronomy and Astrophysics* **426**, 787

Zezas, A. and Fabbiano, G.: 2002, *Astrophysical Journal* **577**, 726

Zwart, S. F. P., Dewi, J., and Maccarone, T.: 2004, *Monthly Notices of the Royal Astronomical Society* **355**, 413

Zwart, S. F. P. and McMillan, S. L. W.: 2002, *Astrophysical Journal* **576**, 899

Appendix A

Catalogue of spectra with *Chandra* data (Chapter 2)

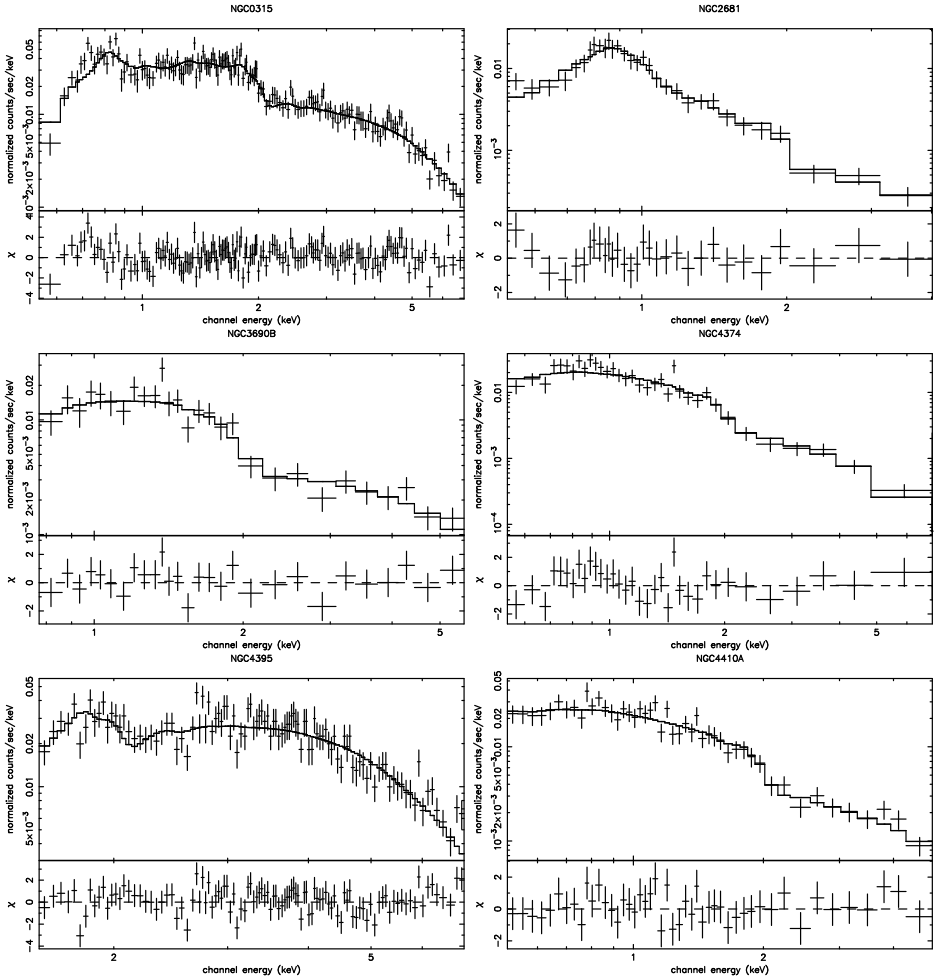

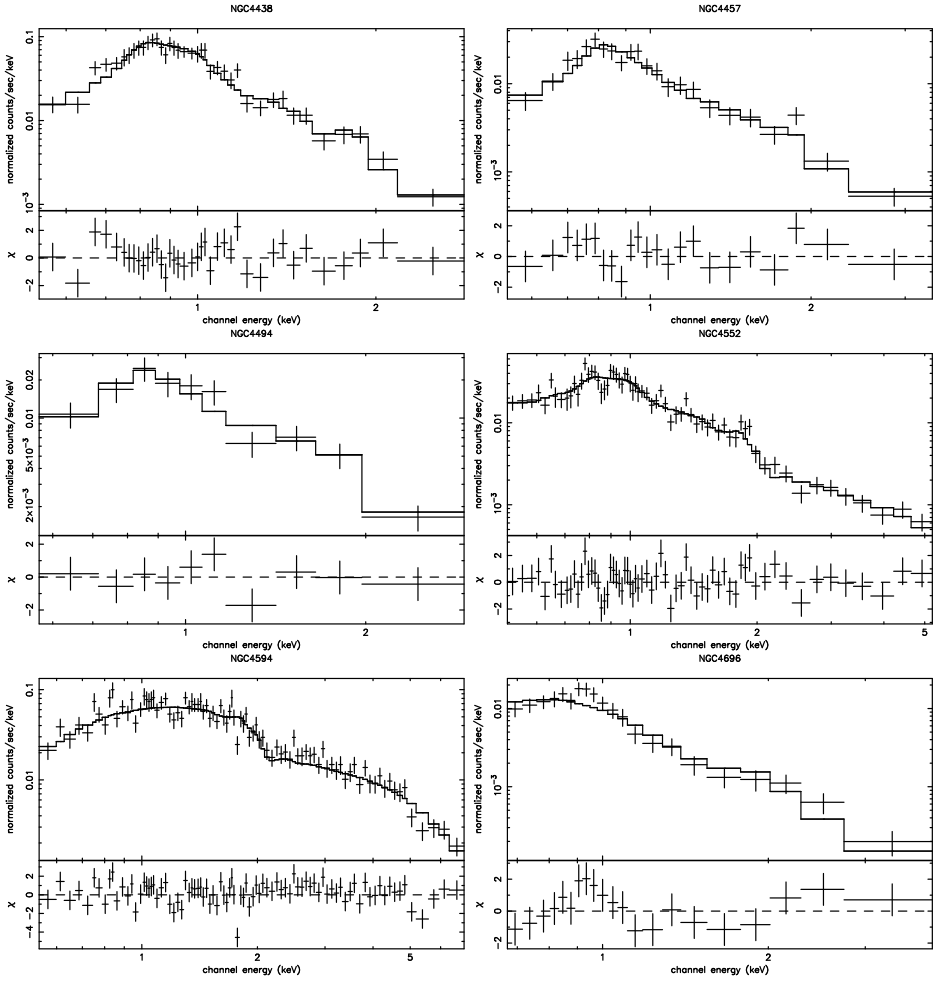
NGC4438
NGC4457
NGC4494
NGC4552
NGC4594
NGC4696
normalized counts/sec/keV
channel energy (keV)
χ

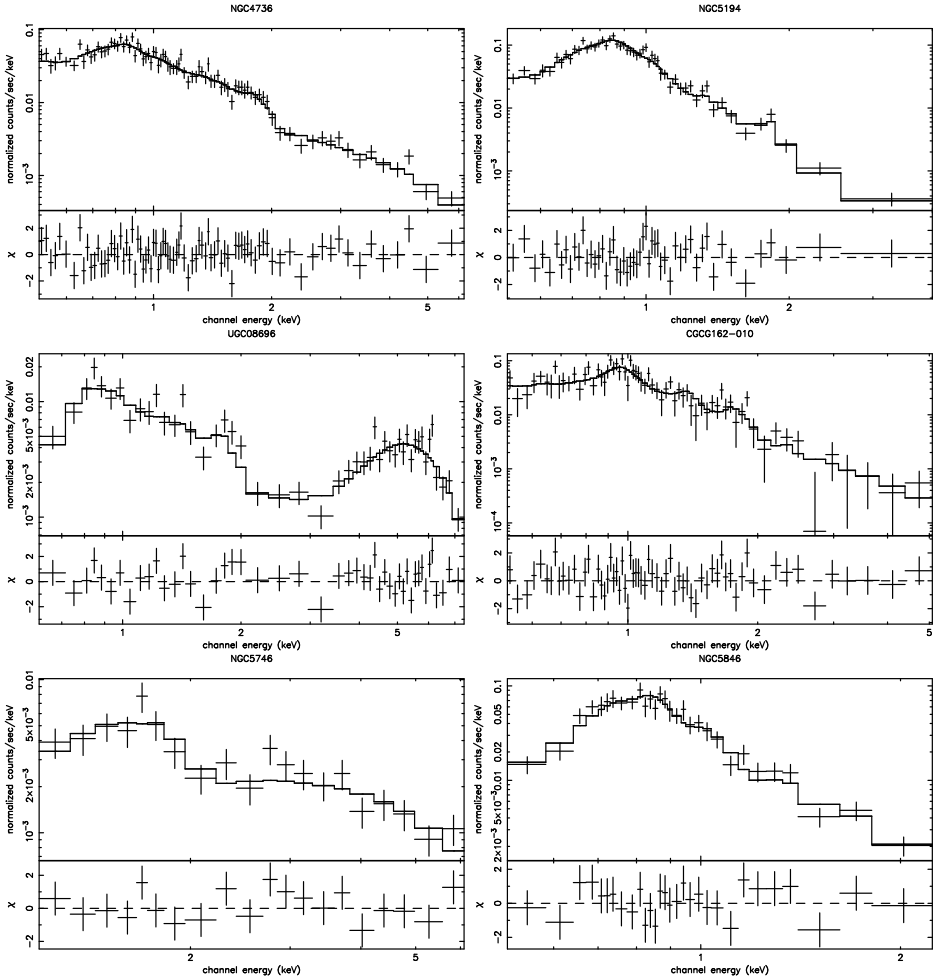
NGC4736
NGC5194
UGC08696
CGCG162−010
NGC5746
NGC5846
normalized counts/sec/keV
χ
channel energy (keV)

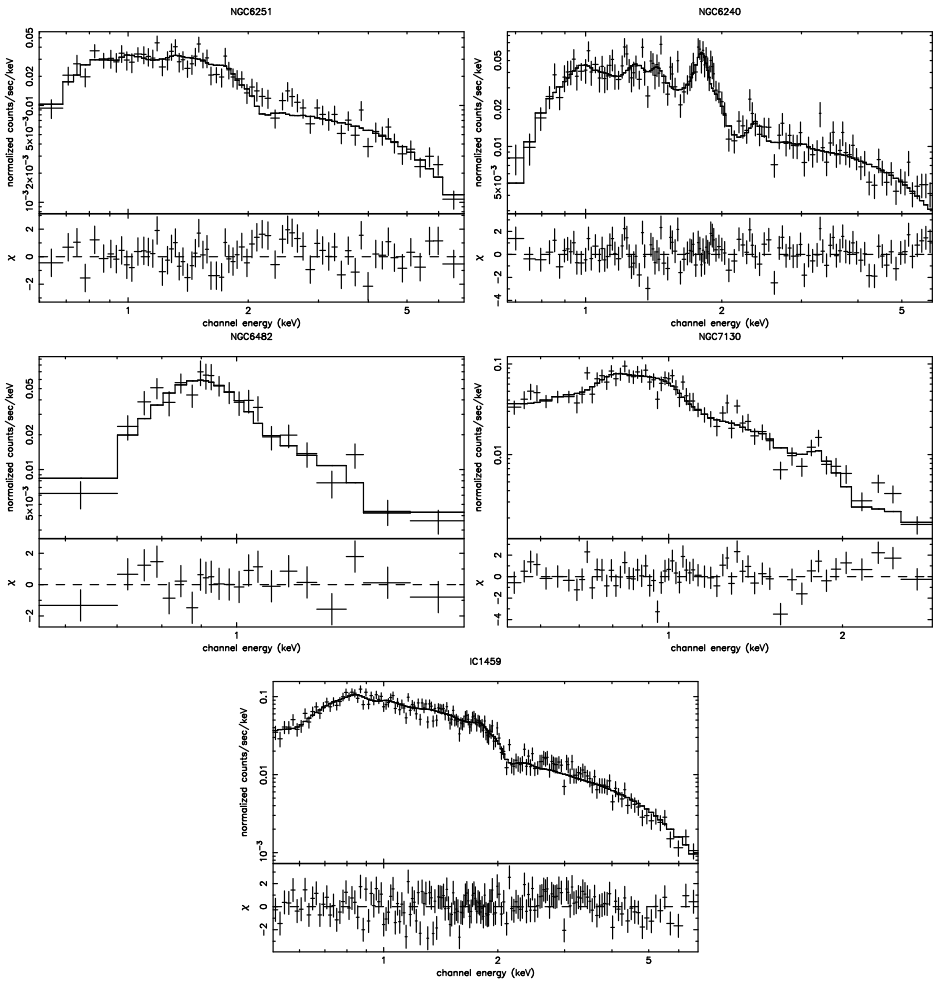

Figure A.1: *ACIS-S spectra of the SF subsample. The solid line corresponds to the best fit model. Residuals from the fitting are presented in the bottom panel.*

Appendix B

Notes on individual sources

NGC 315 (UGC 597, B2 0055+30). NGC 315 is a giant cD radiogalaxy located in the Zwicky cluster 0107.5+3212 (Zwicky et al., 1961, see Appendix F, Fig. F.1), with two-sided well resolved radiojets shown both with the *VLA* and VLBI observations (Venturi et al., 1993; Cotton et al., 1999). Nagar et al. (2005) reported also an unresolved core in addition to the radio jet at VLBI resolutions. The high spatial resolution provided by *Chandra* imaging allowed the detection of X-ray jets, the most striking one being the one along $\sim$10″ to the NW (see Fig. C.1 and Donato et al., 2004; Worrall et al., 2003, 2007) In both studies, based on a short 4.67 ks exposure, they found that the central source is of quite high (2-10 keV) luminosity 10^{41}erg s^{-1} given its AGN character.

With a more recent, longer exposure ($\approx$ 52 ksec) dataset, Satyapal et al. (2005) obtained very similar results (kT=0.54 keV, N_H=0.8 $\times$ 10^{22}cm^{-2}, Γ=1.60, and a hard X-ray luminosity of 4.67 $\times$ 10^{41}erg s^{-1}). Both results do agree with the ones reported in GM+06. Here we present a reanalysis of the longest, previous *Chandra* data ($\approx$ 52 ksec) and analize the 43.6 ksec *XMM-Newton* data finding that both datasets fit with ME2PL with not very discrepant parameters (see Tables 3.9 and 3.19), which leads to a similar (2-10 keV) X-ray luminosity, 5.8 $\times$ 10^{41}erg s^{-1} and 4.2 $\times$ 10^{41}erg s^{-1} respectively. A clear FeKα has been detected with equivalent width of 82 eV. The AGN nature of this galaxy was noted by Ho et al. (1997b), who reported a broad Hα component.

NGC 410 (UGC 735). NGC 410 is the central galaxy of the NORAS cluster RXC 0112.2+3302 (Böhringer et al., 2000), see Appendix F, Fig. F.1. After the *ROSAT* observations new data on the galaxy have not been reported. Here, we analyse the archival 19.6 ksec *XMM-Newton* observations. The bestfit model obtained is MEPL (Γ=2.4, kT=0.69 keV, NH1 = 1.2 $\times$ 10^{21} cm^{-2} and NH2 $<$ 2. $\times$ 10^{21} cm^{-2}).

NGC 474 (UGC 864). This lenticular galaxy is a member of the wide pair Arp 227, together with NGC 470 (see Appendix F, Fig. F.1), which is the dominant member of a loose group. Rampazzo et al. (2006) reported *XMM-Newton* EPIC data for the group. They calculated X-ray luminosities of L_X(0.5-2 keV)= 1.12 $\times$ 10^{39} erg s^{-1} and L_X(2-10 keV) = 6.2 $\times$ 10^{39} erg s^{-1} assuming $\Gamma \sim 1.7$ and galactic column density.

The low count rate of these data does not allow us to perform any spectral fitting. We have computed upper limits in the hard X-ray luminosity of $3.0^{+8.38}_{-0.001} \times 10^{38}$ erg s^{-1} for *Chandra* observations and $6.04^{+326}_{-0.01} \times 10^{37}$ erg s^{-1} for *XMM-Newton*, both consistent with an upper limit of 10^{39} erg s^{-1}, which is roughly consistent with the value quoted by Rampazzo et al. (2006) (2.5×10^{39} erg s^{-1}).

IIIZw 035 (CGPG 0141.8+1650). This galaxy belongs to a close interacting galaxy pair (see Appendix F, Fig. F.1). There are not previous X-ray data reported in the literature. We have analysed both the 14.5 ksec *Chandra* and 16.3 ksec *XMM-Newton* data. Neither have a high enough count-rate for the spectral analysis to be performed. The X-ray morphology shows two diffuse peaks both seen at hard energies, whith the northern one coincident with the LINER nuclear position, see Fig. C.4). Hattori et al. (2004) indicate that the morphological appearance in radio continuum emission suggests that star-forming activity dominates the energetics of the northern galaxy (Pihlstrom et al., 2001); the classification as a LINER may be due to a contribution from shock heating, possibly driven by superwind activity (Taniguchi et al., 1999; Lutz et al., 1999). However Baan and Klockner (2006) by means of observations at 1.4 and 8.4 GHz suggest an AGN nature of the radio continuum emission based in the compactness and flat index spectral nature of the nuclear source (see Tab. 3.31).

NGC 524 (UGC 968). This massive S0 galaxy dominates a small group (see Appendix F, Fig. F.1). The 15.4 ksec *Chandra* ACIS-S data show a morphology with diffuse emission at low energies (< 2 keV) and no X-ray detection in the hard band (2-10 keV), with a total X-ray luminosity amounting to 6.48×10^{38} erg s^{-1}. Filho et al. (2002) reported a slightly resolved 2 mJy core in the center of the optical galaxy from their *VLA* data at 5 GHz and 1″ resolution. They compare their data with those by Wrobel and Heeschen (1991), who detected a 1.4 mJy core at 5″ resolution, concluding that the source has to be compact and have a flattish spectrum. Dwarakanath and Nath (2006) on the contrary, based on the analysis at radiofrequencies, conclude that this group do not show any evidence of either current or past AGN activity.

NGC 835 and NGC 833 (Arp 318A and B ; HCG 16 A and B). Both members of an unusually active compact group, they have been optically classified as LINER and Seyfert 2, respectively (Coziol et al., 2004), and are strongly interacting with each other (see Appendix F, Figs. F.1 and F.2). Only NGC 835 was detected at radiofrequencies (Corbett et al., 2002) as a nuclear compact source. At X-ray frequencies no point sources were detected in neither hard band images (4.5-8* keV or 6-7 keV), but the X-ray soft emission is extended (see Fig. C.7). Turner et al. (2001) analyzed the 40 ksec EPIC *XMM-Newton* first-light observations and confirmed the presence of an AGN in both galaxies A and B. They fitted three components to the EPIC X-ray spectrum of **NGC 833** (Arp 318B): (1) a power-law for the obscured AGN, with Γ=1.8

and N_H=2.4 $\times$ 10^{23}cm^{-2}, (2) an unabsorbed power-law for the radiation scattered into our line of sight by thin, hot plasma directly illuminated by the AGN, and (3) an optically-thin thermal plasma with kT=0.47 keV; the luminosity of the AGN component of 6.2 $\times$ 10^{41} erg s^{-1} turns out to be 100 times brighter than the thermal X-ray emission. The core of **NGC 835** (Arp 318A) shows a very similar spectrum, with absorbed and scattered power laws indicating a heavily obscured AGN (N_H=4.6 $\times$ 10^{23}cm^{-2} and Γ=2.25) of 5.3 $\times$ 10^{41}erg^{-1} (0.5-10 keV) and a soft thermal component with kT=0.51 keV contributing to 2% of the total luminosity. Due to a missidentification, the sources used in GM+06 do not correspond to the nuclear sources we analyse here. FeKα line has been detected in both galaxies with equivalent width of 334 and 774 eV respectively.

NGC 1052. NGC 1052 is the brightest member of a small group (see Appendix F, Fig. F.2) which together with the NGC 1069 group makes up the Cetus I cluster (Wiklind et al., 1995). The X-ray morphology clearly indicates the presence of an unresolved nuclear source in the hard bands (Fig. C.8), in agreement with the classification by Satyapal et al. (2004), that made use of the same dataset. Evidences for the AGN nature of this object have already been given with the detection of (a) broad lines in spectropolarimetric measurements by Barth et al. (1999) and a broad underlying component in Hα reported in Ho et al. (1997b); (b) a variable radio core (Vermeulen et al., 2003); (c) H_20 megamaser emission (Claussen et al., 1998); (d) highly probable UV variability (Maoz et al., 2005). Guainazzi et al. (2000) confirm that its X-ray spectrum may therefore resemble that of Seyfert galaxies with the analysis of its *BeppoSAX* spectrum (0.1-100 keV). They obtain a very good fit with a two-component model for the spectrum, constituted by an absorbed (N_H=2.0 $\times$ 10^{23}cm^{-2}) and rather flat ($\Gamma \approx$1.4) power-law plus a "soft excess" below 2 keV. The corresponding flux in the 2-10 keV energy range is 4.0 $\times$ 10^{-12} erg cm^{-2} s^{-1}. We have best modelled the *Chandra* data with two power-laws with a flat index ($\Gamma = 1.15$) and column density compatible with that reported by Guainazzi et al. (2000), althought we are using a different instrument. Kadler et al. (2004) obtained a much flatter spectral index with another set of *Chandra* data (2.3 ksec) that they atributed to piled up effects. In addition to this, we also analise the 47.2 ksec *XMM-Newton* observation. We find the soft excess reported by Guainazzi et al. (2000), with the best-fit model resulting to be ME2PL ($\Gamma = 1.34$), steeper than the *Chandra* spectrum, and kT=0.60 keV. The FeKα line has been detected with an equivalent width of 144 eV.

NGC 2639 (UGC 4544). This a rather isolated object (Marquez et al., 2003), see Appendix F, Fig. F.1). *XMM-Newton*/pn images show a very faint source with almost no emission detection at hard energies, what argues in favour of classifying it as a SB-like object. The spectral analysis at soft energies results in MEKAL as

the best fit (kT=0.18 keV) with $N_H = 8 \times 10^{21}$ cm^{-2}. However this galaxy is a well known type 1.9 LINER with broad Hα emission (Ho et al., 1997b) and it is one of the best known detections of a water megamaser (Wilson et al., 1995). At radio frequencies Ho and Ulvestad (2001) reported an inverted Spectrum in the compact nuclear source detected. Then it appears that this galaxy can be a very good candidate to a heavily obscured AGN. This could explain the fit at soft energies with a kT value typical of what it is found in some Seyfert 1 like objects (Teng et al., 2005) due to the presence of a warm absorber. Terashima et al. (2002) comment that the large EW (> 1.1 keV) of the FeKα) emission line detected in the *ASCA* data suggests that the nucleus is highly obscured.

NGC 2655 (UGC 4637, Arp 225). Arp 225 is an Sa galaxy which shows traces of a strong interaction or merger event (Mllenhoff and Heidt, 2001): faint outer stellar loops (see Appendix F, Fig. F.2) and extended HI-envelope (Huchtmeier and Richter, 1982). The X-ray *XMM-Newton* morphology of this galaxy shows a clear diffuse extended emission in the softer and harder bands that almost disappears in the medium band (1.0-2.0 keV) (see Fig. C.10). The bestfit model is ME2PL ($\Gamma = 2.48$, kT=0.64 keV, no absorption for the soft component and NH2 $= 3.0 \times 10^{23}$ cm^{-2}). Terashima et al. (2002) comment on the lack of a strong FeKα) fluorescent line in *ASCA* data, ruling out the possibility of "cold" reflection as the origin of the observed flat spectral slope. Ho et al. (1997b) report a questionable detection of a broad band Hα component in its optical spectrum. Moreover, core radio emission has been detected at a flux density of 1.1mJy and indications of polarized light in the nucleus pointing to their AGN nature (Nagar et al., 2000).

NGC 2681 (UGC 4645). A small companion at the same redshift, namely MCG09-15-039, appears in Appendix F, Fig. F.2. An unresolved nuclear source was clearly detected at hard X-ray energies (Fig. C.11). Satyapal et al. (2005), who made use of the same archival *Chandra* ACIS observations of this galaxy, classed them as an AGN-LINER, and derived Γ=1.57 and kT=0.73 keV for an apec plus power-law fit to the nuclear spectrum. These values are in perfect agreement, within the errors, with the parameters we derive for our best model (MEPL) (Γ=1.57 and kT=0.63 keV, see Table 3.9). Ho et al. (1997b) report several arguments for the reality of the broad Hα component derived from the profile fitting, whereas they indicate that the actual parameters of the broad Hα component are not well constrained.

NGC 2685 (UGC 4666, Arp 336). This is a rather isolated object (see Appendix F, Fig. F.2). We report a snapshot (0.86ksec) *XMM-Newton* observation. No nuclear point-like source is detected at hard X-ray, but only a very faint source at high energies (> 2 keV). A (2-10 keV) luminosity of 2.63×10^{39} erg s^{-1} has been estimated assuming a power law (Γ=1.8) and galactic column density, a factor of three lower than the value reported by Cappi et al. (2006), who analysed the same dataset. But

we would like to notice that, in addition to the low count rate in these data, these authors determine a highly unrealistic value for Γ= 0.5, what makes us confident in our results.

UGC 4881 (Arp 55). UGC 4881 is a member of an strongly interacting galaxy pair (see Appendix F, Fig. F.3). We present the analysis of 19 ksec *XMM-Newton* and 14.6 ksec *Chandra* observations. The X-ray morphology (see Fig. C.13) shows two peaks at soft X-rays with no point-like source at high energies (> 2 keV). The best fit for the *XMM-Newton* spectrum is obtained with a MEKAL model (kT=0.19 keV) with a resulting luminosity $L_X(2-10\,\mathrm{keV}) \simeq 10^{41}\,\mathrm{erg\,s^{-1}}$. These values could be uncertain since the two members of the pair are included in the *XMM-Newton* aperture (see Appendix F, Fig. F.3). Althought the low quality of the *Chandra* data does not allow any spectral fitting, we have estimated a very high luminosity of 2.7 $\times$ $10^{40}\mathrm{erg}^{-1}$.

3C 218 (Hydra A). 3C 218 is one of the most luminous radio sources in the local ($z < 0.1$) Universe, only surpassed by Cygnus A. It has been optically identified with the cD2 galaxy Hydra A (Simkin, 1979), which dominates the poor cluster Abell 780 (see Appendix F, Fig. F.3). Its X-ray morphology shows strong thermal emission (showing caves and bubbles) at the whole X-ray energy range, and a point-like source at the nuclear position on the hard band (> 2 keV). Sambruna et al. (2000) discovered with *Chandra* a LLAGN in the LINER harboured by this nearby cD galaxy. They reported the existence of a compact source at energies larger than 2 keV. Their best fit *Chandra* spectrum was found to be an obscured ($N_H = 2.8 \times 10^{22}\ \mathrm{cm}^{-2}$) power law with Γ=1.75 plus an unabsorbed Raymond-Smith with kT=1.05 with abundance 0.1 solar. Here we present *Chandra*/ACIS (80 ksec) and *XMM-Newton*/pn (24 ksec) data. The spectrum for *Chandra* data is fitted by a ME2PL model ($\Gamma = 2.1$ and kT = 1.71 keV) and the *XMM-Newton* data by a MEPL with $\Gamma = 2.2$ and kT = 2.77. It has to be noticed that we obtain a difference in luminosities of two orders of magnitude. This might be due to the large contribution of the diffuse thermal emission at hard X-rays from the cluster thermal emission. Previous studies conclude that both cooling flow and radio jet emission are important (Lane et al., 2004) and also thermal emission form supercavities/bubbles (Wise et al., 2007, based on 227 ksec *Chandra* observations).

NGC 2787 (UGC 4914). This a rather isolated object (see Appendix F, Fig. F.3). Snapshot *Chandra* data of this galaxy were reported by Ho et al. (2001), who estimated an X-ray luminosity of $2 \times 10^{41}\,\mathrm{erg\,s^{-1}}$ by assuming a power-law model with $\Gamma = 1.8$ and galactic column density. We report the analysis of 29.4 ksec *Chandra* and 33 ksec *XMM-Newton* observations. The *Chandra* data have been fitted to a PL model ($\Gamma = 2.3$) while *XMM-Newton* data is better modeled by a moderately obscured (NH2=1.0 $\times$ $10^{22}\mathrm{cm}^{-2}$) ME2PL model. The *Chandra* X-ray morphology

shows a point-like source coincident with the nucleus and an extranuclear source to its SE. Evidences on its AGN nature have been reported at other frequencies. Nagar et al. (2000) confirm its AGN nature at radiofrequencies, based on its flat radio spectrum between 20 and 6 cm. Ho et al. (1997b) reported a fairly prominent broad Hα component classifying it as a type 1.9 LINER. Tremaine et al. (2002) have estimated a mass for the central black hole of $4.1 \times 10^7 M_\odot$.

NGC 2841 (UGC 4966). This is a rather isolated object (see Appendix F, Fig. F.3). The *Chandra* X-ray morphology shows a number of point sources with diffuse emission, one of these coinciding with the nuclear position. We report here the analysis of both *Chandra* and *XMM-Newton* data. Snapshot *Chandra* data of this galaxy was reported previously by Ho et al. (2001). They estimated an X-ray luminosity of 1.81×10^{38} erg s^{-1} ergs/s by assuming a power law with Γ = 1.8 and galactic column density. Our estimated value for the *Chandra* data is a factor of 2 larger than this value. For the *XMM-Newton* spectrum we have obtained the best fit with a ME2PL model with $\Gamma = 2.20$ and kT= 0.58 keV. Ho et al. (1997b) estated that broad Hα emission is absent in this galaxy.

UGC 05101 (IRAS 09320+6134). A clearly perturbed morphology characterises this ultra-luminous infrared galaxy, with a long tail extending to the West (see Appendix F, Fig. F.3). In addition to the hard-band point-like nuclear source, extended emission is seen in both (4.5-8.0* keV) and (6-7 keV) bands in the image obtained from *Chandra* data (Fig. C.17). The evidence of a heavily obscured active galactic nucleus in this galaxy has been provided by Imanishi et al. (2001) and Imanishi et al. (2003), based in near-IR spectroscopy and on its *XMM-Newton* EPIC spectrum, respectively. They fit the spectrum with an absorbed power-law (Γ=1.8 fixed), a narrow Gaussian for the 6.4 keV Fe Kα emission line, which is clearly seen in their spectrum, and a 0.7 keV thermal component; they derive N_H=14×10^{23}cm^{-2} and EW(Fe Kα)=0.41 keV. The resulting (2-10 keV) luminosity ($\sim 5 \times 10^{42}$erg s^{-1}) is within a factor of 2-3 of the values we obtain both from *Chandra* and *XMM-Newton* data. Our best fit model for the spectra is that of a double power-law for *Chandra* data and a ME2PL for *XMM-Newton* data, with consistent spectral slopes for both sets of data. The use of a fixed power law slope of 1.8 to estimate the luminosity can explain the difference between the value we calculate from the spectral fitting and that estimated by Satyapal et al. (2004) for the same *Chandra* dataset. The type 1 AGN nature of the nucleus was already reported by Sanders et al. (1988). Farrah et al. (2003) found that this system is a composite object containing both starburst and AGN contributions, consistent with the result for its optical spectrum (Goncalves et al., 1999). New evidences come from radiofrequencies where it is found a compact nucleus with flat spectral shape (Baan and Klockner, 2006). The Fe-K emission is marginally detected in the analysis of *Chandra* data by Ptak et al. (2003). We have

measured an equivalent width of 278 for the FeKα line.

NGC 3185 (UGC 5554, HCG 44c). It makes up the compact group HCG 44, together with NGC 3193, NGC 3190 and NGC 3187 (see Appendix F, Fig. F.3). Cappi et al. (2006) report their analysis of the *XMM-Newton* available data for this galaxy, finding a very weak nuclear emission with an X-ray spectrum consistent with a power-law with Γ =2.1, which results in a luminosity of 10^{39} ergs/s, in very good agreement with the one we estimate here (see Table 3.27). Ho and Ulvestad (2001) reported this galaxy as marginally detected at 6 cm but not at 20 cm, using *VLA* 1" resolution data.

NGC 3226 (UGC 5617, Arp 94a). Strongly interacting with NGC 3227 (see Appendix F, Fig. F.4), several point sources have been detected at the (4-8) keV band image of this galaxy, with Fe emission unambiguously present in the nucleus. The analysis of HETGS *Chandra* data by George et al. (2001), whose properties strongly suggested that this galaxy hosted a central AGN, resulted in an adequate fit with a photon index Γ=1.94 and N_H=4.8 $\times$ 10^{21}cm^{-2}, with the resulting luminosity L(2-10 keV)$\approx$3.2$\times10^{40}$ erg s^{-1}. The *XMM-Newton* observations of this dwarf elliptical galaxy most probably indicate the presence of a sub-Eddington, super-massive black hole in a radiatively inefficient stage (Gondoin et al., 2004). They conclude that, since the best fit is provided by a bremsstrahlung model absorbed by neutral material, the X-ray emission may therefore be reminiscent of advection-dominated accretion flows. Nevertheless, an acceptable fit is also obtained by including a power-law model (Γ=1.96) absorbed by neutral (N_H=4.1$\times$ 10^{21}cm^{-2}) and ionized material. The resulting (2-10 keV) luminosity, calculated for the distance we use, is 1.8 $\times$ 10^{40} erg s^{-1}, a factor of 4 higher than the one we estimate.

Terashima and Wilson (2003) fit the 22 ksec *Chandra* ACIS nuclear spectrum with a power-law with Γ=2.21 (from 1.62 to 2.76) and N_H=0.93 $\times$ 10^{22}cm^{-2}. Notice that substantial absorption is also derived from the position of this galaxy in the color-color diagrams in GM+06, whereas the power-law index is somewhat steeper (see Table 2.6). We analyze 31 ksec *XMM-Newton* observations finding that the best fit is a combination of two power-laws ($\Gamma = 1.92$, $\mathsf{NH1} = 2.1 \times 10^{21}$ cm^{-2} and $\mathsf{NH2} = 1.2 \times 10^{22}$ cm^{-2}). This is a more complicated model than that proposed by Gondoin et al. (2004). A flat compact radio source has been detected at the nuclear region (Condon et al., 2002; Filho et al., 2006). Ho et al. (1997b) succeeded in extracting a moderately strong broad Hα component from a complicated, three narrow-line component blend.

NGC 3245 (UGC 5663). It forms a wide pair together with NGC 3245A (see Appendix F, Fig. F.4), with cz=1322 km/s. A nuclear source is detected in the (4.5-8.0* keV) band image from *Chandra* data. This agrees with the analysis by Filho et al. (2004) who already noticed a hard nuclear X-ray source coincident with the

optical nucleus. The luminosity they calculated with a fixed Γ=1.7 is in excellent agreement with our estimation. Filho et al. (2002) concluded that at radio frequencies the source could be consistent with a flat and compact spectrum. Wrobel and Heeschen (1991) found an unresolved 3.3 mJy core at 5 GHz, 5″ resolution.

NGC 3379 (UGC 5902, M 105), is the dominant elliptical galaxy in the nearby Leo Group (see Appendix F, Fig. F.4). David et al. (2005) published their study of its X-ray emission as traced by ACIS-S *Chandra* observations. That work is mainly devoted to the analysis of extra-nuclear X-ray sources and diffuse emission, and they derive a power-law index for the diffuse emission of 1.6-1.7, in agreement with the value reported by Georgantopoulos et al. (2002). David et al. (2005) do not fit the spectrum of the nuclear source (their source 1) due to the too low net counts in the S3 chip data for this object. This is also the reason for having neither a fit nor an estimation of the spectral parameters by GM+06. The X-ray image is used for the morphological classification (SB) and for estimating the (2-10 keV) luminosity (1.3×10^{38}erg s^{-1}).

NGC 3414 (UGC 5959, Arp 162). UGC 5959 is a peculiar galaxy, with two companions at very similar redshifts (NGC 3418 and UGC 5958) within 250 kpc (see Appendix F, Fig. F.4). The *Chandra* X-ray morphology shows a point-like source coincident with the optical nucleus. The best spectral fit to the *Chandra* data is a PL with $N_H = 2.1 \times 10^{21}$ cm^{-2} and $\Gamma = 2.0$, which provides a luminosity of $Lx = 9.7 \times 10^{40}$ erg s^{-1}. To our knowledge no previous X-ray data have been reported in the literature. Condon et al. (2002) suggested that the radio source is powered by an AGN. This has been later confirmed with the data reported by Nagar et al. (2005).

NGC 3507 (UGC 6123, KPG 263b). It makes up a wide isolated physical pair (number 263 in Karachentsev's catalogue of isolated pairs) together with NGC 3501 (see Appendix F, Fig. F.4). No hard nuclear point source has been detected in the *Chandra* images of this galaxy (Fig. C.22). The only previously published X-ray study is based on observations obtained with *ASCA*. Terashima et al. (2002) obtained a power-law to be the best model to fit the data, with Γ=1.71 and N_H<7.2 $\times 10^{20}$cm^{-2}. However, our best fit is MEKAL with kT=0.5 keV and absorption consistent with the galactic value. Our estimated luminosity amounts to $Lx = 1.6 \times 10^{37}$ erg s^{-1}, which seems to be much lower than the value reported by Terashima et al. (2002).

NGC 3607 (UGC 6297), is the brightest member of the Leo II group, which NGC 3608 and NGC 3605 also belong to (see Appendix F, Fig. F.4). No hard nuclear point source has been detected in the *Chandra* images of this galaxy (Fig. C.23). No spectral fitting can be made with the data. Based on observations obtained with *ASCA*, Terashima et al. (2002) find no clear evidence for the presence of an AGN in

this LINER, in agreement with our classification as a SB candidate.

NGC 3608 (UGC 6299), member of the Leo II group, it forms a non-interacting pair with NGC 3607 (see Appendix F, Fig. F.5). No hard nuclear point source has been detected in the *Chandra* images of this galaxy (Fig. C.24). The previous X-ray study of this galaxy is that by O'Sullivan et al. (2001), who present a catalogue of X-ray bolometric luminosities for 401 early-type galaxies obtained with *ROSAT* PSPC pointed observations. Adjusted to our adopted distance, this luminosity result to be 1.37×10^{40}erg s^{-1}, about 2 orders of magnitudes brighter than our estimation. However our results are in good agreement with the analysis reported by Flohic et al. (2006), maybe suggesting that O'Sullivan data correspond to extranuclear sources (see Fig. C.24).

NGC 3623 (Arp 317a, M 65). It makes up the Leo Triplet together with NGC 3628 and NGC 3627, with which it forms a non-interacting pair (see Appendix F, Fig. F.5). We report the results on the unique X-ray data provided by *XMM-Newton* observations, althought their quality does not allow a spectral analysis. We have estimated an X-ray luminosity of 2.4×10^{39} erg s^{-1} assuming a power law with spectral index Γ=1.8 and galactic column density. Satyapal et al. (2004) use 1.76 ksec *Chandra* observations to get a luminosity which is in good agreement with our determination. A black hole mass of 10^7 erg s^{-1} has been estimated by Dong and Robertis (2006).

NGC 3627 (UGC 6346, Arp 16, M 66, Arp 317b). It makes up the Leo Triplet together with NGC 3628 and NGC 3623, with which it forms a non-interacting pair (see Appendix F, Fig. F.5). Soft X-ray emission extends over about 2′ in a Northwest-Southeast direction, similar to the extent and orientation of the triple-radio source (Filho et al., 2004). No obvious nuclear X-ray source - hard or soft - was found on the available snapshot *Chandra* image (see Fig. C.26 and Ho et al., 2001). Panessa et al. (2006) noted that another source at 10″ is present in this image with similar flux than that of the nucleus, which probably contaminates other data with worse spatial resolution (see also Georgantopoulos et al., 2002). They derive an upper limit on the *Chandra* (2-10) keV luminosity of 7.6×10^{37}erg s^{-1} with a fixed Γ=1.8. Previous analyses of *ROSAT*, *ASCA* and *BeppoSAX* data resulted in a moderately absorbed power-law component with $\Gamma \approx$ 2-2.5 required to fit the spectra (Roberts and Warwick, 2000; Georgantopoulos et al., 2002; Dadina, 2007). The *XMM-Newton* data do not have enough count-rate for a spectral analysis to be perfomed. Our estimated luminosity assuming a power-law model with a fixed $\Gamma = 1.8$ and galactic absorption is 2.4×10^{39} erg s^{-1}, much larger than the value by Panessa et al. (2006). Its AGN nature was assessed by Filho et al. (2000) based in the compact nuclear source which appears to have a variable flat radio-spectrum.

NGC 3628 (UGC 6350, Arp 317c). It makes up the Leo Triplet together with

NGC 3623 and NGC 3627 (see Appendix F, Fig. F.5). The hard X-ray morphology provided by *Chandra* data shows an unresolved nuclear component that also appears in the Fe image (Fig. C.27). *Chandra* X-ray and ground-based optical Hα, arc-second resolution imaging is studied by Strickland et al. (2004), with the main aim of determining both spectral and spatial properties of the diffuse X-ray emission. They also show the total counts for the nuclear region (an extraction of 1 kpc radius around the dynamical center that, for this galaxy, corresponds to the central 20″), but no spectral fitting was attempted. Our morphological classification does not agree with that of Dudik et al. (2005), who have classified this galaxy as an object displaying no nuclear source according to its morphology in previous *Chandra* ACIS snapshot (1.8 ksec) data; this galaxy is taken as a LINER/transition object and an upper limit of 2.7×10^{37}erg s^{-1} (corrected to our adopted distance) is given for its (2-10 keV) nuclear luminosity, which is consistent with our result. Note that high absorption is derived from the position of this galaxy in the color-color diagrams by GM+06. Here we report 41.6 ksec observation of *XMM-Newton*/pn data. The best fit model is a single power-law ($\Gamma = 1.6$) with $N_H = 4.6 \times 10^{21}$ cm^{-2}. The X-ray luminosity with *XMM-Newton* data is two orders of magnitude brighter than that from *Chandra* data. This can be explained because there are three point-like sources close to the diffuse nucleus, which may be contributing to the *XMM-Newton* aperture. Another explanation could be the high level of variability detected in this galaxy (Roberts et al., 2001).

NGC 3690B (Arp 299, Mrk 171). This galaxy is strongly interacting, in a probable merger, with IC 694 (see Appendix F, Fig. F.5). X-ray emission from *Chandra* data has plenty of features, with a hard unresolved source clearly detected in the nuclear position, which is also seen in the 6-7 keV band (Fig. C.28). The EPIC-pn *XMM-Newton* spatially resolved data have clearly demonstrated the existence of an AGN in NGC 3690, for which a strong 6.4 keV line is detected, and suggested that the nucleus of its companion IC 694 might also host an AGN,[1] since a strong 6.7 keV Fe-Kα line is present (Ballo et al., 2004). *Chandra* and *XMM-Newton* data have been fitted to ME2PL and MEPL, respectively, with ($\Gamma = 3.5$) and kT=0.19 for *Chandra* and ($\Gamma = 1.84$) and kT=0.63 for *XMM-Newton*. The *XMM-Newton* X-ray luminosity results to be almost one order of magnitude brighter than that from *Chandra*. This can be understood due to the inclusion of the companion galaxy NGC 3690A in the *XMM-Newton* extraction. Condon and Broderick (1991) suggested an AGN nature of this source because of its compact flat radio-spectrum.

NGC 3898 (UGC 6787). This object is a member of the cluster of galaxies Abell 1377 (see Appendix F, Fig. F.5). There are not previous reported results on X-ray

[1] However, both galaxies are found in the comparative sample of starburst galaxies in Satyapal et al. (2004)

data for this object in the literature. Here we analyze the available *Chandra* data and find MEPL to be the best fit model ($\Gamma = 1.8$, kT=0.04 keV, $\mathsf{NH1} = 1.4 \times 10^{22} \mathsf{cm}^{-2}$ and $\mathsf{NH2} < 6 \times 10^{21} \mathsf{cm}^{-2}$) to describe the X-ray spectral energy distribution. The X-ray morphology shows a point-like source only at soft energies, questioning its AGN nature. Thus, we have classified this object as SB-like object. Ho et al. (1997b) adopted the conservative assumption that broad Hα is not present due to the ambiguity of its detection, but they claim that it would be highly desirable to verify this with data of higher S/N.

NGC 3945 (UGC 6860). This is a rather isolated object (see Appendix F, Fig. F.6). We have detected a nuclear unresolved source at hard energies with *Chandra* data (Fig. C.30), leading to an AGN-like classification. At softer energies (0.4-1 keV) it shows a ring like or arm like structure of diffuse extended emission. The spectral analysis of the nucleus gives as best fit model a single PL with $\Gamma = 2.6$ and column density consistent with the galactic value. There are not previous reported X-ray data in the literature for this object. Nagar et al. (2005) detect a compact continuum radiosource.

NGC 3998 (UGC 6946). Five galaxies (NGC 3990, NGC 3977, NGC 3972, NGC 3982 and UGC 6919) are seen within 250 kpc (see Appendix F, Fig. F.6), all but one at cz compatible with sharing the same physical association. The AGN nature of this galaxy was assed by Ho et al. (1997b) based on the clear detection of a broad Hα line, the detection of a variable radio core (Filho et al., 2002) and a 20% UV flux variation reported by Maoz et al. (2005). Ptak et al. (2004) published the analysis of the same 10 ks *XMM-Newton* data on this LINER galaxy. They fitted the X-ray spectrum with a simple-absorber power-law with Γ=1.88, $\mathsf{N_H} = 3.3 \times 10^{20}$ cm^{-2} and obtained an observed flux F(2-10 keV) = 1.1 $\times 10^{-11}$ cm^{-2} s^{-1}, already in agreement with previously published data from *BeppoSAX* (Pellegrini et al., 2000; Georgantopoulos et al., 2002; Dadina, 2007) and *ASCA* (Terashima et al., 2000, 2002). Our spectral fitting for *XMM-Newton* data results in a single PL with spectral index Γ=1.87 at $\mathsf{N_H} = 2.0 \times 10^{20}$ cm^{-2}. However, the fitting to the *Chandra* spectrum is improved when using a model with two power-laws and a thermal contribution (see Tables 3.9 and 3.19). Both sets of data gives the same value for the X-ray luminosity. A *BeppoSAX* observation (Pellegrini et al., 2000) showed that the Fe Kα line was not detected to an EW upper limit of 40 eV. Nevertheless, in the *ASCA* spectrum by Terashima et al. (2002) an Fe Kα line is marginally detected at 6.4 keV.

NGC 4036 (UGC 7005). It forms a wide pair (see Appendix F, Fig. F.6) together with NGC 4041 (cz=1234 km/s). The *Chandra* images show a point-like source within diffuse emission extending less than 5″ (Fig. C.32). Also several knotty regions are present within 20″ radius. We estimate $\mathsf{Lx}(2-10\ \mathsf{keV}) = 1 \times 10^{39}$ erg s^{-1} by assuming a single PL model with ($\Gamma = 1.8$ fixed) and galactic absorption. Its AGN nature

is also confirmed by the optical data, since Ho et al. (1997b) reported a faint, broad Hα line.

NGC 4111 (UGC 7103). At least four galaxies are found within 250 kpc (see Appendix F, Fig. F.6) with redshifts from 600 to 900 km/s. A hard nuclear point source has been detected for this galaxy (Fig. C.33). A previous X-ray spectral analysis was based in *ASCA* data by Terashima et al. (2000) (see also Terashima et al., 2002) who could not fit the spectrum with a single-component model, but instead they required a combination of a power-law together with a Raymond-Smith plasma, with Γ=0.9, kT=0.65 keV and $N_H = 1.4 \times 10^{20}$ cm^{-2}. These parameters agree with those estimated from its position in the color-color diagrams by GM+06. We have fitted the *Chandra* spectrum with ME2PL ($\Gamma = 3.0$, kT=0.66 keV, $NH1 = 4.7 \times 10^{21}$ cm^{-2} and $NH2 = 3.8 \times 10^{22}$ cm^{-2}) which leads to an estimated hard luminosity of 2.5 $\times 10^{40}$erg s^{-1}, a factor of 3 brighter than Terashima et al.'s estimation. The agreement is remarkably good taking into account the different instruments used and the different models assumed for the spectral fitting.

NGC 4125 (UGC 7118). It forms a pair with NGC 4121, at 3.6 arcmin (see Appendix F, Fig. F.6) and less than 60 km/s in cz. Figure C.34 shows the presence of a nuclear hard point-like source. The best fit that Georgantopoulos et al. (2002) obtained for the central 2′ *BeppoSAX* spectrum is provided by an absorbed power-law with Γ=2.52 and N_H=3$\times$ 10^{22}cm^{-2}, that resulted in L(2-10 keV)=0.68$\times$ 10^{40} erg s^{-1}. Based on the same *Chandra* ACIS dataset, Satyapal et al. (2004) class this galaxy among those revealing a hard nuclear source embedded in soft diffuse emission. They estimate the luminosity by assuming an intrinsic power-law slope of 1.8, which results in L(2-10 keV)=7.3$\times$ 10^{38} erg s^{-1}, in very good agreement with the value estimated by GM+06. We provide here a new fit to the *Chandra* data, with a best-fit MEPL ($\Gamma = 2.32$ and kT=0.57 keV). The 35.3 ksec *XMM-Newton* data are reproduced by an unabsorbed MEPL ($\Gamma = 2.36$ and kT=0.54 keV). The much larger luminosity for *Chandra* data are difficult to understand but it may be attributed to the difference in the column density between both sets of data. In principle a larger luminosity should be expected for *XMM-Newton* data since in addition to the nucleus, an ULX to the NE is included in this extraction aperture.

IRAS 12112+0305. This merging system (see Appendix F, Fig. F.6) contains two separate nuclei with a pair of tidal tails (Scoville et al., 2000). Very faint extended X-ray emission has been detected in this Ultraluminous Infrared Galaxy with no evidence of unresolved hard nuclear emission. Franceschini et al. (2003) presented *XMM-Newton* first results for this galaxy and made a formal fitting to the spectrum with MEPL in spite of the low count-rate of the data. We have not tried any spectral fitting and estimated an X-ray luminosity L(2-10 keV)=1.5$\times$ 10^{41} erg s^{-1}, which is in very well agreement with Franceschini et al.'s value. Condon and Broderick (1991)

detect a compact radio core with a flat continuum.

NGC 4261 (UGC 7360, 3C 270). NGC 4261 is the main galaxy in a group of 33 galaxies (Nolthenius, 1993) in the Virgo West cloud (see Appendix F, Fig. F.7). Noel-Storr et al. (2003) pointed out this galaxy to host a nuclear dust disk together with a twin radio jet morphology in the *VLA* and VLBI images. The nuclear hard band emission of this galaxy is clearly unresolved both in the (4.5-8.0* keV) and 6-7 keV bands (Fig. C.36). The various features seen at soft energies (Fig. C.36) were already shown by Donato et al. (2004), who analysed its *Chandra* ACIS data for the core component (core radius of 0.98″); they fit it with a PL+apec model with Γ=1.09, kT=0.60 keV, and a high column density N_H=7.0$\times$ 10^{22}cm^{-2}, reported to be the largest intrinsic column density among the 25 radio galaxies in their study. These parameters agree with those obtained by Rinn et al. (2005) and Satyapal et al. (2005) for the same data. Zezas et al. (2005) published the analysis of the same 35ks *Chandra* ACIS-S observations we use here. They reported a point-like emission above 4.0 keV and the evidence for an X-ray jet component down to arc-second scales from the nucleus (barely visible in our Fig. C.36). A three-component model was given as the best fit for the X-ray spectrum of the nuclear 2″: a heavily obscured flat power-law (Γ=1.54 and N_H=8.4$\times$ 10^{22}cm^{-2}), a less absorbed steeper power-law (Γ=2.25 and $N_H < 3.7\times 10^{20}$cm^{-2}), and a thermal component (kT=0.50 keV), which resulted in L(2-10 keV)=10.8$\times$ 10^{40} erg s^{-1}, in agreement with our results. They reported an equally good fit with a single power-law (Γ=1.37) seen through a partially covering absorber (N_H=7.7$\times$ 10^{22}cm^{-2}, f_{cov}=0.92) plus a thermal component. GM+06 did not include this object in the subsample with spectral fits due to its complexity which gave as unexpected parameters with any of the five models we tested. We provide here an acceptable fit by using ME2PL.

Sambruna et al. (2003) published its nuclear EPIC-pn *XMM-Newton* spectrum (the central 10″), which was best-fitted with a two-component model with a power law (Γ=1.4) absorbed by a column density of $N_H \approx 4\times 10^{22}$cm^{-2} plus a thermal component with kT$\approx$0.7 keV (in agreement with *Chandra* spectral results by Gliozzi et al. (2003) and Chiaberge et al. (2003)); an unresolved FeK emission line with EW $\approx$ 0.28 keV was detected at $\sim$7 keV. They also reported short-term flux variability from the nucleus (timescale of 3-5 ks), which they argued as being originated in the inner jet. We analyse 27 ksec *XMM-Newton* data finding that the bestfit is ME2PL (Γ=2.38, kT=0.62 keV, $\mathsf{NH1} = 2.2 \times 10^{21}$ cm^{-2} and $\mathsf{NH2} = 1.4 \times 10^{23}$ cm^{-2}), which is a more complicated model than Sambruna et al. (2003) proposed, with a temperature compatible with theirs but a higher value for the spectral index. Our best fit to the *XMM-Newton* spectrum agrees with that obtained for *Chandra* data with consistent parameters. The reported luminosity is also consistent ($\mathsf{Lx}(2-10\ \mathsf{keV}) = 1.3$ and 1.5×10^{41} erg s^{-1}, respectively). No obvious signs of broad Hα have been reported

in optical spectroscopic data either from the ground (Ho et al., 1997b) or from small-aperture (0.1″) HST spectra (Ferrarese et al., 1996).

NGC 4278 (M 98). It is a member of a group together with NGC 4314, with 3 of its members visible in Appendix F, Fig. F.7. Ho et al. (2001) used snapshot (1.43 ksec) *Chandra* data to class the X-ray morphology of this galaxy as type I, i.e. dominated by a nuclear source (see also Dudik et al., 2005). The same dataset is used by Terashima and Wilson (2003) who, in addition to the unresolved nucleus, report the presence of a faint elongated structure about 50″ long along PA ≈ 70 in the (0.5-2 keV) band. Their best spectral fitting corresponds to an unabsorbed power-law with Γ= 1.64, after the correction of a slight pile-up effect. They also reported flux variability from the comparison between *Chandra* and previous *ASCA* data. We fitted the same ≈ 100 ksec dataset with ME2PL ($\Gamma = 2.37$, kT=0.57 keV). The best fit model we derive for the 30.5 ksec *XMM-Newton* data 2PL ($\Gamma = 2.3$, $\mathsf{NH1} = 6 \times 10^{20}$ cm^{-2}, $\mathsf{NH2} = 7.2 \times 10^{22}$ cm^{-2}). An equally good fit is obtained with MEPL with $\Gamma = 1.99$, kT=0.65 keV, $\mathsf{NH1} = 3.9 \times 10^{21}$ cm^{-2}, $\mathsf{NH2} = 1.0 \times 10^{20}$ cm^{-2} The estimated *XMM-Newton* hard X-ray luminosity is a factor of 10 brighter than that from *Chandra* data This difference can be in part explained as due to the contamination by a number of point-like sources around the AGN that can be seen on *Chandra* X-ray image (Fig. C.36 and Tab. 3.23). The AGN nature of this source was well known since earlies 80's when Jones (1984) observed this object using VLBI and found that the core flux density is 180 and 190 mJy at 18 and 6 cm, on size scales less than 5 and less than 1 mas, respectively. Later on, Ho et al. (1997b) classified it as a type 1.9 LINER based on the broad component detected in the Hα line. Nagar et al. (2005) have detected a radiojet at 2cm.

NGC 4314 (UGC 7443). It is a member of a group together with NGC 4278, wich can be seen in the SW corner in Appendix F, Fig. F.7. No nuclear source has been detected in the hard X-ray band images from *Chandra* data (Fig. C.38). Satyapal et al. (2004) used the same *Chandra* ACIS dataset to classify this galaxy among those exhibiting multiple, hard off-nuclear point sources of comparable brightness to the nuclear source. With an assumed power-law index of 1.8, the corresponding luminosity, corrected to our adopted distance, results in L(2-10 keV)=8$\times$ 10^{37} erg s^{-1}, in excellent agreement with the one that was estimated by GM+06. We report here the analysis of the 22 ksec *XMM-Newton* data. We have found that the X-ray spectral distribution can be best fitted by MEPL ($\Gamma = 1.5$, kT=0.24 keV, $\mathsf{N_H} = 2.7 \times 10^{21}$ cm^{-2}).

NGC 4321 (UGC 7450, M 100). NGC 4321 is a well-studied, grand design spiral galaxy, located in the Virgo Cluster (see Appendix F, Fig. F.7). Based on snapshot imaging data, Ho and Ulvestad (2001) classed its *Chandra* X-ray morphology as type I, i.e., with a dominant nuclear source at variance with our results as an SB candi-

date. Roberts et al. (2001) analysed previous *ASCA* data and derived a best model for the spectral fitting with an absorbed power-law (N_H=0.2$\times 10^{22}$cm^{-2} and Γ=1.9) and a MEKAL (kT=0.67 keV) components; these parameters are far from the range we have derived from the analysis of the available *XMM-Newton* and *Chandra* data, which agree perfectly well. No evidence for an AGN is found at radio frequencies. Filho et al. (2000, 2006) found a resolved extended source at 6cm.

NGC 4374 (UGC 7494, 3C 272.1, M 84). NGC 4374 is one of the brightest giant elliptical galaxies in the center of the Virgo cluster (see Appendix F, Fig. F.7). It shows strong radio emission and a two-sided jet emerging from its compact core (Xu et al., 2000). Bower et al. (1998) find a black hole mass of (0.9-2.6) $\times$ 10^9 $M_\odot$ from velocities measured in the central emission-gas disk. An unresolved nuclear source is detected both in (4.5-8.0* keV) and 6-7 keV band images from *Chandra* data (Fig. C.40). Satyapal et al. (2004) have already described the X-ray morphology traced by the same *Chandra* ACIS dataset of this galaxy as revealing a hard nuclear source embedded in soft diffuse emission. The *Chandra* ACIS-S data are also analysed by Finoguenov and Jones (2001)[2]; they report a remarkable interaction of the radio lobes and the diffuse X-ray emission, and provide the parameters for a fit with an absorbed (N_H=2.7$\times$ 10^{21}cm^{-2}) power law (Γ=2.3) and the corresponding L(0.5-10 keV)=4.7$\times$ 10^{39} erg s^{-1}, all in very good agreement with the ones we give in GM+06. These values somewhat differ from those obtained from the *ASCA* spectrum (Terashima et al., 2002), most probably due to the different spatial resolutions.

NGC 4410A (UGC 7535, Mrk 1325). NGC 4410A is a member of a compact group of galaxies (see Appendix F, Fig. F.7), being NGC 4410A associated with the *VLA* radio source (Hummel et al., 1986). Both (4.5-8* keV) and 6-7 keV band images show the unresolved nature of the nuclear source at these energies (Fig. C.41). The same ACIS-S *Chandra* observations we use for the NGC 4410 group are presented in Smith et al. (2003), who obtained an adequate fit for the spectrum of the inner 1″ with a power law with $\Gamma\approx$2 and a fixed N_H=5$\times$ 10^{20}cm^{-2}, in agreement with a previous analysis of *ROSAT* X-ray observations (Tschoke et al., 1999). The best fit model by GM+06 only needs the inclusion of a power law with Γ=1.75 (consistent with theirs within the errors). The reanalysis of *Chandra* data results in a best fit model MEPL with Γ = 1.77, kT=0.30 keV and N_H1=5.1$\times$ 10^{21}cm^{-2} and no absorption for the hard component. This fit agrees with the reported by GM+06. AGN nature of this object was obtained throught the detection of a rather broad Hα component by Donahue et al. (2002).

NGC 4438 (UGC 7574, Arp 120b). This galaxy is in a pair with NGC 4435 (see

[2]See also Kataoka and Stawarz (2005) for the analysis of the two extra-nuclear knots.

Appendix F, Fig. F.8) in the Virgo cluster (Rauscher, 1995). Ho et al. (1997a) reported this galaxy as that with the weakest broad Hα nucleus. The results from 25 ks *Chandra* ACIS-S observations of this galaxy are also presented in Machacek et al. (2004), who suggest the presence of an AGN, based on the steep spectral index and the location of the hard emission at the center of the galaxy, in contrast to our morphological classification. The spectrum of the central 5″ is claimed to be best-fitted by a combination of an absorbed power law (with N_H=2.9$\times 10^{22}$cm^{-2} and a fixed Γ=2.0) and a MEKAL with kT=0.58 keV thermal component, providing L(2-10 keV)=2.5$\times$ 10^{39} erg s^{-1}. Nevertheless, Satyapal et al. (2005) class this galaxy as a non AGN-LINER based on the same ACIS *Chandra* dataset, in agreement with GM+06 classification. The new fit for *Chandra* data results in MEPL with kT=0.52 keV, Γ=1.91 and N_H=3.7$\times$ 10^{21}cm^{-2}, wich is consistent, within the errors, with that provided by GM+06.

NGC 4457 (UGC 7609). This is a rather isolated object in the Virgo Cluster , with an unphysical companion within 250 kpc (UGC 7644 at cz=4222 km/s). Unresolved hard X-ray emission is seen in the nucleus on this galaxy (Fig. C.43). The spectral analysis of the same ACIS *Chandra* data by Satyapal et al. (2005) gives Γ=1.57, kT=0.69 keV, and no additional absorption, in very good agreement with GM+06 results. The best fit model reported here is also MEPL, with compatible parameters but with a larger column density, $NH1 = 3.7 \times 10^{21}$ cm^{-2}.

NGC 4459 (UGC 7614). With NGC 4468 at 8.5 arcmin and NGC 4474 at 13.5 arcmin to the E-NE, NGC 4477 and NGC 4479 are the two similar-sized galaxies to the SE within 250kpc (see Appendix F, Fig. F.8) close in redshift. GM+06 morphologically classified this galaxy as a SB candidate (see Fig. C.44), in agreement with Satyapal et al. (2005) who, also based on these ACIS *Chandra* data, gave no additional X-ray information on this object. A mass of $M_{BH} = 7 \times 10^7 M_\odot$ has been reported for its nuclear black hole (Tremaine et al., 2002, based on Space Telescope Imaging Spectrograph (STIS) measurements of ionized-gas disks by Sarzi et al. (2001)) .

NGC 4486 (UGC 7654, Virgo A, Arp 152, 3C 274, M 87). This well known giant elliptical galaxy located at the center of the Virgo cluster (see Appendix F, Fig. F.8), hosts a very strong central radio source and a synchrotron jet which is visible from radio to X-ray wavelengths (Marshall et al., 2002). Both the unresolved nuclear emission and the jet-like feature extending $\sim$15″ to the W-NW, in the direction of the optical jet, are seen in Fig. C.45. Deep 500 ksec *Chandra* observations of this galaxy are shown in Forman et al. (2005), where the same salient features present in our Fig. C.45 can be seen, with X-ray jets clearly detected, but unfortunately no spectral analysis is made. Donato et al. (2004) analyse both *Chandra* and *XMM-Newton* data providing a radius for the core of 0.22″. Dudik et al. (2005), based on 38 ksec *Chandra* observations, classed it among objects exhibiting a dominant hard nuclear point source and estimated its luminosity as L(2-10 keV)=3.3$\times$ 10^{40} erg s^{-1} with a

fixed Γ=1.8 power law, in good agreement with the one estimated by GM+06 with the same dataset. Here we use a much longer exposure time dataset (≈ 100 ksec) and improve the fitting by ME2PL ($\Gamma = 2.4$, kT= 0.82, $\mathsf{NH1} = 1.0 \times 10^{21}$ cm^{-2} and $\mathsf{NH2} = 3.96 \times 10^{22}$ cm^{-2}), what results in a luminosity of 7.2×10^{41} erg s^{-1}, 20 times lager than the value obtained by Forman et al. (2005). The spectrum extracted from a 19 ksec *XMM-Newton* observation suffers from strong pile-up effects, so the resulting parameters will not be discussed any further. Noel-Storr et al. (2003) found by using optical spectroscopic STIS data that a broad component is needed to fit the spectrum. A black hole of mass $M_{BH} \approx 2.6{\times}10^9$ M$\odot$ is found by Lauer et al. (1992). The active nucleus in M87 emits a nonstellar continuum, which is found to vary in strength over time in UV (Perlman et al., 2003; Maoz et al., 2005), optical (Tsvetanov et al., 1998) and X-rays (Harris et al., 1997).

NGC 4494 (UGC 7662). This elliptical galaxy is located in the Coma I cloud (see Appendix F, Fig. F.8). Hard nuclear emission from *Chandra* data is point-like (Fig. C.46). The *XMM-Newton* EPIC spectrum extracted from a 45″ region has been published by O'Sullivan and Ponman (2004). A MEPL model results in their best model for the spectral fitting, for which they get Γ=1.5 (consistent with GM+06 value) but for hydrogen column density fixed at the Galactic value (N_H=1.56$\times$ 10^{20}cm^{-2}) and kT=0.25 keV. Dudik et al. (2005) classed it as a hard nuclear point-dominated source and estimated L(2-10 keV)=7.2$\times$ 10^{38} erg s^{-1} with a fixed Γ=1.8 power law, about a factor of 6 fainter than the one GM+06 calculated with the spectral fitting. The new fitted model agrees with that reported in GM+06. We have also analised the 24.5 ksec *XMM-Newton* observation, obtaining a single PL as bestfit model with a spectral index consistent with *Chandra* spectral index and absorption consistent with galactic absorption.

NGC 4552 (UGC 7760, M 89). This Virgo elliptical galaxy (see Appendix F, Fig. F.8) has no detected broad band Hα component (Cappellari et al., 1999); its nuclear source shows long-term variability at UV wavelengths (Cappellari et al., 1999; Maoz et al., 2005) and a radio jet with VLBI observations (Nagar et al., 2005). This galaxy shows an unresolved source in the hard X-rays band over an extended nebulosity with the peak of emission coincident with the galaxy center determined from 2MASS data (Fig. C.47). Xu et al. (2005) found from *Chandra* ACIS-S data that the central source is the brightest in the field and that it coincides with the optical/IR/radio center of the galaxy within 0.5″. The X-ray-identified source is compact and variable on short time scales of 1 h. Their best-fitted model of the source is consistent with an absorbed power-law with spectral index Γ=2.24, in rather good agreement with the *ASCA* data reported by Colbert and Mushotzky (1999). The inferred luminosity in the 2-10 keV is 4×10^{39} erg s^{-1}, consistent with our result (2.6$\times$ 10^{39}erg s^{-1}). Their main conclusion based on the variability, the spectral analysis,

and multi-wavelength data is that the central source is more likely a low-luminosity AGN than contribution from LMXBs (Low Mass X-ray Binaries). GM+06 best-fit parameters are consistent with a model of a power law (Γ=1.81) plus a thermal RS (kT= 0.83 keV), in much better agreement with the results by Filho et al. (2004) on the analysis of *Chandra* archival data, with Γ=1.51 and kT=0.95. The new *Chandra* spectral analysis is consistent with those obtained before. We also report 32 ksec *XMM-Newton* observation. The bestfit model and parameters agree with these obtained with *Chandra* data. However the X-ray luminosity is a factor of 10 larger than *Chandra* data ($\mathrm{Lx}(2-10\ \mathrm{keV}) = 1\times10^{40}\ \mathrm{erg\ s^{-1}}$). This difference can be easily explained by the contribution of point-like sources within the *XMM-Newton* extraction region that can be seen in the hard X-ray image (see Fig. C.47 and Table 3.23).

NGC 4589 (UGC 7797). It is part of a small group (Wiklind et al. 1995), from wich NGC 4648 and NGC 4572 are visible in Appendix F, Fig. F.9. Roberts et al. (1991) already reported it as a faint X-ray source. We present here the new 54 ksec *Chandra* data for this galaxy, which allow to derive a luminosity $\mathrm{Lx}(2-10\ \mathrm{keV}) = 7.9\times10^{38}\ \mathrm{erg\ s^{-1}}$). We cannot perform a proper spectral fitting due to the low count rate. The X-ray morphology shows a diffuse emission without any point-like source at hard energies ($>$ 2keV). However a radio jet has been reported by Nagar et al. (2005), pointing to its AGN nature.

NGC 4579 (UGC 7796, M 58). Another galaxy (NGC 4564) lies in the field within 250 kpc (see Appendix F, Fig. F.9, SW corner), which is close in redshift (cz=1142 km/s). NGC 4579 shows a compact nuclear source sitting in a diffuse halo (Fig. C.49), as already reported by Ho and Ulvestad (2001). Eracleous et al. (2002) fitted the compact unresolved central source detected in *Chandra* X-ray data, coincident with the broad-line region detected in UV by Barth et al. (2002), with a simple power-law spectra with Γ=1.88, which gives an estimated luminosity of 1.7×10^{41}erg s^{-1}. Dewangan et al. (2004) presented *XMM-Newton* data to search for the presence of an FeKα line. The best-fit spectrum is rather complex: an absorbed power-law with Γ=1.77 plus a narrow Gaussian at 6.4 keV and a broad Gaussian at 6.79 keV with FWHM $\sim$ 20.000 km s^{-1}. This broad component is interpreted as arising from the inner accretion disk. The estimated luminosity amounts to 1.2×10^{40}erg s^{-1}, lower than both Eracleous's estimation and GM+06 (1.4×10^{41}erg s^{-1}). We have made a new analysis on both 30 ksec *Chandra* and 19.6 ksec *XMM-Newton* data. The spectrum extracted from *XMM-Newton* observations suffers from strong pile-up effects, so the resulting parameters will not be discussed any further. The fitting to *Chandra* data gives MEPL with $\Gamma = 1.58$, kT=0.20 keV and column densities for the soft and hard frequencies $\mathrm{N_H} = 5\times10^{21}\ \mathrm{cm^{-2}}$. The derived X-ray luminosity is $\sim 10^{41}\ \mathrm{erg\ s^{-1}}$, consistent with those by Barth et al. (2002) and GM+06. The AGN

nature of this LINER is confirmed by the detection of broad wings in the Hα line Stauffer (1982); Keel (1983); Filippenko and Sargent (1985); Ho et al. (1997b) along with broad lines in the UV (Maoz et al., 1998), large UV variability (Barth et al., 1996; Maoz et al., 1998, 2005) and a flat-spectrum radio core (Hummel et al., 1987; Nagar et al., 2005).

NGC 4596 (UGC 7828). It forms a wide pair (see Appendix F, Fig. F.9) together with NGC 4608 (cz=1864 km/s). This galaxy is very faint at X-ray frequencies, showing diffuse X-ray morphology, from a *Chandra* observation, in all the spectral bands (Fig. C.50). In fact, information on its spectral properties could not be obtained based on the present data due to the lack of sufficient counts in the hard band (4.5-8.0* keV). No previous X-ray data have been reported for this galaxy. A black hole mass of 7.8$\times$ 10^7 $M_\odot$ is calculated by Tremaine et al. (2002) based on Space Telescope Imaging Spectrograph (STIS) measurements of ionized-gas disks by Sarzi et al. (2001).

NGC 4594 (M 104, Sombrero Galaxy). The famous galaxy NGC 4594, with no evidence of a similar size galaxy within 250 kpc (see Appendix F, Fig. F.9), was one of the earliest galaxies to show evidences for the possible presence of a central supermassive (up to 10^9 $M_\odot$) black hole (Kormendy, 1988). Its nucleus shows large short-term variability in the UV (Maoz et al., 2005) and show a radio compact core Its X-ray morphology shows a compact unresolved nuclear source on top of a diffuse halo (Fig. C.51). Dudik et al. (2005) used the classification by Ho and Ulvestad (2001) based on snapshot *Chandra* observations ($<$ 2 ksec), that classed it with the objects that exhibit a dominant hard nuclear point source. We have made for the *Chandra* spectrum a new analysis and found a best fit model consistent with a single PL ($\Gamma = 1.56$ with $N_H = 1.9 \times 10^{21}$ cm^{-2}). This is in close agreement, within the errors, with the spectral fitting values provided by GM+06 ($\Gamma = 1.41$ with $N_H = 2.0 \times 10^{21}$ cm^{-2}). We also present here the 15.8 ksec *XMM-Newton* spectrum, which is better modelled with ME2PL ($\Gamma = 2.05$, $N_H = 6.4 \times 10^{21}$ cm^{-2} and kT = 0.69 keV). Pellegrini et al. (2003) presented a spectral analysis based on 40 ksec *XMM-Newton* of the 7″ central nuclear source, which they derive to be consistent with an absorbed power law with Γ=1.88 and a column density of N_H=1.8$\times$ 10^{21}cm^{-2}. The value of our estimated 2-10 keV luminosity, 1.6$\times$ 10^{40} erg s^{-1}, agrees fairly well with that reported by Pellegrini from *XMM-Newton*. The *XMM-Newton* computed hard X-ray luminosity is a factor of 1.7 higher than that obtained from *Chandra* data. The morphology of hard X-rays and the larger extraction aperture of *XMM-Newton* data cannot explain this difference.

NGC 4636 (UGC 7878). It belongs to a galaxy group Mahtessian (number 98j in 1998), but it shows no companion within 250 kpc (see Appendix F, Fig. F.9). This galaxy does not show emission at high energies (Fig. C.52), althought a moderately

strong broad component at Hα was detected by Ho et al. (1997b) in the starlight-subtracted optical spectrum. *Chandra* data do not have high enough quality to allow a proper fitting to the spectrum. The difference in our estimation of the X-ray luminosity (1.77×10^{39}erg s^{-1}) and the value reported by Loewenstein et al. (2001) for the nucleus (2×10^{38}erg s^{-1}) is due to the different apertures used, 13″ and 3″, respectively. Xu et al. (2002) and O'Sullivan et al. (2005) presented *XMM-Newton* data for this source and find that it can be consistent with thermal plasma with a temperature kT between 0.53 and 0.71 keV. We present the 16.4 ksec *XMM-Newton* observation. The extracted nuclear spectrum is better modelled with MEPL ($\Gamma = 2.9$ and kT=0.54 keV) with no additional absorption. The arm-like structure reported by Jones et al. (2002) at soft energies can be produced by shocks driven by symmetric off-center outbursts, preventing the deposition of gas in the center. O'Sullivan et al. (2005) suggest that the X-ray morphology can be the result of a past AGN that is quiescent at the present. There is a two orders of magnitude difference in the luminosities obtained with *XMM-Newton* data compared to *Chandra* data, which can be attributed to the diffuse emission at hard X-rays shown in *Chandra* images (see Fig. C.52).

NGC 4676A and B (Arp 242, The Mice Galaxy). These two galaxies are the members of the well known interacting pair named "The Mice" (Arp 242, see Appendix F, Figs. F.9 and F.10). No high energy X-rays emission is detected (Fig. C.53) for component A, but it is present for component B (Fig. C.54). Read (2003) presented the first *Chandra* analysis of the Mice Galaxy and found a compact source in component B with a rather diffuse emission in A. Their spectral fitting in B is both consistent with MEKAL and power law models. We did not perform any fitting due to poor counting statistics. From the color-color diagrams and based on the same dataset, GM+06 concluded that the spectrum for component A is consistent with a power law with a spectral index in the range 0.8-1.2. GM+06 did not make any estimation for component B since the errors in the count-rate for the hardest band is greater than 80%. GM+06 estimated the luminosities for both components which agree remarkably well with the results by Read (2003), who explain the X-ray emission as produced by starbursts in both components. Our new estimation is also in agreement with these previously published values.

NGC 4698 (UGC 7970). This seems to be a rather isolated object, since no companion is visible within 250 kpc (see Appendix F, Fig. F.10). This galaxy shows a very faint, high-energy X-ray emission from its central region. The largest extension is found at intermediate energies, between 1 and 4 keV (Fig. C.55). Georgantopoulos and Zezas (2003) made a careful analysis of the *Chandra* data on this source and found that the X-ray nuclear position coincides with the faint radio source reported by Ho and Ulvestad (2001). They find that the best-fit model consists of an absorbed

power law with Γ=2.18 and column density of N_H=5 $\times$ 10^{20}cm^{-2}, which gives a a nuclear luminosity of 10^{39}erg s^{-1}. GM+06 found, from the color-color diagrams obtained from the same *Chandra* data, that they may be well reproduced by a combined model with a power law with Γ=[1.2-1.6] and a thermal component with kT=[0.7-0.8] keV, what results in a luminosity fainter by a factor of two than that estimated by Georgantopoulos and Zezas (2003). Cappi et al. (2006) fit its *XMM-Newton* spectrum with a single power law model with Γ=2.0 and get L(2-10 keV)=1.6$\times$ 10^{39}erg s $^{-1}$, a factor of 3 brighter than our determination from *Chandra* data. Our *XMM-Newton* (2-10 keV) luminosity is consistent with the result reported by Cappi et al. (2006). The discrepancies between both measurements can be explained because of the off-nuclear point sources located within the *XMM-Newton* extraction region. No trace of broad Hα is visible in the relatively high S/N spectrum presented by Ho et al. (1997b).

NGC 4696 (Abell 3526). NGC 4696 is the brightest member of the rich Centaurus Cluster, Abell 3526 (see Appendix F, Fig. F.10). This galaxy is rather diffuse at high X-ray energies, having a clear nuclear halo morphology at soft energies (Fig. C.56). In fact, Satyapal et al. (2004) classed it as an object that reveals a hard nuclear point source embedded in soft diffuse emission. Taylor et al. (2006) used 196.6 ksec *Chandra* data, extracted the nuclear source with a 0.9" aperture, and obtained the best-fit model by a MEKAL thermal plasma with kT=0.75 keV and abundance 0.22 solar. Rinn et al. (2005) fit its *XMM-Newton* spectrum with a thermal model with kT=0.7 keV but with a matellicity 1.2 times solar. At variance with them, GM+06 best-fit model was a power law but with a rather high and unrealistic spectral index of 4.26. In spite of this difference, the estimated luminosities are within a factor of 2 (6$\times$ 10^{39}erg s^{-1} and 1.2$\times$ 10^{40}erg s^{-1} for our analysis and Taylor's, respectively). GM+06 classified this source as a good candidate for a Starburst due to the absence of a nuclear-unresolved source at hard energies (Fig. C.56). Nevertheless, the VLBA data reported by Taylor and collaborators reveal a weak nucleus and a broad, one-sided jet extending over 25 pc, suggesting an AGN nature of this peculiar source. We have reanalysed the same *Chandra* data than in GM+06 and obtained that the best-fit model is MEPL ($\Gamma = 3.1$ and kT=0.67 keV) without additional absorption. The X-ray luminosity is now 1 $\times$ 10^{40} erg s^{-1}. The available *XMM-Newton* data (40 ksec) produce a spectrum with strong pile-up effects, so it will not be used any further.

NGC 4736 (UGC 7996, M 94). This is a rather isolated object in terms of similar size galaxies within 250 kpc projected distance (see Appendix F, Fig. F.10). An unresolved nuclear source was reported for this galaxy using 0.15 arcsec resolution *VLA* data at 2cm (Nagar et al., 2005). Maoz et al. (2005) reported a factor of 2.5 long-term variability at UV. This galaxy shows a large number of unresolved compact sources in the few central arcseconds, which makes the extraction of the true nuclear source

rather difficult (Fig. C.57). The high abundance of extranuclear sources can be due to the blue knots and HII regions located in an external ring (Roberts et al., 2001; Maoz et al., 2005)). With the same *Chandra* dataset we have used for this galaxy, Eracleous et al. (2002) identified 3 X-ray sources in the nuclear region, all of them showing hard spectra with power law indices ranging from 1.13, for the brightest one, to 1.8 for X-3, and luminosities in the 2-10 keV band between $4\times\ 10^{38}$ erg s^{-1} and 9.1×10^{39} erg s^{-1}. We assign the source X-2 by Eracleous to be the nucleus of the galaxy since it coincides with the 2MASS near-IR nucleus within 0.82″. Eracleous et al. (2002) stressed the complications of defining an AGN or SB character to this source, suggesting that even if the brightest source is associated with an AGN it will only contribute 20% to the energy balance in X-rays. The radio monitoring observations made by Kording et al. (2005) with the VLBI found a double structure, with the radio position N4736-b coinciding with our X-ray nucleus. From this double structure the brightest knot N4736-b also appears to be variable, pointing to an AGN nature for this low luminosity AGN. Our new fit to *Chandra* data agrees with that reported in GM+06 (MEPL). We report also our analysis on 16.8 ksec *XMM-Newton* data. The spectrum is modelized by a ME2PL. An order of magnitude difference is found between the luminosities obtained from *Chandra* and *XMM-Newton* data as expected due to the inclusion of all the X-ray sources mentioned by Eracleous et al. (2002) in the *XMM-Newton* extraction aperture (see Table 3.23). *ASCA* and *ROSAT* results are given by Roberts et al. (1999) and Roberts et al. (2001), where they reported a marginal detection of an ionized Fe K emission line. Terashima et al. (2002) found a possible hint of Fe K emission in the *ASCA* spectrum. In our *XMM-Newton* spectrum there is only marginal evidence for such an emission line (see Appendices E and E).

NGC 5005 (UGC 8256). This is a rather isolated object with no similar size galaxies within 250 kpc projected distance (see Appendix F, Fig. F.10), but two galaxies (NGC 5002 at cz=1091 km/s and NGC 5014 at cz=1126 km/s) are just out of the 250 kpc box. A broad Hα component was found in its optical spectrum Terashima et al. (2002); Ho et al. (1997b). Its *ASCA* X-ray spectrum (Terashima et al., 2002) was fitted with an absorbed (N_H=0.1×10^{22}cm^{-2}) power-law with $\Gamma = 0.97$, and a thermal (Raymond-Smith) component with kT=0.76 keV. They also reported a factor about 2 variability for this source. Dudik et al. (2005) classed its *Chandra* X-ray morphology as type III, i.e., a nuclear source embedded in diffuse emission; their spectral fitting provided N_H=1.1×10^{20}cm^{-2}, Γ=1.9 and kT=0.9 keV. Guainazzi et al. (2005b) analysed both *Chandra* and *XMM-Newton* data, to disclaim the *Compton-thick* nature of this source (Risaliti et al., 1999), deriving $N_H = 3\times\ 10^{22}$ cm^{-2} and $\Gamma = 1.6$. Gallo et al. (2006) obtained, with the same *XMM-Newton* dataset, $N_H < 1.4 \times 10^{20}$ cm^{-2} and $\Gamma = 1.58$, and a total (2-10) keV luminosity of $\approx 10^{40}$ erg s^{-1}. We report

our results on the available *XMM-Newton* observations (0.86 ksec). The best fit model is a MEPL model with ($\Gamma = 1.5$ and kT=0.27 keV) with a column density of 6×10^{21} cm^{-2}, even lower that in Guainazzi et al. (2005a), and a luminosity of $Lx(2-10\ keV) = 2 \times 10^{40}$ erg s^{-1}.

NGC 5055 (UGC 8334, M 63). Only a dwarf spiral, namely UGC 8313, at very similar redshift (cz=593 km/s) appears close to this galaxy (see Appendix F, Fig. F.10). Its shows a clearly unresolved nuclear source coincident with the 2MASS position for the nucleus (Fig. C.59). No previous study of *Chandra* data has been reported. The only data available were *ROSAT* PSPC and HRI observations (Read et al., 1997; Roberts and Warwick, 2000) that pointed to the nucleated nature of this source within their low spatial resolution (10″ at best). In the course of an investigation of ULXs over a sample of 313 nearby galaxies, Liu and Bregman (2005) found 10 ULX in this galaxy, one of which is close to the nucleus with a luminosity variation from 0.96 and 1.59×10^{39}erg s^{-1} in 1.6 days. The new *Chandra* data can be fitted with a PL model ($\Gamma = 2.3$), with a very low luminosity ($Lx = 6 \times 10^{37}$ erg s^{-1}). This seems to be consistent with the spatially resolved UV source detected by (Maoz et al., 1998, 2005), which they reported as an extended, non-varying source, who suggested a young star origin to the observed emission. The 0.2″ resolution observations by Nagar et al. (2000) give an upper limit of 1.1 mJy to any small-scale radio emission at 15 GHz. Ho et al. (1997b) classified it as a type 1.9 LINER based in the detection of a broad Hα component.

Mrk 266NE (NGC 5256, UGC 8632, IZw 67). Mrk 266 is a merging system (see Appendix F, Fig. F.11) with two nuclei separated by 10″ (Hutchings and Neff, 1988; Wang et al., 1997): a Seyfert 2 nucleus to the southwest and a LINER nucleus to the northeast. Here we pay attention to the LINER nucleus. Its X-ray morphology shows the double structure of these merging, luminous infrared system with the northeast nucleus brighter than the southwestern one. Also the southwest nucleus shows hard emission being more diffuse (Fig. C.60). Our nuclear morphology agrees with that reported by Satyapal et al. (2004). Here we find the best fit for the *Chandra* spectrum to be ME2PL ($N_H = 2.2 \times 10^{23}$ cm^{-2}, $\Gamma = 1.34$ and kT=0.83 keV). The resulting X-ray luminosity is 4.6×10^{41} erg s^{-1}. We also report *XMM-Newton* data which seem to be consistent with the same model but with a steeper spectral index ($\Gamma = 2.7$) and an X-ray luminosity a bit larger but consistent with *Chandra* data. A clear FeKα has been detected with equivalent width of 276 eV.

UGC 08696 (Mrk 273, IRAS 13428+5608). Mrk 273 is one of the prototypical ultraluminous galaxies, showing a very complex structure at optical frequencies with a double nucleus, with a projected separation of ≈ 1″, and a long tidal tail, indicative of a merging system (see Appendix F, Fig. F.11). A compact flat spectrum radio source has been detected between 2 and 6 cm (Baan and Klockner, 2006). At high

X-ray energies only the northern nucleus is detected (Fig. C.61), which is coincident with the compact radio source shown in VLBI observations (Cole et al., 1999; Carilli and Taylor, 2000). Based on *Chandra* ACIS imaging, Satyapal et al. (2004) classed this galaxy among those revealing a hard nuclear source embedded in soft diffuse emission. X-ray *Chandra* data have been previously analysed by (Xia et al., 2002), who carefully studied both the nucleus and the extended emission. They showed that the compact nucleus is well described by an absorbed power law (N_H= 4.1×10^{20}cm^{-2}, Γ=2.1, L(2-10 keV)=$2.9\times$ 10^{42} erg s^{-1}) plus a narrow FeKα line. The most remarkable result of this analysis is that the spectrum of the central 10" is consistent with $1.5Z_{\odot}$ metallicity, whereas the extended halo seems to be consistent with a thermal plasma with 0.1 $Z_{\odot}$ metallicity. The results reported by Ptak et al. (2003) on the same *Chandra* dataset (the only available up to now) point out that most of the observed X-ray emission (95%) comes from the nucleus. GM+06 best-fit model agrees with those data within the errors (Γ=1.74 , kT=0.75 keV, N_H=3.9×10^{20}cm^{-2} and L(2-10 keV)=1.5×10^{42} erg s^{-1}, see Tables 2.5 and 2.6). Our new best fit to the *Chandra* data is consistent with a ME2PL model with a column density 10 times higher than previouly reported and almost a factor of ten larger X-ray luminosity. In addition, we report the results for the available 18 ksec *XMM-Newton* observation obtaining the same bestfit model with consistent spectral parameters and luminosity. Using *XMM-Newton* data, Balestra et al. (2005) analysed the FeKα line and concluded that, alike the case of NGC 6240, the line is the result of the superposition of neutral FeKα and a blend of highly ionized lines of FeXXV and FeXXVI. We have measured an equivalent width of 266 eV for the FeKα line.

CGCG 162-010 (Abell 1795, 4C 26.42). This galaxy is the central cD galaxy of the cluster A1795 (see Appendix F, Fig. F.11), which hosts the powerful type I radio source 4C26.42. The X-ray morphology shows a rather diffuse emission at high energies and a very clear long filament at soft energies (Fig. C.62). A full description of the nature of this filament was made in Crawford et al. (2005), who attributed the observed structure to a large event of star formation induced by the interaction of the radio jet with the intra-cluster medium. Satyapal et al. (2004) classed this galaxy among those revealing a hard nuclear source embedded in soft diffuse emission, based on *Chandra* ACIS imaging. Nevertheless, Donato et al. (2004), investigating the nature of the X-ray central compact core in a sample of type I radio galaxies, classified this galaxy among sources without a detected compact core, in agreement with GM+06 classification. The X-ray spectroscopic analysis of GM+06 results in this object being one of the five most luminous in the sample, with a value for the luminosity in very good agreement with that estimated by Satyapal et al. (2004) for an intrinsic power-law slope of 1.8 for the same dataset (see Table 2.5). Here we report a new analysis on these 20 ksec *Chandra* data and 42.3 ksec *XMM-Newton* data. The

spectrum extracted from *Chandra* data is better fitted with ME (kT=1.1 keV) whereas that from *XMM-Newton* data is better described by MEPL ($\Gamma = 2.1$ and kT=3.3 keV). The hard X-ray luminosity estimated from *XMM-Newton* data appears to be three orders of magnitude brighter than the *Chandra* value. These large differencies can be atributed to the contribution of an extranuclear hard X-ray component from the cooling flow of the galaxy cluster (Fabian, 1994). In fact, the difference vanishes for the spectrum extracted from *Chandra* data and 25″ aperture.

NGC 5363 (UGC 8847). It makes a wide pair together with NGC 5364 (cz=1241), in a group with several smaller galaxies, as NGC 5356 and NGC 5360 (see Appendix F, Fig. F.11). We report here for the first time the analysis on archival 19.3 ksec *XMM-Newton* observations. The extracted spectrum is better fitted with ME2PL ($\Gamma = 2.14$ and kT=0.61 keV). Evidences for its AGN nature can be found in the radio data reported by Nagar et al. (2005).

IC 4395 (UGC 9141). This galaxy is disturbed by a neighboring edge-on galaxy, UGC 9141 at cz=1102 km/s) (see Appendix F, Fig. F.11). The only previously published X-ray data on this galaxy correspond to the *XMM-Newton* RGS spectrum by Guainazzi and Bianchi (2007), in which neither of the studied emission lines have been detected. We report the first analysis of archival 18 ksec *XMM-Newton* observation, that results in MEPL ($\Gamma = 1.78$ and kT=0.26 keV) with no additional absorption as the best fit.

IRAS 14348-1447. IRAS 14348-1447 is part of a merging galaxy pair (see Appendix F, Fig. F.11). Our *Chandra* image shows a diffuse morphology in the whole X-ray energy range, but does not allow any kind of spectral analysis. We estimate a (2-10 keV) X-ray luminosity of 1×10^{41} erg s^{-1} by assuming a single power-law with fixed spectral index to 1.8 and galactic absorption. Franceschini et al. (2003) analysed the same *XMM-Newton* dataset presented in this paper, deriving a two component model as the best fit, with a thermal component with kT$\approx$0.62 keV, and an absorbed power-law with $\Gamma \approx 2.2$ and $N_H > 10^{21}$ cm^{-2} accounting for a significant hard X-ray component. They described the (0.2-10) keV X-ray morphology at larger spatial scales (2×2 arcminutes), with a bow-like structure extending about 30″ in the NS direction, together with another relatively bright blob at about 20″ to the SE which lacks any optical counterpart. The spectrum we have extracted from *XMM-Newton* data is fitted with an unabsorbed ME with kT=3.67 keV; this value for the temperature is a rather extreme, but no other model is able to provide a good fit with physically reasonable parameters. The derived luminosity is 4.9×10^{41}erg s^{-1}, consistent with the value estimated with *Chandra* data.

NGC 5746 (UGC 9499). This galaxy is part of a very wide galaxy pair with NGC 5740 (cz=1572 km/s), at $\approx$ 18′ (out of the plotted field of view in Appendix

F, Fig. F.12). No previous X-ray data analysis have been reported. Here we make use of the archival *Chandra* observations, that indicate an X-ray morphology showing a clearly compact, unresolved nuclear source (Fig. C.66). We obtain that a single power-law model ($\Gamma = 1.28$) with moderate obscuration ($N_H = 6 \times 10^{21}$ cm^{-2}) can explain the observed spectrum. The analysis reported by GM+06 with the same data, both the fitting and the position in the color-color diagrams, provided very similar results. Nagar et al. (2002) detected a compact radio source suggesting the AGN nature of the nuclear source in this galaxy.

NGC 5813 (UGC 9655). NGC 5813 belongs to the group of galaxies #50 in the catalog by de Vaucouleurs (1975), whith NGC 5846 being the brightest member of the group; the closest galaxy to NGC 5813 is NGC 5814 at 4.8 arcmin to the S-SE (see Appendix F, Fig. F.12), but it lies too far away to be a physical companion (cz=10581 km/s). The X-ray morphology is extremely diffuse, with very extended emission at softer energies and without any emission at hard energies. We present the analysis on the spectra extracted from 48.4 ksec *Chandra* and 28 ksec *XMM-Newton* observations. Both *Chandra* and *XMM-Newton* data are best fitted with a MEPL model. The fitting parameters are compatible, excepting for the hydrogen column density (consistent with zero for *Chandra* data and 2.6×10^{21} cm^{-2} for *XMM-Newton* data). This leads to a high discrepancy between *Chandra* and *XMM-Newton* luminosities (6.3×10^{38} erg s^{-1} and 1×10^{40} erg s^{-1}, respectivelly). This discrepancy can be explained as due to the inclusion in the *XMM-Newton* spectrum of diffuse emission coming from the core galaxy cluster group. In fact, the higher luminosity is recovered when the aperture used from extracting the spectrum with *Chandra* data is fixed to 25″ (see Table 3.23). At radiofrequencies Nagar et al. (2005) found a well detected compact radiocore.

NGC 5838 (UGC 9692, CGCG 020-057). Also belonging to the NGC 5846 group, a number of small galaxies are seen within 250 kpc (see Appendix F, Fig. F.12). There is not previous reported X-ray data in the literature. We present the analysis on the available 13.6 ksec *Chandra* observations, for which unfortunatelly no spectral fitting can be made due to the low count-rate. The estimated hard X-ray luminosity is 1.6×10^{39} erg s^{-1} assuming a power-law model with fixed spectral index to 1.8 and galactic absorption. The hard X-ray morphology appears extended and diffuse with a faint nuclear source. Filho et al. (2002) detected a slightly resolved 2.2 mJy source, and confirm its compactness from subarcsecond-resolution 8.4 GHz images. Based on previous data at radio frequencies, they also conclude that the nuclear radio source in NGC 5838 must have a flat radio spectrum.

NGC 5846 (UGC 9706). NGC 5846 is the brightest member of the G50 group in the catalog of de Vaucouleurs (1975). In Appendix F, Fig. F.12 the two galaxies closest to it are the two small ones to the W (NGC 5845, at cz=1458 km/s) and NGC 5839,

at 1225 km/s); the barred spiral to the E is NGC 5850, at 2556 km/s, and hence it does not conform a close interacting pair. Based on *Chandra* data, Trinchieri and Goudfrooij (2002) revealed a complex X-ray morphology with no clear nuclear identification (see also Fig. C.69). They detected, however, a large amount of individual, compact sources in the luminosity range from 3 to 20×10^{38} erg s^{-1}. Filho et al. (2004) reanalysed the data already presented in Trinchieri and Goudfrooij (2002) and reported a weak, hard (2-10 keV) nuclear source with Γ=2.29, which is compatible within the errors with the value we obtain from the spectral fitting. Satyapal et al. (2005) analysed the *Chandra* data of this galaxy that they classed within non-AGN LINERs, fitting its spectrum with a single thermal model with kT=0.65 keV, exactly the same as in GM+06 for our single RS model. We have reanalysed the spectra extracted from *Chandra* and *XMM-Newton* data, that result to best-fitted by MEPL for *Chandra* and ME2PL for *XMM-Newton*. At radiofrequencies it appears as a clearly compact radio core with a flat continuum (Filho et al., 2000, 2006).

NGC 5866 (UGC 9723). With several galaxies in the field of view in Appendix in Fig. F.12, two of them are physically close to it, namely NGC 5666A (cz=585 km/s) and NGC 5826 (cz=823 km/s). It forms a wide physical group with NGC 5879 (at 80 arcmin and cz=929 km/s) and NGC 5907 (at 85 arcmin and cz=779 km/s). The data for this galaxy reveals a rather complex morphology at hard X-ray energies with an identifiable nuclear region and extended emission in the northwest direction (Fig. C.70). Previous X-ray data analysis by Pellegrini (1994) based on *ROSAT* PSPC observations, pointed out a high excess of soft X-ray emission in S0 galaxies. Filho et al. (2004) and Terashima and Wilson (2003) failed to detect any hard nuclear X-ray emission in the *Chandra* image of this galaxy, and Satyapal et al. (2005) classed it as a non-AGN-LINER, which agrees with GM+06 morphological classification. We estimate a hard X-ray luminosity $\mathrm{Lx}(2-10\ \mathrm{keV}) = 2\times 10^{38}\ \mathrm{erg\ s^{-1}}$. Multifrequency radio observations suggest it harbors a compact, flat-spectrum radio core Hummel (1980); Wrobel and Heeschen (1991); Nagar et al. (2005); Filho et al. (2000, 2004); Falcke et al. (2000).

IZw 107 (Mkn 848, VV 705). Mark 848S is a Luminous Infrared Galaxy (Goldader et al., 1997) belonging to a close pair (see Appendix F, Fig. F.12) of interacting galaxies (Armus et al., 1990). The *Chandra* X-ray imaging (see Fig. C.71) shows a diffuse source at the nuclear position and a point-like source to its North. The spectrum extracted from *XMM-Newton* data is better fitted with a single PL ($\Gamma = 2.3$) without additional absorption. The reported X-ray Luminosity is $1.6\times 10^{41}\ \mathrm{erg\ s^{-1}}$.

NGC 6251 (UGC 10501). Paired with NGC 6252 at 2.4 arcmin (cz=6428 km/s) (see Appendix F, Fig. F.13), this is a well-known radio galaxy hosting a giant radio jet (Birkinshaw and Worrall, 1993; Urry and Padovani, 1995; Sudou and Taniguchi, 2000). The high-energy X-ray morphology shows a well-defined unresolved nu-

clear source without any extended halo (Fig. C.72). Guainazzi et al. (2003) reported a full analysis of the nuclear energy source comparing *Chandra*, *BeppoSAX*, and *ASCA* data. They found that the spectrum can be modeled with a combination of a thermal plasma at kT=1.4 keV, plus a power law with Γ=1.76 and N_H=1.6$\times$ 10^{21}cm^{-2}, but they do not find evidence for the broad FeKα claimed in previous *ASCA* observations. However, the high sensitivity of *XMM-Newton* leads Gliozzi et al. (2004) to suggest again that such a broad (σ= 0.6 keV) FeKα line at 6.4 keV with an EW=0.22 keV is really there. The presence of an accretion disk in addition to the jet were suggested for explaining the origin of the X-ray emission. Chiaberge et al. (2003) modelled the spectral energy distribution from Γ-ray to radio frequencies and found that it was consistent with a synchrotron self-compton model with an unexpected high resemblance to blazar-like objects. This model, together with the dispute over the existence of FeKα, lead Evans et al. (2005) to favor the relativistic jet emission as the main component of the observed emission. We report here the analysis of the spectra extracted from 25.4 ksec *Chandra* and 41 ksec *XMM-Newton* data. *Chandra* results are consistent with our previous analysis (GM+06). *XMM-Newton* data is better reproduced by ME2PL. The hard X-ray luminosity calculated from *XMM-Newton* data is one order of magnitude brighter than that obtained from *Chandra* data, which cannot be interpreted as due to an aperture effect (Table 3.24).

NGC 6240 (IC 4625, UGC 10592, 4C 02.44). This is a very well-known ultraluminous infrared merger remnant (see Appendix F, Fig. F.13) with a strong nonthermal radio excess and two nuclei separated by $\approx$2″. Carral et al. (1990) report a compact radio source at 15 GHz. Making use of the same dataset we analyse here, Komossa et al. (2003) discovered a binary AGN in the galaxy coincident with the optical nucleus. They appear as compact-unresolved at energies between 2.5-8 keV. With the same dataset we use here, Satyapal et al. (2004) classed it as an object that reveals a hard nuclear point source embedded in soft diffuse emission. The spectroscopic analysis shows a very hard radiation for both nuclei, with Γ=0.2 for the one to the South and 0.9 for the one to the Northeast. The FeKα emission line is present in both nuclei. Ptak et al. (2003) pointed out to the complexity of the nuclear spectrum of this galaxy and constructed a more complex model that, in addition to the standard MEKAL and power law components, also included a Gaussian fit for the FeKα and a Compton reflection component with different column densities. To give an idea of the complexity of the source, let us point out that Boller et al. (2003) best-modeled the FeKα line as resolved into 3 narrow lines: a neutral FeKα line at 6.4 keV, an ionized line at 6.7 keV, and a blend of higher ionized lines (FeXXVI and Fe Kβ line) at 7.0 keV. For consistency with the statistical analysis, we modelled the continuum spectrum with the combination of a thermal plus a power law component, without taking the complexity of the FeKα line into account. High absorption was derived

for this source from both the spectral fitting and the estimation from color-color diagrams by GM+06. We have fitted the spectra of this source, obtained from both *Chandra* and *XMM-Newton* data, with ME2PL. The hard X-ray luminosity is one order of magnitude brighter in the spectrum from *XMM-Newton* data compared to that from *Chandra* data. This cannot be totally explained considering that the two nuclear sources are included in the *XMM-Newton* aperture 3.24. A clear FeKα been detected in our data with equivalent width of 378 keV (see Table 3.29).

IRAS 17208-0014. This Ultraluminous Infrared source has an optical morphology characterised by a single nucleus surrounded by a disturbed disk (see Appendix F, Fig. F.13) containing several compact star clusters, with a single tail. Baan and Klockner (2006) detected a compact flat spectrum nuclear radio source. Its X-ray nuclear emission appears to be unresolved at high energies (Fig. C.74). Risaliti et al. (1999) analysed luminous IR galaxies in X-rays with *BeppoSAX* to investigate the 2-10 keV nature of their emission and classified this object as a star forming galaxy with quite a large X-ray luminosity (L(2-10 keV)=1×10^{42} erg s^{-1}). Franceschini et al. (2003) reported their analysis on *XMM-Newton* data for a sample of 10 ULIRGs and found that for this galaxy the observations are equally consistent with a model of a thermal plasma with a temperature kT=0.75 keV plus a power law component with Γ=2.26 and N_H=1.1×10^{22}cm^{-2}, and a thermal component with a temperature kT=0.74 keV plus a cut-off power law component with Γ=1.30 and N_H=2.6×10^{21}cm^{-2}, leading in both cases to similar luminosities on the order of a few times 10^{41}erg s^{-1}. Based on the lack of FeKα emission line and the close value between the SFR estimated through the far IR emission and the X-ray emission, they suggested that the X-ray emission had a starburst origin. GM+06 did not tried to fit the spectrum extracted from *Chandra* data due to low count rate; from the position in the color-color diagrams, this galaxy seemed to be consistent with high column density and a combined model with a power law index between 1.6 and 2.0 and a temperature in the range 0.6-0.8 keV. Ptak et al. (2003) analysed the same *Chandra* data on this object and found that the best fit to the global spectrum is provided by a combined power law (Γ=1.68) and thermal (kT=0.35 keV) with N_H=0.52×10^{22}cm^{-2} model. The nuclear luminosity is estimated to be L(2-10 keV)=4.2×10^{41} erg s^{-1}, a factor of 3 brighter than the value from GM+06. We report here the analysis of the spectra extracted from 14.6 ksec *Chandra* and 14 ksec *XMM-Newton* observations on this source. *Chandra* data are better explained with a PL with a spectral index of 1.6, while *XMM-Newton* data are better described by MEKAL (kT=0.64 keV). We report a luminosity of 1.6×10^{41} erg s^{-1} calculated from *Chandra* data, close to what it was reported before. *XMM-Newton* data result in a lower value (1.7×10^{40} erg s^{-1}). The low count rate of these observations donot allow to favour any of the results.

NGC 6482 (UGC 11009). This galaxy is the brightest member of a fossil group

(see Appendix F, Fig. F.13). Based on different *Chandra* observations that those reported here, Khosroshahi et al. (2004) analysed the temperature profile of the group, but not for the individuals. *Chandra* data on this source shows no hard nuclear source (Fig. C.75) associated with the compact radio source detected by Goudfrooij et al. (1994). The spectral analysis shows that the data are consistent with a thermal plasma at kT=0.68 keV in GM+06. The *Chandra* analysis performed here is consistent with the values obtained before. We have also analysed 6.7 ksec *XMM-Newton* data finding that the best-fit is provided by MEKAL with a temperature of 0.7 keV (also consistent with that from *Chandra* data). The hard X-ray luminosity results to be almost one order of magnitude for *XMM-Newton* data. This discrepancy can be attributed to the extended emission around the nucleus. The nuclear spectrum is better-fitted by a single thermal component, maybe due to the contribution of the emission from the galaxy group. In fact, a very similar spectrum is recovered when using a 25″ extraction with *Chandra* data.

NGC 7130 (IC 5135, IRAS 21453-3511), is a peculiar galaxy that has no close companions (see Appendix F, Fig. F.13), since the closest projected companion AM2145-351 is at z=0.1. It shows a well-defined nuclear source at high X-ray energies (Fig. C.76). Since most of the UV emission is spectrally characteristic of star formation (Thuan, 1984; Gonzalez-Delgado et al., 2004), Levenson et al. (2005) used the same *Chandra* dataset than we use in this paper; they tried to decompose the AGN and Starburst contributions and found that the AGN contribution manifested mainly at higher energies (> 3 keV). They found that the obscuration of the nucleus is *Compton-thick*, which prevents the detection of the intrinsic emission in the *Chandra* bandpass below 8 keV. The spectral fitting is not statistically acceptable for this source in GM+06 but now, with our refined method, we have that ME2PL shows an acceptable fit (Γ=2.7, kT=0.76 keV, $\mathsf{NH2} = 8.6 \times 10^{23}\ \mathsf{cm}^{-2}$). A clear FeK$\alpha$ has been measured with equivalent width 382 eV.

NGC 7285 (Arp 93). NGC 7285 is a member of the close interacting pair Arp 93, together with NGC 7284 at 0.5 arcmin (see Appendix F, Fig. F.13) and cz=4681 km/s. No previous X-ray data have been reported. Here we present the 27.2 ksec *XMM-Newton* observations on this source. The spectral analysis gives MEPL as the best fit with: Γ=1.6, kT=0.13 keV, $\mathsf{NH1} = 6.8 \times 10^{21}\ \mathsf{cm}^{-2}$ and $\mathsf{NH2} = 8.7 \times 10^{21}\ \mathsf{cm}^{-2}$. An equally good fit is obtained with 2PL, with Γ=1.69, $\mathsf{NH1} = 8. \times 10^{20}\ \mathsf{cm}^{-2}$ and $\mathsf{NH2} = 1.7 \times 10^{22}\ \mathsf{cm}^{-2}$. A clear FeK$\alpha$ has been measured with equivalent width 212 eV.

NGC 7331 (UGC 12113). This is a quite isolated object in terms of not having any large companion at similar redshift (see Appendix F, Fig. F.14) althought sometimes it has been considered in interaction with a member of the Stephan Quintet (Dumke et al., 1995). Stockdale et al. (1998) and Roberts and Warwick (2000) used *ROSAT*

data to point out the AGN nature of this galaxy. The hard X-ray image extracted from the only available *Chandra* dataset does not show any evidence of a nuclear source, being very diffuse at high energies (Fig. C.78). Note that Filho et al. (2004) described this galaxy as hosting a hard (2-10 keV) X-ray nucleus, but Satyapal et al. (2004) classed it as an object exhibiting multiple, hard off-nuclear point sources of comparable brightness to the nuclear source, based on the same data. The parameters estimated by GM+06 from its position in color-color diagrams are consistent with a spectral index 2-2.6 and a temperature 0.7 keV. The estimation of the luminosity by Satyapal et al. (2004) for an intrinsic power slope of 1.8 is in perfect agreement with GM+06. Gallo et al. (2006) presented the *XMM-Newton* data on this source and found that the spectrum is consistent with a thermal component at kT=0.49 keV plus a power law with Γ=1.79, giving a luminosity that is a factor of 10 larger than that in GM+06 and this work. There is only 49 counts in the 0.5-10.0 keV band of the spectrum extracted from 0.8 ksec *XMM-Newton* data. We estimate an X-ray luminosity with *XMM-Newton* data in good agreement with Gallo et al. (2006) results. The diference in luminosities between *Chandra* and *XMM-Newton* is attributed to the off-nuclear point-like sources seen in the *Chandra* hard energy band images (see Fig. C.78).

IC 1459 (IC 5265). IC 1459 is a giant elliptical in a loose group with several spiral galaxies, the most conspicuous in Appendix F, Fig. F.14 being IC 6269B (cz=2870 km/s) and IC 5264 (cz=1940 km/s). A variety of indicators suggesting a recent merger are present in this galaxy, as a nuclear dust lane (Sparks et al., 1985), an ionized gas disk and a number of shells (Forbes et al., 1994). At X-ray frequencies, this galaxy presents an unresolved nuclear source on top of a diffuse halo at high energies (Fig. C.79), in agreement with the classification by Satyapal et al. (2004). A compact radio core has been detected (Slee et al., 1994). Fabbiano et al. (2003), based on a different set of data , found that it shows a rather weak (L(2-10 keV)=8.0$\times$ 10^{40} erg s^{-1}) unabsorbed nuclear X-ray source with Γ=1.88 and a faint FeKα line at 6.4 keV. These characteristics correspond to a normal AGN radiating at sub-Eddington luminosities, at 3$\times$ 10^{-7} below the Eddington limit. They suggest that ADAF solutions can explain the X-ray spectrum, but these models failed to explain the high radio power of its compact source (Drinkwater et al., 1997). The fitting parameters from GM+06 are in remarkably good agreement with theirs (Γ=1.89, kT=0.30 keV and L(2-10 keV)=3.6$\times$ 10^{40} erg s^{-1}). We report here the results of the analysis of the nuclear spectra extracted from 53 ksec *Chandra* and 26.9 ksec *XMM-Newton* data. The former is better fitted by ME2PL with $\Gamma = 2.17$, kT = 0.61 keV and column densities $\mathsf{NH1} = 2.0 \times 10^{21}$ cm^{-2} and $\mathsf{NH2} = 1.3 \times 10^{22}$ cm^{-2}. The spectrum extracted from *XMM-Newton* data shows a MEPL best-fit with spectral index and hydrogen column density NH1 consistent with that reported before. The differ-

ence in luminosities dissapears when comparing *Chandra* and *XMM-Newton* spectra obtained with the same aperture.

NPM1G-12.0625 (Abell 2597). The brightest galaxy in Abell 2597 cluster (see Appendix F, Fig. F.14). Sarazin et al. (1995) found a nuclear radiosource consisting of unresolved nuclear emission and two diffuse lobes. Previous X-ray data on this galaxy referred to the analysis of the extended emission in its parent cluster (Pointecouteau et al., 2005; Morris and Fabian, 2005), but less attention was paid to the nuclear emission. Satyapal et al. (2004) classed its X-ray morphology based on 40 ksecs *Chandra* data, as those of objects revealing a nuclear point source embeded in difuse emission. We report the analysis of the nuclear spectra extracted from 59 ksec *Chandra* and 89.6 ksec *XMM-Newton* data. *Chandra* data are better fitted by MEPL and *XMM-Newton* with ME2PL with a consistent value of the spectral index, although high. The reported temperature is much lower in the case of *Chandra* data (kT=0.31 keV) compared with *XMM-Newton* data (kT=2.7 keV). This higher value in *XMM-Newton* data is an aperture effect since there is a strong hard diffuse component related to the cluster emission (see Tables 3.24 and 3.25).

NGC 7743 (UGC 12759). No other similar-sized galaxy is seen within 250 kpc (see Appendix F, Fig. F.14). This LINER appears not to have a broad Hα component (Terashima et al., 2000). It is the only object in the sample by Terashima et al. (2002) with no need of a power-law component to fit its *ASCA* spectrum, what is interpreted as a possible *Compton-thick* nature for this object. A clear compact flat spectrum radio core has been detected by Ho and Ulvestad (2001). In fact, it appears as a *Compton-thick* candidate in the study by Panessa et al. (2006). Our *XMM-Newton* spectrum covers up to $\simeq$5 keV, and is better fitted by MEPL with $\Gamma = 3.16$, kT=0.26 keV, $\mathsf{NH1} = 3.5 \times 10^{21}$ cm^{-2} and $\mathsf{NH2} = 1.7 \times 10^{22}$ cm^{-2}. We stress that $\chi^2_r = 1.76$, which is the smallest value we get, but the count number is at the low limit of our requirements and the spectral fit is therefore not reliable.

Bibliography

Armus, L., Heckman, T. M., and Miley, G. K.: 1990, *Astrophysical Journal* **364**, 471

Baan, W. A. and Klockner, H.-R.: 2006, *Astronomy and Astrophysics* **449**, 559

Balestra, I., Boller, T., Gallo, L., Lutz, D., and Hess, S.: 2005, *Astronomy and Astrophysics* **442**, 469

Ballo, L., Braito, V., Ceca, R. D., Maraschi, L., Tavecchio, F., and Dadina, M.: 2004, *Astrophysical Journal* **600**, 634

Barth, A. J., Filippenko, A. V., and Moran, E. C.: 1999, *\apj* **525**, 673

Barth, A. J., Ho, L. C., and Sargent, W. L. W.: 2002, *Astronomical Journal* **124**, 2607

Barth, A. J., Reichert, G. A., Filippenko, A. V., Ho, L. C., Shields, J. C., Mushotzky, R. F., and Puchnarewicz, E. M.: 1996, *Astronomical Journal* **112**, 1829

Birkinshaw, M. and Worrall, D. M.: 1993, *Astrophysical Journal* **412**, 568

Böhringer, H., Voges, W., Huchra, J. P., McLean, B., Giacconi, R., Rosati, P., Burg, R., Mader, J., Schuecker, P., Simi, D., Komossa, S., Reiprich, T. H., Retzlaff, J., and Trmper, J.: 2000, *Astrophysical Journal Supplement Series* **129**, 435

Boller, T., Keil, R., Hasinger, G., Costantini, E., Fujimoto, R., Anabuki, N., Lehmann, I., and Gallo, L.: 2003, *Astronomy and Astrophysics* **411**, 63

Bower, G. A., Green, R. F., Danks, A., Gull, T., Heap, S., Hutchings, J., Joseph, C., Kaiser, M. E., Kimble, R., Kraemer, S., Weistrop, D., Woodgate, B., Lindler, D., Hill, R. S., Malumuth, E. M., Baum, S., Sarajedini, V., Heckman, T. M., Wilson, A. S., and Richstone, D. O.: 1998, *Astrophysical Journal* **492**, L111

Cappellari, M., Renzini, A., Greggio, L., di Serego Alighieri, S., Buson, L. M., Burstein, D., and Bertola, F.: 1999, *Astrophysical Journal* **519**, 117

Cappi, M., Panessa, F., Bassani, L., Dadina, M., Dicocco, G., Comastri, A., della Ceca, R., Filippenko, A. V., Gianotti, F., Ho, L. C., Malaguti, G., Mulchaey, J. S., Palumbo, G. G. C., Piconcelli, E., Sargent, W. L. W., Stephen, J., Trifoglio, M., and Weaver, K. A.: 2006, *Astronomy and Astrophysics* **446**, 459

Carilli, C. L. and Taylor, G. B.: 2000, *Astrophysical Journal* **532**, L95

Carral, P., Turner, J. L., and Ho, P. T. P.: 1990, *Astrophysical Journal* **362**, 434

Chiaberge, M., Gilli, R., Capetti, A., and Macchetto, F. D.: 2003, *Astrophysical Journal* **597**, 166

Claussen, M. J., Diamond, P. J., Braatz, J. A., Wilson, A. S., and Henkel, C.: 1998, *Astrophysical Journal* **500**, L129

Colbert, E. J. M. and Mushotzky, R. F.: 1999, *Astrophysical Journal* **519**, 89

Cole, G. H. J., Pedlar, A., Holloway, A. J., and Mundell, C. G.: 1999, *Monthly Notices of the Royal Astronomical Society* **310**, 1033

Condon, J. J. and Broderick, J. J.: 1991, *Astronomical Journal* **102**, 1663

Condon, J. J., Cotton, W. D., and Broderick, J. J.: 2002, *Astronomical Journal* **124**, 675

Corbett, E. A., Norris, R. P., Heisler, C. A., Dopita, M. A., Appleton, P., Struck, C., Murphy, T., Marston, A., Charmandaris, V., Kewley, L., and Zezas, A. L.: 2002, *Astrophysical Journal* **564**, 650

Cotton, W. D., Feretti, L., Giovannini, G., Lara, L., and Venturi, T.: 1999, *Astrophysical Journal* **519**, 108

Coziol, R., Brinks, E., and Bravo-Alfaro, H.: 2004, *Astronomical Journal* **128**, 68

Crawford, C. S., Sanders, J. S., and Fabian, A. C.: 2005, *Monthly Notices of the Royal Astronomical Society* **361**, 17

Dadina, M.: 2007, *Astronomy and Astrophysics* **461**, 1209

David, L. P., Jones, C., Forman, W., and Murray, S. S.: 2005, *Astrophysical Journal* **635**, 1053

de Vaucouleurs, G.: 1975, *Social Studies of Science* **9**, 557

Dewangan, G. C., Griffiths, R. E., Matteo, T. D., and Schurch, N. J.: 2004, *Astrophysical Journal* **607**, 788

Donahue, M., Smith, B. J., and Stocke, J. T.: 2002, *Astronomical Journal* **123**, 1922

Donato, D., Sambruna, R. M., and Gliozzi, M.: 2004, *Astrophysical Journal* **617**, 915

Dong, X. Y. and Robertis, M. M. D.: 2006, *Astronomical Journal* **131**, 1236

Drinkwater, M. J., Webster, R. L., Francis, P. J., Condon, J. J., Ellison, S. L., Jauncey, D. L., Lovell, J., Peterson, B. A., and Savage, A.: 1997, *Monthly Notices of the Royal Astronomical Society* **284**, 85

Dudik, R. P., Satyapal, S., Gliozzi, M., and Sambruna, R. M.: 2005, *Astrophysical Journal* **620**, 113

Dumke, M., Krause, M., Wielebinski, R., and Klein, U.: 1995, *Astronomy and Astrophysics* **302**, 691

Dwarakanath, K. S. and Nath, B. B.: 2006, *Astrophysical Journal* **653**, L9

Eracleous, M., Shields, J. C., Chartas, G., and Moran, E. C.: 2002, *Astrophysical Journal* **565**, 108

Evans, D. A., Hardcastle, M. J., Croston, J. H., Worrall, D. M., and Birkinshaw, M.: 2005, *Monthly Notices of the Royal Astronomical Society* **359**, 363

Fabbiano, G., Elvis, M., Markoff, S., Siemiginowska, A., Pellegrini, S., Zezas, A., Nicastro, F., Trinchieri, G., and McDowell, J.: 2003, *Astrophysical Journal* **588**, 175

Fabian, A. C.: 1994, *Annual Review of Astronomy and Astrophysics* **32**, 277

Falcke, H., Nagar, N. M., Wilson, A. S., and Ulvestad, J. S.: 2000, *Astrophysical Journal* **542**, 197

Farrah, D., Afonso, J., Efstathiou, A., Rowan-Robinson, M., Fox, M., and Clements, D.: 2003, *Monthly Notices of the Royal Astronomical Society* **343**, 585

Ferrarese, L., Ford, H. C., and Jaffe, W.: 1996, *Astrophysical Journal* **470**, 444

Filho, M. E., Barthel, P. D., and Ho, L. C.: 2000, *Astrophysical Journal Supplement Series* **129**, 93

Filho, M. E., Barthel, P. D., and Ho, L. C.: 2002, *Astrophysical Journal Supplement Series* **142**, 223

Filho, M. E., Barthel, P. D., and Ho, L. C.: 2006, *Astronomy and Astrophysics* **451**, 71

Filho, M. E., Fraternali, F., Markoff, S., Nagar, N. M., Barthel, P. D., Ho, L. C., and Yuan, F.: 2004, *Astronomy and Astrophysics* **418**, 429

Filippenko, A. V. and Sargent, W. L. W.: 1985, *Astrophysical Journal Supplement Series* **57**, 503

Finoguenov, A. and Jones, C.: 2001, *Astrophysical Journal* **547**, L107

Flohic, H. M. L. G., Eracleous, M., Chartas, G., Shields, J. C., and Moran, E. C.: 2006, *Astrophysical Journal* **647**, 140

Forbes, D. A., Thomson, R. C., Groom, W., and Williger, G. M.: 1994, *Astronomical Journal* **107**, 1713

Forman, W., Nulsen, P., Heinz, S., Owen, F., Eilek, J., Vikhlinin, A., Markevitch, M., Kraft, R., Churazov, E., and Jones, C.: 2005, *Astrophysical Journal* **635**, 894

Franceschini, A., Braito, V., Persic, M., Ceca, R. D., Bassani, L., Cappi, M., Malaguti, P., Palumbo, G. G. C., Risaliti, G., Salvati, M., and Severgnini, P.: 2003, *Monthly Notices of the Royal Astronomical Society* **343**, 1181

Gallo, L. C., Lehmann, I., Pietsch, W., Boller, T., Brinkmann, W., Friedrich, P., and Grupe, D.: 2006, *Monthly Notices of the Royal Astronomical Society* **365**, 688

Georgantopoulos, I., Panessa, F., Akylas, A., Zezas, A., Cappi, M., and Comastri, A.: 2002, *Astronomy and Astrophysics* **386**, 60

Georgantopoulos, I. and Zezas, A.: 2003, *Astrophysical Journal* **594**, 704

George, I. M., Mushotzky, R. F., Yaqoob, T., Turner, T. J., Kraemer, S., Ptak, A. F., Nandra, K., Crenshaw, D. M., and Netzer, H.: 2001, *Astrophysical Journal* **559**, 167

Gliozzi, M., Sambruna, R. M., and Brandt, W. N.: 2003, A&A **408**, 949

Gliozzi, M., Sambruna, R. M., Brandt, W. N., Mushotzky, R., and Eracleous, M.: 2004, *Astronomy and Astrophysics* **413**, 139

Goldader, J. D., Joseph, R. D., Doyon, R., and Sanders, D. B.: 1997, *Astrophysical Journal* **474**, 104

Goncalves, A. C., Veron-Cetty, M.-P., and Veron, P.: 1999, *Astronomy and Astrophysics Supplement Series* **135**, 437

Gondoin, P., Orr, A., and Siddiqui, H.: 2004, *Astronomy and Astrophysics* **420**, 905

Gonzalez-Delgado, R. M., Fernandes, R. C., P\'erez, E., Martins, L. P., Storchi-Bergmann, T., Schmitt, H., Heckman, T., and Leitherer, C.: 2004, *Astrophysical Journal* **605**, 127

Goudfrooij, P., de Jong, T., Hansen, L., and Norgaard-Nielsen, H. U.: 1994, *Monthly Notices of the Royal Astronomical Society* **271**, 833

Guainazzi, M. and Bianchi, S.: 2007, *Monthly Notices of the Royal Astronomical Society* **374**, 1290

Guainazzi, M., Fabian, A. C., Iwasawa, K., Matt, G., and Fiore, F.: 2005a, *Monthly Notices of the Royal Astronomical Society* **356**, 295

Guainazzi, M., Grandi, P., Comastri, A., and Matt, G.: 2003, *Astronomy and Astrophysics* **410**, 131

Guainazzi, M., Matt, G., and Perola, G. C.: 2005b, *Astronomy and Astrophysics* **444**, 119

Guainazzi, M., Oosterbroek, T., Antonelli, L. A., and Matt, G.: 2000, *Astronomy and Astrophysics* **364**, L80

Harris, D. E., Biretta, J. A., and Junor, W.: 1997, *Monthly Notices of the Royal Astronomical Society* **284**, L21

Hattori, T., Yoshida, M., Ohtani, H., Sugai, H., Ishigaki, T., Sasaki, M., Hayashi, T., Ozaki, S., Ishii, M., and Kawai, A.: 2004, *Astronomical Journal* **127**, 736

Ho, L. C., Feigelson, E. D., Townsley, L. K., Sambruna, R. M., Garmire, G. P., Brandt, W. N., Filippenko, A. V., Griffiths, R. E., Ptak, A. F., and Sargent, W. L. W.: 2001, *Astrophysical Journal* **549**, L51

Ho, L. C., Filippenko, A. V., and Sargent, W. L. W.: 1997a, *Astrophysical Journal* **487**, 568

Ho, L. C., Filippenko, A. V., Sargent, W. L. W., and Peng, C. Y.: 1997b, *Astrophysical Journal Supplement Series* **112**, 391

Ho, L. C. and Ulvestad, J. S.: 2001, *Astrophysical Journal Supplement Series* **133**, 77

Huchtmeier, W. K. and Richter, O.-G.: 1982, *Astronomy and Astrophysics* **109**, 331

Hummel, E.: 1980, *Astronomy and Astrophysics Supplement Series* **41**, 151

Hummel, E., Kotanyi, C. G., and van Gorkom, J. H.: 1986, *Astronomy and Astrophysics* **155**, 161

Hummel, E., van der Hulst, J. M., Keel, W. C., and Kennicutt, R. C.: 1987, *Astronomy and Astrophysics Supplement Series* **70**, 517

Hutchings, J. B. and Neff, S. G.: 1988, *Astronomical Journal* **96**, 1575

Imanishi, M., Dudley, C. C., and Maloney, P. R.: 2001, *Astrophysical Journal* **558**, L93

Imanishi, M., Terashima, Y., Anabuki, N., and Nakagawa, T.: 2003, *Astrophysical Journal* **596**, L167

Jones, C., Forman, W., Vikhlinin, A., Markevitch, M., David, L., Warmflash, A., Murray, S., and Nulsen, P. E. J.: 2002, *Astrophysical Journal* **567**, L115

Jones, D. L.: 1984, *Astrophysical Journal* **287**, 33

Kadler, M., Kerp, J., Ros, E., Falcke, H., Pogge, R. W., and Zensus, J. A.: 2004, *Astronomy and Astrophysics* **420**, 467

Kataoka, J. and Stawarz, L.: 2005, *Astrophysical Journal* **622**, 797

Keel, W. C.: 1983, *Astrophysical Journal* **269**, 466

Khosroshahi, H. G., Jones, L. R., and Ponman, T. J.: 2004, *Monthly Notices of the Royal Astronomical Society* **349**, 1240

Komossa, S., Burwitz, V., Hasinger, G., Predehl, P., Kaastra, J. S., and Ikebe, Y.: 2003, *Astrophysical Journal* **582**, L15

Kording, E., Colbert, E., and Falcke, H.: 2005, *Astronomy and Astrophysics* **436**, 427

Kormendy, J.: 1988, *Astrophysical Journal* **335**, 40

Lane, W. M., Clarke, T. E., Taylor, G. B., Perley, R. A., and Kassim, N. E.: 2004, AJ **127**, 48

Lauer, T. R., Faber, S. M., Lynds, R. C., Baum, W. A., Ewald, S. P., Groth, E. J., Hester, J. J., Holtzman, J. A., Kristian, J., Light, R. M., O'Neil, E. J., Schneider, D. P., Shaya, E. J., and Westphal, J. A.: 1992, *Astronomical Journal* **103**, 703

Levenson, N. A., Weaver, K. A., Heckman, T. M., Awaki, H., and Terashima, Y.: 2005, *Astrophysical Journal* **618**, 167

Liu, J.-F. and Bregman, J. N.: 2005, *Astrophysical Journal Supplement Series* **157**, 59

Loewenstein, M., Mushotzky, R. F., Angelini, L., Arnaud, K. A., and Quataert, E.: 2001, *Astrophysical Journal* **555**, L21

Lutz, D., Veilleux, S., and Genzel, R.: 1999, ApJL **517**, L13

Machacek, M. E., Jones, C., and Forman, W. R.: 2004, *Astrophysical Journal* **610**, 183

Mahtessian, A. P.: 1998, *Astrophysics* **41**, 308

Maoz, D., Koratkar, A., Shields, J. C., Ho, L. C., Filippenko, A. V., and Sternberg, A.: 1998, *Astronomical Journal* **116**, 55

Maoz, D., Nagar, N. M., Falcke, H., and Wilson, A. S.: 2005, *Astrophysical Journal* **625**, 699

Marquez, I., Masegosa, J., Durret, F., Delgado, R. M. G., Moles, M., Maza, J., Perez, E., and Roth, M.: 2003, *Astronomy and Astrophysics* **409**, 459

Marshall, H. L., Miller, B. P., Davis, D. S., Perlman, E. S., Wise, M., Canizares, C. R., and Harris, D. E.: 2002, *Astrophysical Journal* **564**, 683

Morris, R. G. and Fabian, A. C.: 2005, *Monthly Notices of the Royal Astronomical Society* **358**, 585

Mllenhoff, C. and Heidt, J.: 2001, *Astronomy and Astrophysics* **368**, 16

Nagar, N. M., Falcke, H., and Wilson, A. S.: 2005, *Astronomy and Astrophysics* **435**, 521

Nagar, N. M., Falcke, H., Wilson, A. S., and Ho, L. C.: 2000, *Astrophysical Journal* **542**, 186

Nagar, N. M., Falcke, H., Wilson, A. S., and Ulvestad, J. S.: 2002, *Astronomy and Astrophysics* **392**, 53

Noel-Storr, J., Baum, S. A., Kleijn, G. V., van der Marel, R. P., O'Dea, C. P., de Zeeuw, P. T., and Carollo, C. M.: 2003, *Astrophysical Journal Supplement Series* **148**, 419

Nolthenius, R.: 1993, *Astrophysical Journal Supplement Series* **85**, 1

O'Sullivan, E., Forbes, D. A., and Ponman, T. J.: 2001, *Monthly Notices of the Royal Astronomical Society* **328**, 461

O'Sullivan, E. and Ponman, T. J.: 2004, *Monthly Notices of the Royal Astronomical Society* **349**, 535

O'Sullivan, E., Vrtilek, J. M., and Kempner, J. C.: 2005, *Astrophysical Journal* **624**, L77

Panessa, F., Bassani, L., Cappi, M., Dadina, M., Barcons, X., Carrera, F. J., Ho, L. C., and Iwasawa, K.: 2006, *Astronomy and Astrophysics* **455**, 173

Pellegrini, S.: 1994, *Astronomy and Astrophysics* **292**, 395

Pellegrini, S., Baldi, A., Fabbiano, G., and Kim, D.-W.: 2003, *Astrophysical Journal* **597**, 175

Pellegrini, S., Cappi, M., Bassani, L., della Ceca, R., and Palumbo, G. G. C.: 2000, *Astronomy and Astrophysics* **360**, 878

Perlman, E. S., Harris, D. E., Biretta, J. A., Sparks, W. B., and Macchetto, F. D.: 2003, *Astrophysical Journal* **599**, L65

Pihlstrom, Y. M., Conway, J. E., Booth, R. S., Diamond, P. J., and Polatidis, A. G.: 2001, *Astronomy and Astrophysics* **377**, 413

Pointecouteau, E., Arnaud, M., and Pratt, G. W.: 2005, *Astronomy and Astrophysics* **435**, 1

Ptak, A., Heckman, T., Levenson, N. A., Weaver, K., and Strickland, D.: 2003, *Astrophysical Journal* **592**, 782

Ptak, A., Terashima, Y., Ho, L. C., and Quataert, E.: 2004, *Astrophysical Journal* **606**, 173

Rampazzo, R., Alexander, P., Carignan, C., Clemens, M. S., Cullen, H., Garrido, O., Marcelin, M., Sheth, K., and Trinchieri, G.: 2006, *Monthly Notices of the Royal Astronomical Society* **368**, 851

Rauscher, B. J.: 1995, *Astronomical Journal* **109**, 1608

Read, A. M.: 2003, *Monthly Notices of the Royal Astronomical Society* **342**, 715

Read, A. M., Ponman, T. J., and Strickland, D. K.: 1997, *Monthly Notices of the Royal Astronomical Society* **286**, 626

Rinn, A. S., Sambruna, R. M., and Gliozzi, M.: 2005, *Astrophysical Journal* **621**, 167

Risaliti, G., Maiolino, R., and Salvati, M.: 1999, *Astrophysical Journal* **522**, 157

Roberts, M. S., Hogg, D. E., Bregman, J. N., Forman, W. R., and Jones, C.: 1991, *Astrophysical Journal Supplement Series* **75**, 751

Roberts, T. P., Schurch, N. J., and Warwick, R. S.: 2001, *Monthly Notices of the Royal Astronomical Society* **324**, 737

Roberts, T. P. and Warwick, R. S.: 2000, *Monthly Notices of the Royal Astronomical Society* **315**, 98

Roberts, T. P., Warwick, R. S., and Ohashi, T.: 1999, *Monthly Notices of the Royal Astronomical Society* **304**, 52

Sambruna, R. M., Chartas, G., Eracleous, M., Mushotzky, R. F., and Nousek, J. A.: 2000, *Astrophysical Journal* **532**, L91

Sambruna, R. M., Gliozzi, M., Eracleous, M., Brandt, W. N., and Mushotzky, R.: 2003, ApJL **586**, L37

Sanders, D. B., Soifer, B. T., Elias, J. H., Madore, B. F., Matthews, K., Neugebauer, G., and Scoville, N. Z.: 1988, *Astrophysical Journal* **325**, 74

Sarazin, C. L., Burns, J. O., Roettiger, K., and McNamara, B. R.: 1995, *Astrophysical Journal* **447**, 559

Sarzi, M., Rix, H.-W., Shields, J. C., Rudnick, G., Ho, L. C., McIntosh, D. H., Filippenko, A. V., and Sargent, W. L. W.: 2001, *Astrophysical Journal* **550**, 65

Satyapal, S., Dudik, R. P., O'Halloran, B., and Gliozzi, M.: 2005, *Astrophysical Journal* **633**, 86

Satyapal, S., Sambruna, R. M., and Dudik, R. P.: 2004, *Astronomy and Astrophysics* **414**, 825

Scoville, N. Z., Evans, A. S., Thompson, R., Rieke, M., Hines, D. C., Low, F. J., Dinshaw, N., Surace, J. A., and Armus, L.: 2000, *Astronomical Journal* **119**, 991

Simkin, S. M.: 1979, *Astrophysical Journal* **234**, 56

Slee, O. B., Sadler, E. M., Reynolds, J. E., and Ekers, R. D.: 1994, *Monthly Notices of the Royal Astronomical Society* **269**, 928

Smith, B. J., Nowak, M., Donahue, M., and Stocke, J.: 2003, *Astronomical Journal* **126**, 1763

Sparks, W. B., Wall, J. V., Thorne, D. J., Jorden, P. R., van Breda, I. G., Rudd, P. J., and Jorgensen, H. E.: 1985, *Monthly Notices of the Royal Astronomical Society* **217**, 87

Stauffer, J. R.: 1982, *Astrophysical Journal Supplement Series* **50**, 517

Stockdale, C. J., Romanishin, W., and Cowan, J. J.: 1998, *Astrophysical Journal* **508**, L33

Strickland, D. K., Heckman, T. M., Colbert, E. J. M., Hoopes, C. G., and Weaver, K. A.: 2004, *Astrophysical Journal Supplement Series* **151**, 193

Sudou, H. and Taniguchi, Y.: 2000, *Astronomical Journal* **120**, 697

Taniguchi, Y., Trentham, N., and Ikeuchi, S.: 1999, *Astrophysical Journal* **526**, L13

Taylor, G. B., Sanders, J. S., Fabian, A. C., and Allen, S. W.: 2006, *Monthly Notices of the Royal Astronomical Society* **365**, 705

Teng, S. H., Wilson, A. S., Veilleux, S., Young, A. J., Sanders, D. B., and Nagar, N. M.: 2005, *Astrophysical Journal* **633**, 664

Terashima, Y., Ho, L. C., Ptak, A. F., Mushotzky, R. F., Serlemitsos, P. J., Yaqoob, T., and Kunieda, H.: 2000, *Astrophysical Journal* **533**, 729

Terashima, Y., Iyomoto, N., Ho, L. C., and Ptak, A. F.: 2002, *Astrophysical Journal Supplement Series* **139**, 1

Terashima, Y. and Wilson, A. S.: 2003, *Astrophysical Journal* **583**, 145

Thuan, T. X.: 1984, *Astrophysical Journal* **281**, 126

Tremaine, S., Gebhardt, K., Bender, R., Bower, G., Dressler, A., Faber, S. M., Filippenko, A. V., Green, R., Grillmair, C., Ho, L. C., Kormendy, J., Lauer, T. R., Magorrian, J., Pinkney, J., and Richstone, D.: 2002, *Astrophysical Journal* **574**, 740

Trinchieri, G. and Goudfrooij, P.: 2002, *Astronomy and Astrophysics* **386**, 472

Tschoke, D., Hensler, G., and Junkes, N.: 1999, *Astronomy and Astrophysics* **343**, 373

Tsvetanov, Z. I., Hartig, G. F., Ford, H. C., Dopita, M. A., Kriss, G. A., Pei, Y. C., Dressel, L. L., and Harms, R. J.: 1998, *Astrophysical Journal* **493**, L83

Turner, M. J. L., Reeves, J. N., Ponman, T. J., Arnaud, M., Barbera, M., Bennie, P. J., Boer, M., Briel, U., Butler, I., Clavel, J., Dhez, P., Cordova, F., Santos, S. D., Ferrando, P., Ghizzardi, S., Goodall, C. V., Griffiths, R. G., Hochedez, J. F., Holland, A. D., Jansen, F., Kendziorra, E., Lagostina, A., Laine, R., Palombara, N. L., Lortholary, M., Mason, K. O., Molendi, S., Pigot, C., Priedhorsky, W., Reppin, C., Rothenflug, R., Salvetat, P., Sauvageot, J., Schmitt, D., Sembay, S., Short, A., Stroder, L., Trifoglio, M., Trumper, J., Vercellone, S., Vigroux, L., Villa, G., and Ward, M.: 2001, *Astronomy and Astrophysics* **365**, L110

Urry, C. M. and Padovani, P.: 1995, *Publications of the Astronomical Society of the Pacific* **107**, 803

Venturi, T., Giovannini, G., Feretti, L., Comoretto, G., and Wehrle, A. E.: 1993, *Astrophysical Journal* **408**, 81

Vermeulen, R. C., Ros, E., Kellermann, K. I., Cohen, M. H., Zensus, J. A., and van Langevelde, H. J.: 2003, *Astronomy and Astrophysics* **401**, 113

Wang, J., Heckman, T. M., and Lehnert, M. D.: 1997, *Astrophysical Journal* **491**, 114

Wiklind, T., Combes, F., and Henkel, C.: 1995, *Astronomy and Astrophysics* **297**, 643

Wilson, A. S., Braatz, J. A., and Henkel, C.: 1995, *Astrophysical Journal* **455**, L127

Wise, M. W., McNamara, B. R., Nulsen, P. E. J., Houck, J. C., and David, L. P.: 2007, *Astrophysical Journal* **659**, 1153

Worrall, D. M., Birkinshaw, M., and Hardcastle, M. J.: 2003, *Monthly Notices of the Royal Astronomical Society* **343**, L73

Worrall, D. M., Birkinshaw, M., Laing, R. A., Cotton, W. D., and Bridle, A. H.: 2007, *Monthly Notices of the Royal Astronomical Society* **380**, 2

Wrobel, J. M. and Heeschen, D. S.: 1991, *Astronomical Journal* **101**, 148

Xia, X. Y., Xue, S. J., Mao, S., Boller, T., Deng, Z. G., and Wu, H.: 2002, *Astrophysical Journal* **564**, 196

Xu, C., Baum, S. A., O'Dea, C. P., Wrobel, J. M., and Condon, J. J.: 2000, *Astronomical Journal* **120**, 2950

Xu, H., Kahn, S. M., Peterson, J. R., Behar, E., Paerels, F. B. S., Mushotzky, R. F., Jernigan, J. G., Brinkman, A. C., and Makishima, K.: 2002, *Astrophysical Journal* **579**, 600

Xu, Y., Xu, H., Zhang, Z., Kundu, A., Wang, Y., and Wu, X.-P.: 2005, *Astrophysical Journal* **631**, 809

Zezas, A., Birkinshaw, M., Worrall, D. M., Peters, A., and Fabbiano, G.: 2005, *\apj* **627**, 711

Zwicky, F., Herzog, E., and Wild, P.: 1961, *Catalogue of galaxies and of clusters of galaxies, Vol. I*

Appendix C

Catalogue of LINER images

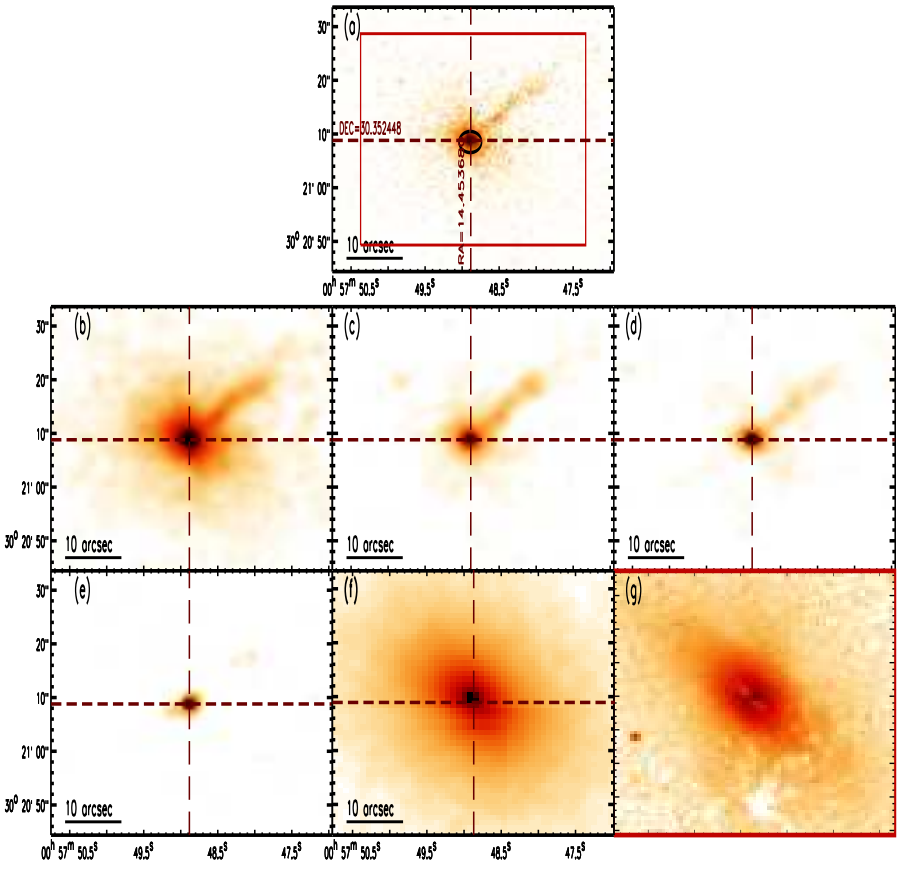

Figure C.1: *NGC 315*

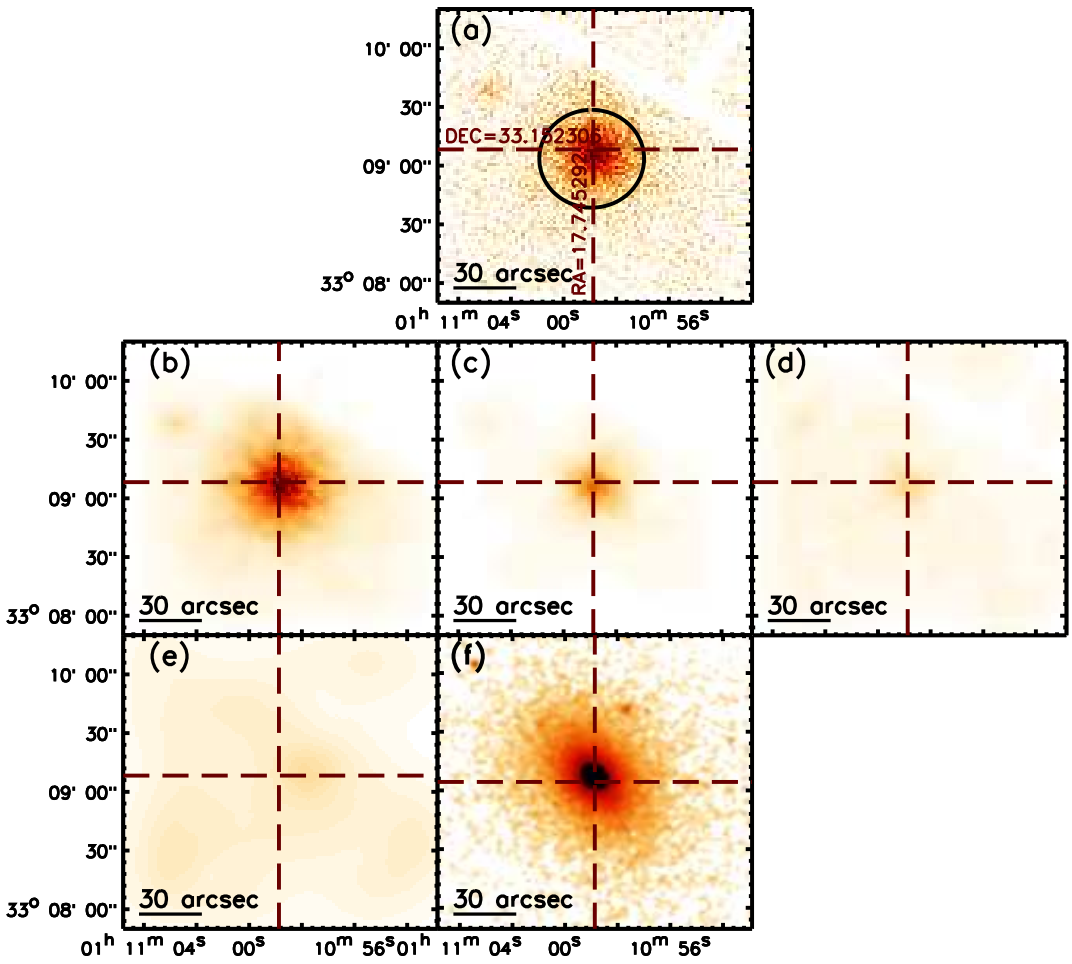

Figure C.2: *NGC410 (XMM-Newton)*

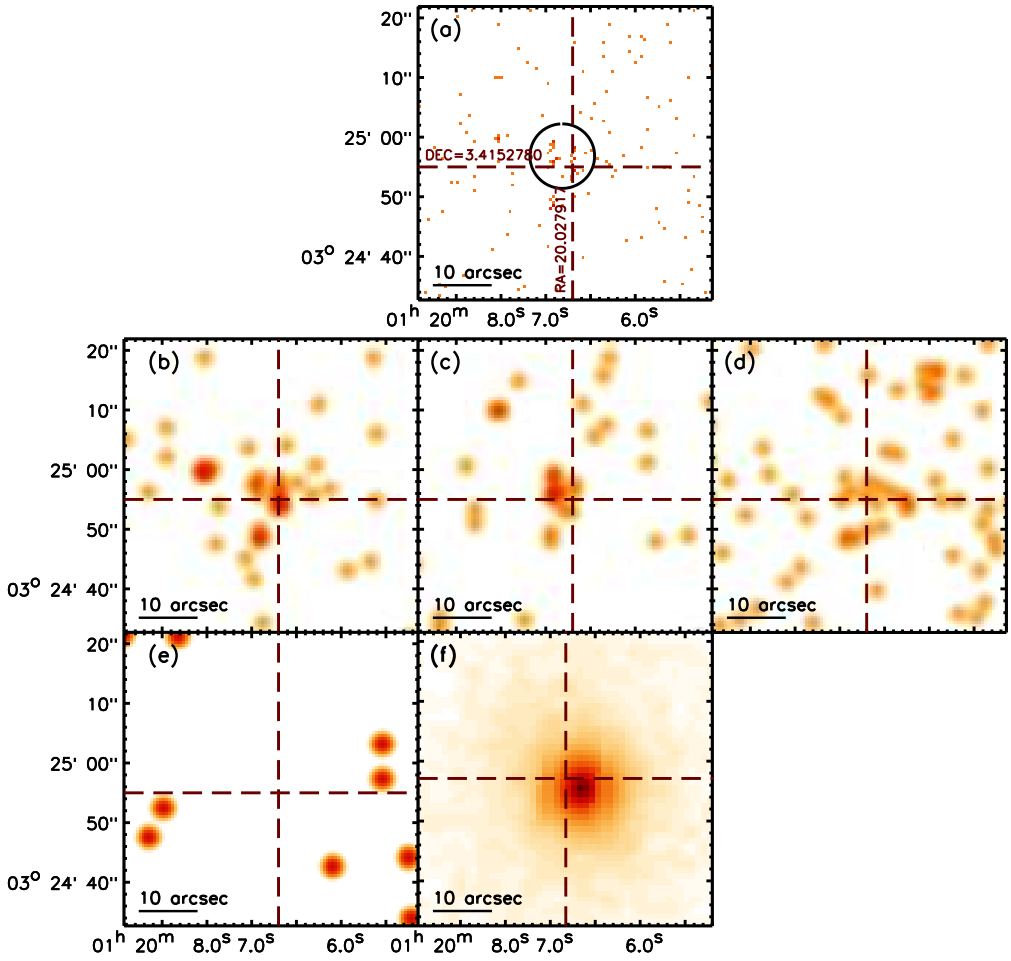

Figure C.3: *NGC 474*

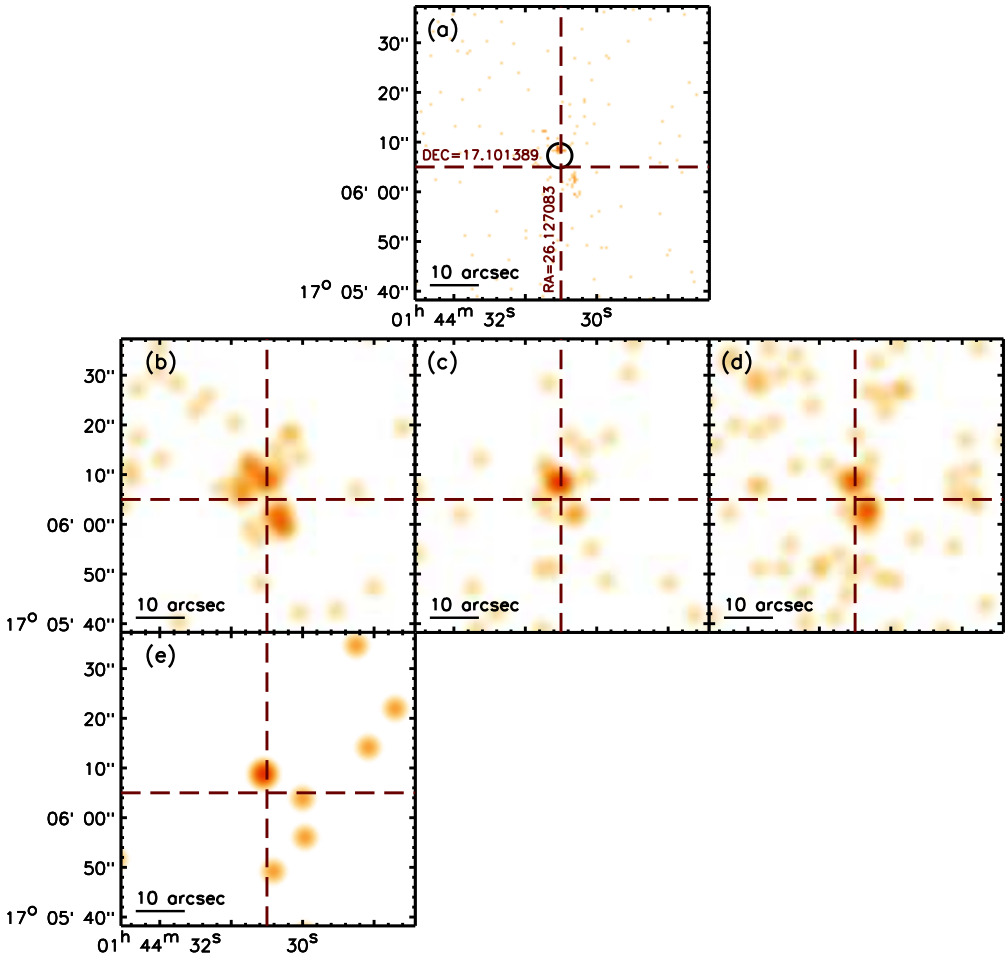

Figure C.4: *IIIZW035*

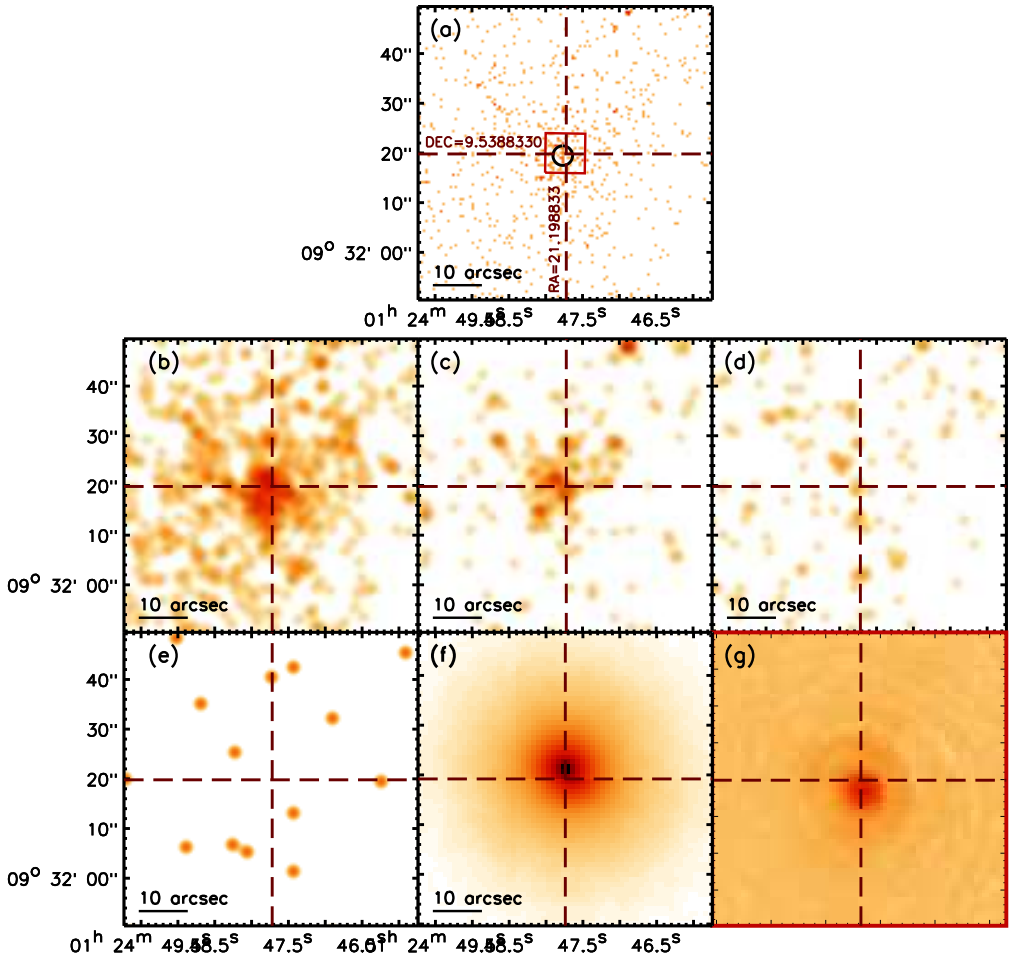

Figure C.5: *UGC 968*

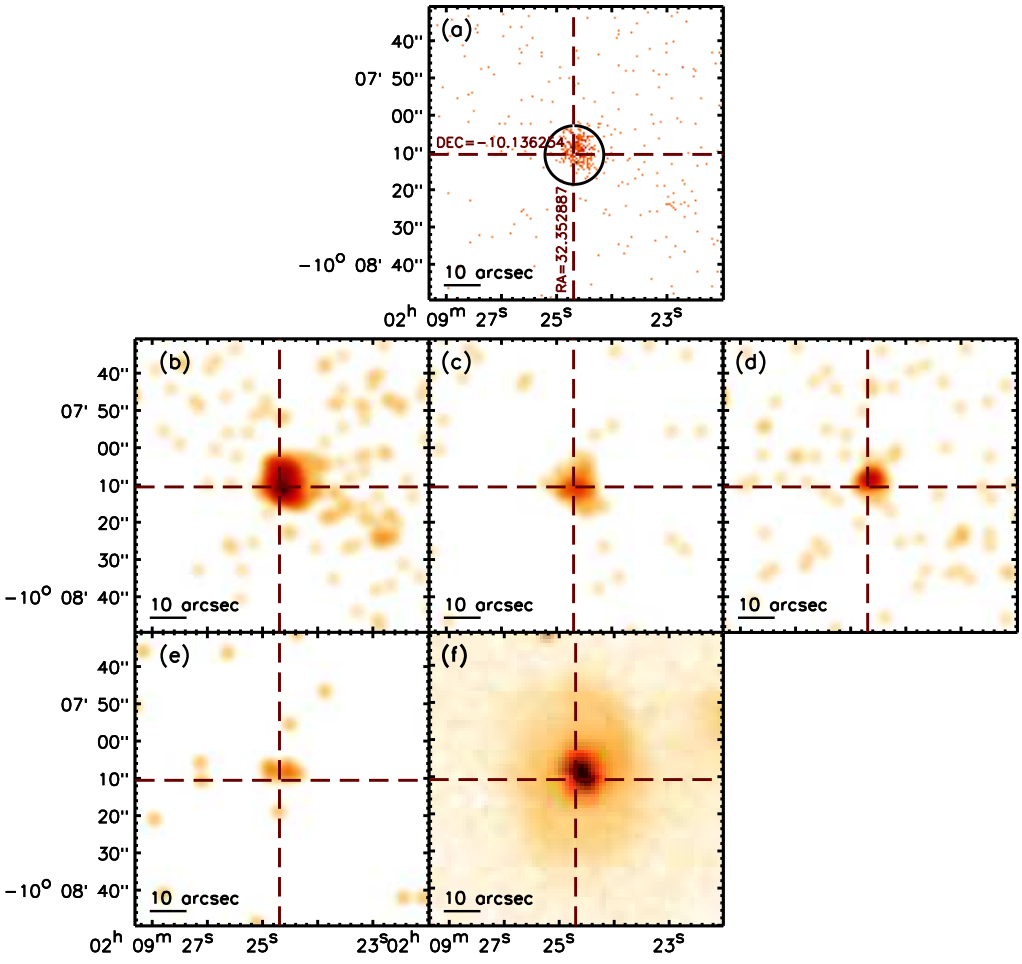

Figure C.6: *ARP318A*

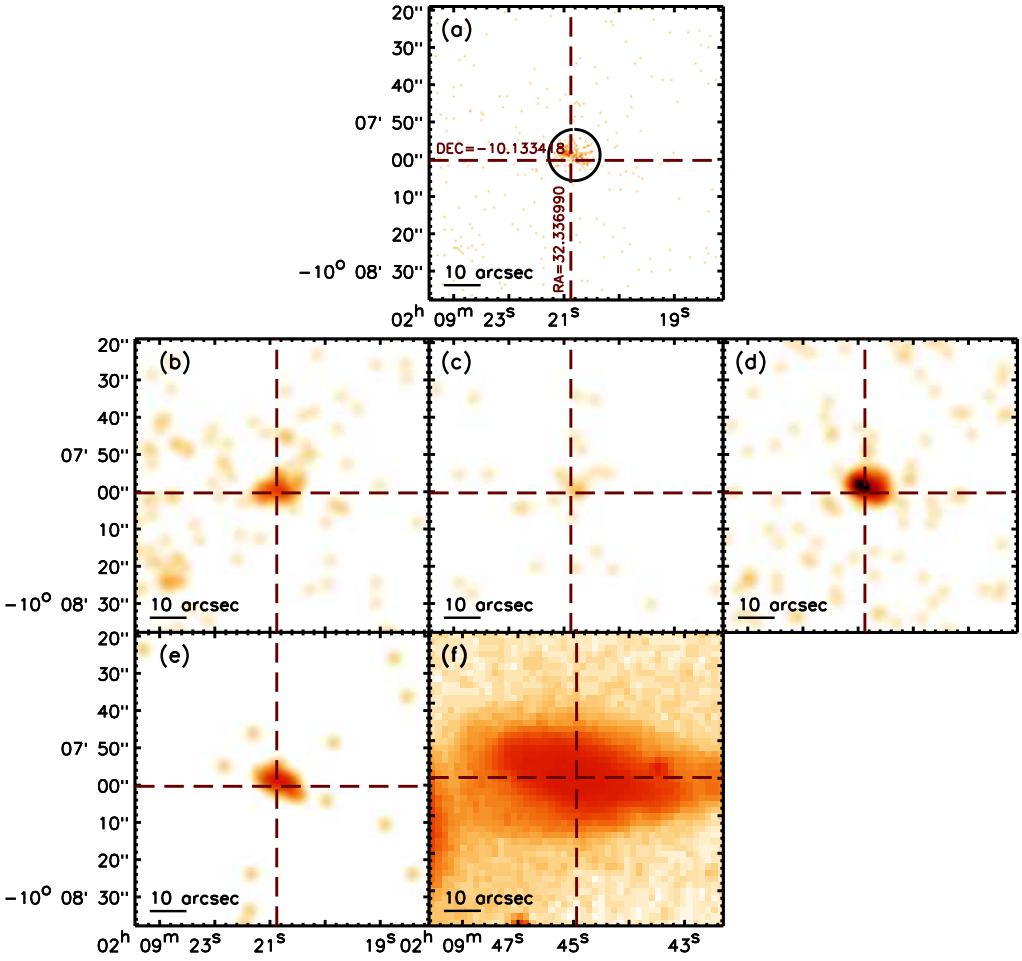

Figure C.7: *ARP318B*

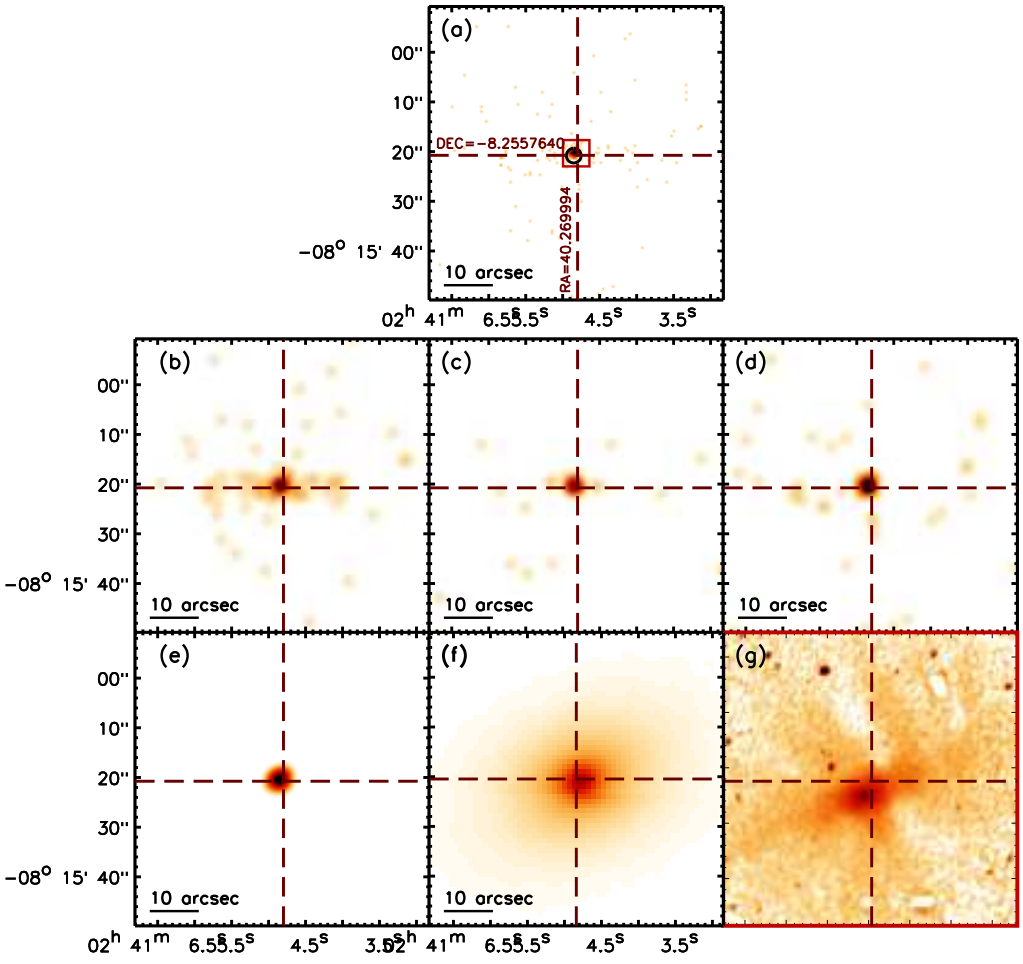

Figure C.8: *NGC1052*

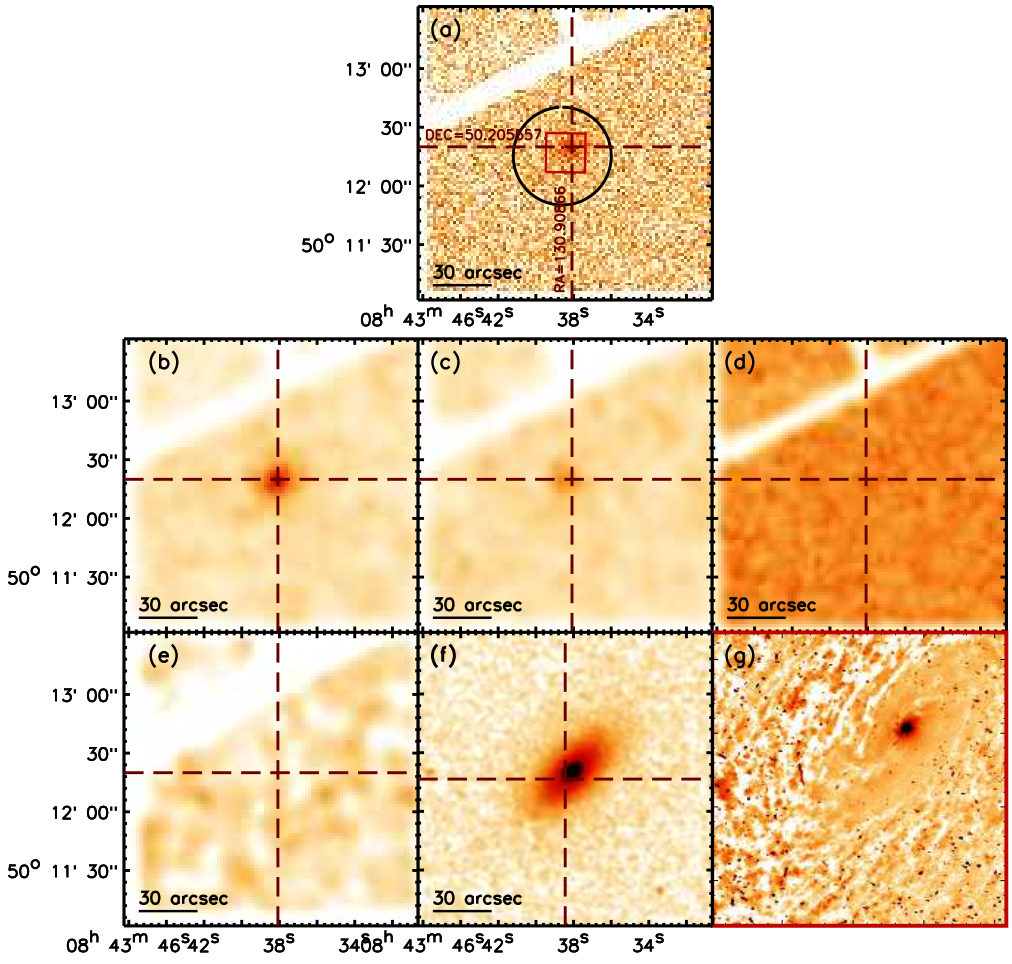

Figure C.9: *NGC2639 (XMM-Newton)*

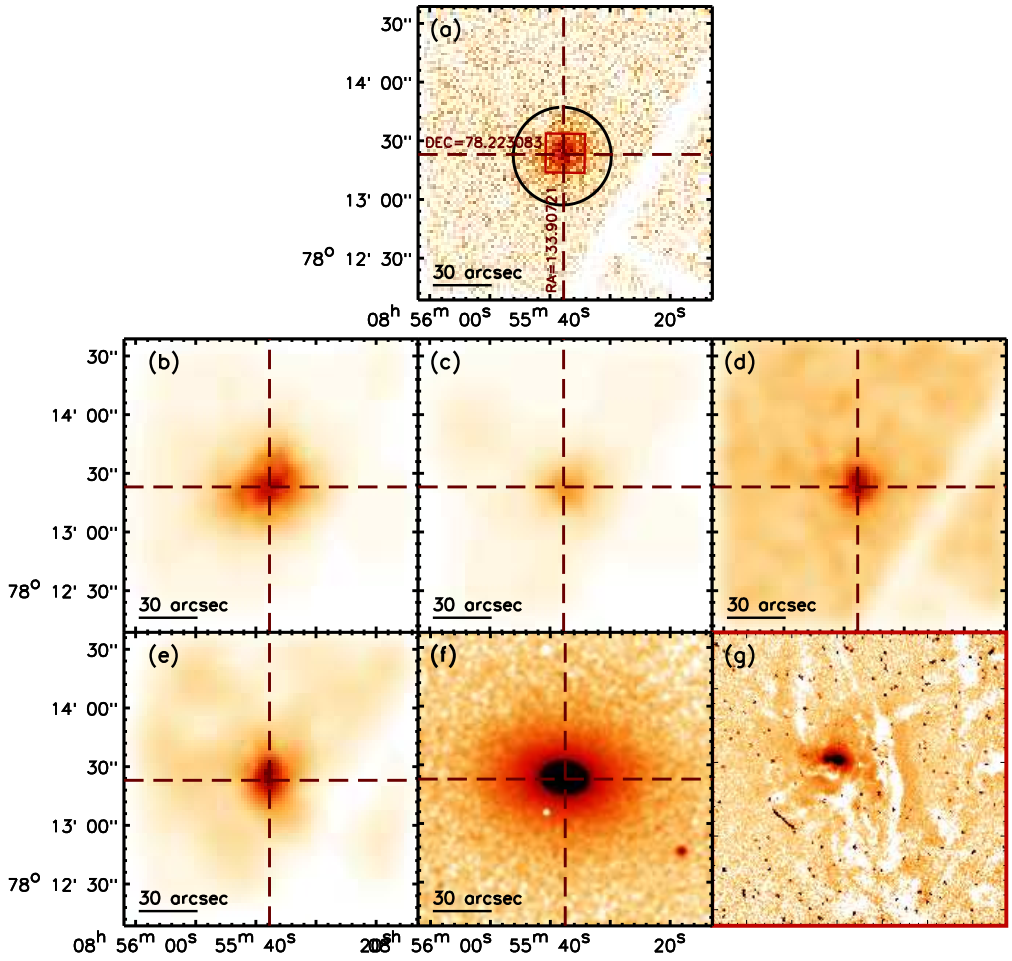

Figure C.10: *NGC2655 (XMM-Newton)*

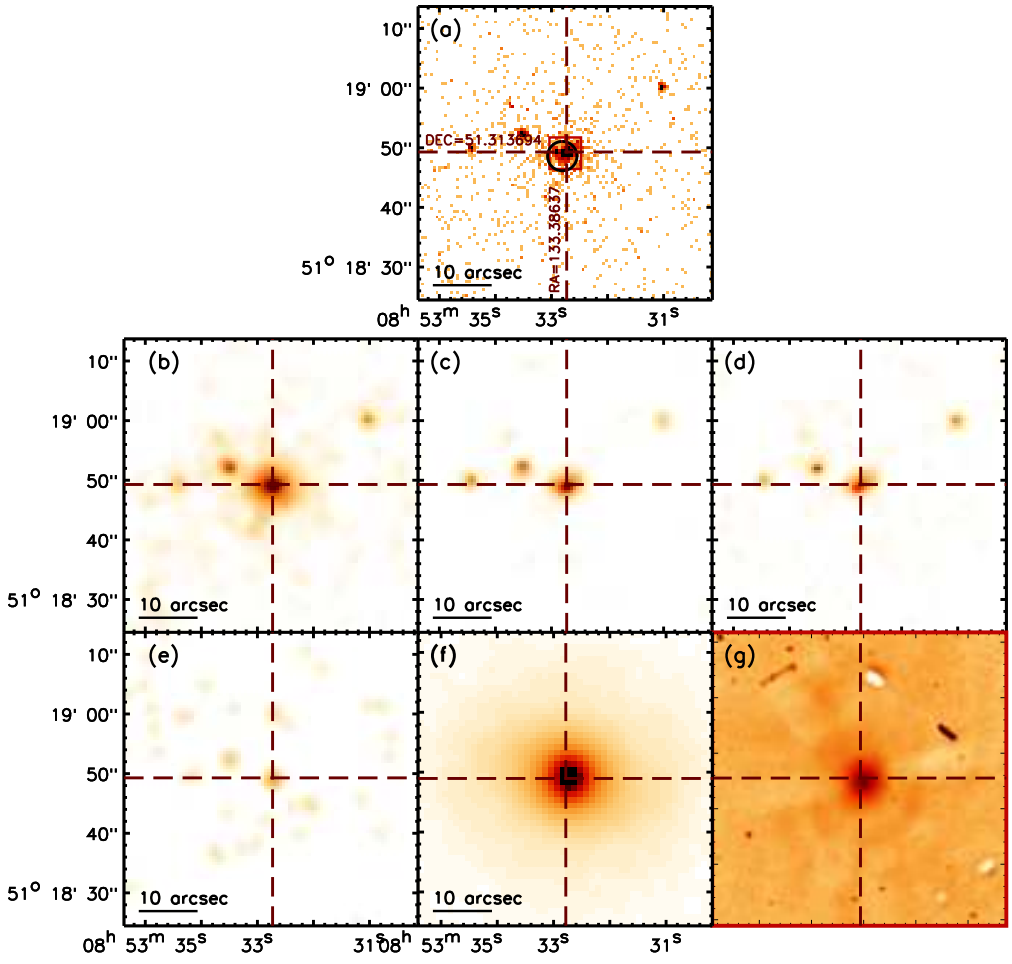

Figure C.11: *NGC2681*

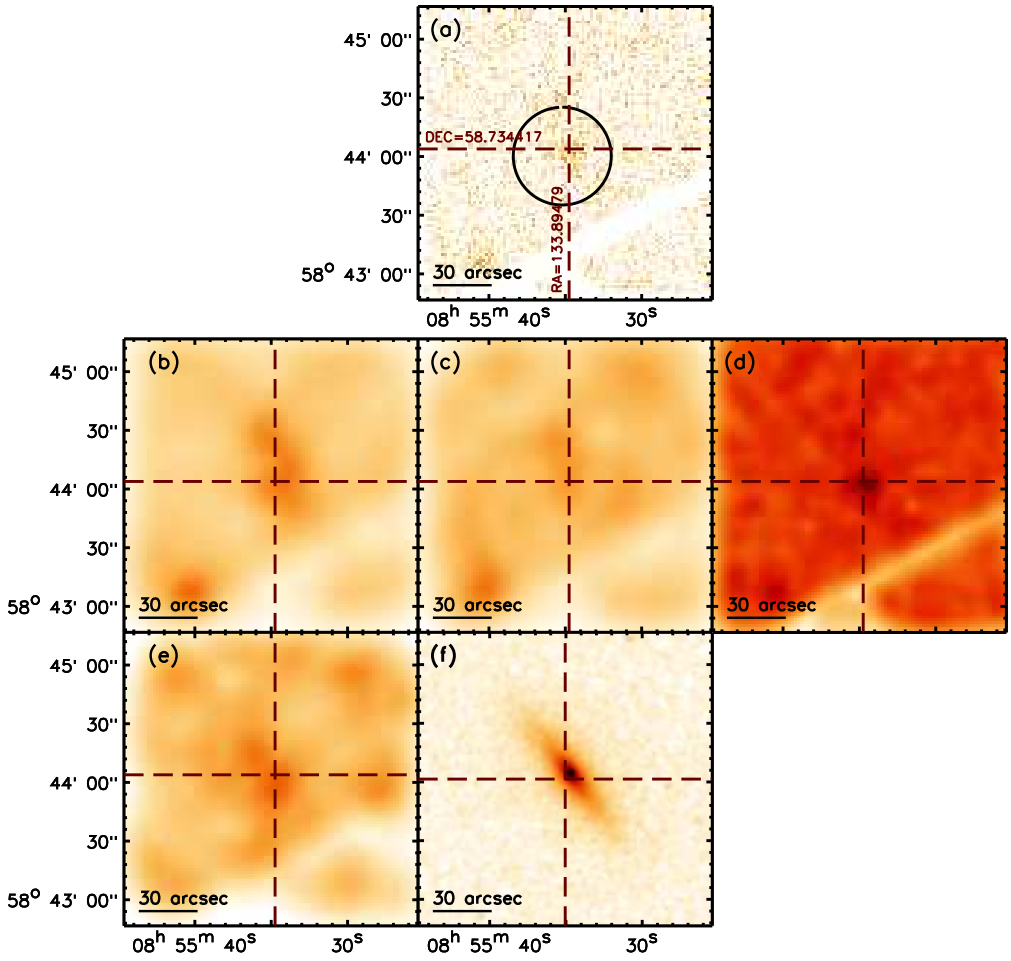

Figure C.12: *NGC2685 (XMM-Newton)*

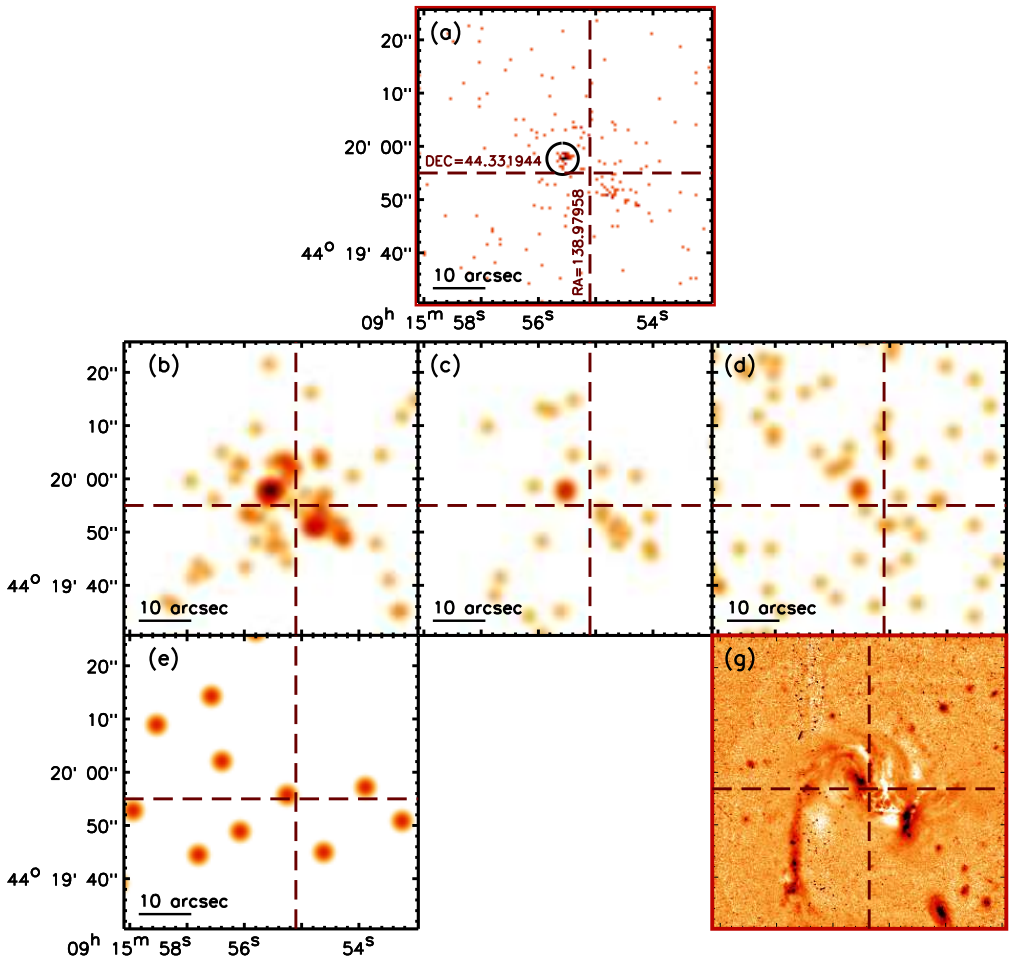

Figure C.13: *UGC4881*

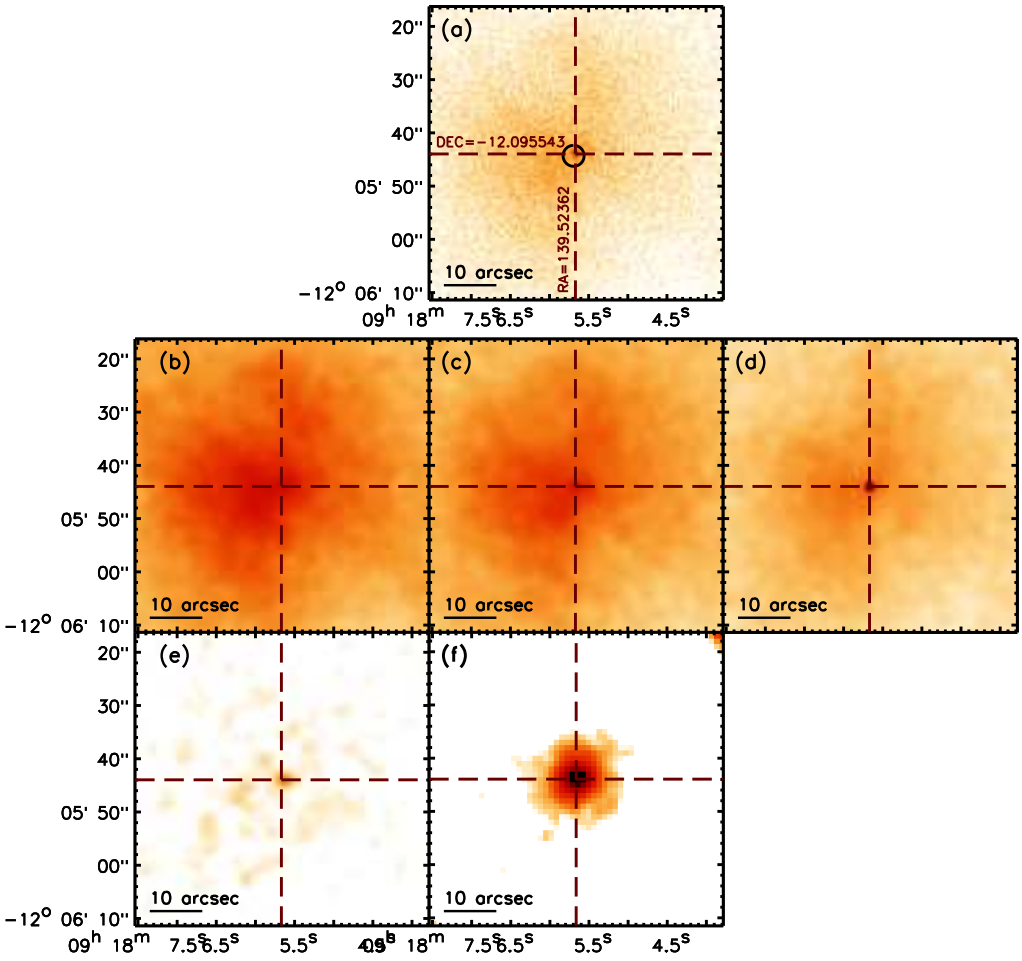

Figure C.14: *3C218*

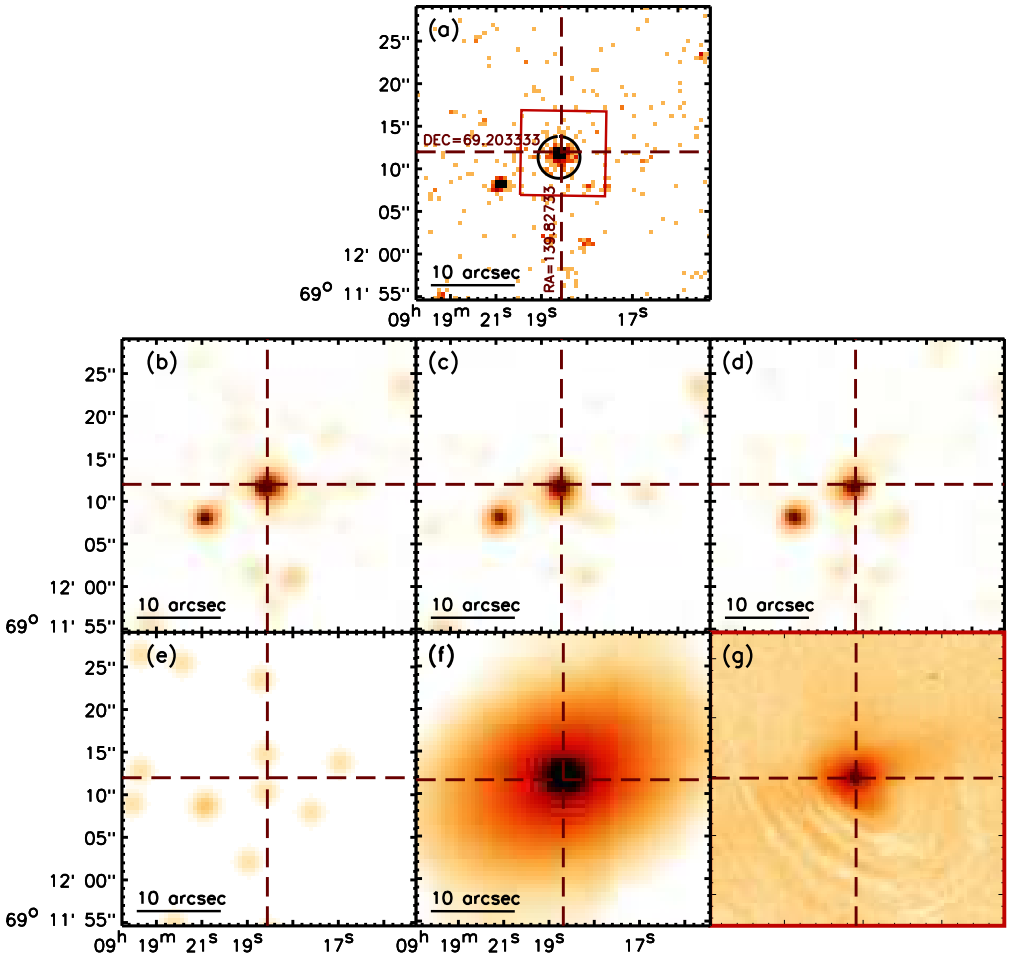

Figure C.15: *NGC2787*

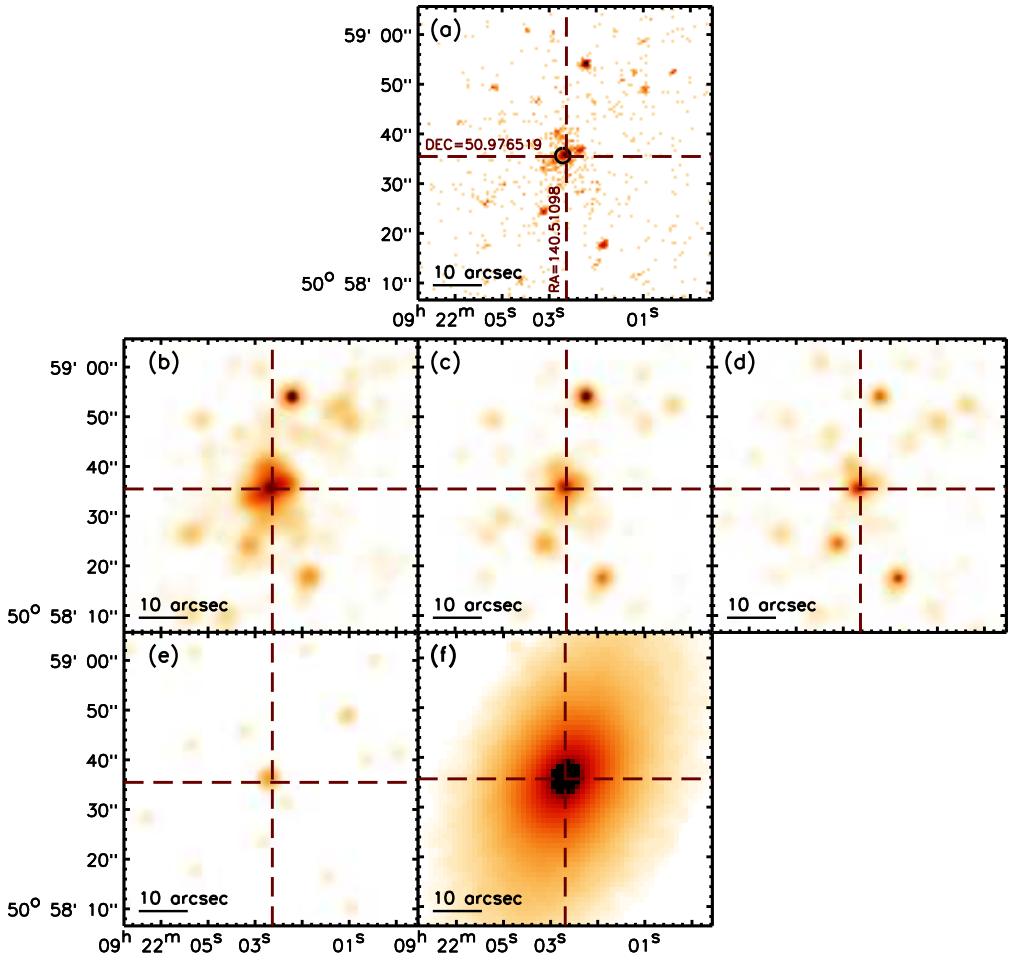

Figure C.16: *NGC2841*

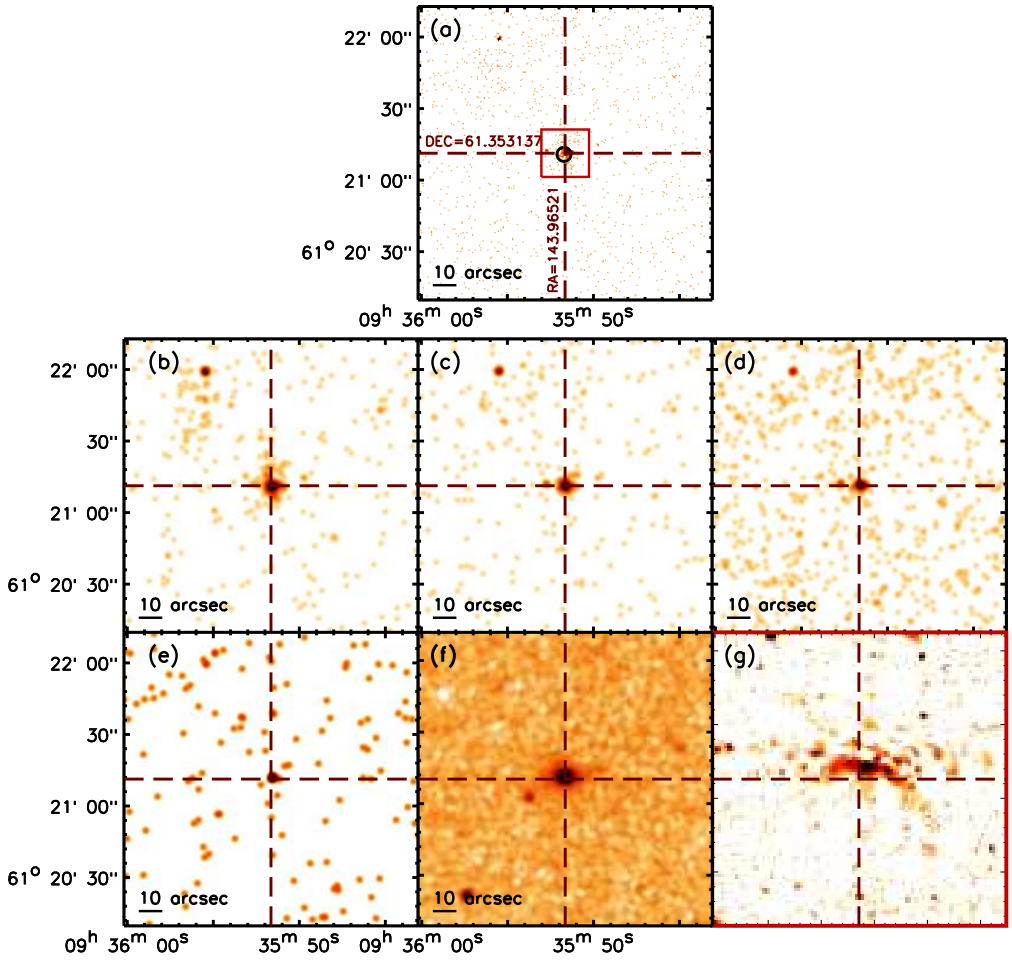

Figure C.17: *UGC05101*

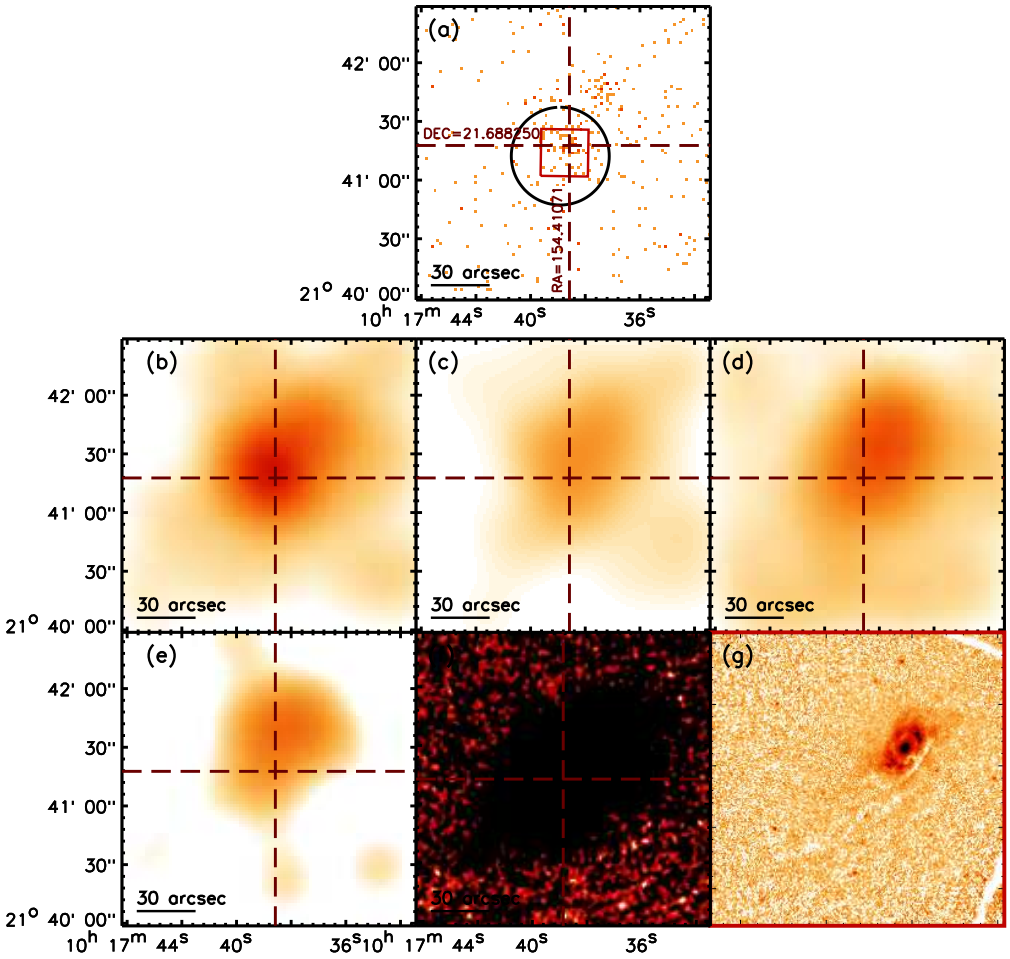

Figure C.18: *NGC3185 (XMM-Newton)*

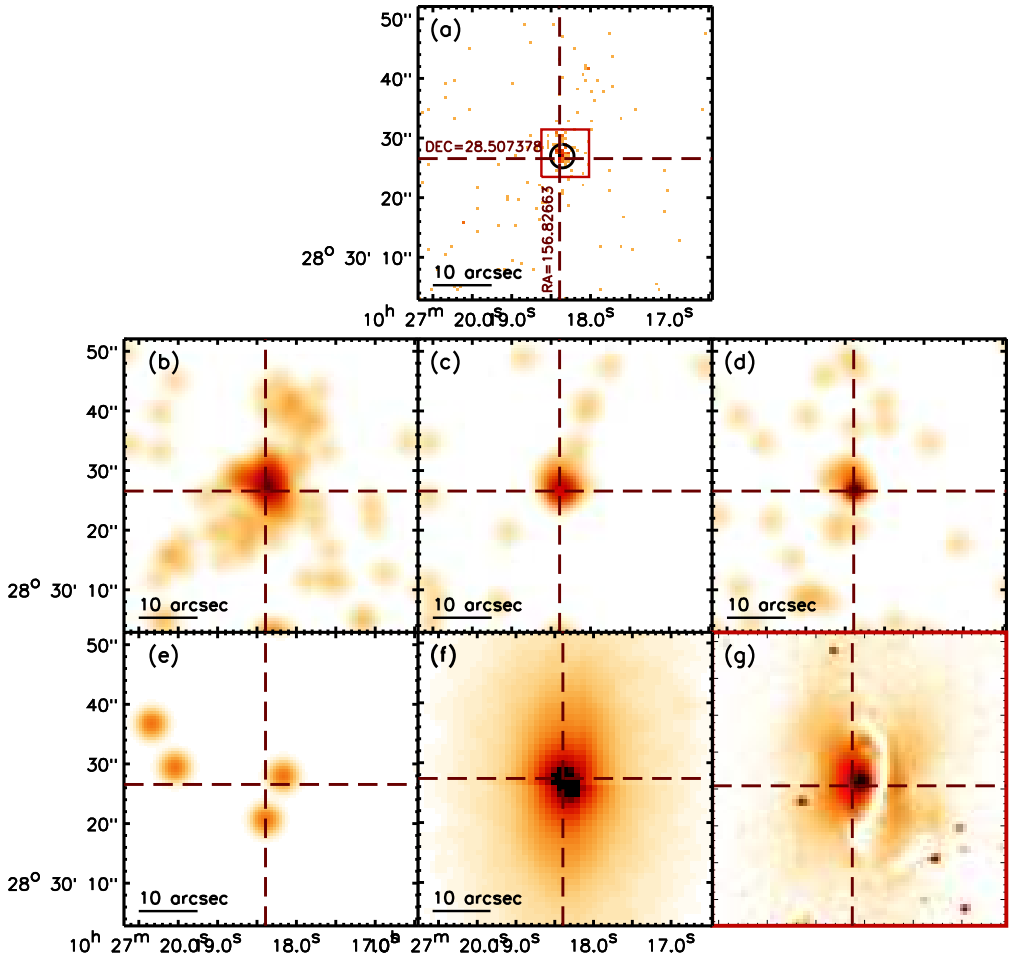

Figure C.19: *NGC3245*

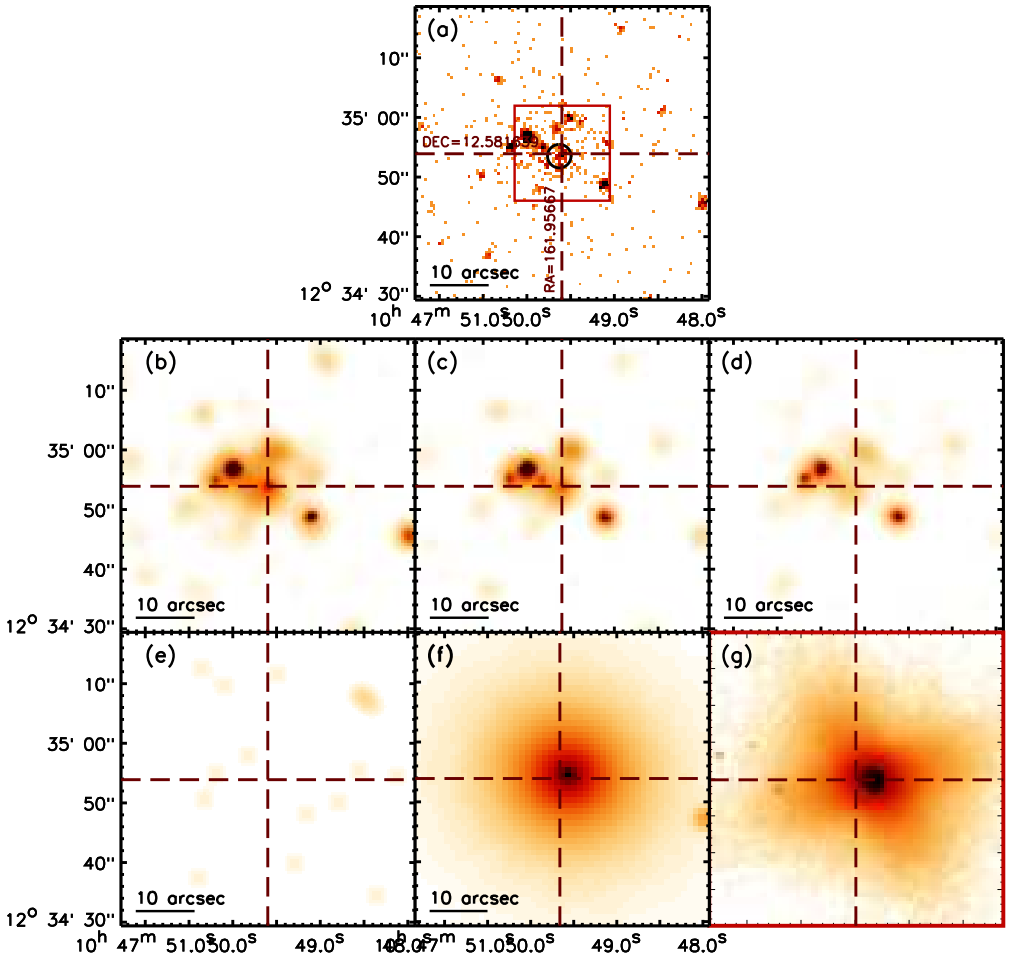

Figure C.20: *NGC3379*

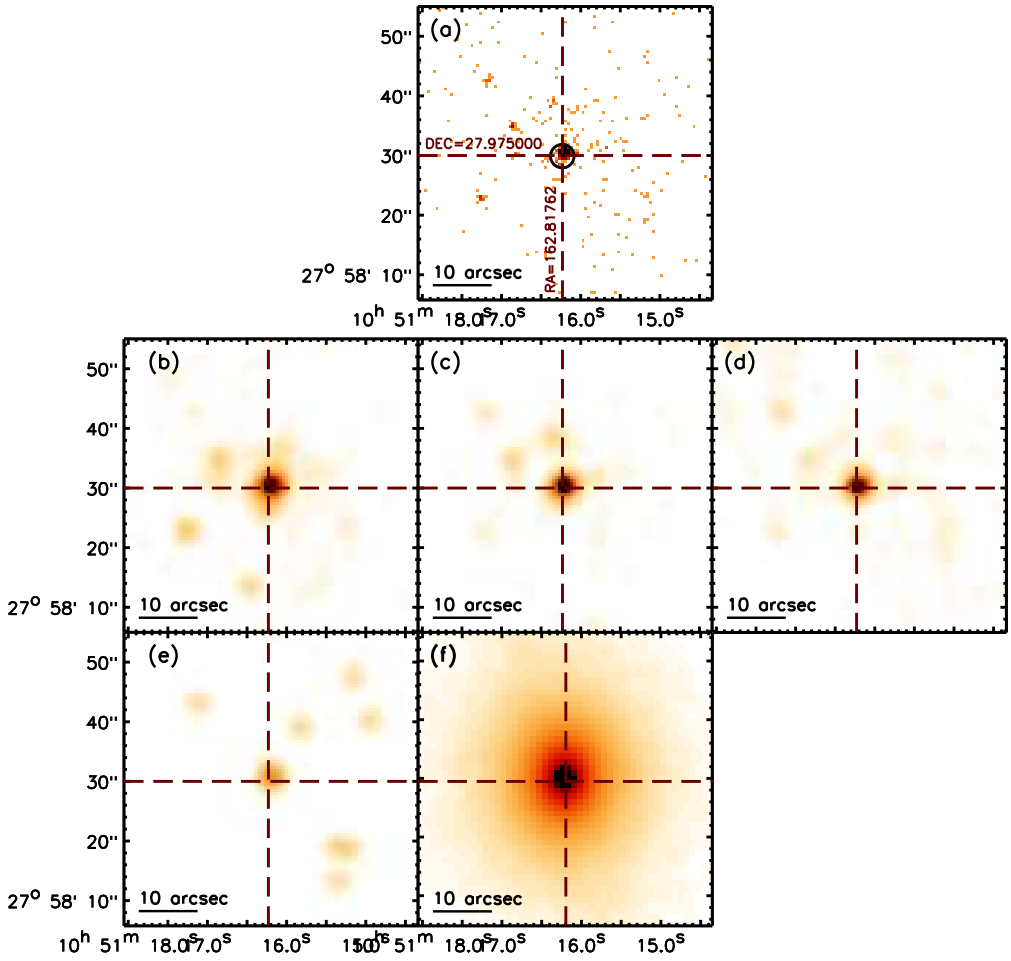

Figure C.21: *UGC5959*

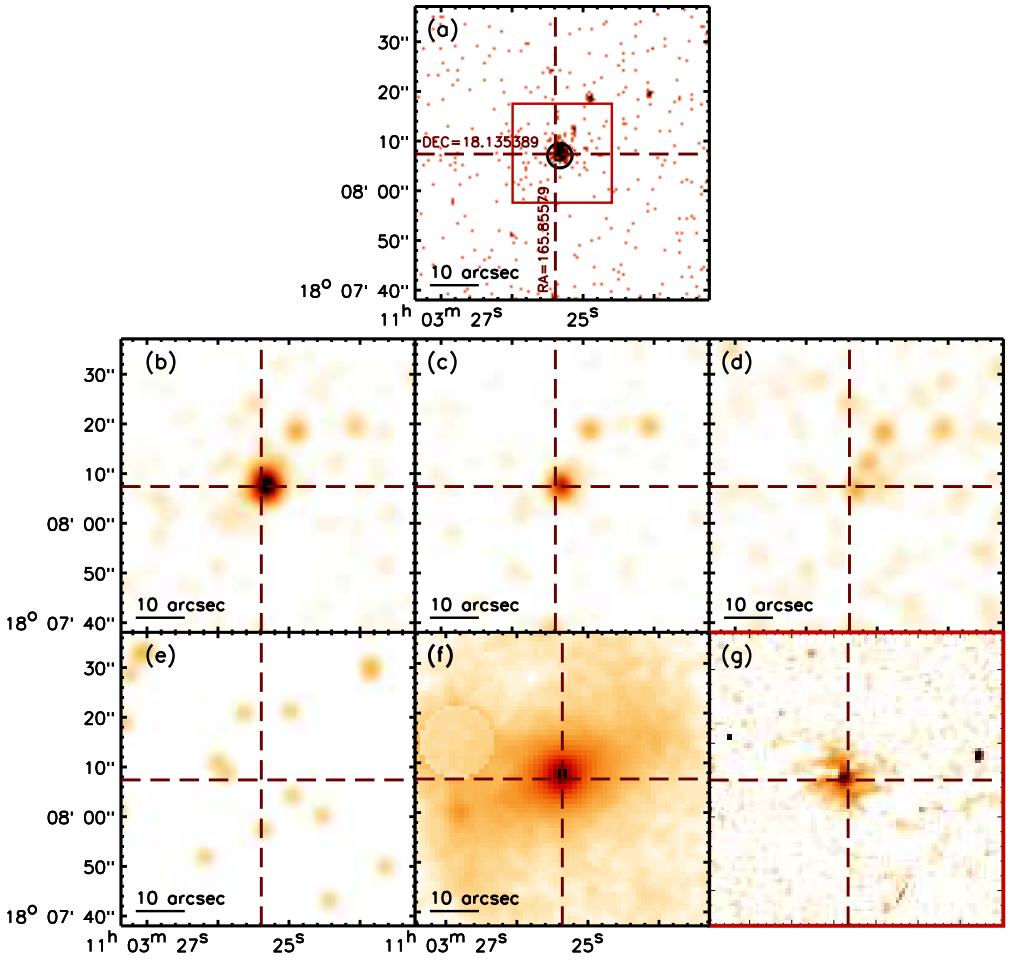

Figure C.22: *NGC3507*

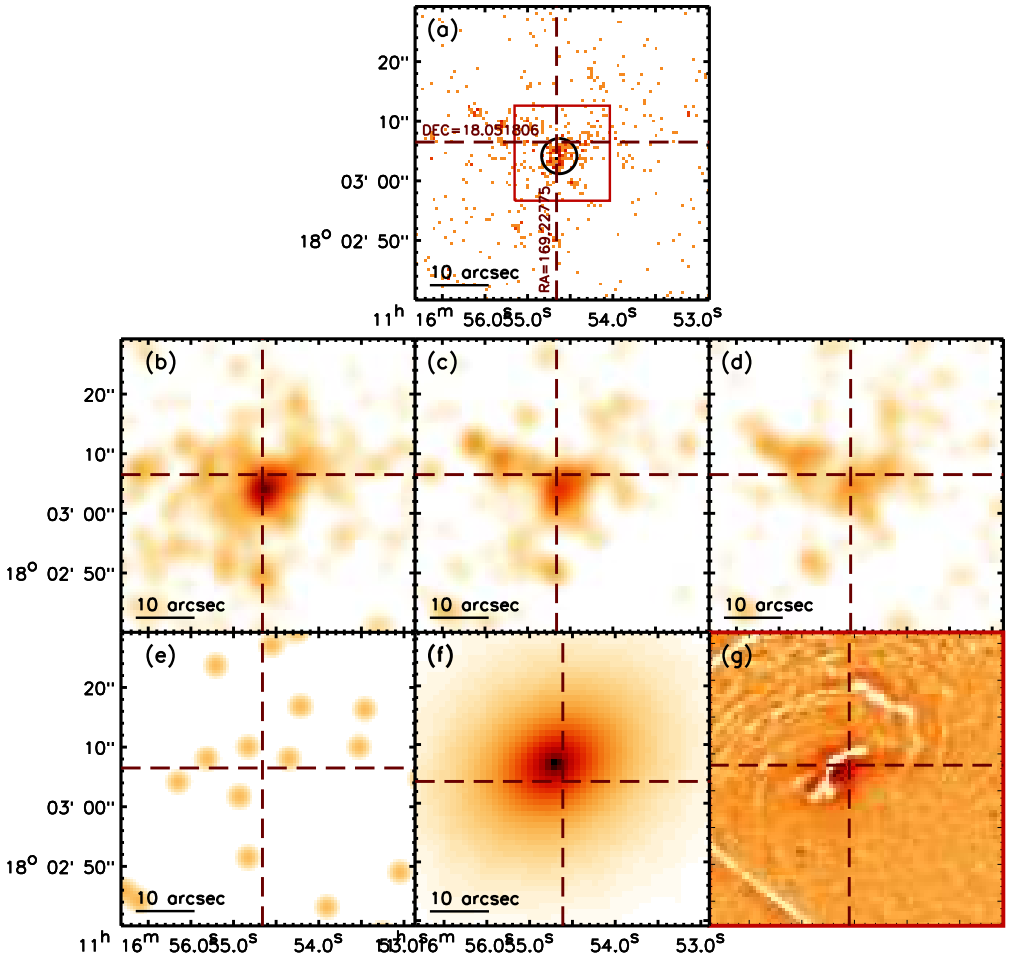

Figure C.23: *NGC3607*

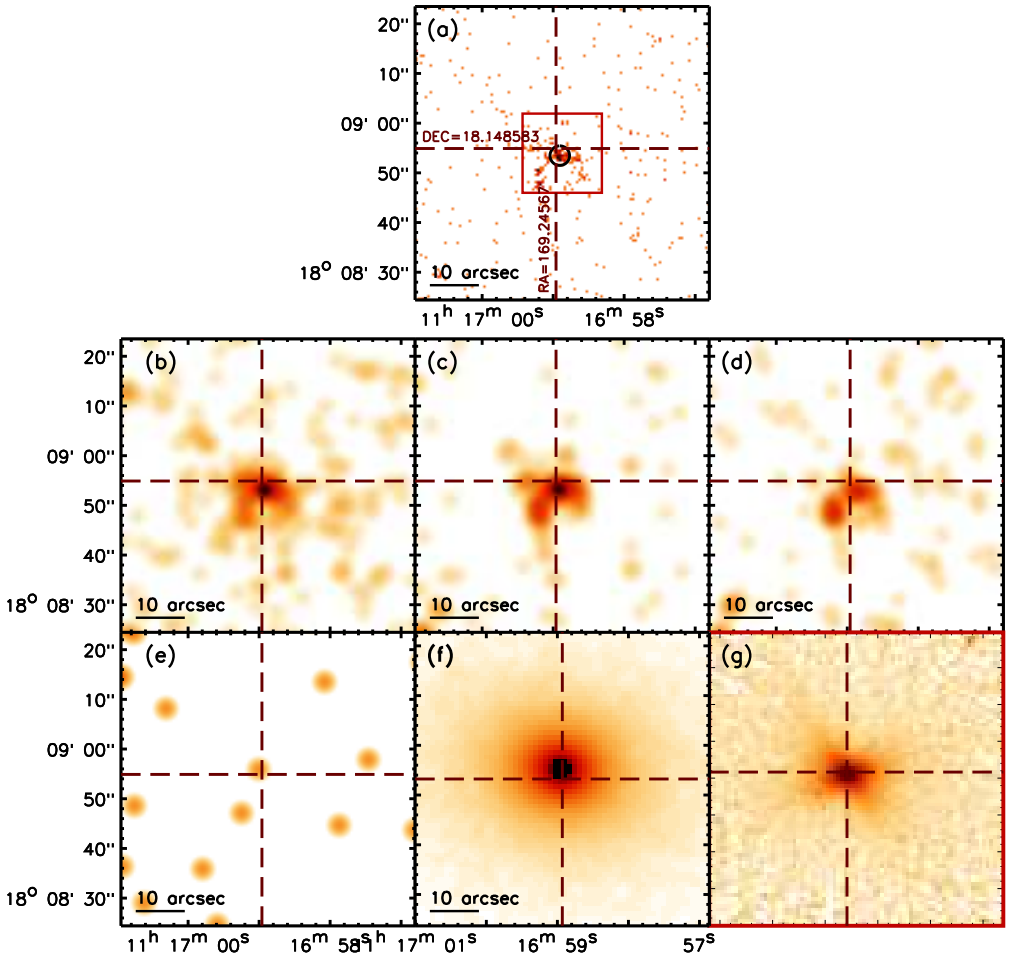

Figure C.24: *NGC3608*

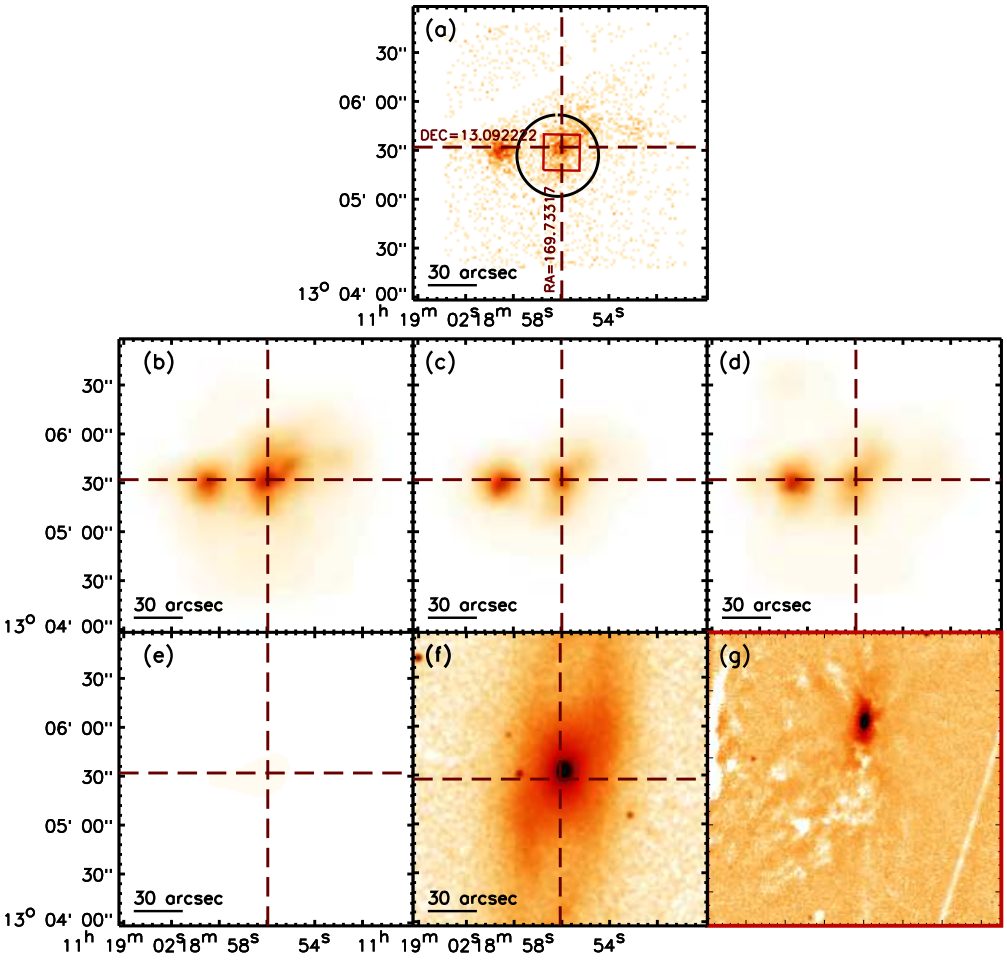

Figure C.25: *NGC3623 (XMM-Newton)*

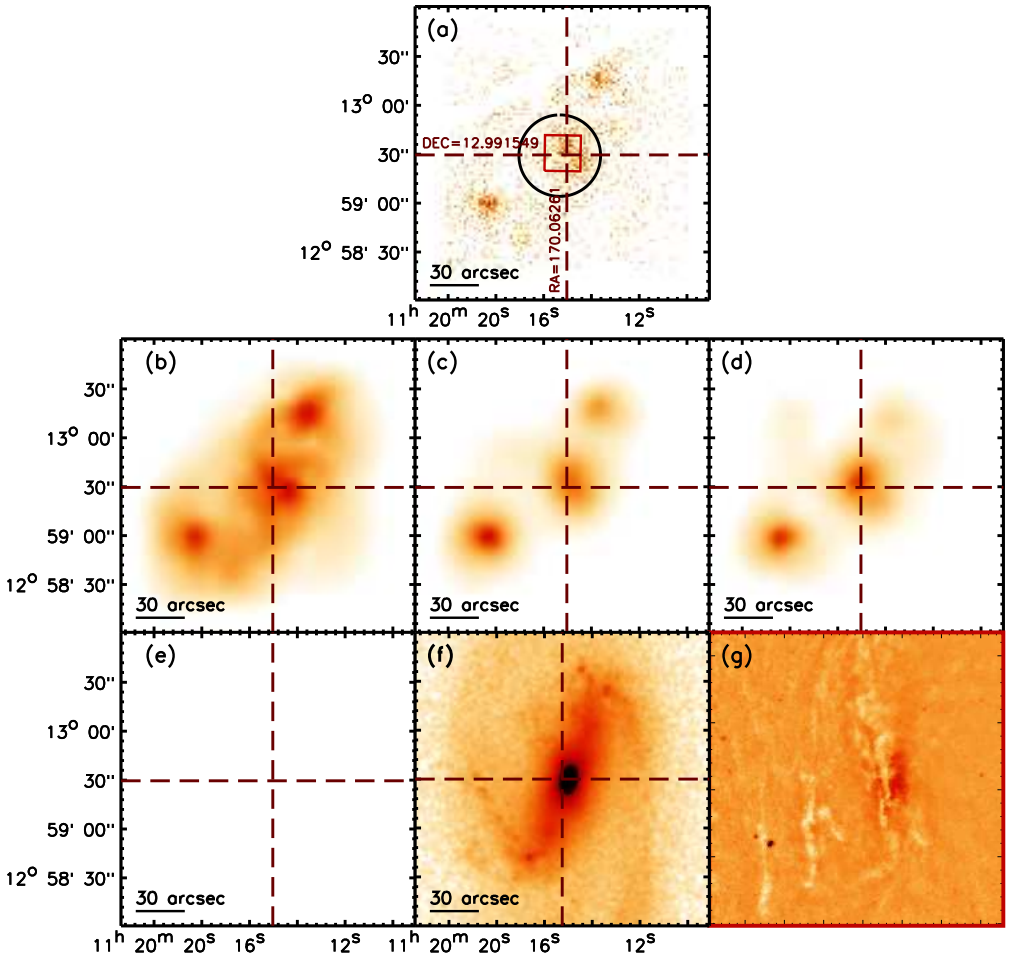

Figure C.26: *NGC3627 (XMM-Newton)*

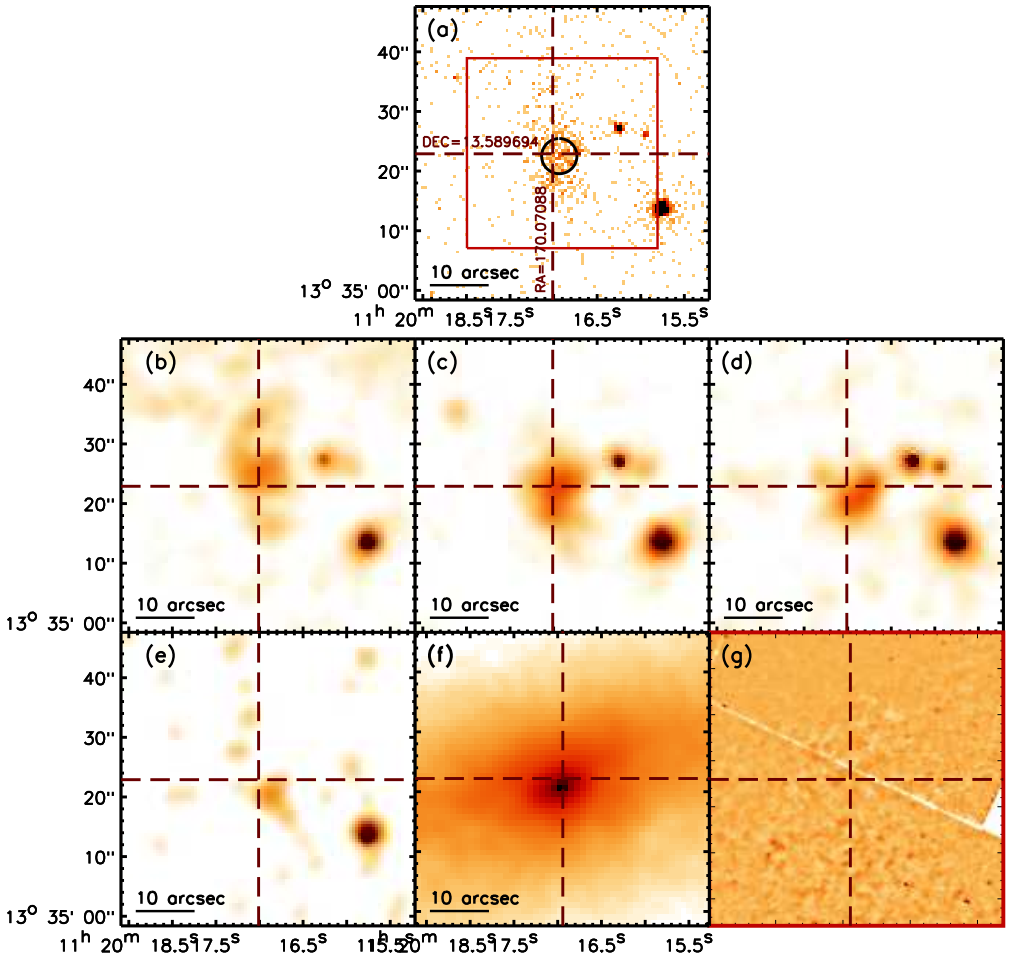

Figure C.27: *NGC3628*

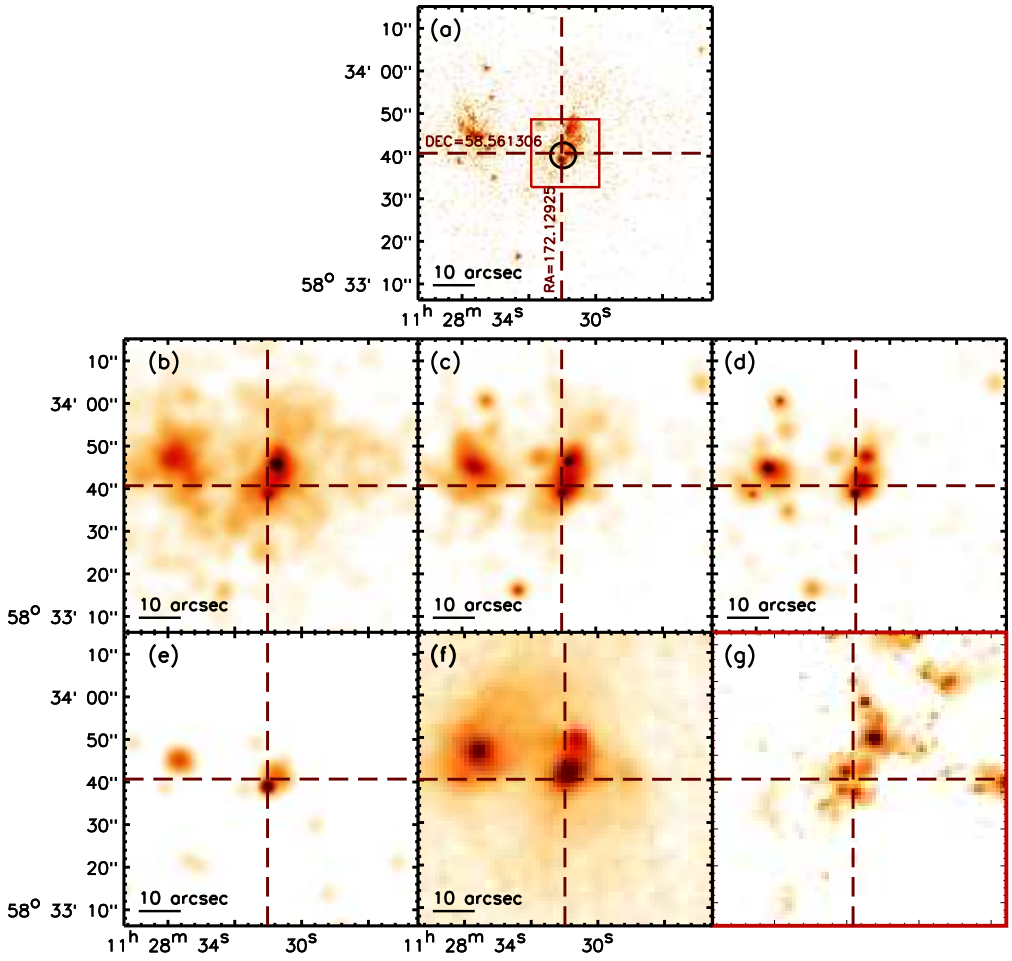

Figure C.28: *NGC3690*

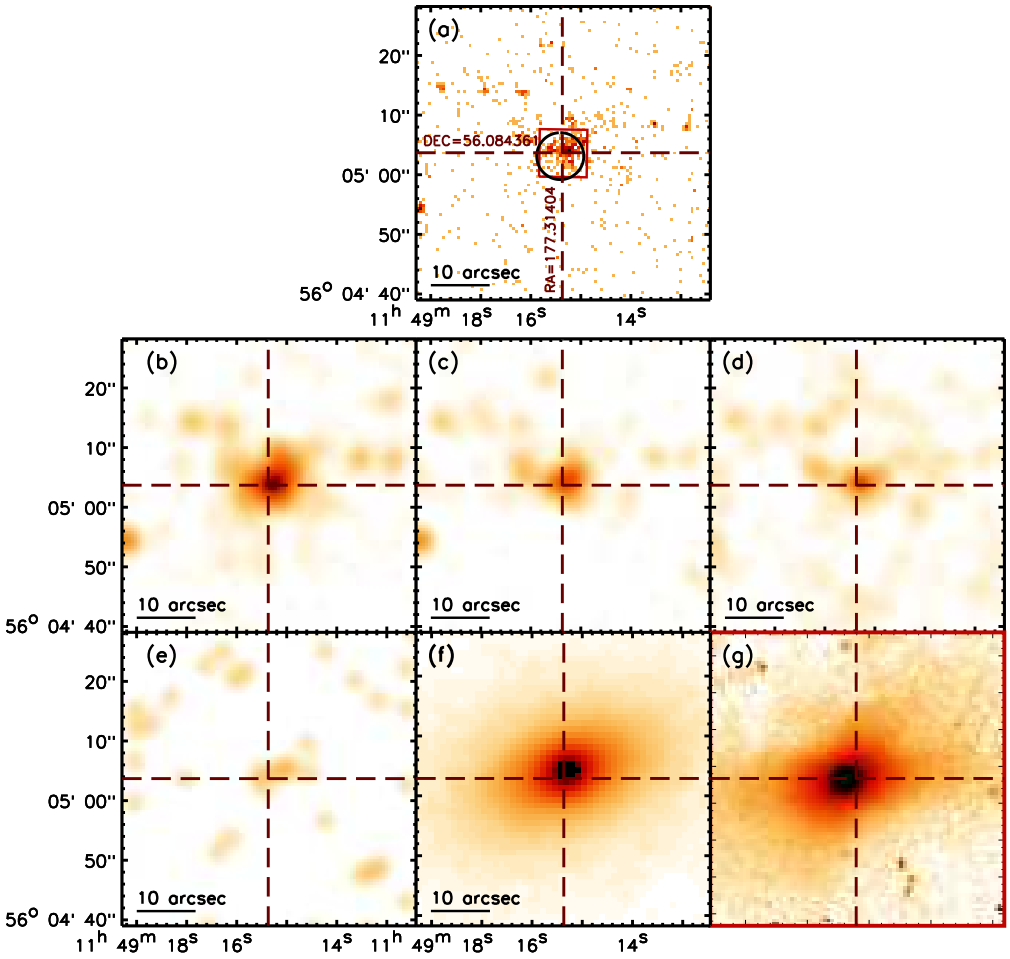

Figure C.29: *NGC3898*

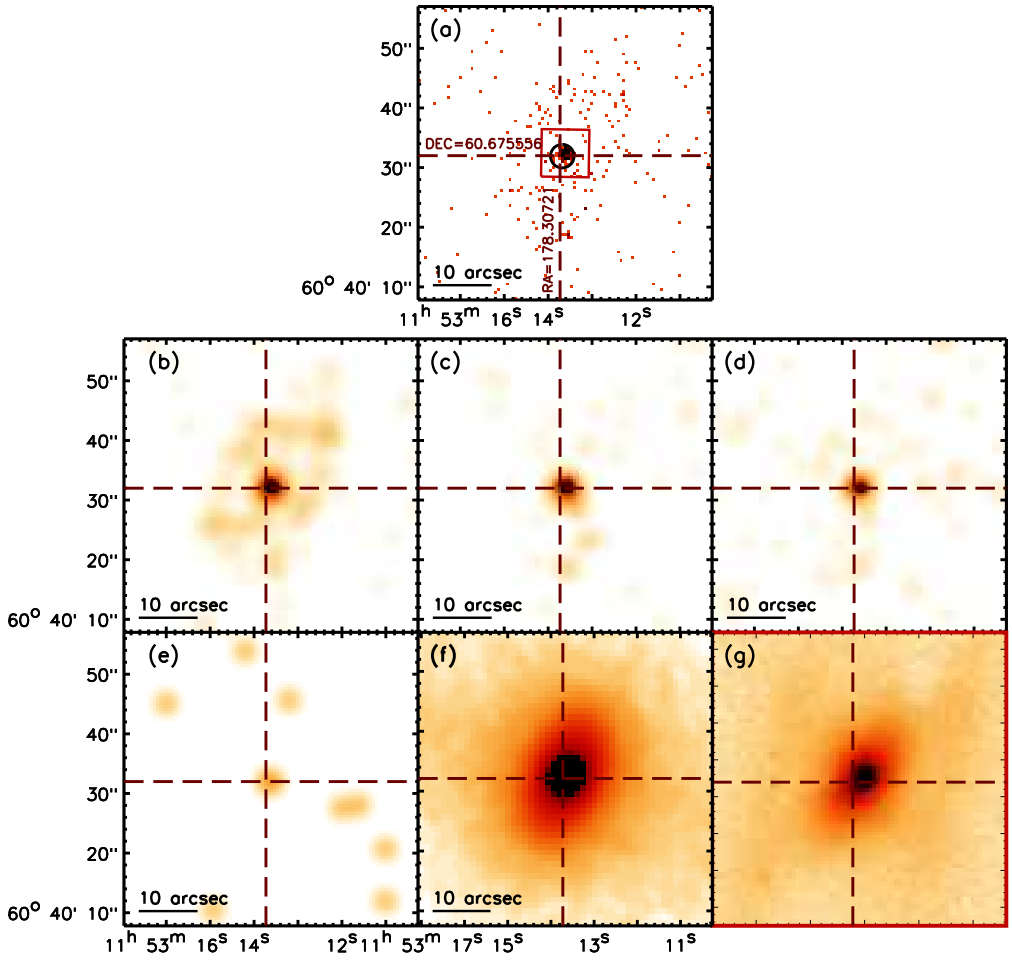

Figure C.30: *UGC6860*

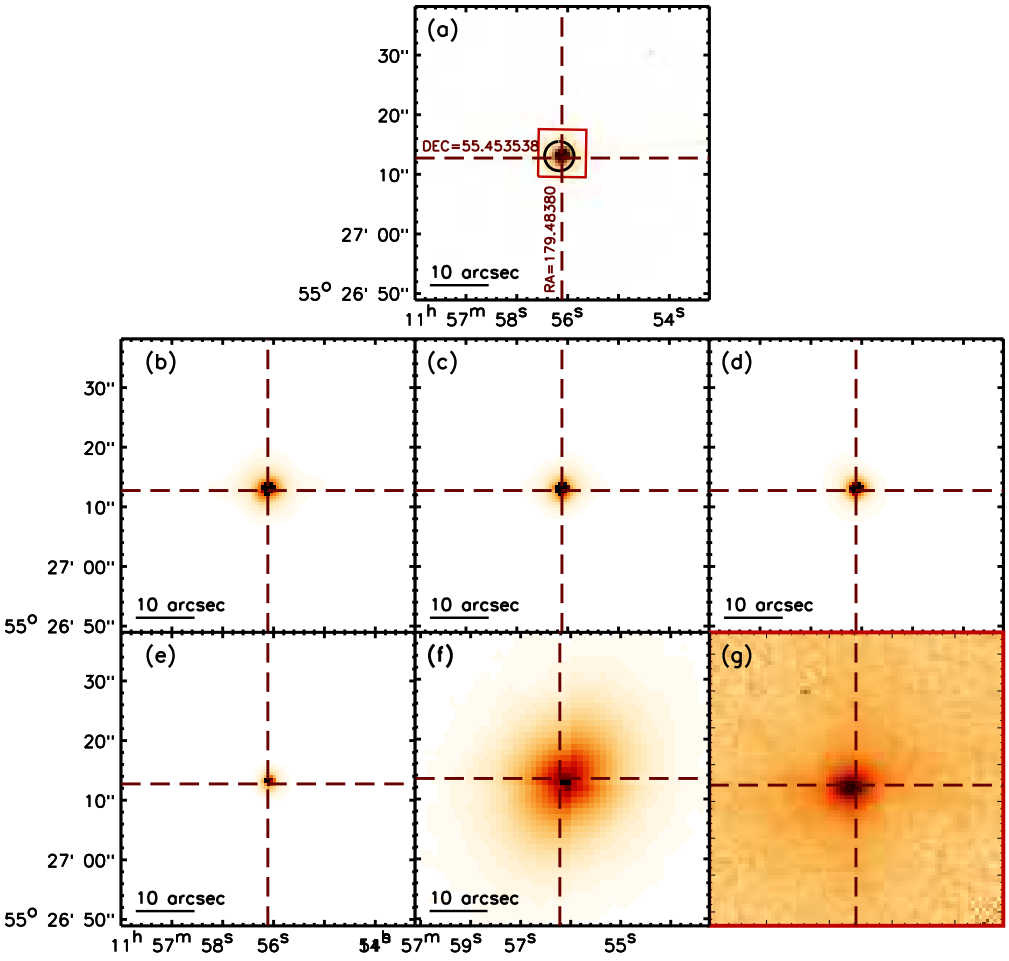

Figure C.31: *UGC6946*

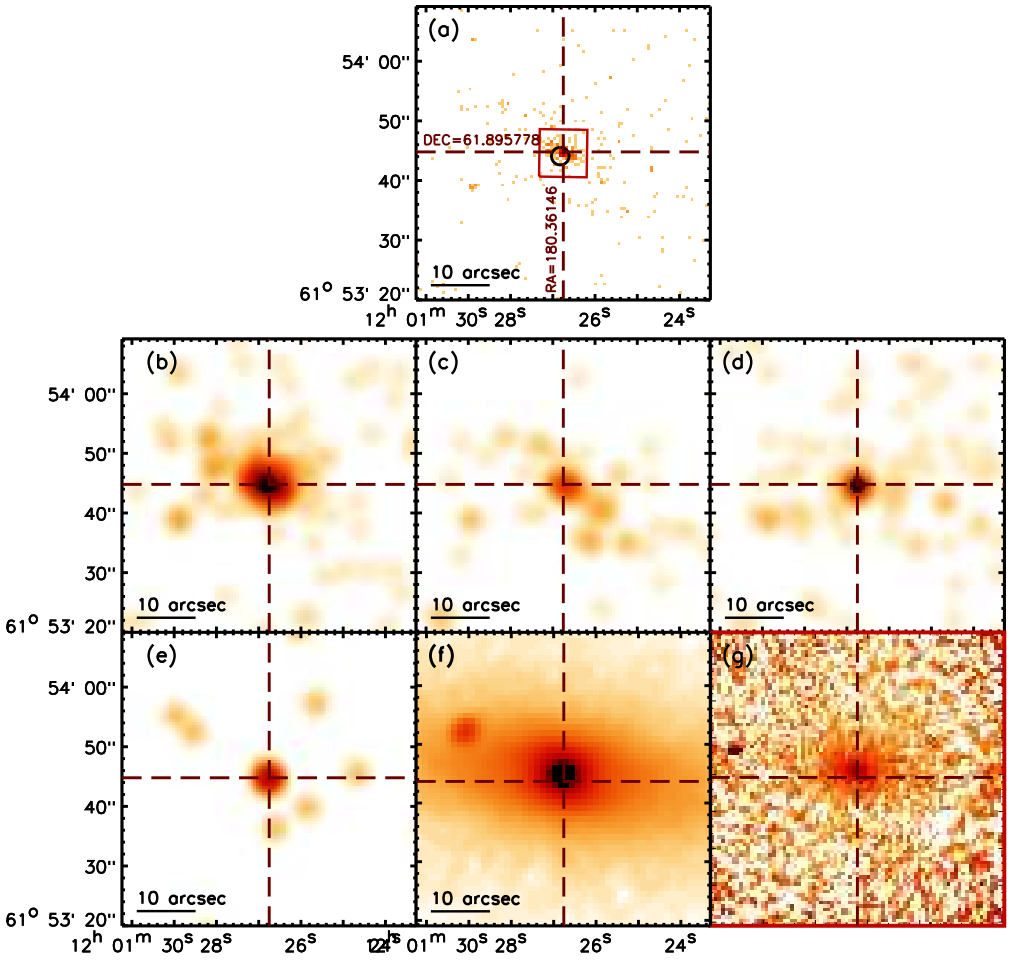

Figure C.32: *UGC7005*

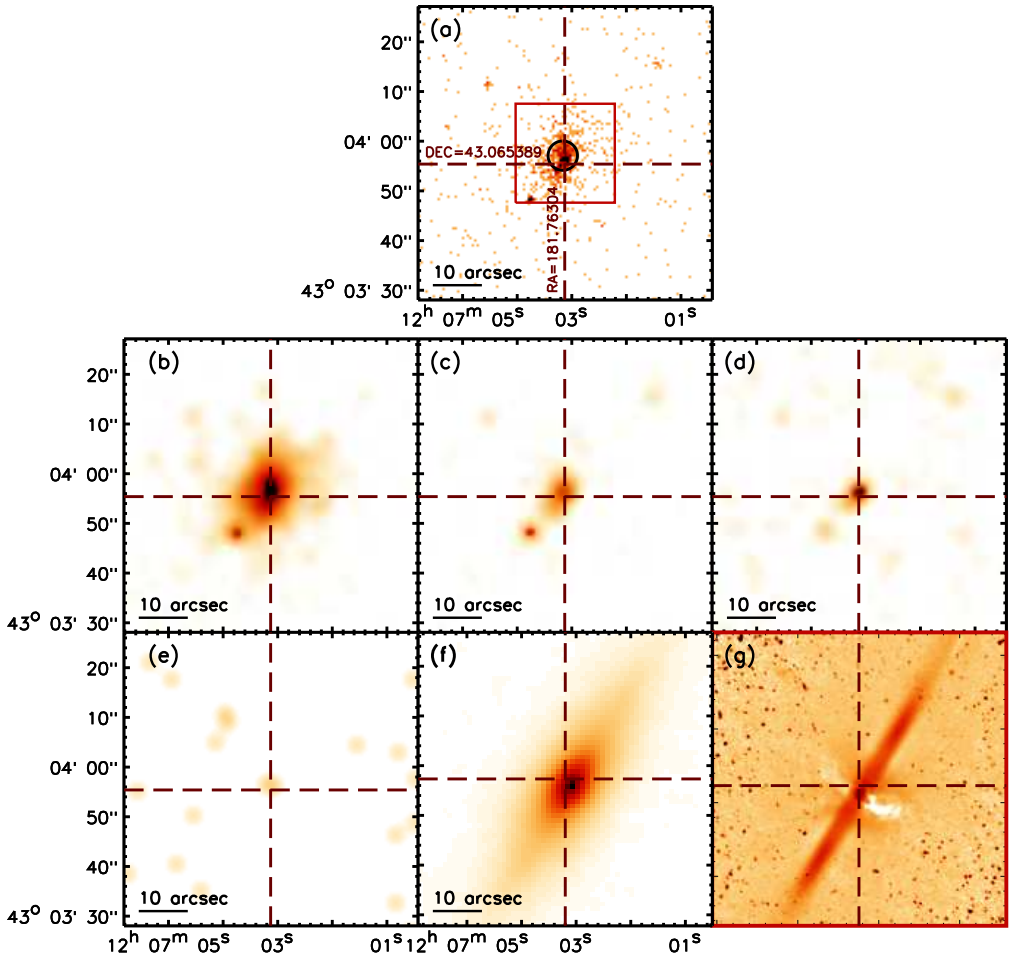

Figure C.33: *NGC4111*

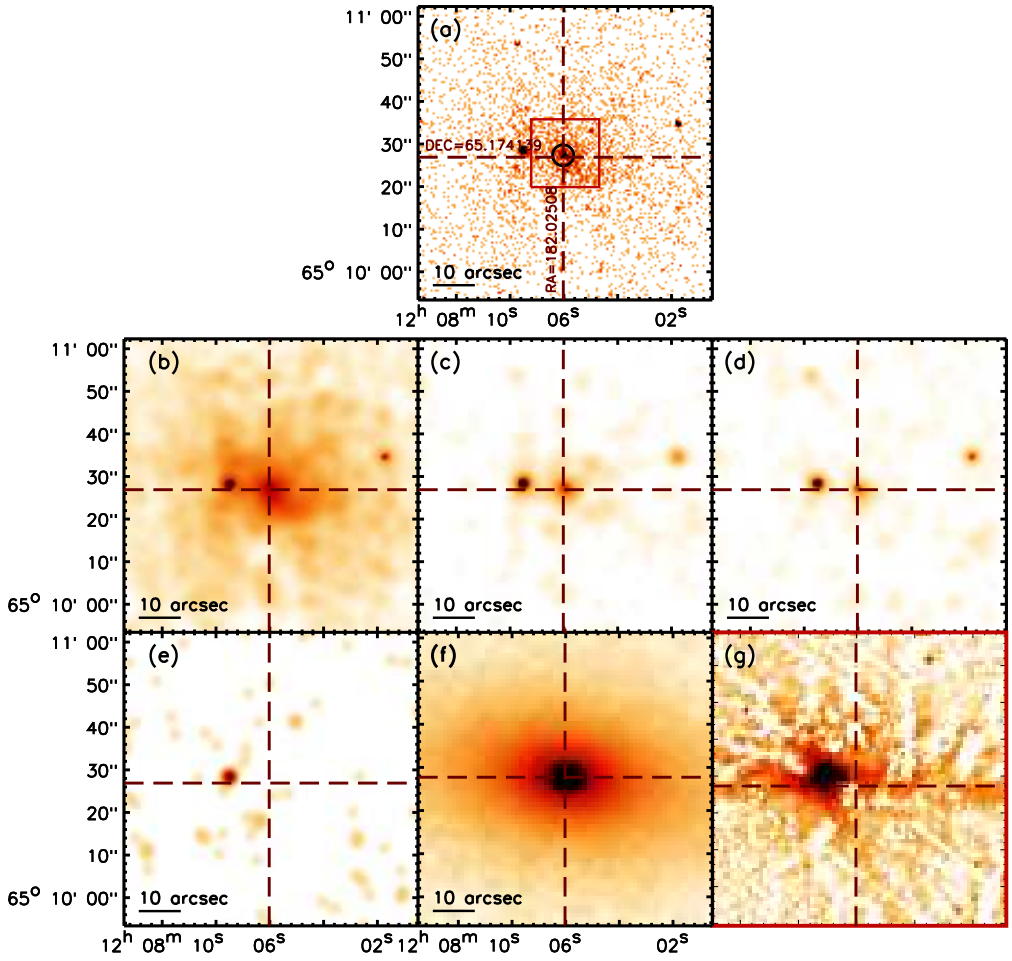

Figure C.34: *NGC4125*

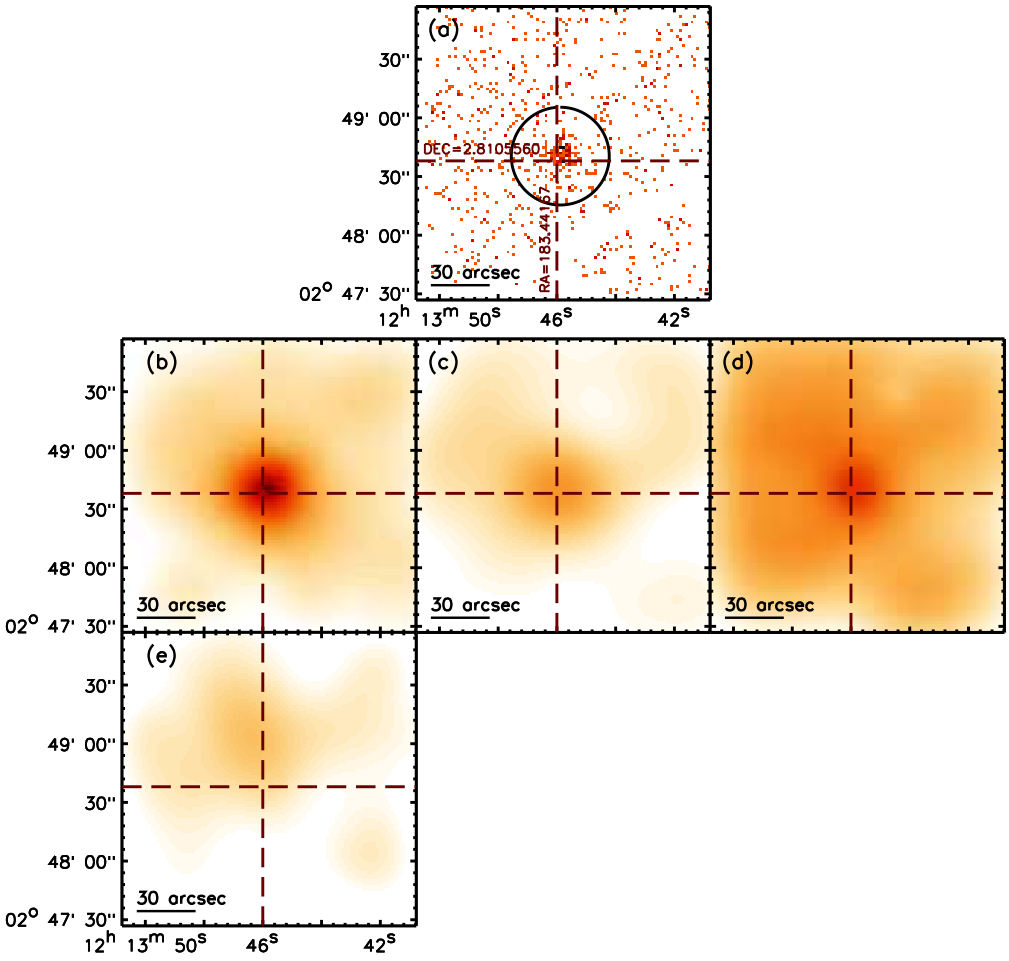

Figure C.35: *IRAS12112+0305 (XMM-Newton)*

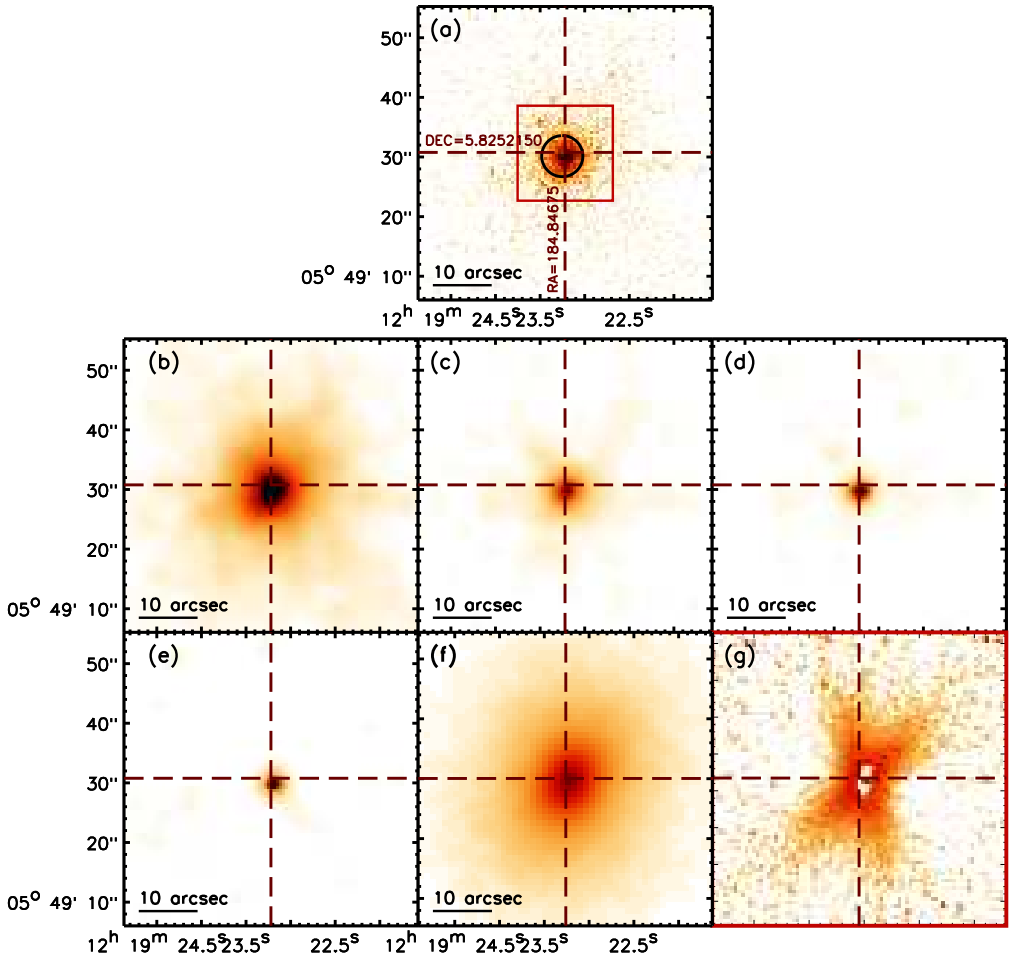

Figure C.36: *NGC4261*

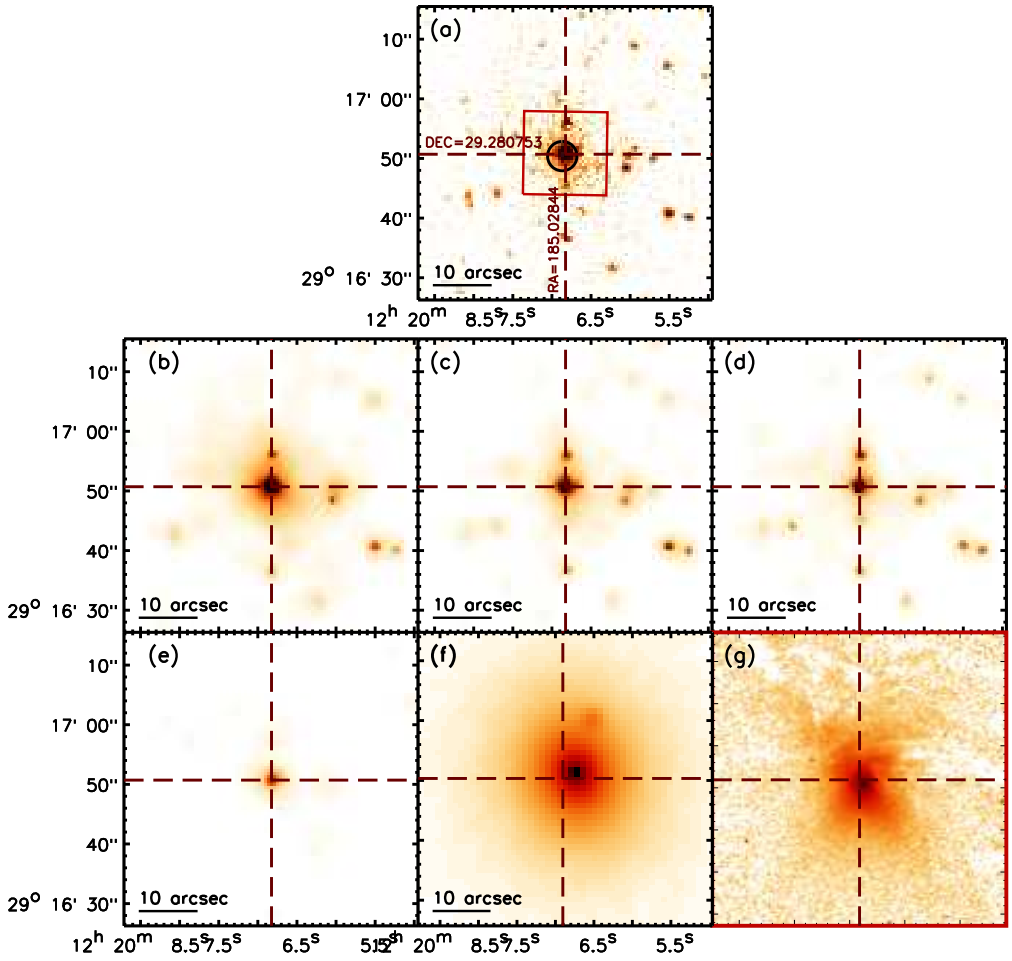

Figure C.37: *NGC4278*

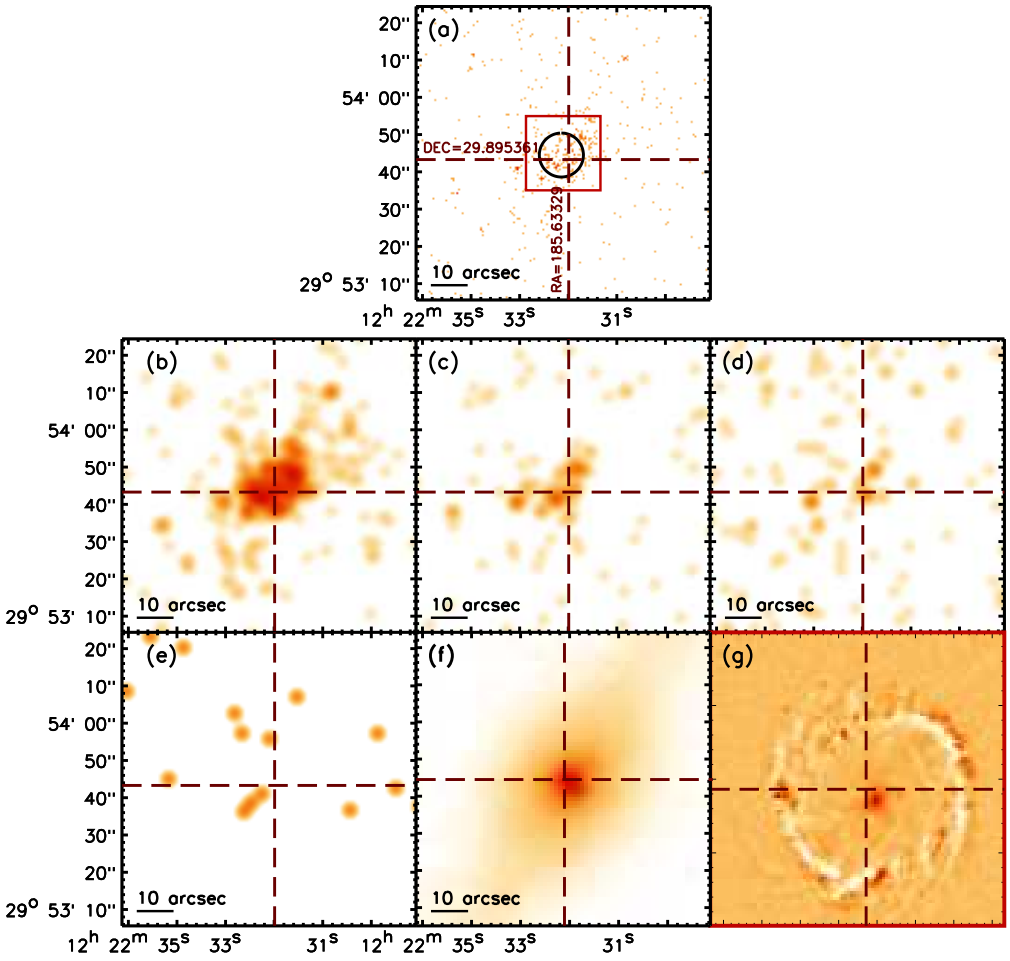

Figure C.38: *NGC4314*

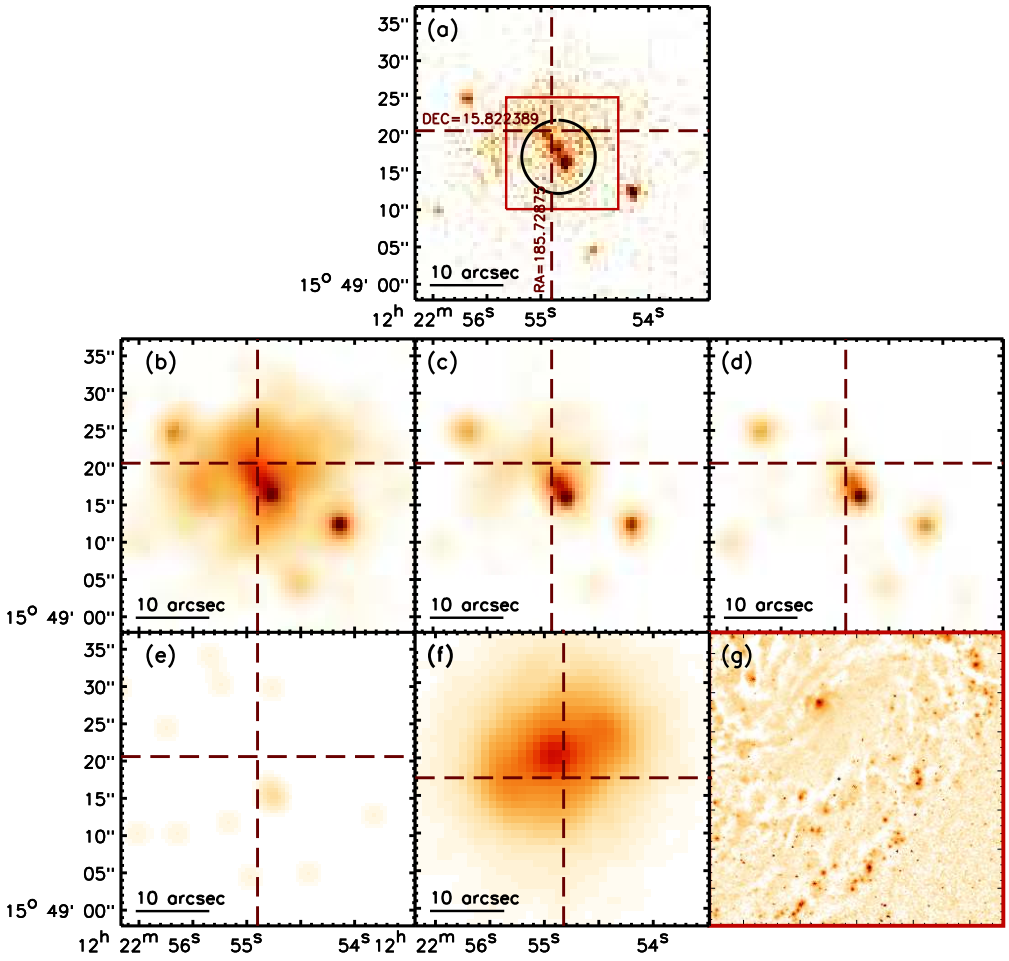

Figure C.39: *NGC4321*

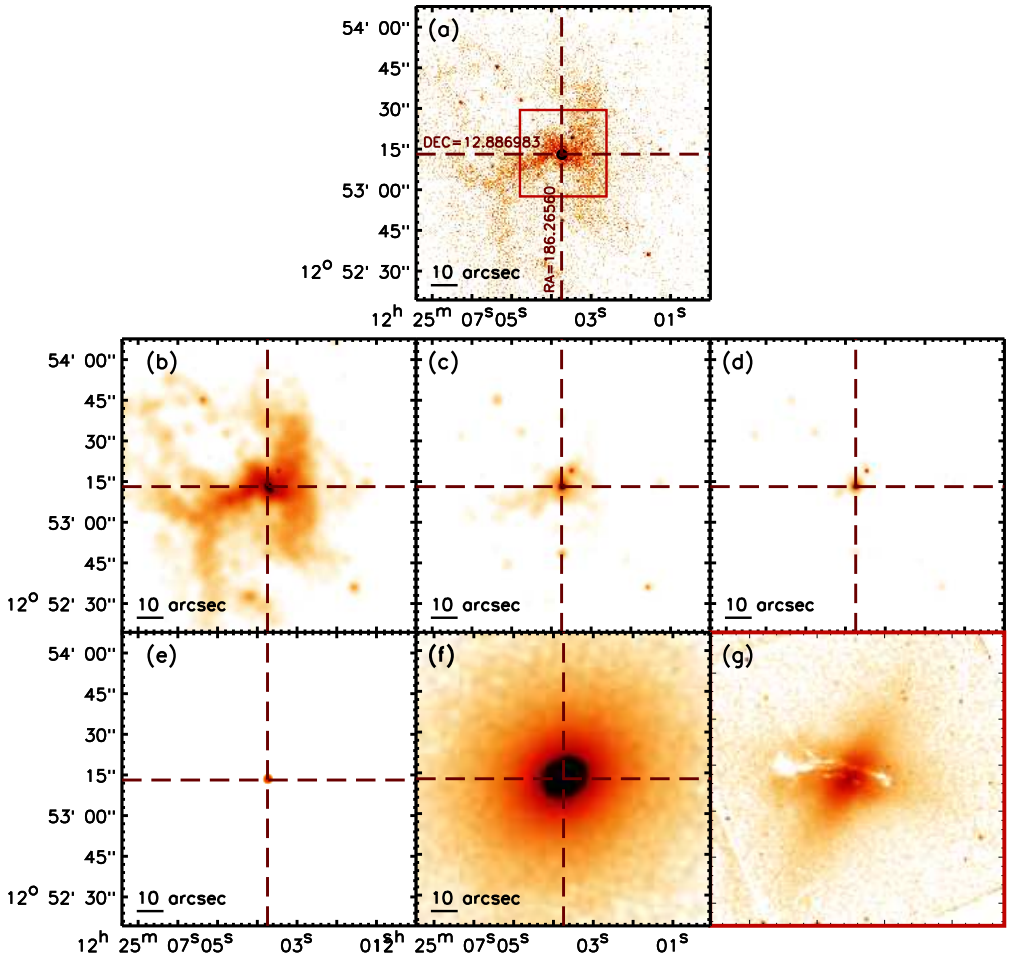

Figure C.40: *NGC4374*

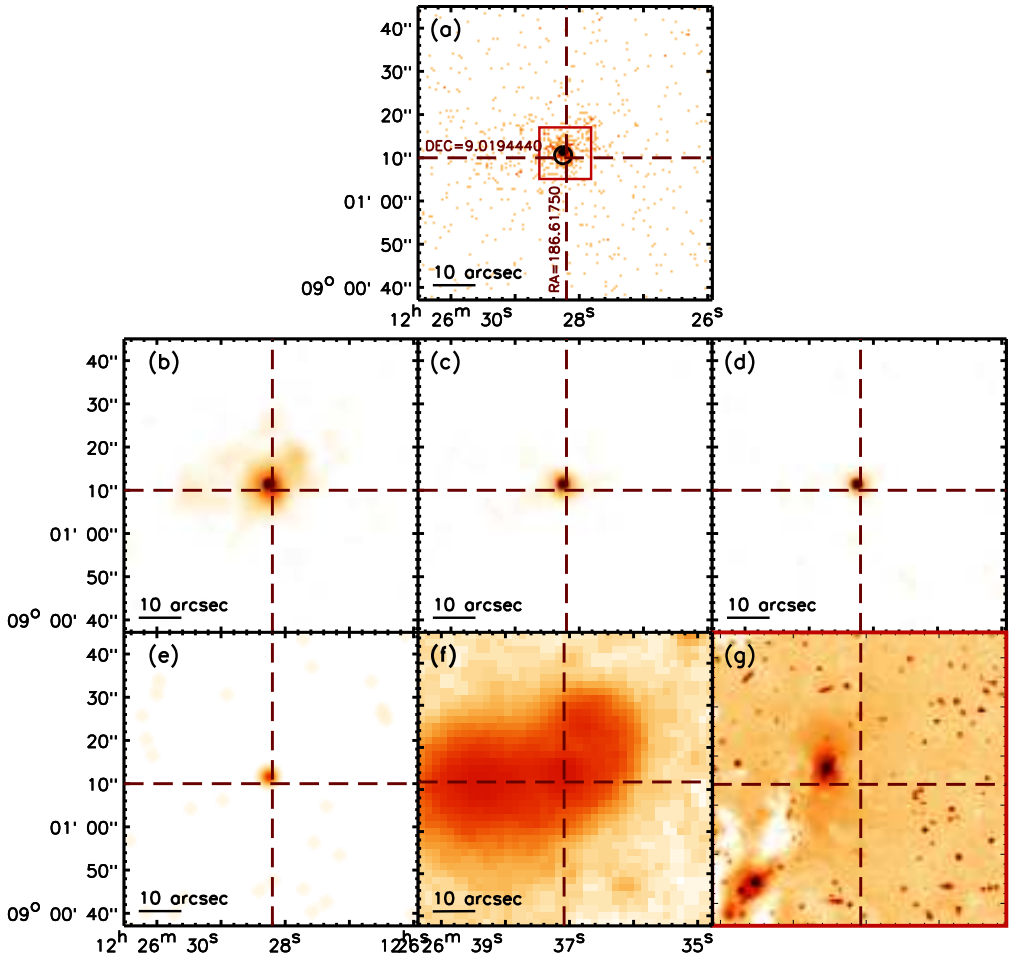

Figure C.41: *NGC4410*

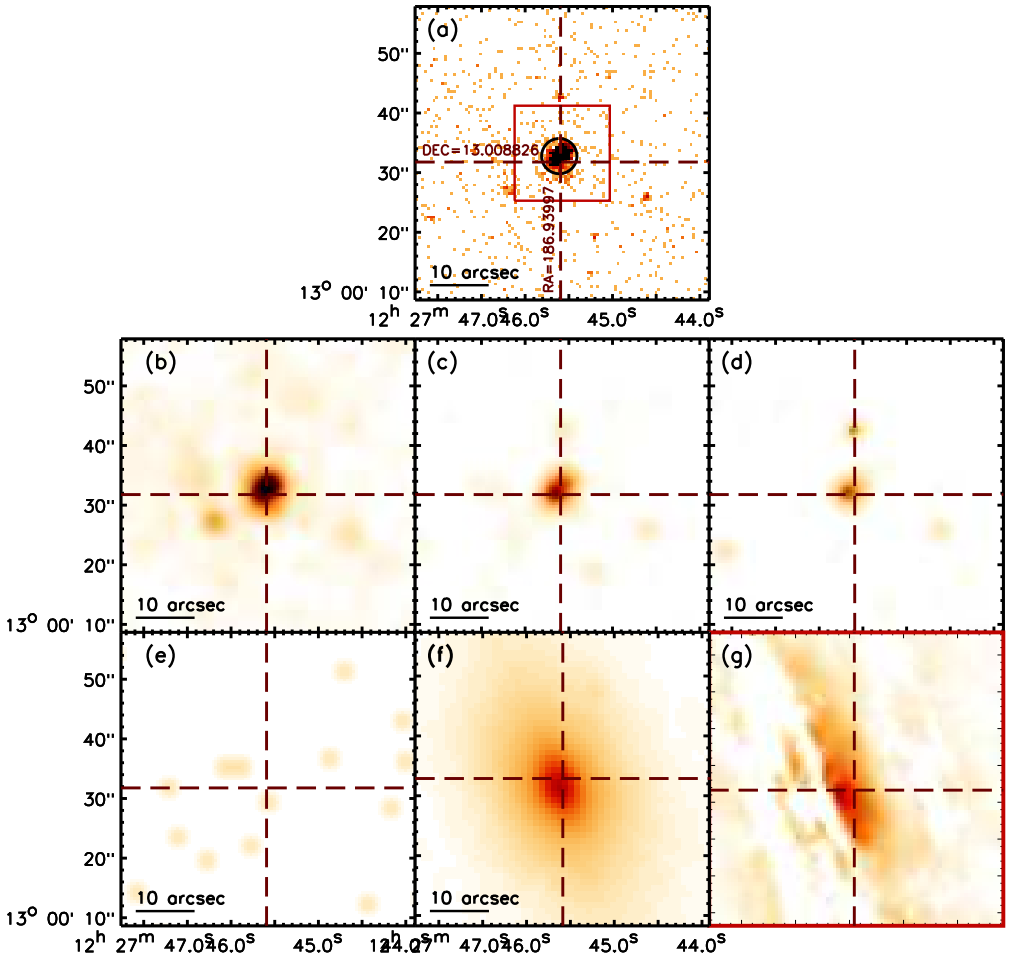

Figure C.42: *NGC4438*

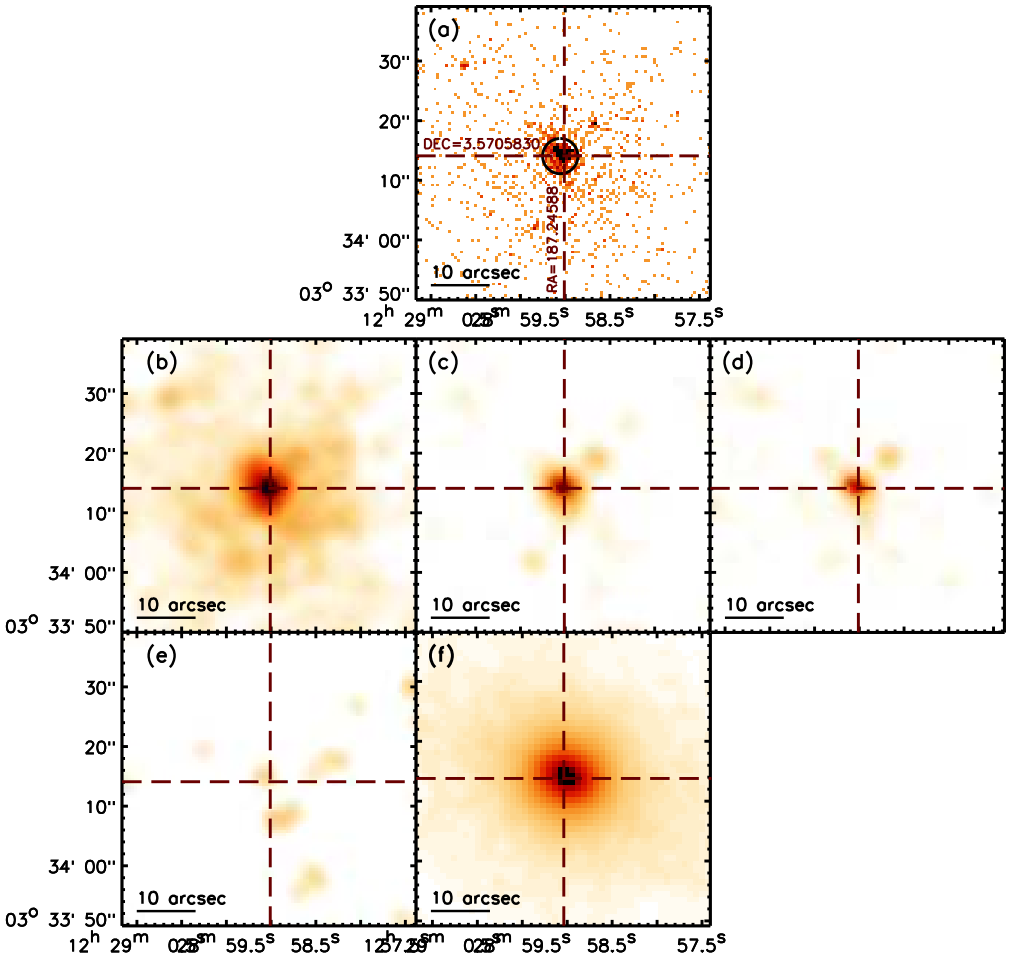

Figure C.43: *NGC4457*

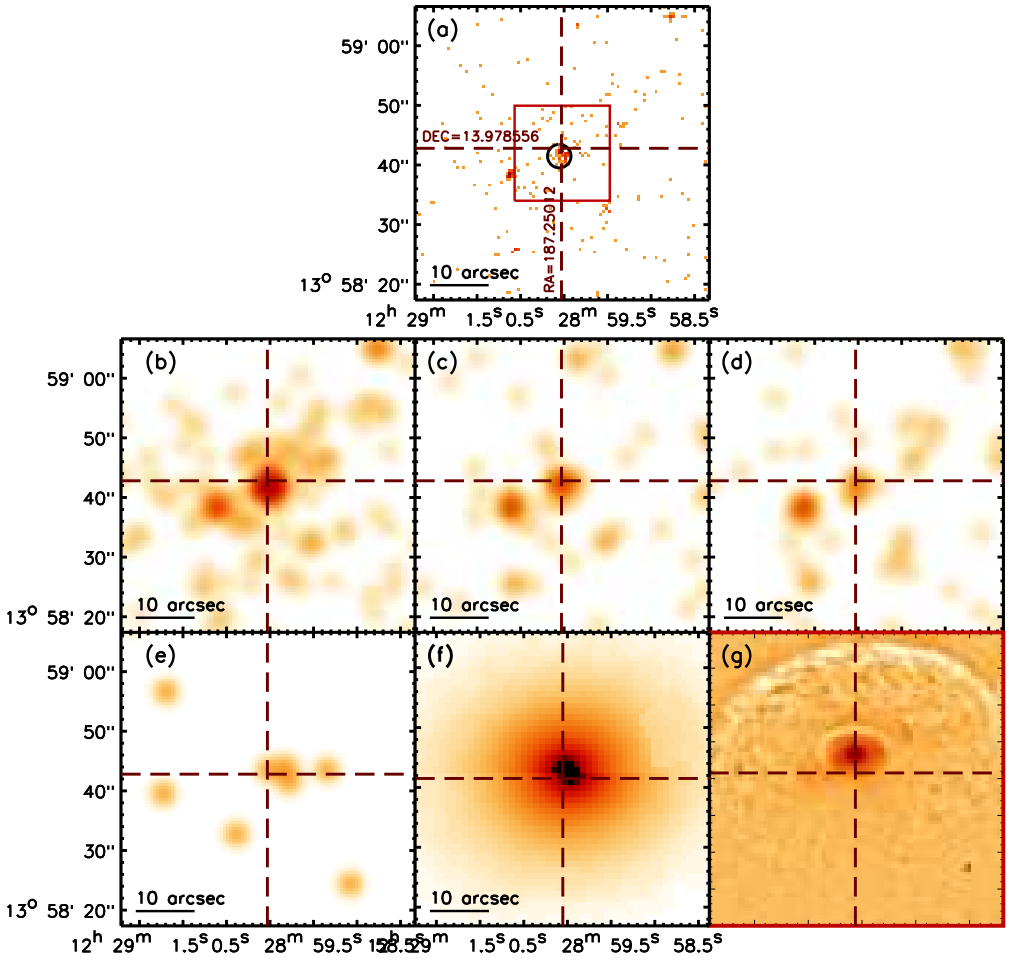

Figure C.44: *NGC4459*

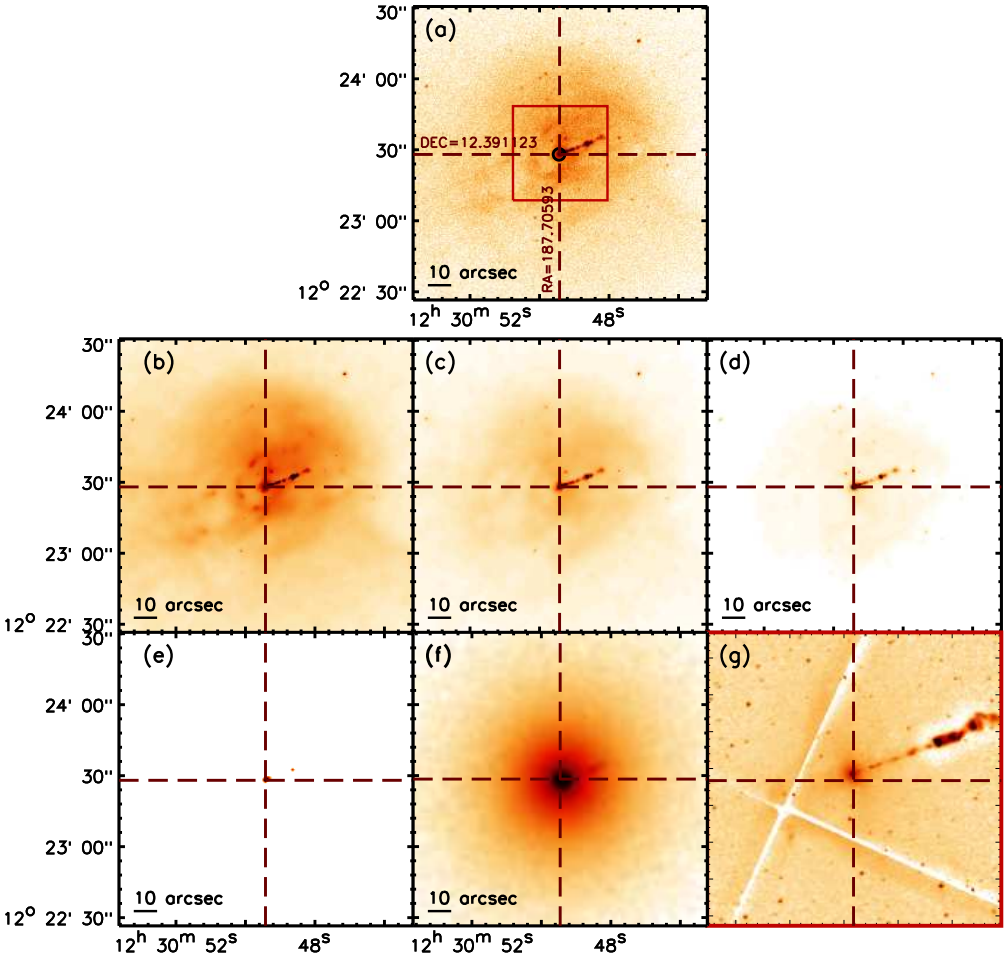

Figure C.45: *NGC4486*

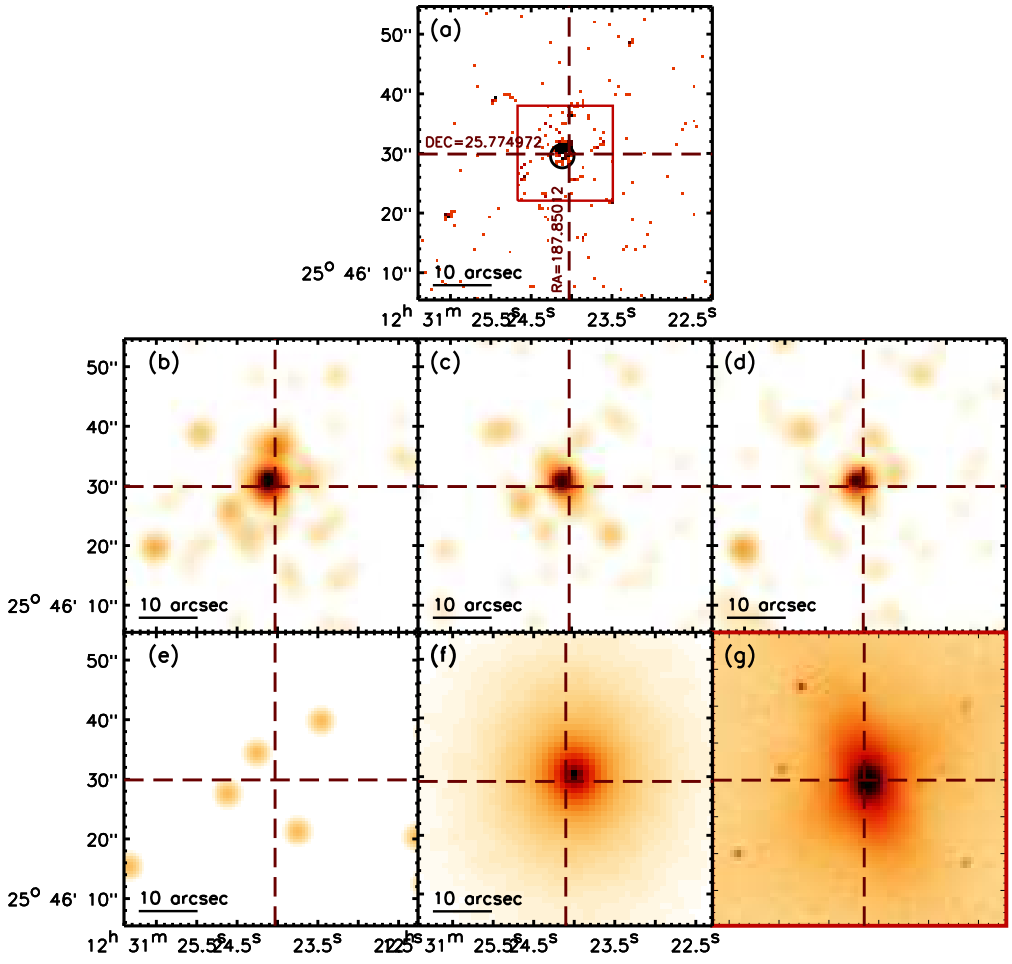

Figure C.46: *NGC4494*

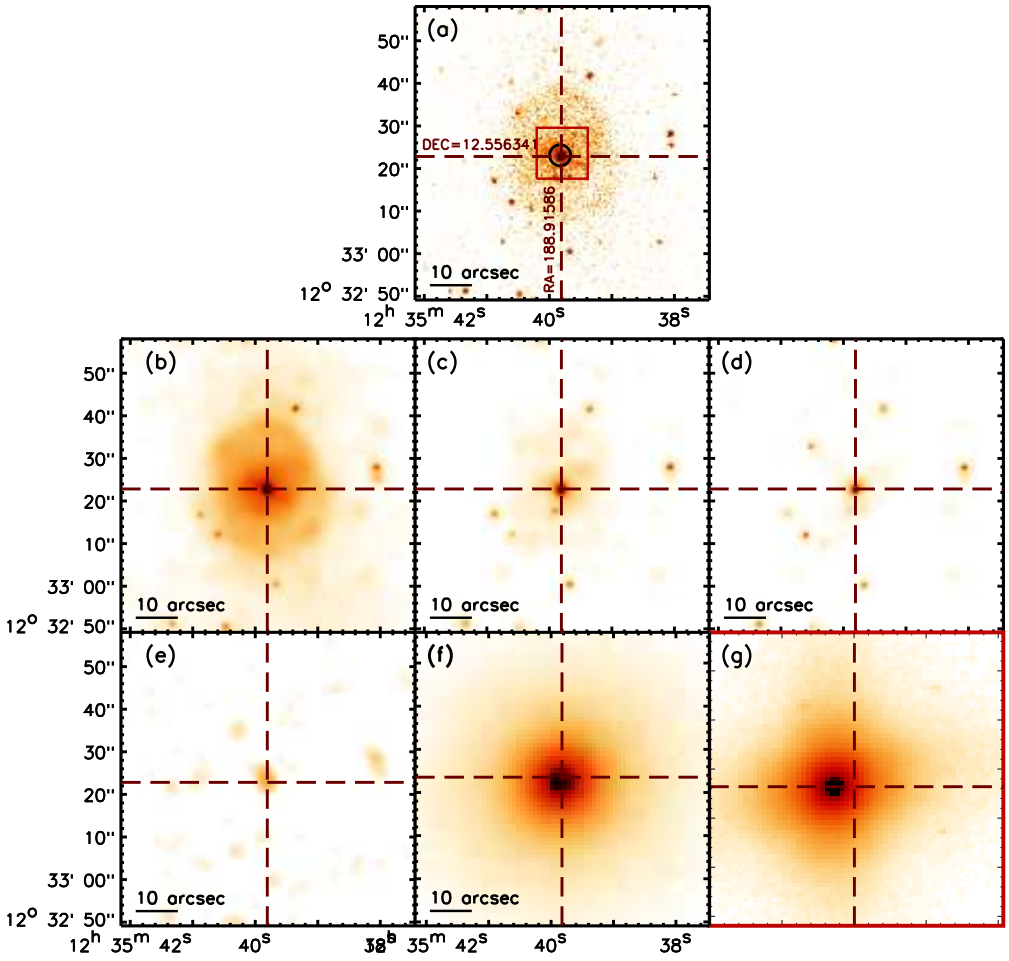

Figure C.47: *NGC4552*

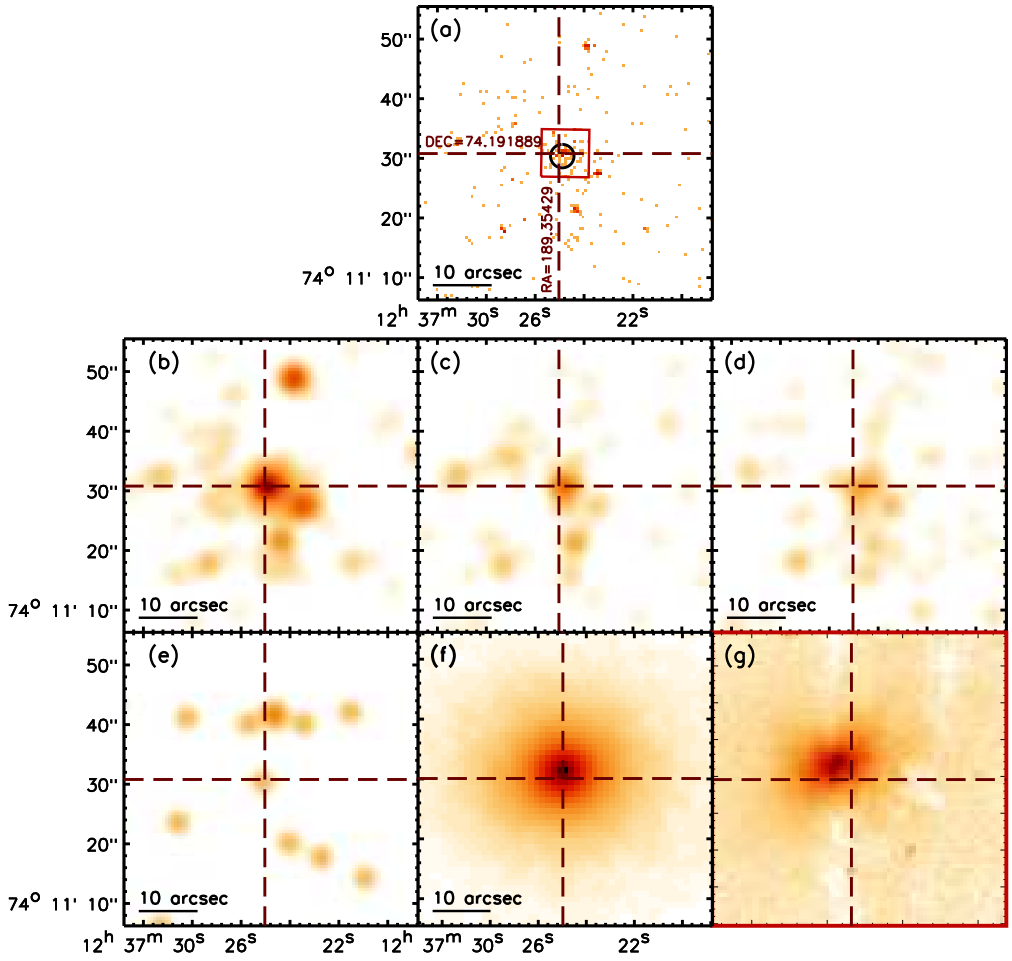

Figure C.48: *UGC7797*

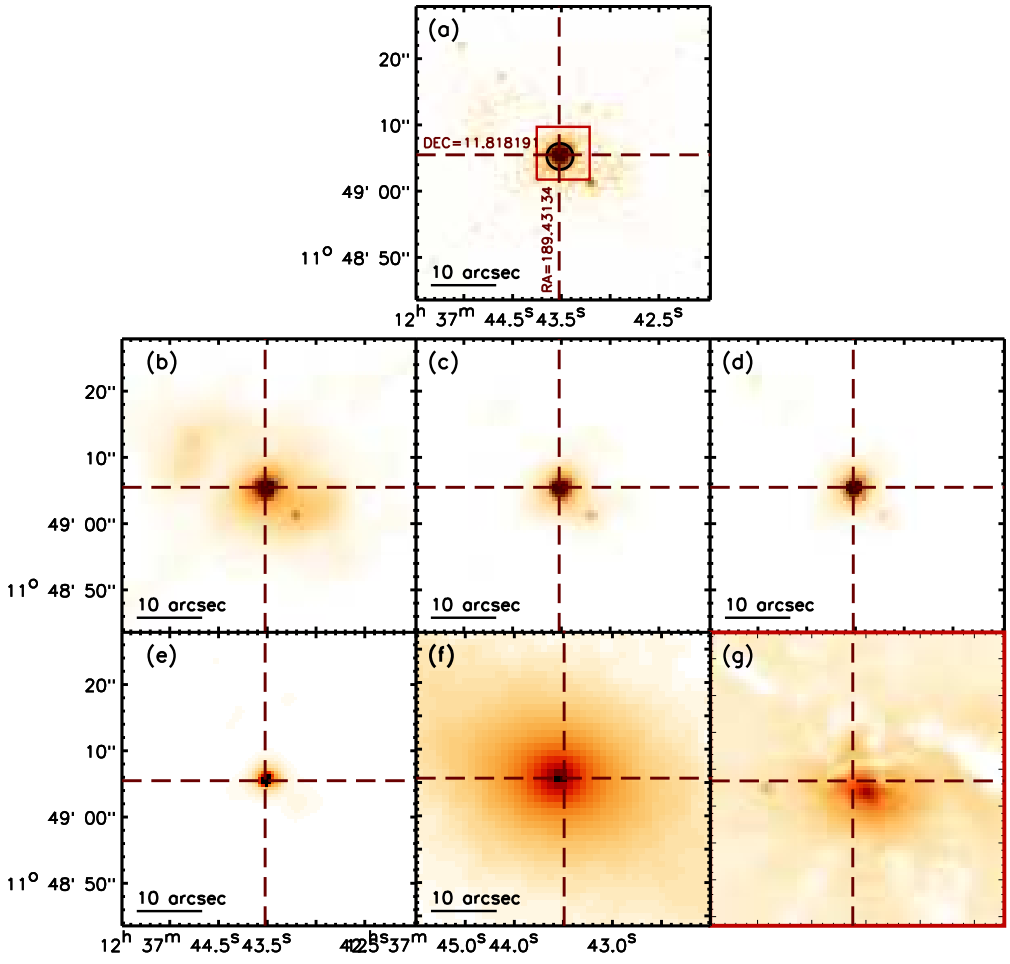

Figure C.49: *NGC4579*

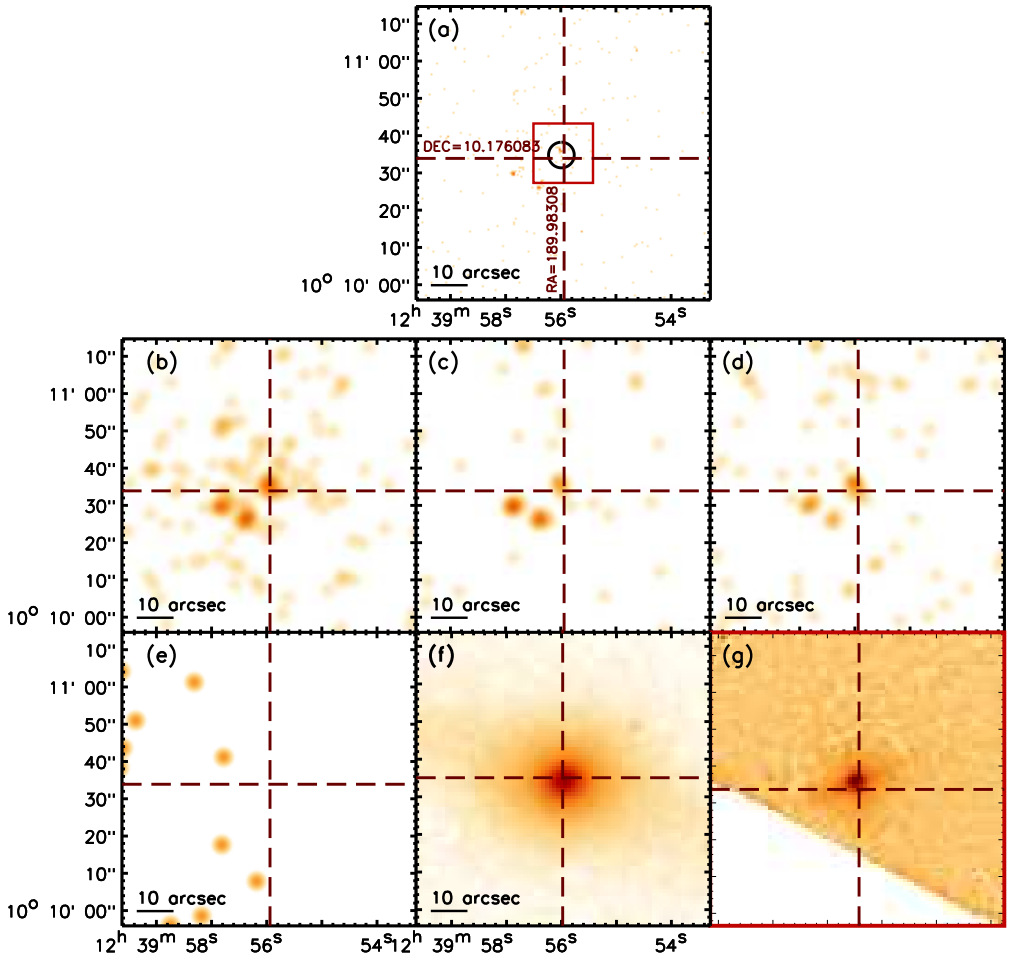

Figure C.50: *NGC4596*

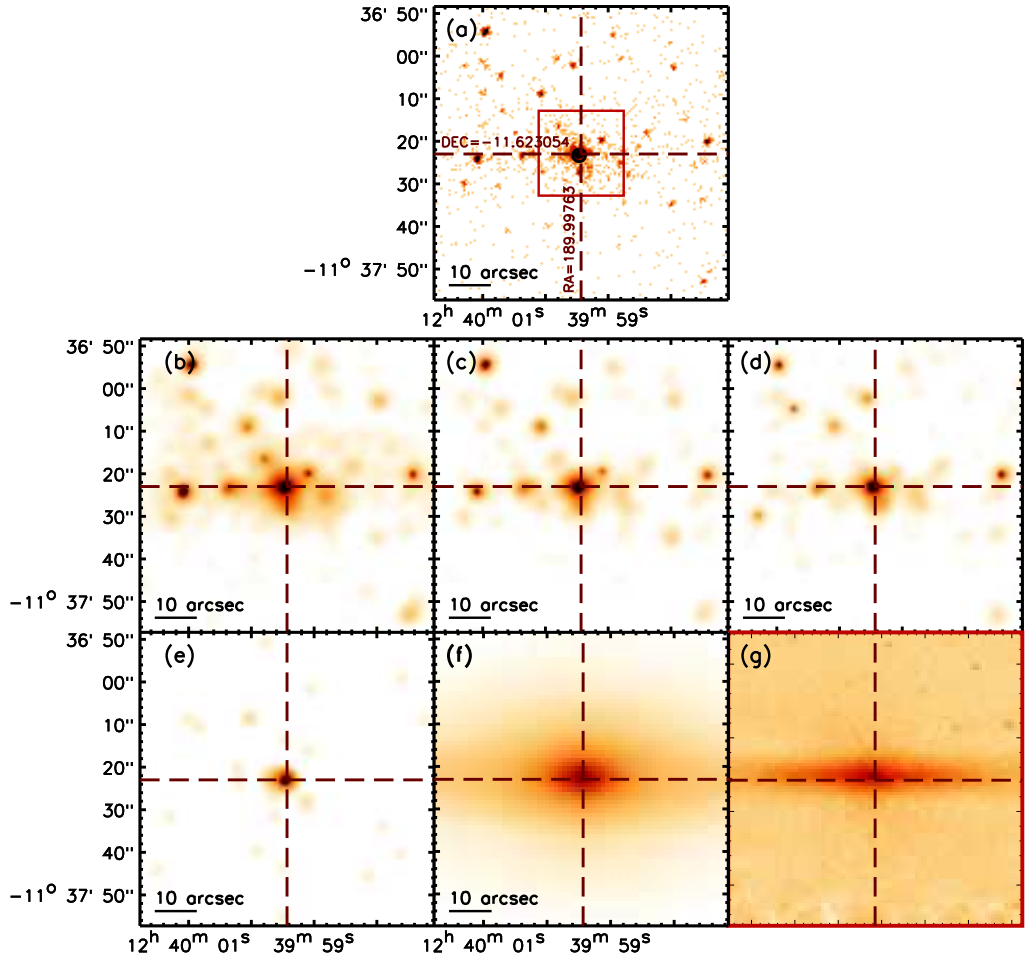

Figure C.51: *NGC4594*

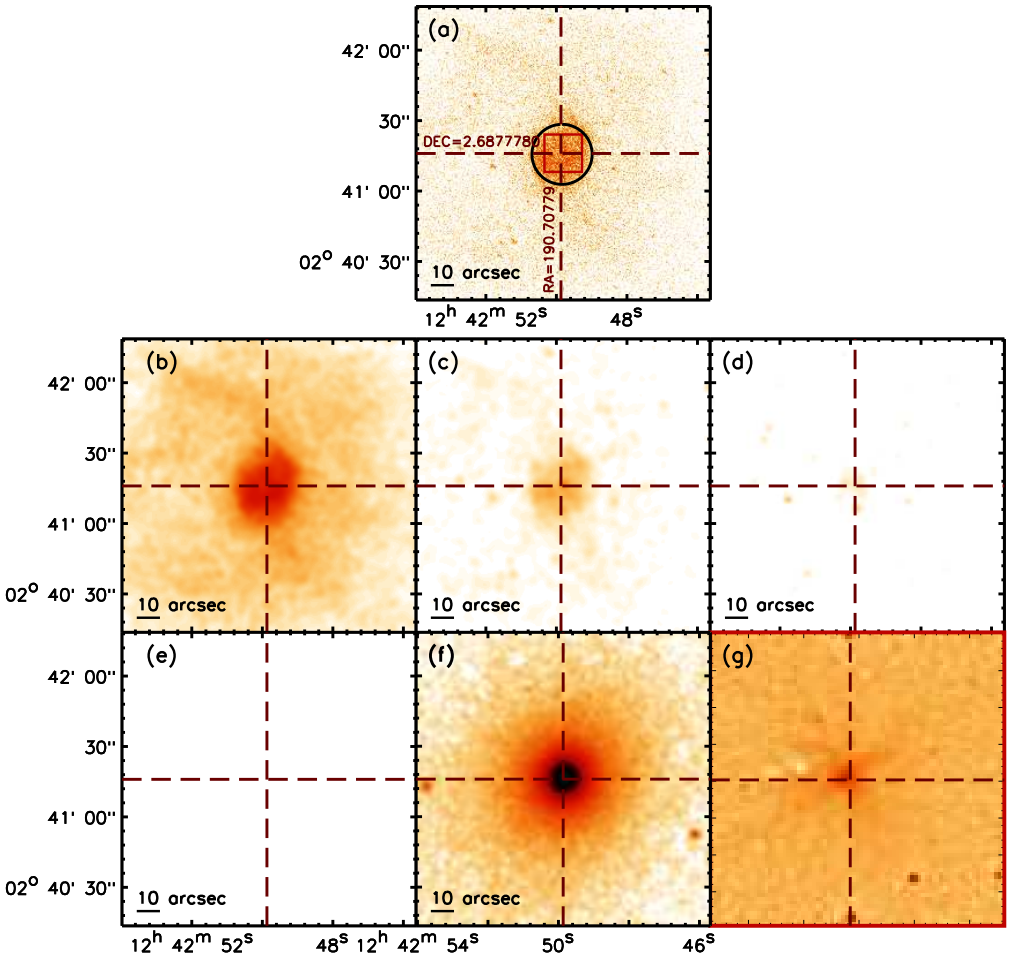

Figure C.52: *NGC4636*

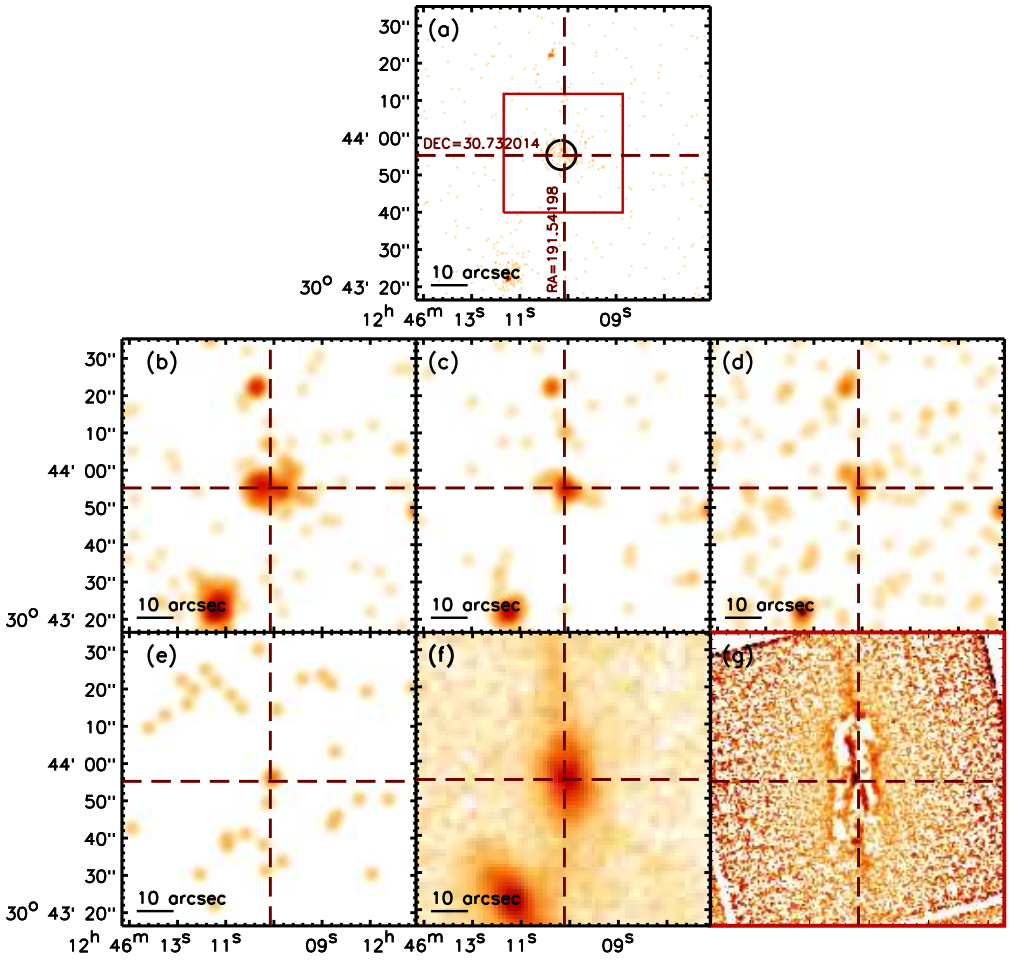

Figure C.53: *NGC4676A*

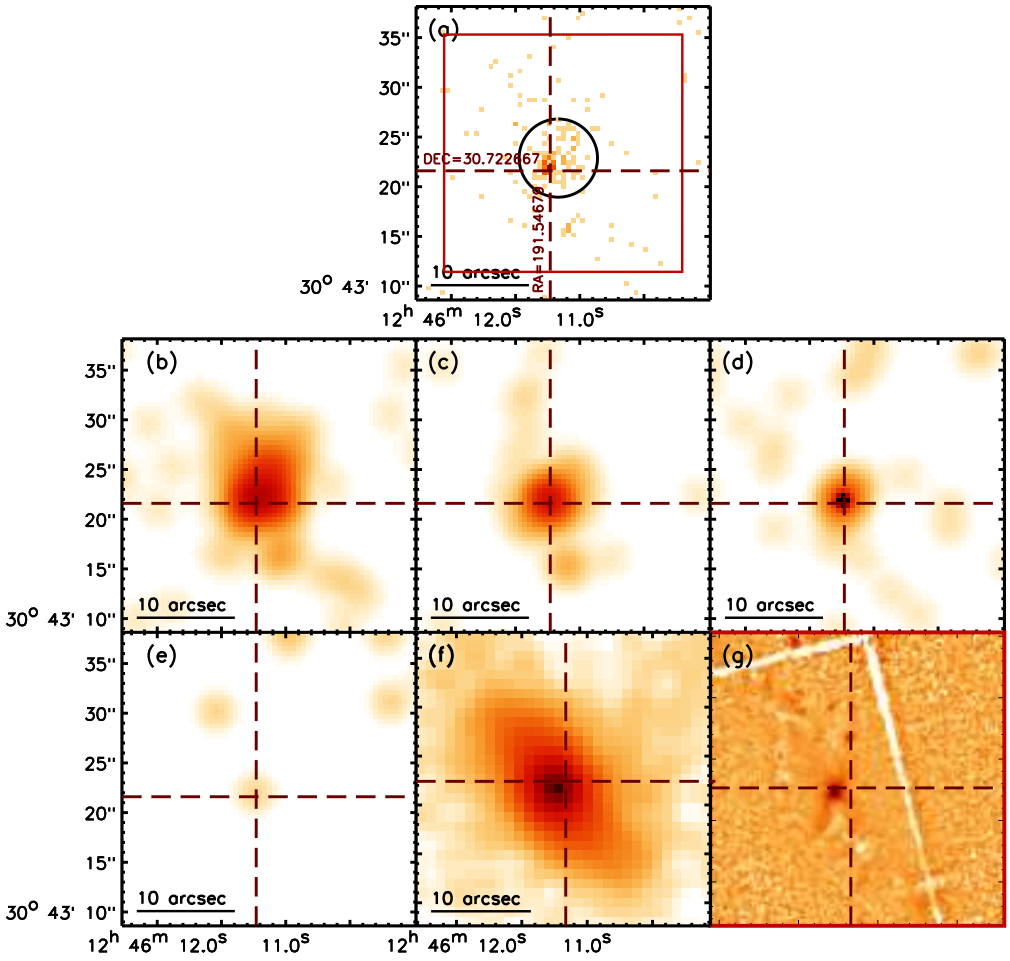

Figure C.54: *NGC4676B*

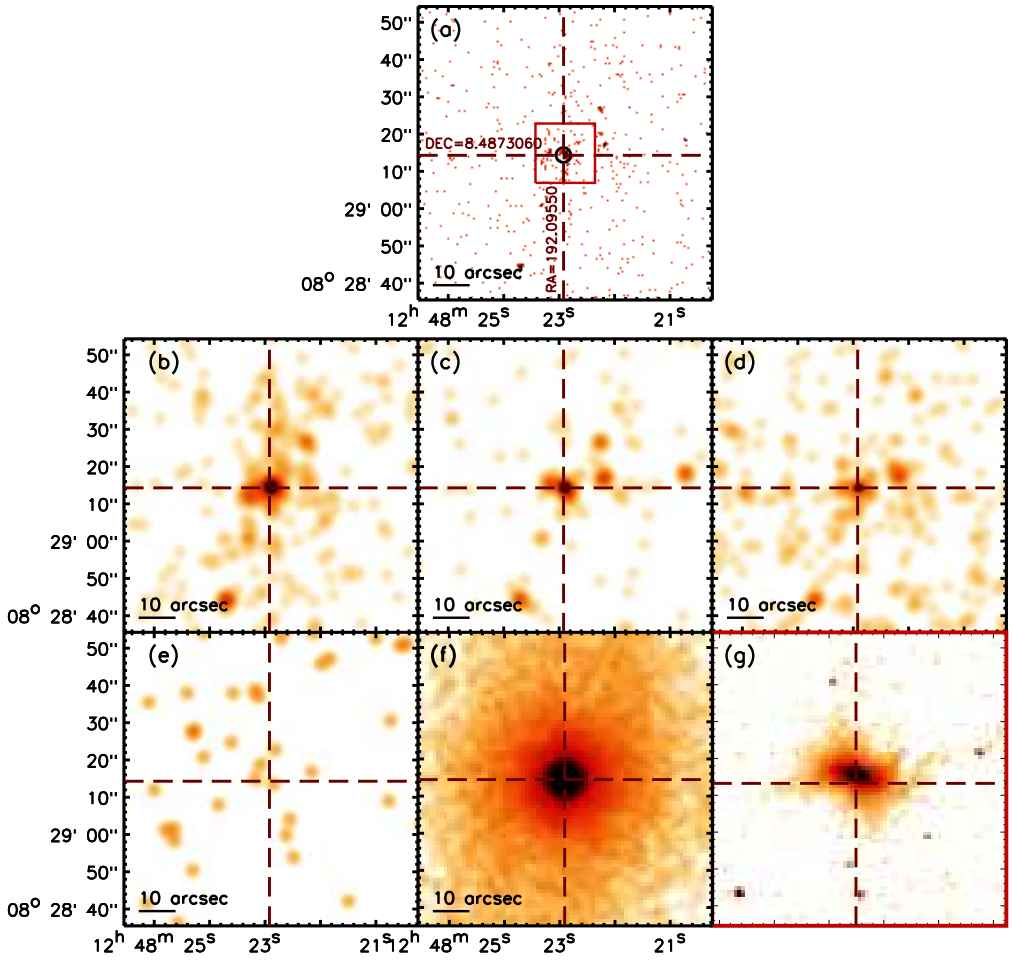

Figure C.55: *NGC4698*

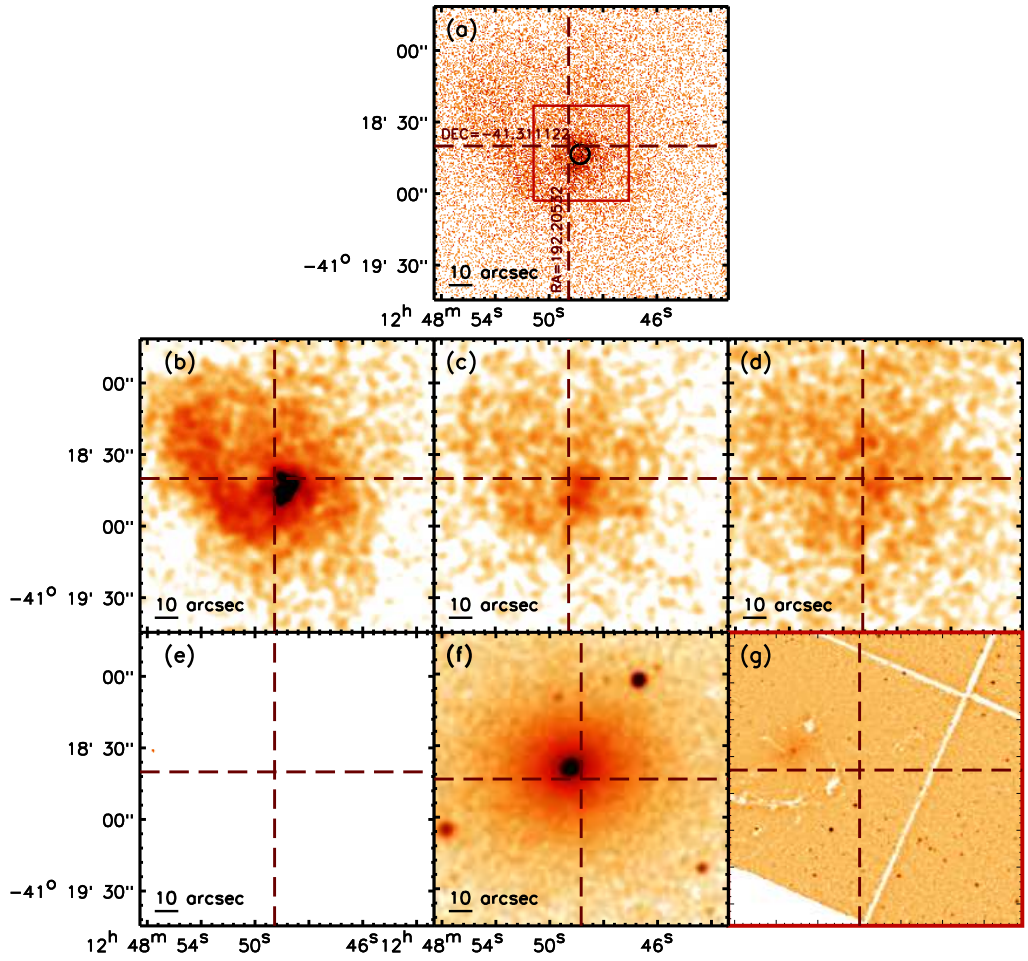

Figure C.56: *NGC4696*

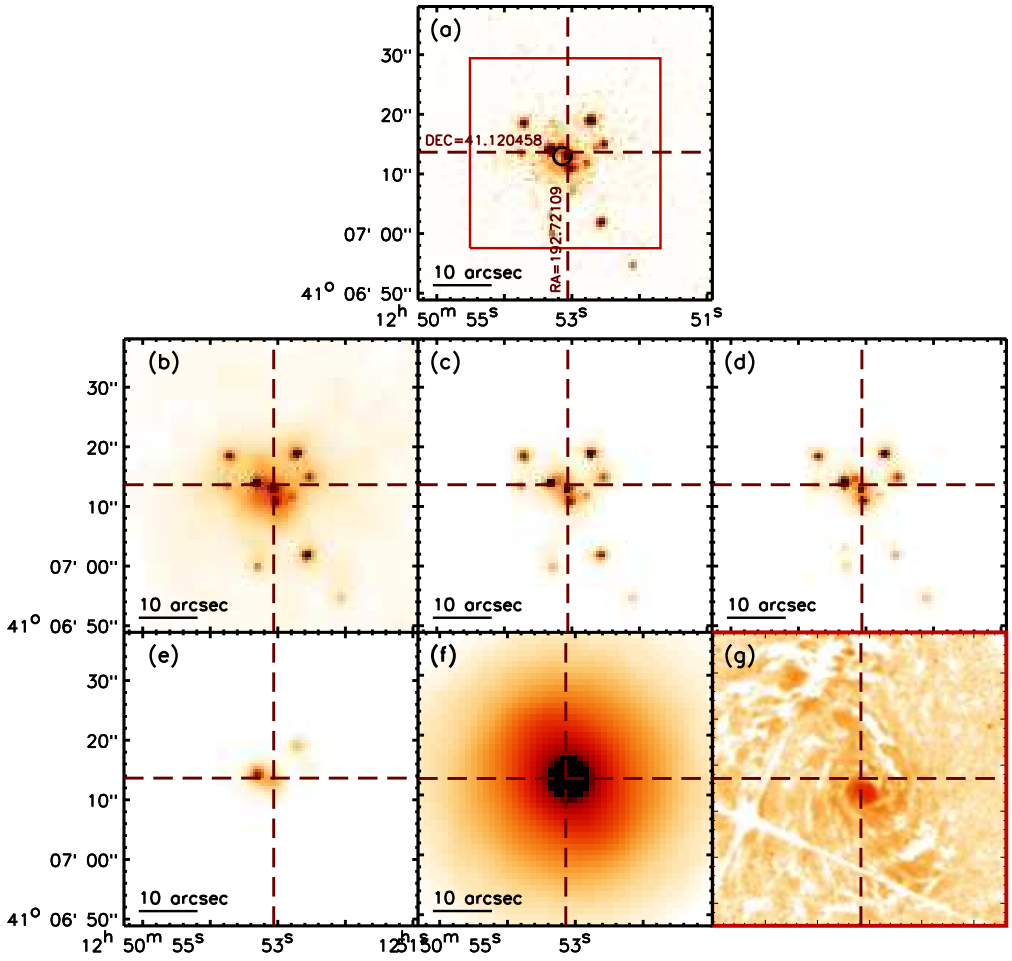

Figure C.57: *NGC4736*

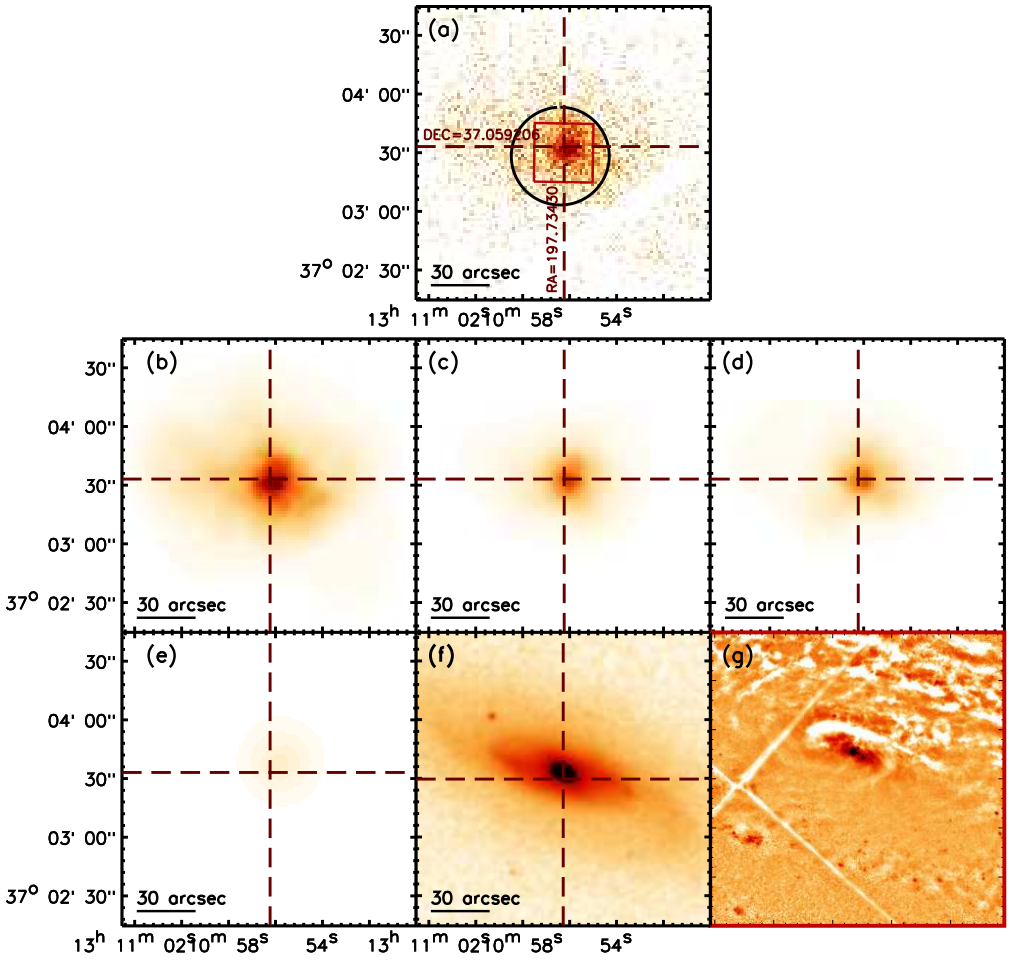

Figure C.58: *NGC5005 (XMM-Newton)*

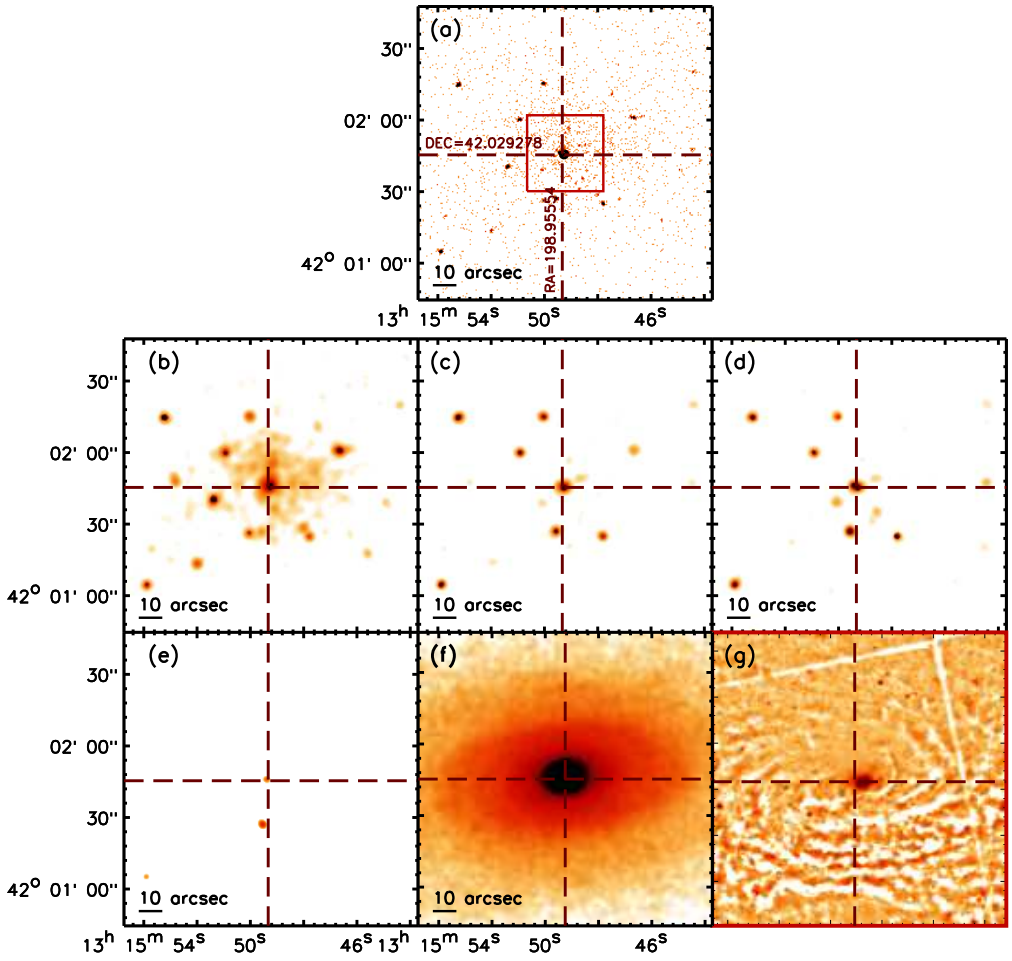

Figure C.59: *NGC5055*

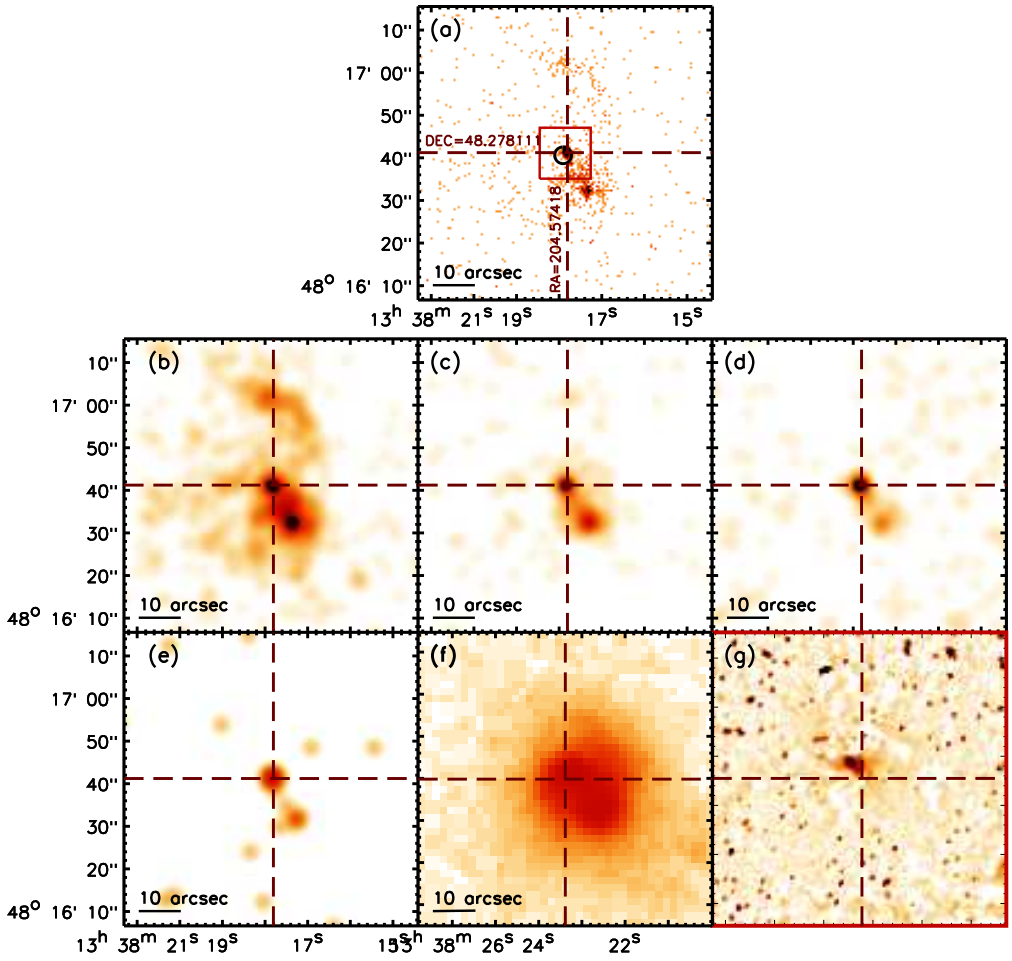

Figure C.60: *MRK266NE*

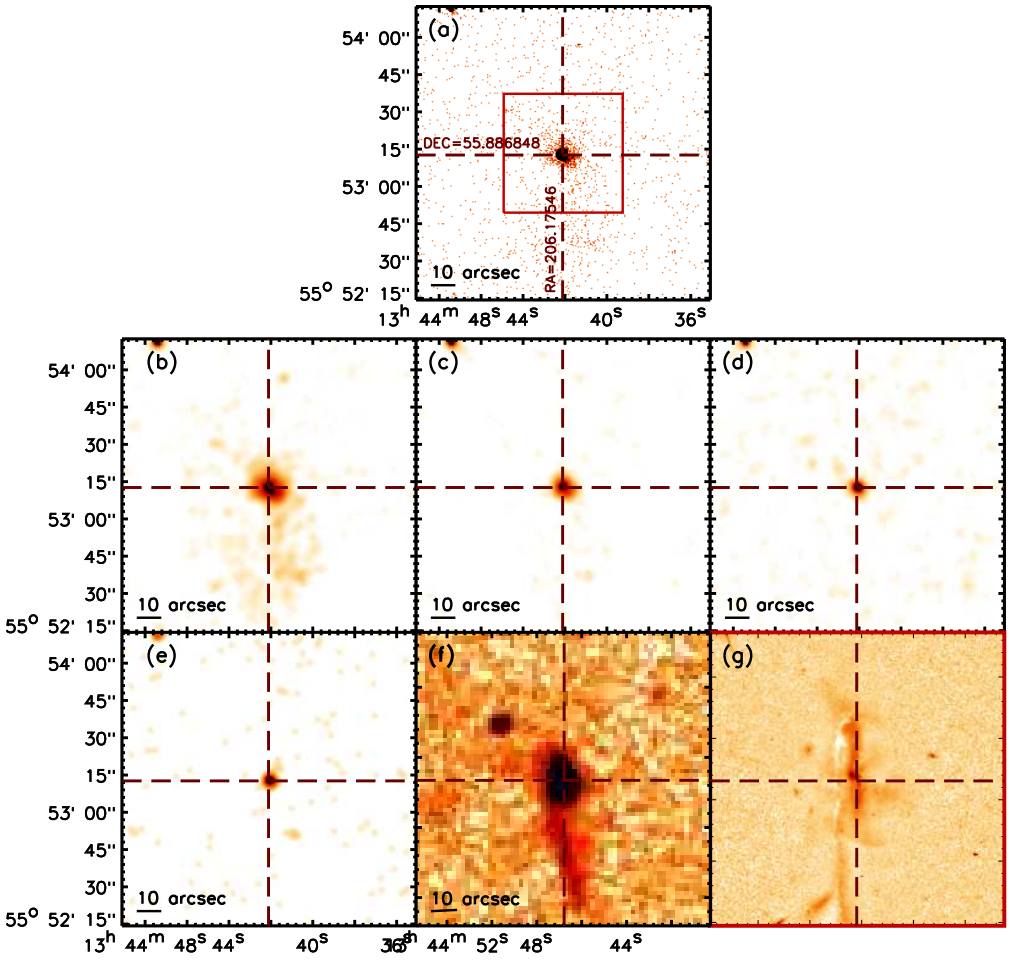

Figure C.61: *UGC08696*

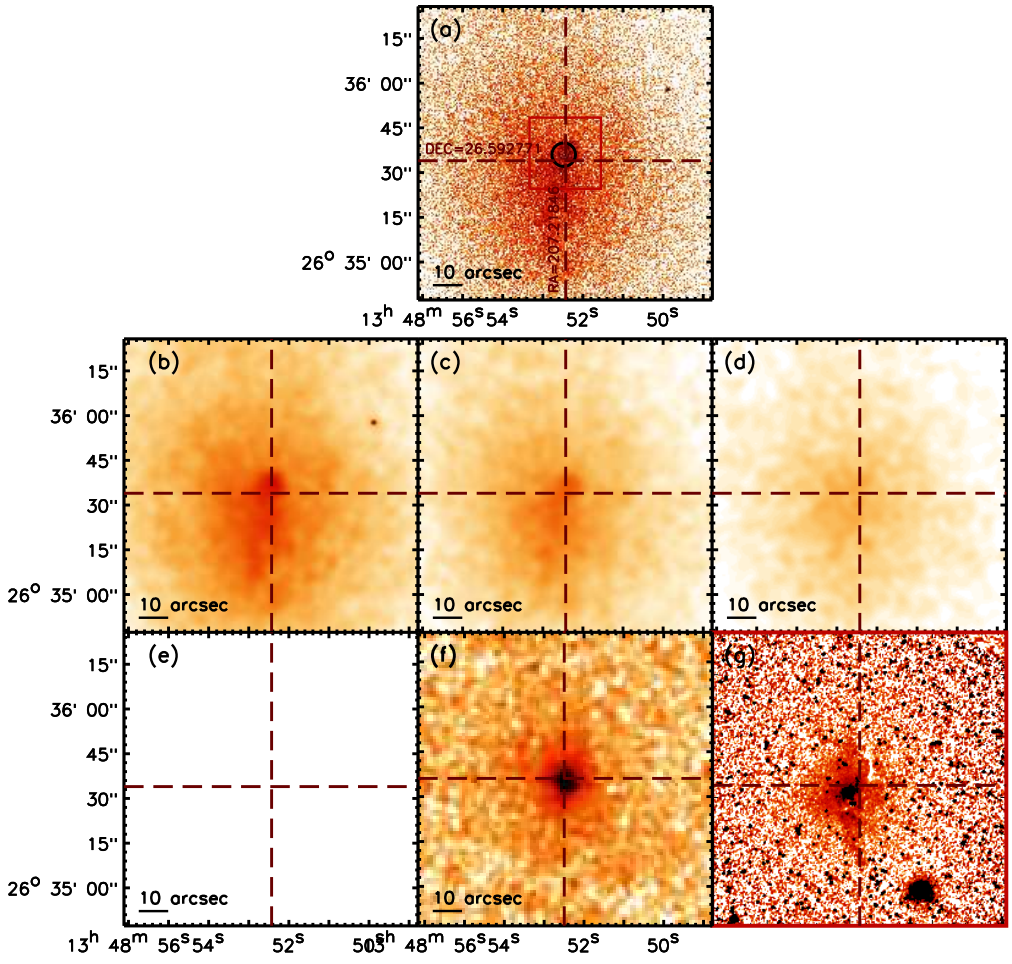

Figure C.62: *CGCG162-010*

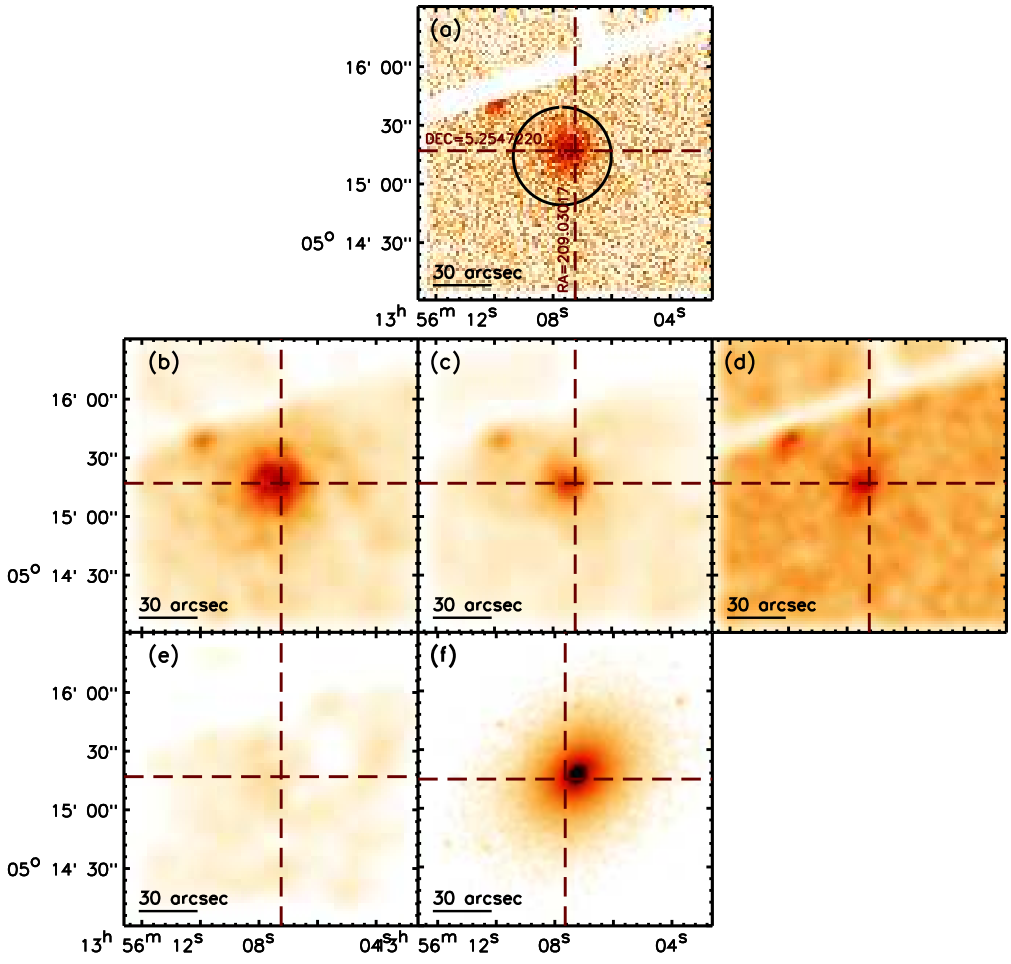

Figure C.63: *NGC5363 (XMM-Newton)*

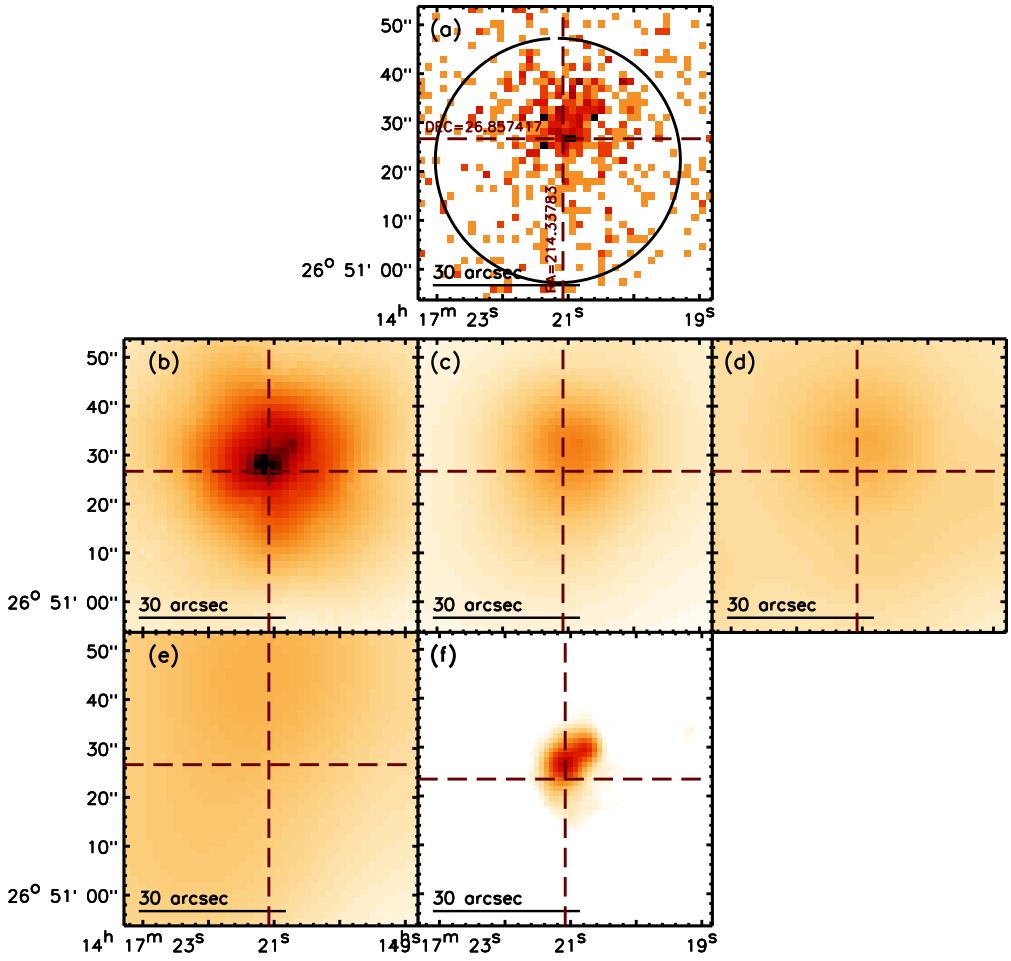

Figure C.64: *IC4395 (XMM-Newton)*

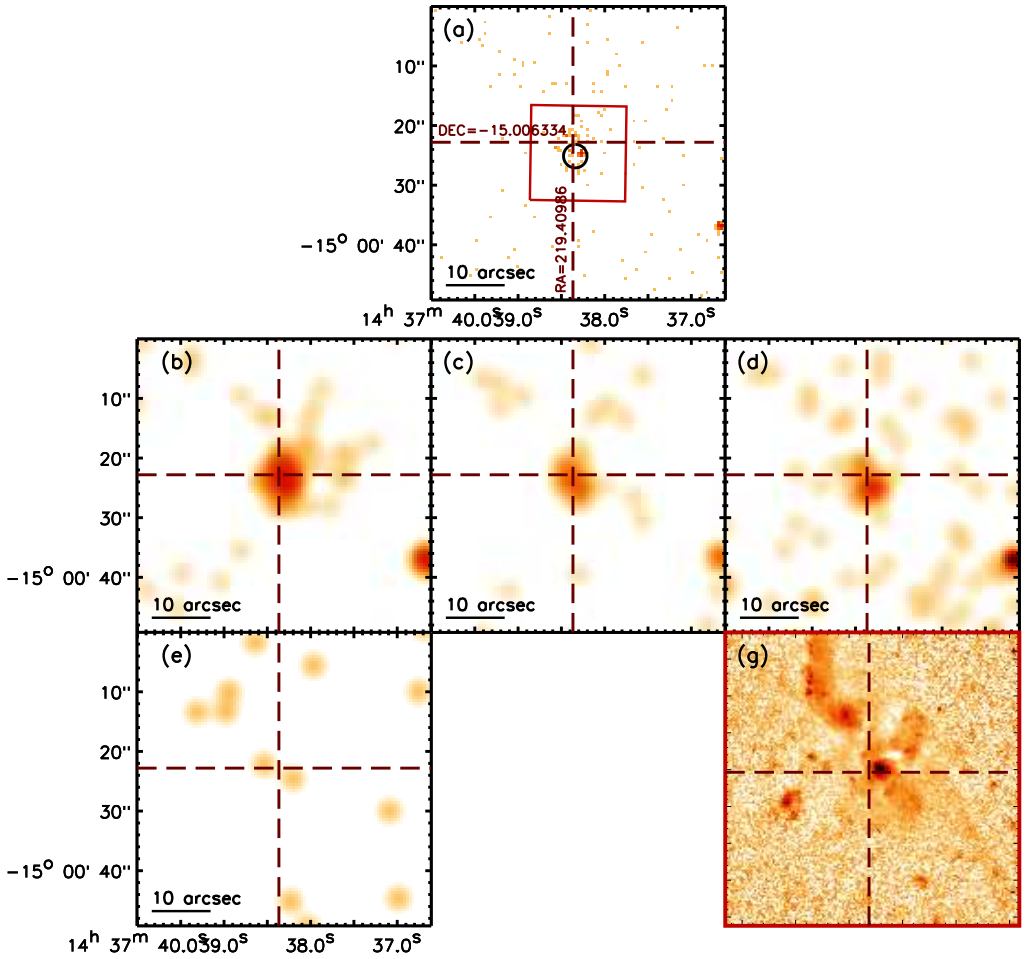

Figure C.65: *IRAS14348-1447*

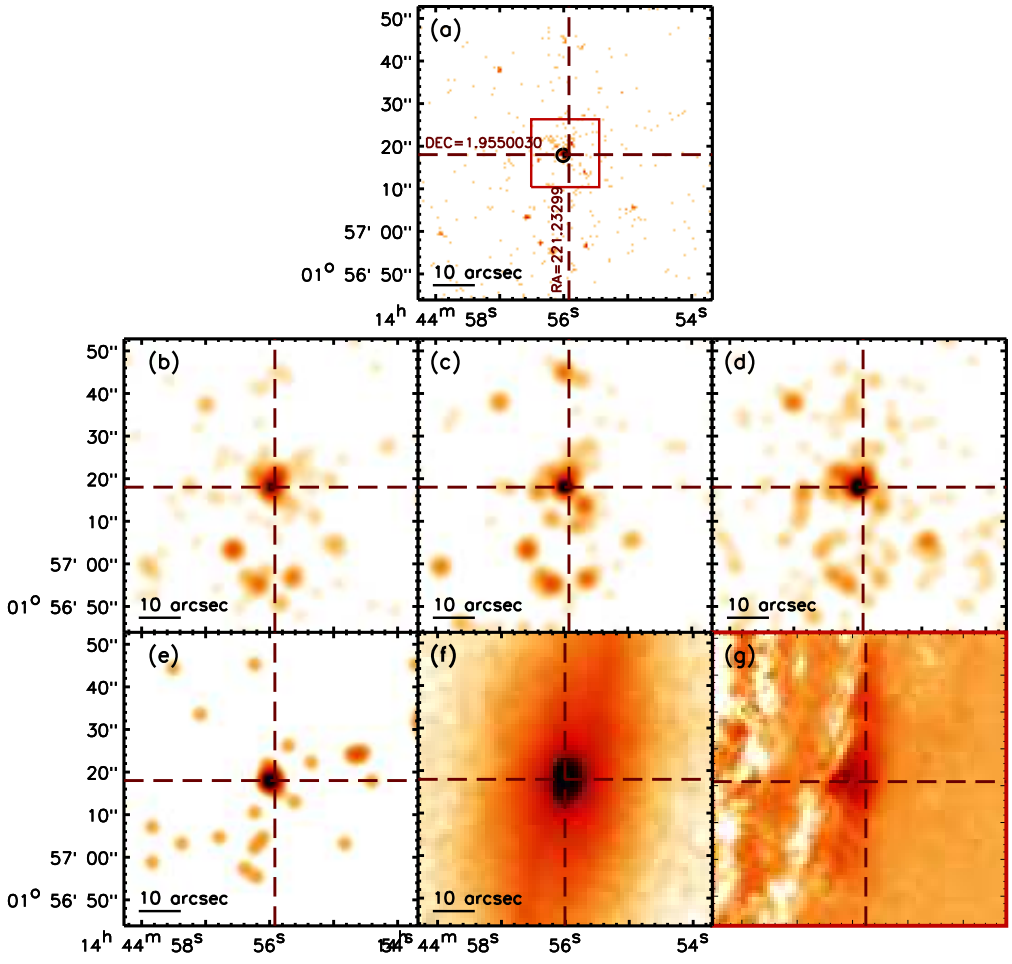

Figure C.66: *NGC5746*

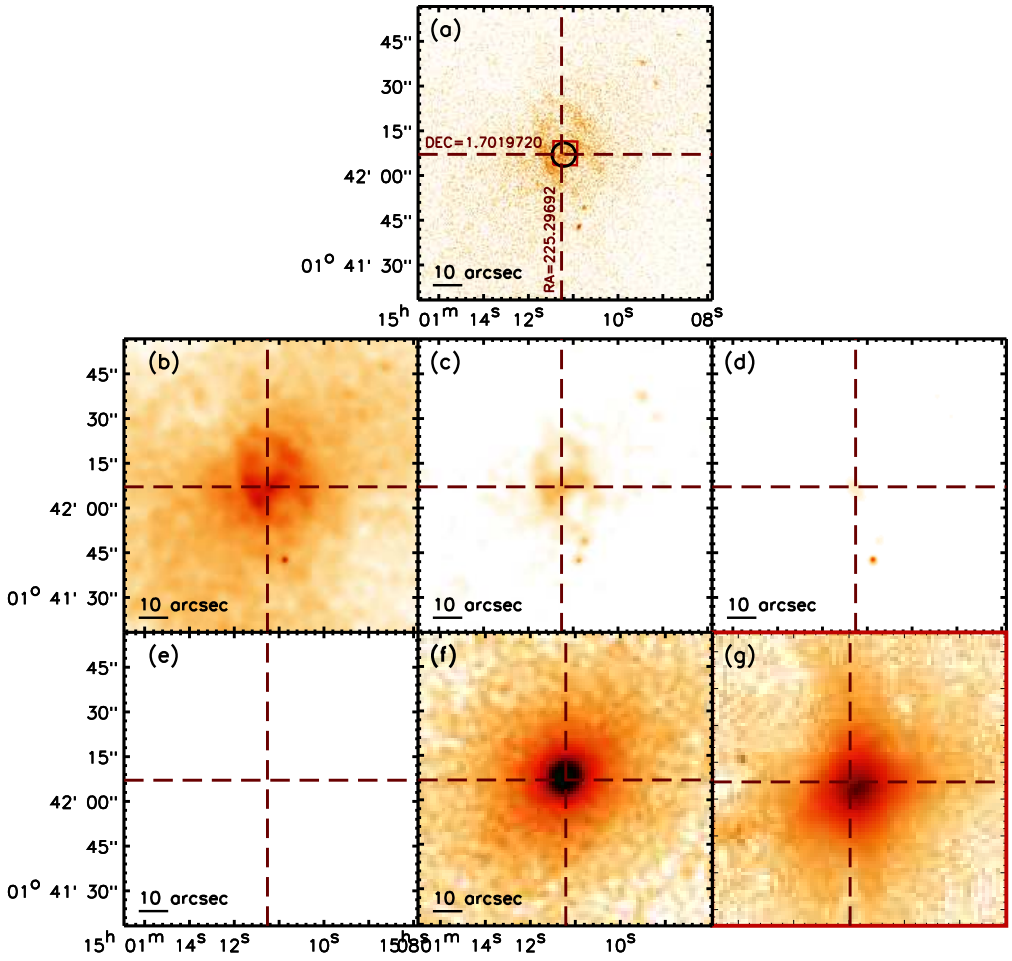

Figure C.67: *NGC5813*

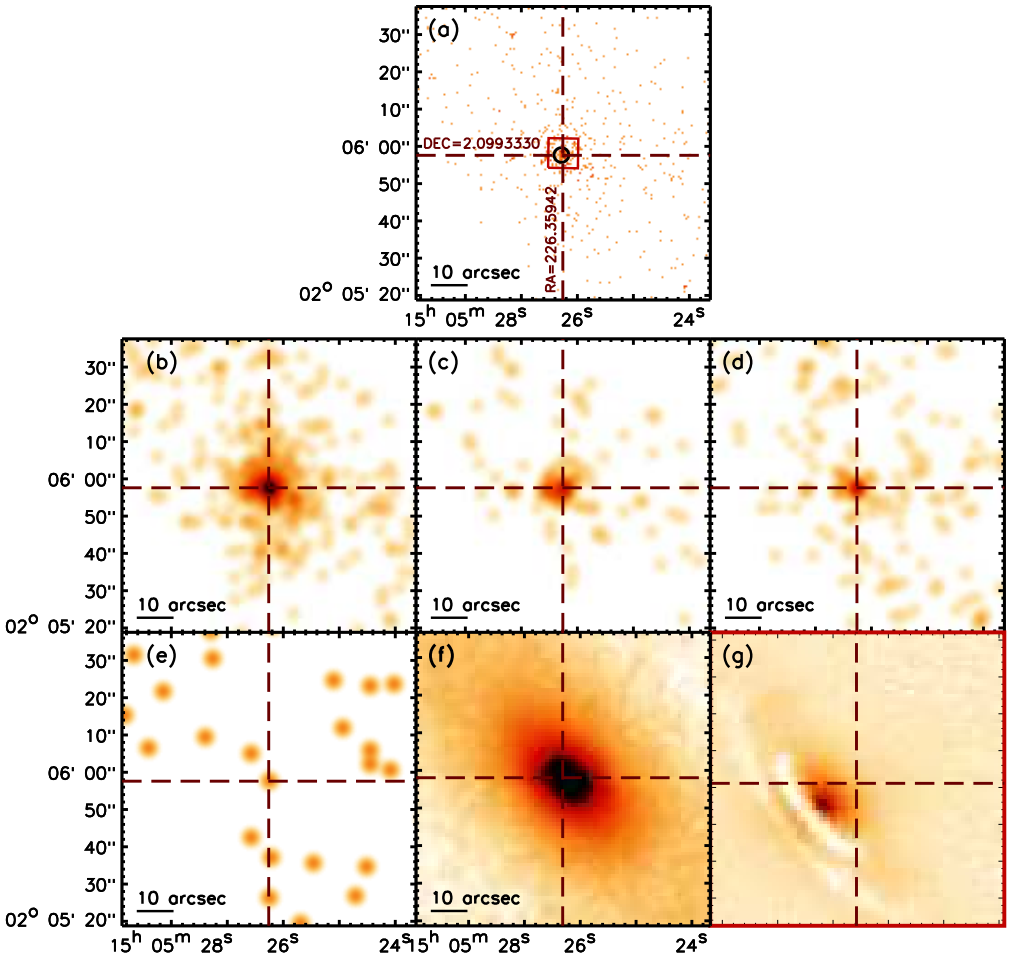

Figure C.68: *UGC9692*

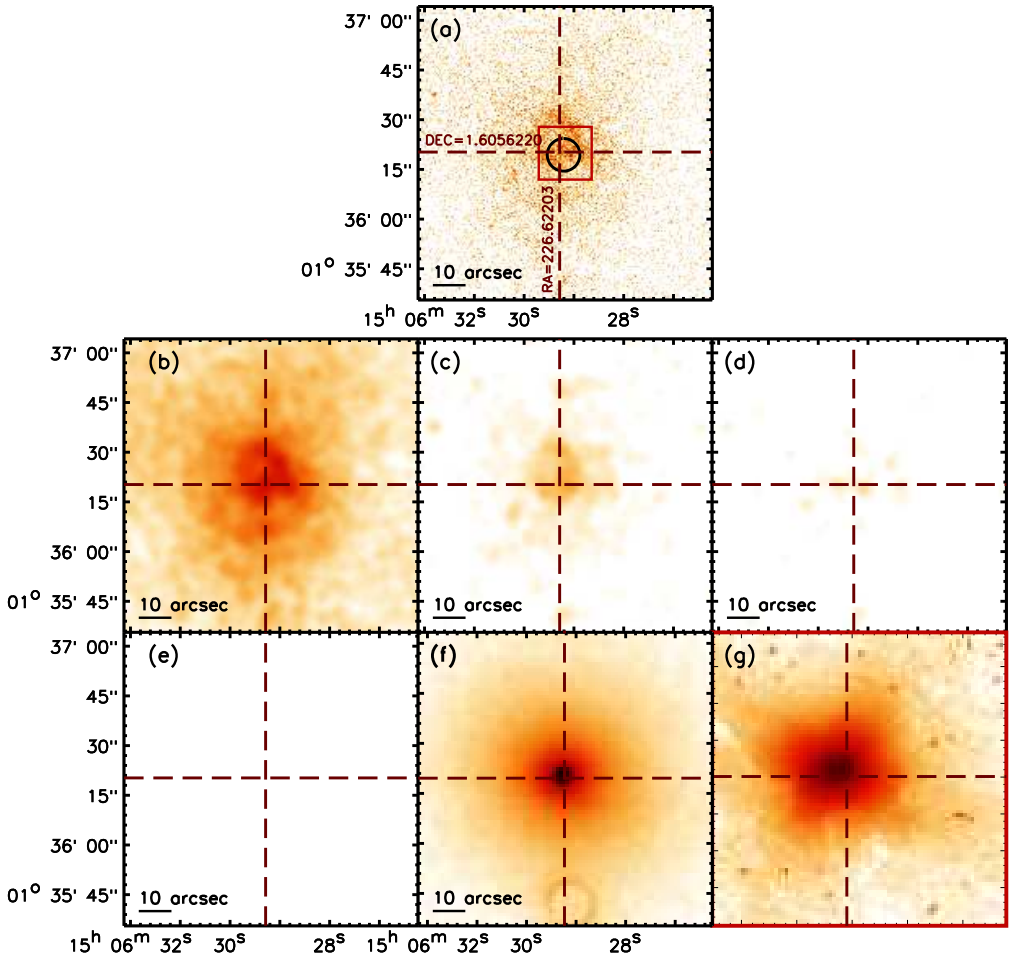

Figure C.69: *NGC5846*

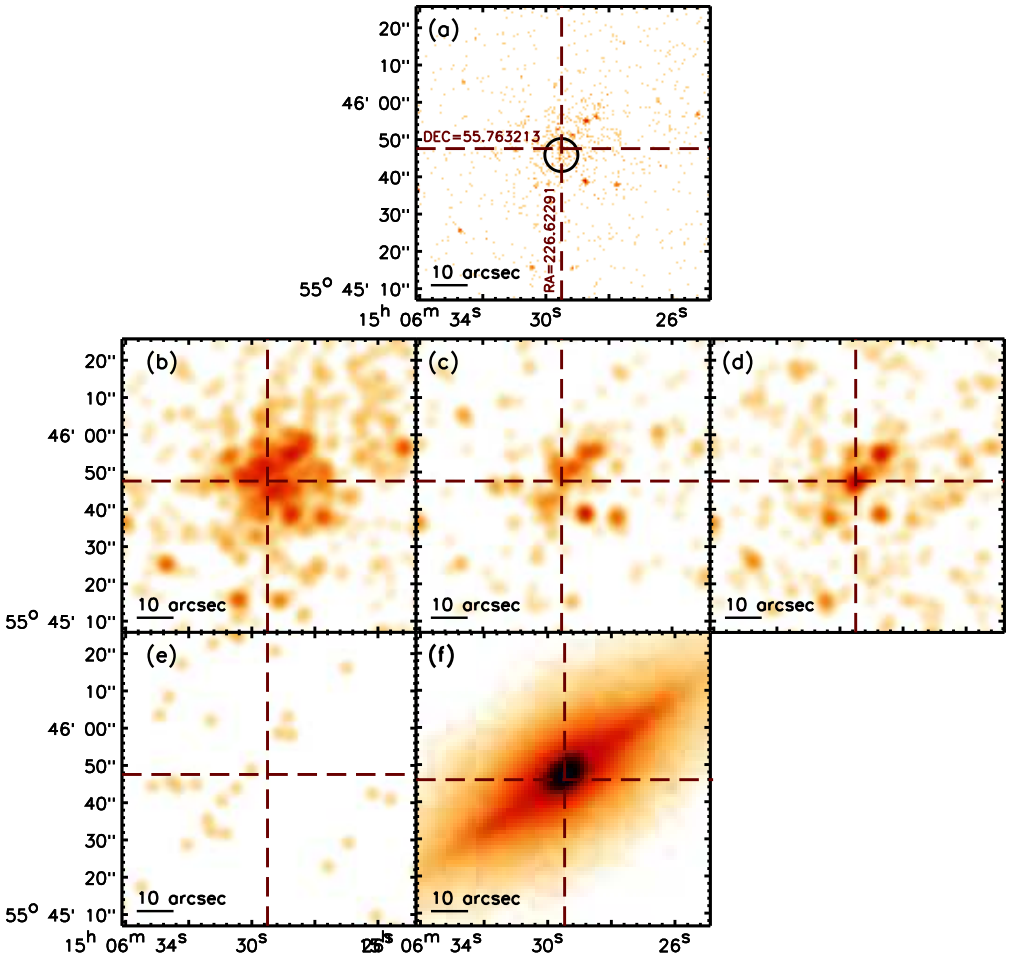

Figure C.70: *NGC5866*

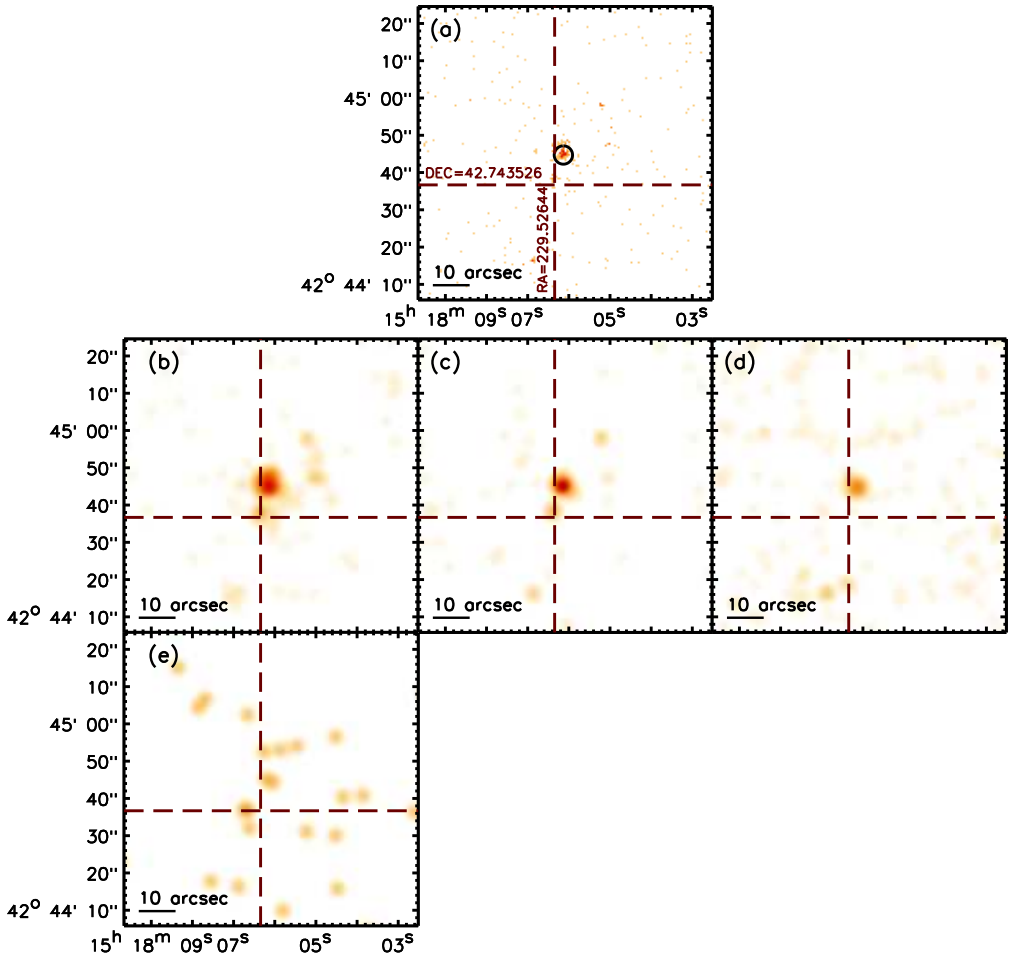

Figure C.71: *IZw107 (Mkn848)*

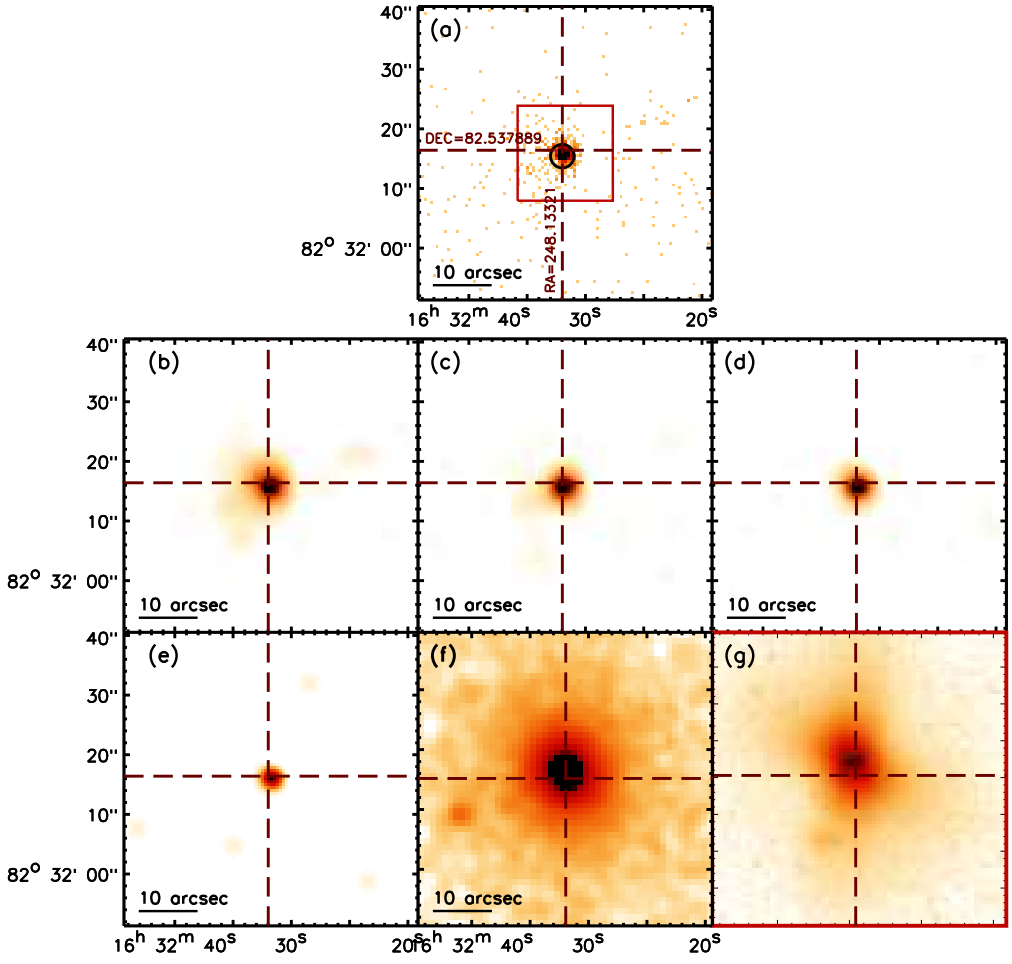

Figure C.72: *NGC6251*

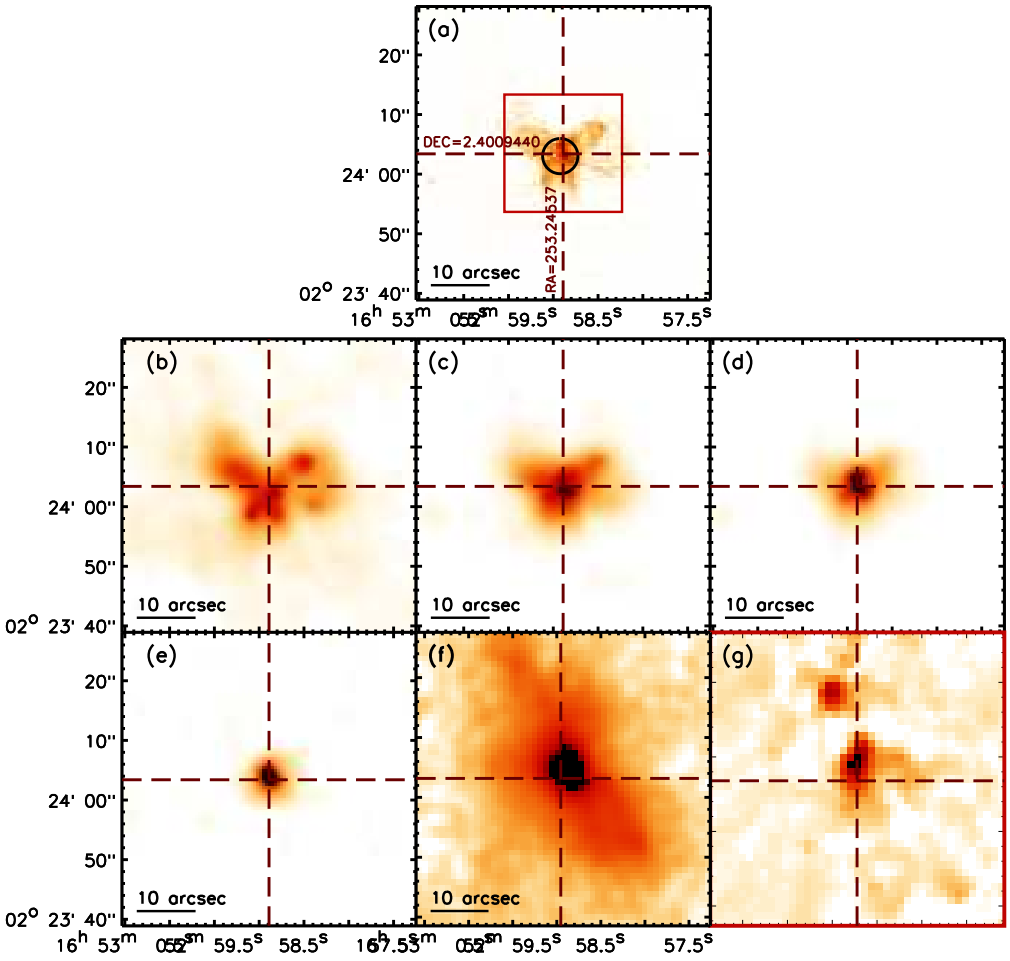

Figure C.73: *NGC6240*

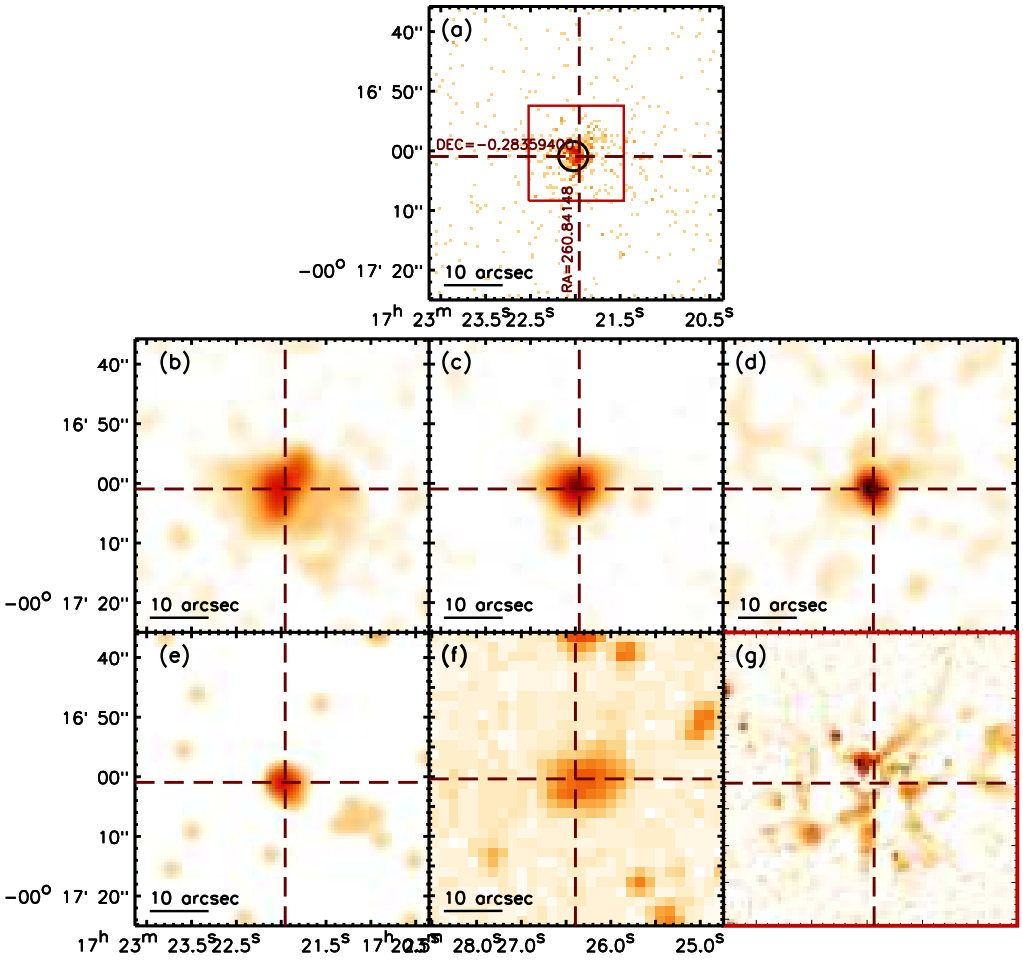

Figure C.74: *IRAS1720-0014*

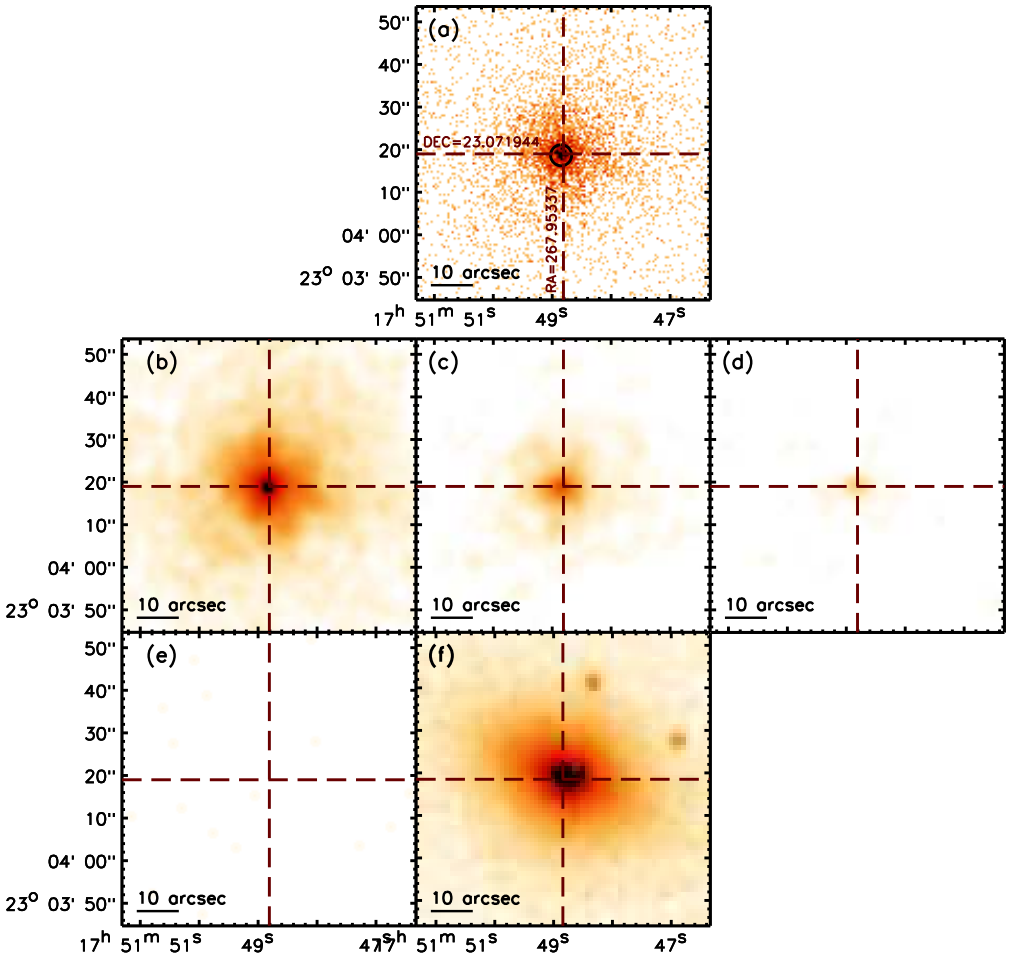

Figure C.75: *NGC6482*

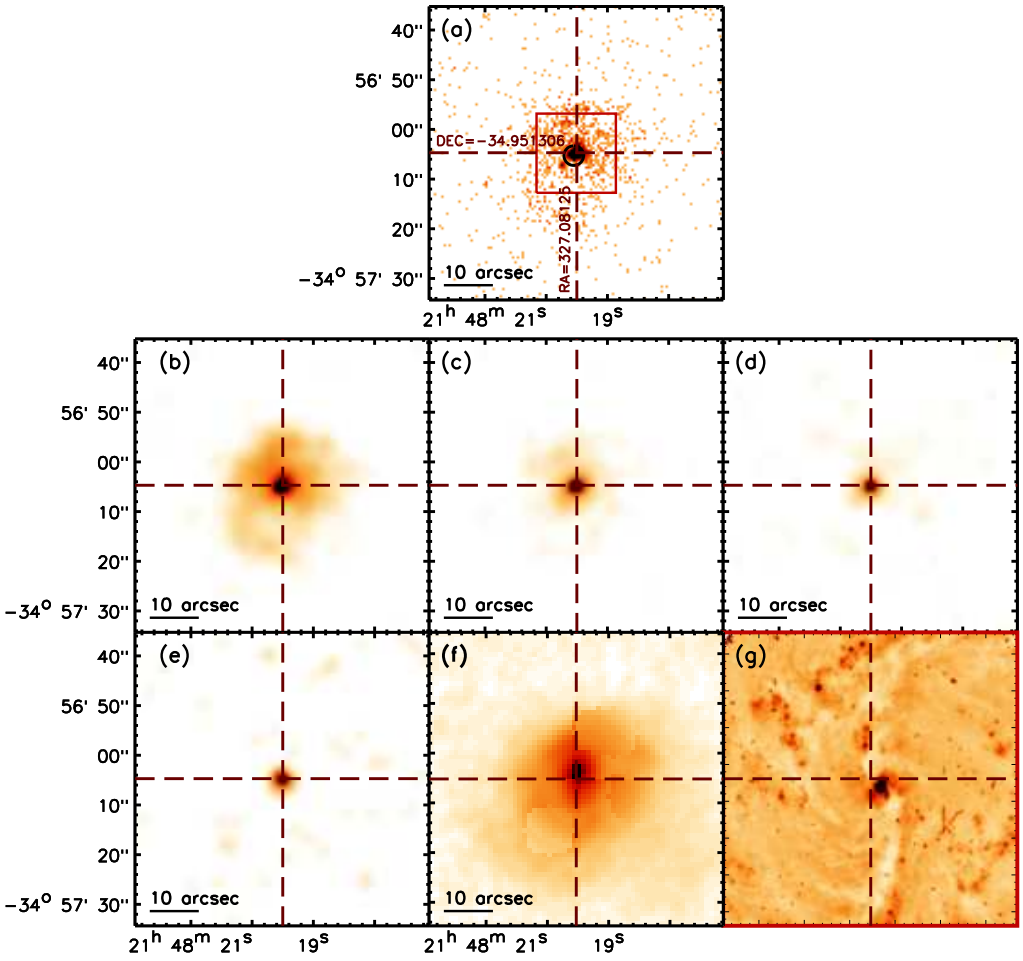

Figure C.76: *NGC7130*

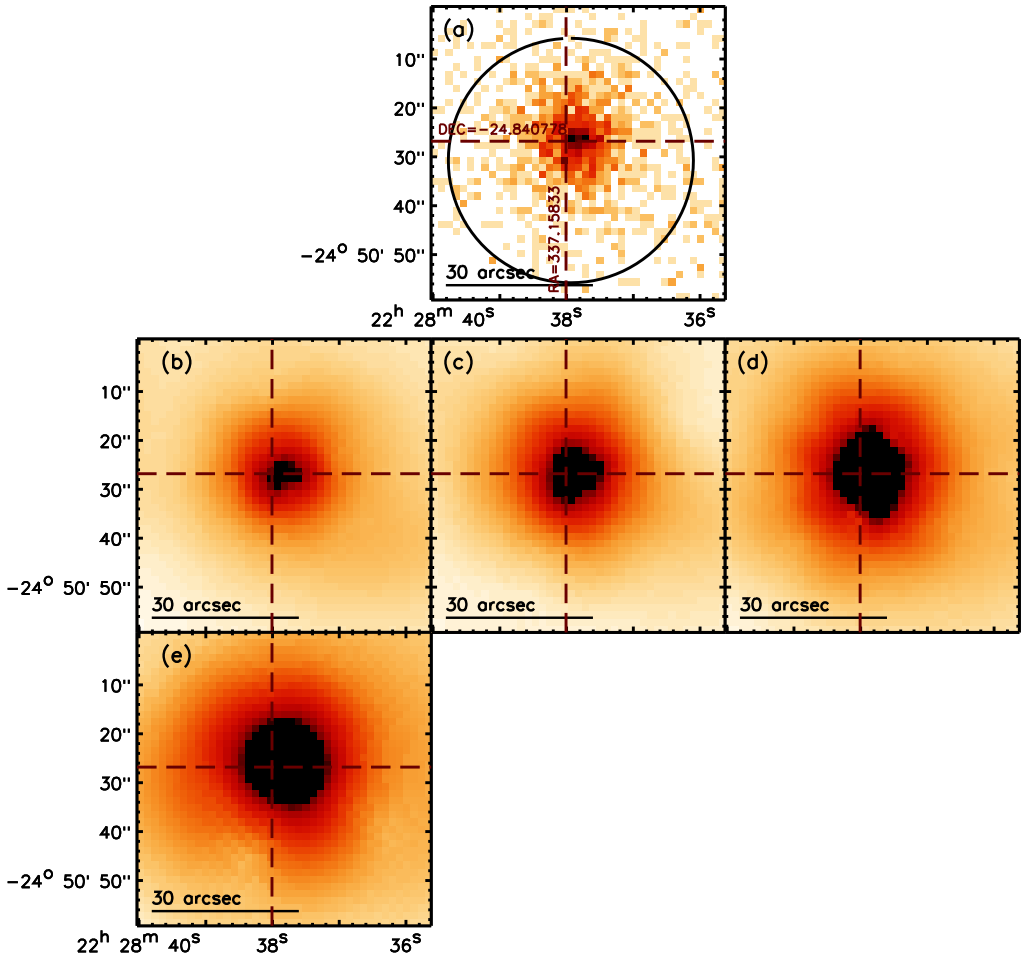

Figure C.77: *NGC7285 (XMM-Newton)*

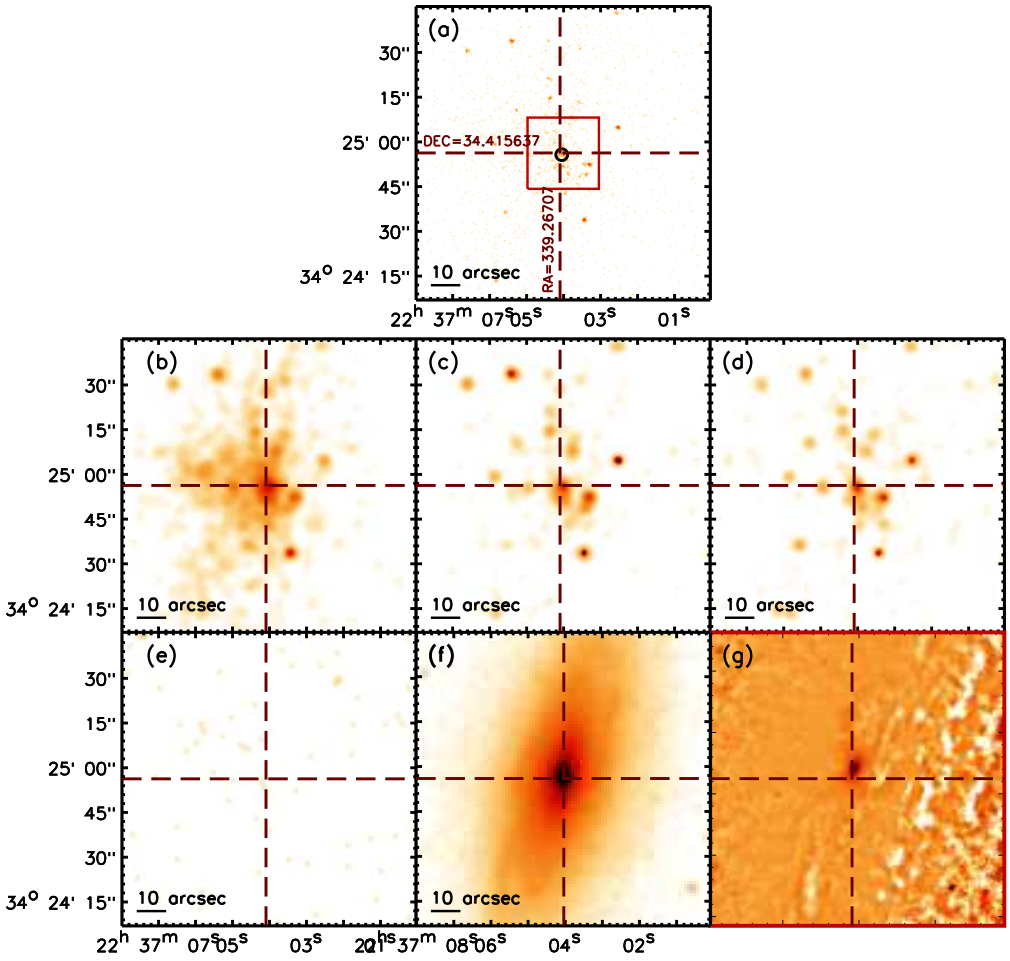

Figure C.78: *NGC 7331*

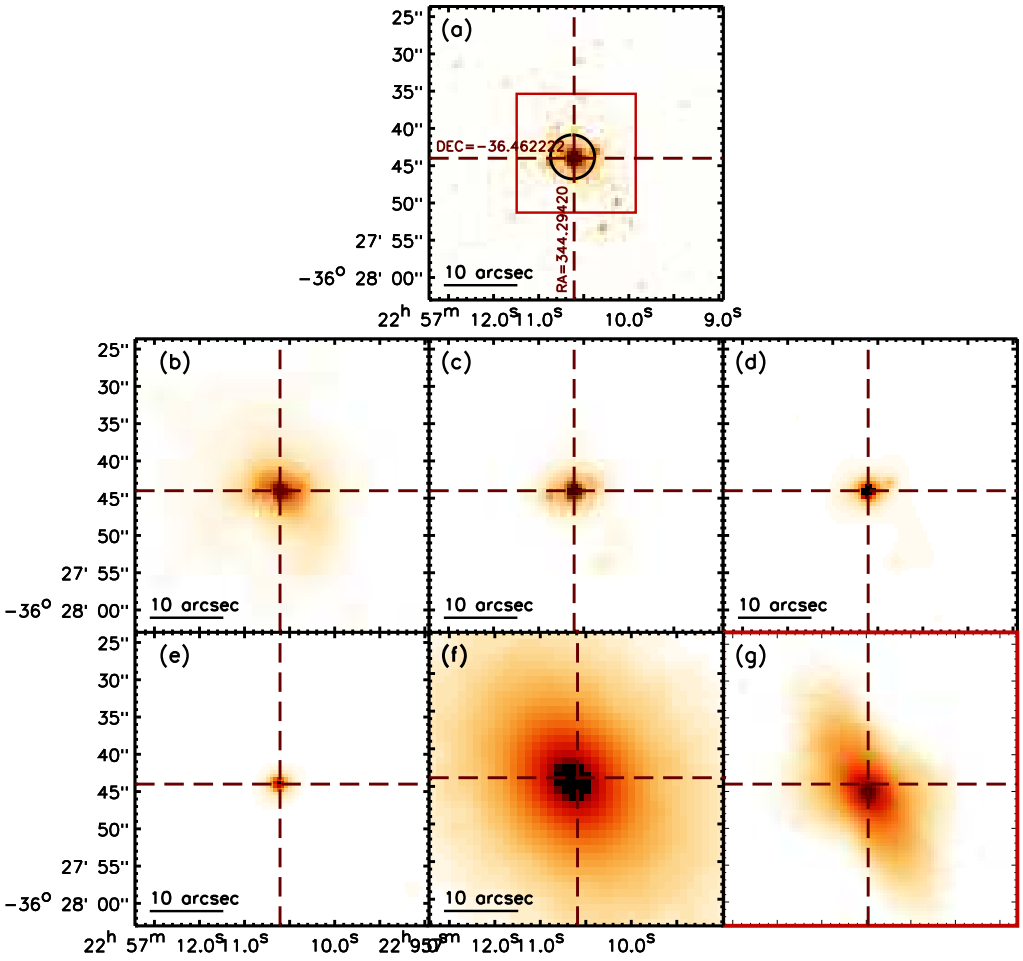

Figure C.79: *IC1459*

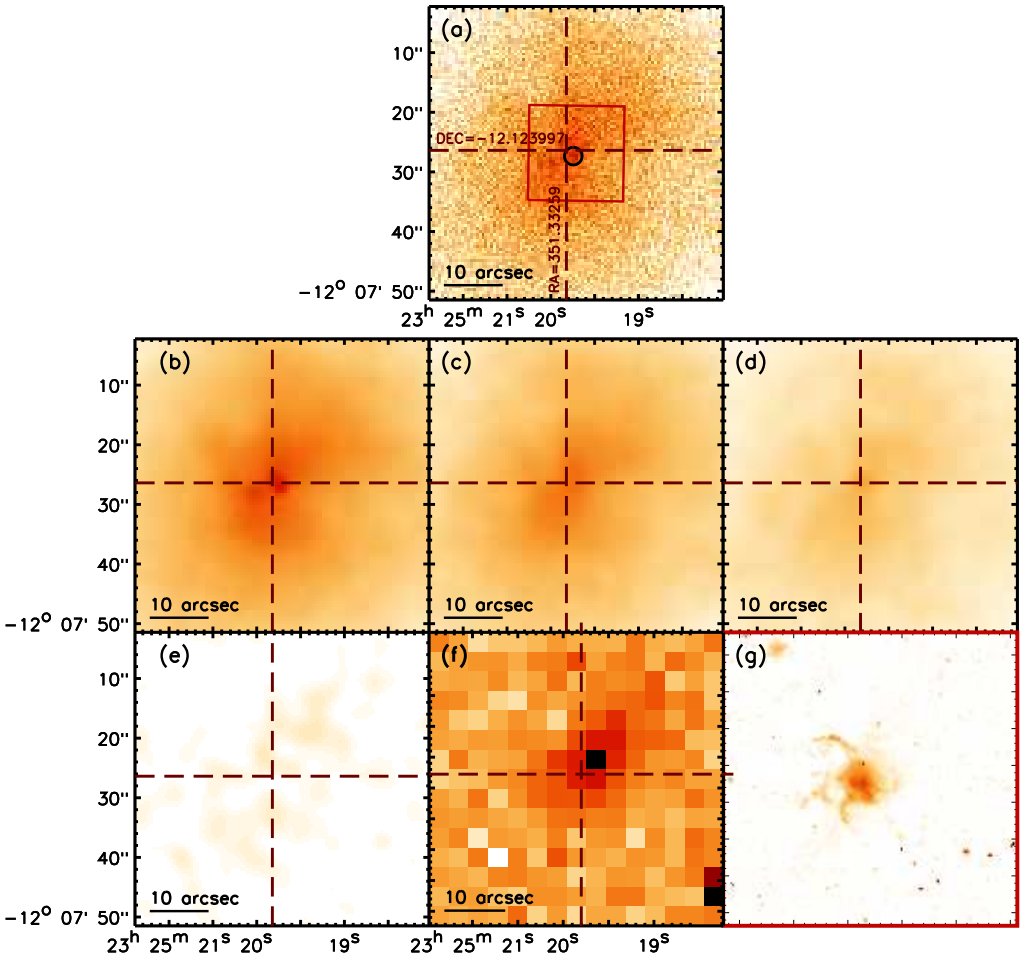

Figure C.80: *NPM1G-12.0625*

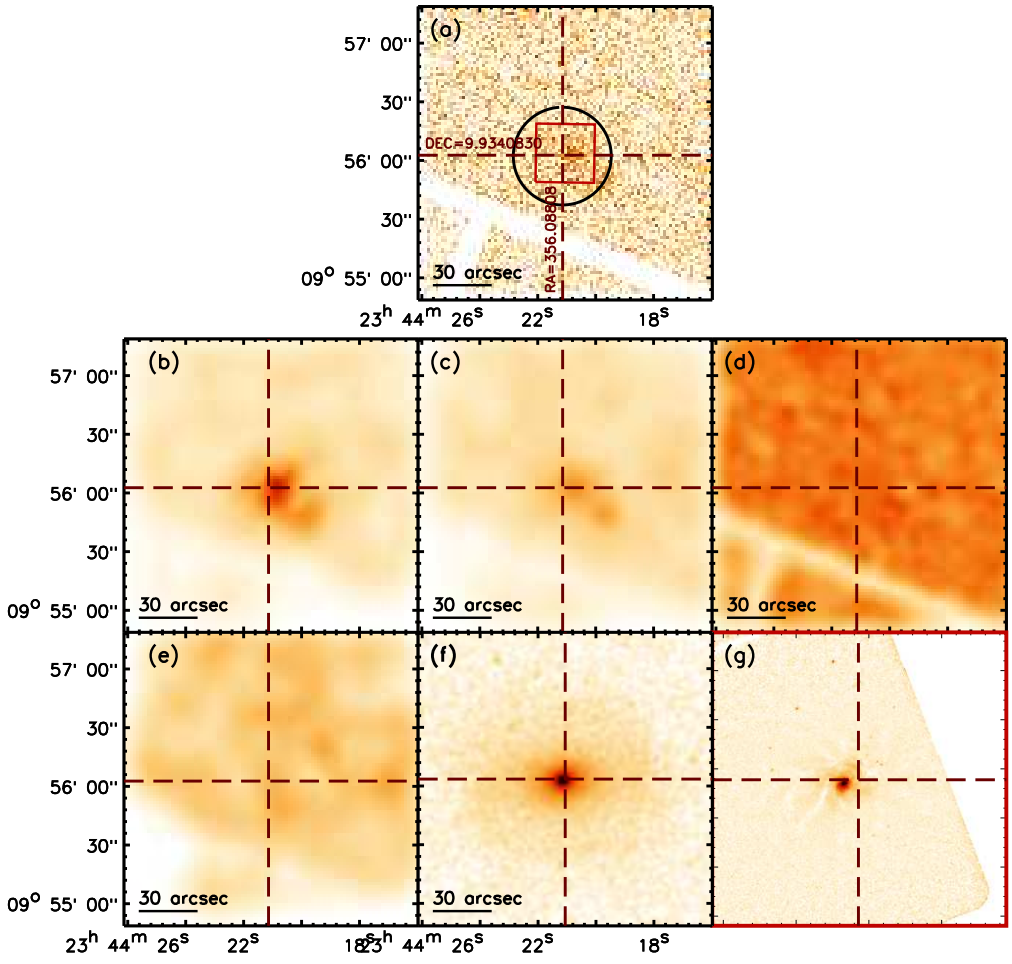

Figure C.81: *NGC7743 (XMM-Newton)*

Appendix D

Catalogue of spectra with *Chandra* data (Chapter 3)

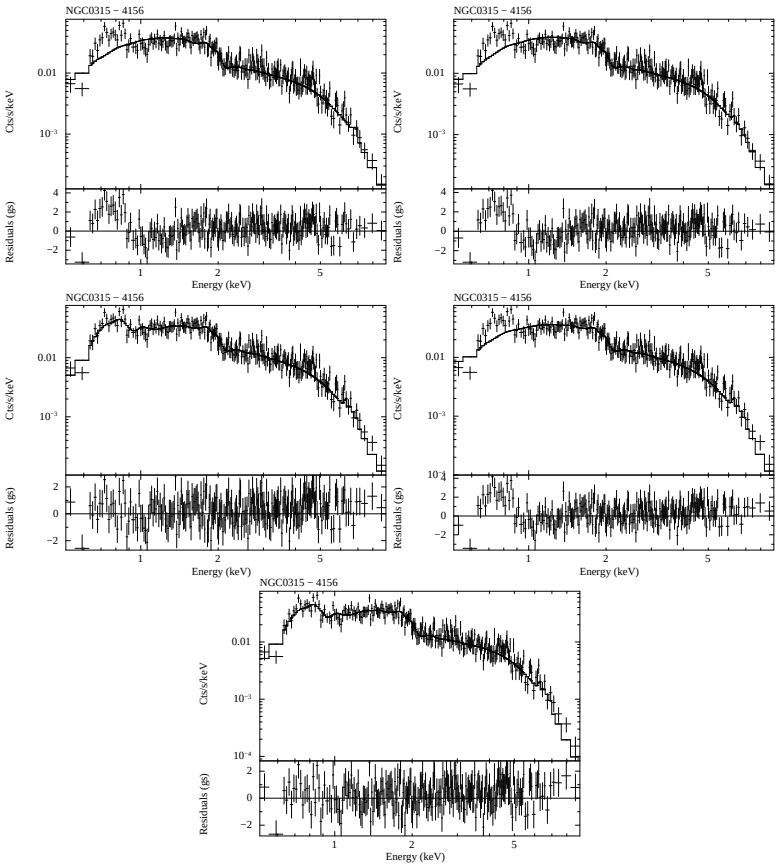

Figure D.1: *Spectral fits of NGC0315. (Top-left): Thermal model (MEKAL), (Top-right): Power-law model, (Center-left): Power-law plus thermal model, (Center-right): Two power-law model, (Bottom): Two power-law plus thermal model.*

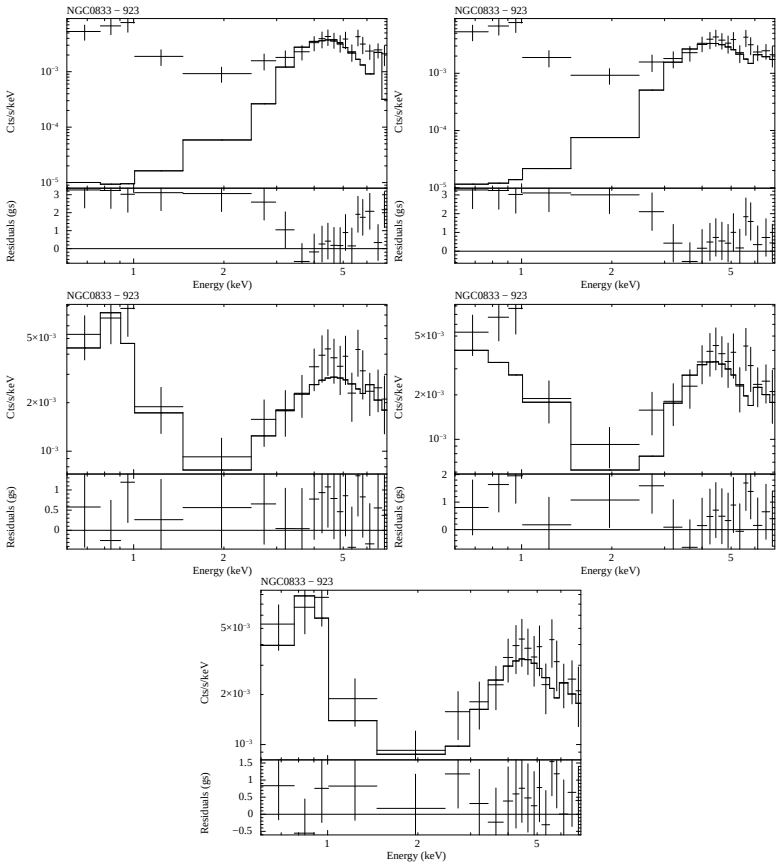

Figure D.2: *Spectral fits of NGC0833. (Top-left): Thermal model (MEKAL), (Top-right): Power-law model, (Center-left): Power-law plus thermal model, (Center-right): Two power-law model, (Bottom): Two power-law plus thermal model.*

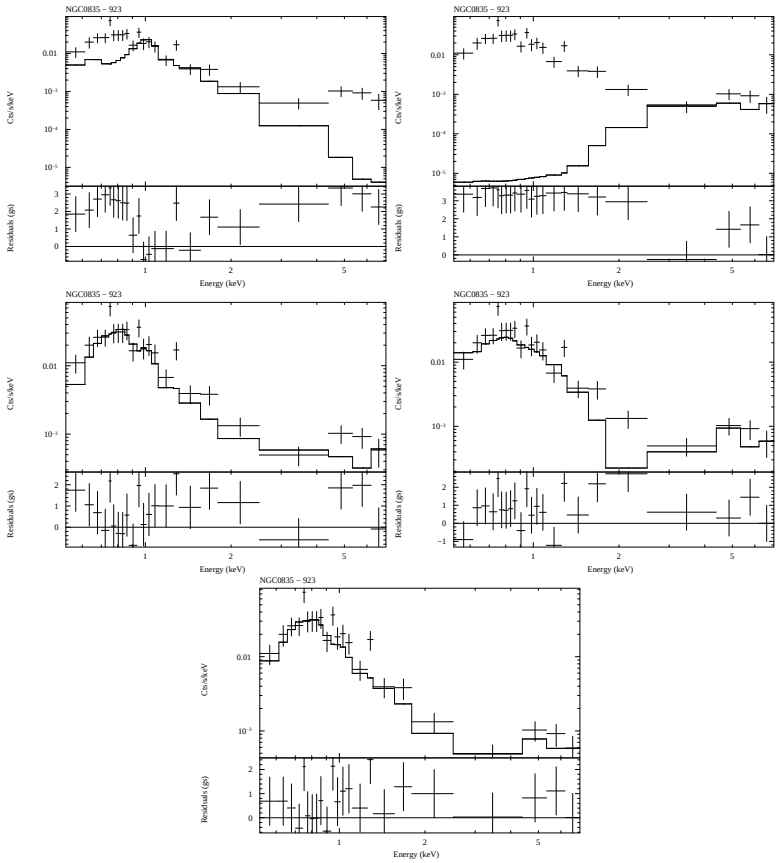

Figure D.3: *Spectral fits of NGC0835. (Top-left): Thermal model (MEKAL), (Top-right): Power-law model, (Center-left): Power-law plus thermal model, (Center-right): Two power-law model, (Bottom): Two power-law plus thermal model.*

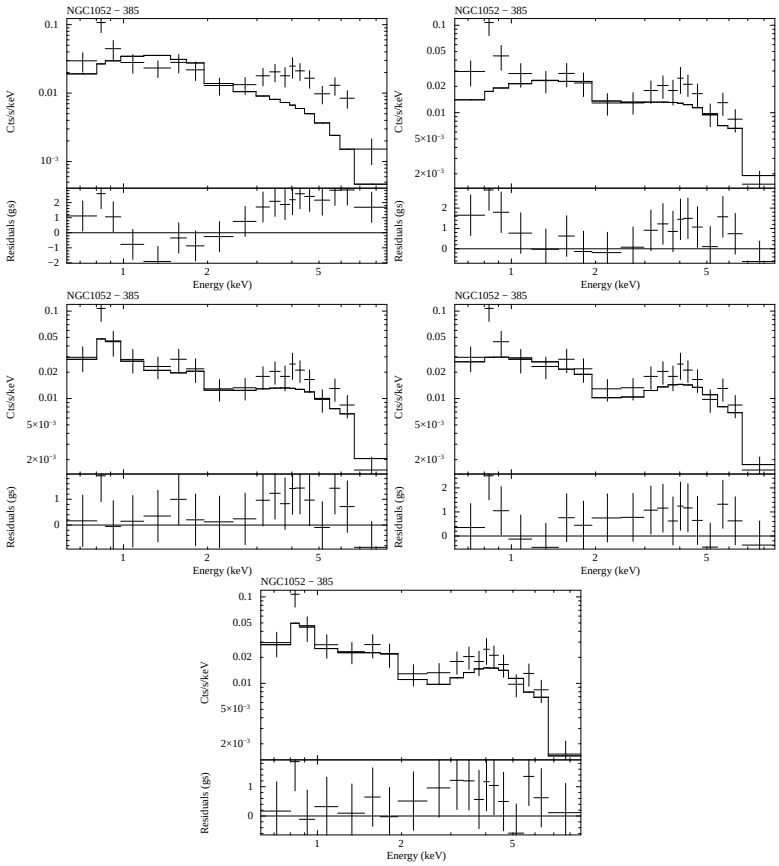

Figure D.4: *Spectral fits of NGC1052. (Top-left): Thermal model (MEKAL), (Top-right): Power-law model, (Center-left): Power-law plus thermal model, (Center-right): Two power-law model, (Bottom): Two power-law plus thermal model.*

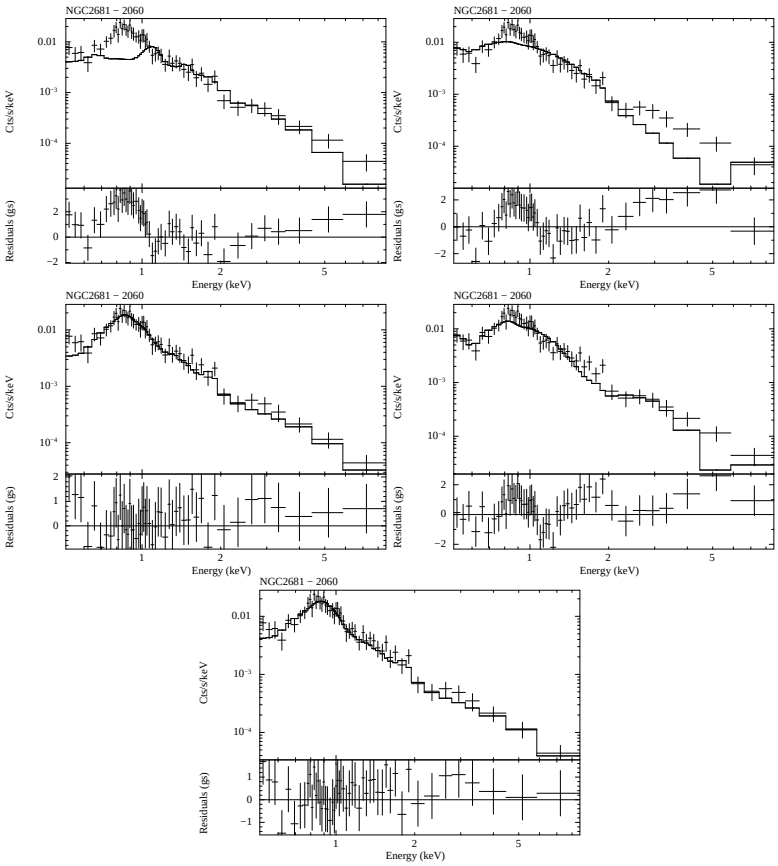

Figure D.5: *Spectral fits of NGC2681. (Top-left): Thermal model (MEKAL), (Top-right): Power-law model, (Center-left): Power-law plus thermal model, (Center-right): Two power-law model, (Bottom): Two power-law plus thermal model.*

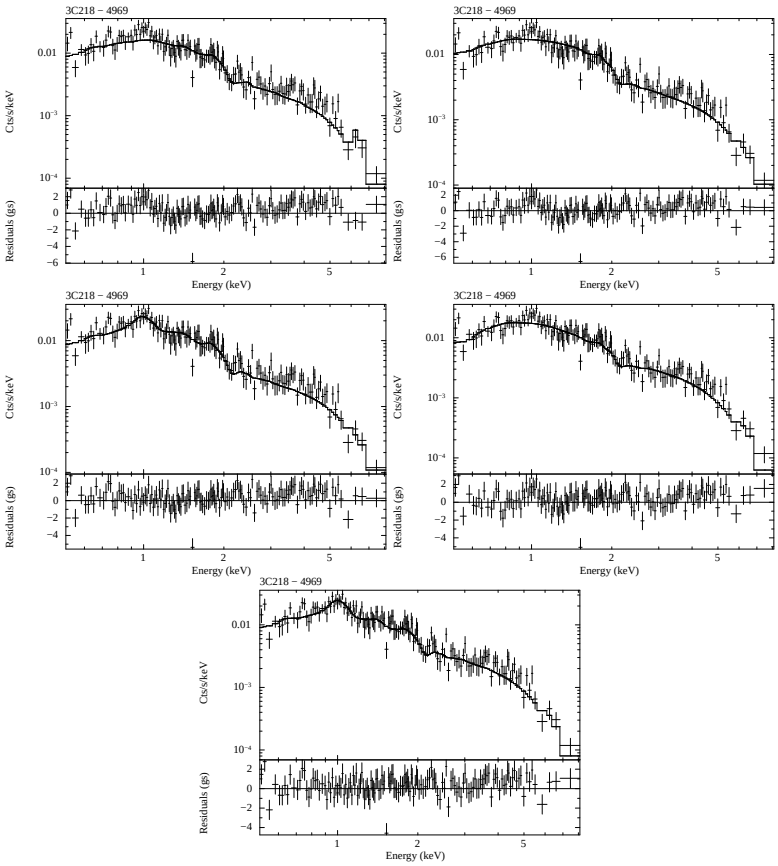

Figure D.6: *Spectral fits of 3C218. (Top-left): Thermal model (MEKAL), (Top-right): Power-law model, (Center-left): Power-law plus thermal model, (Center-right): Two power-law model, (Bottom): Two power-law plus thermal model.*

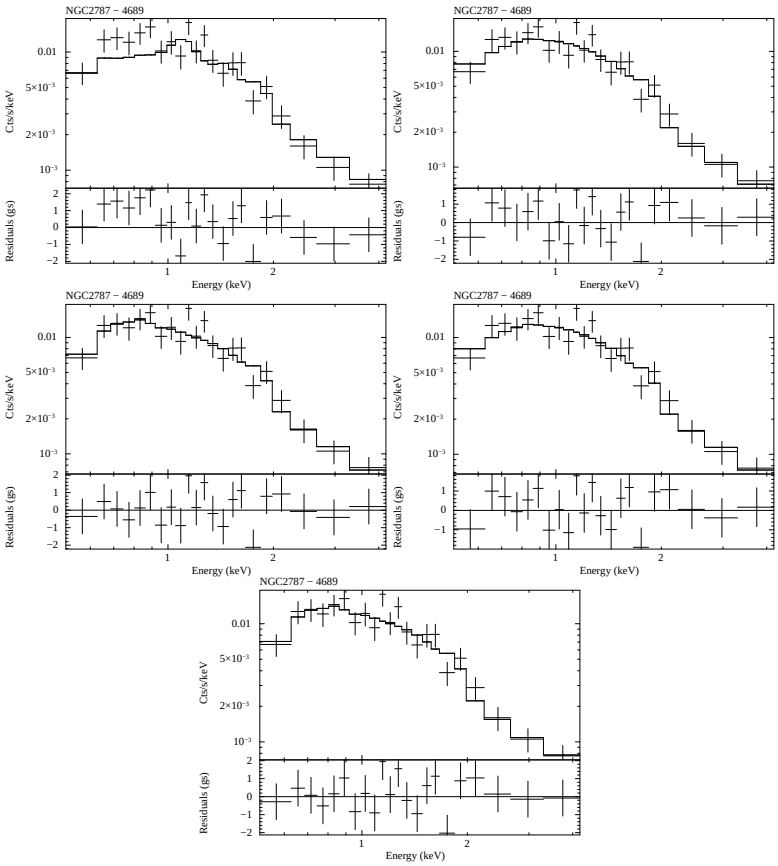

Figure D.7: *Spectral fits of NGC2787. (Top-left): Thermal model (MEKAL), (Top-right): Power-law model, (Center-left): Power-law plus thermal model, (Center-right): Two power-law model, (Bottom): Two power-law plus thermal model.*

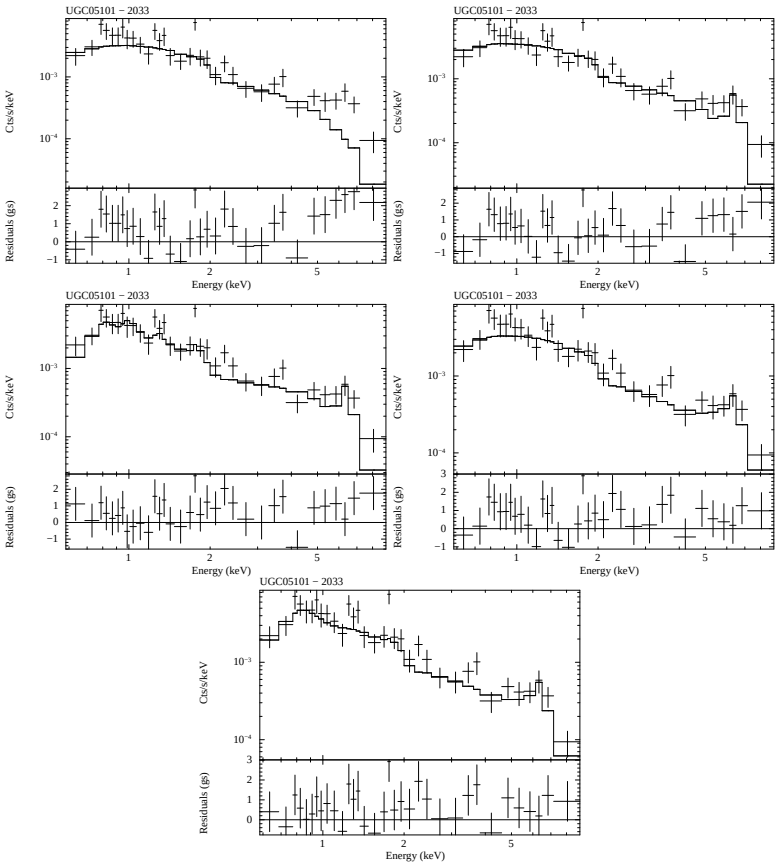

Figure D.8: *Spectral fits of UGC05101. (Top-left): Thermal model (MEKAL), (Top-right): Power-law model, (Center-left): Power-law plus thermal model, (Center-right): Two power-law model, (Bottom): Two power-law plus thermal model.*

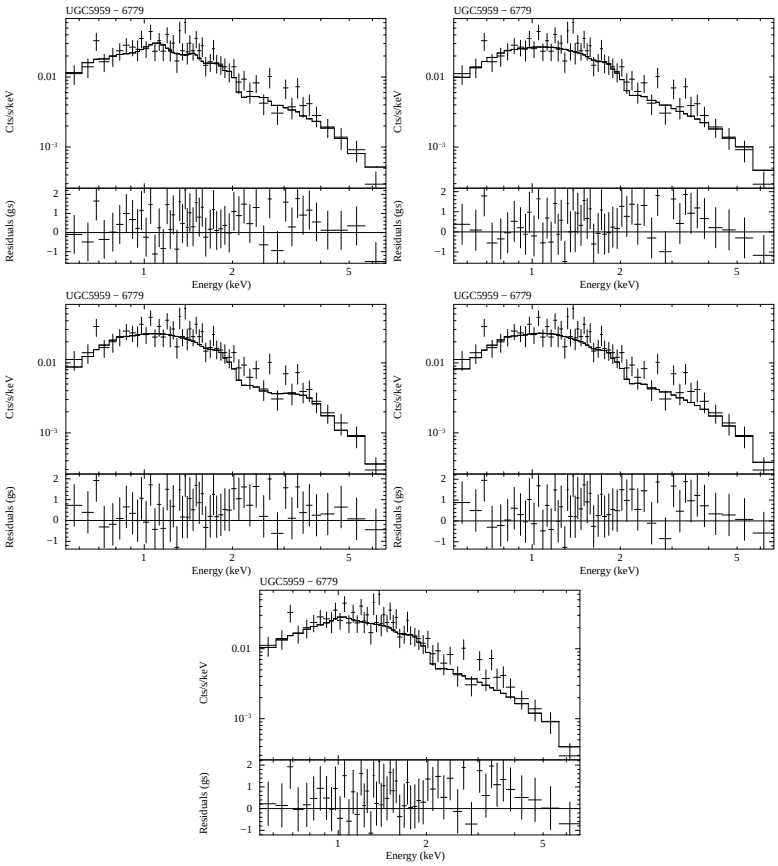

Figure D.9: *Spectral fits of UGC5959. (Top-left): Thermal model (MEKAL), (Top-right): Power-law model, (Center-left): Power-law plus thermal model, (Center-right): Two power-law model, (Bottom): Two power-law plus thermal model.*

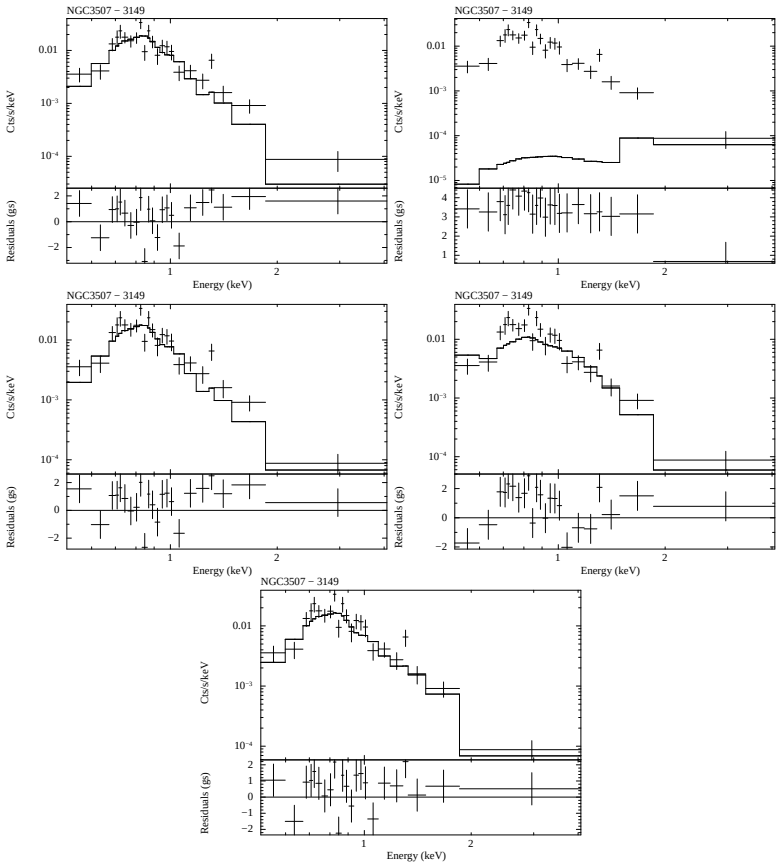

Figure D.10: *Spectral fits of NGC3507. (Top-left): Thermal model (MEKAL), (Top-right): Power-law model, (Center-left): Power-law plus thermal model, (Center-right): Two power-law model, (Bottom): Two power-law plus thermal model.*

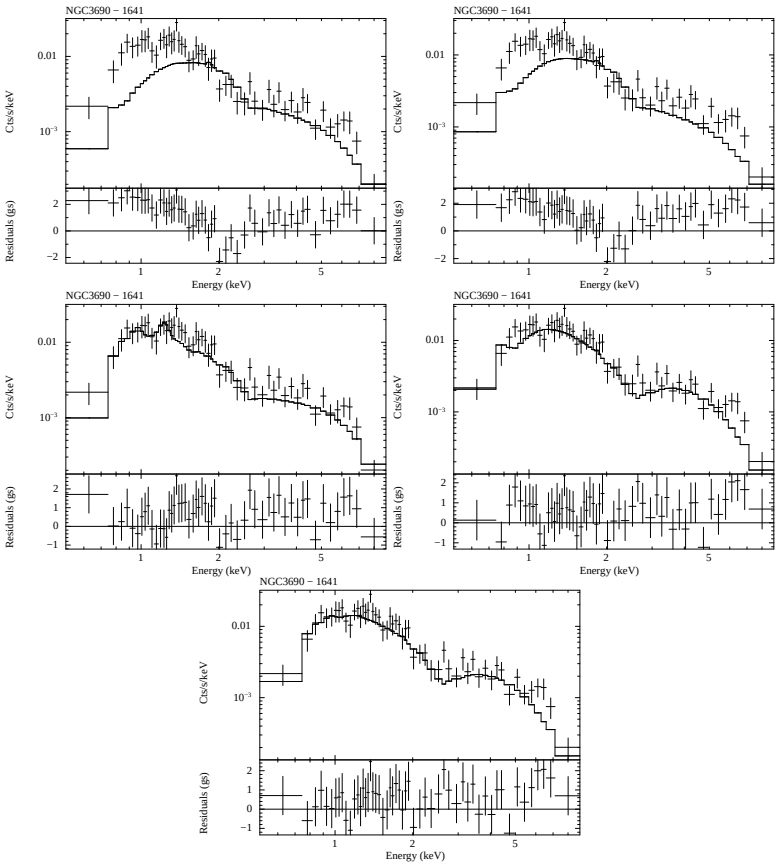

Figure D.11: *Spectral fits of NGC3690. (Top-left): Thermal model (MEKAL), (Top-right): Power-law model, (Center-left): Power-law plus thermal model, (Center-right): Two power-law model, (Bottom): Two power-law plus thermal model.*

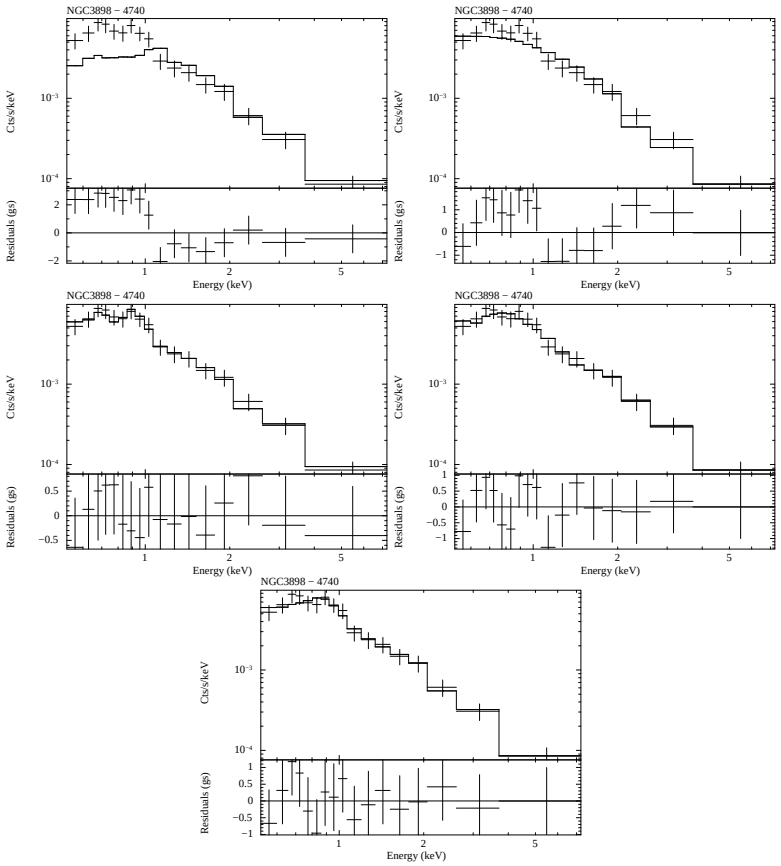

Figure D.12: *Spectral fits of NGC3898. (Top-left): Thermal model (MEKAL), (Top-right): Power-law model, (Center-left): Power-law plus thermal model, (Center-right): Two power-law model, (Bottom): Two power-law plus thermal model.*

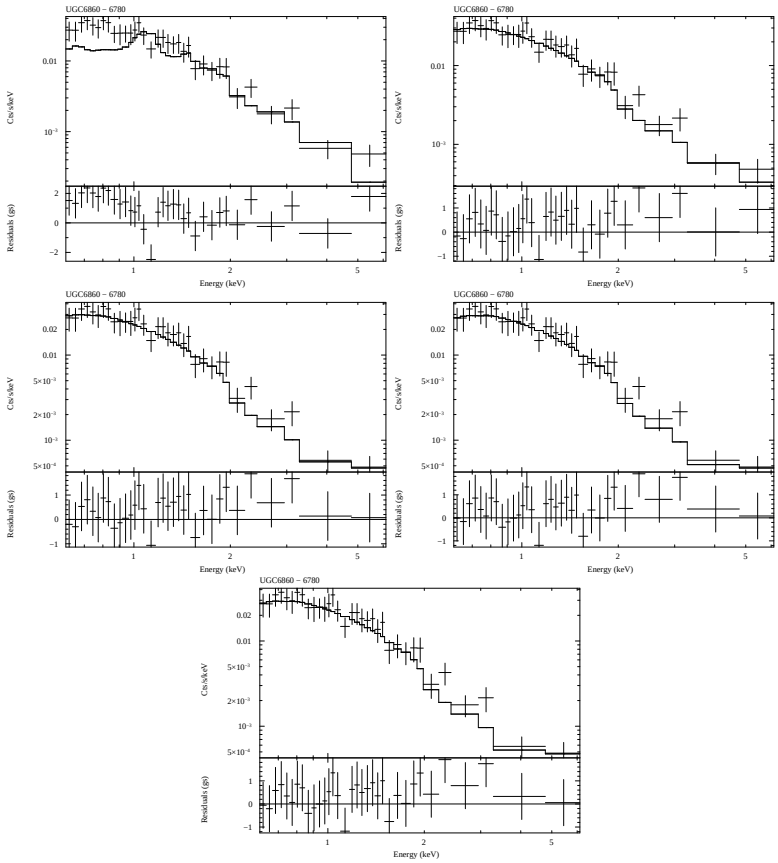

Figure D.13: *Spectral fits of UGC6860. (Top-left): Thermal model (MEKAL), (Top-right): Power-law model, (Center-left): Power-law plus thermal model, (Center-right): Two power-law model, (Bottom): Two power-law plus thermal model.*

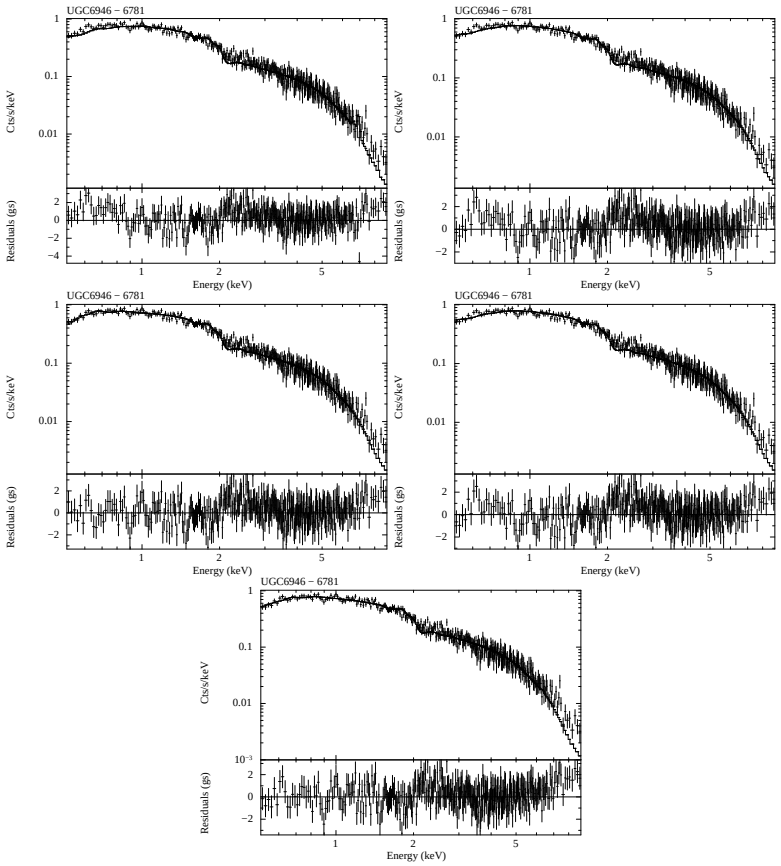

Figure D.14: *Spectral fits of UGC6946. (Top-left): Thermal model (MEKAL), (Top-right): Power-law model, (Center-left): Power-law plus thermal model, (Center-right): Two power-law model, (Bottom): Two power-law plus thermal model.*

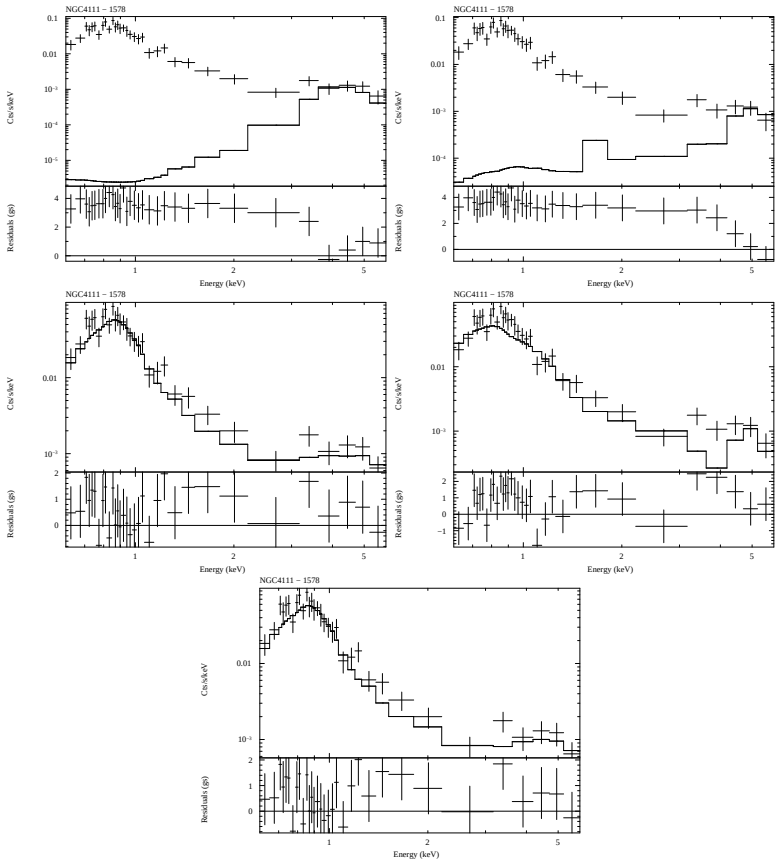

Figure D.15: *Spectral fits of NGC4111. (Top-left): Thermal model (MEKAL), (Top-right): Power-law model, (Center-left): Power-law plus thermal model, (Center-right): Two power-law model, (Bottom): Two power-law plus thermal model.*

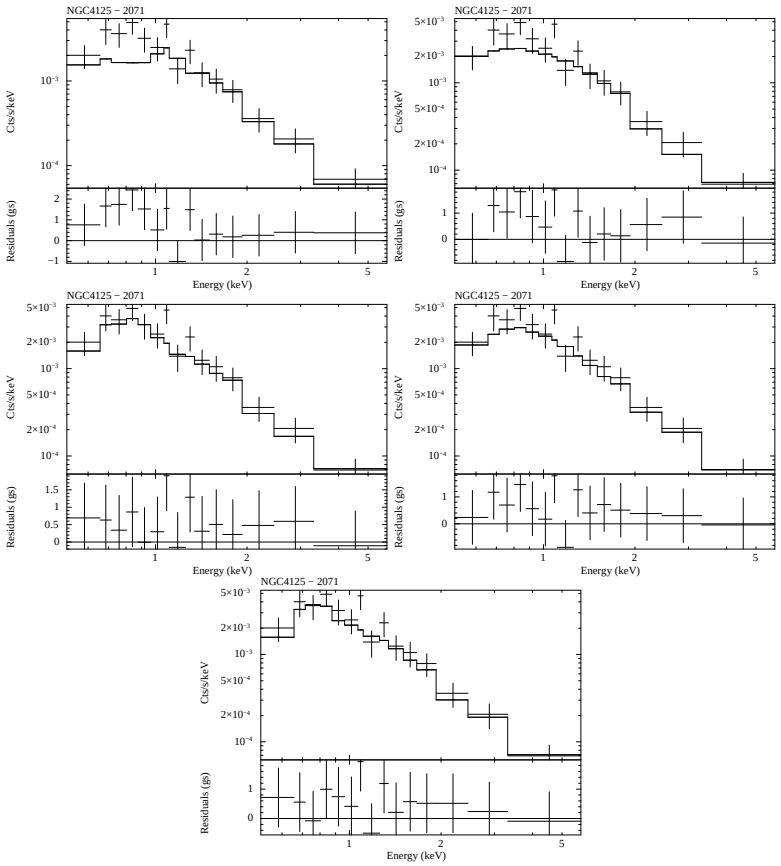

Figure D.16: *Spectral fits of NGC4125. (Top-left): Thermal model (MEKAL), (Top-right): Power-law model, (Center-left): Power-law plus thermal model, (Center-right): Two power-law model, (Bottom): Two power-law plus thermal model.*

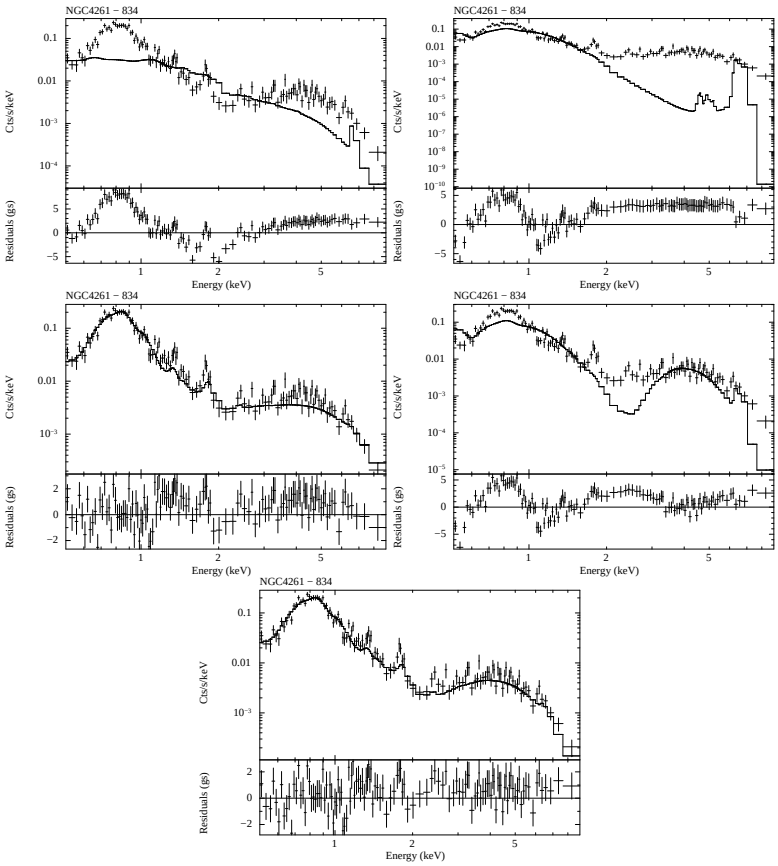

Figure D.17: *Spectral fits of NGC4261. (Top-left): Thermal model (MEKAL), (Top-right): Power-law model, (Center-left): Power-law plus thermal model, (Center-right): Two power-law model, (Bottom): Two power-law plus thermal model.*

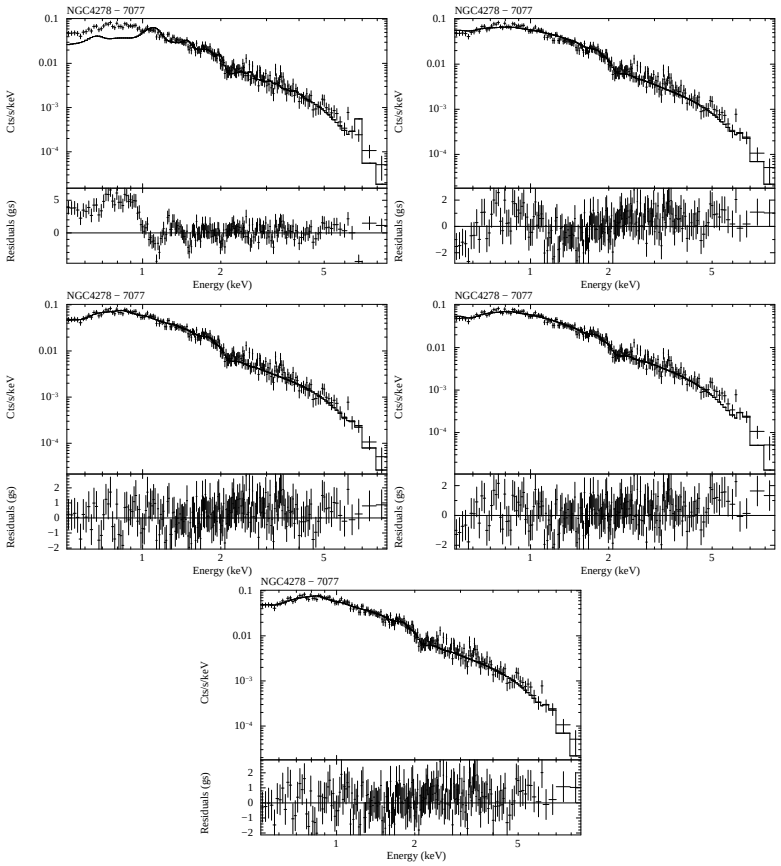

Figure D.18: *Spectral fits of NGC4278. (Top-left): Thermal model (MEKAL), (Top-right): Power-law model, (Center-left): Power-law plus thermal model, (Center-right): Two power-law model, (Bottom): Two power-law plus thermal model.*

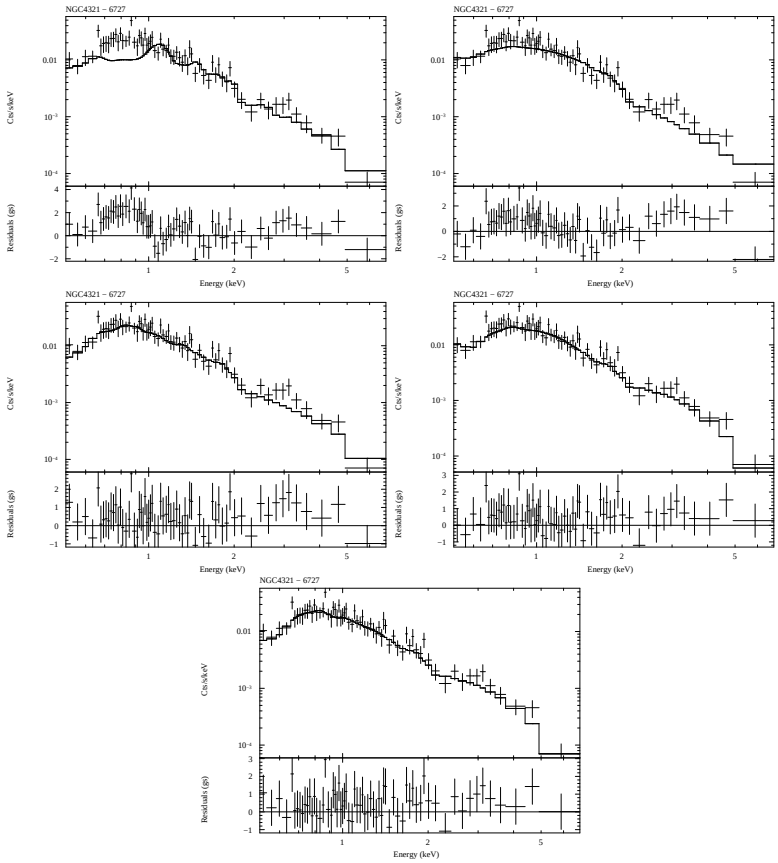

Figure D.19: *Spectral fits of NGC4321. (Top-left): Thermal model (MEKAL), (Top-right): Power-law model, (Center-left): Power-law plus thermal model, (Center-right): Two power-law model, (Bottom): Two power-law plus thermal model.*

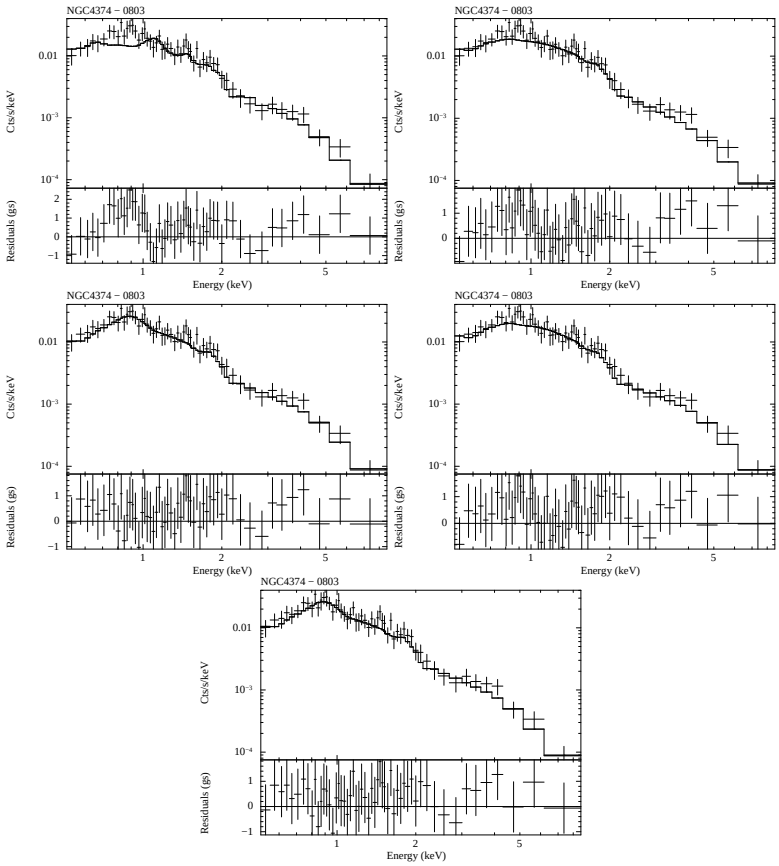

Figure D.20: *Spectral fits of NGC4374. (Top-left): Thermal model (MEKAL), (Top-right): Power-law model, (Center-left): Power-law plus thermal model, (Center-right): Two power-law model, (Bottom): Two power-law plus thermal model.*

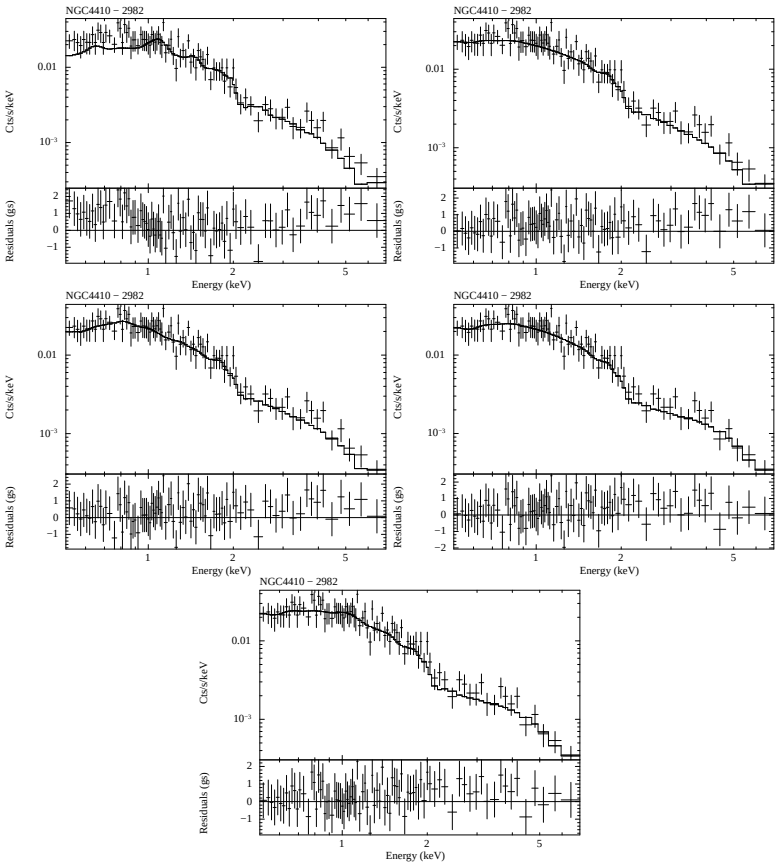

Figure D.21: *Spectral fits of NGC4410. (Top-left): Thermal model (MEKAL), (Top-right): Power-law model, (Center-left): Power-law plus thermal model, (Center-right): Two power-law model, (Bottom): Two power-law plus thermal model.*

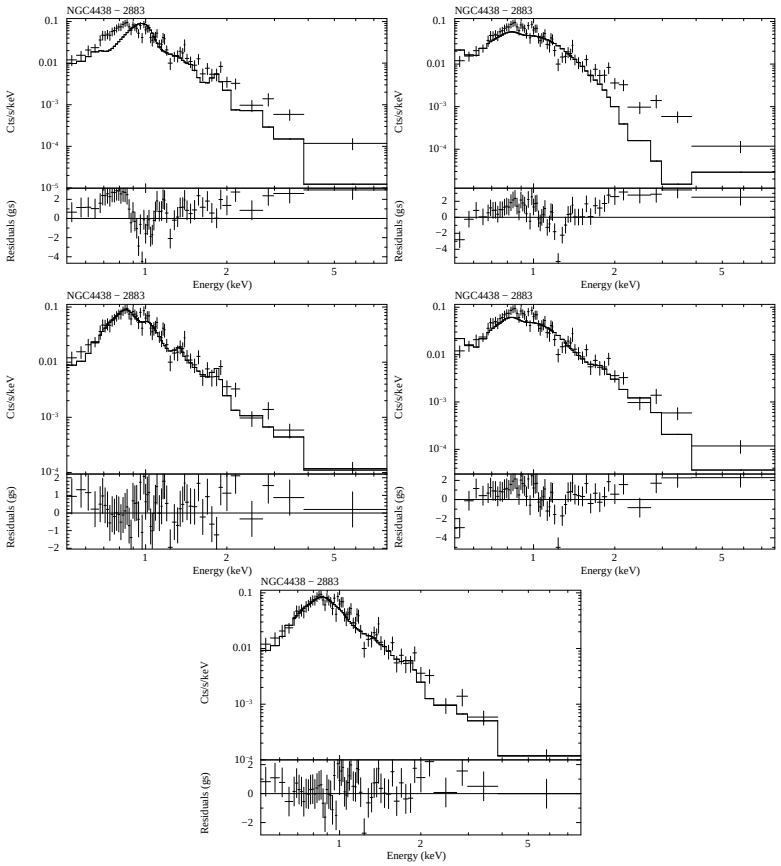

Figure D.22: *Spectral fits of NGC4438. (Top-left): Thermal model (MEKAL), (Top-right): Power-law model, (Center-left): Power-law plus thermal model, (Center-right): Two power-law model, (Bottom): Two power-law plus thermal model.*

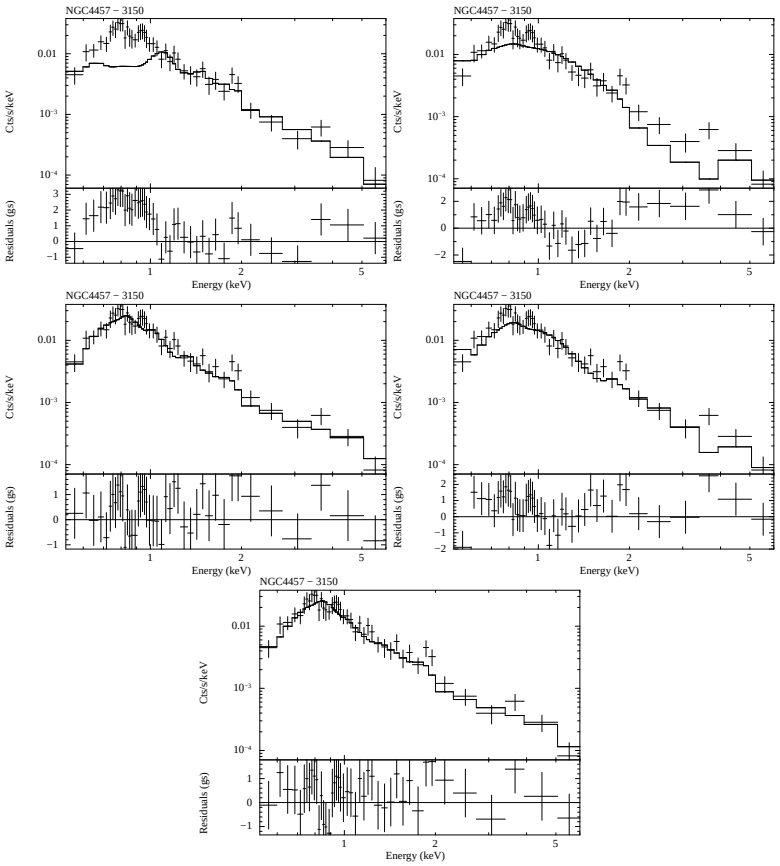

Figure D.23: *Spectral fits of NGC4457. (Top-left): Thermal model (MEKAL), (Top-right): Power-law model, (Center-left): Power-law plus thermal model, (Center-right): Two power-law model, (Bottom): Two power-law plus thermal model.*

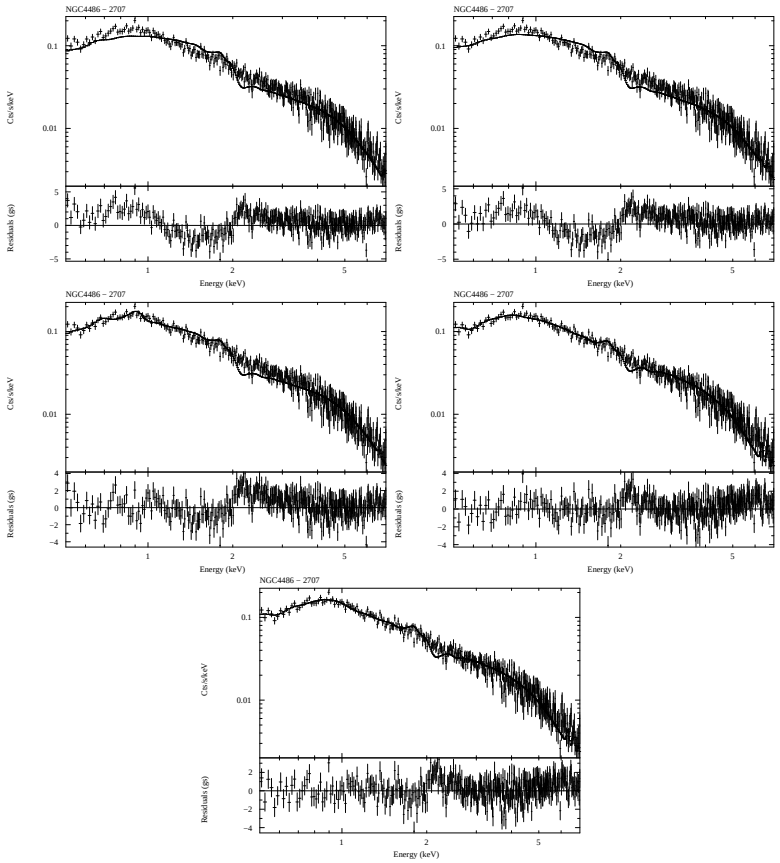

Figure D.24: *Spectral fits of NGC4486. (Top-left): Thermal model (MEKAL), (Top-right): Power-law model, (Center-left): Power-law plus thermal model, (Center-right): Two power-law model, (Bottom): Two power-law plus thermal model.*

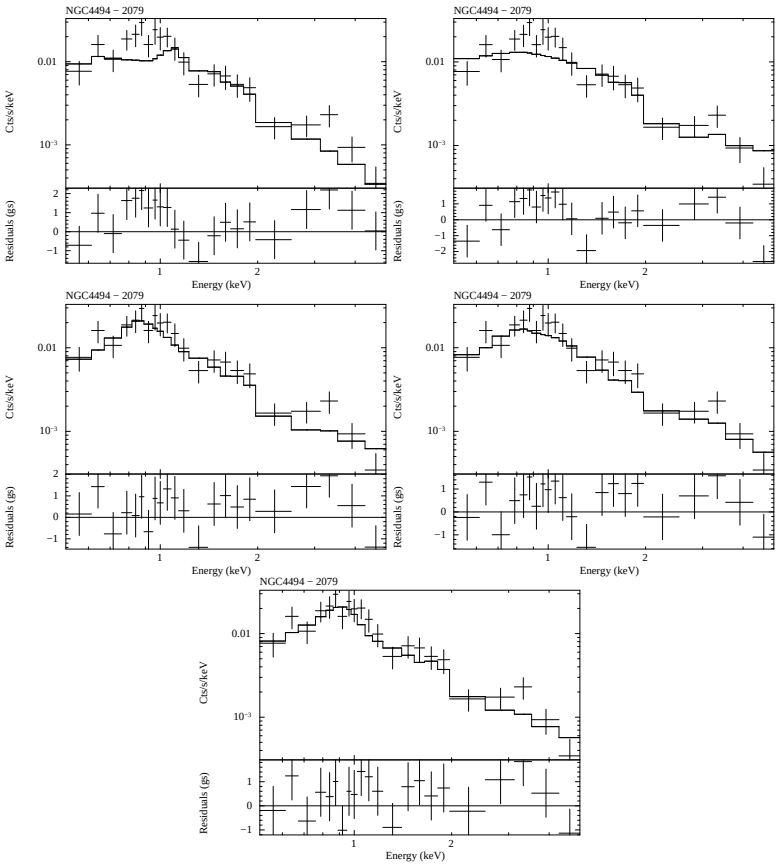

Figure D.25: *Spectral fits of NGC4494. (Top-left): Thermal model (MEKAL), (Top-right): Power-law model, (Center-left): Power-law plus thermal model, (Center-right): Two power-law model, (Bottom): Two power-law plus thermal model.*

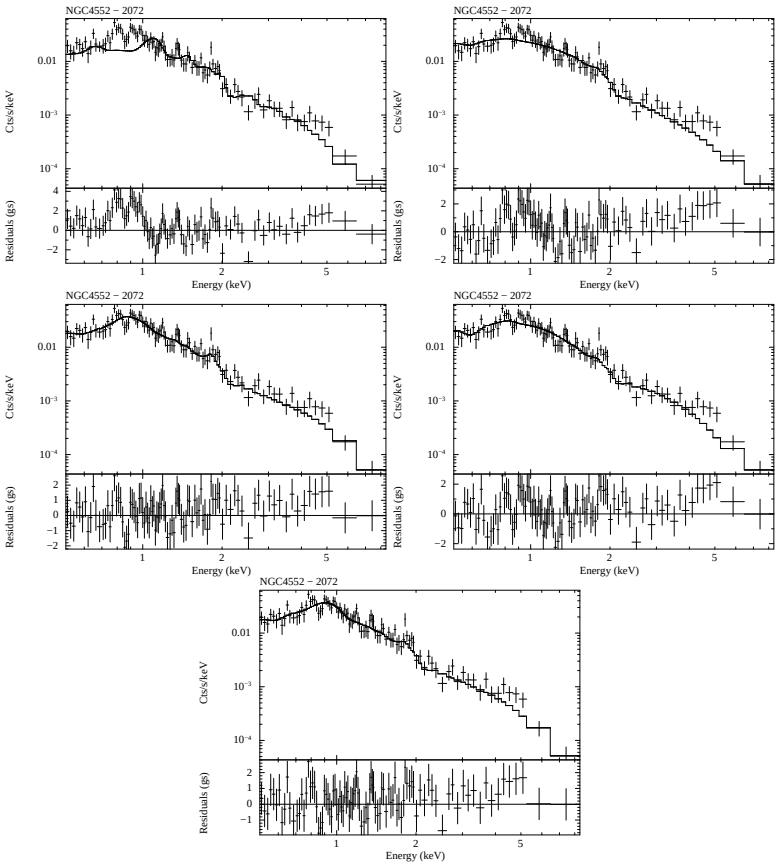

Figure D.26: *Spectral fits of NGC4552. (Top-left): Thermal model (MEKAL), (Top-right): Power-law model, (Center-left): Power-law plus thermal model, (Center-right): Two power-law model, (Bottom): Two power-law plus thermal model.*

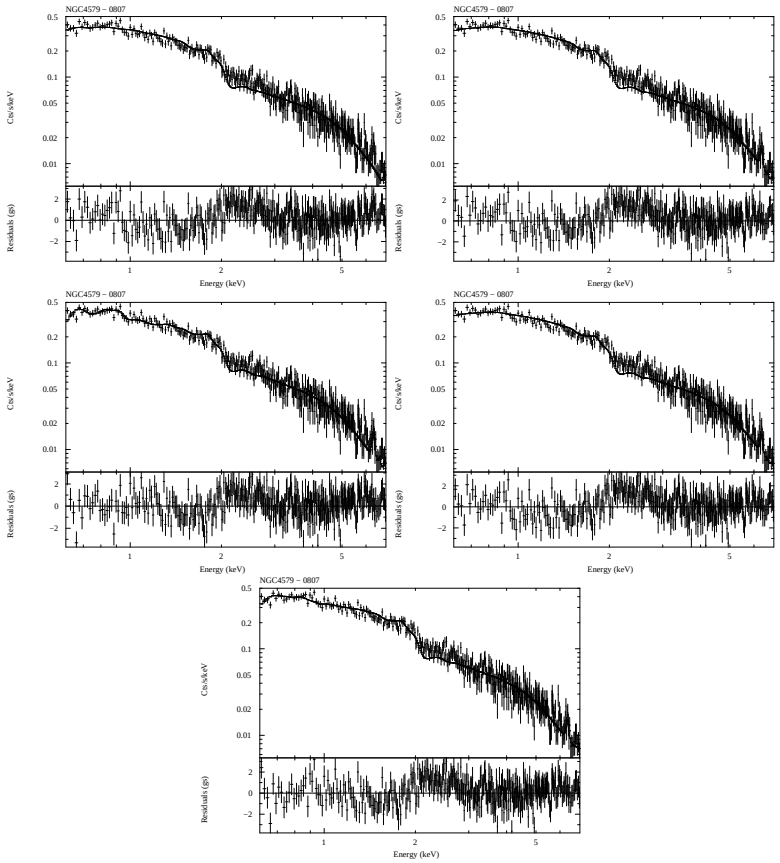

Figure D.27: *Spectral fits of NGC4579. (Top-left): Thermal model (MEKAL), (Top-right): Power-law model, (Center-left): Power-law plus thermal model, (Center-right): Two power-law model, (Bottom): Two power-law plus thermal model.*

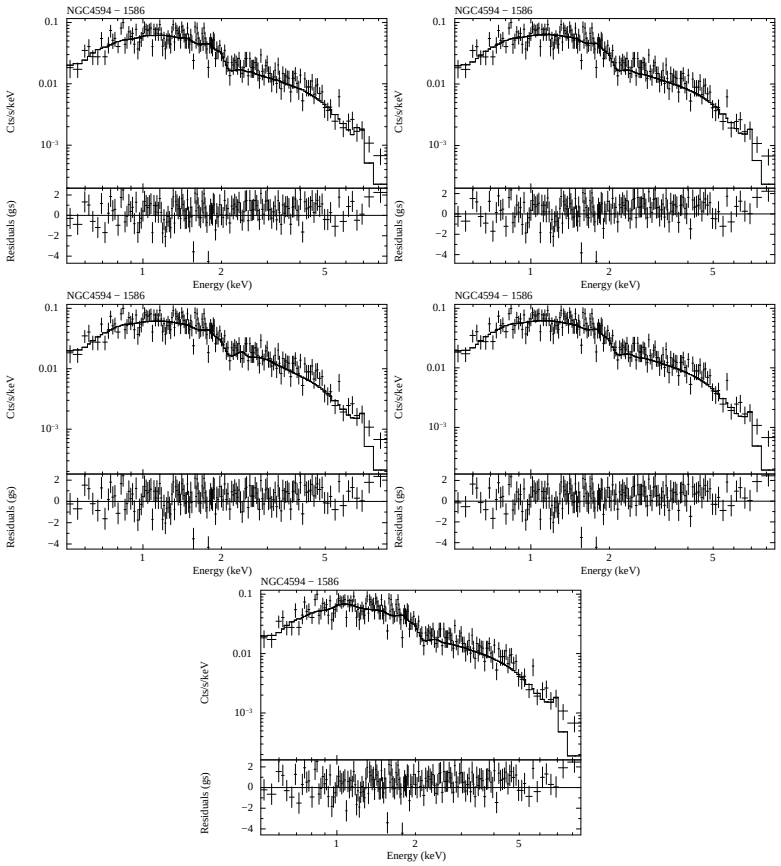

Figure D.28: *Spectral fits of NGC4594. (Top-left): Thermal model (MEKAL), (Top-right): Power-law model, (Center-left): Power-law plus thermal model, (Center-right): Two power-law model, (Bottom): Two power-law plus thermal model.*

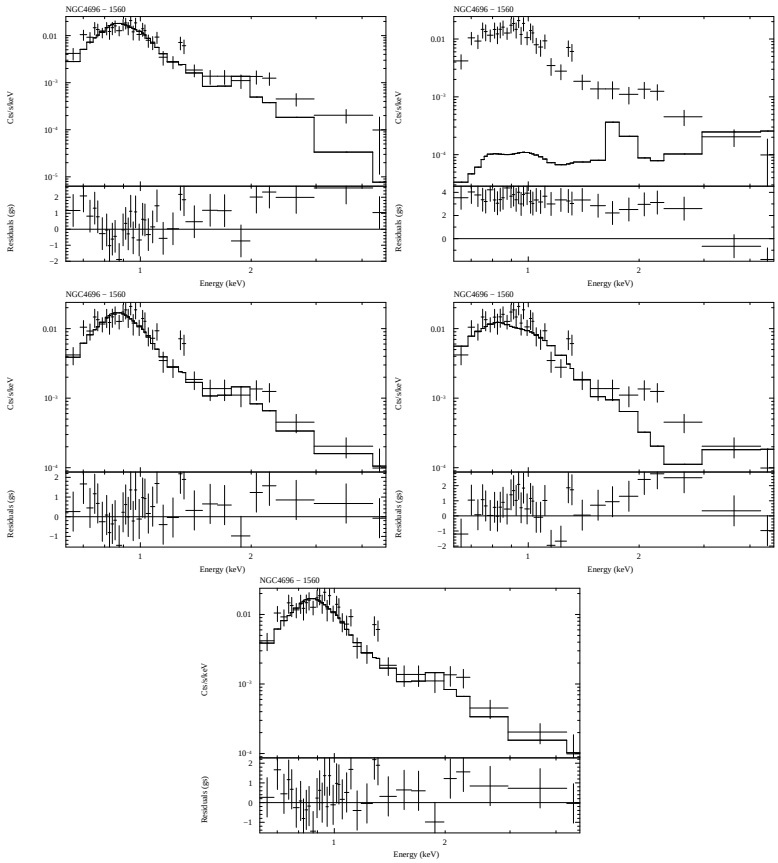

Figure D.29: *Spectral fits of NGC4696. (Top-left): Thermal model (MEKAL), (Top-right): Power-law model, (Center-left): Power-law plus thermal model, (Center-right): Two power-law model, (Bottom): Two power-law plus thermal model.*

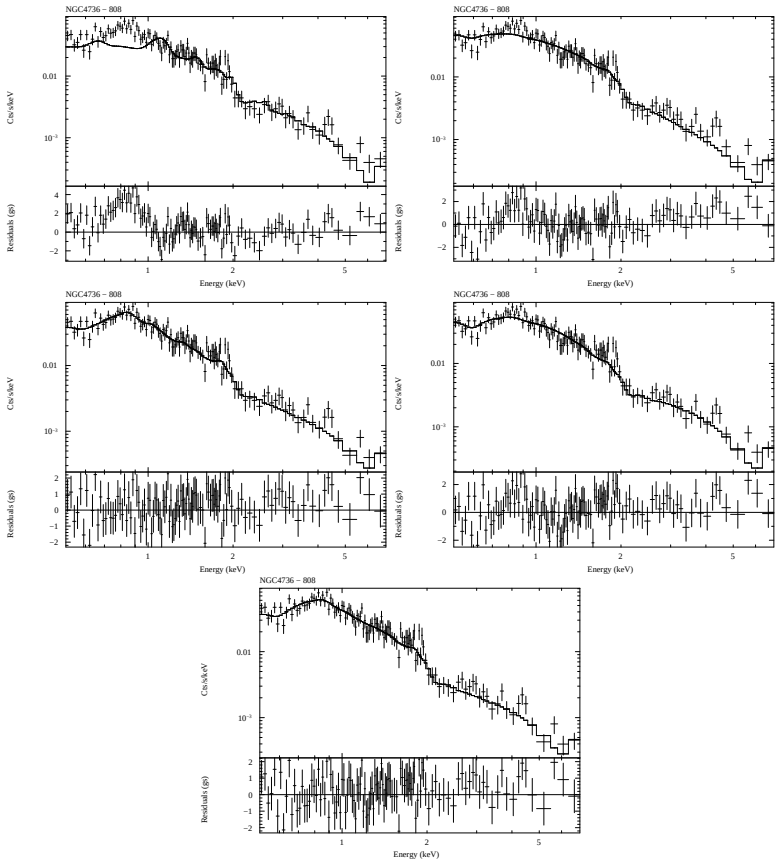

Figure D.30: *Spectral fits of NGC4736. (Top-left): Thermal model (MEKAL), (Top-right): Power-law model, (Center-left): Power-law plus thermal model, (Center-right): Two power-law model, (Bottom): Two power-law plus thermal model.*

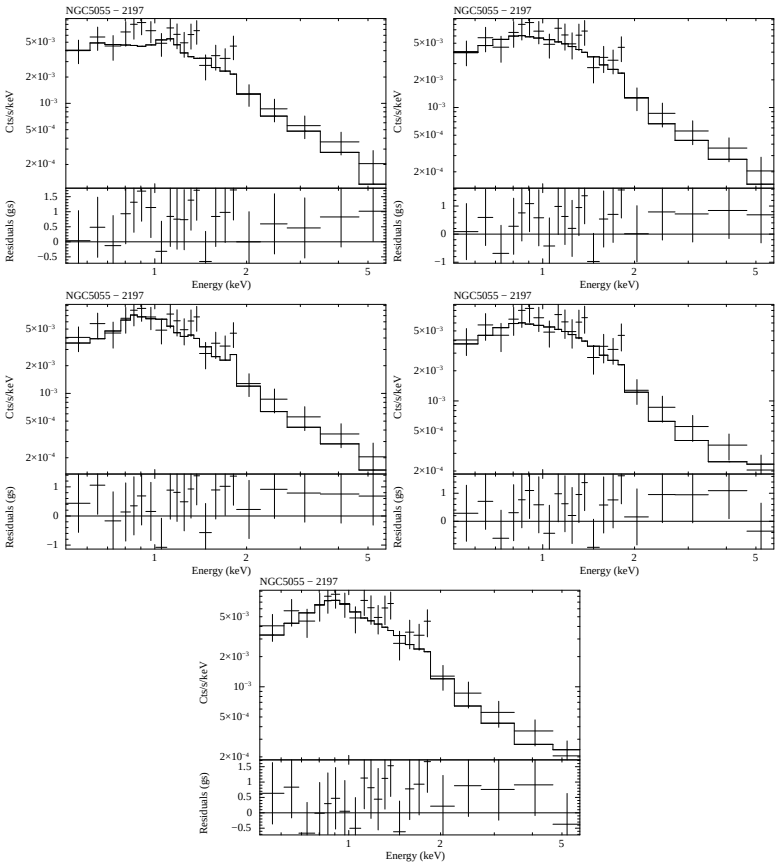

Figure D.31: *Spectral fits of NGC5055. (Top-left): Thermal model (MEKAL), (Top-right): Power-law model, (Center-left): Power-law plus thermal model, (Center-right): Two power-law model, (Bottom): Two power-law plus thermal model.*

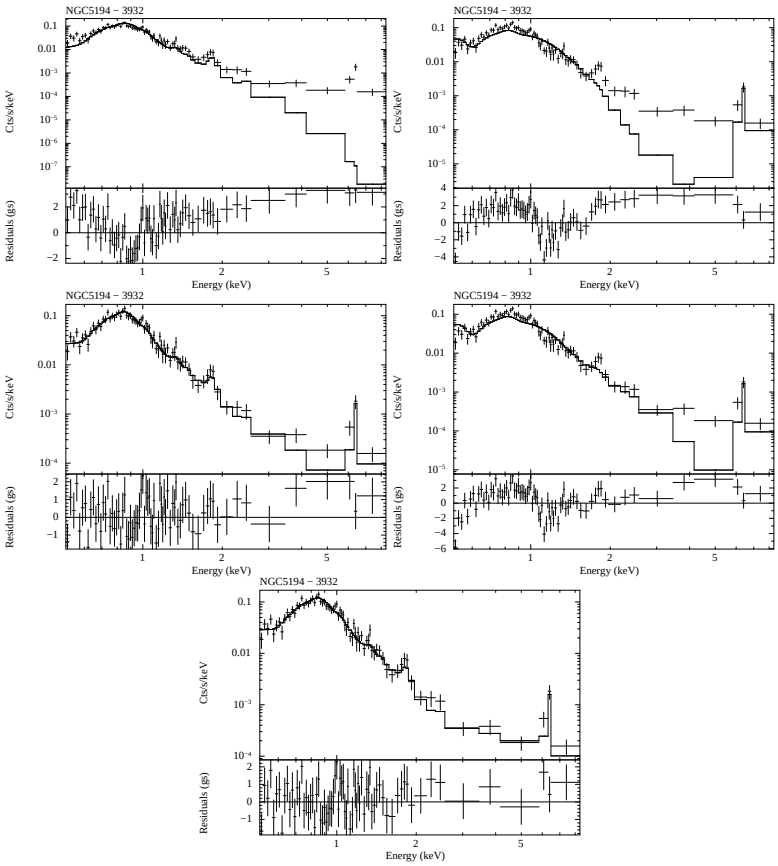

Figure D.32: *Spectral fits of NGC5194. (Top-left): Thermal model (MEKAL), (Top-right): Power-law model, (Center-left): Power-law plus thermal model, (Center-right): Two power-law model, (Bottom): Two power-law plus thermal model.*

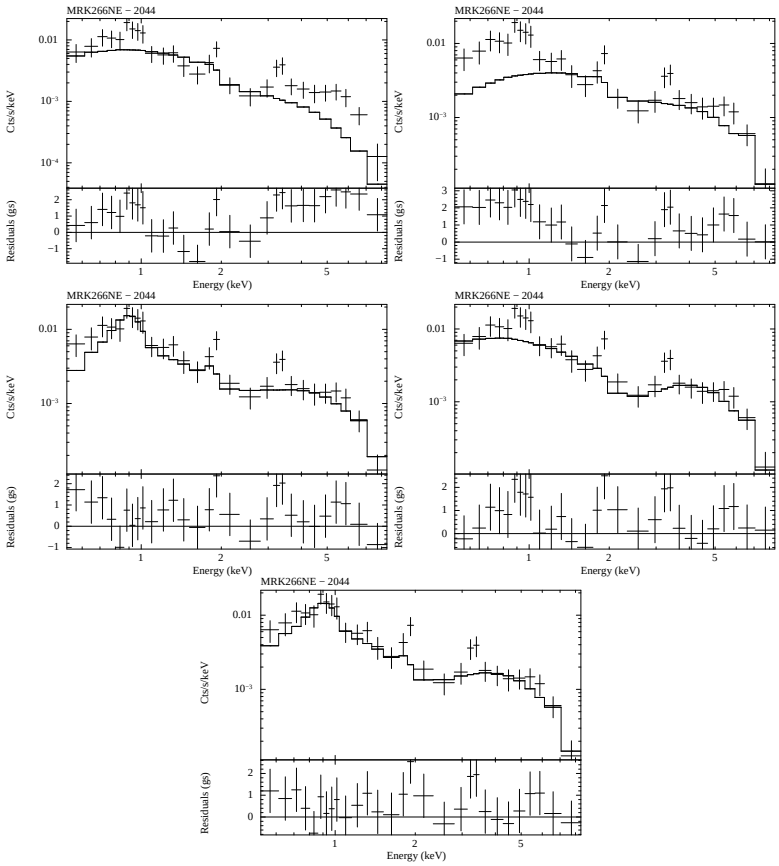

Figure D.33: *Spectral fits of MRK266NE. (Top-left): Thermal model (MEKAL), (Top-right): Power-law model, (Center-left): Power-law plus thermal model, (Center-right): Two power-law model, (Bottom): Two power-law plus thermal model.*

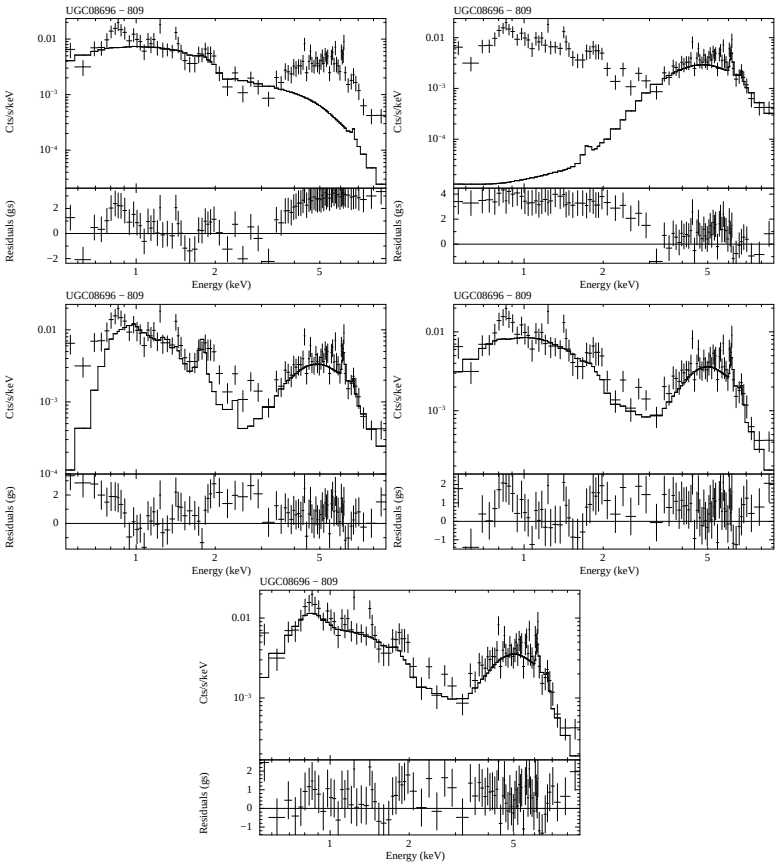

Figure D.34: *Spectral fits of UGC08696. (Top-left): Thermal model (MEKAL), (Top-right): Power-law model, (Center-left): Power-law plus thermal model, (Center-right): Two power-law model, (Bottom): Two power-law plus thermal model.*

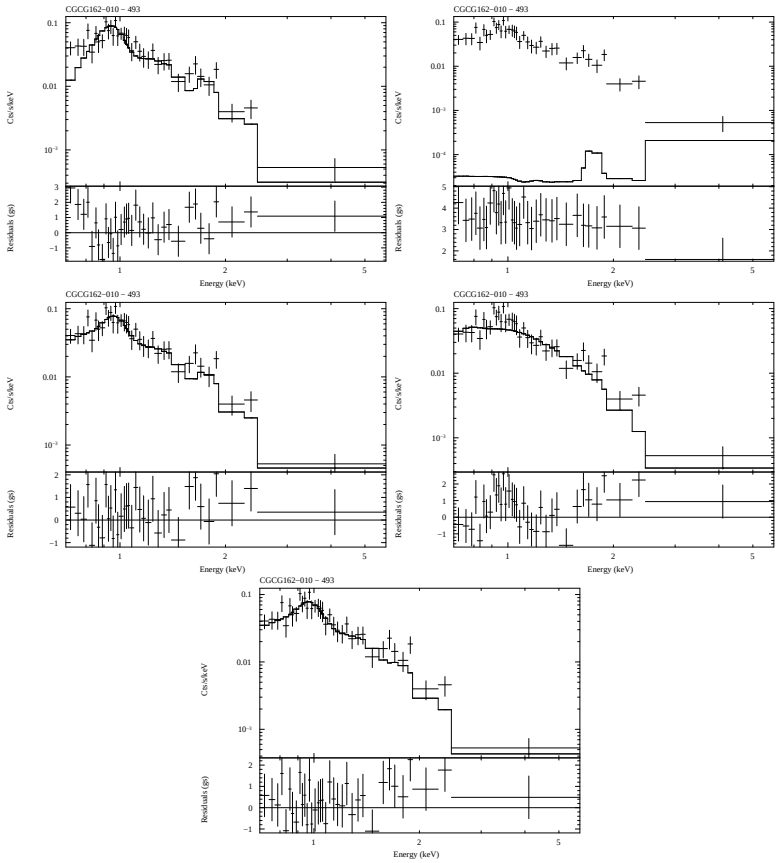

Figure D.35: *Spectral fits of CGCG162-010. (Top-left): Thermal model (MEKAL), (Top-right): Power-law model, (Center-left): Power-law plus thermal model, (Center-right): Two power-law model, (Bottom): Two power-law plus thermal model.*

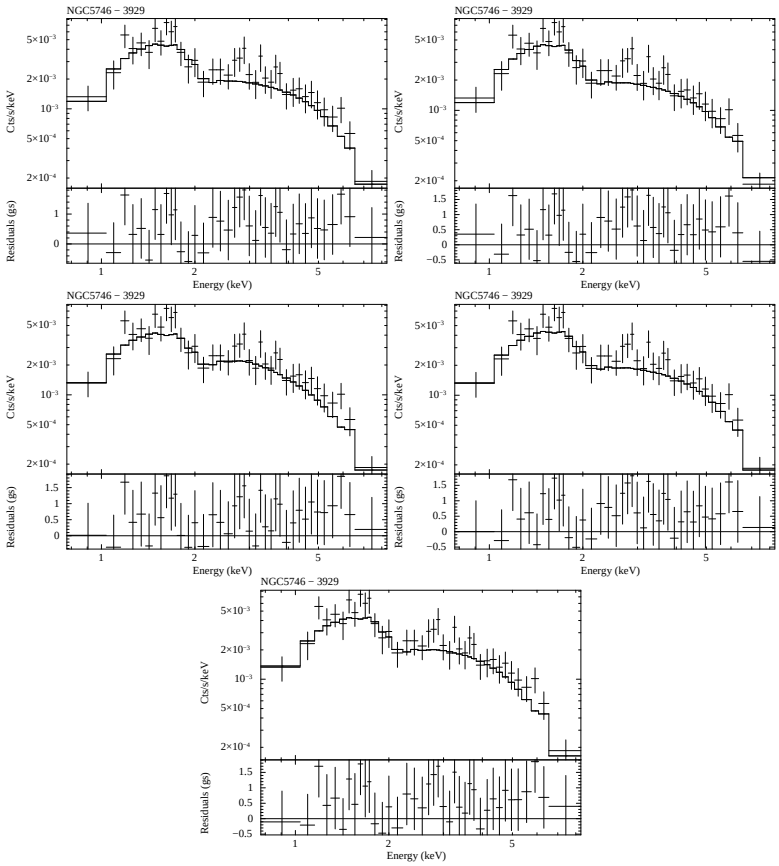

Figure D.36: *Spectral fits of NGC5746. (Top-left): Thermal model (MEKAL), (Top-right): Power-law model, (Center-left): Power-law plus thermal model, (Center-right): Two power-law model, (Bottom): Two power-law plus thermal model.*

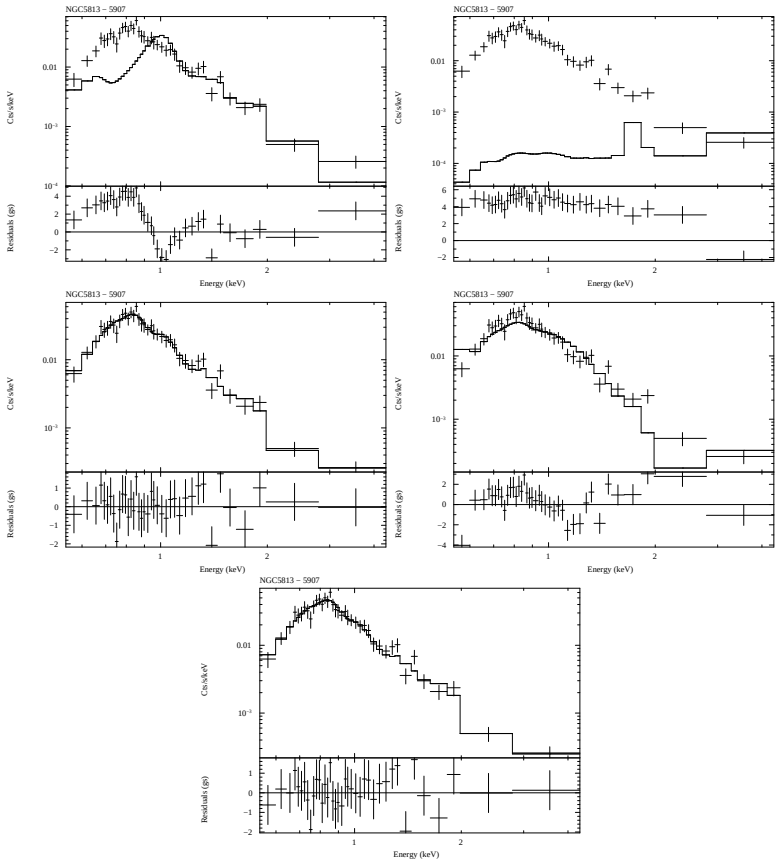

Figure D.37: *Spectral fits of NGC5813. (Top-left): Thermal model (MEKAL), (Top-right): Power-law model, (Center-left): Power-law plus thermal model, (Center-right): Two power-law model, (Bottom): Two power-law plus thermal model.*

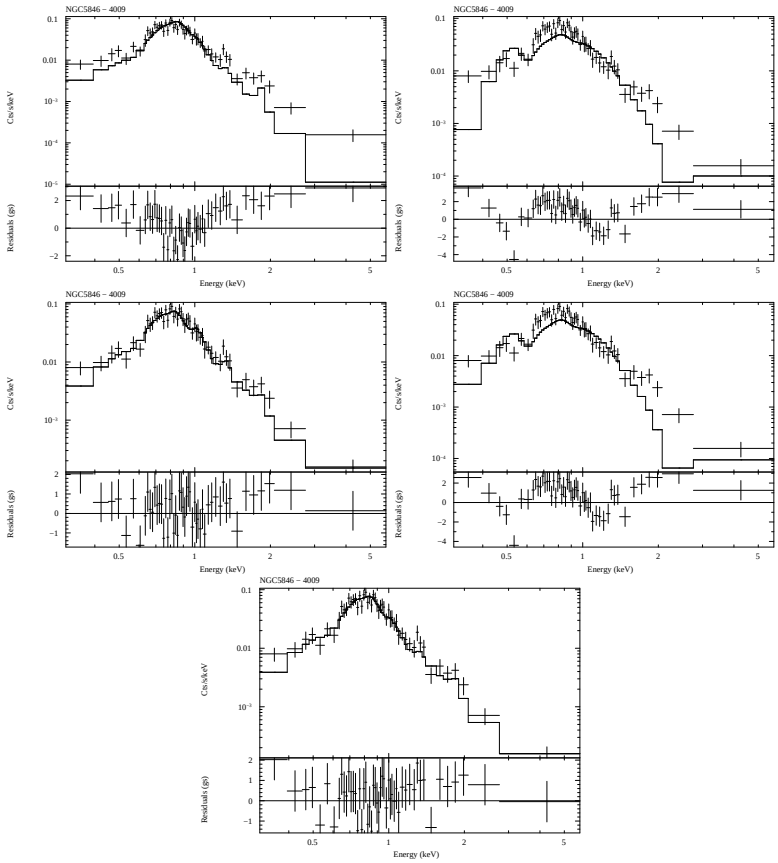

Figure D.38: *Spectral fits of NGC5846. (Top-left): Thermal model (MEKAL), (Top-right): Power-law model, (Center-left): Power-law plus thermal model, (Center-right): Two power-law model, (Bottom): Two power-law plus thermal model.*

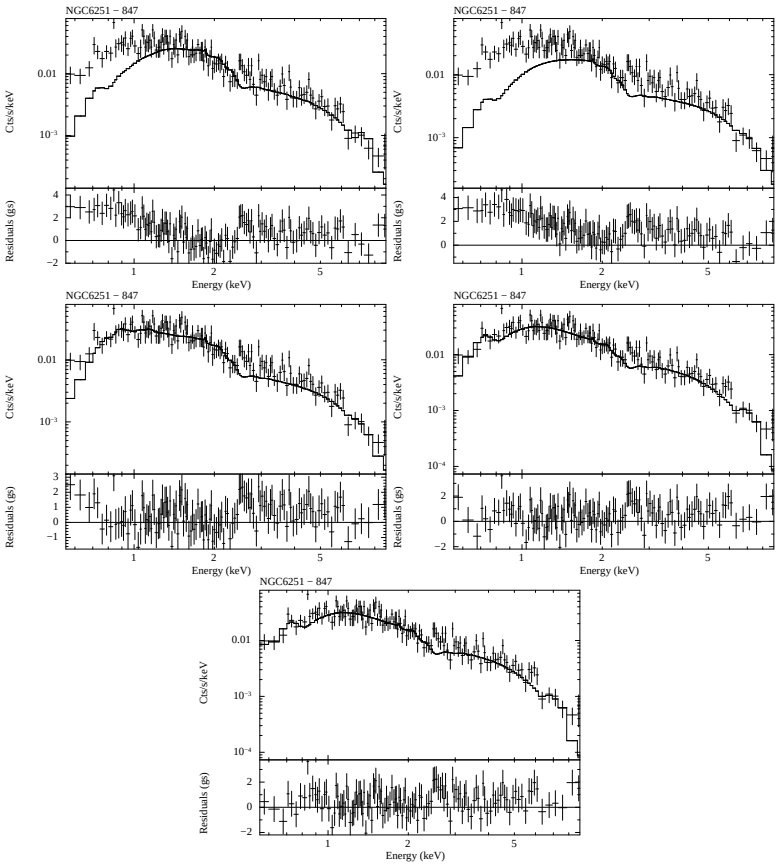

Figure D.39: *Spectral fits of NGC6251. (Top-left): Thermal model (MEKAL), (Top-right): Power-law model, (Center-left): Power-law plus thermal model, (Center-right): Two power-law model, (Bottom): Two power-law plus thermal model.*

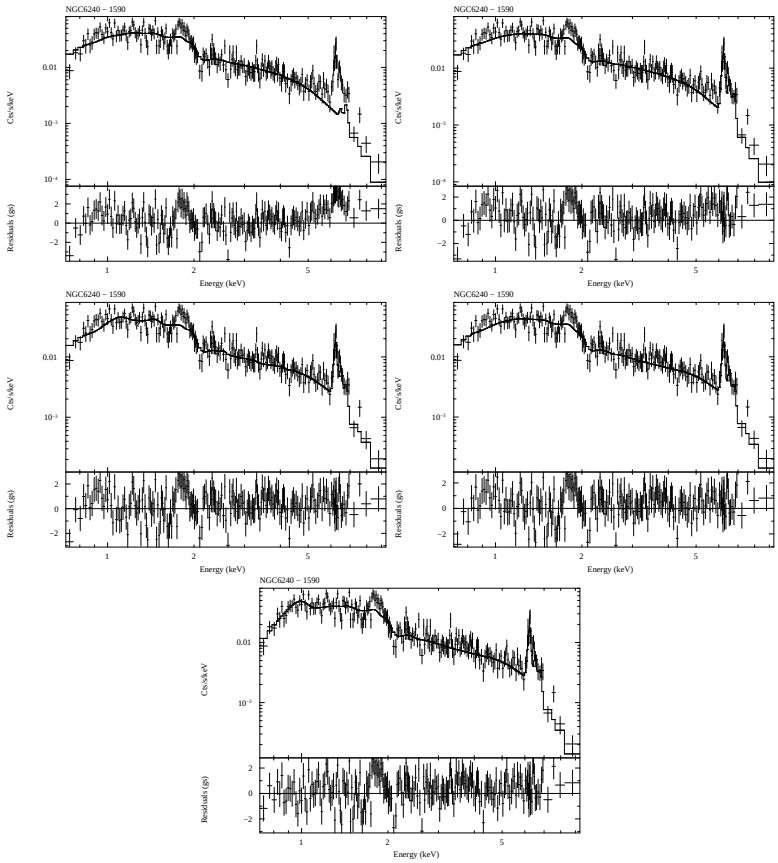

Figure D.40: *Spectral fits of NGC6240. (Top-left): Thermal model (MEKAL), (Top-right): Power-law model, (Center-left): Power-law plus thermal model, (Center-right): Two power-law model, (Bottom): Two power-law plus thermal model.*

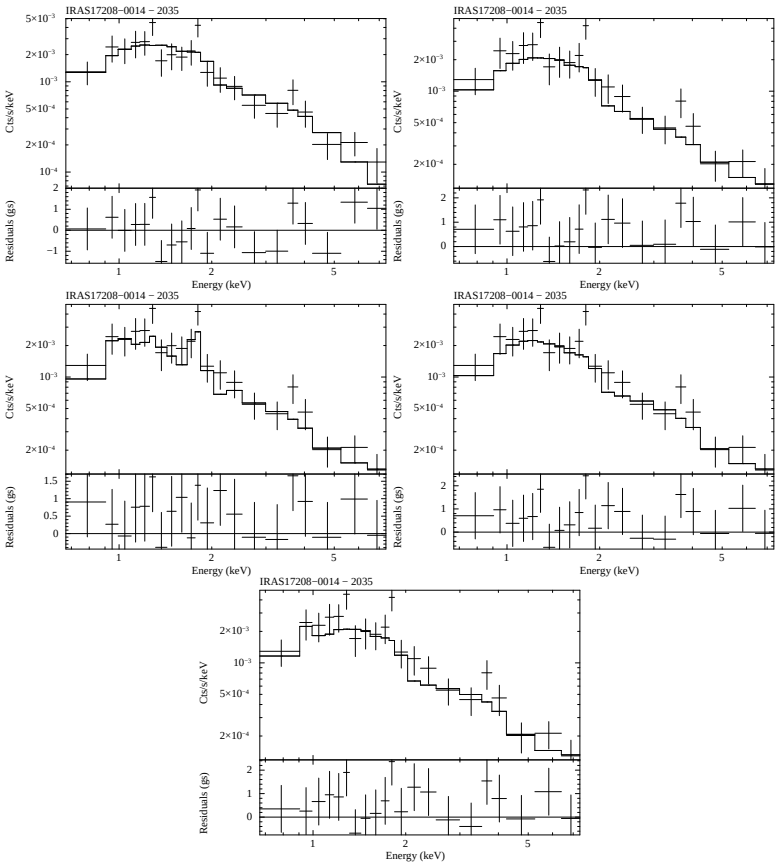

Figure D.41: *Spectral fits of IRAS17208-0014. (Top-left): Thermal model (MEKAL), (Top-right): Power-law model, (Center-left): Power-law plus thermal model, (Center-right): Two power-law model, (Bottom): Two power-law plus thermal model.*

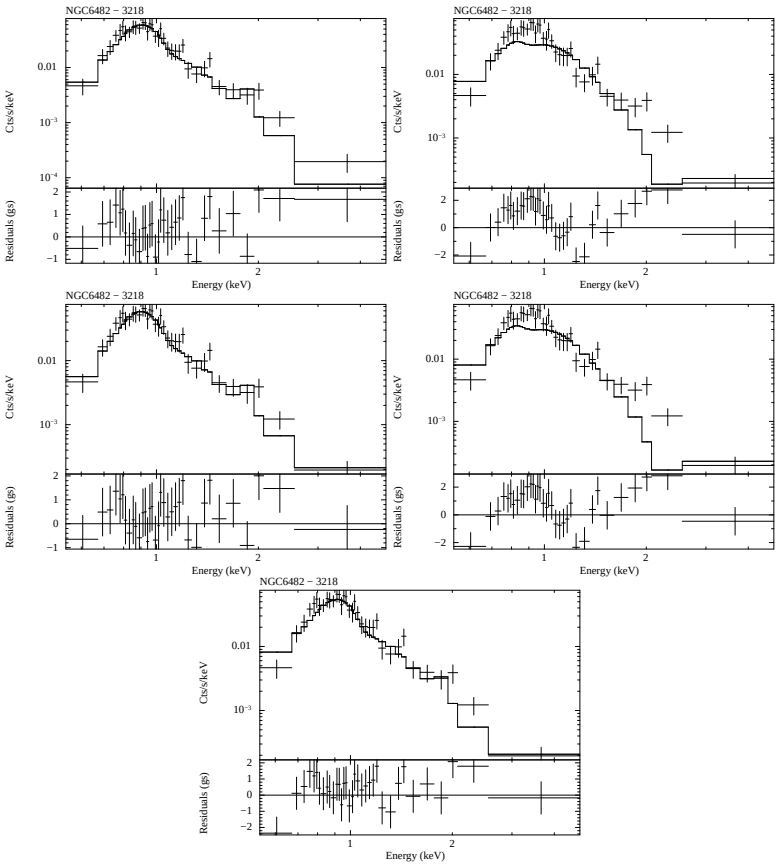

Figure D.42: *Spectral fits of NGC6482. (Top-left): Thermal model (MEKAL), (Top-right): Power-law model, (Center-left): Power-law plus thermal model, (Center-right): Two power-law model, (Bottom): Two power-law plus thermal model.*

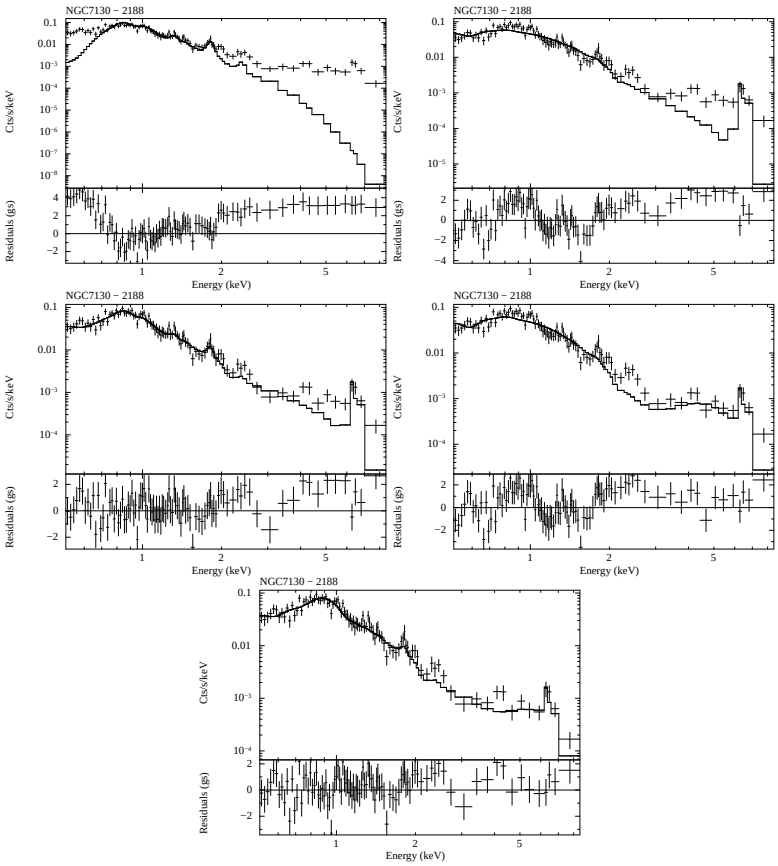

Figure D.43: *Spectral fits of NGC7130. (Top-left): Thermal model (MEKAL), (Top-right): Power-law model, (Center-left): Power-law plus thermal model, (Center-right): Two power-law model, (Bottom): Two power-law plus thermal model.*

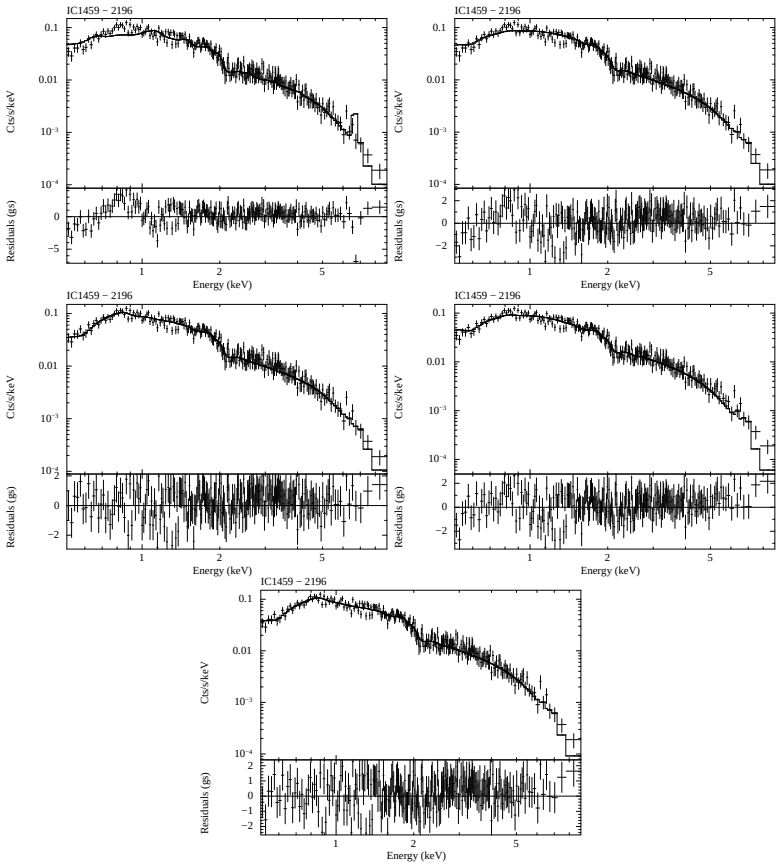

Figure D.44: *Spectral fits of IC1459. (Top-left): Thermal model (MEKAL), (Top-right): Power-law model, (Center-left): Power-law plus thermal model, (Center-right): Two power-law model, (Bottom): Two power-law plus thermal model.*

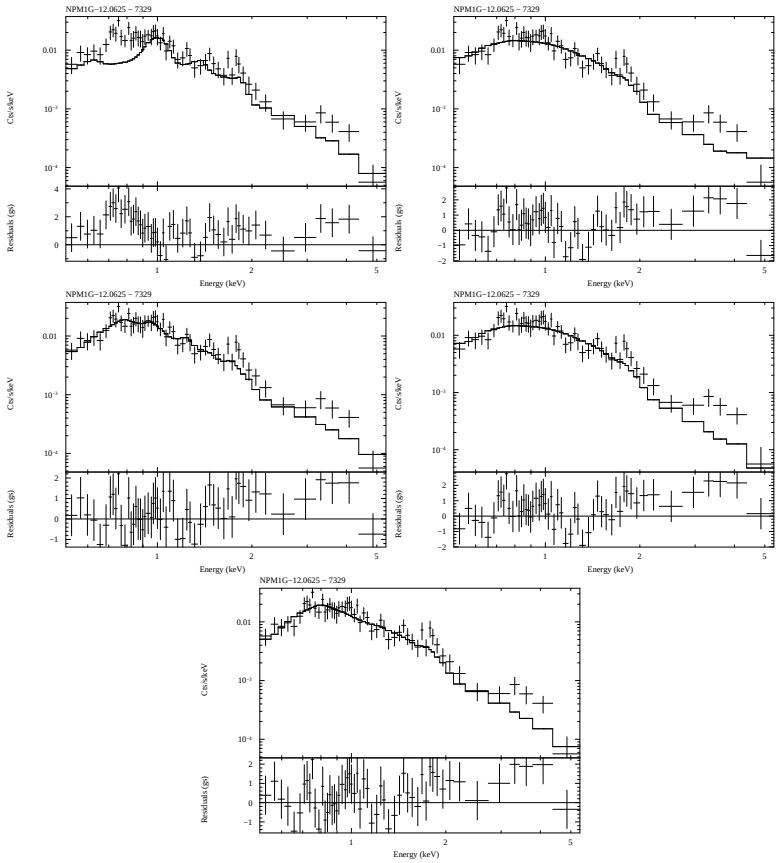

Figure D.45: *Spectral fits of NPM1G-12.0625. (Top-left): Thermal model (MEKAL), (Top-right): Power-law model, (Center-left): Power-law plus thermal model, (Center-right): Two power-law model, (Bottom): Two power-law plus thermal model.*

Appendix E

Catalogue of spectra with *XMM-Newton* data (Chapter 3)

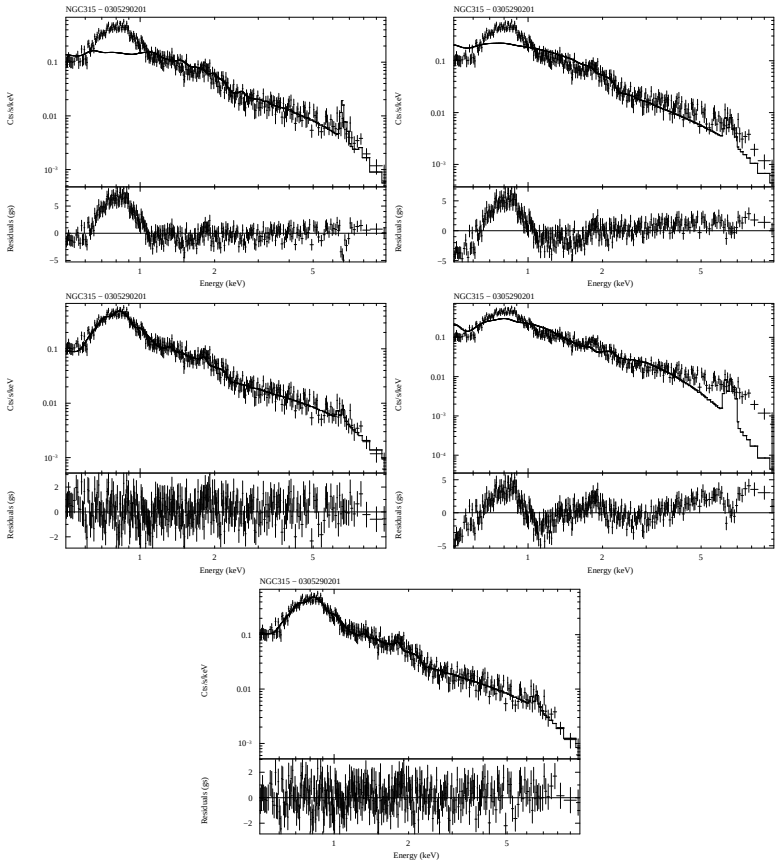

Figure E.1: *Spectral fits of NGC315. (Top-left): Thermal model (MEKAL), (Top-right): Power-law model, (Center-left): Power-law plus thermal model, (Center-right): Two power-law model, (Bottom): Two power-law plus thermal model.*

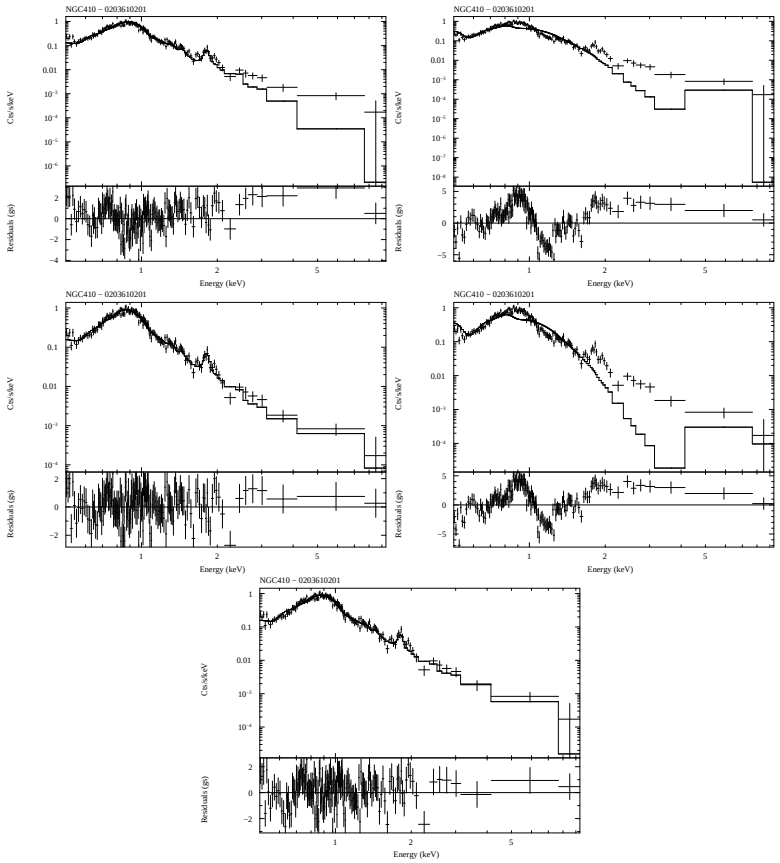

Figure E.2: *Spectral fits of NGC410. (Top-left): Thermal model (MEKAL), (Top-right): Power-law model, (Center-left): Power-law plus thermal model, (Center-right): Two power-law model, (Bottom): Two power-law plus thermal model.*

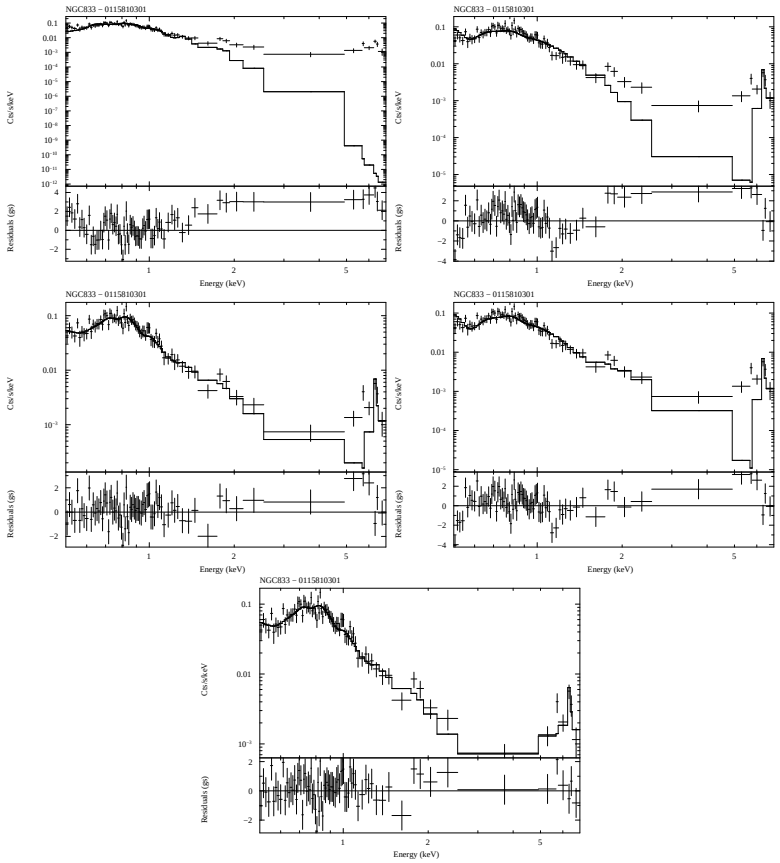

Figure E.3: *Spectral fits of NGC835. (Top-left): Thermal model (MEKAL), (Top-right): Power-law model, (Center-left): Power-law plus thermal model, (Center-right): Two power-law model, (Bottom): Two power-law plus thermal model.*

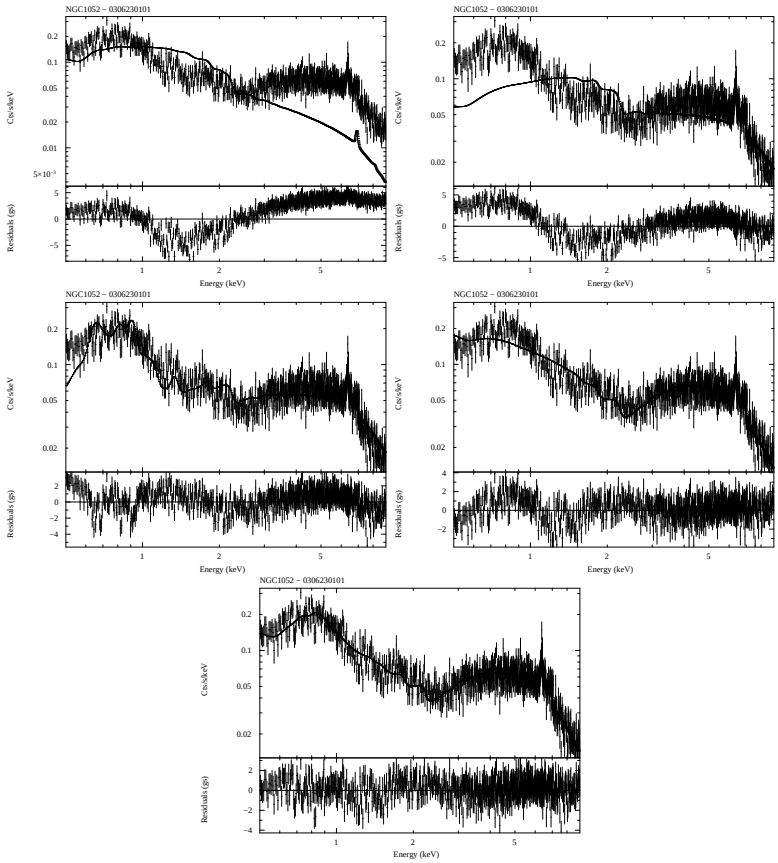

Figure E.4: *Spectral fits of NGC1052. (Top-left): Thermal model (MEKAL), (Top-right): Power-law model, (Center-left): Power-law plus thermal model, (Center-right): Two power-law model, (Bottom): Two power-law plus thermal model.*

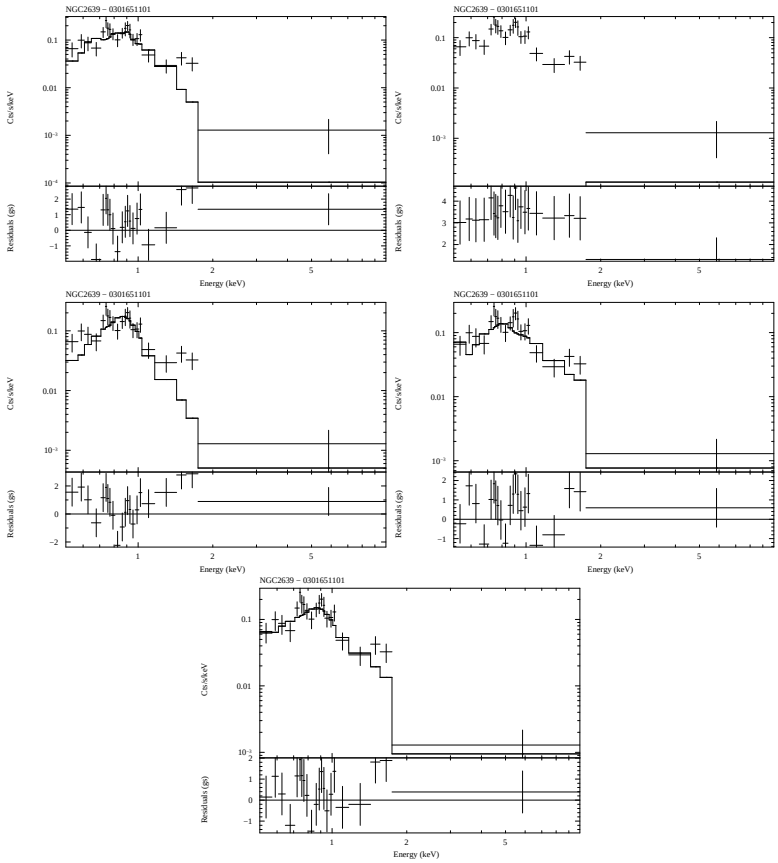

Figure E.5: *Spectral fits of NGC2639. (Top-left): Thermal model (MEKAL), (Top-right): Power-law model, (Center-left): Power-law plus thermal model, (Center-right): Two power-law model, (Bottom): Two power-law plus thermal model.*

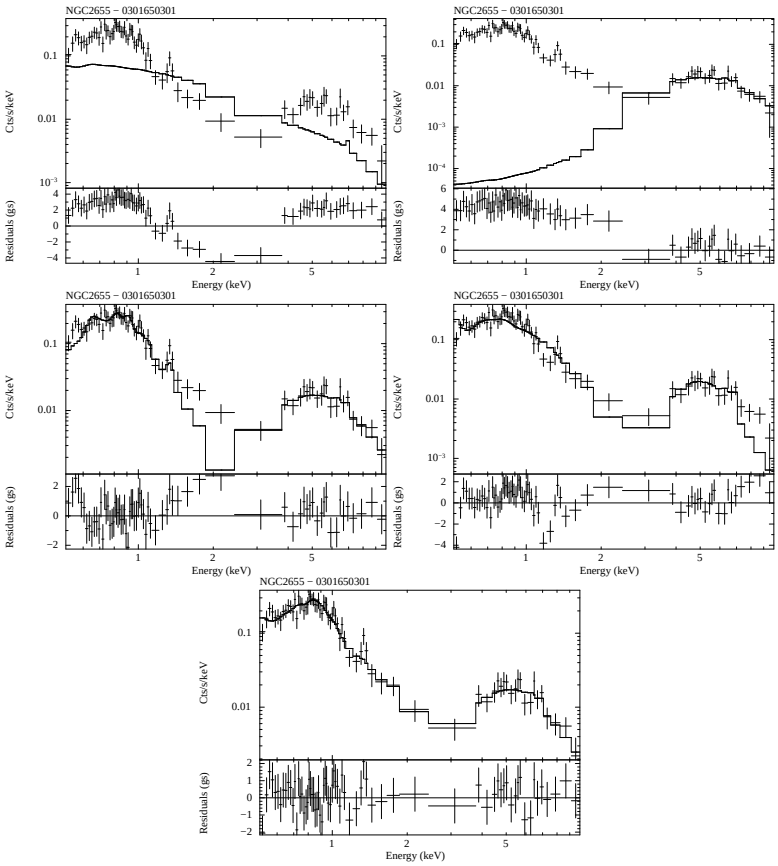

Figure E.6: *Spectral fits of NGC2655. (Top-left): Thermal model (MEKAL), (Top-right): Power-law model, (Center-left): Power-law plus thermal model, (Center-right): Two power-law model, (Bottom): Two power-law plus thermal model.*

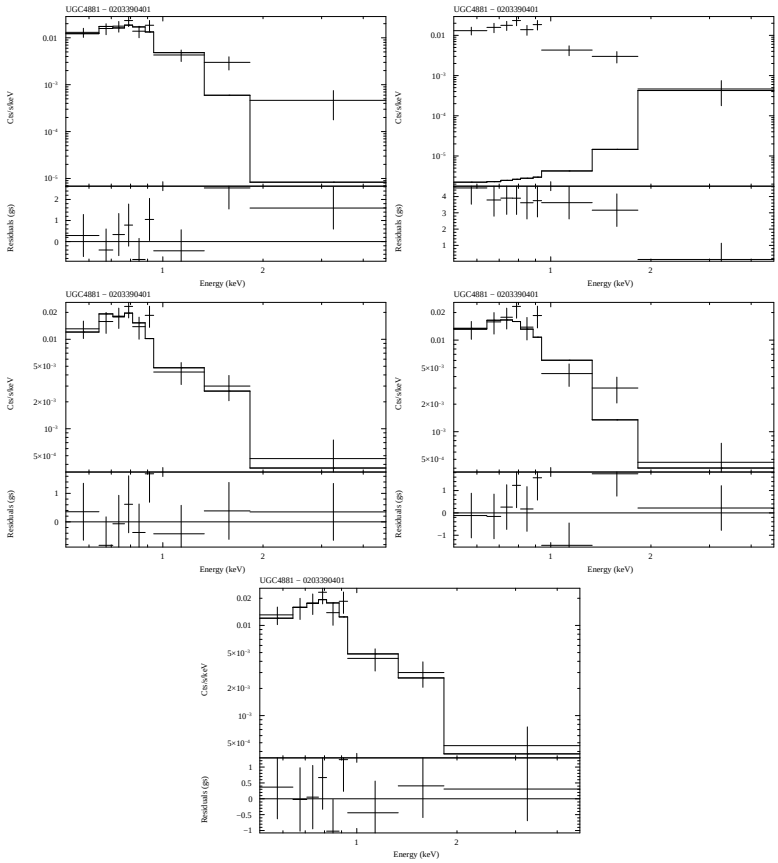

Figure E.7: *Spectral fits of UGC4881. (Top-left): Thermal model (MEKAL), (Top-right): Power-law model, (Center-left): Power-law plus thermal model, (Center-right): Two power-law model, (Bottom): Two power-law plus thermal model.*

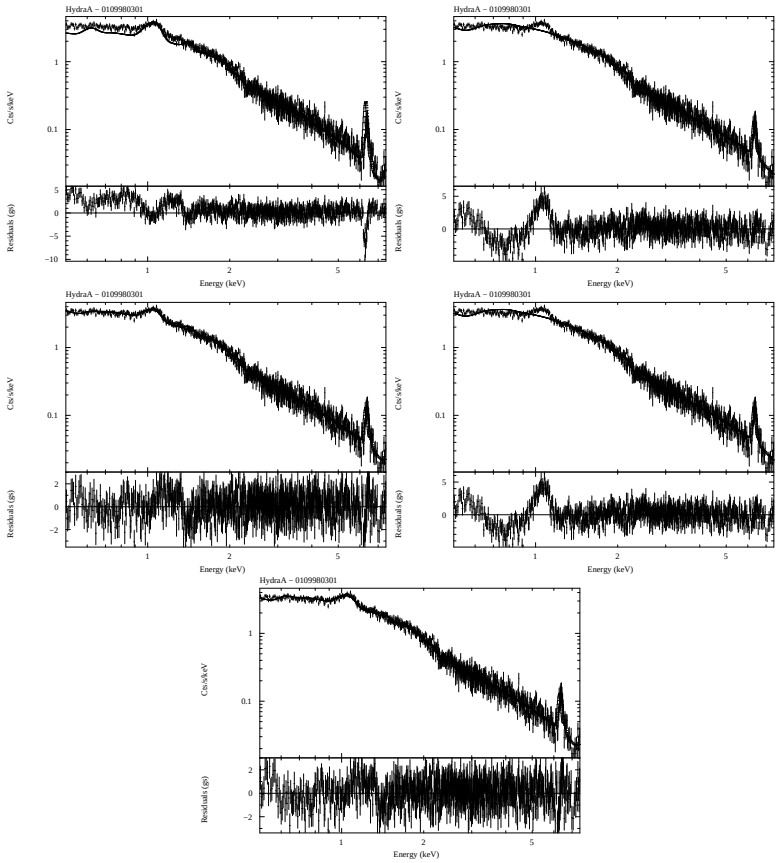

Figure E.8: *Spectral fits of HydraA. (Top-left): Thermal model (MEKAL), (Top-right): Power-law model, (Center-left): Power-law plus thermal model, (Center-right): Two power-law model, (Bottom): Two power-law plus thermal model.*

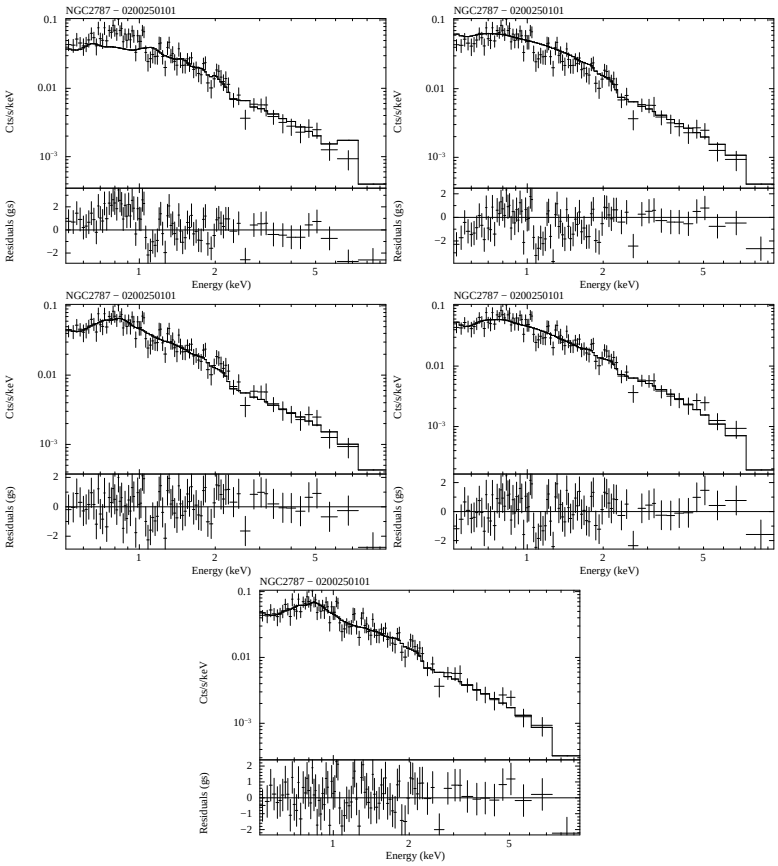

Figure E.9: *Spectral fits of NGC2787. (Top-left): Thermal model (MEKAL), (Top-right): Power-law model, (Center-left): Power-law plus thermal model, (Center-right): Two power-law model, (Bottom): Two power-law plus thermal model.*

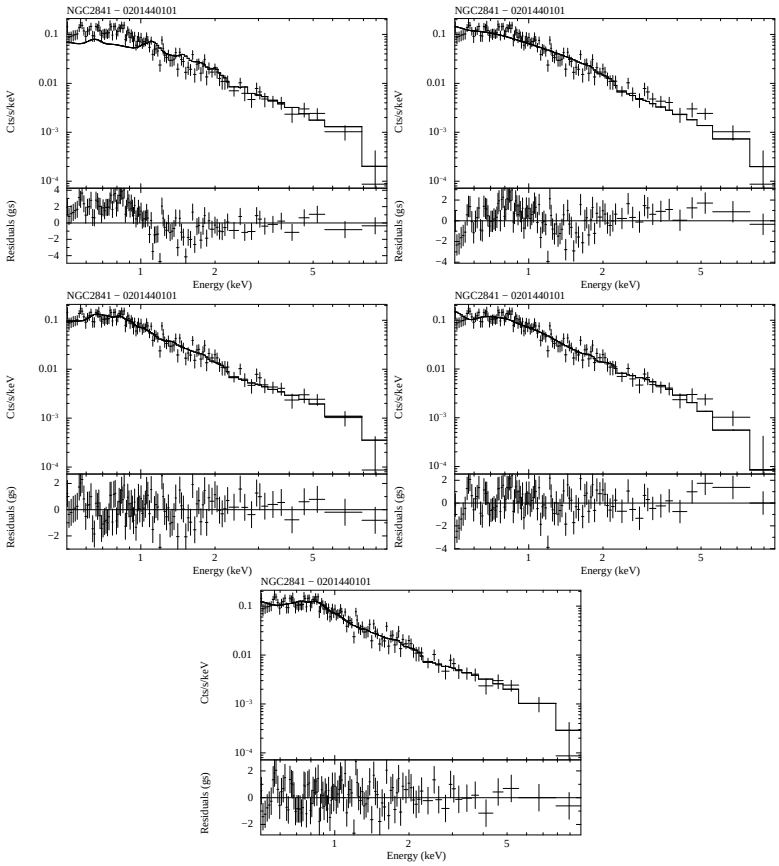

Figure E.10: *Spectral fits of NGC2841. (Top-left): Thermal model (MEKAL), (Top-right): Power-law model, (Center-left): Power-law plus thermal model, (Center-right): Two power-law model, (Bottom): Two power-law plus thermal model.*

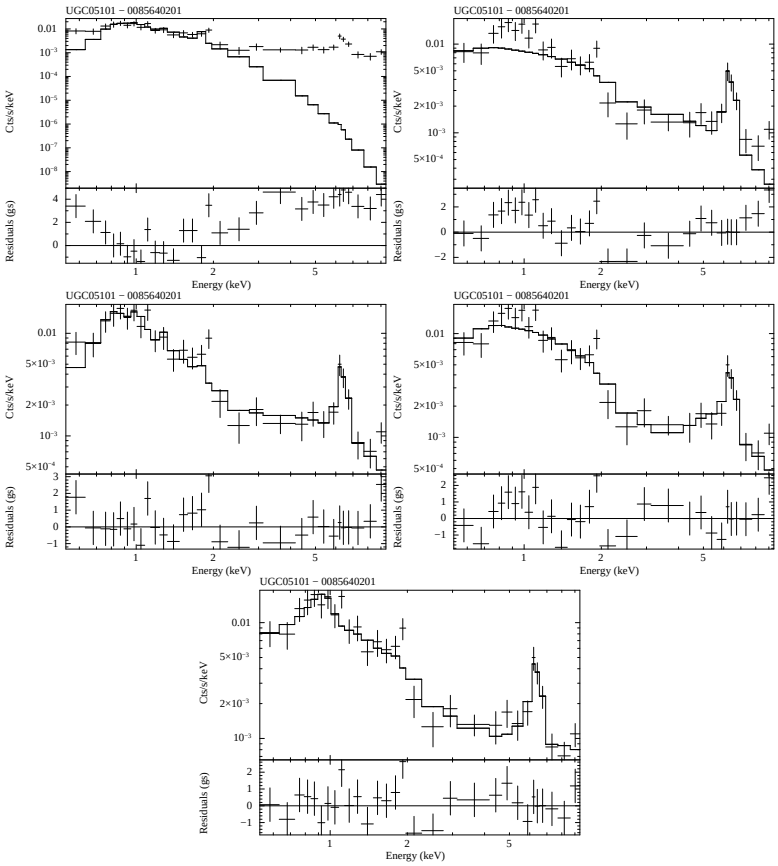

Figure E.11: *Spectral fits of UGC05101. (Top-left): Thermal model (MEKAL), (Top-right): Power-law model, (Center-left): Power-law plus thermal model, (Center-right): Two power-law model, (Bottom): Two power-law plus thermal model.*

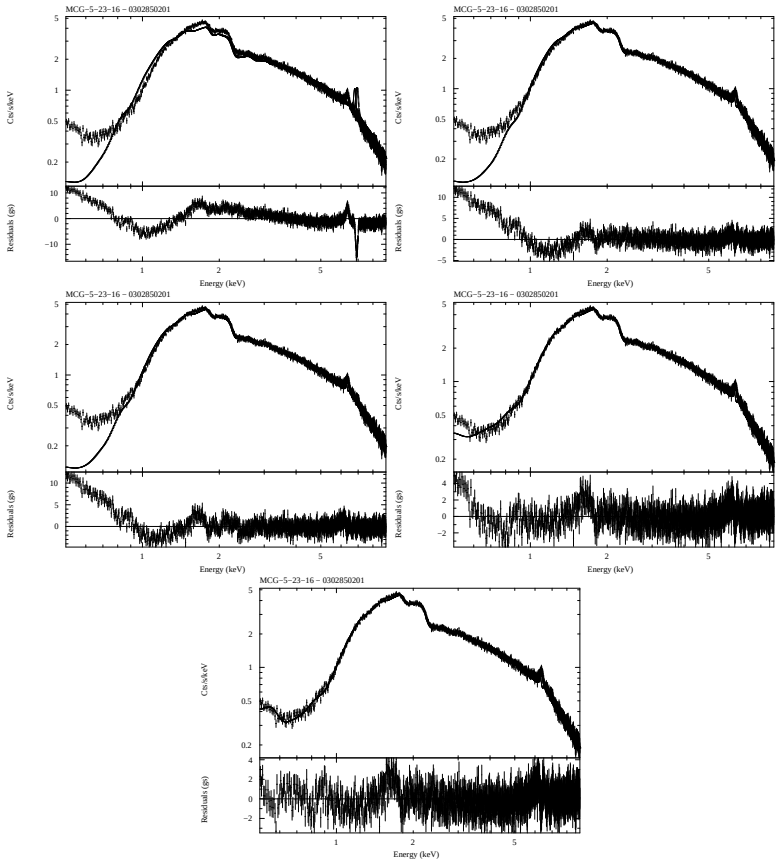

Figure E.12: *Spectral fits of MCG-5-23-16. (Top-left): Thermal model (MEKAL), (Top-right): Power-law model, (Center-left): Power-law plus thermal model, (Center-right): Two power-law model, (Bottom): Two power-law plus thermal model.*

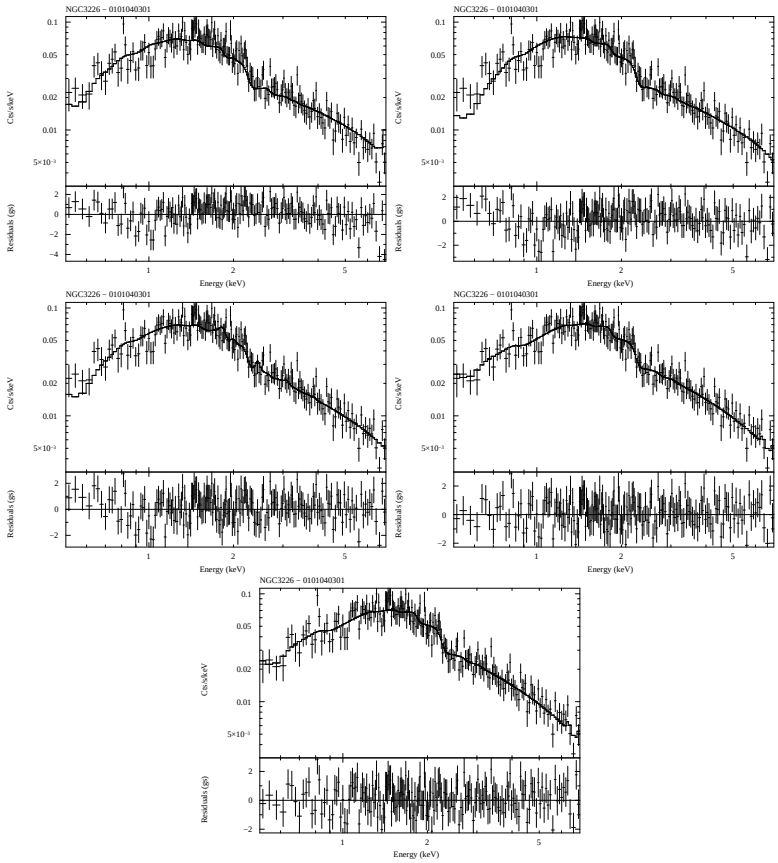

Figure E.13: *Spectral fits of NGC3226. (Top-left): Thermal model (MEKAL), (Top-right): Power-law model, (Center-left): Power-law plus thermal model, (Center-right): Two power-law model, (Bottom): Two power-law plus thermal model.*

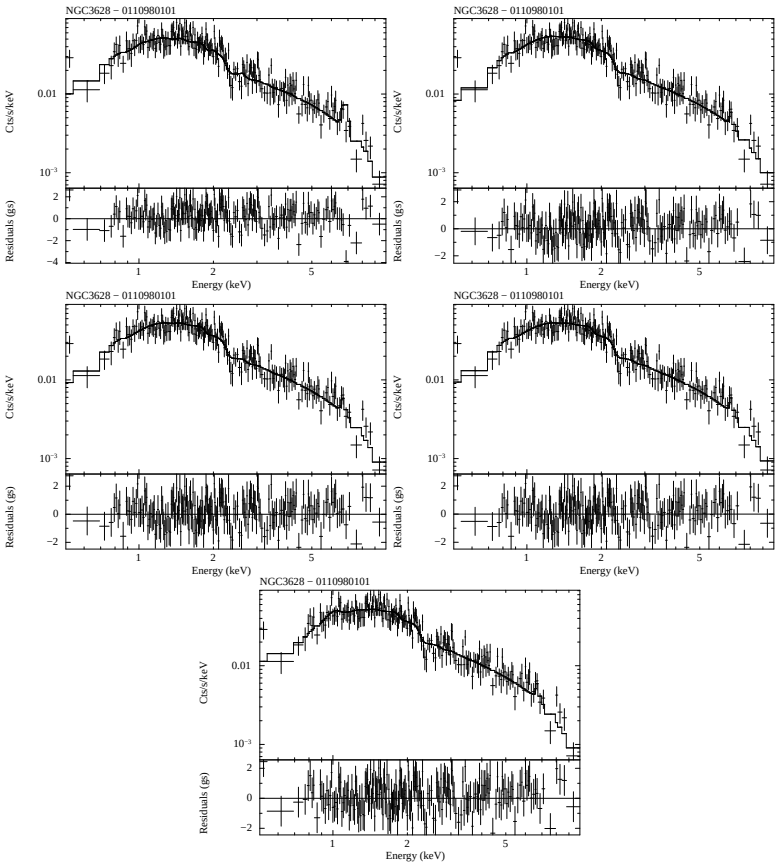

Figure E.14: *Spectral fits of NGC3628. (Top-left): Thermal model (MEKAL), (Top-right): Power-law model, (Center-left): Power-law plus thermal model, (Center-right): Two power-law model, (Bottom): Two power-law plus thermal model.*

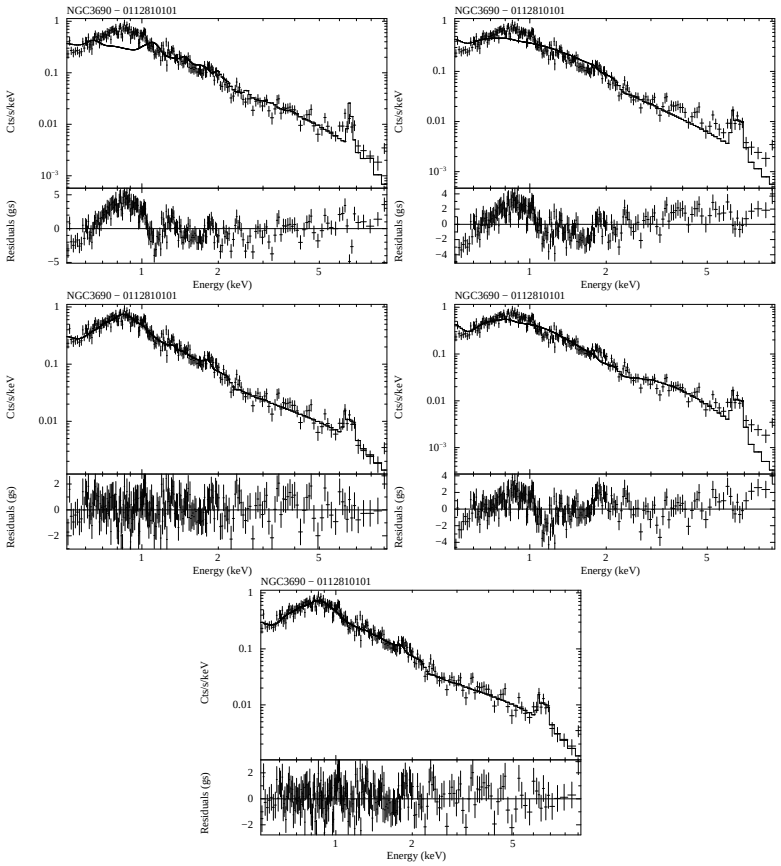

Figure E.15: *Spectral fits of NGC3690. (Top-left): Thermal model (MEKAL), (Top-right): Power-law model, (Center-left): Power-law plus thermal model, (Center-right): Two power-law model, (Bottom): Two power-law plus thermal model.*

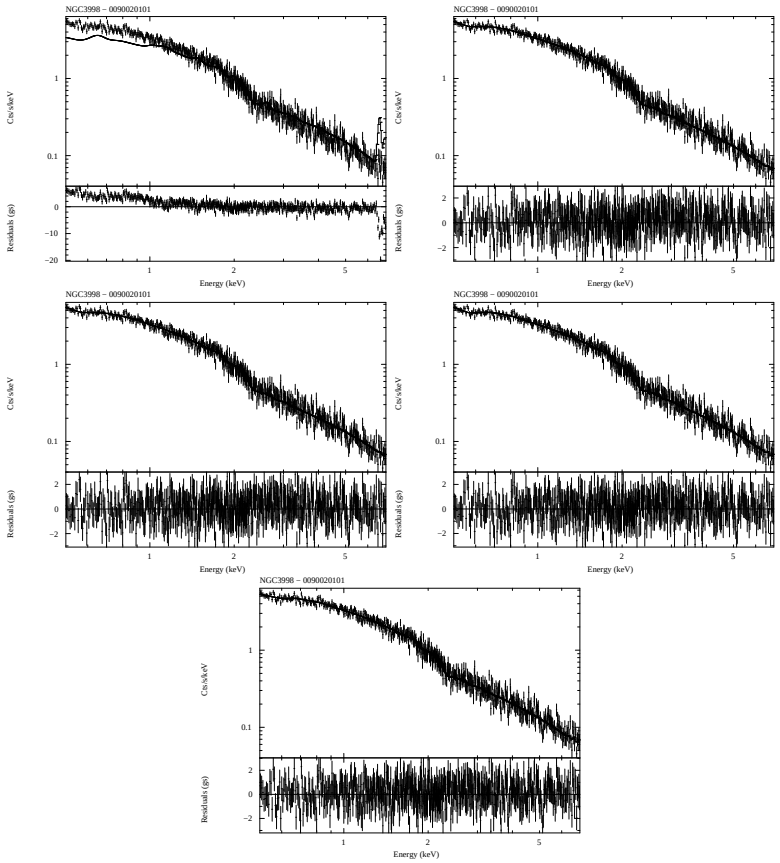

Figure E.16: *Spectral fits of NGC3998. (Top-left): Thermal model (MEKAL), (Top-right): Power-law model, (Center-left): Power-law plus thermal model, (Center-right): Two power-law model, (Bottom): Two power-law plus thermal model.*

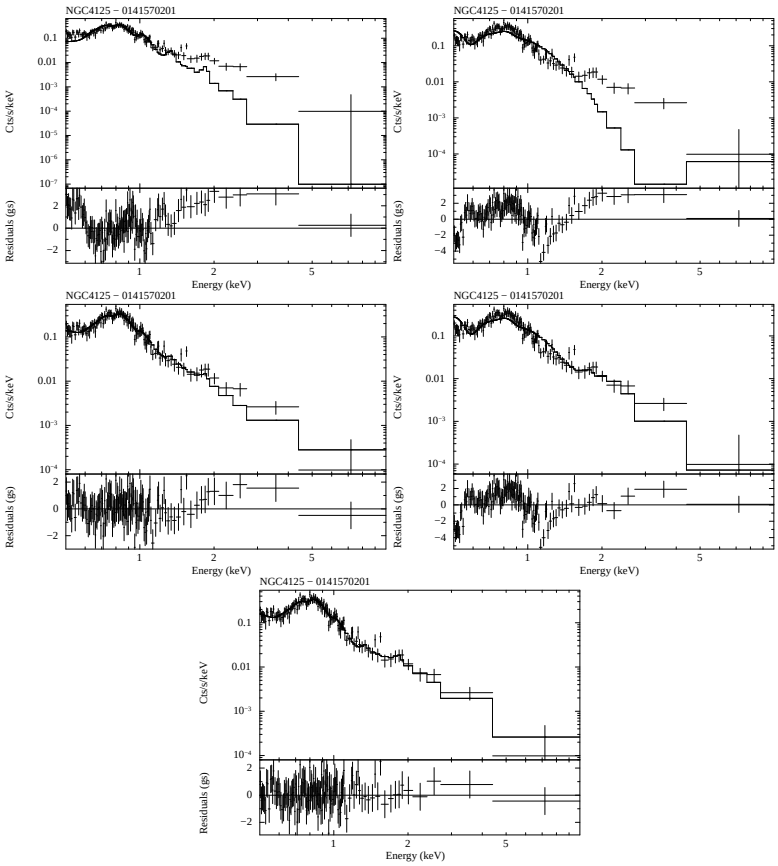

Figure E.17: *Spectral fits of NGC4125. (Top-left): Thermal model (MEKAL), (Top-right): Power-law model, (Center-left): Power-law plus thermal model, (Center-right): Two power-law model, (Bottom): Two power-law plus thermal model.*

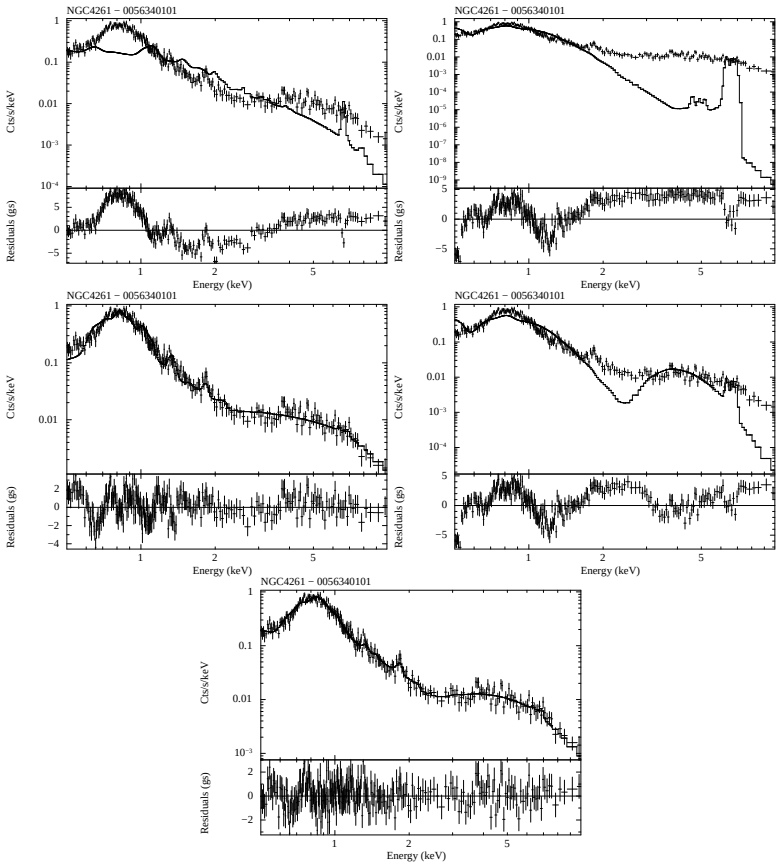

Figure E.18: *Spectral fits of NGC4261. (Top-left): Thermal model (MEKAL), (Top-right): Power-law model, (Center-left): Power-law plus thermal model, (Center-right): Two power-law model, (Bottom): Two power-law plus thermal model.*

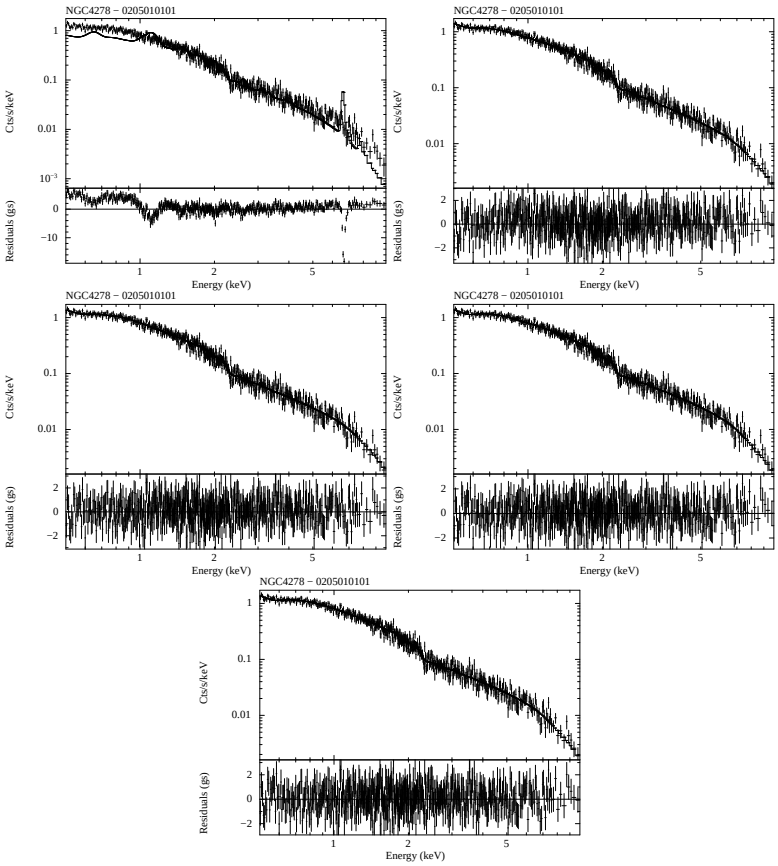

Figure E.19: *Spectral fits of NGC4278. (Top-left): Thermal model (MEKAL), (Top-right): Power-law model, (Center-left): Power-law plus thermal model, (Center-right): Two power-law model, (Bottom): Two power-law plus thermal model.*

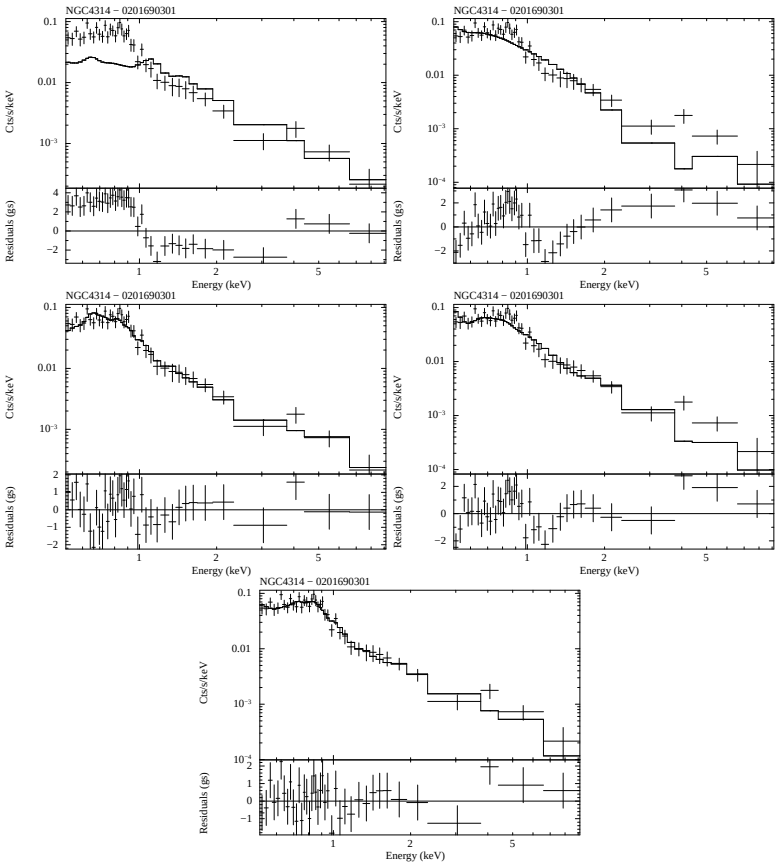

Figure E.20: *Spectral fits of NGC4314. (Top-left): Thermal model (MEKAL), (Top-right): Power-law model, (Center-left): Power-law plus thermal model, (Center-right): Two power-law model, (Bottom): Two power-law plus thermal model.*

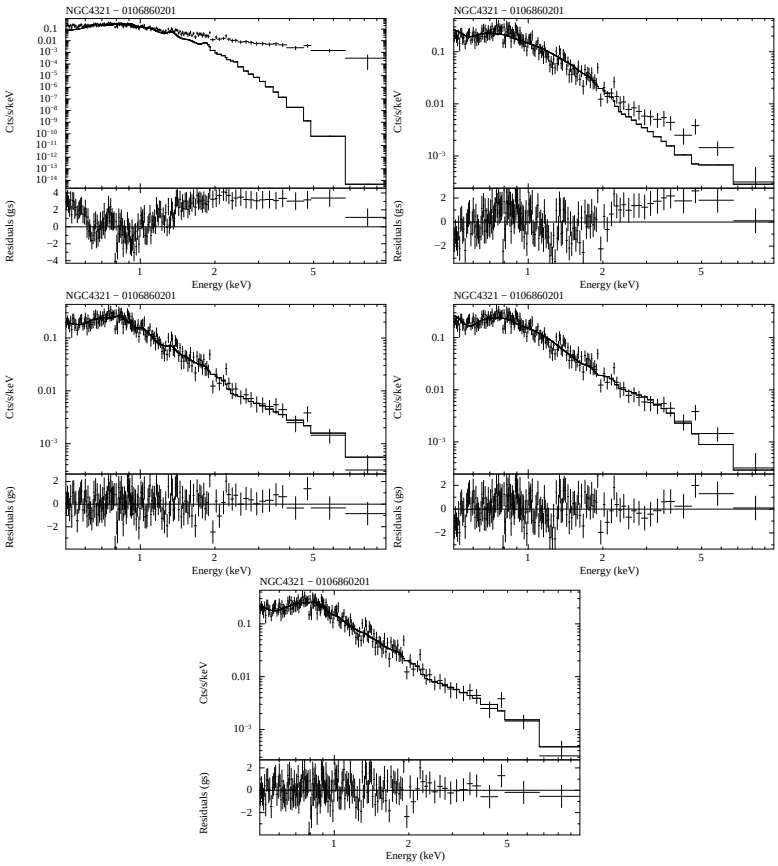

Figure E.21: *Spectral fits of NGC4321. (Top-left): Thermal model (MEKAL), (Top-right): Power-law model, (Center-left): Power-law plus thermal model, (Center-right): Two power-law model, (Bottom): Two power-law plus thermal model.*

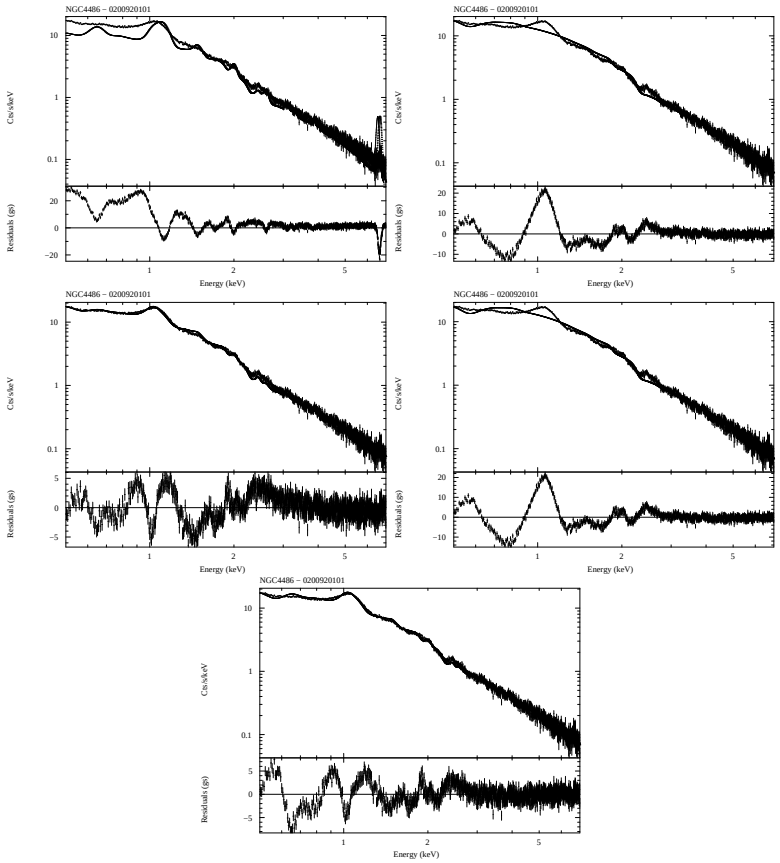

Figure E.22: *Spectral fits of NGC4486. (Top-left): Thermal model (MEKAL), (Top-right): Power-law model, (Center-left): Power-law plus thermal model, (Center-right): Two power-law model, (Bottom): Two power-law plus thermal model.*

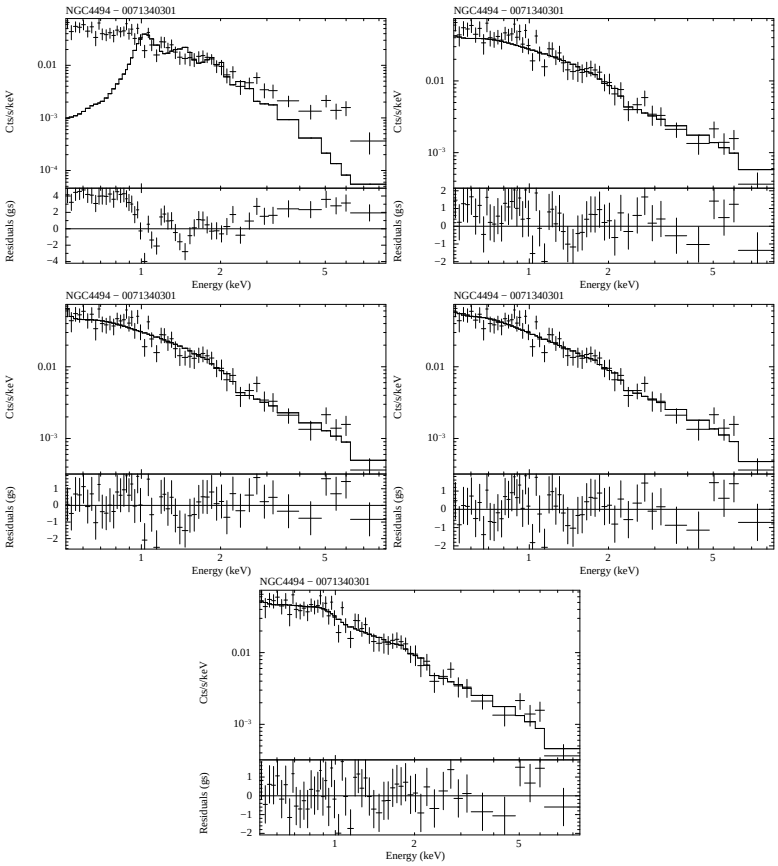

Figure E.23: *Spectral fits of NGC4494. (Top-left): Thermal model (MEKAL), (Top-right): Power-law model, (Center-left): Power-law plus thermal model, (Center-right): Two power-law model, (Bottom): Two power-law plus thermal model.*

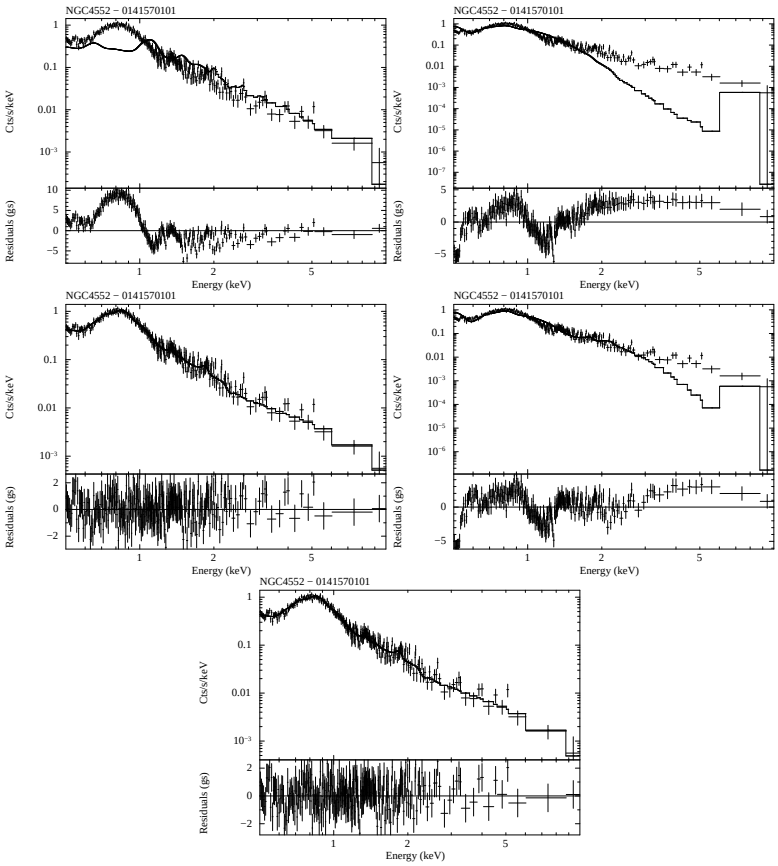

Figure E.24: *Spectral fits of NGC4552. (Top-left): Thermal model (MEKAL), (Top-right): Power-law model, (Center-left): Power-law plus thermal model, (Center-right): Two power-law model, (Bottom): Two power-law plus thermal model.*

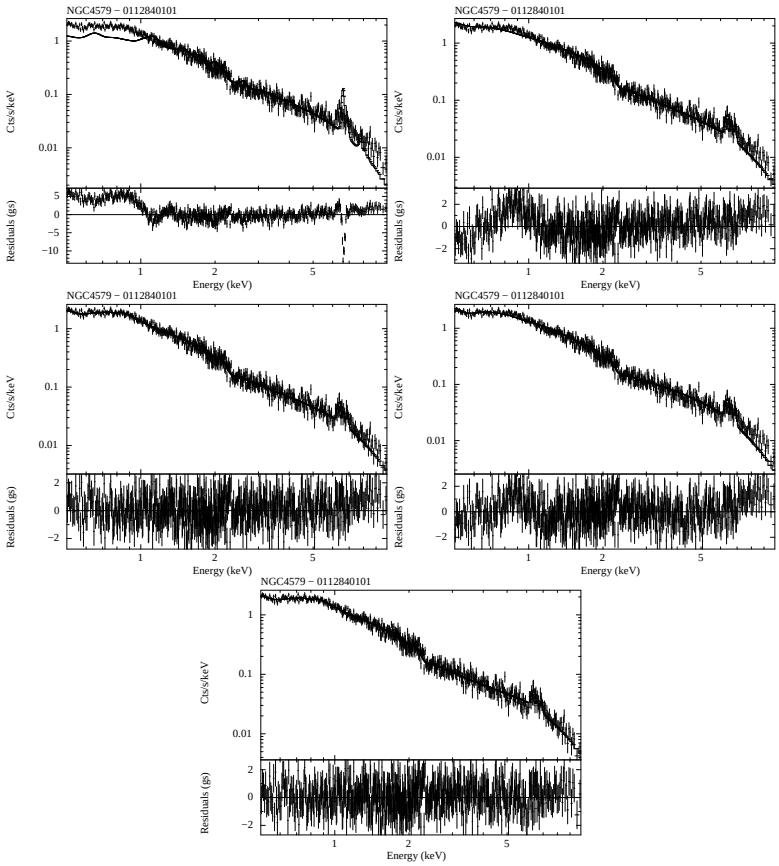

Figure E.25: *Spectral fits of NGC4579. (Top-left): Thermal model (MEKAL), (Top-right): Power-law model, (Center-left): Power-law plus thermal model, (Center-right): Two power-law model, (Bottom): Two power-law plus thermal model.*

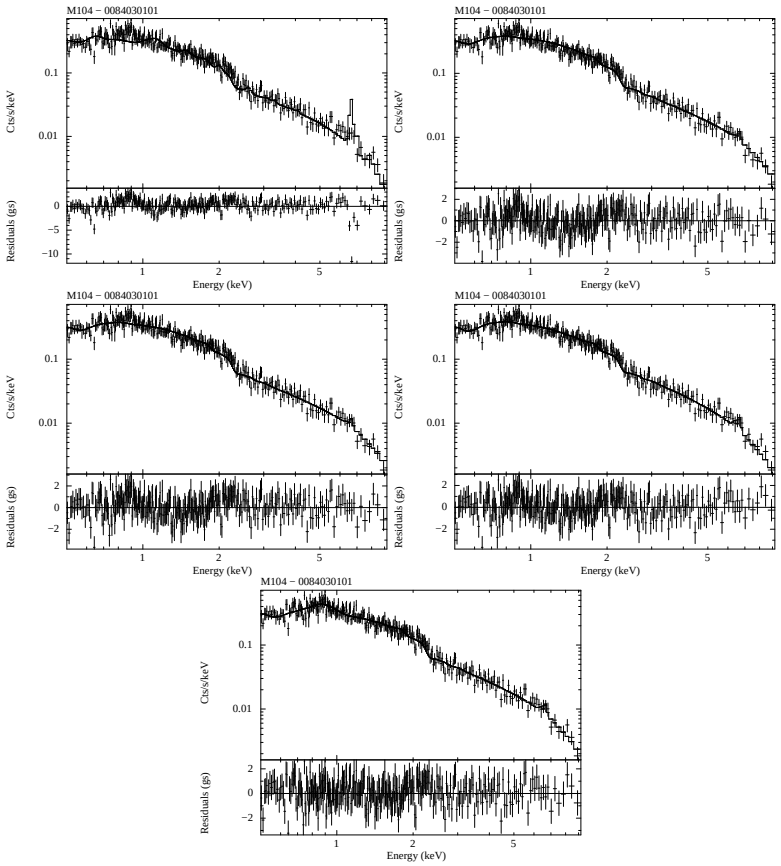

Figure E.26: *Spectral fits of NGC4594. (Top-left): Thermal model (MEKAL), (Top-right): Power-law model, (Center-left): Power-law plus thermal model, (Center-right): Two power-law model, (Bottom): Two power-law plus thermal model.*

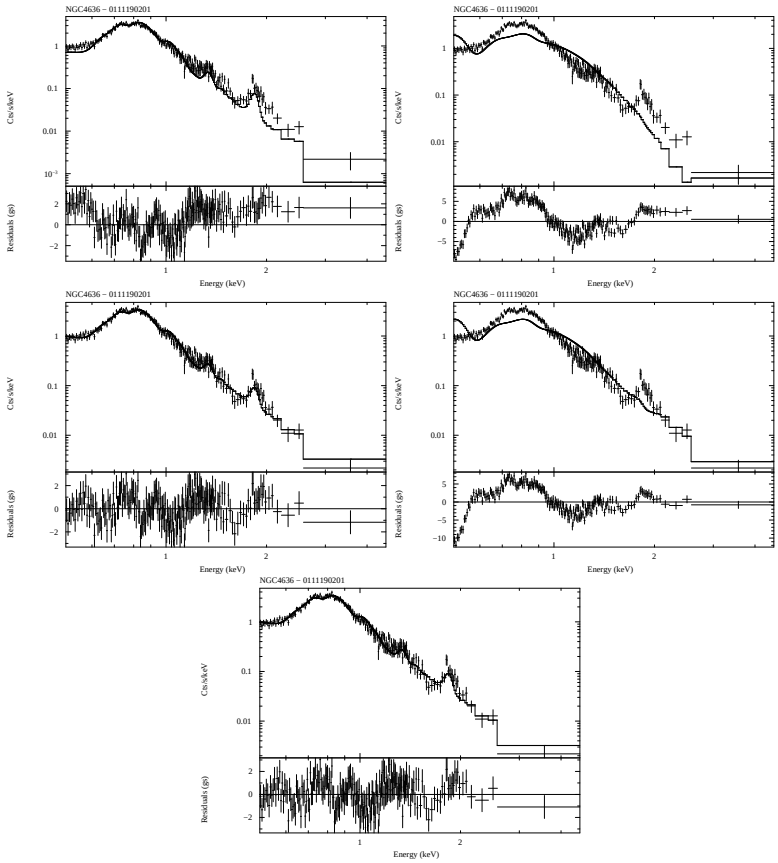

Figure E.27: *Spectral fits of NGC4636. (Top-left): Thermal model (MEKAL), (Top-right): Power-law model, (Center-left): Power-law plus thermal model, (Center-right): Two power-law model, (Bottom): Two power-law plus thermal model.*

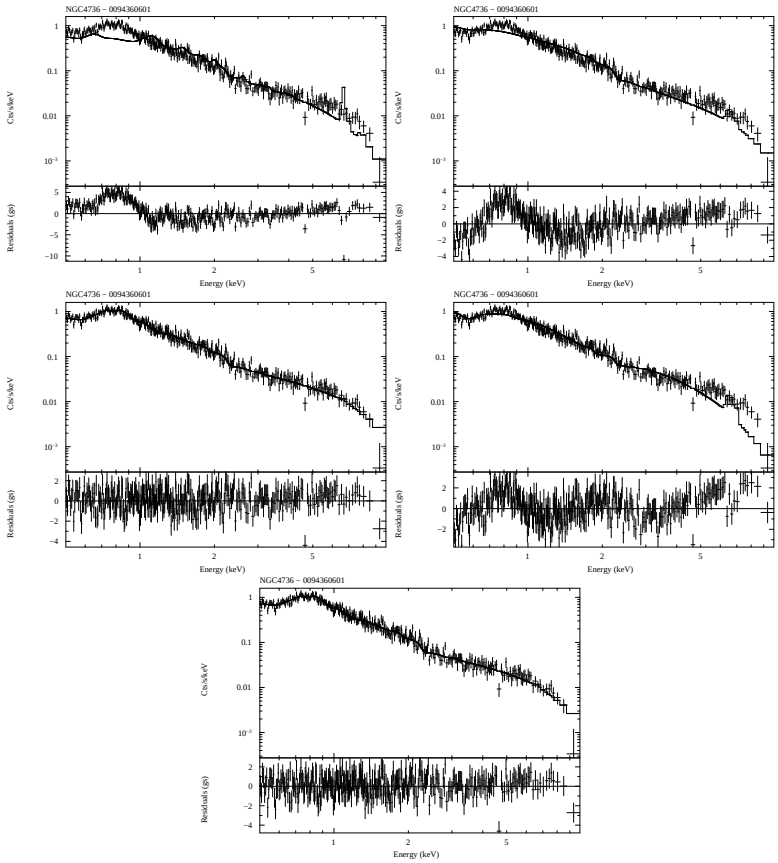

Figure E.28: *Spectral fits of NGC4736. (Top-left): Thermal model (MEKAL), (Top-right): Power-law model, (Center-left): Power-law plus thermal model, (Center-right): Two power-law model, (Bottom): Two power-law plus thermal model.*

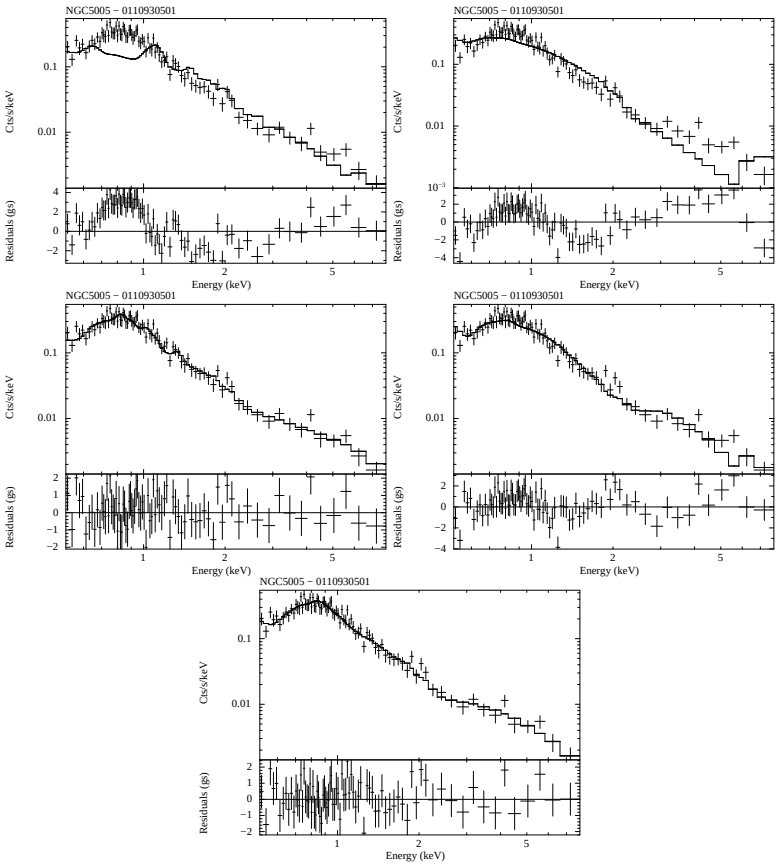

Figure E.29: *Spectral fits of NGC5005. (Top-left): Thermal model (MEKAL), (Top-right): Power-law model, (Center-left): Power-law plus thermal model, (Center-right): Two power-law model, (Bottom): Two power-law plus thermal model.*

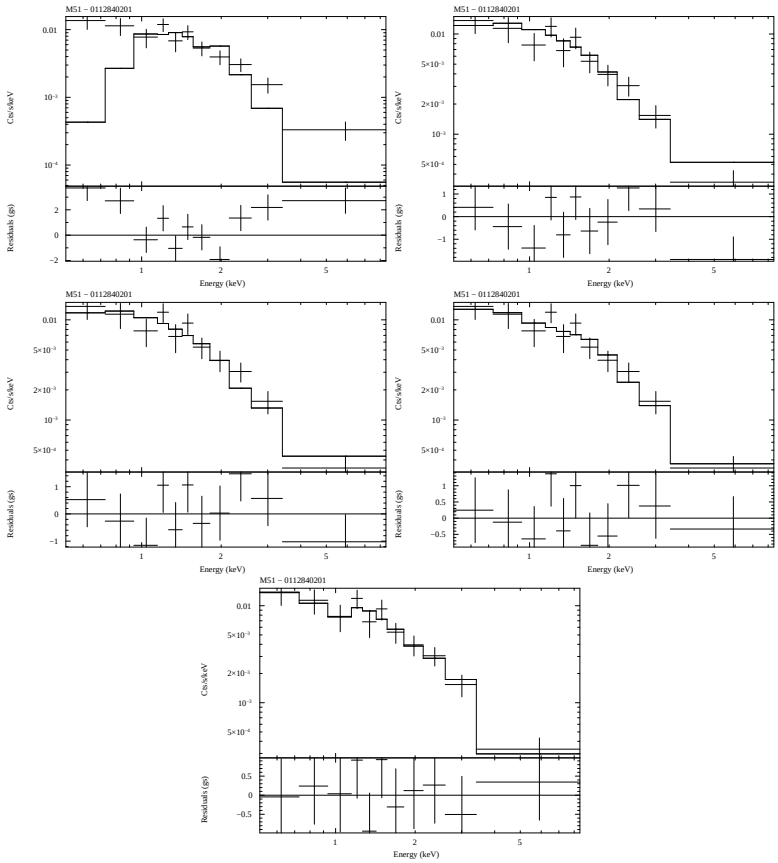

Figure E.30: *Spectral fits of NGC5194. (Top-left): Thermal model (MEKAL), (Top-right): Power-law model, (Center-left): Power-law plus thermal model, (Center-right): Two power-law model, (Bottom): Two power-law plus thermal model.*

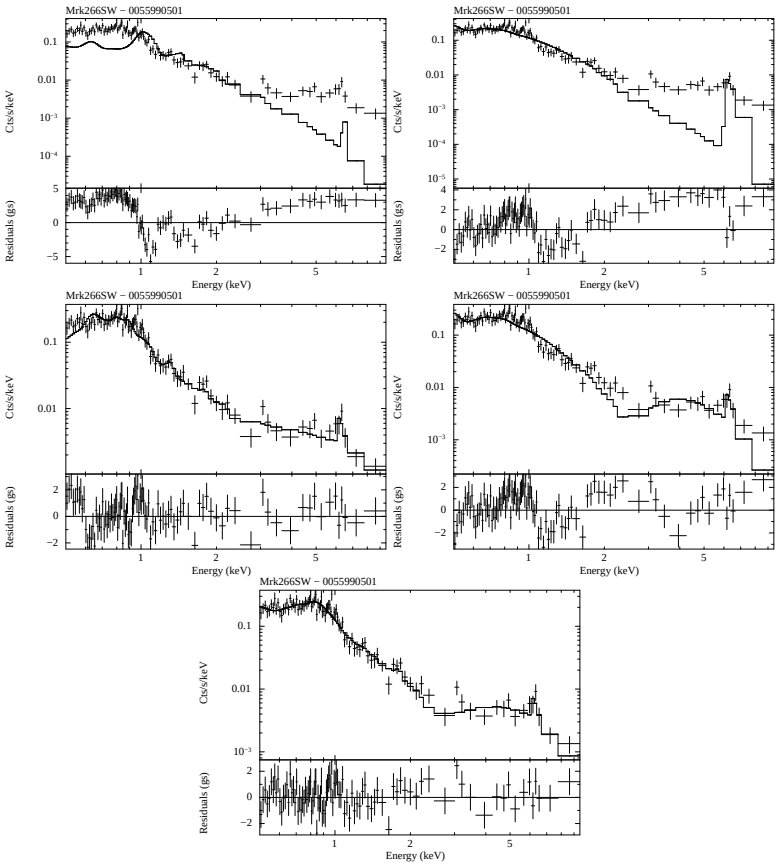

Figure E.31: *Spectral fits of Mrk266SW. (Top-left): Thermal model (MEKAL), (Top-right): Power-law model, (Center-left): Power-law plus thermal model, (Center-right): Two power-law model, (Bottom): Two power-law plus thermal model.*

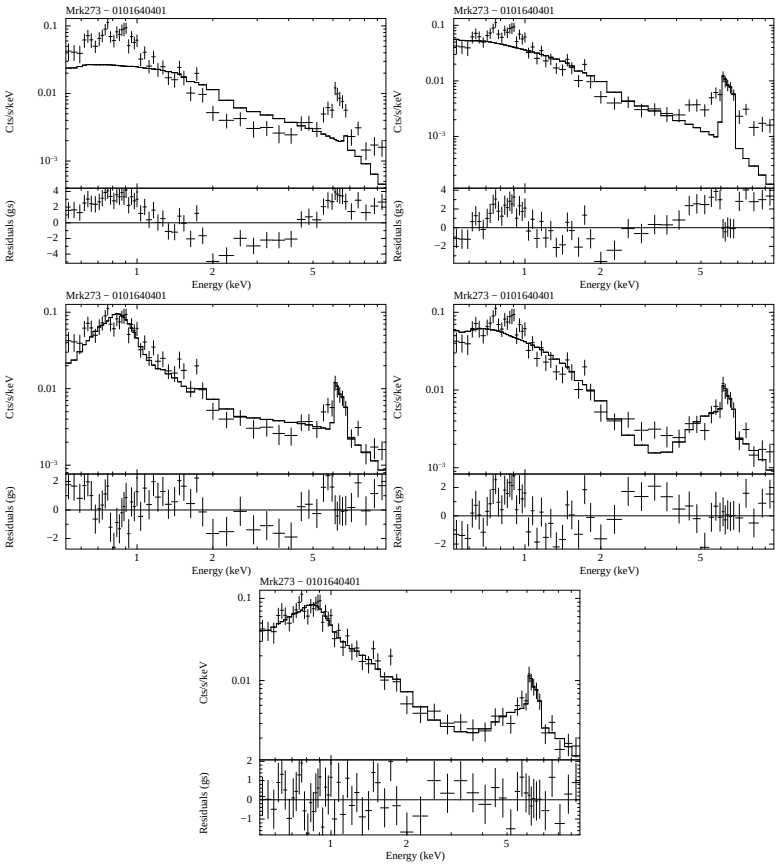

Figure E.32: *Spectral fits of UGC08696. (Top-left): Thermal model (MEKAL), (Top-right): Power-law model, (Center-left): Power-law plus thermal model, (Center-right): Two power-law model, (Bottom): Two power-law plus thermal model.*

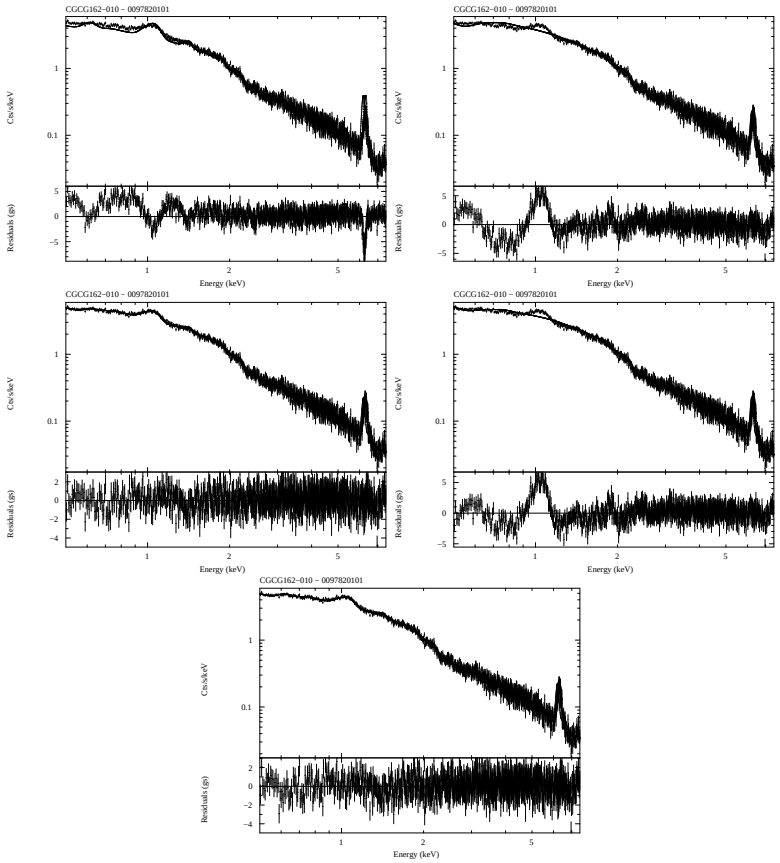

Figure E.33: *Spectral fits of CGCG162-010. (Top-left): Thermal model (MEKAL), (Top-right): Power-law model, (Center-left): Power-law plus thermal model, (Center-right): Two power-law model, (Bottom): Two power-law plus thermal model.*

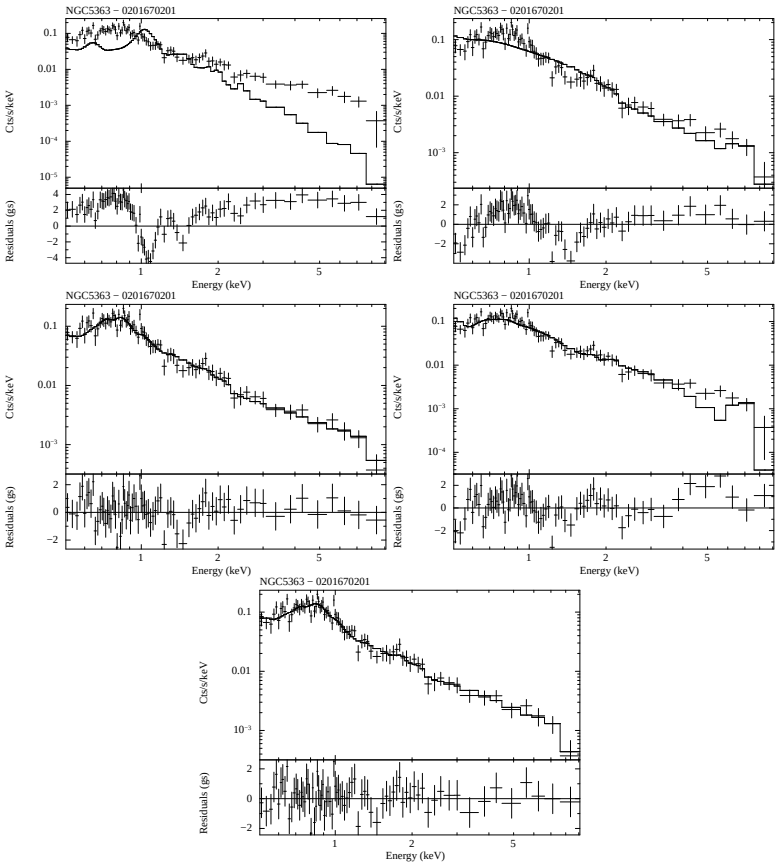

Figure E.34: *Spectral fits of NGC5363. (Top-left): Thermal model (MEKAL), (Top-right): Power-law model, (Center-left): Power-law plus thermal model, (Center-right): Two power-law model, (Bottom): Two power-law plus thermal model.*

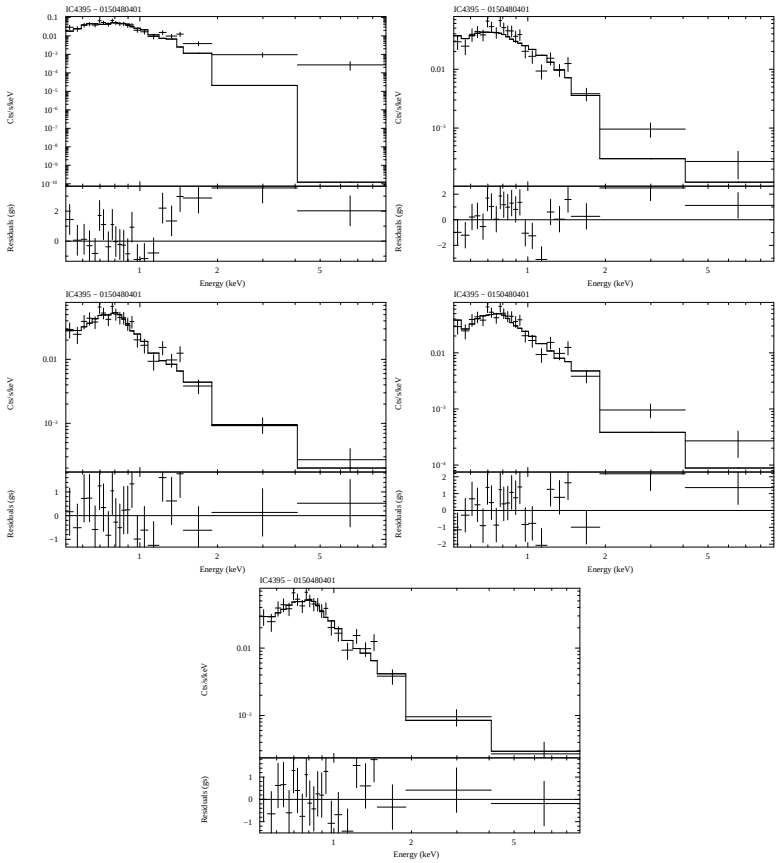

Figure E.35: *Spectral fits of IC4395. (Top-left): Thermal model (MEKAL), (Top-right): Power-law model, (Center-left): Power-law plus thermal model, (Center-right): Two power-law model, (Bottom): Two power-law plus thermal model.*

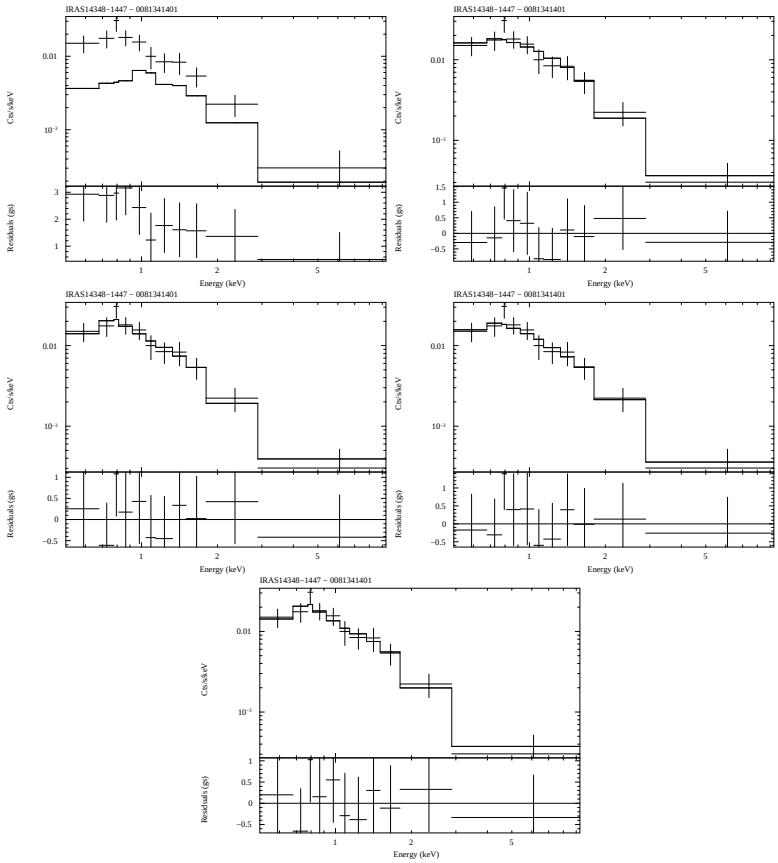

Figure E.36: *Spectral fits of IRAS14348-1447. (Top-left): Thermal model (MEKAL), (Top-right): Power-law model, (Center-left): Power-law plus thermal model, (Center-right): Two power-law model, (Bottom): Two power-law plus thermal model.*

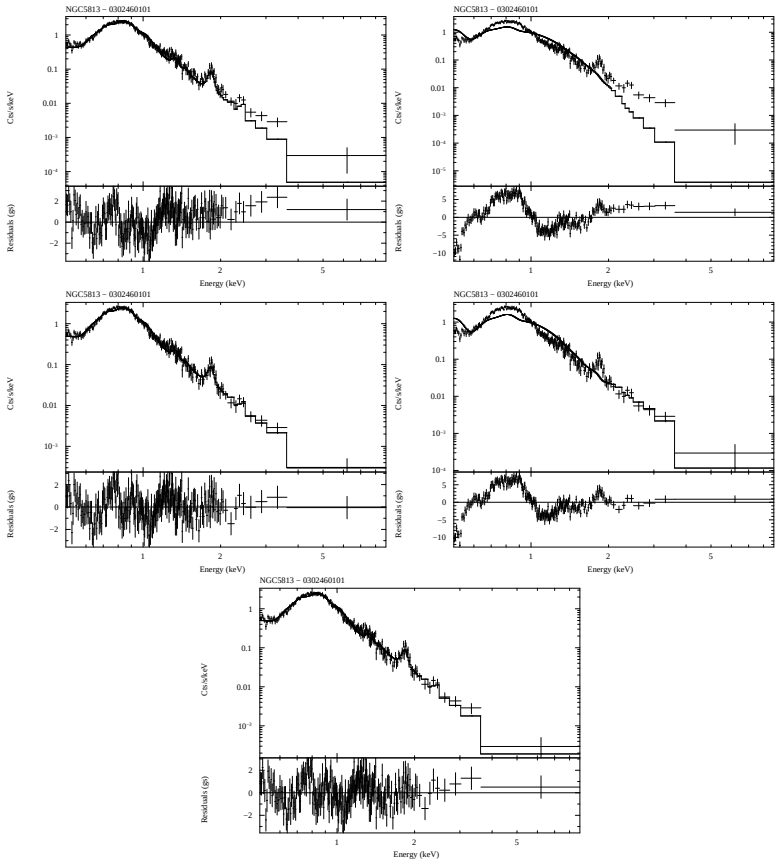

Figure E.37: *Spectral fits of NGC5813. (Top-left): Thermal model (MEKAL), (Top-right): Power-law model, (Center-left): Power-law plus thermal model, (Center-right): Two power-law model, (Bottom): Two power-law plus thermal model.*

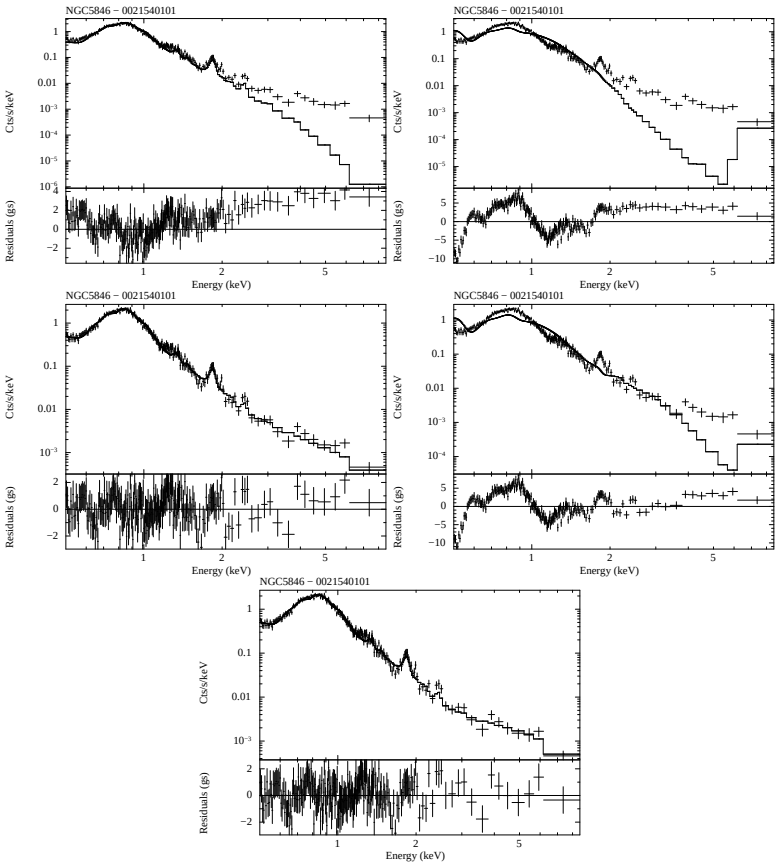

Figure E.38: *Spectral fits of NGC5846. (Top-left): Thermal model (MEKAL), (Top-right): Power-law model, (Center-left): Power-law plus thermal model, (Center-right): Two power-law model, (Bottom): Two power-law plus thermal model.*

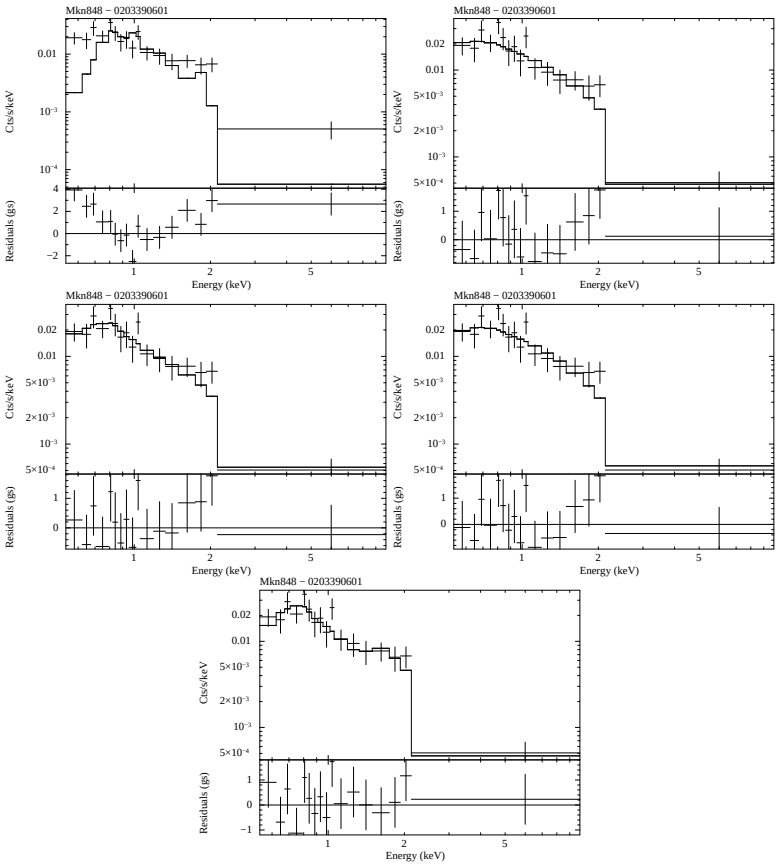

Figure E.39: *Spectral fits of Mkn848. (Top-left): Thermal model (MEKAL), (Top-right): Power-law model, (Center-left): Power-law plus thermal model, (Center-right): Two power-law model, (Bottom): Two power-law plus thermal model.*

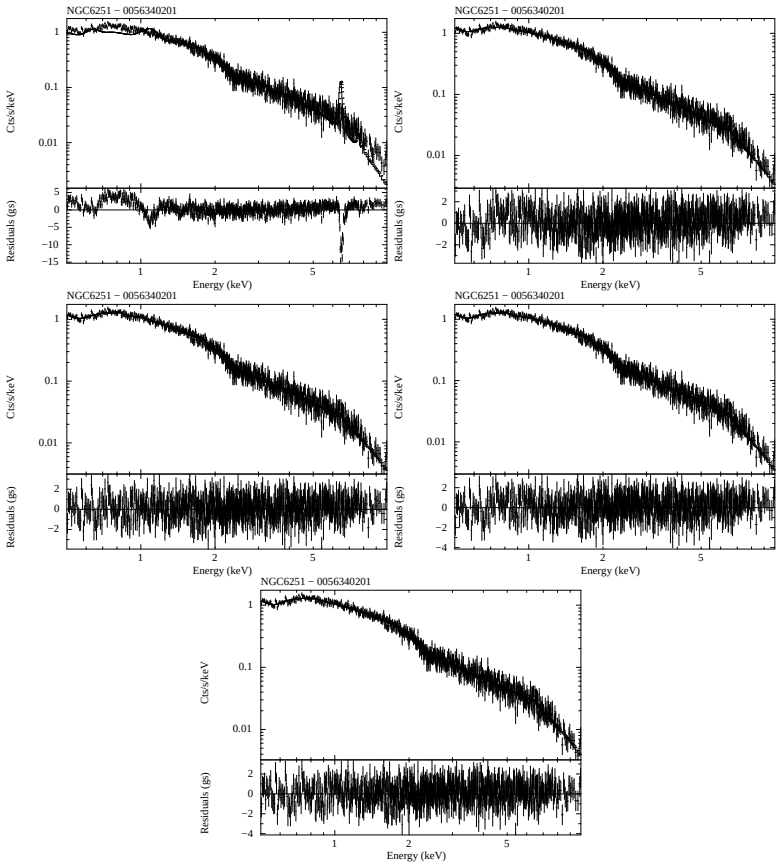

Figure E.40: *Spectral fits of NGC6251. (Top-left): Thermal model (MEKAL), (Top-right): Power-law model, (Center-left): Power-law plus thermal model, (Center-right): Two power-law model, (Bottom): Two power-law plus thermal model.*

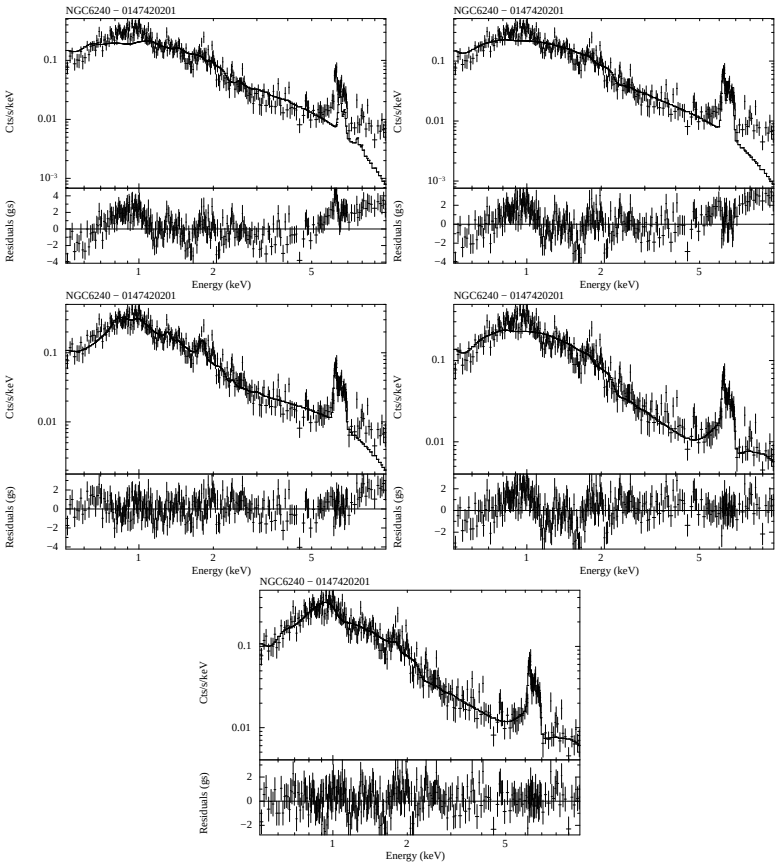

Figure E.41: *Spectral fits of NGC6240. (Top-left): Thermal model (MEKAL), (Top-right): Power-law model, (Center-left): Power-law plus thermal model, (Center-right): Two power-law model, (Bottom): Two power-law plus thermal model.*

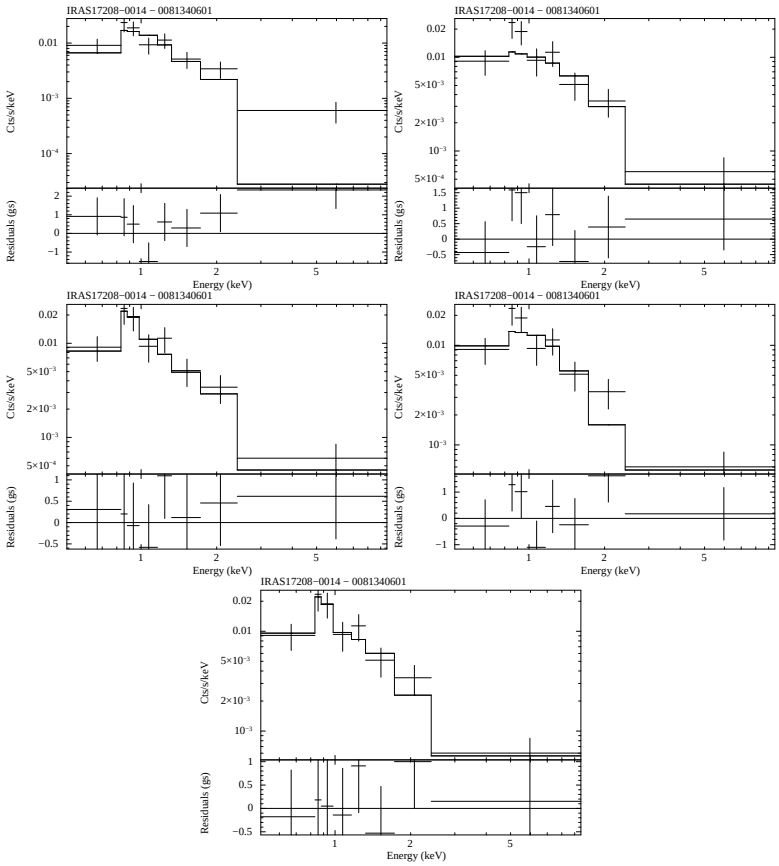

Figure E.42: *Spectral fits of IRAS17208-0014. (Top-left): Thermal model (MEKAL), (Top-right): Power-law model, (Center-left): Power-law plus thermal model, (Center-right): Two power-law model, (Bottom): Two power-law plus thermal model.*

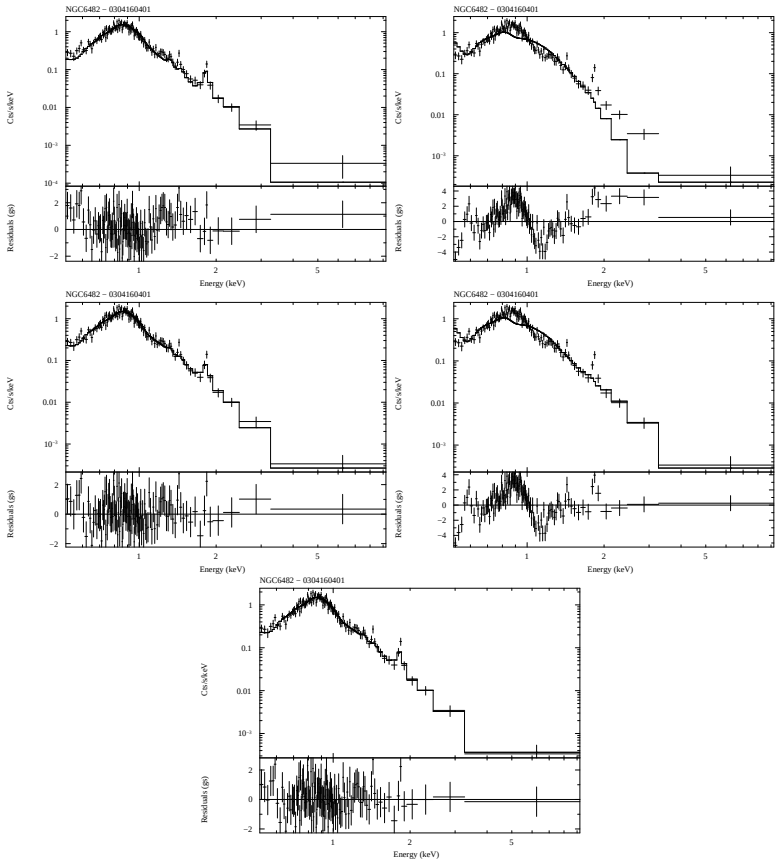

Figure E.43: *Spectral fits of NGC6482. (Top-left): Thermal model (MEKAL), (Top-right): Power-law model, (Center-left): Power-law plus thermal model, (Center-right): Two power-law model, (Bottom): Two power-law plus thermal model.*

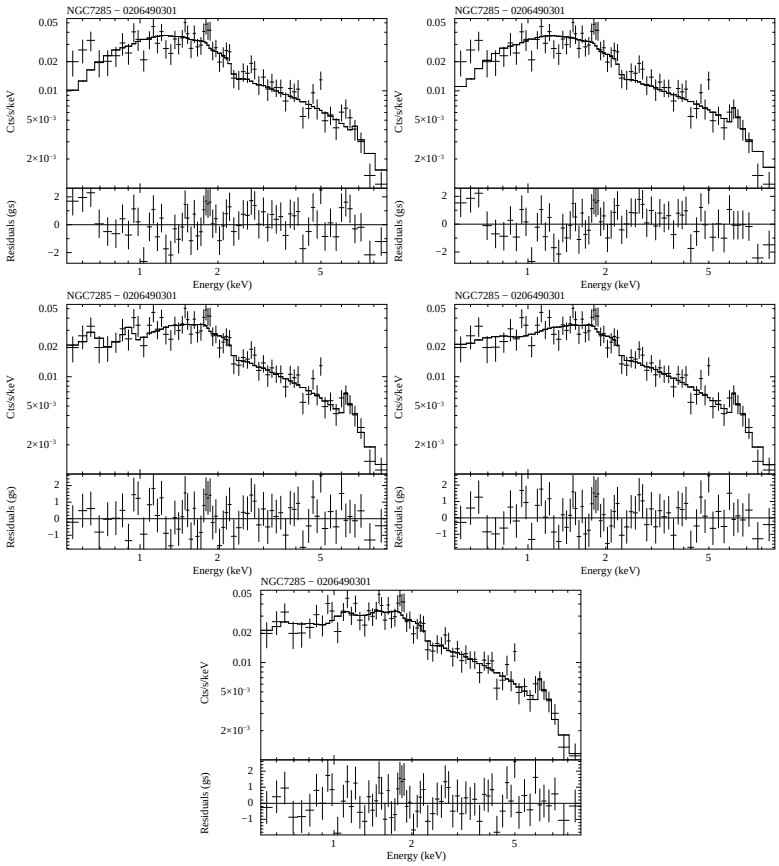

Figure E.44: *Spectral fits of NGC7285. (Top-left): Thermal model (MEKAL), (Top-right): Power-law model, (Center-left): Power-law plus thermal model, (Center-right): Two power-law model, (Bottom): Two power-law plus thermal model.*

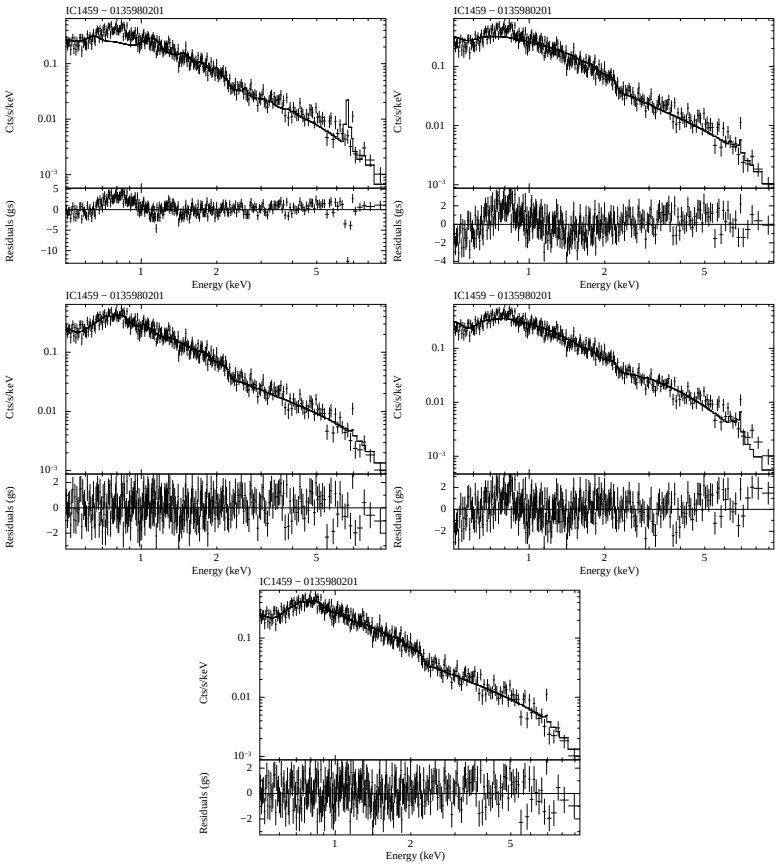

Figure E.45: *Spectral fits of IC1459. (Top-left): Thermal model (MEKAL), (Top-right): Power-law model, (Center-left): Power-law plus thermal model, (Center-right): Two power-law model, (Bottom): Two power-law plus thermal model.*

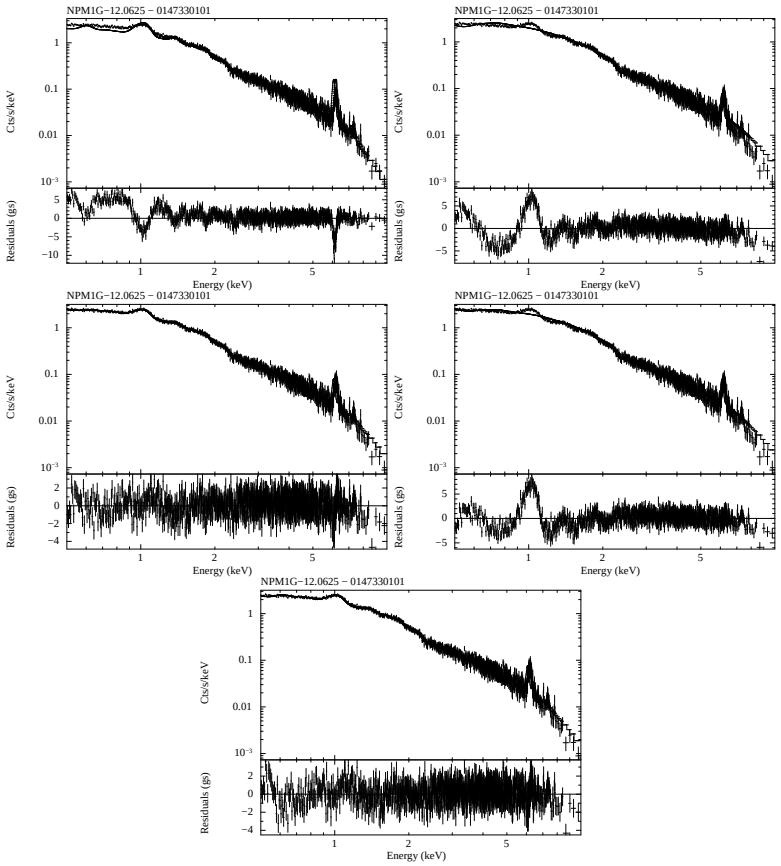

Figure E.46: *Spectral fits of NPM1G-12.0625. (Top-left): Thermal model (MEKAL), (Top-right): Power-law model, (Center-left): Power-law plus thermal model, (Center-right): Two power-law model, (Bottom): Two power-law plus thermal model.*

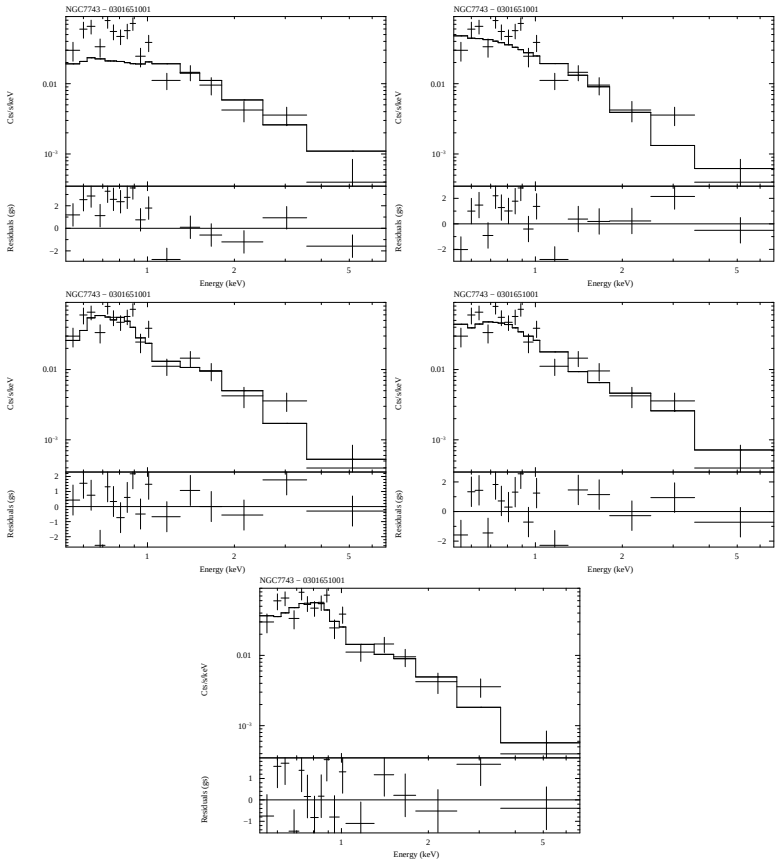

Figure E.47: *Spectral fits of NGC7743. (Top-left): Thermal model (MEKAL), (Top-right): Power-law model, (Center-left): Power-law plus thermal model, (Center-right): Two power-law model, (Bottom): Two power-law plus thermal model.*

Appendix F

DSS images of LINERs in 150 kpc-side boxes

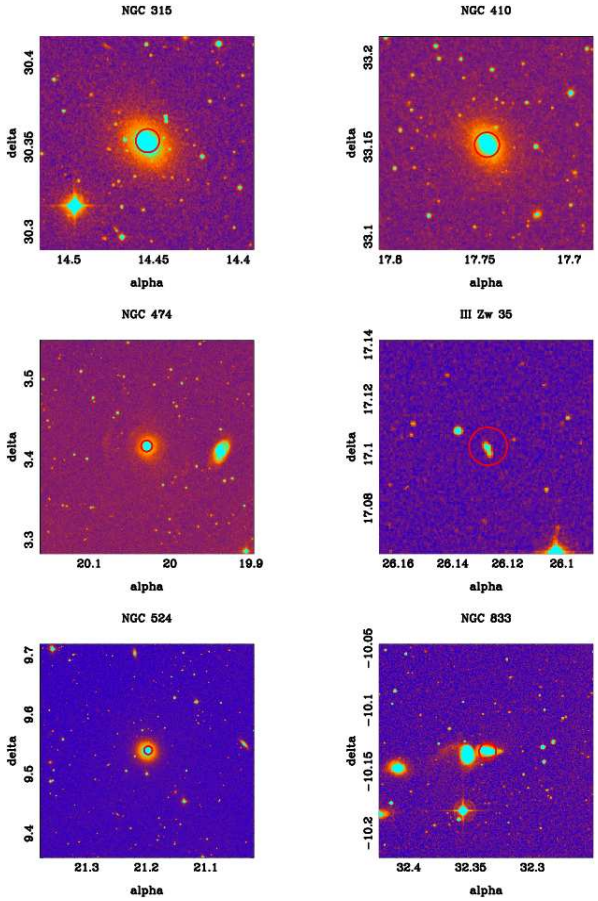

Figure F.1: *Images from the Digital Sky Survey showing boxes of 150 kpc on a side, based on distances provided in Tab. 3.1. The red circle indicates de 25″ extraction region for* XMM-Newton *spectra. Galaxies with label numbers from 1 to 6.*

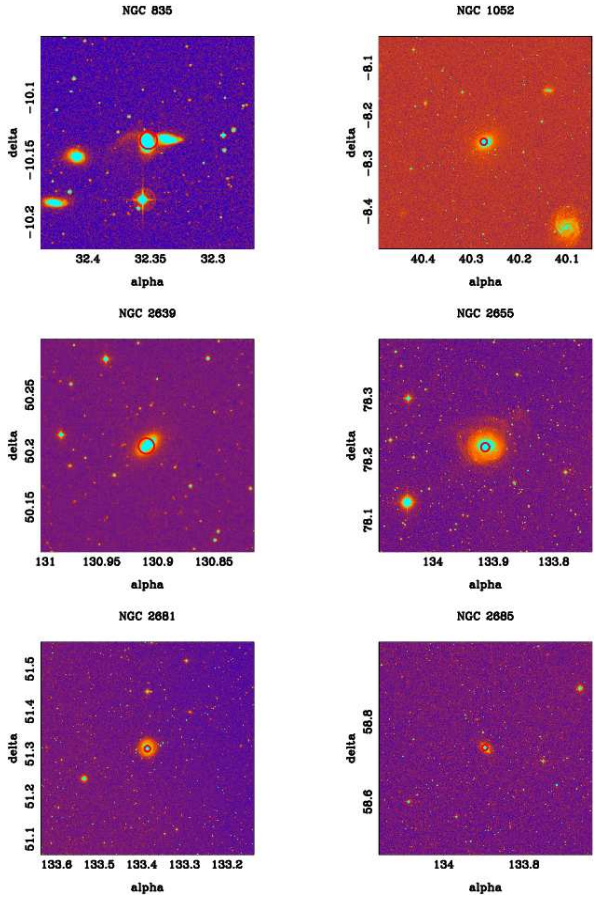

Figure F.2: *Same as F.1 but for galaxies with label numbers from 7 to 12*

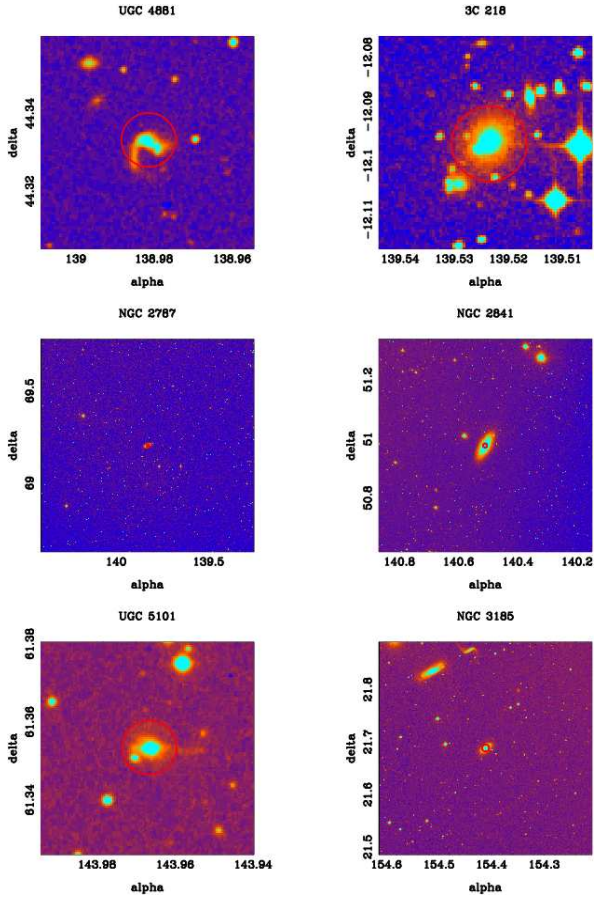

Figure F.3: *Same as F.1 but for galaxies with label numbers from 13 to 18*

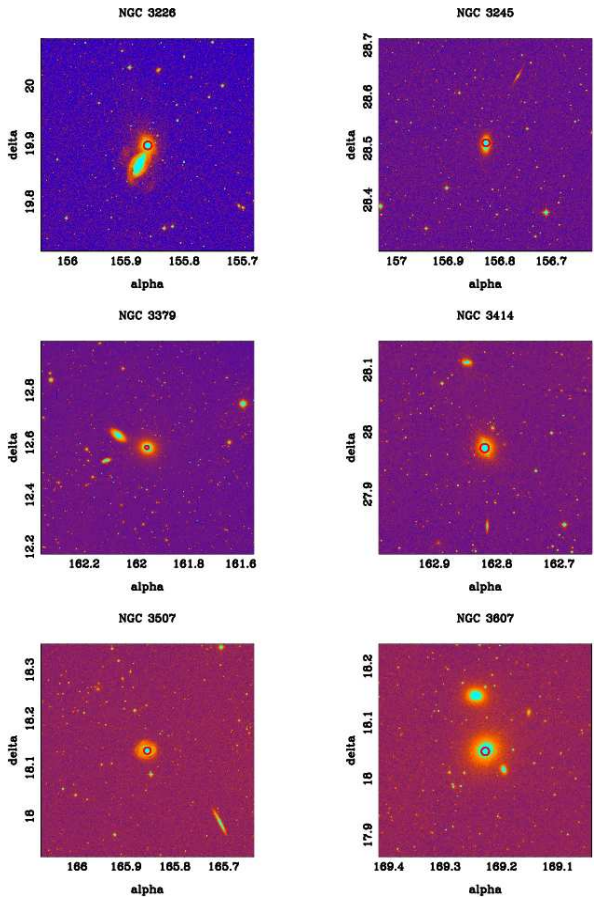

Figure F.4: *Same as F.1 but for galaxies with label numbers from 19 to 24*

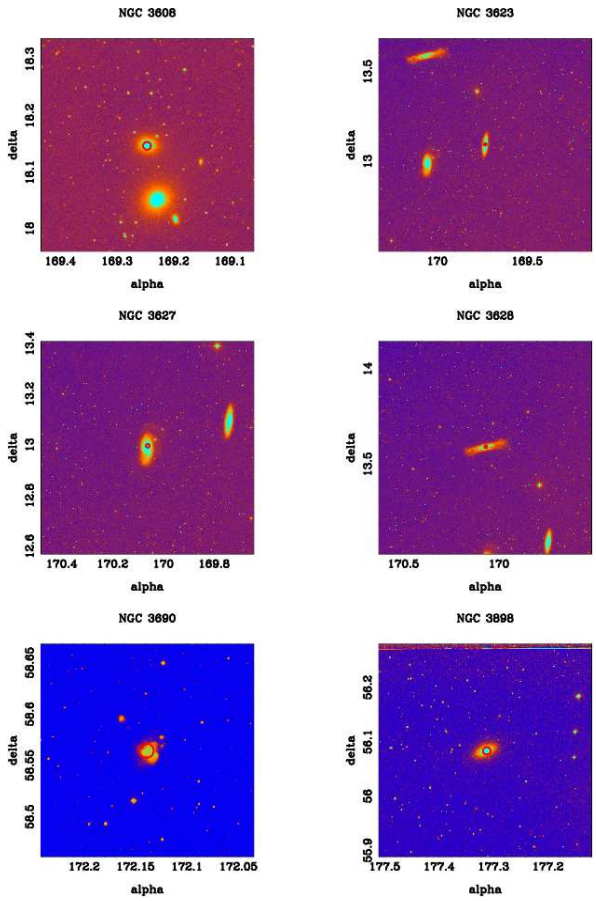

Figure F.5: *Same as F.1 but for galaxies with label numbers from 25 to 30*

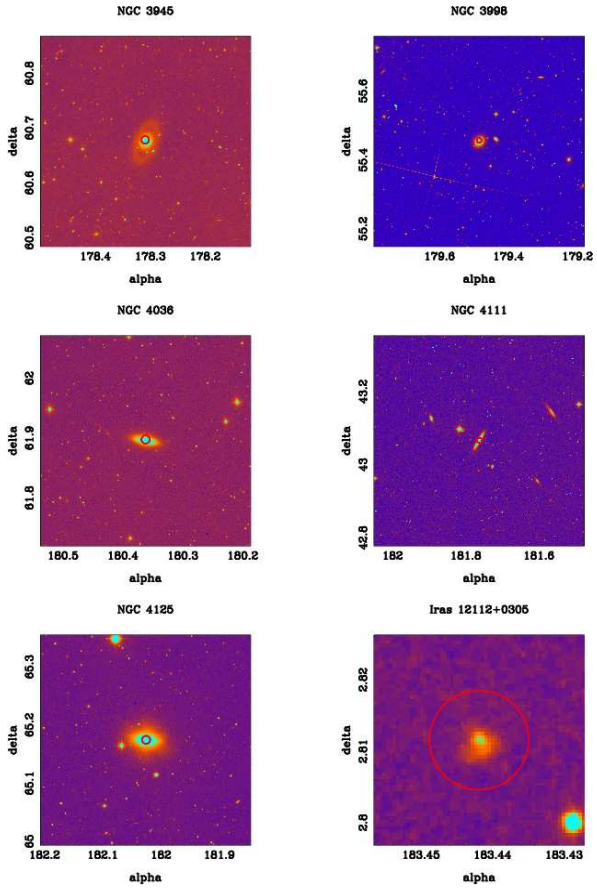

Figure F.6: *Same as F.1 but for galaxies with label numbers from 31 to 36*

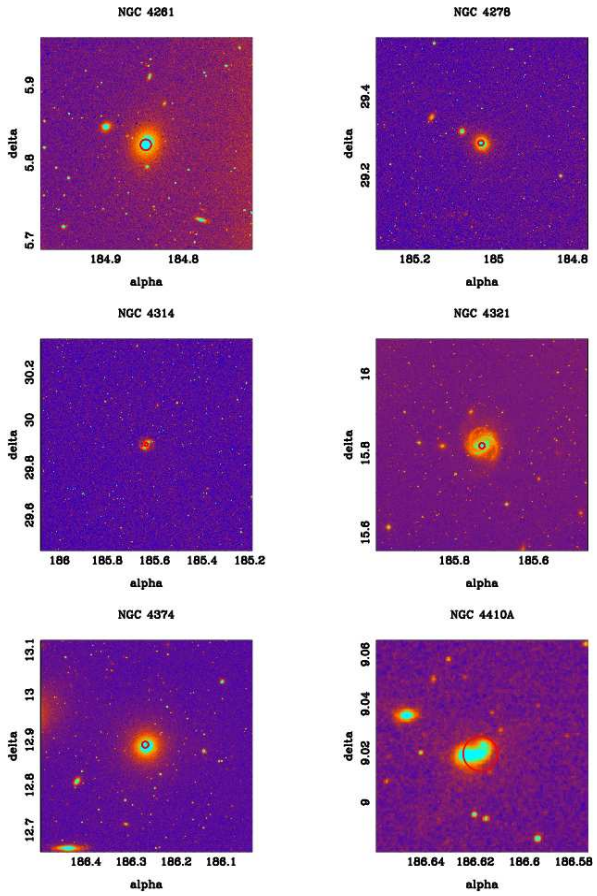

Figure F.7: *Same as F.1 but for galaxies with label numbers from 37 to 42*

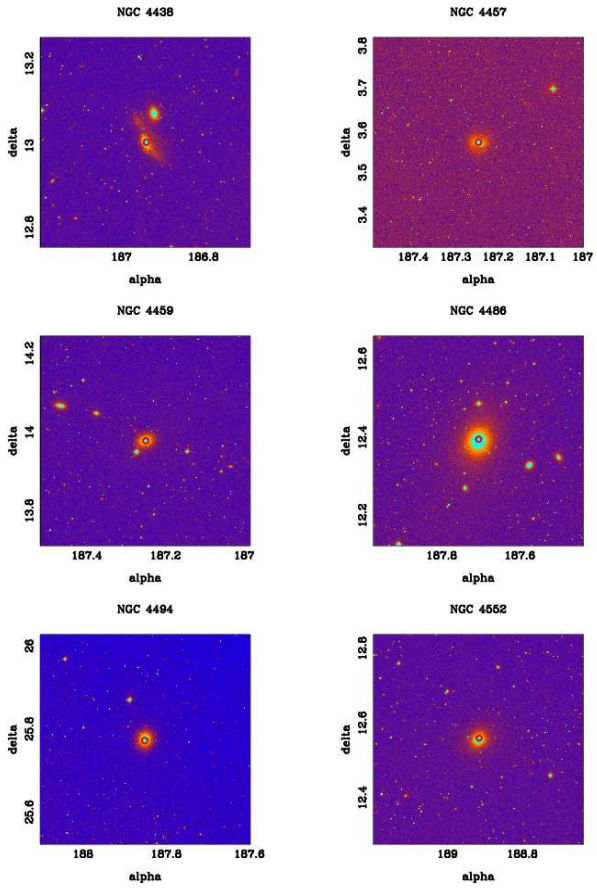

Figure F.8: *Same as F.1 but for galaxies with label numbers from 43 to 48*

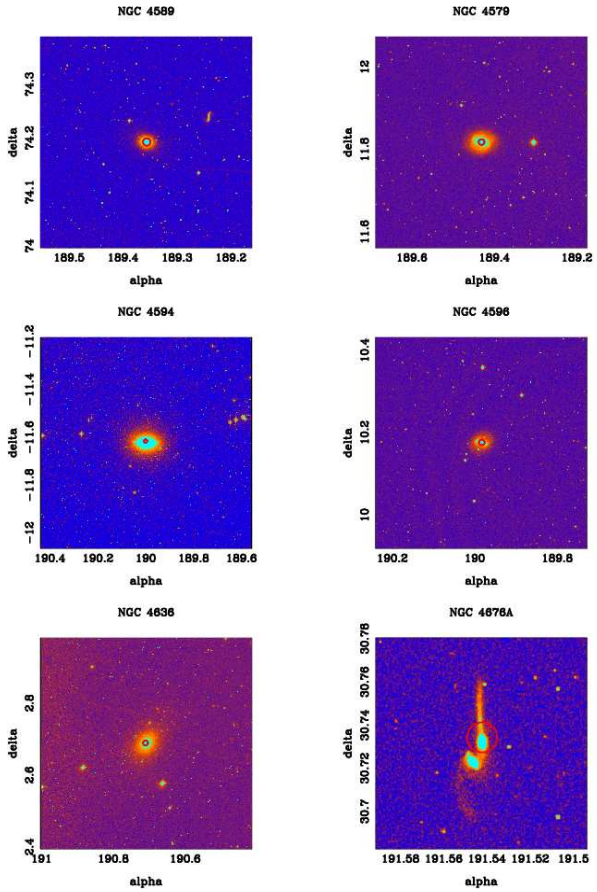

Figure F.9: *Same as F.1 but for galaxies with label numbers from 49 to 54*

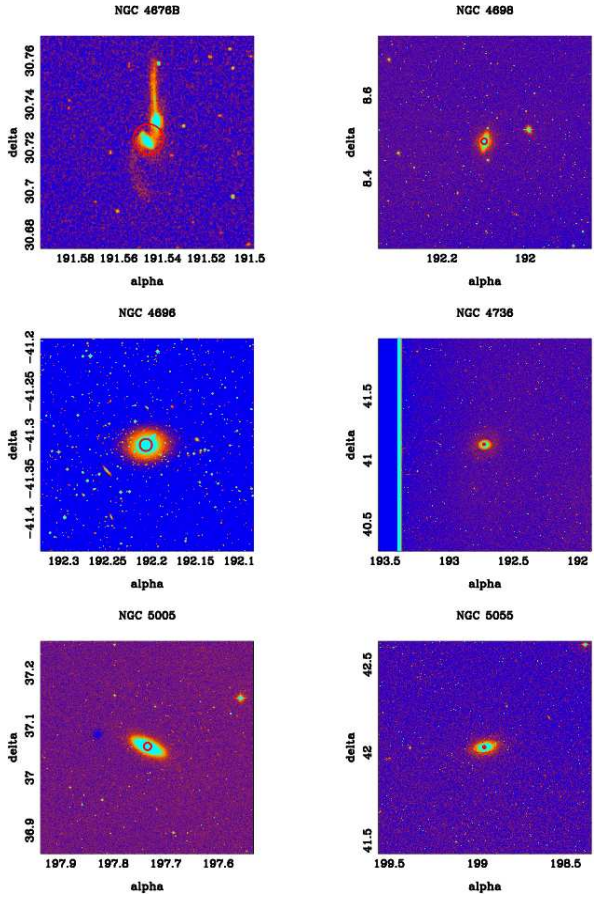

Figure F.10: *Same as F.1 but for galaxies with label numbers from 55 to 60*

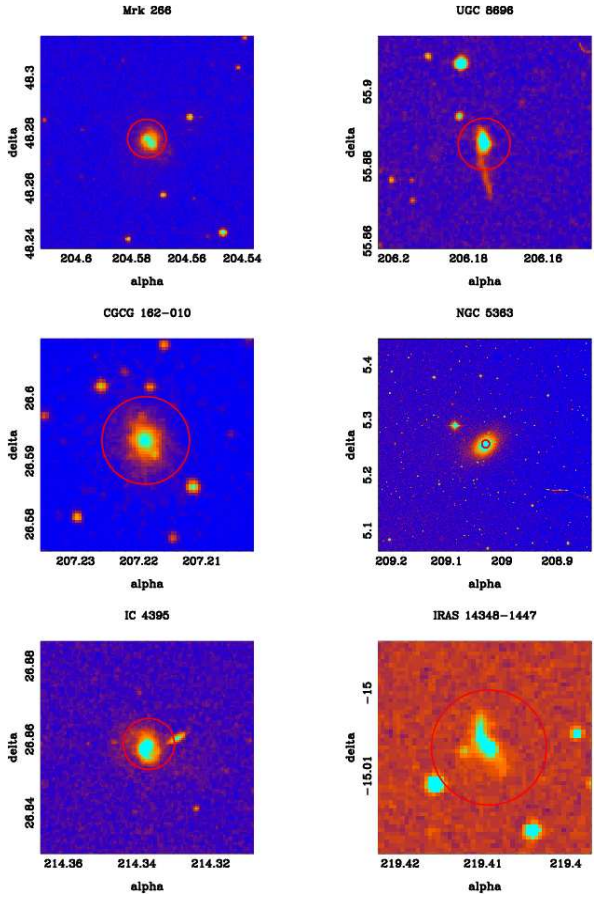

Figure F.11: *Same as F.1 but for galaxies with label numbers from 61 to 66*

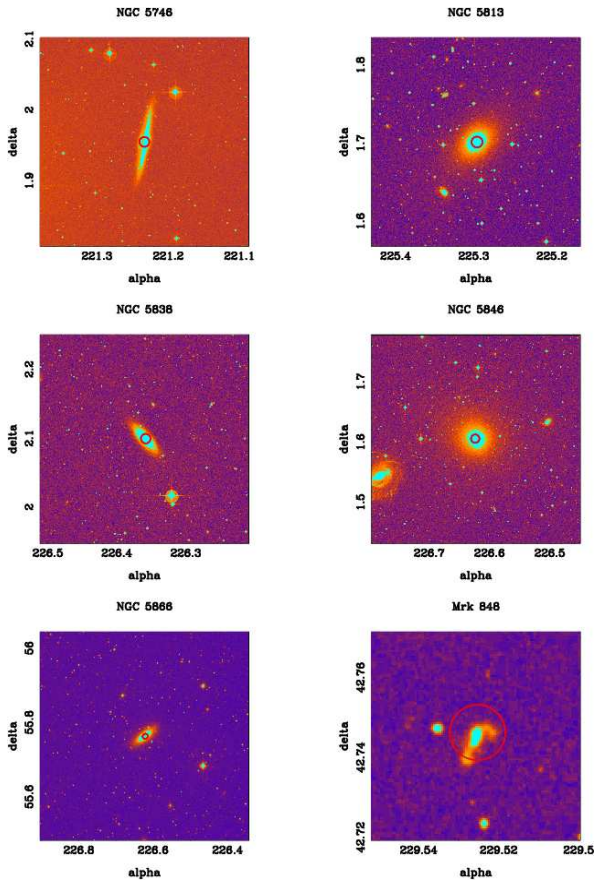

Figure F.12: *Same as F.1 but for galaxies with label numbers from 67 to 72*

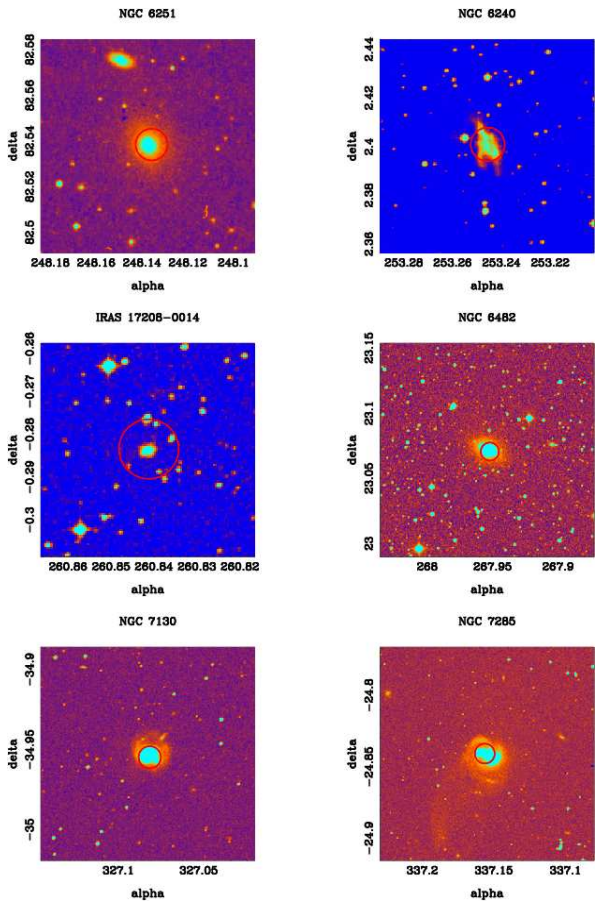

Figure F.13: *Same as F.1 but for galaxies with label numbers from 73 to 78*

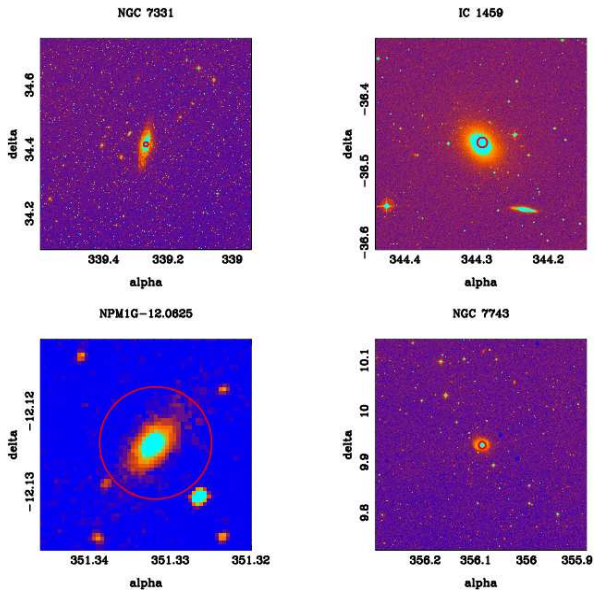

Figure F.14: *Same as F.1 but for galaxies with label numbers from 79 to 82*